Global Analysis of Predicted and Observed Dynamic Topography

Fred D. Richards

A dissertation submitted for the degree of
Doctor of Philosophy
at the University of Cambridge

Jesus College
May 2018

Global Analysis of Predicted and Observed Dynamic Topography

Fred D. Richards

While the bulk of topography on Earth is generated and maintained by variations in the thickness and density of crust and lithosphere, a significant time-variable contribution is expected as a result of convective flow in the underlying mantle. For over three decades, this dynamic topography has been calculated numerically from inferred density structure and radial viscosity profiles. Resulting models predict ± 2 km of long wavelength (i.e., $\sim 20{,}000$ km) dynamic topography with minor contributions at wavelengths shorter than $\sim 5{,}000$ km. Recently, observational studies have revealed that, at the longest wavelengths, dynamic topography variation is $\sim 30\%$ that predicted, with ± 1 km amplitudes recovered at shorter wavelengths. Here, the existing database of water-loaded basement depths is streamlined, revised and augmented. By fitting increasingly sophisticated thermal models to a combined database of these oceanic basement depths and corrected heat flow measurements, the average thermal structure of oceanic lithosphere is constrained. Significantly, optimal models are consistent with invariable geochemical and seismological constraints whilst yielding similar values of mantle potential temperature and plate thickness, irrespective of whether heat flow, subsidence or both are fit. After recalculating residual depth anomalies relative to optimal age-depth subsidence and combining them with continental constraints from gravity anomalies, a global spherical harmonic representation is generated. Although, long wavelength dynamic topography increases by $\sim 40\%$ in the revised observation-based model, spectral analysis confirms that a fundamental discrepancy between observations and predictions remains. Significantly, residual depth anomalies reveal a $\sim 4{,}000$ km-scale eastward tilt across the Indian Peninsula. This asymmetry extends onshore from the high-elevation Western Ghats in the west to the Krishna-Godavari floodplains in the east. Calibrated inverse modelling of drainage networks suggest that the tilt of the peninsula grew principally in Neogene times with vertical motions linked to asthenospheric temperature anomalies. Uplift rates of up to 0.1 mm a^{-1} place important constraints on the spatio-temporal evolution of dynamic topography and suggest that rates of transient vertical motion exceed those predicted by many modelling studies. Most numerical models excise the upper ~ 300 km of Earth's mantle and are unable to reconstruct the wavelength and rate of uplift observed across Peninsular India. By contrast, through conversion of upper mantle shear wave velocities to density using a calibrated anelastic parameterisation, it is shown that shorter wavelength (i.e., $\leqslant 5{,}000$ km) dynamic topography, can mostly be explained by $\pm 150°$C asthenospheric temperature anomalies. Inclusion of anelastically corrected density structure in whole-mantle instantaneous flow models also serves to reduce discrepancy between predictions and observations of dynamic topography at long wavelengths. Residual mismatch between observations and predictions is further improved if the basal 300–600 km of large low shear wave velocity regions in the deep mantle are geochemically distinct and negatively buoyant. Finally, inverse modelling of geoid, dynamic topography, gravity and core-mantle boundary topography observations using adapted density structure suggests that geodynamic constraints can be acceptably fit using plausible radial viscosity profiles, contradicting a long-standing assertion that modest long wavelength dynamic topography is incompatible with geoid observations.

Publications arising from this dissertation

Parts of Chapter 2 and 3 are based on:

Richards F. D., M. J. Hoggard, L. R. Cowton & N. J. White (2018), Reassessing Thermal Relationships between Basement Depth, Heat Flow and Age within the Oceanic Realm, *Journal of Geophysical Research: Solid Earth*, under review.

Part of Chapter 4 is based on:

Richards F. D., M. J. Hoggard & N. J. White (2016), Cenozoic Epeirogeny of the Indian Peninsula. *Geochemistry, Geophysics, Geosystems*, Vol. 17, 4920-4954.

Declaration

This dissertation describes my original work except where acknowledgement is made in the text. It does not exceed the page limit and is not substantially the same as any work that has been, or is being submitted to any other university for any degree, diploma or any other qualification.

<div align="right">

Fred D. Richards

May 2018

</div>

Per me si va ne la città dolente,
per me si va ne l'etterno dolore,
per me si va tra la perduta gente.
Giustizia mosse il mio alto fattore:
fecemi la divina potestate,
la somma sapienza e 'l primo amore.
Dinanzi a me non fuor cose create
se non etterne, e io etterno duro.
Lasciate ogni speranza, voi ch'entrate

Inferno Canto III
La Divina Commedia
Dante Alighieri

Acknowledgements

I would first like to thank the many wonderful people who have contributed to my work, well-being and scientific development throughout the last four years. Huge thanks go to Nicky White for his direction and help in structuring my thoughts. Special thanks go to Mark Hoggard who has been both a mentor and a friend, no one else has had such a profound influence on my science and it has been a real pleasure to work on so many projects together. I am very grateful to Sia Ghelichkani and Lorenzo Colli who have been great collaborators, their expertise in the more mathematically challenging areas of this project has been enormously helpful. Harriet Lau has also been a great help throughout and I must thank her for sharing her tidal tomography models. Closer to home, I have really enjoyed working with Laurence Cowton, Marthe Klöcking, Simon Stephenson, Paddy Ball and Fergus McNab. I am also very grateful for the scientific guidance and friendship of a number of excellent people that have graced the Drum during my time in Cambridge: Jacqueline Austermann, Alex Dickinson, Kathy Gunn, Conor O'Malley, Ross Parnell-Turner and Verónica Rodríguez-Tribaldos.

Paul Bellingham and Ken McDermott at ION Geophysical, Neil Hodgson at Spectrum Geo and Alex Bump at BP deserve a special mention for providing access to various seismic datasets. It has also been a pleasure to meet and interact with Richard Corfield, Mark Ireland and Alistair Crosby amongst many others.

Special thanks go to my academic friends John Rudge and Alex Copley for their support throughout my Ph.D. Conversations with David Al-Attar, Sanne Cottaar, Keith Priestley and Dan McKenzie have also been hugely influential and helpful throughout the past four years.

I would like to thank my girlfriend Isabel Reid without whom I would have lost my sanity long before completing this piece of work. Her encouragement to take the odd break from writing, stellar cooking and general concern about my overwhelmingly pork-based diet have been invaluable in keeping me going. I must also thank my parents for their constant support and encouragement throughout my doctoral studies.

Finally, I would like to heartily thank Sarah Riley-Smith, who allowed me to lodge with her for rather longer than she had originally expected. I will miss her generosity, hospitality and our long discussions on everything from politics to art history. Caroline and Charles Kingdon have also been fantastic hosts for the last few months of my Ph.D and I thank them for allowing me to defile their fridge on occasion with Co-op ready meals.

Contents

List of Figures

List of Tables

Notation table

Notation	Parameter	Dimensions
A	Seafloor area	m^2
A'	Upstream drainage area	m^2
A_B	Background stress relaxation amplitude	dimensionless
A_η	Viscosity reduction factor	dimensionless
A_P	Peak stress relaxation amplitude	dimensionless
α	Thermal expansivity	K^{-1}
α_B	Background stress relaxation gradient	dimensionless
α_f	Flexural parameter	km
b	Boundary radius	km
B_r	Reference strain rate	s^{-1}
δb	Boundary dynamic topography	km
β	Poroelastic coefficient	dimensionless
C	Core-mantle boundary topography	km
$C_{2,0}$	Core-mantle boundary excess ellipticity	m
C_c	Crustal loading correction	km
C_p	Specific heat capacity	J kg^{-1} K^{-1}
C_s	Sediment loading correction	km
γ	Viscosity reduction factor	dimensionless
d	Grain size	mm
d_r	Reference grain size	1 mm
D	Flexural rigidity	N m
E	Erosion rate	m Ma^{-1}
E_a	Activation energy	kJ mol^{-1}
E_Y	Young's modulus	N m^{-2}
$\dot{\epsilon}$	Strain rate	s^{-1}
F	Fractional disturbance of heat flow	dimensionless
f	Frequency	Hz
f'	Time-normalised frequency	Hz
f_{lm}	Expansion coefficient	dimensionless
f_M	Maxwell frequency	Hz
g	Gravitational acceleration	m s^{-2}
G	Anisotropy coefficient	dimensionless
G	Gravitational constant	6.67$\times$ 10 $^{-11}$ m^3 kg^{-1} s^{-2}
γ_r	Reference gravitational acceleration at surface	9.8196 m s^{-2}
Δg	Gravity anomaly	mGal
h	Channel thickness	km
H	Heat flow	W m^{-2}
H_1	Oceanic plate V_S misfit	dimensionless

Continued overleaf...

Notation	Parameter	Dimensions
H_2	Adiabatic V_S misfit	dimensionless
H_3	Nodule V_S misfit	dimensionless
H_4	Attenuation misfit	dimensionless
H_5	Viscosity misfit	dimensionless
H_a	Activation enthalpy	J mol^{-1}
H_w	Weighted misfit	dimensionless
η	Viscosity	Pas
η^*	Viscosity contrast	Pas
η_r	Reference viscosity	Pas
η_l	Lithospheric viscosity	Pas
$\eta_l m$	Lower mantle viscosity	Pas
$\eta_u m$	Upper mantle viscosity	Pas
$\eta_t z$	Transition zone viscosity	Pas
θ	Co-latitude	$^{\circ}$
J	Cost function	dimensionless
J^*	Complex compliance	GPa^{-1}
J_1	Storage compliance	GPa^{-1}
J_2	Loss compliance	GPa^{-1}
k	Thermal conductivity	W m^{-1} K^{-1}
k_{lat}	Lattice thermal conductivity	W m^{-1} K^{-1}
k_{rad}	Radiative thermal conductivity	W m^{-1} K^{-1}
K	Bulk modulus	GPa
K_l^C	Core-mantle boundary topography kernel	dimensionless
$K_l^{\Delta g}$	Gravity anomaly kernel	dimensionless
K_l^N	Geoid kernel	dimensionless
K_l^S	Dynamic topography kernel	dimensionless
K_l^Z	Dynamic admittance kernel	dimensionless
κ	Thermal diffusivity	m^2 s^{-1}
κ_e	Erosional diffusivity	m^2 Ma^{-1}
l	Spherical harmonic degree	dimensionless
l_{max}	Maximum spherical harmonic degree	dimensionless
L_r	River length	m
λ	Wavelength	km
λ'	Longitude	$^{\circ}$
λ_1	Gradient damping parameter	km^{-2}
λ_2	Norm damping parameter	km^{-2}
λ_c	Compaction decay length scale	km
λ_S	Spatial smoothing parameter	dimensionless
λ_T	Temporal smoothing parameter	dimensionless
λ_η	Viscosity smoothing parameter	dimensionless
$\lambda\phi$	Melt viscosity coefficient	dimensionless

Notation	Parameter	Dimensions
m	Spherical harmonic order	dimensionless
m'	Concavity index	dimensionless
m_d	Grain size exponent	dimensionless
M_b	Body wave magnitude	dimensionless
M_C	Core-mantle boundary excess ellipticity misfit	dimensionless
$M_{\Delta g}$	Free-air gravity anomaly misfit	dimensionless
M_N	Geoid misfit	dimensionless
M_S	Dynamic topography misfit	dimensionless
μ	Shear modulus	GPa
μ_U	Unrelaxed shear modulus	GPa
μ_U^0	Surface unrelaxed shear modulus	GPa
n	Number of samples	dimensionless
n'	Concavity index	dimensionless
N	Geoid anomaly	m
Na_8	Na_2O concentration per 8 wt. % MgO	dimensionless
ν	Poisson's ratio	dimensionless
p	Asymptotic significance	dimensionless
P	Pressure	Pa
P_0	Surface pressure	GPa
$P_{bounded}$	Bounded parameter	variable
$P_{internal}$	Internally varied parameter	variable
P_l	Spectral power	km^2
P_{max}	Maximum parameter value	variable
P_{min}	Minimum parameter value	variable
P_r	Reference pressure	GPa
P_{tz-lm}	Transition zone-lower mantle penalty function	dimensionless
P_{um-tz}	Upper mantle-transition zone penalty function	dimensionless
ϕ	Fractional porosity of sediment	dimensionless
$\phi_\circ$	Initial porosity of sediment	dimensionless
ϕ_L	Lithosphere-asthenosphere boundary temperature coefficient	dimensionless
φ	Latitude	$^\circ$
Q	Cumulative oceanic heat flow	TW
Q_s	Total amount of rock eroded	km
Q^{-1}	Attenuation	dimensionless
Q_S^{-1}	Shear wave attenuation	dimensionless
r	Pearson correlation coefficient	dimensionless
r'	Radius	km
$r_{\Delta g}$	Free-air gravity anomaly correlation	dimensionless
r_N	Geoid correlation	dimensionless
r_S	Dynamic topography correlation	dimensionless
R	Gas constant	8.314 J mol^{-1} K^{-1}

Notation	Parameter	Dimensions
$R_\oplus$	Earth radius	6371 km
R_1	Model roughness	dimensionless
R_C	Core-mantle boundary radius	3480 km
R_ρ	Shear wave velocity-density conversion factor	dimensionless
ρ	Density	Mg m^{-3}
$\rho_\circ$	Mantle density at 0° C	Mg m^{-3}
$\overline{\rho_c}$	Mean density of oceanic crust	Mg m^{-3}
ρ_a	Asthenospheric mantle density	Mg m^{-3}
ρ_b	Density at compensation depth	Mg m^{-3}
ρ_{cu}	Upper crustal density	Mg m^{-3}
ρ_m	Mantle density	Mg m^{-3}
ρ_r	Reference density	Mg m^{-3}
ρ_s	Infilling sediment density	Mg m^{-3}
$\overline{\rho_s}$	Bulk sediment density	Mg m^{-3}
ρ_{sg}	Solid grain density	Mg m^{-3}
ρ_w	Water density	Mg m^{-3}
$\Delta\rho_a$	Density contrast between mantle and water	Mg m^{-3}
S	Sedimentation rate	m s^{-1}
$\mathbb{S}^2$	Unit two sphere	dimensionless
σ	Standard deviation or error	variable
σ_a	Asperity stress	MPa
σ_p	Peierl's stress	MPa
σ_P	Width of stress relaxation peak	dimensionless
t	Time	s
t_c	Two-way travel time crustal thickness	s
t_s	Two-way travel time sediment thickness	s
Δt	Finite difference timestep	s
t	Time	s
T	Temperature	$^\circ$C
T'	Homologous temperature	dimensionless
$T_\circ$	Background asthenospheric temperature	$^\circ$C
T_0	Surface temperature	$^\circ$C
T_e	Elastic thickness	km
T_L	Critical isotherm defining lithospheric thickness	$^\circ$C
T_p	Mantle potential temperature	$^\circ$C
T_r	Reference temperature	$^\circ$C
T_s	Solidus temperature	$^\circ$C
T_η	Critical homologous temperature	dimensionless
ΔT	Temperature anomaly	$^\circ$C
τ_G	Landscape response time	Ma
τ_M	Normalised Maxwell period	s

Notation	Parameter	Dimensions
τ_P'	Peak stress relaxation timescale	s
τ_S	Shear wave period	s
τ_S'	Normalised shear wave period	s
$\tau_{r'r'}$	Radial normal stress	Pa
U	Uplift rate	m Ma^{-1}
ΔU	Gravitational potential anomaly	m^2 s^{-2}
$\overline{v_c}$	Acoustic velocity of oceanic crust	km s^{-1}
v	Advective coefficient of erosion	m$^{1-2m'}$ Ma^{-1}
v_{sg}	Acoustic velocity of solid grains	km s^{-1}
v_w	Acoustic velocity of water	km s^{-1}
V_a	Activation volume	mm^3 mol^{-1}

Chapter 1

Introduction

The bulk of Earth's surface topography is maintained by thickness and density variations within the mechanically strong crust and lithosphere (Airy, 1855; Pratt, 1855). This isostatic component of topography explains the development of high elevation mountain belts in response to crustal thickening and subsidence of the seafloor away from ocean ridges as the lithosphere cools and densifies. However, it has long been recognised that not all topography seems to obey the principles of isostasy. For example, sections of the Mid-Atlantic Ridge either side of Iceland are elevated close to sea-level, ~ 2 km above the isostatically expected value of ~ 2.5 km (White & McKenzie, 1989). By contrast, the mid-ocean ridge overlying the Australian-Antarctic Discordance lies in ~ 4 km of water, ~ 1.5 km deeper than expected. These ± 2 km anomalies have long been attributed to the changing pattern of convective circulation within the underlying mantle (Menard, 1973; McKenzie, 1977). Even before the first satellite observations of Earth's gravity and topography, Pekeris (1935) demonstrated that, assuming the Earth's interior is convecting, normal stresses arising from mantle flow will deflect the Earth's surface. The lithosphere is elevated above buoyant, upwelling regions, whilst sinking, positive density anomalies draw the Earth's surface down (Griggs, 1939). The spatio-temporal evolution of this dynamic topography therefore places useful constraints on the internal viscosity and density structure of the convecting mantle.

In the decades following these initial advances, improvements in satellite observations, development of seismic tomographic techniques, increases in computing power, theoretical advances and experimental insights have combined to greatly expand understanding of convection within the Earth (Runcorn, 1965; Dziewonski & Anderson, 1984). The Earth's characteristic Rayleigh number is estimated to be $\sim 10^8$, suggesting that the mantle convects vigorously on geological timescales (Turcotte & Schubert, 2002). In this context, the planform of mantle convection will constantly change with time and both computational and analogue models of mantle convection predict a diverse range of features and patterns. These features includes upwelling sheets, small-scale convective rolls and localised plumes that may extend from the core-mantle boundary to the surface

---

or originate from internal boundaries within the upper mantle (McKenzie *et al.*, 1973; Yuen *et al.*, 1994; Davies, 1992; van Hunen *et al.*, 2003; Davies & Davies, 2009). As a result, dynamic topography is expected to be ubiquitous, have a complex surface expression and be preserved in the geological record.

With the development of the first seismic tomography models of Earth's mantle it became possible to link internal wave speed anomalies to mantle density heterogeneity (Dziewonski & Anderson, 1984). Using this input density structure alongside estimates of viscosity from glacial isostatic adjustment studies, Hager *et al.* (1985) modelled instantaneous mantle flow to make the first global prediction of present-day dynamic topography. Since this pioneering study, as computational techniques and constraint on internal density structure have improved, increasingly complex predictive models have been developed (e.g. Ricard *et al.*, 1993; Bunge *et al.*, 2003). Despite these significant advances, dynamic topography predictions have changed relatively little: all outputs are dominated by degree two structure (i.e. wavelengths of $\sim 20,000$ km; Flament *et al.*, 2013).

By contrast, understanding of mantle convection from an observational perspective has, historically, been limited by a dearth of relevant observational data, owing largely to poor constraint on isostatic topography. The protracted tectonic histories of continents, and associated density structure complexity, complicates analysis of continental isostasy. However, oceanic lithosphere is both thinner and less chemically heterogeneous, simplifying assessment of its isostatic state. If well constrained corrections can be made for seafloor subsidence as a function of age, sedimentary loading and anomalous crustal thickness, the resulting 'residual depth anomalies' can be used to infer the pattern of present-day dynamic topography. Thanks largely to the proliferation of high-resolution seismic reflection images collected by the hydrocarbon industry, it has recently become possible to make accurate oceanic residual depth measurements throughout the global ocean (Winterbourne *et al.*, 2009; Hoggard *et al.*, 2017). The residual depth dataset places important observational constraint on present-day dynamic topography and differs from geodynamic predictions in two important respects. First, at the longest wavelengths (i.e. $\sim 20,000$ km) recovered amplitudes are approximately one order of magnitude smaller than observations, although the spatial pattern of dynamic topography is similar. Secondly, the observational field contains significantly greater short-wavelength ($\lambda \leqslant 5,000$ km) signal. This mismatch suggests that predictive models have some fundamental shortcomings which require addressing before they can be applied to the study of past dynamic topography. Furthermore, the more rapid evolution of dynamic topography indicated by substantial short-wavelength dynamic topography variation has important implications

for our understanding of eustatic sea-level records, landscape development and Earth's viscosity structure. Temporal evolution of dynamic topography is difficult to observe due to incompleteness of the geological record, sparsity of palaeo-elevation markers and convolution of dynamic signals with vertical motions from other sources. However, detailed analysis of margin stratigraphy and landscape evolution can be used to extract past vertical motions and place important constraints on time-dependent convective support.

This dissertation has three key aims. First, provide the best possible constraint on present-day dynamic topography by augmenting an existing database of oceanic residual depths with new data and a more accurate lithospheric cooling model. This new dataset is turned into a globally continuous map and spectrally analysed. Secondly, place constraints on characteristic timescales over which dynamic topography evolves by analysing the Cenozoic uplift and denudation history of the Indian Peninsula. Finally, explore the large disagreement that exists between observations and predictions of dynamic topography, focusing initially on short-wavelength ($\lambda \leqslant 5,000$ km) and then longer-wavelength ($\lambda \sim 20,000$ km) discrepancies. A new predictive geodynamic model is developed with important implications for our understanding of Earth's internal density and viscosity structure.

1.1   Dissertation Structure

Chapter 2: Thermal Models of Oceanic Lithosphere

By assembling and fitting an updated database of water-loaded basement depths, in conjunction with a pre-existing oceanic heat flow compilation, a revised thermal model of the oceanic lithosphere is developed that yields equally good fit to both sets of measurements whilst honouring geochemical constraints of mantle potential temperature. Experimentally determined temperature, pressure and compositional dependence of mantle and crustal thermal parameters are shown to be essential in determining values of plate thickness, mantle potential temperature and zero-age ridge depth that yield good fit to both subsidence and heat flow data, in addition to seismological constraints on lithosphere-asthenosphere boundary depths. Finally, predicted plate cooling-derived gravity field is calculated for the optimal model and used to identify residual anomalies that may relate to sub-lithospheric processes.

Chapter 3: Global Residual Depth Measurements

Water-loaded oceanic basement depths are converted into a revised and augmented compila-

tion of oceanic residual depth anomalies using age-depth subsidence predicted by the optimal model obtained in Chapter 2. 123 new additions to the database fill important gaps in the pre-existing database and are examined within a regional context. The residual depth database is then combined with shiptrack bathymetry constraints and scaled long wavelength free-air gravity anomalies onshore to create a revised observation-based dynamic topography dataset. Finally, a globally continuous spherical harmonic representation of these observations is generated and compared to previously published estimates of dynamic topography.

Chapter 4: Dynamic Topography of India

The eastward tilt visible in the topography of the Indian Peninsula is shown to extend offshore into the oceanic realm, giving a total wavelength of $\sim 4{,}000$ km. The low elastic thickness of the region, obtained using admittance analysis, shows that this topography is not maintained by flexural loading alone. Calibrated joint inversion of 530 river profiles is undertaken to determine the spatio-temporal evolution of rock uplift over the peninsula, revealing that most of the present-day topography developed in Neogene times with uplift rates of up to 0.1 mm a^{-1}. Independent constraints from low-temperature thermochronology, sedimentary flux observations and sequence stratigraphic architecture along Indian margins corroborate fluvial incision and changes in base-level associated with the recovered uplift history. Flexural modelling demonstrates that $\sim 70\%$ of post-Deccan uplift across the Indian peninsula must arise from sub-plate sources. Geodynamic predictions derived from shear wave velocity tomography demonstrate that a west-east gradient in dynamic topography arising from $\sim \pm 100$ °C upper mantle temperature anomalies can explain present-day residual depth. Possible causes for implied late Cenozoic changes in mantle circulation beneath India are explored. Finally, the implications of rapid rates of dynamic uplift and subsidence observed across India are discussed in terms of global dynamic topography evolution.

Chapter 5: Asthenospheric Temperature Anomalies

Observations of global dynamic topography reveal significantly larger amplitudes at short wavelengths ($\lambda \leqslant 5{,}000$ km) than predicted by geodynamic models. The principal cause of this discrepancy is shown to be excision of the uppermost ~ 250 km of the mantle in many models. Shear wave velocity (V_S) anomalies in this asthenospheric layer, corrected for the effects of lithospheric cooling, show strong spatial anti-correlation with dynamic topography. To accurately assess the dynamic topography contribution of the asthenosphere, an accurate conversion between V_S, temperature and density anomalies is calibrated using an experimen-

tally derived anelasticity model that predicts temperatures consistent with independent geochemical constraints. Inclusion of these $150 \pm 50\ ^\circ\text{C}$ asthenospheric temperature anomalies in geodynamic predictions yields significantly improved fit to observations of short-wavelength dynamic topography.

Chapter 6: Reconciling Observations & Predictions of Dynamic Topography

Upper mantle V_S tomography models are combined with global models in the lower mantle to update geodynamic predictions of global dynamic topography from instantaneous flow calculations. Conversion of V_S into temperature using calibrated anelasticity models significantly reduces amplitude misfit between predicted and observed dynamic topography and geoid constraints. Presence of $\sim 1\%$ density anomalies in the basal portions of large low shear wave velocity provinces (LLSVPs) is shown to explain large misfits between dynamic topography and geoid at degree two ($\lambda \sim 20{,}000$ km). Full reconciliation of observations and predictions of dynamic topography, geoid, gravity and CMB topography is achieved by simultaneously inverting dynamic topography and geoid constraints to optimise the radial viscosity profile of the Earth.

Chapter 7: Conclusions and Further Work

Chapter 2

Thermal Models of Oceanic Lithosphere

The observed subsidence and heat flow of oceanic seafloor as a function of age places significant constraints upon the thermal evolution of lithospheric plates (Turcotte & Oxburgh, 1967; McKenzie, 1967). By combining an understanding of this behaviour with the depth distribution of intraplate earthquakes, it is possible to make inferences about the rheological properties of oceanic lithosphere, which affect the way in which rigid plates transmit elastic stresses and bend under loads (Watts & Zhong, 2000; McKenzie *et al.*, 2005; Craig *et al.*, 2014). This thermal structure also plays a primary role in the generation of anisotropic fabrics and the pooling of melts at the lithosphere-asthenosphere boundary (Turcotte & Schubert, 2002; Burgos *et al.*, 2014; Stern *et al.*, 2015). Finally, a quantitative understanding of plate behaviour through time enables accurate residual depth anomalies to be isolated that relate to other geological processes such as mantle convection and flexure. Measurements of oceanic residual depth anomalies play a key role in helping to estimate spatial patterns of dynamic topography, which in turn enables the viscosity and density structure of the upper and lower mantle to be constrained (Hager *et al.*, 1985).

In the 1970s, regional and sometimes global compilations of age-depth and heat flow observations were used to build simple models of the cooling of oceanic lithosphere (Lister, 1972; Parsons & Sclater, 1977). Two principal models were proposed: a half-space model, in which the lithospheric plate cools and thickens indefinitely as a function of age, and a plate model, in which the lithospheric plate also cools and thickens but approaches a finite thickness that is controlled by convective resupply of basal heat, probably related to the growth of a Rayleigh-Taylor instability at the base of the plate (Parsons & McKenzie, 1978; Yuen & Fleitout, 1985; Davaille & Jaupart, 1994; Huang & Zhong, 2005). Both models are based upon solutions of the heat flow equation for purely vertical conduction, with different boundary conditions. A half-space model involves conductive cooling of a semi-infinite mantle half-space with fixed surface temperature along the upper boundary and the initial temperature with depth at the ridge axis (Turcotte & Oxburgh, 1969). For plate models, the principal difference is that temperature along a basal boundary is also fixed to mimic this resupply

of heat (McKenzie, 1967). These calculations yield the temperature distribution within oceanic lithosphere as a function of age.

Turcotte & Oxburgh (1967) used a simple half-space model to argue that age-depth observations from young lithosphere can be accounted for by cooling and thickening of an evolving plate. Parsons & Sclater (1977) extended age-depth observations for the North Pacific and North Atlantic oceans out to 160 Ma and concluded that these observations are better fitted using a plate, rather than a half-space model. Using a simple inverse approach, they obtained a plate thickness of 125 $\pm$ 10 km, a basal and axial temperature of 1350 $\pm$ 275°C, and a thermal expansion coefficient of 3.2 $\pm$ 1.1 $\times$ 10^{-5} K^{-1}. This plate model was broadly compatible with existing heat flow observations. Subsequently, Stein & Stein (1992) jointly inverted a revised compilation of age-depth and heat flow observations from the North Pacific and northwest Atlantic oceans to constrain their plate model. They favoured a thinner plate thickness of 95 km, an increased temperature of 1450°C, and a thermal expansion coefficient of 3.1 $\times$ 10^{-5} K^{-1}.

The analytical approach that underpins both of these modelling strategies ignores horizontal conduction of heat and radioactive heat generation, which is thought to be minor in oceanic lithosphere (McKenzie, 1967; Jaupart & Mareschal, 2007). The model also assumes that the thermal conductivity, k, the thermal expansion coefficient, α, and the heat capacity, C_P, of cooling peridotitic mantle are constant. McKenzie *et al.* (2005) showed that the thermal structure of a cooling plate can be calculated numerically using experimentally determined values of k, α and C_P that vary as a function of temperature. In addition, they argued that, if decompression melting yields an oceanic crustal thickness of $\sim$ 7 km, the potential temperature at which the plate forms can be fixed at 1315°C. In their revised plate model, which incorporates an axial melting zone, they match age-depth observations from the north Pacific Ocean (Parsons & Sclater, 1977) and selected heat flow observations (Sclater *et al.*, 1980). Their optimal model has a plate thickness of 106 km and a potential temperature of 1315°C. By including the temperature dependence of k, α and C_P, McKenzie *et al.* (2005) predicted that the seismogenic thickness of oceanic lithosphere approximately corresponds to the depth to the 600°C isotherm. More recently, increasingly sophisticated plate models that include lithostatic pressure, mineralogic phase transitions, and hydrothermal circulation within oceanic crust have been developed (Afonso *et al.*, 2007; Grose & Afonso, 2013; Korenaga & Korenaga, 2016; Schmeling *et al.*, 2017).

The purpose of revisiting this well-known problem is threefold. First, the merits of exploiting a revised and augmented global database of age-depth observations are outlined (Hoggard *et al.*, 2017).
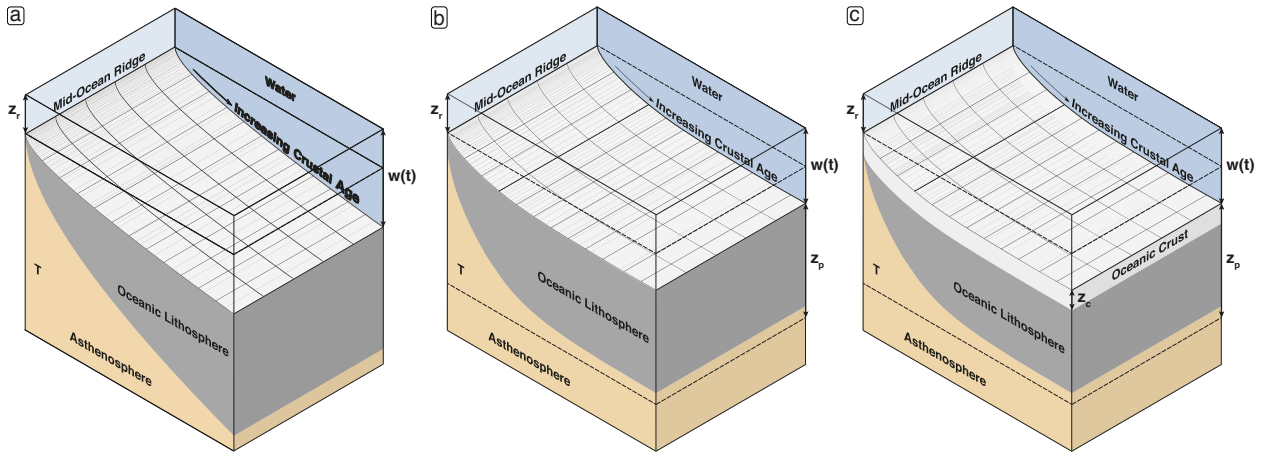
Figure 2.1: Schematic diagrams of models for the thermal cooling of oceanic lithosphere. (a) Half-space cooling model; $w(t)$ = water depth through time; z_r = water depth at the ridge axis; T = temperature at the ridge axis. (b) Simple plate cooling model; z_p = plate thickness; T = temperature at the ridge axis and basal boundary. (c) Complete plate cooling model; z_c = thickness of oceanic crustal layer; T = mantle potential temperature.

An important aim is to exploit this database in conjunction with a global inventory of revised heat flow measurements (Hasterok *et al.*, 2011). Secondly, both of these databases are jointly inverted using an increasingly sophisticated suite of models to constrain the thermal structure of oceanic lithosphere. The intention is to identify an optimal model that yields the best fit to combined age-depth and heat flow databases, whilst simultaneously honouring independent constraints on mantle potential temperature, seismologic observations and laboratory experiments on the thermal properties of olivine. Thirdly, the resulting thermal structure is used to examine rheological properties relating to the seismogenic thickness and depth of the lithosphere-asthenosphere boundary. Expected free-air gravity anomalies are also recalculated within the oceanic realm.

2.1   Assembly of Observational Databases

2.1.1   Age-Depth Measurements

An understanding of the thermal evolution of oceanic lithosphere depends upon the availability of a sufficiently accurate and comprehensive database of age-depth measurements. Water-loaded depth to the top of oceanic basement can be accurately determined provided that the thickness and density of both the overlying sedimentary pile and oceanic crust are known. It is also important to exclude regions of the oceanic floor where flexural bending occurs (e.g. trenches, seamounts, plateaux). In the original age-depth compilations used by Parsons & Sclater (1977) and by Stein

& Stein (1992), observations were principally extracted from abundant ship-track records of the North Pacific and North Atlantic oceans. This strategy was later adapted and applied to greater amounts of ship-track records to ensure that regions with significant (but unknown) thicknesses of sediment, with seamounts and plateaux, and with long wavelength free-air gravity anomalies were excluded (see, e.g. Hillier & Watts, 2005; Crosby *et al.*, 2006; Korenaga & Korenaga, 2008). One disadvantage of this approach is that the resultant compilations are largely restricted to the Pacific plate and they also tend to be biased toward younger plate ages.

Here, a global strategy is implemented that exploits the comprehensive compilation of 1240 seismic reflection profiles together with 302 modern (i.e. wide-angle) and 395 legacy (i.e. refraction) experiments from Hoggard *et al.* (2017), combined with ~200 new seismic reflection profiles, to produce a database of water-loaded basement depth as a function of age (Appendix A). Ages are assigned to the basement depth measurements using the magnetic reversal history of Müller *et al.* (2016) that has been augmented by including oceanic crust from the Black Sea, from the Caspian Sea, from the eastern Mediterranean Sea, and from the New Caledonian and Aleutian basins. Gridding artefacts within the Gulf of California and along the Mohns Ridge have also been corrected using age constraints (Müller *et al.*, 2008; Figure 2.2a).

The quality of this compilation relies on the ability to accurately correct for both sedimentary and crustal loading. Most modern seismic reflection profiles clearly image both the sediment-basement and the Moho interfaces (Figure 2.2b,c). Simple calibration schemes are used to convert the two-way travel time measured for each mapped interface on a seismic reflection profile into the equivalent water-loaded correction (e.g. Czarnota *et al.*, 2013). Sedimentary and crustal corrections have been applied to 1,160 spot measurements, each of which has a typical uncertainty of ± 120 m. An additional 870 spot measurements have been included that have only been corrected for sedimentary loading. In these cases, regional crustal thickness is estimated as either thicker or thinner than average based on adjacent lines and the presence of seamounts or fracture zones. The sign of the crustal correction is therefore estimated, but not its absolute magnitude. However, the crustal correction is often small compared to the sedimentary correction, so these estimates still provide useful upper or lower bounds. Each of the 2,030 spot measurements of age-depth represents an average over a $1°$ bin.

Figure 2.2d shows the distribution of water-loaded depth to basement as a function of plate age (see Appendix B). Maximum (thicker crust) or minimum (thinner crust) estimates are shown as downwards and upwards pointing triangles, respectively. Circles represent measurements where the
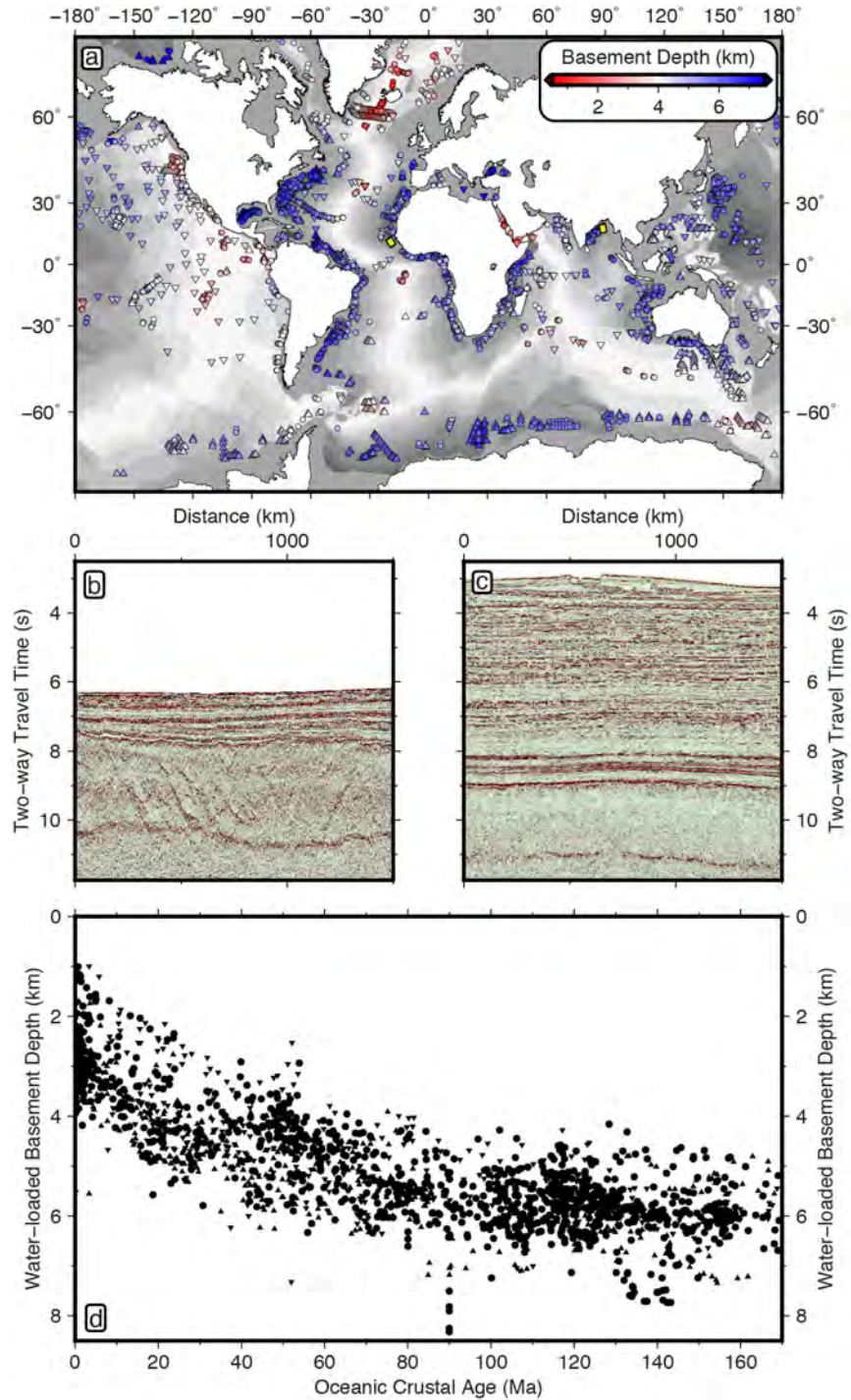
Figure 2.2: Oceanic age-depth database. (a) Map showing global distribution of 2,030 water-loaded depths to oceanic basement from Hoggard *et al.* (2017); circles = data with both sedimentary and crustal corrections; upward/downward pointing triangles = lower/upper estimates of depth for which only sedimentary corrections are applied; yellow lines offshore northwest Africa and offshore east India = locations of example seismic reflection profiles shown in (b) and (c), respectively; grey background shading = updated oceanic plate age. (b) Seismic reflection profile offshore Guinea-Bissau, northwest Africa. Note seabed at ∼ 6.5 s, top of oceanic basement at ∼ 7.5 s and Moho at ∼ 10.5 s. (c) Seismic reflection profile offshore east India. Note seabed at ∼ 2 s, top of oceanic basement at ∼ 9 s and Moho at ∼ 11.5 s. (d) 2,030 water-loaded depths to oceanic basement plotted as function of plate age.

crustal correction has also been applied. This distribution reveals how oceanic lithosphere subsides as a function of time but it is overprinted by considerable scatter that is thought to be directly, or indirectly, generated by the pattern of sub-plate mantle circulation (Hoggard *et al.*, 2017). In order to exploit this distribution of age-depth measurements to place constraints on the thermal evolution of oceanic lithosphere, it is necessary to assume that dynamic topography is roughly evenly distributed as a function of plate age. Importantly, this assumption is common to all studies that use these age-depth measurements, with the exception of Crosby & McKenzie (2009) where gravity anomalies were used as a proxy to explicitly remove dynamic topography. Since the aim here is to understand how the thermal structure of oceanic lithosphere evolves, it is desirable to exploit this distribution of age-depth measurements in conjunction with a global database of heat flow measurements. An important advantage of exploiting two suites of different observations is that any potential trade-off between model parameters can be mitigated (Stein & Stein, 1992).

2.1.2   Heat Flow Measurements

A compilation of heat flow measurements is developed that is corrected in several significant ways. The decay of heat flow through the oceanic basement as a function of plate age provides an additional constraint on the thermal structure of the oceanic plate. A key advantage of exploiting heat flow measurements is that the long thermal time constant for oceanic lithosphere acts as a buffer against sensitivity to transient temperature perturbations within the underlying asthenospheric mantle. However, the effects of hydrothermal circulation can bias heat flow measurements, especially within younger portions of oceanic lithosphere (Lister, 1972). For this reason, particular attention has been paid to applying a series of corrections.

A global database comprising 23,428 heat flow measurements has been recently assembled by Hasterok *et al.* (2011). First, those measurements that lie upon oceanic crust, as defined by a revised oceanic age grid (Müller *et al.*, 2016), are identified. Heat flow measurements are then filtered to remove artefacts and spatially binned over $0.1°$ regions, with the median value selected from each bin. This approach reduces the predominance of very dense, high resolution local studies within the global database.

It is desirable to minimise the impact of hydrothermal circulation on this database. It has been documented that thin sedimentary cover and the existence of a rugose sediment-basement interface can promote hydrothermal circulation (Lister, 1972). Hasterok *et al.* (2011) described a set of

criteria that are designed to minimise these effects, including removal of measurements where sedimentary thickness is less than 400 m, which are located within 60 km of a seamount, or which occur on large igneous provinces. These filters significantly reduce scatter and improve the correlation of heat flow measurements as a function of plate age. The same filters are applied to measurements from oceanic crust that is younger than 65 Ma. Sedimentary thicknesses are extracted from the NGDC_v2 grid (Whittaker *et al.*, 2013). Where appropriate, regions with no measurements are infilled by exploiting values from the CRUST1.0 compilation (Laske *et al.*, 2013). The seamount inventory is taken from Wessel *et al.* (2010) and the distribution of large igneous provinces is from Coffin & Eldholm (1994). Note that no measurements are culled using theoretical cooling models in order to sidestep potential circularity (*contra* Hasterok *et al.*, 2011). Significantly, a consequence of spatial binning is that no individual measurements have values > 500 mW m^{-2} above the running mean.

These hydrothermal filtering criteria have not been applied to measurements from oceanic crust that is older than 65 Ma since hydrothermal circulation is thought to be negligible for older ages (Stein & Stein, 1992; Hasterok, 2013). Should these filtering criteria be applied to measurements older than 65 Ma data, fewer measurements are selected, which leads to a small increase in interquartile ranges and to greater scatter between age bins. The resultant median heat flow values do not systematically change, which is consistent with the expectation of reduced hydrothermal circulation. For this reason, all measurements from oceanic crust that is older than 65 Ma are retained (Figure 2.3a).

The rate at which sediment is deposited on the seabed also affects heat flow measurements. Since sediment has an initial temperature that is equal to bottom water, this deposition acts to depress the geothermal profile, which gives rise to an underestimate of heat flow. An analytical solution that describes the magnitude of this effect is provided by Von Herzen & Uyeda (1963), who assumed that sedimentation rate and thermal diffusivity are constant as a function of time and that the effects of sedimentary compaction and hydrothermal circulation are negligible. In the absence of internal heat generation, their expression can be simplified to give the fractional disturbance, F, of the geothermal profile at the seabed

$$F = 1 + 2Y^2 \text{erfc}(Y) - \text{erf}(Y) - \frac{2Y}{\sqrt{\pi}} \exp(-Y^2) \tag{2.1}$$

where $Y = \frac{1}{2} U t^{\frac{1}{2}} \kappa^{-\frac{1}{2}}$, U is a constant sedimentation rate, t is time since onset of sedimentation and κ is thermal diffusivity. Following Hasterok *et al.* (2011), the value of U is approximated by dividing total sedimentary thickness by plate age. For a thermal diffusivity of 0.25 mm^2 s^{-1}, 60%
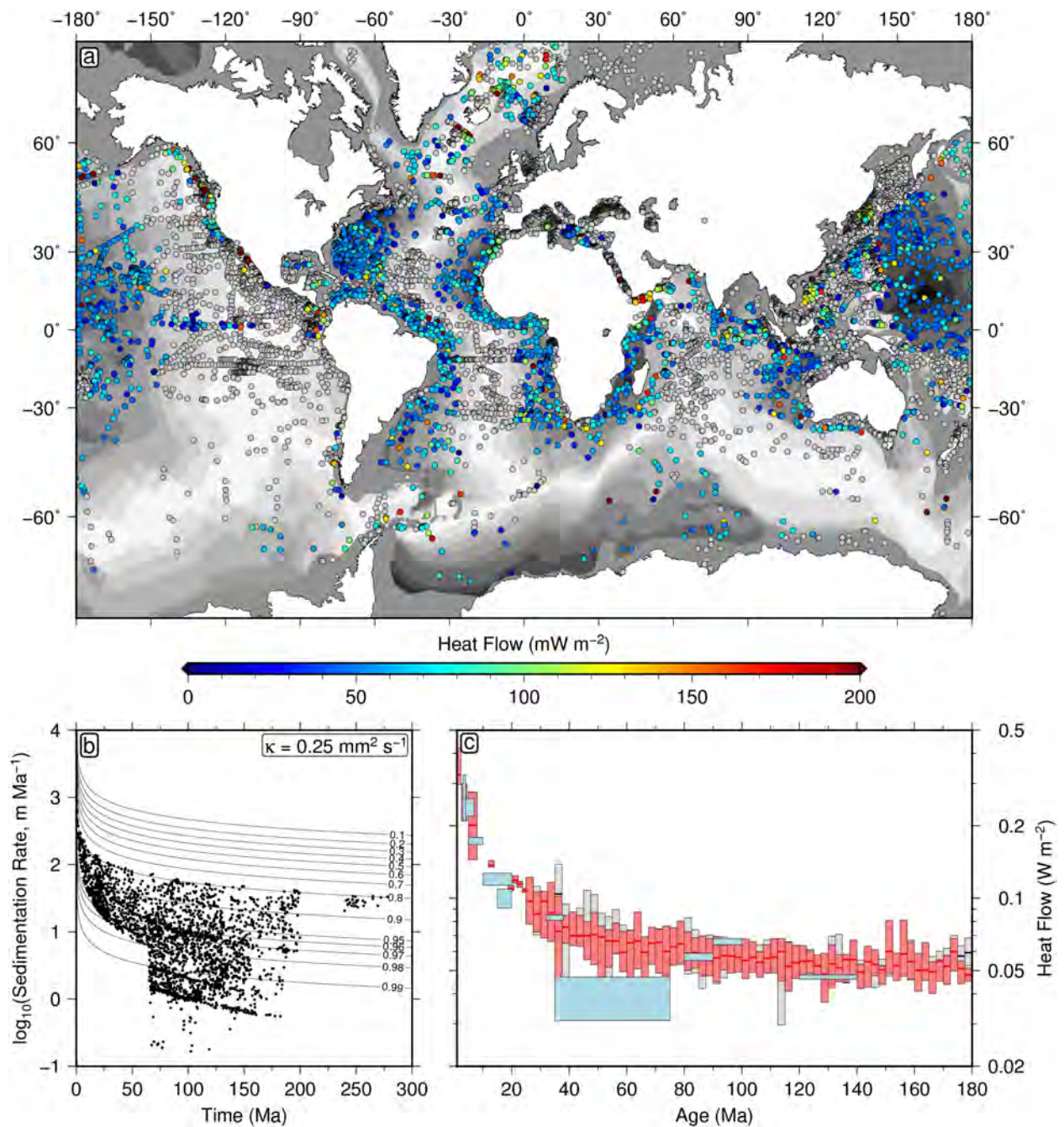
Figure 2.3: Heat flow database. (a) Map showing global distribution of heat flow measurements from Hasterok *et al.* (2011); coloured circles = measurements that pass the filtering process; grey circles = measurements removed during filtering process; grey background shading = updated oceanic plate age. (b) Sedimentation correction to heat flow measurements from Equation (2.1) using a thermal diffusivity of $\kappa = 0.25$ mm^2 s^{-1}; black circles = heat flow measurements; contours represent fractional disturbance of heat flow due to sedimentation (see Equation 2.1). (c) Observed heat flow plotted as function of plate age. Gray line/box = median and interquartile range of sediment-corrected heat flow measurements from Hasterok (2013); light red line/box = median and interquartile range of sediment-corrected heat flow measurements from updated compilation; light blue boxes = heat flow database of Sclater *et al.* (1980) used in McKenzie *et al.* (2005).

of the remaining measurements within the heat flow database require a sedimentary correction of less than 5% and 91% are corrected by $< 20\%$ (Figure 2.3b). Measurements requiring significant correction occur either on young oceanic crust or on crust with large sedimentation rates such as major deltas and sedimentary basins surrounded by elevated continental lithosphere like the Black, Mediterranean and Caspian Seas. The assumption of constant sedimentation rate may not hold in some of these regions rendering the sediment correction more uncertain (Guliyev *et al.*, 2003). The correction procedure leaves 3766 adjusted heat flow measurements, which are binned into 2.5 Myr windows. Discarding measurements that require sedimentation corrections greater than either 20% results in increased variability in young age bins, but does not significantly alter heat flow statistics for ages that exceed ~ 40 Ma. Heat flow values for plate ages greater than 168 Ma are excluded from the following analysis to avoid giving undue weight to measurements in potentially anomalous locations such as the Caspian Sea.

The effect of using different thermal diffusivity values has been tested over a range that encompasses values typically encountered for carbonaceous sediments (κ=0.1–0.5 mm^2 s^{-1}; Waples & Waples 2004). Reducing diffusivity gives rise to greater variation of geothermal profiles and larger sedimentary corrections. However, a value of $\kappa = 0.1$ mm^2 s^{-1} increases median heat flow values by less than 3% at young ages and has an even smaller effect on older bins. A value of $\kappa = 0.5$ mm^2 s^{-1} systematically reduces the median heat flow within each bin by $< 2\%$ for ages greater than 15 Ma. These minor adjustments are significantly smaller than the interquartile range for each bin, which suggests that uncertainty in the value of thermal diffusivity has a minor impact on resultant heat flow values.

The resultant heat flow statistics show that very high values of > 180 mW m^{-2} occur at young plate ages, decreasing to 100 ± 20 mW m^{-2} by 20 Ma. At 60 Ma, heat flow measurements are 65 ± 15 mW m^{-2} and steadily decrease to 50 ± 8 mW m^{-2} for ages > 125 Ma. It has been suggested that, despite global filtering of measurements to limit the effects of hydrothermal circulation, a significant hydrothermal deficit still exists for plate ages of < 25 Ma (Hasterok, 2013). A handful of detailed, high resolution analyses have been carried out at specific locations on young oceanic crust where there is a dense coverage of both heat flow and seismic reflection surveys (Hasterok *et al.*, 2011). Compared with these results, the corrected and binned database may systematically underpredict actual heat flow measurements by 25–40% within this age range. Hasterok (2013) suggests that average heat flow values for ages < 25 Ma should instead be taken from these specific sites, despite the increased spatial bias. Following this approach, these values are adopted for

< 25 Ma lithosphere, whereas the global compilation is used for older age bins (see Appendix C).

2.2   Modelling Strategy

After adiabatically upwelling beneath the mid-ocean ridge, mantle material is transported laterally at a rate that is governed by plate spreading. This material progressively cools as it moves further away from the ridge. Provided that the half-spreading rate exceeds $\sim$ 10 mm a^{-1}, the horizontal component of heat conduction can be regarded as negligible (McKenzie *et al.*, 2005). Furthermore, heat generation by radioactive decay only makes a minor contribution within the oceanic realm.

Pioneering models of the thermal evolution of oceanic lithosphere assumed constant values of physical parameters that govern thermal evolution. The most important parameters are thermal conductivity, k, thermal expansivity, α, and isobaric specific heat capacity, C_P (Turcotte & Oxburgh, 1967; Parsons & Sclater, 1977; Stein & Stein, 1992; Turcotte & Schubert, 2002). Despite the success of thermal models that assume constant values of these parameters, McKenzie *et al.* (2005) re-examined this approach by taking into account their temperature dependence. Laboratory studies demonstrate that k, α and C_P vary significantly over temperature and pressure ranges that are deemed appropriate to the upper mantle (Berman & Aranovich, 1996; Bouhifd *et al.*, 1996; Hofmeister & Pertermann, 2008). McKenzie *et al.* (2005) also included the effects of adiabatic decompression melting at the ridge axis while Grose & Afonso (2013) and Korenaga & Korenaga (2016) allowed for differences in the thermal properties of oceanic crust and mantle.

Cooling oceanic lithosphere is advected horizontally from the ridge axis at a fixed velocity, and the evolution of its temperature structure depends only upon age for plate velocities $\geqslant$ 10 mm a^{-1} when horizontal conduction is insignificant. The thermal structure can be calculated using a generalised form of the one-dimensional heat equation in a reference frame that moves horizontally with the spreading lithosphere,

$$\frac{\partial\left[\rho(T,P,X)C_P(T,X)T\right]}{\partial t} = \frac{\partial}{\partial z}\left(k(T,P,X)\frac{\partial T}{\partial z}\right), \tag{2.2}$$

where t is time, z is depth, and ρ is density while T, P and X refer to temperature, pressure and composition. In this equation, k and ρ vary as functions of T, P and X. C_P depends only upon temperature and composition since it has a negligible dependence on pressure (Hofmeister, 2007).

Although simple analytical solutions exist for the half-space and plate models when thermal pa-

rameters are constant, Equation (2.2) must be solved numerically when thermal parameters vary as a function of temperature, pressure and composition (Turcotte & Schubert, 2002; McKenzie *et al.*, 2005). Here, the applicability of the half-space cooling and plate models are explored. The constant heat flow model of Doin & Fleitout (1996) is not considered since it requires the existence of steep temperature gradients at the base of the cooling plate close to the ridge axis. This requirement is incompatible with the expected axial temperature profile which is dominantly controlled by adiabatic decompression and melting.

Following McKenzie *et al.* (2005), if an expression for the integral

$$G = \int k(T) dT \qquad (2.3)$$

can be found, then Equation (2.2) can be reformulated as

$$\frac{\partial T}{\partial t} = \frac{1}{\rho C_P} \frac{\partial^2 G}{\partial z^2} - \frac{T}{\rho C_P} \frac{\partial (\rho C_P)}{\partial t} \qquad (2.4)$$

where the second term on the right is considerably smaller than the first. Equation (2.4) is solved numerically with an unconditionally stable time- and space-centred Crank-Nicholson finite-difference scheme and a predictor-corrector step (Press *et al.*, 1996). Accordingly, Equation (2.4) is recast as

$$T_j^{n+1} + A \left(-\frac{k_{j+\frac{1}{2}}^m}{\Delta z_j^m} T_{j+1}^{n+1} + \left(\frac{k_{j+\frac{1}{2}}^m}{\Delta z_j^m} + \frac{k_{j-\frac{1}{2}}^m}{\Delta z_{j-1}^m} \right) T_j^{n+1} - \frac{k_{j-\frac{1}{2}}^m}{\Delta z_{j-1}^m} T_{j-1}^{n+1} \right)$$
$$= T_j^n + A \left(\frac{k_{j+\frac{1}{2}}^m}{\Delta z_j^m} T_{j+1}^n - \left(\frac{k_{j+\frac{1}{2}}^m}{\Delta z_j^m} + \frac{k_{j-\frac{1}{2}}^m}{\Delta z_{j-1}^m} \right) T_j^n + \frac{k_{j-\frac{1}{2}}^m}{\Delta z_{j-1}^m} T_{j-1}^n \right) + B$$

where

$$A = \frac{\Delta t}{\left(\rho_j^m C_{P\,j}^m \left(\Delta z_j^m + \Delta z_{j-1}^m \right) \right)}, \qquad (2.5)$$

Δt is the time step, Δz is the mesh spacing and k_j^n represents the value of the variable k at $z = j\Delta z$ and $t = n\Delta t$. For the predictor step, $m = n$ and for the corrector step, $m = n + \frac{1}{2}$. B is included as a correction that represents the $\frac{T}{\rho C_P} \frac{\partial (\rho C_P)}{\partial t}$ term in Equation (2.4). For the predictor step the expression

$$B = -\frac{T_j^n \left(\rho_j^n C_{P\,j}^n - \rho_j^{n-1} C_{P\,j}^{n-1} \right)}{\rho_j^n C_{P\,j}^n}. \qquad (2.6)$$

is employed and for the corrector step

$$B = -\frac{\left(T_j^{n+1} + T_j^n\right)\left(\rho_j^{n+1} C_{P\,j}^{\,n+1} - \rho_j^n C_{P\,j}^{\,n}\right)}{\left(\rho_j^{n+1} C_{P\,j}^{\,n+1} + \rho_j^n C_{P\,j}^{\,n}\right)}.$$ (2.7)

is applied.

These sets of equations are solved by tridiagonal elimination (Press *et al.*, 1996). For incompressible models, Δz_j^m has a constant value of 1 km whilst in compressible models, Δz_j^m is space-centred and scales with thermal contraction. The timestep, $\Delta T = 5$ kyr, and the magnitude of the corrector step drops below $0.1°$C by 1.4 Ma, reducing to $< 0.01°$C by 18 Ma.

A suite of half-space and plate models using both constant and variable thermal parameters have been analysed and compared with age-depth and heat flow observations. The analytical half-space and plate models with constant thermal parameters have a constant temperature, T, assigned to the ridge axis and ridge axis/basal boundary, respectively. The numerical models with non-constant parameters use a more realistic temperature structure for these boundaries. In these models, a potential temperature, T_P, is selected and combined with a plate thickness to calculate the absolute temperature along the basal boundary. The initial ridge axis temperature profile is calculated using this same adiabatic gradient except where it intersects the solidus for anhydrous lherzolite and undergoes decompression melting (Katz *et al.*, 2003). The geothermal gradient above this depth is calculated using the melting parameterisation of Shorttle *et al.* (2014) which yields crustal thicknesses of 0.01–41.10 km for the potential temperature range 1100–1650°C. Temperature is assumed to linearly decrease from the melting parameterisation value at 7 km depth to 0°C at the surface. Realistic variations in this initial temperature profile have a negligible effect on inferred values of potential temperature, plate thickness and depth of ridge axis. A summary of all the models tested here is provided in Table 2.1.

Thermal models that predict the development of oceanic lithosphere should be consistent with independent constraints for the axial temperature structure derived from either the thickness of oceanic crust or the geochemistry of mid-ocean ridge basalts (McKenzie *et al.*, 2005). Global compilations of marine seismic experiments yield an average crustal thickness of 6.9 ± 2.2 km (White *et al.*, 1992; Hoggard *et al.*, 2017). Within our melting parameterisation, 6.9 ± 2.2 km of oceanic crust is produced when the potential temperature is $1331 \pm 35°$C. If the mantle is hydrated by, for example, 113 ppm the inferred potential temperature would decrease by $\sim 11°$C (Brown & Lesher, 2016). This inferred potential temperature is also dependent upon globally averaged

modal proportions of fertile pyroxenite, lherzolite and harzburgite within the melting region. These proportions remain relatively poorly constrained, but if the mass fraction of fertile pyroxenite is up to $\sim 5\%_{px}$, inferred potential temperature decreases by $\sim 6°C\ \%_{px}^{-1}$ (Shorttle *et al.*, 2014). An alternative suite of constraints comes from analysis of mid-ocean ridge basalt geochemistry. A variety of petrologic and geochemical studies all yield similar estimates for ambient mantle potential temperatures (e.g. 1250–1350°C: Katsura *et al.*, 2004; 1280–1400°C: Herzberg *et al.*, 2007; 1314–1464°C: Dalton *et al.*, 2014; $1318^{+44}_{-32}°$C: Matthews *et al.*, 2016). Geochemical and geophysical arguments are therefore consistent with ambient potential temperatures of $T = 1340 \pm 60°$C.

2.3   Age-Depth and Heat Flow Calculations

For the half-space cooling model with constant thermal parameters, plate subsidence, w, as a function of time, t, is calculated analytically using

$$w(t) = z_r + \frac{2\rho_m \alpha (T - T_0)}{(\rho_m - \rho_w)} \sqrt{\frac{\kappa t}{\pi}}, \tag{2.8}$$

where z_r is water depth at the ridge axis, $\rho_m = 3.33$ Mg m^{-3} is the density of mantle at 0°C, $\rho_w = 1.03$ Mg m^{-3} is the density of seawater, $\alpha = 3.28 \times 10^{-5}$ K^{-1} is the thermal expansion coefficient, T is the temperature of the ridge axis, $T_0 = 0°$C is surface temperature and $\kappa = k/(\rho_m C_P) = 0.8044 \times 10^{-6}$ m^2 s^{-1} is thermal diffusivity. For the simple plate model with constant thermal parameters, w is calculated analytically using

$$w(t) = z_r + \frac{\rho_m \alpha (T - T_0) z_p}{2(\rho_m - \rho_w)} \left[1 - \frac{8}{\pi^2} \sum_{i=0}^{N} \frac{1}{(1 + 2i)^2} \exp{-\frac{\kappa(1 + 2i)^2 \pi^2 t}{z_p^2}} \right], \tag{2.9}$$

where z_p is the equilibrium plate thickness, T is the temperature of the ridge axis and basal boundary and i is an integer whose maximum value $N = 10$ is chosen to ensure appropriate convergence. For incompressible plate models that include temperature-dependent parameters,

$$w(t) = z_r + \frac{1}{\rho_m - \rho_w} \left[\int_0^{z_p} \rho(0, z) dz - \int_0^{z_p} \rho(t, z) dz \right] \tag{2.10}$$

is used. For compressible plate models that include both temperature- and pressure-dependent parameters,

$$w(t) = z_r + \frac{\rho_b}{\rho_b - \rho_w(t)} \int_0^{z_p} \left[1 - \frac{\rho(0, z')}{\rho(t, z')} \right] dz', \tag{2.11}$$

is used, where z' is the Lagrangian depth coordinate that contracts vertically with compression, ρ_b is the density at the depth of compensation (i.e. the shallowest depth where $\rho(t, z')$ and $\rho(0, z')$ are equal) and $\rho_w(t) = 1.028 + 0.0048w(t)$ Mg m^{-3} (where $w(t)$ is given in km) in order to account for the compressibility of seawater (Grose & Afonso, 2013).

For the half-space cooling model, surface heat flow, H, is calculated analytically using

$$H(t) = \frac{k(T - T_0)}{\sqrt{\pi \kappa t}}, \tag{2.12}$$

where $k = 3.138$ W m^{-1} °C^{-1} is the thermal conductivity (Parsons & Sclater, 1977). For the simple plate model with constant thermal parameters, H is given by

$$H(t) = \frac{k(T - T_0)}{z_p} \left[1 + 2 \sum_{i=1}^{N} \exp \frac{-\kappa i^2 \pi^2 t}{z_p^2} \right]. \tag{2.13}$$

For all other plate models, surface heat flow is calculated numerically using

$$H(n\Delta t) = \frac{k_0^n(T_1^n - T_0^n)}{\Delta z_0^n}, \tag{2.14}$$

where n is the time step of magnitude Δt, k_0^n is the surface conductivity and Δz_0 is the depth increment at the surface.

In order to minimise the misfit between observed and calculated subsidence, a trial function

$$\chi_s = \sqrt{\frac{1}{M} \sum_{i=1}^{M} \left(\frac{w_i^o - w_i^c}{\sigma_i} \right)^2}, \tag{2.15}$$

is chosen where w_i^o and w_i^c are the observed and calculated values of water-loaded subsidence, σ_i is the standard deviation of observed subsidence (~ 700 m), and $M = 2,030$ is the number of measurements. These subsidence observations are not binned since an uneven age distribution could give rise to an unintended bias toward regions with large positive or negative residual depth anomalies. Subsidence observations from seafloor that is younger than 5 Ma are excluded in order to sidestep the possible effects of vigorous hydrothermal circulation near the ridge axis.

The misfit between observed and calculated heat flow is minimised using a similar trial function

$$\chi_h = \sqrt{\frac{1}{M} \sum_{i=1}^{M} \left(\frac{H_i^o - H_i^c}{\sigma_i^*} \right)^2}, \tag{2.16}$$

where H_i^o and H_i^c are the observed and calculated values of heat flow, $M = 2,904$ is the number of measurements and σ_i^* is defined as the interquartile range divided by 1.349, in accordance with the statistical analysis of Hasterok *et al.* (2011). As before, observations from seafloor that is younger than 5 Ma are excluded. Observations from seafloor older than 168 Ma in order have been excised to avoid unintended bias.

These two misfit functions are equally weighted and combined into a single misfit function given by

$$\chi_t = \sqrt{\frac{(\chi_s)^2 + (\chi_h)^2}{2}}. \tag{2.17}$$

For the half-space cooling model there are two adjustable parameters: the water depth at the ridge axis, z_r, and the axial temperature, T. The simple analytical plate model has three adjustable parameters: z_r, the plate thickness, z_p, and the temperature of the basal boundary and ridge axis, T. For the more complex plate models, T is mantle potential temperature. Given the small number of dimensions, the misfit space is easily interrogated using parameter sweeps, which enables the shape of the misfit function to be determined and the global minimum identified. In such sweeps, T is typically varied between 1100 and 1600°C at intervals of 25°C, z_r is varied between 1.5 and 3 km at intervals of 0.05 km, and z_p is varied between 50 and 210 km at intervals of 5 km.

2.4   Model Assessment

The principal aim of this chapter is to show how revised databases of basement subsidence and heat flow can be used to identify the thermal model which best represents the average behaviour of oceanic lithosphere. The optimal model has several qualities. First, it should have the ability to jointly fit subsidence and heat flow observations. Secondly, it should predict an axial temperature that agrees with independent geochemical and petrologic constraints. Finally, the simplest physical model is sought that is consistent with both experimental data on the thermal properties of minerals and a range of separate observations, such as earthquake hypocentral depths and lithospheric thickness measurements.

2.4.1   Half-Space Cooling Models

In its simplest form, this model yields an excellent fit between observed and calculated plate subsidence as a function of time (Figure 2.4a). Unfortunately, the predicted value of axial temperature

is $T = 1003°C$, which is considerably less than that determined by petrologic observations (e.g. 1280–1400°C; Herzberg *et al.*, 2007). Although there is a negative trade-off between T and z_r, it is evident that T cannot be increased by the required amount of about 300°C without both an unreasonably large decrease in z_r and an unreasonably large increase in χ_t (Figure 2.4c).
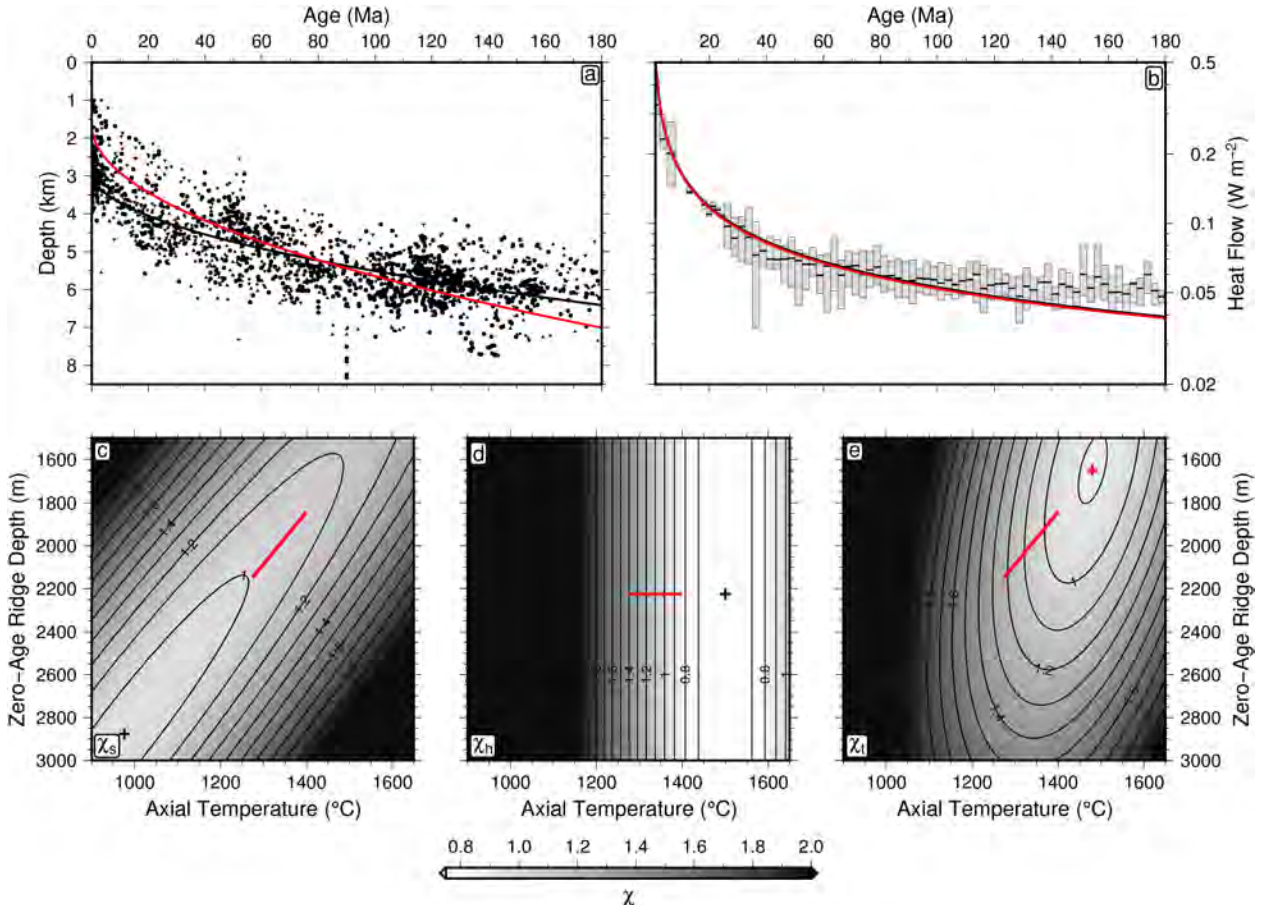
Figure 2.4: Half-space cooling model. (a) Water-loaded depth to oceanic basement as function of plate age (Figure 2.2d); black line = optimal relationship obtained by only fitting age-depth observations; red line = optimal relationship from joint fit of age-depth and heat flow observations. (b) Surface heat flow as function of plate age (Figure 2.3c); grey boxes with horizontal bars = interquartile ranges and median values of sediment-corrected heat flow measurements; black line = optimal relationship obtained by only fitting heat flow observations; red line = optimal relationship from joint fit of age-depth and heat flow observations. (c) Misfit between observed and calculated age-depth observations, χ_s, as function of axial temperature and zero-age ridge depth; black cross = misfit minimum; red bar = optimal parameters when axial temperature is fixed at $1340 \pm 60°C$. (d) Same for misfit between observed and calculated heat flow, χ_h. (e) Same for joint misfit, χ_t, between observed and calculated age-depth and heat flow observations; red cross = global minimum used to generate red curves in panels (a) and (b).

When subsidence and heat flow measurements are jointly fitted, the half-space cooling model tends to overpredict subsidence and to underpredict heat flow for plate ages of greater than ~ 80 Ma

(Figure 2.4a and 2.4b). This residual misfit is most marked for the oldest heat flow observations. Furthermore, the calculated value of T is almost $100°$C greater than the upper bound proposed by Herzberg *et al.* (2007). The failure to reproduce the observed flattening of heat flow and subsidence for older plates, and the mismatch to independent axial temperature constraints, demonstrates that half-space cooling models do not provide an adequate approximation of the average thermal structure of oceanic lithosphere (Figure 2.4c–e).

2.4.2   Plate Models

It has previously been demonstrated that a simple analytical plate model provides an adequate fit to combined subsidence and heat flow observations (Figure 2.5; Parsons & Sclater, 1977; Stein & Stein, 1992). Here, it is shown that the revised databases of both sets of observations can be accurately fitted with a residual misfit of $\chi_t \sim 0.8$. A global minimum exists at $T = 1493°$ C, $z_p = 106$ km and $z_r = 2.20$ km. Notably, if the approach of Parsons & Sclater (1977) is repeated by only fitting subsidence data, minimum misfit is recovered when $T = 1325°$C and $z_p = 130$ km, which is very similar to their original result (i.e. $T = 1333°$C, $z_p = 120$ km). In comparison, results for the combined subsidence and heat flow fit closely agree with those of Stein & Stein (1992) who retrieve a hotter and thinner plate ($T = 1450°$C, $z_p = 90$ km) in their jointly fitted model.

It is clear that a simple plate model yields an improved fit to the combined database of subsidence and heat flow observations in comparison to the half-space cooling model (Figure 2.5; Table 2.1). However, the recovered axial temperature of $T = 1493°$C is significantly hotter than the independent constraints of 1280–1400°C. A predicted zero-age ridge depth of $z_r = 2.20$ km is also shallow compared to the global average of ~ 2.8 km (Gale *et al.*, 2014). Importantly, there is a mismatch in optimal parameters desired by the subsidence versus the heat flow data (Figures 2.5c and 2.5d). The shape of the combined misfit function offers little room for manoeuvre in terms of trade-off between plate thickness and temperature (Figure 2.5e). These discrepancies imply that despite the apparent success of the simple plate model, a more complex approach is required.

Temperature- & Pressure-Dependent Parameterisations

Here, the scheme described by McKenzie *et al.* (2005) is followed in which a more physically realistic parameterisation of conductivity, k, expansivity, α and heat capacity, C_P, is included within the framework of the plate model. In the first instance, models were benchmarked against
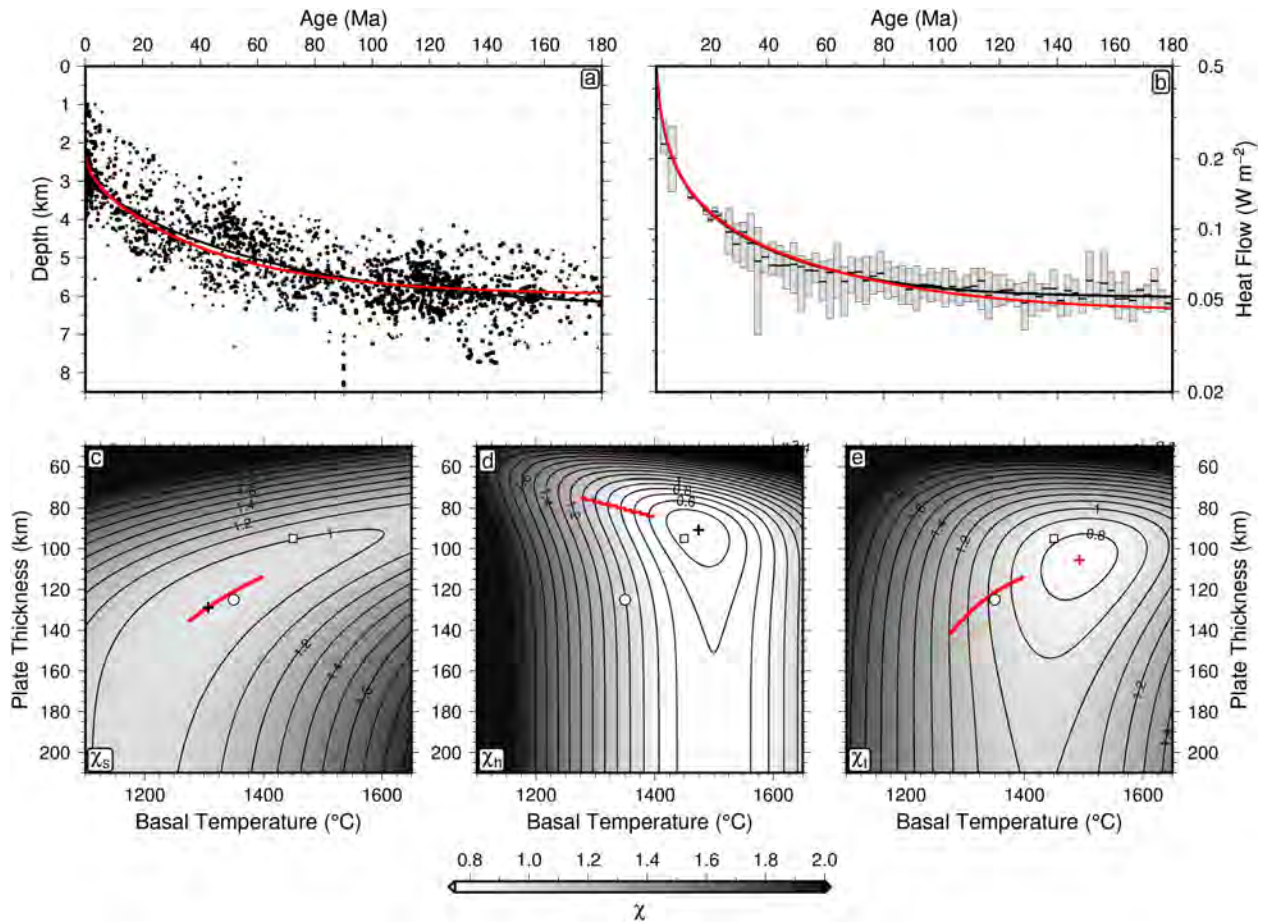
Figure 2.5: Simple plate model. (a) Water-loaded depth to oceanic basement as function of plate age (Figure 2.2d); black line = optimal relationship obtained by only fitting age-depth observations; red line = optimal relationship from joint fit of age-depth and heat flow observations. (b) Surface heat flow as function of plate age (Figure 2.3c); grey boxes with horizontal bars = interquartile ranges and median values of sediment-corrected heat flow measurements; black line = optimal relationship obtained by only fitting heat flow observations; red line = optimal relationship from joint fit of age-depth and heat flow observations. (c) Misfit between observed and calculated age-depth observations, χ_s, as function of axial/basal temperature and plate thickness, sliced at best-fitting zero-age depth of 2.35 km; black cross = misfit minimum; red bar = optimal parameters when axial temperature is fixed at $1340 \pm 60°$C; white circle = optimal result of Parsons & Sclater (1977); white square = optimal result of Stein & Stein (1992). (d) Same for misfit between observed and calculated heat flow, χ_h. (e) Same for joint misfit, χ_t, between observed and calculated age-depth and heat flow observations, sliced at best-fitting zero-age depth of 2.20 km; red cross = global minimum used to generate red curves in panels (a) and (b).

their temperature-dependent approach which generates an excellent fit to both subsidence and heat flow observations (Figure 2.6a and 2.6b; Table 2.1). The shape of the misfit function shows that there is a global minimum at $T = 1407°$C, $z_p = 95$ km and $z_r = 2.51$ km (Figure 2.6c–2.6e). This result is $\sim 85°$C cooler than obtained for the simple plate model, but it is hotter and thinner than that calculated by McKenzie *et al.* (2005) who independently fixed $T = 1315°$C and $z_r = 2.5$ km
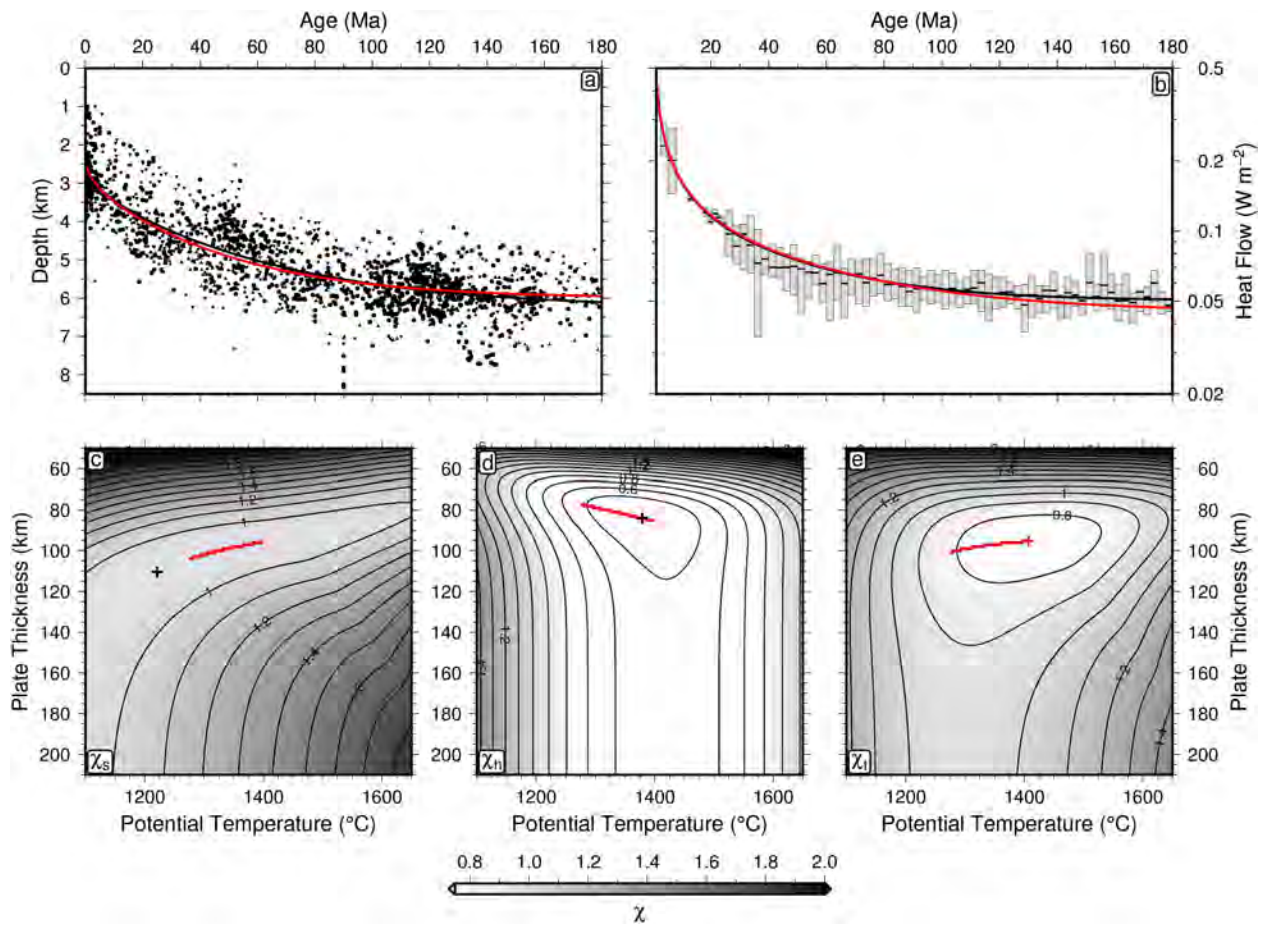
Figure 2.6: Temperature-dependent plate model. (a) Water-loaded depth to oceanic basement as function of plate age (Figure 2.2d); black line = optimal relationship obtained by only fitting age-depth observations; red line = optimal relationship from joint fit of age-depth and heat flow observations. (b) Surface heat flow as function of plate age (Figure 2.3c); grey boxes with horizontal bars = interquartile ranges and median values of sediment-corrected heat flow measurements; black line = optimal relationship obtained by only fitting heat flow observations; red line = optimal relationship from joint fit of age-depth and heat flow observations. (c) Misfit between observed and calculated age-depth observations, χ_s, as function of potential temperature and plate thickness, sliced at best-fitting zero-age depth of 2.55 km; black cross = misfit minimum; red bar = optimal parameters when axial temperature is fixed at $1340 \pm 60°$C. (d) Same for misfit between observed and calculated heat flow, χ_h. (e) Same for joint misfit, χ_t, between observed and calculated age-depth and heat flow observations, sliced at best-fitting zero-age depth of 2.51 km; red cross = global minimum used to generate red curves in panels (a) and (b).

to obtain an equilibrium plate thickness of 106 km. Thus there remains a significant discrepancy between the retrieved values of T and z_p compared with those expected from independent petrologic and seismologic constraints (Herzberg *et al.*, 2007; Burgos *et al.*, 2014; Steinberger & Becker, 2017).

The laboratory results upon which the temperature dependence of conductivity, thermal expansivity and isobaric heat capacity are based have associated uncertainties (Figure 2.7a, c & e). The
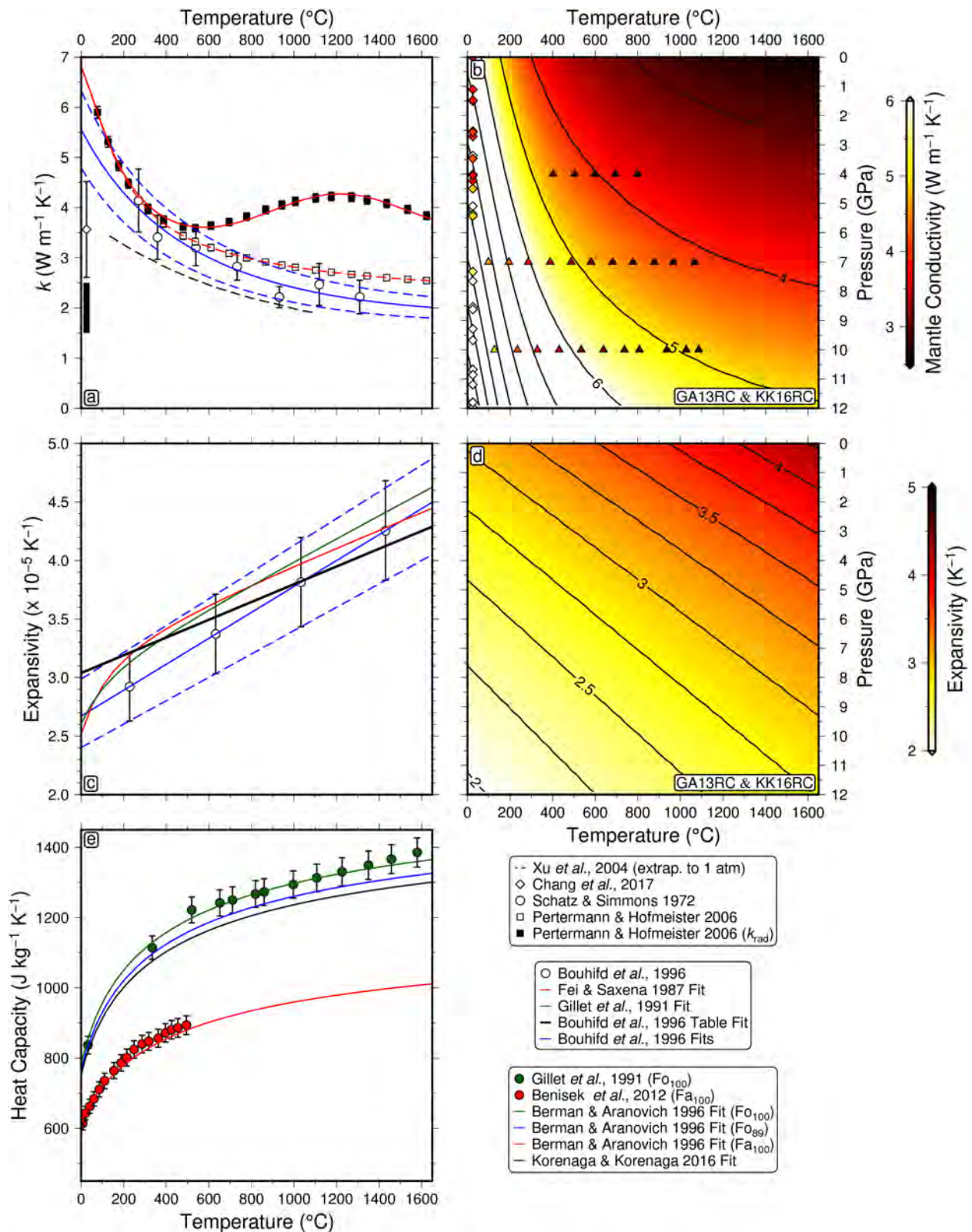
Figure 2.7 *(previous page)*: **Temperature- and pressure-dependence of conductivity, expansivity and heat capacity.** (a) Thermal conductivity, k, plotted as function of temperature for constant pressure of 0.1 MPa. Squares with error bars and solid red line = forsterite lattice conductivity measurements from Pertermann & Hofmeister (2006) combined with 5 mm radiative conductivity measurements of Hofmeister (2005); triangles and red dashed line = forsterite lattice conductivity measurements from Pertermann & Hofmeister (2006); circles with error bars fitted with solid/dashed blue lines = forsterite conductivity measurements from Schatz & Simmons (1972) where dashed lines represent $\pm 1\sigma$; diamond with error bar = forsterite lattice conductivity measurement for anhydrous olivine from Chang *et al.* (2017); vertical black bar = range of estimates for conductivity of basalt (Kelemen *et al.*, 2004). (b) Contour map of forsterite lattice thermal conductivity as function of temperature and pressure based upon fitting measurements from Pertermann & Hofmeister (2006) using pressure dependence of Hofmeister (2007). Diamonds = forsterite lattice conductivity measurements for anhydrous olivine data from Chang *et al.* (2017); inverted triangles = forsterite lattice conductivity measurements from Xu *et al.* (2004). (c) Thermal expansivity of forsterite plotted as function of temperature for constant pressure of 0.1 MPa. Circles with error bars fitted with solid/dashed blue lines = measurements from Bouhifd *et al.* (1996) where dashed lines represent $\pm 1\sigma$; red/green lines = relationships used by Fei & Saxena (1987) and Gillet *et al.* (1991), respectively. (d) Contour map of thermal expansivity of forsterite as function of temperature and pressure based upon parameterisation of Grose & Afonso (2013) and Korenaga & Korenaga (2016). (e) Heat capacity plotted as function of temperature. Circles with error bars and red line = fayalite measurements from Benisek *et al.* (2012) fitting using fayalite parameterisation of Berman (1988); triangles with error bars and green line = forsterite measurements from Gillet *et al.* (1991) using forsterite parameterisation of Berman (1988); blue line = parameterisation of Berman (1988) assuming 11% fayalite and 89% fosterite; black line = parameterisation described by Equation (2) from Korenaga & Korenaga (2016). Note that pressure dependence over the relevant range of plate thicknesses is negligible (Hofmeister, 2007).

sensitivity of results to these uncertainties has been examined by carrying out a series of misfit function sweeps for temperature, plate thickness and zero-age ridge depth using parameterisations fitted to both upper and lower bounds of these experimental datasets. For example, heat capacity was varied by changing the forsterite-fayalite ratio, in accordance with the expected range within the mantle (i.e. Fo_{84}–Fo_{92}). This variation produced $\pm 13^\circ$C change in predicted temperature but negligible change in both plate thickness and zero-age ridge depth. Varying thermal expansivity between its upper and lower bounds made negligible difference to temperature and resulted in only ± 2.5 km change in plate thickness. However, zero-age ridge depth varied by ± 0.22 km. Finally, the temperature-dependence of thermal conductivity is varied in accordance with the upper and lower bounds of experimental measurements made by Schatz & Simmons (1972) and exploited by McKenzie *et al.* (2005). This variation yields a $\pm 115^\circ$C change in predicted temperature, a ± 5 km change in plate thickness, and a minimal (± 0.01 km) change in zero-age ridge depth.

It is clear that the temperature dependence of thermal conductivity has the most significant effect upon plate parameters (McKenzie *et al.*, 2005). Fortunately, modern experiments based upon
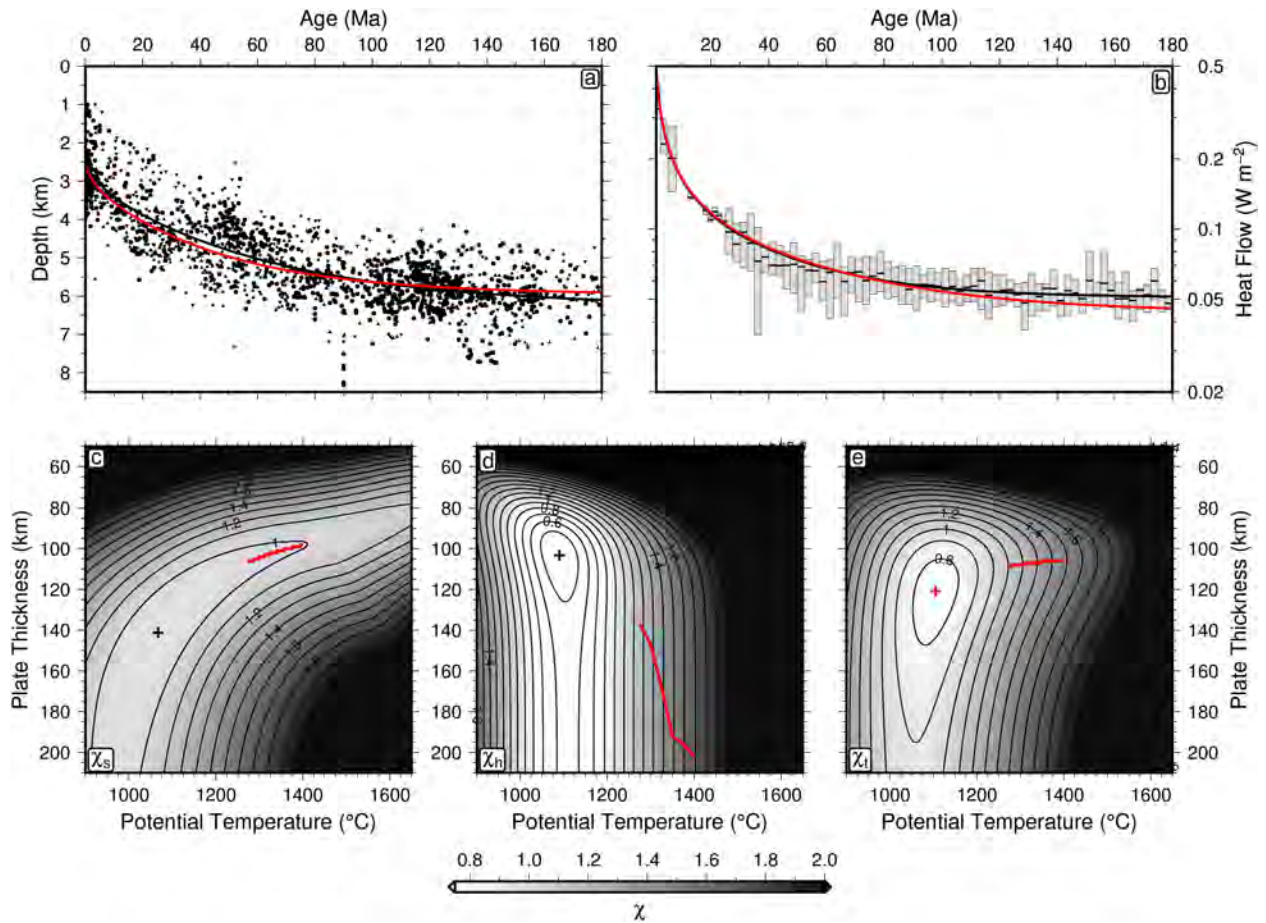
**Figure 2.8: Temperature-dependent plate model with updated olivine conductivity model.** (a) Water-loaded depth to oceanic basement as function of plate age (Figure 2.2d); black line = optimal relationship obtained by only fitting age-depth observations; red line = optimal relationship from joint fit of age-depth and heat flow observations. (b) Surface heat flow as function of plate age (Figure 2.3c); grey boxes with horizontal bars = interquartile ranges and median values of sediment-corrected heat flow measurements; black line = optimal relationship obtained by only fitting heat flow observations; red line = optimal relationship from joint fit of age-depth and heat flow observations. (c) Misfit between observed and calculated age-depth observations, χ_s, as function of potential temperature and plate thickness, sliced at best-fitting zero-age depth of 2.43 km; black cross = misfit minimum; red bar = optimal parameters when axial temperature is fixed at $1340 \pm 60°$C. (d) Same for misfit between observed and calculated heat flow, χ_h. (e) Same for joint misfit, χ_t, between observed and calculated age-depth and heat flow observations, sliced at best-fitting zero-age depth of 2.55 km; red cross = global minimum used to generate red curves in panels (a) and (b).

laser flash analysis yield better resolved measurements with smaller uncertainties compared with the older measurements of Schatz & Simmons (1972) that use a contact method (Figure 2.7a; Hofmeister, 2005; Pertermann & Hofmeister, 2006). These modern experiments also show that the original measurements of Schatz & Simmons (1972) together with the radiative conductivity parameterisation of Hofmeister (1999) that were used by McKenzie *et al.* (2005) tend to underesti-

mate the thermal conductivity of olivine by 20–30%. If a conductivity parameterisation consistent with these more recent developments is used instead, uncertainty in the recovered value of T is reduced. Zero-age ridge depth and plate thickness have values of 2.55 km and 121 km, respectively. However, the increase in the value of k for olivine now yields an optimal potential temperature of $1105°C$, which is $\sim 175°C$ below the lower bound of independent constraints. Optimal thermal
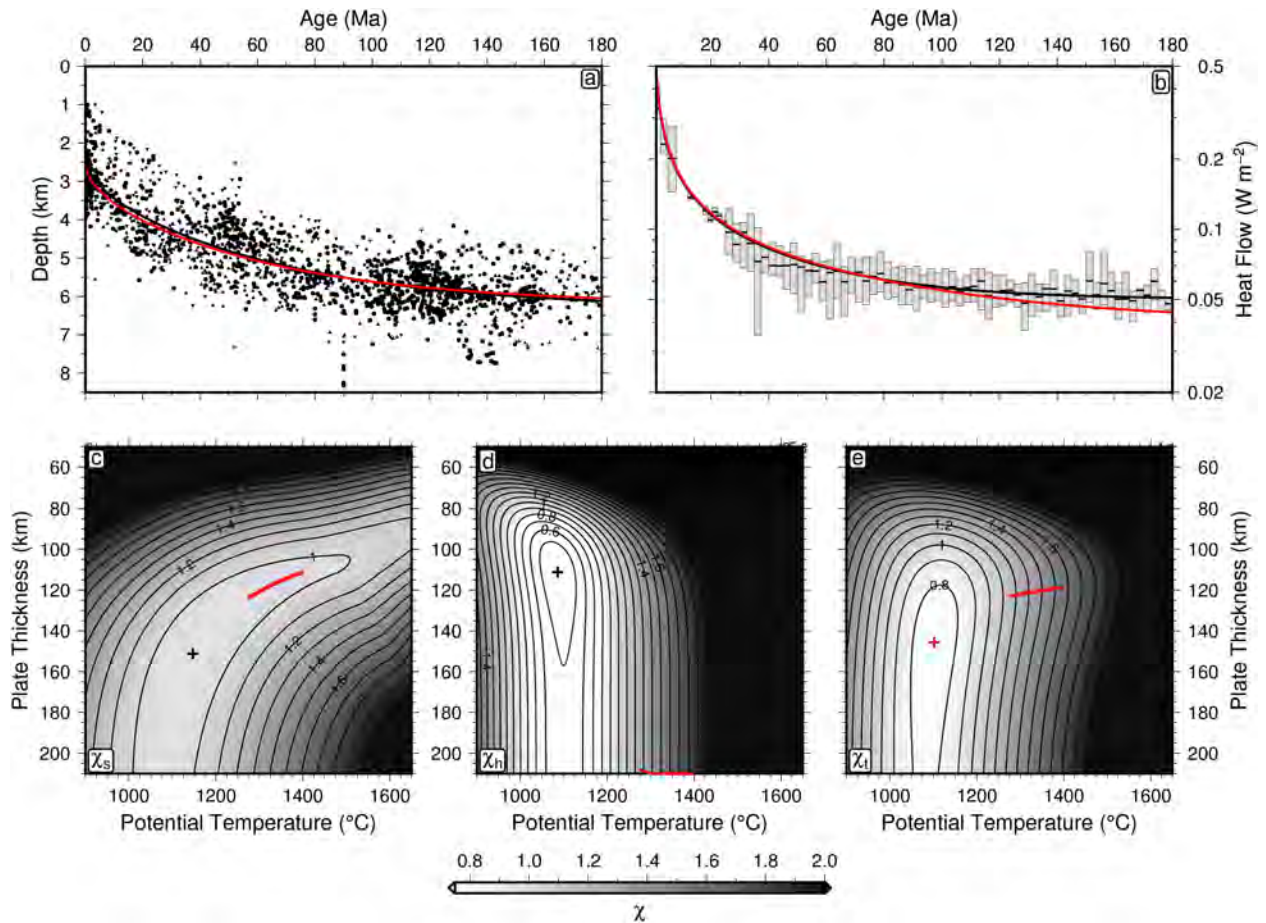
Figure 2.9: Pressure and temperature-dependent plate model with no oceanic crust.
(a) Water-loaded depth to oceanic basement as function of plate age (Figure 2.2d); black line = optimal relationship obtained by only fitting age-depth observations; red line = optimal relationship from joint fit of age-depth and heat flow observations. (b) Surface heat flow as function of plate age (Figure 2.3c); grey boxes with horizontal bars = interquartile ranges and median values of sediment-corrected heat flow measurements; black line = optimal relationship obtained by only fitting heat flow observations; red line = optimal relationship from joint fit of age-depth and heat flow observations. (c) Misfit between observed and calculated age-depth observations, χ_s, as function of potential temperature and plate thickness, sliced at best-fitting zero-age depth of 2.44 km; black cross = misfit minimum; red bar = optimal parameters when axial temperature is fixed at $1340 \pm 60°C$. (d) Same for misfit between observed and calculated heat flow, χ_h. (e) Same for joint misfit, χ_t, between observed and calculated age-depth and heat flow observations, sliced at best-fitting zero-age depth of 2.62 km; red cross = global minimum used to generate red curves in panels (a) and (b).

parameters for the subsidence and heat flow data still do not coincide. It can therefore be inferred that the physics of lithospheric cooling is not adequately represented by an olivine-based, purely temperature-dependent model alone.

Experimental observations also demonstrate that thermal conductivity and expansivity (but not specific heat capacity) vary significantly over pressure ranges relevant to lithospheric plates (Figure 2.7b & 2.7d; Hofmeister, 2007). The pressure dependency of k and α are incorporated into a revised plate model (Table 2.1). Once again, an adequate fit to subsidence and heat flow observations is obtained where the residual value of χ_t is less than 1. In this case, the locus of the global minimum shifts slightly to $T = 1102°C$, $z_p = 146$ km and $z_r = 2.62$ km. It is concluded that the inclusion of pressure dependence makes little discernible difference to the potential temperature discrepancy.

Complete Plate Model

Finally, one additional issue is explored that may help to resolve the temperature discrepancy. Although the assumption of pure olivine is probably an appropriate approximation for oceanic mantle lithosphere, it constitutes $< 5\%$ of oceanic crust (White & Klein, 2013). Instead, plagioclase feldspar is the dominant phase ($\sim 50\%$ – the remainder being primarily pyroxene), which has a thermal conductivity that is $\sim 25\%$ that of olivine. Thus the oceanic crustal layer has an insulating effect upon the underlying mantle lithosphere.

Grose & Afonso (2013) have used a geometric mixing rule to estimate the conductivity of an aggregate comprised of plagioclase feldspar, diopside and olivine which yields a value of 2.65 W m^{-1} °C^{-1} at room temperature and pressure. Ocean drilling program results have reported thermal conductivities of $\sim$2 W m^{-1} °C^{-1} for basalt and gabbro at equivalent conditions (Kelemen *et al.*, 2004). These values are smaller than the geometric mean calculated by Grose & Afonso (2013), but are more consistent with the results of a harmonic mean mixing rule which yields 2.21 W m^{-1} °C^{-1}.

A revised plate model, that includes 7 km-thick oceanic crust with temperature-dependent conductivity based upon a harmonic mean of the parameterisation described by Grose & Afonso (2013), yields $T = 1304°C$, $z_p = 135$ km and $z_r = 2.64$ km (Figure 2.10). This result changes minimally if a constant value of $k = 2$ W m^{-1} °C^{-1} is used ($T = 1308°C$, $z_p = 133$ km and $z_r = 2.72$ km). Fixing the potential temperature to $1333°C$ yields only a 3% increase in residual misfit to the combined heat flow and subsidence databases (Figure 2.7a & b). Importantly, consistent values of T, z_p
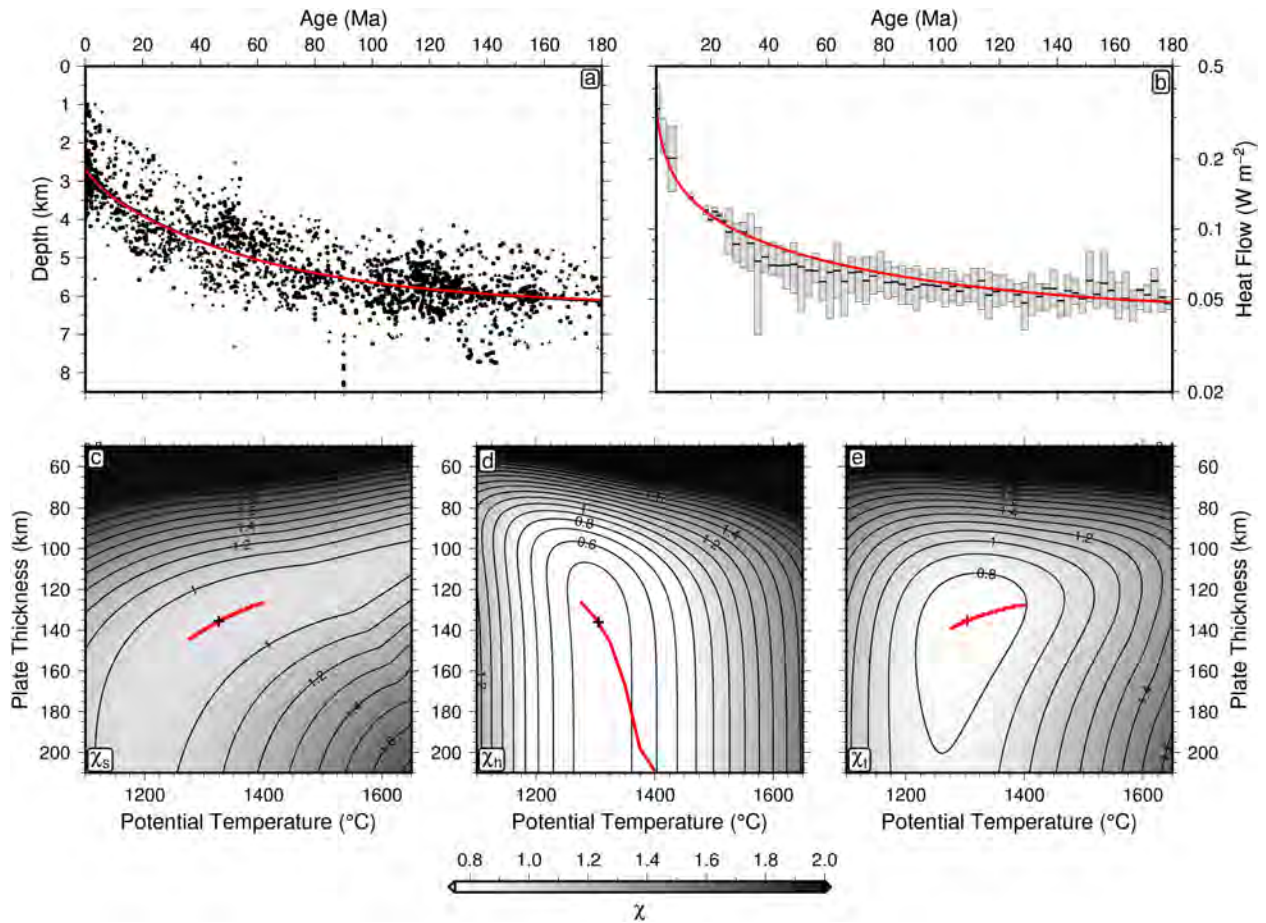
Figure 2.10: Complete plate model. (a) Water-loaded depth to oceanic basement as function of plate age (Figure 2.2d); black line = optimal relationship obtained by only fitting age-depth observations; red line = optimal relationship from joint fit of age-depth and heat flow observations. (b) Surface heat flow as function of plate age (Figure 2.3c); grey boxes with horizontal bars = interquartile ranges and median values of sediment-corrected heat flow measurements; black line = optimal relationship obtained by only fitting heat flow observations; red line = optimal relationship from joint fit of age-depth and heat flow observations. (c) Misfit between observed and calculated age-depth observations, χ_s, as function of potential temperature and plate thickness, sliced at best-fitting zero-age depth of 2.60 km; black cross = misfit minimum; red bar = optimal parameters when axial temperature is fixed at $1340 \pm 60°$C. (d) Same for misfit between observed and calculated heat flow, χ_h. (e) Same for joint misfit, χ_t, between observed and calculated age-depth and heat flow observations, sliced at best-fitting zero-age depth of 2.64 km; red cross = global minimum used to generate red curves in panels (a) and (b). Note that subsidence and heat flow misfit minima give similar values of potential temperature and plate thickness.

and z_r are obtained regardless of whether subsidence and heat flow measurements are jointly or separately fitted. Significantly, the retrieved potential temperature of $1304°$C is now in agreement with independent constraints of 1280–$1400°$C.

Table 2.1: Summary of model results fit to heat flow and subsidence simultaneously. Details on model setup and best-fitting parameters for cases where T is a free parameter or T is fixed to an independently constrained value of 1333°C. z_c = crustal thickness; T- and P-dependence indicate parameterisations used in each model, MJP05 = parameters from McKenzie et al. (2005), GA13 = parameters from Grose & Afonso (2013) and KK16 = parameters from Korenaga & Korenaga (2016); T = best-fitting mantle temperature; z_p = best-fitting plate thickness; z_r = best-fitting zero-age ridge depth; χ_t = joint misfit value at these conditions; Q = predicted cumulative oceanic heat flux; $[X]_{gchem}$ subscripts indicate values when temperature is fixed at 1333°C. HSCk = half-space cooling model with constant parameters; Pk = simple plate model with constant parameters; MR* = plate model with temperature-dependent parameters following McKenzie et al. (2005); KR = plate model with temperature-dependent parameters and revised olivine conductivity model of Pertermann & Hofmeister (2006); KRC = plate model with temperature- and pressure-dependent parameters; KRCCk = complete plate model with constant conductivity of 2 W m^{-1} °C^{-1}; KRCC = complete plate model with temperature- and pressure-dependent parameters, including 7 km thick oceanic crust with constant conductivity; including 7 km thick oceanic crust with temperature- and pressure-dependent conductivity based on harmonic mean of plagioclase, clinopyroxene and olivine conductivities from Grose & Afonso (2013).

Model	z_c (km)	T-dependence	P-dependence	T (°C)	z_p (km)	z_r (m)	χ_t	$[z_p]_{gchem}$ (km)	$[z_r]_{gchem}$ (m)	$[\chi_t]_{gchem}$	Q (TW)	$[Q]_{gchem}$ (TW)
HSCk	0	None	None	1480	—	1656	0.900	—	<2000	1.073	28.68	25.82
Pk	0	None	None	1493	106	2204	0.749	125	2300	1.022	29.91	29.64
MR*	0	MJP05	None	1407	95	2508	0.731	93	2616	0.753	28.71	27.87
KR	0	KK16 & GA13	None	1105	121	2548	0.749	123	<2000	1.208	28.97	33.38
KRC	0	KK16 & GA13	GA13	1102	146	2624	0.743	144	2056	1.283	28.94	33.78
KRCCk	7	KK16 & GA13	GA13	1308	133	2720	0.728	136	2660	0.731	27.09	27.45
KRCC	7	KK16 & GA13	GA13	1304	135	2640	0.726	136	2584	0.732	27.53	27.96

Table 2.2: Summary of model results fit to subsidence and heat flow separately. Best-fitting parameters for unconstrained mantle potential temperature. Model abbreviations as in caption of Table 2.1. Subscripts denote whether fit is to subsidence ($_s$) or heat flow data ($_h$) only.

Model	T_s (°C)	$[z_p]_s$ (km)	$[z_r]_s$ (m)	χ_s	T_h (°C)	$[z_p]_h$ (km)	χ_h
HSCk	1005	–	2816	0.951	1500	–	0.606
Pk	1307	129	2352	0.927	1474	91	0.414
MR*	1221	110	2548	0.927	1379	84	0.406
KR	1067	141	2432	0.927	1090	103	0.411
KRC	1147	151	2444	0.927	1086	111	0.409
KRCCk	1308	136	2684	0.928	1311	136	0.444
KRCC	1325	136	2604	0.927	1305	136	0.441

2.5   Implications

2.5.1   Intraplate Earthquakes

Thermal models of oceanic lithosphere can be used to track particular isothermal contours as a function of plate age (Figure 2.11). It is instructive to compare different thermal models with the depths of intraplate earthquakes in order to place constraints on the rheologic behaviour of oceanic lithosphere. Wiens & Stein (1983) showed that the maximum depth of oceanic intraplate seismicity seems bounded by the 700–800°C isothermal contour from the plate model of Parsons & Sclater (1977) (Figure 2.11a). They concluded that, above this temperature, oceanic lithosphere cannot support the stresses required to achieve seismic failure. McKenzie *et al.* (2005) revisited this issue and showed that almost all intraplate earthquakes occur at depths that are cooler than the 600°C isothermal surface (Figure 2.11b). Subsequently, Craig *et al.* (2014) reanalysed the source parameters of earthquakes that occur beneath in the vicinity of outer rises of oceanic plates. By combining their results with the thermal model of McKenzie *et al.* (2005), they suggested that the seismic-aseismic transition matched the 600°C isothermal surface and that this match agreed with other seismological and experimental studies where a limit of 600°C was determined.

In contrast, the revised thermal model suggested that the seismic-aseismic transition better matches the 700°C isothermal surface (Figure 2.11c). This revised estimate is a direct consequence of the fact that the thermal model is based upon jointly fitting both subsidence and heat flow observations. It also includes the effects of pressure-dependence and low conductivity crust. In contrast, McKenzie
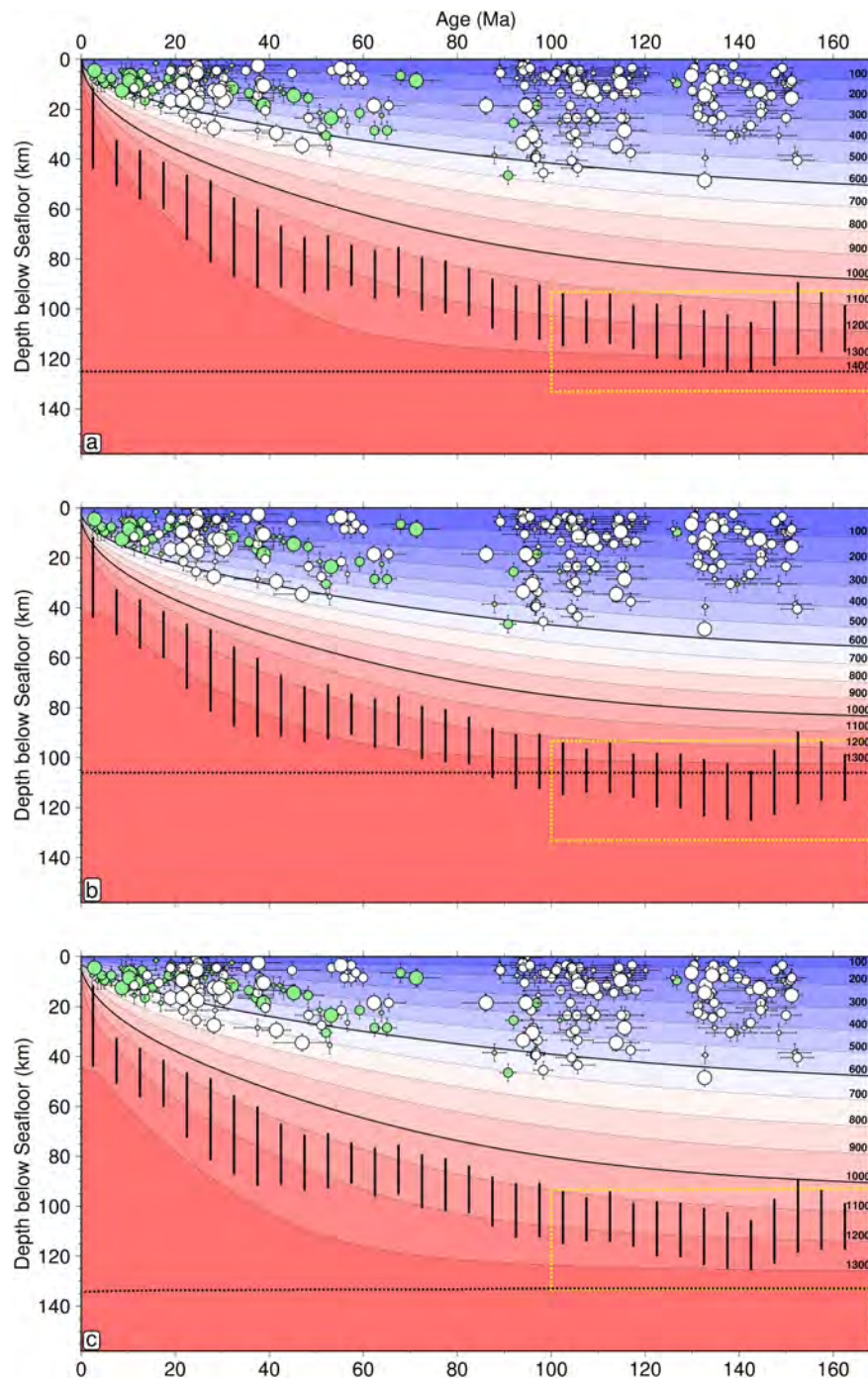
Figure 2.11: Thermal structure of oceanic lithosphere. (a) Simple analytical plate model using the published values found by Parsons & Sclater (1977); numbered contours = isothermal surfaces plotted in degrees Celsius; green and white circles with error bars = oceanic intraplate and outer rise earthquakes from Craig *et al.* (2014) where small/medium/large circles = M_b <5.5, 5.5–6.5 and >6.5; vertical black bars = depth to lithosphere-asthenosphere boundary in Pacific Ocean based upon peak variations in azimuthal anisotropy (Burgos *et al.*, 2014); dashed box = envelope of depths to lithosphere-asthenosphere boundary for plate ages >100 Ma (Steinberger & Becker, 2017); horizontal black dashed line = base of plate model. (b) Same for temperature-dependent plate model using parameter values from McKenzie *et al.* (2005). (c) Same for our optimal complete plate model using updated P-T-dependence of thermal parameters and a 7 km layer of oceanic crust.

et al. (2005) considered only the temperature dependence of olivine thermal parameters and fitted a spatially limited database of subsidence observations from the North Pacific plate (Parsons & Sclater, 1977). These differences in model parameterisation and data fitting result in a best-fitting plate thickness of 135 km, 30 km thicker than that proposed by McKenzie *et al.* (2005). The $100°$C difference between these results and those of Craig *et al.* (2014) is significant and has obvious implications for plate rheology. For example, Boettcher *et al.* (2007) argue that the strength and frictional behaviour of olivine aggregates is entirely consistent with a transition from velocity weakening to velocity strengthening at approximately $600°$C. Following Goetze (1978), who carried out indentation creep tests on single olivine crystals, they calculate the yield stress at an asperity, σ_a, using

$$\sigma_a = \sigma_p \left[1 - \left(\frac{-RT}{H} \ln \frac{\dot{\epsilon}}{B_r} \right)^{1/2} \right] \tag{2.18}$$

where the Peierl's stress $\sigma_p = 8500$ MPa, the gas constant $R = 8.314$ J mol^{-1} K^{-1}, the activation enthalpy $H_a = 5.4 \times 10^5$ J mol^{-1}, and the reference strain rate $B_r = 5.7 \times 10^{11}$ s^{-1}. The original form of this equation is given by Stocker & Ashby (1973) and by Goetze (1978). It arises from the fact that at low temperatures the glide motion of dislocations within the crystal lattice become dominant. In non-metals such as olivine, the lattice itself resists dislocation motion so that a finite, and often large, stress is required to move a dislocation. This frictional resistance is known as the Peierl's stress. Attempts to formulate rate equations for plastic flow in the rate limiting case are not wholly satisfactory but the observations are reasonably well described by Equation 2.18. Dislocation flow in this high stress regime is sometimes referred to as the power law breakdown regime. Goetze (1978) compiled low pressure creep experiments that were carried out on dry polycrystalline olivine aggregates which he used to determine the linear relationship between σ_a and $\sqrt{T}$. In Figure 2.12a, these measurements are refitted. The vertical intercept yields $\sigma_p = 8900 \pm 400$ MPa and the slope yields $H_a = 5.13 \times 10^5$ J mol^{-1}.

When extrapolating the results of creep experiments from a strain rate of 10^{-5} s^{-1} to geologic strain rates, the most significant source of uncertainty concerns the value of H_a, the activation enthalpy. Goetze (1978) summarises experimental data which suggest that $H_a = (5.23 \pm 0.63) \times 10^5$ J/mol. Subsequently, a considerable number of studies have been carried out which suggest that $H_a = (5.35 \pm 0.35) \times 10^5$ J/mol (see, e.g. Kohlstedt & Goetze, 1974; Kirby & Kronenberg, 1987; Kohlstedt *et al.*, 1995). Following Boettcher *et al.* (2007), the results of Goetze (1978) are extrapolated to geologic strain rates of 10^{-15}–10^{-12} s^{-1} (Figure 2.12b). However, this extrapolation suggests that the switch from the velocity weakening to velocity strengthening regime, which is regarded as a
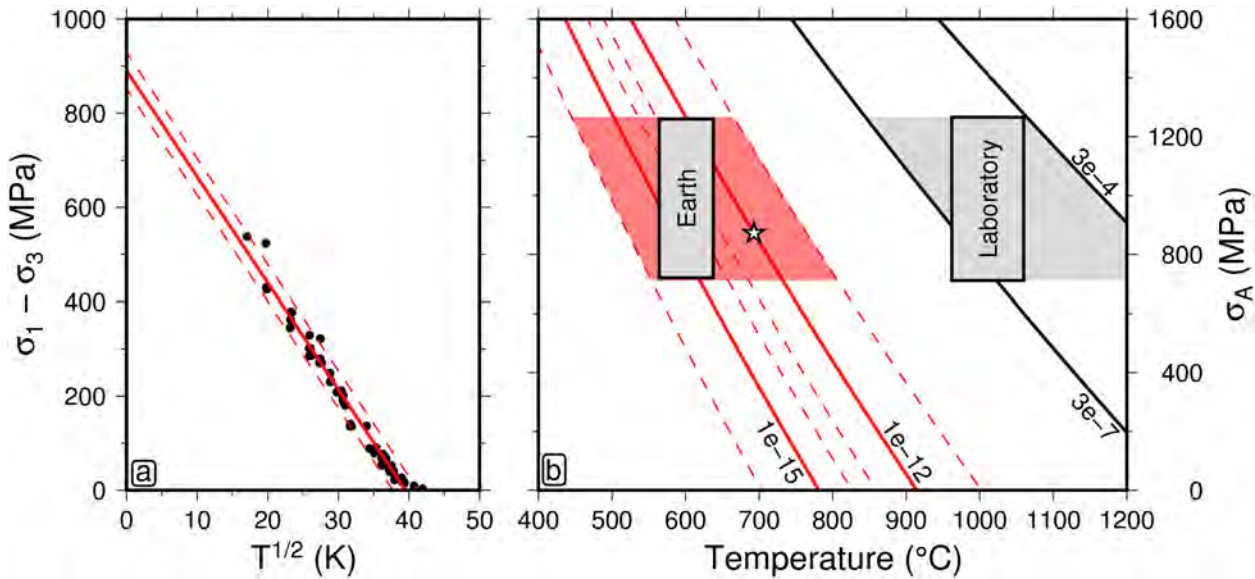
Figure 2.12: Rheologic scaling calculations. (a) Asperity stress, σ_a, plotted as function of temperature, $\sqrt{T}$ for suite of experimental measurements carried out on dry polycrystalline olivine aggregates, redigitised from Goetze (1978). Solid circles = creep measurements corrected to reference strain rate of 10^{-5} s^{-1}; solid/dashed red lines = best-fitting linear relationship $\pm 2\sigma$ uncertainty. (b) Scaling between laboratory experiments and geologic conditions redrawn from Boettcher *et al.* (2007). Labelled black lines = relationships between σ_a and T for observed (i.e. laboratory) strain rates; labelled red lines = relationships between σ_a and T for extrapolated (i.e. geologic) strain rates, pairs of red dashed lines show variations arising from uncertainty in the activation enthalpy $H_a = 540 \pm 40$ kJ mol^{-1}; labelled grey boxes = conditions at which transition from velocity-weakening to velocity strengthening behaviour occurs taken from Boettcher *et al.* (2007); grey/red polygons = range of temperature estimates for σ_a range of 800–1200 MPa; star = temperature estimate from optimal complete plate model for base of seismogenic zone (Figure 2.11c).

proxy for the seismic-aseismic transition, may occurs at temperatures as high as $700 \pm 50^\circ$C, instead of at 600°C as Boettcher *et al.* (2007) state. This revised estimate is consistent with the results shown in Figure 2.11c and with recent laboratory studies (King & Marone, 2012).

2.5.2   Lithospheric Thickness Measurements

A range of seismologic approaches have been used to estimate lithospheric thickness in the oceanic realm. Unfortunately, this topic is complicated by a variety of different definitions for this boundary, including depth to a particular velocity contour, depth at which lateral velocity variation ceases, depth of maximum negative velocity gradient, depth to which conductive cooling extends, depth at which there is a marked change in anisotropy, and depth at which attenuation peaks (e.g. Eaton *et al.*, 2009).

Body and surface wave tomographic studies have shown that lateral velocity variations as a function of age persist down to depths of ~ 150 km (Priestley & McKenzie, 2013). Steinberger & Becker (2017) determine the evolution of lithospheric thickness by defining a critical isotherm, $T_L = T_0 + \phi_L(T - T_0)$, where $T_0 = 0°$C is surface temperature, T represents the geochemically constrained mantle potential temperature of $1333°$C, and $\phi_L = 0.843$ represents an arbitrary fraction of the temperature difference corresponding to the lithosphere-asthenosphere boundary. By applying this relationship to a suite of tomographic models, the authors estimate an average depth down to the lithosphere-asthenosphere boundary beneath old oceanic lithosphere of 109 ± 22 km. These studies provide useful bounds but suffer from limited vertical resolution such that predicted lithosphere-asthenosphere boundaries determined by tomographic inversion can be highly dependent upon the starting model.

ScS reverberations, SS precursors, Sp and Ps conversions all arise from impedance contrasts at depth and so have also been used to place constraints on lithospheric thickness (Rychert *et al.*, 2012; Schmerr, 2012). Whilst these measurements have improved vertical resolution, independent information about velocity structure above the putative discontinuity is needed to adequately depth migrate events. It is also unclear whether the imaged discontinuities actually represent the lithosphere-asthenosphere boundary. One suggested alternative is that these represent frozen-in radial anisotropy related to decompression melting at the ridge axis (Auer *et al.*, 2015; Hansen *et al.*, 2016).

Deep seismic reflection and refraction surveys have also been carried out with a view to imaging the transition from a high-velocity 'lid' to a lower velocity zone (Thybo, 2006; Stern *et al.*, 2015). Results are broadly consistent with the depth of peak azimuthal anisotropy variations and shear wave gradients from Burgos *et al.* (2014), who obtained thicknesses of ~ 115 km in older ocean basins (Figure 2.11; Table 2.3). These observations have been corroborated by other seismic anisotropy studies that focussed exclusively on the Pacific shear wave velocity structure (Yuan & Romanowicz, 2010; Beghein *et al.*, 2014). Values of 90–120 km obtained by Bagley & Revenaugh (2008) and Kawakatsu *et al.* (2009) through receiver function analysis of > 100 Ma Pacific plate also fall within the range.

It is important to note that the depth to the lithosphere-asthenosphere boundary is not necessarily expected to coincide with a single isotherm as any rheologic transition is probably also dependent upon confining pressure and strain rate (Hansen *et al.*, 2016). Nevertheless, many studies have simply adopted a temperature of $1100°$C for the critical isotherm, with a realistic range of $1120 \pm$

80°C (Pollack & Chapman, 1977; Steinberger & Becker, 2017).

Isothermal surfaces calculated using half-space cooling models strongly cross-cut the seismologically determined lithospheric thicknesses at old ages. This discrepancy further suggests that half-space models are poor representations of oceanic thermal structure. As lithosphere cools and thickens over time, the temperature of the rheological transition— if it changes at all— would be expected to increase rather than decrease as a consequence of increasing confining pressure. The simple (i.e. constant parameter) plate model and the temperature-dependent model that implements the parameterisation of McKenzie et $al.$ (2005) both tend to underpredict lithospheric thickness (Figure 2.11b). However, a complete (i.e. compressible temperature- and pressure-dependent) model yields a reasonably good match with seismologically constrained estimates of the lithosphere-asthenosphere boundary. In particular, the peak change in orientation of azimuthal anisotropy observed in the Pacific Ocean appears to be strongly related to the 1200 ± 50°C isotherm (Figure 2.11c; Burgos et $al.$, 2014). This match strengthens the validity of the optimal thermal structure.

Multiple studies have suggested that the elastic thickness of the oceanic lithosphere increases as a function of age, roughly following the depth to the 300–600°C isotherm (Watts & Zhong, 2000; Watts et $al.$, 2013). By contrast, reanalysis of flexural bending at oceanic trenches found that elastic thickness correlates poorly with plate age if bending moment and load magnitude are not prescribed a $priori$ (Bry & White, 2007). The optimal plate model determined here does not significantly affect the conclusions of these previous analyses.

Table 2.3: Comparison of thermal structure and seismic constraints. T_S = seismogenic thickness-controlling isotherm; z_L = average depth at $t \geqslant 100$ of T_L isotherm where $\phi_L = 0.843$; upper and lower bounds correspond to $\phi_L = 0.9$ and $\phi_L = 0.78$, respectively. $[X]_{gchem}$ subscripts indicate values when temperature is fixed at 1333°C. Model abbreviations as in caption of Table 2.1.

Model	T_S (km)	$[T_S]_{gchem}$ (km)	z_L (km)	$[z_L]_{gchem}$ (km)
HSCk	728	653	132^{+20}_{-16}	131^{+20}_{-16}
Pk	760	658	96^{+7}_{-7}	109^{+9}_{-10}
MR*	628	607	90^{+4}_{-5}	90^{+4}_{-5}
KR	471	561	107^{+7}_{-8}	113^{+7}_{-8}
KRC	485	589	116^{+10}_{-10}	118^{+9}_{-10}
KRCCk	728	742	108^{+10}_{-10}	108^{+10}_{-10}
KRCC	693	708	108^{+10}_{-10}	109^{+9}_{-10}

2.5.3   Gravitational Response of Plate Model

Our optimal thermal structure can be used to calculate the associated isostatic gravity field generated by plate spreading, from which residual features related to flexure and mantle convection can be isolated in observed gravity fields. Here, the approach outlined by Crosby *et al.* (2006) is adopted. First, the adapted oceanic age grid of Müller *et al.* (2016) is expanded into spherical harmonic coefficients up to and including degree and order 90. Secondly, a grid of anomalous gravitational potential, $\Delta U(x, y)$, is calculated on this filtered age grid using

$$\Delta U(x, y) = -2\pi G \left[\frac{(\rho_m - \rho_w) w(x, y)^2}{2} + \int_0^{z_p} z \Delta \rho(x, y, z) dz \right], \qquad (2.19)$$

where $\Delta \rho$ is the density contrast between a vertical column of hot asthenosphere at the ridge axis and a column of cooling and thickening lithosphere away from the ridge axis, w is plate subsidence, z_p is plate thickness, $z = 0$ is at the seabed, ρ_m is mantle density at $0°$C and ρ_w is the density of water. Thirdly, the grid of $\Delta U(x, y)$ values is fitted using real spherical harmonics up to degree 120, generating a suite of coefficients C_{lm} and S_{lm} (where l is the degree and m is the order). Finally, the predicted free-air gravity field can be calculated by

$$\Delta g = -\frac{1}{R} \sum_{l=0}^{120} (l+1) \sum_{m=0}^{l} \left[C_{lm} \cos(m\lambda') + S_{lm} \sin(m\lambda') \right] \bar{P}_{lm}(\cos\theta), \qquad (2.20)$$

where $\bar{P}_{lm}$ is the normalised Legendre polynomial, λ' is longitude, θ is co-latitude and $R = 6371$ km is the Earth's radius (Figure 2.13a).

Isolating the corresponding plate cooling signal in satellite-based gravity observations is complicated by the superposition of other unrelated signals within the waveband of interest. While this complication rules out the use of gravitational predictions as a direct constraint on thermal evolution, it is encouraging that complete plate models matches large-scale features well. In particular, the general reduction of spreading rates from the Pacific, through Indian and into the Atlantic Oceans results in predictions for an increasingly large anomaly on young oceanic lithosphere that is matched by observed gravity anomalies (Figure 2.13b–2.13d). The negative gravity anomaly observed in the Pacific Ocean at ages < 70 Ma correlates with a long wavelength gravity signal, implying that negative dynamic topography near the East Pacific Rise ridge axis may be responsible for deviations away from the plate cooling signal in this part of the basin (Figure 2.13b).
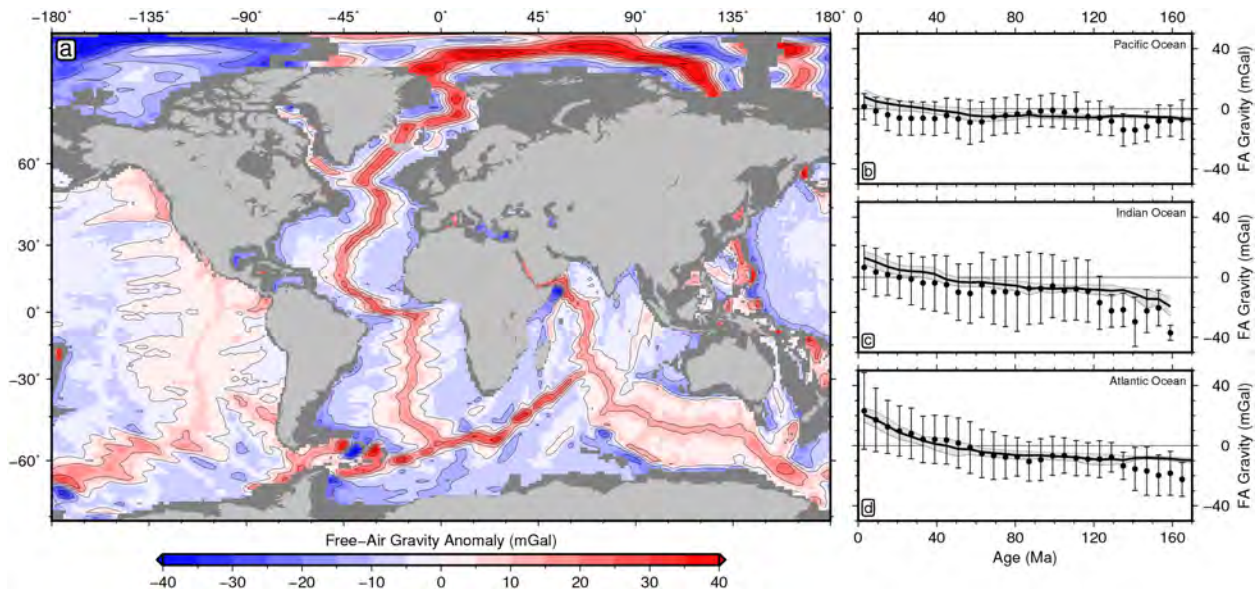
Figure 2.13: Observed and calculated gravity fields. (a) Gravity field predicted from optimal complete plate model and updated age grid; contour interval = 10 mGal. (b) Solid line/grey envelope = mean and standard deviation of predicted gravity anomalies for Pacific Ocean binned as function of plate age, excluding regions with anomalous oceanic crust determined by Crosby *et al.* (2006); solid circles with vertical bars = observed stacked gravity field (Sandwell *et al.*, 2014). (c) Same for Indian Ocean. (d) Same for Atlantic Ocean.

2.6   Comparison with Previous Results

The modelling approach adopted here differs in two respects from previously published work. First, improved and revised datasets for both subsidence and heat flow are applied to provide better constraints on physical parameters. Secondly, additional complexity is only added to models when it is required to reconcile available geophysical and geochemical datasets. Moreover, previous studies that apply temperature- and pressure-dependent parameters have either set temperature at the ridge axis or investigated a narrow range of potential temperatures (McKenzie *et al.*, 2005; Grose & Afonso, 2013; Korenaga & Korenaga, 2016). Here, ridge depth, potential temperature and plate thickness are varied over a wide range in order to identify global minima. This approach enables inconsistencies between parameter values required to fit either subsidence or heat flow observations to be identified. Other studies of oceanic plate evolution have investigated regional differences in subsidence and heat flow measurements (Parsons & Sclater, 1977; Crosby *et al.*, 2006). Since the principal aim is to constrain the thermal structure that best represents globally averaged behaviour and since there is substantial sampling bias between basins, inter-basin variation has not been investigated here.

As thermal models have become more physically realistic, it is generally true that the discrepancies between best-fitting parameters required to individually fit subsidence and heat flow observations have reduced (Tables 2.1, 2.2 & 2.4). This result suggests that temperature- and pressure-dependent parameterisations of thermal properties based on laboratory experiments are valid and scalable.

It has been suggested in previous studies that experimentally determined thermal expansivity values may lead to overestimates of thermal contraction in the real Earth, giving rise to underestimates of potential temperature using the approach adopted here (Pollack, 1980; Korenaga, 2007a; Grose, 2012). However, it should be noted that the model with the best fit has $T = 1304°C$, close to independent constraints of $T = 1333°C$. This geochemically constrained potential temperature becomes the best-fitting model if thermal expansivity is reduced by $\sim 1\%$, well within the $\pm 0.3 \times 10^{-5} \ K^{-1}$ experimental uncertainty bounds (Bouhifd *et al.*, 1996). Consequently, it may not be necessary to appeal to incomplete thermal relaxation or to differences in mineral assemblage in order to account for the apparent expansivity deficit (cf. Korenaga, 2007b; Grose & Afonso, 2013).

Although potentially significant, the effects of phase changes during thermal evolution is harder to assess with any degree of confidence since experimental constraints on thermal expansivity, heat capacity and conductivity at relevant P-T conditions are poorly constrained for many mineral constituents (Schutt & Lesher, 2006). The P-T conditions at phase changes and the associated density transformations are also dependent upon composition, volatile content and oxidation state, all of which are uncertain (Jennings & Holland, 2015). Consequently, implementation of age-dependent phase changes introduces additional, unwarranted, degrees of freedom that are not required by the current observations. Korenaga & Korenaga (2016) have used the pMELTS algorithm to determine the effects of melt extraction and phase changes on equilibrium mineral assemblages, but much of the thermodynamic database relies upon parameter estimations or upon extrapolation of temperature and pressure derivatives that depart considerably from experimental constraints (Berman, 1988; Ghiorso *et al.*, 2002; Ueki & Iwamori, 2013). Although their approximation of the temperature and pressure dependence for C_P and k_{rad} yield improved results compared with Grose & Afonso (2013), the inferred increase in subsidence rate of $\sim 80 \ m \ Myr^{-1}$ at ~ 20 Ma attributed to the spinel-garnet transition has not been identified within subsidence observations. Improved understanding and additional constraints are clearly required relating to the P-T-X conditions and density changes associated with this transformation. Should this significant increase in inferred subsidence rate be confirmed with observations, the effective thermal expansivity must be significantly lower than experimental predictions and incomplete thermal relaxation could then be

invoked to address the discrepancy (Korenaga, 2007b).

A significant difference between the temperature- and pressure-dependent plate model proposed here and previous efforts is that the equilibrated plate thickness is greater and neither expansivity nor conductivity have been artificially adjusted. A larger plate thickness reflects both the relatively smaller thermal contraction encountered close to the base of the plate due to an increase in confining pressure and the insulating effect of low conductivity oceanic crust, which reduces the rate of heat extraction. It is this latter effect that leads to lower potential temperatures compared with only temperature-dependent models with no crustal layer (e.g. McKenzie *et al.*, 2005). The larger plate thickness retrieved using a compressible model is more consistent with existing seismological constraints (Figure 2.11; Goutorbe, 2010; Burgos *et al.*, 2014; Steinberger & Becker, 2017). In general, inclusion of more physically realistic model parameters tends to result in an improved fit to the available independent geophysical and geochemical constraints. This behaviour suggests that the complete plate model represents a good approximation of average oceanic lithospheric thermal structure as a function of age.

Table 2.4: Summary of previously published model results. PS77 = Parsons & Sclater (1977); SS92 = Stein & Stein (1992); MJP05 = McKenzie *et al.* (2005); GA13 = Grose & Afonso (2013); KK16 = Korenaga & Korenaga (2016); KKRC = complete plate model. * Fit is only calculated up to 100 Ma as model prediction is truncated at this age–other misfit calculations are carried out up to 170 Ma.

Model	χ_s (m)	χ_h (W m^{-2})	χ_t
PS77	0.965	1.263	1.124
SS92	1.029	0.505	0.810
MJP05	0.951	0.772	0.866
GA13	0.965	0.644	0.820
KK16*	1.432	0.444	1.060
KRCC	0.927	0.441	0.726

The complete plate model can also be used to investigate the Earth's heat budget. Total surface heat flow is estimated at 46 ± 3 TW, of which $Q = 29.7 \pm 1.3$ TW conducts out of the oceanic plates estimated from previous cooling models (Pollack *et al.*, 1993; Jaupart & Mareschal, 2007; Lay & Buffett, 2008; Davies & Davies, 2010; Hasterok, 2013). Updating the value of Q is straightforward

by combining the oceanic age grid with the expression

$$Q = \int_0^t H(t) \frac{dA}{dt} dt, \qquad (2.21)$$

where A is total seafloor area of a given age, t, and $H(t)$ is the predicted surface heat flow for that age.

The optimal plate model yields a total oceanic heat flux of $Q = 27.5$ TW, increasing to $Q = 28.0$ TW when mantle potential temperature is fixed at $1333°$C (Table 2.1). These values are $\sim 7\%$ lower than previous estimates. The optimal plate model with no P-T dependence or oceanic crust gives values of ~ 29.9 TW. Total heat flow therefore decreases by ~ 2 TW when P-T dependence and a lower conductivity crustal layer are included, giving rise to a similar overall heat flux but at reduced potential temperatures. However, the new reduced value of $Q \approx 28$ TW is difficult to independently confirm in the absence of a comprehensive global heat flow database free from hydrothermal circulation and sediment blanketing effects. The integrated basal heat flow into the base of oceanic lithosphere is 4.7 TW for the complete plate model, suggesting that $> 15\%$ of surface heat flow is provided by resupply of heat beneath older oceanic plates away from the passive upwelling zone beneath the ridge axis.

2.7   Summary

By fitting a range of increasingly sophisticated thermal models to a combined database of oceanic basement depths and corrected heat flow measurements, the optimal temperature structure of oceanic lithospheric plates has been identified. This model is then evaluated in the context of seismologic and petrologic constraints for plate thickness, melt generation and rheologic structure. Half-space cooling models consistently yield poor quality fits to the combined database for plate ages of >100 Ma. As more physically realistic parameters are incorporated into the plate model, residual misfit progressively reduces and, significantly, potential temperature and plate thickness estimates converge upon independently determined values when compositional dependence, temperature dependence, pressure dependence and compressibility are progressively included. This improvement underlines the applicability and scalability of experimental datasets.

The complete plate model also provides good visual fits to variations in the gravitational field as a function of plate age. The optimal plate model yields a potential temperature of $1304 \pm 60°$C

and a plate thickness of 135 ± 30 km. This potential temperature is similar to that required to generate an average thickness oceanic crust from an anhydrous peridotite source (Katz *et al.*, 2003; McKenzie *et al.*, 2005; Shorttle *et al.*, 2014).

The optimal model predicts that the integrated oceanic heat flow is $\sim$ 28 TW, which is slightly lower than previous estimates, and that the base of the seismogenic zone is controlled by the 700°C, rather than the 600°C, isothermal surface. The largest contribution to these differences and the reason for an improved fit to observational constraints is the insulating effect of the low conductivity oceanic crust. A corollary of this proposed model is that calculated residual depth anomalies are probably more secure. Furthermore, empirical calibration of shear wave velocity and temperature can be refined (see Chapter 5).

Chapter 3

Global Residual Depth Measurements

The bulk of topography on Earth is generated by changes in the thickness and density of the lithosphere (Airy, 1855; Pratt, 1855). The dominance of this isostatic signal means that accurate determination of dynamic topography relies on the extent to which crustal and lithospheric thickness and density structure can be constrained (Hager *et al.*, 1985; Flament *et al.*, 2013). The protracted tectonic history of the continents has resulted in complex density and thickness variations that make it difficult to place constraints on the amplitude of isostatically generated topography. However, the structure of oceanic lithosphere is substantially simpler and better understood (Oxburgh & Parmentier, 1977; Turcotte & Schubert, 2002). Away from oceanic plateaux and seamounts, oceanic crustal thickness is relatively uniform in density and thickness (7.1 ± 0.8 km), while the density and thickness of the oceanic lithosphere evolves according to conductive cooling in a predictable manner (Parsons & Sclater, 1977; White *et al.*, 1992). Thus, provided that variations in the thickness and density of sediment and oceanic crust are well constrained, the isostatic component of topography can be calculated and subtracted to determine residual depth anomalies. These residual depth anomalies, where distant from locations subject to plate flexure, can be related to sub-crustal density anomalies and provide an useful bound on the amplitude of dynamic topography.

The study of these bathymetric deviations has a long history. Menard (1973) originated the term 'residual depth anomalies' and compiled the first map of Pacific observations. Cochran & Talwani (1977) and Crough & Jarrard (1981) then expanded this analysis throughout the oceans, finding large (> 500 m) positive anomalies associated with the Hawaii, Rio Grande Rise, Kerguelen, Azores and North Atlantic regions. ~ -1 km negative anomalies were identified across the East Pacific Rise and the Australian-Antarctic Discordance. Since constraints for sediment thickness were generally unavailable, notably close to continental margins, these initial studies focussed on regions in the centre of ocean basins where sediment thicknesses are assumed to be minimal. Sediment density was also assumed to be constant and an attempt was made to correct for anomalous crustal thickness.

Isostatic corrections in thickly sedimented regions were improved by applying simple compaction laws to better determine the depth-dependent variation of sediment density and seismic velocity (Le Douaran & Parsons, 1982; Crough, 1983). Residual depth anomalies were then recalculated, verifying the existence of ± 1 km variation on wavelengths of $\sim 1{,}000$–$2{,}500$ km (Cazenave *et al.*, 1988). Up to this point, crustal thickness variation had largely been ignored. Crosby *et al.* (2006) attempted to address the crustal issue by excising regions of anomalously thick crust using gravity and topography signatures but made no explicit correction for crustal thickness elsewhere.

Since the first residual depth anomalies were measured, the quantity and quality of oceanic seismic reflection datasets has dramatically increased. These data, principally acquired by the hydrocarbon industry, allow for clear delineation of the seabed, sediment-basement interface and Moho across large areas of oceanic basins. Winterbourne *et al.* (2009, 2014) exploited this seismic database to build a compilation of spot measurements of residual depth that correct for variable sedimentary and crustal thickness. Finally, Hoggard *et al.* (2017) refined calibrations between seismic velocity, density and thickness of sediment and oceanic crust, while expanding the residual depth dataset of Winterbourne *et al.* (2014). This latest study represents the best constraint to date on present-day residual depths.

In this chapter, the existing database of residual depth anomalies is augmented, streamlined and revised. First, the methodology for calculating residual depth anomalies is revisited and the impact of using different age-depth subsidence models is assessed. Next, water-loaded basement depths are corrected using age-depth subsidence predicted by the complete thermal model of oceanic lithosphere developed in Chapter 2. 123 additional residual depth measurements are added to the pre-existing database that fill significant gaps within the Gulf of Mexico, and along the South American and African margins. These additional data points are analysed together with the existing database to place constraints on regional dynamic topography. The global residual depth data is then combined with shiptrack bathymetry offshore and scaled long wavelength free-air gravity anomalies onshore to create an updated observation-based estimate of present-day dynamic topography. Finally, a globally continuous spherical harmonic representation of this revised database is generated and compared with previously published results.

3.1   Residual Depth Measurements

∼200 new seismic reflection profiles, generously provided by Spectrum Geo Ltd., were analysed to identify *bona fide* oceanic crust and sections with clearly imaged sediment-basement and Moho interfaces. 123 seismic profiles were identified that met these criteria. Seabed and sediment-basement interfaces are picked on all these profiles. The Moho is also interpreted where imaging quality permits unambiguous identification of this interface (Figure 3.1). The locations and interpretations of these profiles are given in Table A.1.
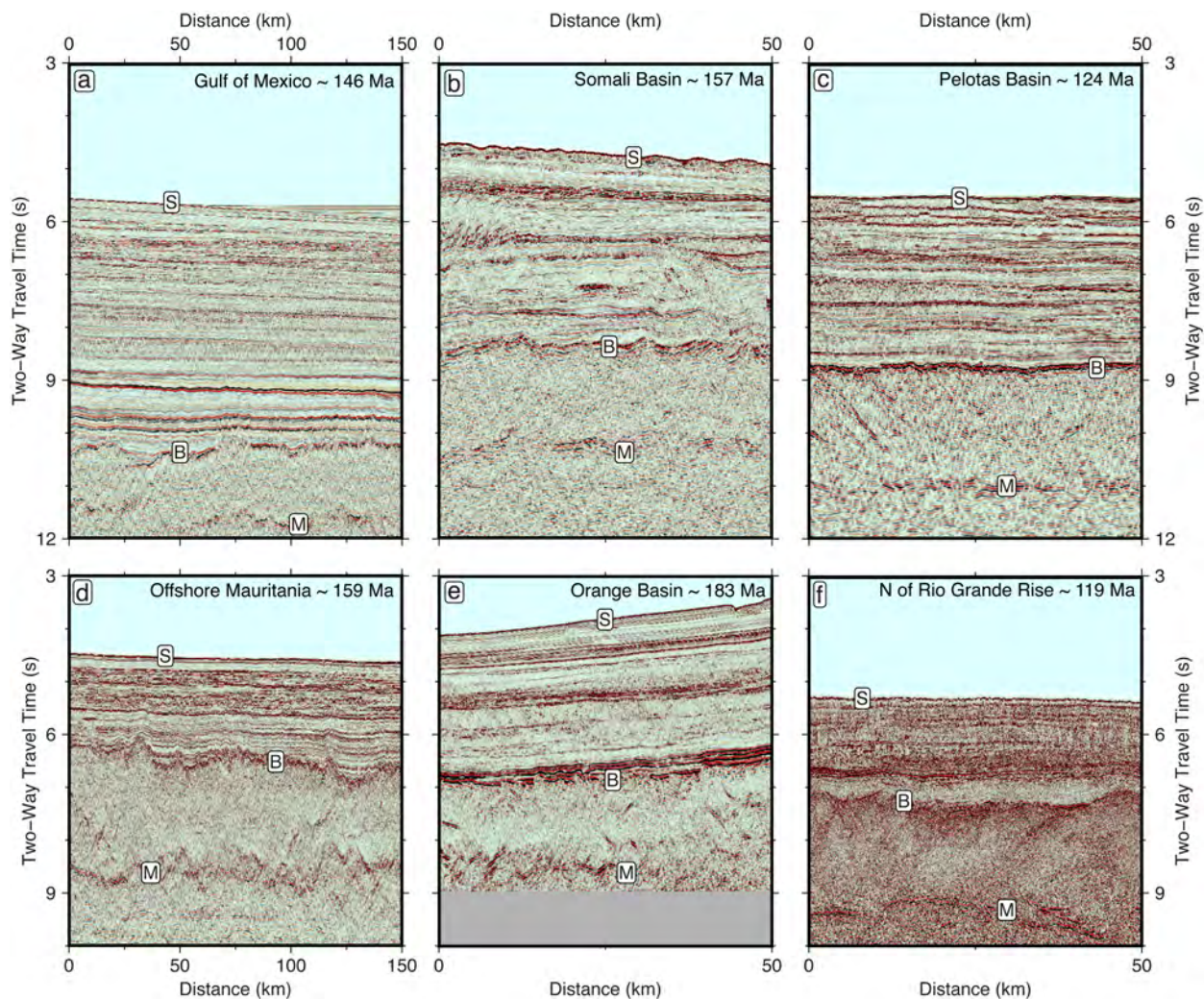
Figure 3.1: Seismic reflection profiles on old ocean floor. (a) Seismic reflection profile of ∼ 146 Ma oceanic crust from southern Gulf of Mexico. S = seabed; B = sediment-basement interface; M = Moho (i.e. base of crust). (b) Southern Somali Basin (∼ 157 Ma). (c) Pelotas Basin (∼ 124 Ma). (d) Offshore Mauritania (∼ 159 Ma). (e) Orange Basin (∼ 183 Ma). (f) North of Rio Grande Rise (∼ 119 Ma). Crustal ages from adapted magnetic reversal history grid of (Müller *et al.*, 2016). Locations shown in Figures 3.4–3.10. Seismic data courtesy of Spectrum Geo Ltd. and shown with permission.
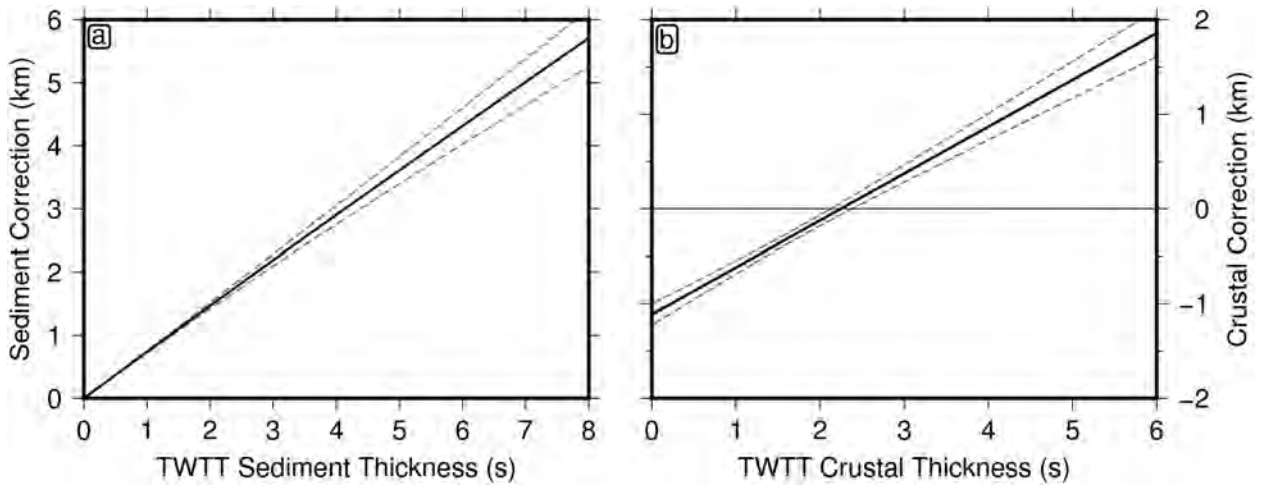
Figure 3.2: Sediment and crustal corrections. (a) Isostatic correction for sediment loading. Solid/dashed line = sedimentary correction plotted as function of sediment thickness in two-way travel time (TWTT) with $\pm 1\sigma$ standard deviation. Standard deviation includes uncertainties in all input parameters in Equation 3.1. (b) Isostatic correction for crustal thickness variation. Solid/dashed line = crustal correction plotted as function of crustal thickness in TWTT with 1σ standard deviation arising from uncertainties in velocity and density.

Variable thicknesses of sediment and crustal layers in two-way travel time were converted to an equivalent water load using the method outlined in Czarnota *et al.* (2013) and Hoggard *et al.* (2017) to determine water-loaded basement depth along each section. The sedimentary correction is calculated as a function of sediment thickness, z_s, using

$$C_s = \left(\frac{\rho_a - \overline{\rho_s}}{\rho_a - \rho_w} \right) z_s \tag{3.1}$$

where ρ_a is the density of the asthenosphere (3.20 ± 0.02 Mg m^{-3}), ρ_w is the density of water (1.03 ± 0.01 Mg m^{-3}) and $\overline{\rho_s}$ is the average density of the sedimentary column (Figure 3.2a). Seismic reflection profiles are acquired as a function of two-way travel time (TWTT) and so a velocity model is applied to convert these values into true thicknesses, z_s. There are 43 locations in the global database in which seismic reflection and seismic refraction profiles intersect, yielding a set of data points for which sediment thickness is known in both TWTT and depth. A velocity model can therefore be calibrated by fitting the 43 tie points with a parameterisation that accounts for compaction using the expression

$$\frac{t_s}{2} = \frac{z}{v_{sg}} + \phi_\circ \lambda_c \left(\frac{1}{v_w} - \frac{1}{v_{sg}} \right) \left[1 - \exp\left(\frac{-z}{\lambda_c} \right) \right], \tag{3.2}$$

where t_s is sediment thickness in TWTT, v_{sg} is the solid grain acoustic velocity (5.5 ± 0.5 km s^{-1}),

v_w is the acoustic velocity of water (1.5 ± 0.01 km s^{-1}), $\phi_\circ$ is the initial porosity and λ_c is the compaction decay length (Christensen, 1982). Optimal values of $\phi_\circ$, λ_c and v_{sg} are determined by performing a parameter sweep to find values that minimise the RMS misfit between the calculated and observed time-depth relationship. The smallest RMS misfit is obtained when $v_{sg} = 5.5$ km s^{-1}, $\phi_\circ = 0.61$ and $\lambda_c = 3.9$ km. These parameters can then be used to calculate $\overline{\rho_s}$ as a function depth using

$$\overline{\rho_s}(z) = \rho_{sg} + \frac{\phi_\circ \lambda_c}{z}(\rho_w - \rho_{sg})\left[1 - \exp\left(\frac{-z}{\lambda_c}\right)\right] \tag{3.3}$$

where ρ_{sg} is the density of solid grains (2.65 ± 0.5 Mg m^{-3}; Athy, 1930). Czarnota et $al.$ (2013) and Hoggard et $al.$ (2017) carefully propagated uncertainties in velocity, density and compaction parameters through the calculations to determine characteristic errors. Error is $< \pm 100$ m for sediment thicknesses below 3 km but progressively increases as a function of thickness to $\sim \pm 250$ m at sediment thicknesses of 5 km. Sediment thickness varies considerably throughout the oceanic realm (0–12 km), yielding sedimentary corrections of comparable magnitude (Figure 3.2a; Whittaker et $al.$, 2013). Accurately determining the sedimentary correction, as outlined above, is therefore of importance when constraining residual depth anomalies.

Variations in oceanic crustal thickness also contribute to deviations in water-loaded basement depth. This variability is accounted for through isostatic replacement of crustal thicknesses that differ from the global average of 7.1 km with an equivalent water load (White et $al.$, 1992). The crustal correction is given by

$$C_c = \left(\frac{\rho_a - \overline{\rho_c}}{\rho_a - \rho_w}\right)(z_c - 7.1km) \tag{3.4}$$

where z_c and $\overline{\rho_c}$ (2.86 ± 0.03 Mg m^{-3}) are the thickness and average density of oceanic crust, respectively (Carlson & Herrick, 1990). Crustal thickness in TWTT, t_c, is converted into true thickness, z_c, using the bulk velocity, $\overline{v_c} = 6.28 \pm 0.34$ km s^{-1}, determined from waveform modelling of modern wide-angle seismic experiments (Hoggard et $al.$, 2017). The crustal correction rarely exceeds 200 m and is thus of secondary importance to the sedimentary correction when calculating oceanic residual depths (Figure 3.2b).

Isostatic corrections for variation in sediment and crustal thickness have been applied to 123 interpreted sections of the seismic profiles assembled here (Appendix A). Isostatically corrected basement depths are then averaged over 1° bins and assigned ages to according to the revised grid of Müller et $al.$ (2016), yielding 123 water-loaded basement depth measurements. These additional data points were combined with the existing dataset of Hoggard et $al.$ (2017) in Chapter 2 to create

an accurate global database that places important constraints on the rate and extent of conductive cooling of the oceanic lithosphere.

Cooling and thickening of oceanic lithosphere plays the dominant role in the temporal evolution of bathymetry. As a result, this background behaviour is removed from the water-loaded basement depth measurements to isolate residual depth anomalies. Hoggard *et al.* (2016) have shown that the amplitude and wavelength of these residual depth anomalies do not strongly rely upon the exact reference model. Nevertheless, it is instructive to examine the extent to which residual depth measurements are influenced by the different thermal models tested in Chapter 2. Oceanic residual topography anomalies calculated using the half-space cooling model have a mean value that is offset from zero and a large amount of variance (Figure 3.3a & d). Residual depths calculated with simple analytical plate models are skewed towards low residual depths since hot basal temperatures are required to simultaneously fit heat flow measurements (cf. Stein & Stein, 1992; Figure 3.3b & e). These hotter temperatures cause subsidence to 'flatten' at shallower depths, causing residual depth measurements on old seafloor to exhibit a negative skew. By contrast, anomalies measured using the complete plate model are symmetrical about zero irrespective of plate age, with minimal skewness where one standard deviation is ± 0.65 km (Figure 3.3c & f). The pattern, amplitude and wavelength of residual depth anomalies is similar to that calculated by Hoggard *et al.* (2017).

Some previous residual depth studies used the half-space cooling model as a reference model, leading to significant amplitudes of residual topography at older ages (Cazenave & Lago, 1991; Lithgow-Bertelloni & Silver, 1998; Korenaga & Korenaga, 2008). As has been demonstrated in Chapter 2, this model fails to adequately characterise the average thermal structure of oceanic lithosphere and is unable to fit known independent geophysical and geochemical constraints. The seafloor 'flattening' that causes observed subsidence to deviate from half-space cooling predictions is a general feature of old oceanic lithosphere, although the mechanism responsible is subject to debate (Parsons & Sclater, 1977; Morgan & Smith, 1992; Hillier & Watts, 2005; Korenaga & Korenaga, 2008; Hillier, 2010; Korenaga, 2015).

Marty & Cazenave (1989) suggested that, rather than recording the maximum amplitude of convectively maintained topography, residual topographic anomalies may instead represent 'frozen-in' thermal anomalies that were present at the ridge axis when lithosphere was initially generated. To test this hypothesis, thermal models are calculated for plate thicknesses of 80–150 km using a range of axial temperature anomalies that are compatible with geochemically inferred limits (i.e. 1315–1550°C; Dalton *et al.*, 2014). Initial basal temperature is fixed through time and resulting
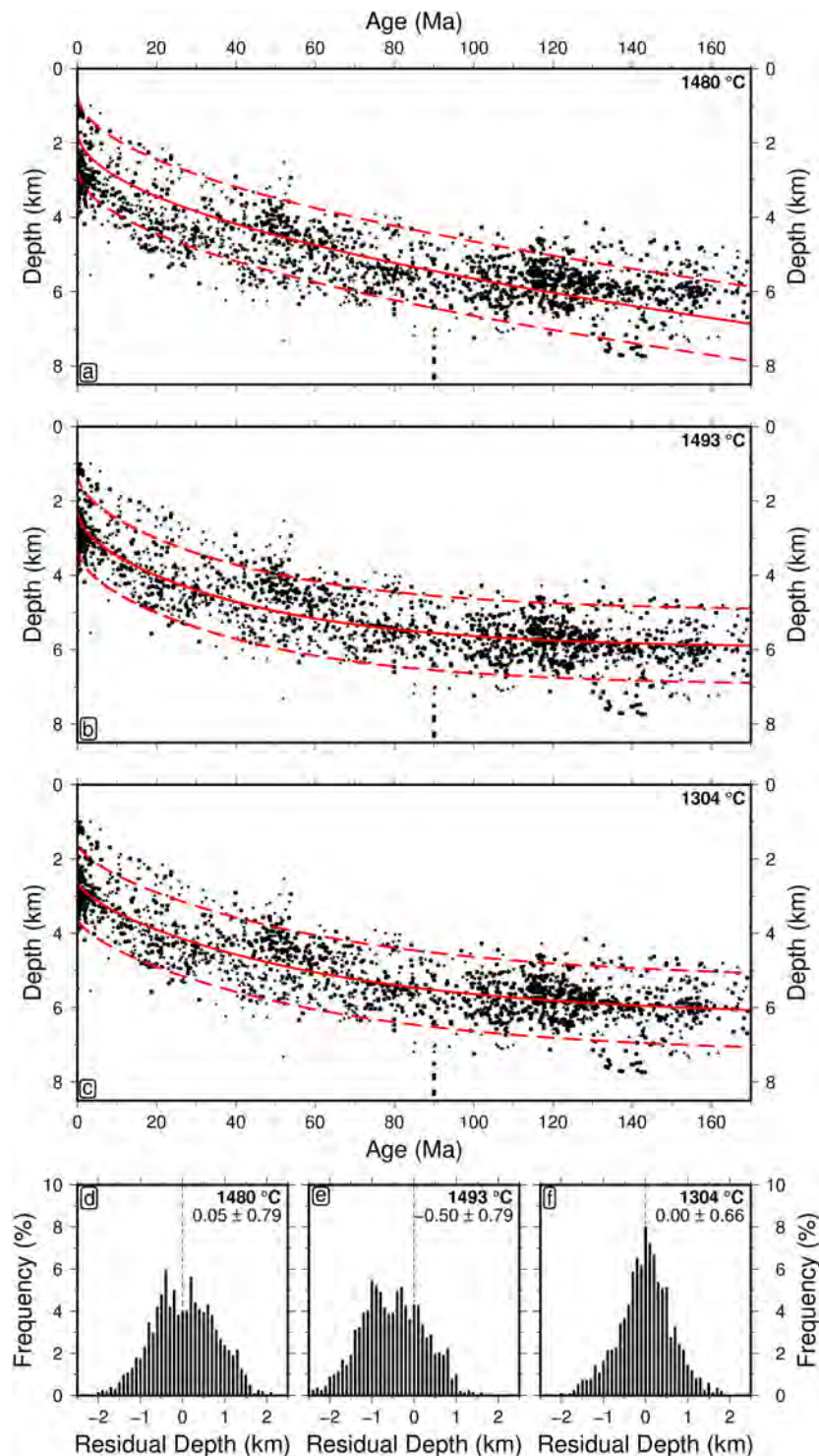
Figure 3.3: Residual depth anomalies. (a) Water-loaded depth to oceanic basement observations plotted as function of plate age (Figure 2.2d); solid/dashed red lines = optimal age-depth relationship ±1 km from half-space cooling obtained for joint fit of subsidence and heat flow observations which has axial temperature of 1480°C. (b) Same for simple analytical plate model which has axial/basal temperature of 1493°C. (c) Same for complete plate model which has potential temperature of 1304°C. (d) Histogram of residual depth anomalies with respect to half-space cooling model shown in panel (a). Mean and standard deviation in top right-hand corner. (e) Same with respect to simple plate model shown in panel (b). (f) Same with respect to complete plate model shown in panel (c).

subsidence patterns are compared. This suite of models show that mean and maximum differences in predicted subsidence are 280–430 m and 300–530 m, respectively. An average amplitude of ± 175 m in these severe tests suggests that putative ridge-generated thermal anomalies are unlikely to be the primary cause of residual depth anomalies. A lack of symmetric distributions of residual topography and gravity anomalies either side of spreading centres, combined with stratigraphic evidence for the vertical mobility of these features through time, point to sub-lithospheric convective processes as the most plausible driving mechanism (e.g. Czarnota *et al.*, 2013; Hoggard *et al.*, 2017).

Recent studies of residual depth anomalies have exploited the reference model of Crosby & McKenzie (2009), which is based on direct observations of ocean floor subsidence (Winterbourne *et al.*, 2014; Hoggard *et al.*, 2016, 2017). This empirical analysis used long wavelength free-air gravity anomalies to delineate and remove areas significantly affected by dynamic topography (Crosby *et al.*, 2006). Oceanic plateaux and regions of thin crust identified in gravity and bathymetry data were also manually excised to remove isostatic signals related to crustal thickness variation. In contrast to thermal models, the resulting age-depth subsidence relationship exhibits a convex-up shape between 73 Ma and 156 Ma. This excursion probably represents the onset of Rayleigh-Taylor instability at the lithosphere-asthenosphere boundary. As dynamic topography is defined here as time-dependent deviations in surface elevation generated by mantle convection, the bathymetric anomaly caused by this small-scale convection should be considered as a dynamic contribution. Thus, instead of applying the Crosby & McKenzie (2009) age-depth relationship, residual depth anomalies are calculated by subtracting the age-depth subsidence predicted by an optimal plate model (see Chapter 2) from global water-loaded basement depth measurements.

The resultant residual depth anomaly database provides important constraints on the amplitude of dynamic topography throughout the oceanic realm. 123 of the 2,030 residual depth anomaly measurements are new and provide useful data coverage in a number of areas that were originally poorly sampled. Here, these residual depth anomalies are examined within a regional context.

3.1.1   Gulf of Mexico & Caribbean Sea

The oceanic crust in the Gulf of Mexico probably formed at a Jurassic spreading centre (Buffler & Sawyer, 1985). Rifting occurred in response to the anti-clockwise rotation of the Yucatan block away from the Louisiana margin along a transform fault running north-south along the western

edge of the basin (Ross & Scotese, 1988; Schouten & Klitgord, 1994; Le Roy *et al.*, 2008). 20 residual depth measurements have been added to the southern Gulf of Mexico, 17 of which have been corrected for both sediment thickness and crustal thickness variation (Figure 3.1a & 3.4b).
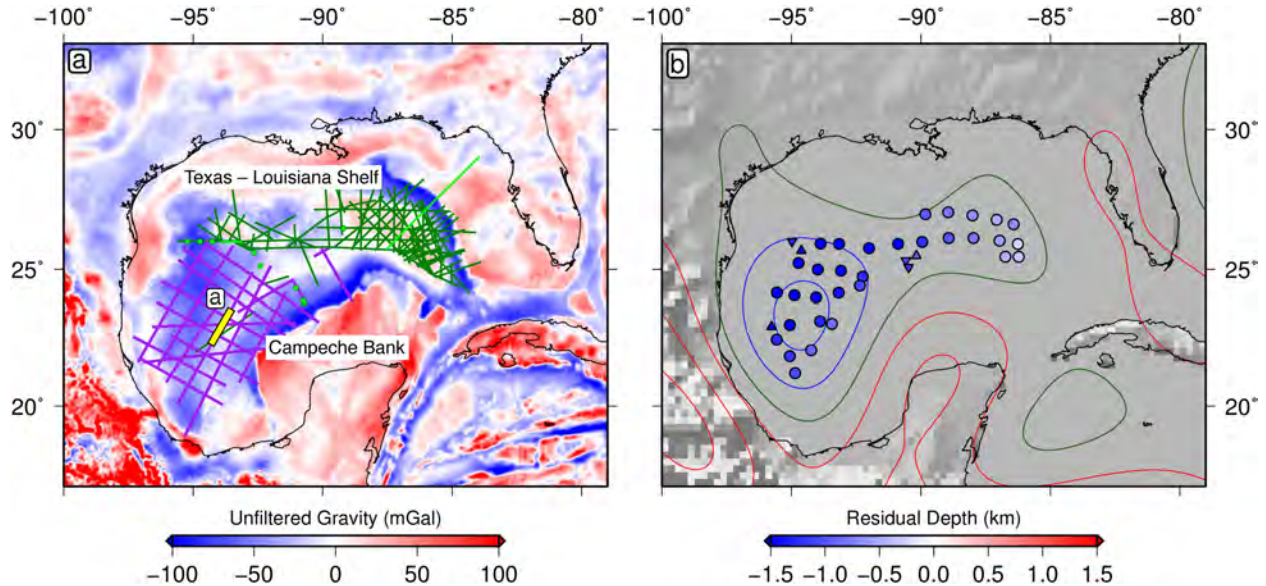
Figure 3.4: Seismic profile locations and residual depth measurements in the Gulf of Mexico. (a) Location map. Dark green lines = pre-existing seismic reflection profiles; light green lines = pre-existing seismic wide-angle and refraction data; light green circles = vintage slope-intercept experiments; purple = new seismic reflection profiles; yellow bar = location of seismic profile in Figure 3.1a. (b) Residual depth map. Circles = measurements with crustal and sedimentary correction; upward/downward pointing triangles = measurements with sedimentary correction, direction of arrow indicates whether estimate is an upper or lower bound. Long wavelength free-air gravity anomaly (1,000 km $\geqslant$ λ $\geqslant$ 5,000 km) is contoured at 25 mGal intervals; red = positive; blue = negative; green = neutral.

Calculated residual depth anomalies reveal the southern Gulf of Mexico to be amongst the most drawn down regions on Earth with values ranging from -1.8 km in the southwestern Gulf of Mexico to -0.3 km along the eastern edge of the basin (Figure 3.4b). The $\sim$ 1.5 m km^{-1} gradient in dynamic topography shown by this pattern is amongst the steepest observed globally and spatially correlates with long wavelength gravity anomalies (Figure 3.4b). The short wavelength dynamic topographic variation combined with the positive correlation between gravity and residual depth suggest that the density anomalies responsible for the observed gradient are located in the shallow mantle (Colli *et al.*, 2016).

The timing of drawdown responsible for anomalously deep basement depths in the Gulf of Mexico is the subject of debate. Miocene destabilisation of Jurassic salt layers around the Texas-Lousiana shelf has been attributed to tilting of the continental margin and may be linked to the deepening

of the Gulf of Mexico further offshore (Peel *et al.*, 1995; Rowan *et al.*, 2004). However, there is also stratigraphic evidence for an earlier phase of drawdown commencing at the Paleocene-Eocene boundary (Cossey *et al.*, 2016). Geodynamic modelling studies also suggest that rapid downwelling may have initiated around ~ 50 Ma due to the subduction and ensuing eclogitisation of the Hess Rise conjugate, an anomalously thick oceanic plateau (Wang *et al.*, 2017). The uncertainties concerning this timing may be resolved through stratigraphic analysis along the southern margin of the basin since the effects of halokinesis are largely absent, rendering interpretation of recorded changes in palaeo-water depth and accommodation space less ambiguous.

Outside of the Gulf of Mexico, two residual depth points were added in the Atlantic Ocean off the east coast of Barbados with an average residual depth of +300 m. Although observations are sparse in this region, preventing accurate delineation of trends, measurement of positive residual topography in close proximity to the Lesser Antilles subduction zone suggests that long wavelength downwelling associated with slab sinking may be locally counteracted here by positive thermal anomalies behind the slab. However, the relative proximity of the data points to the Lesser Antilles trench (~ 300 km) makes it difficult to rule out a flexural contribution to these anomalies without independent constraint on the elastic thickness of the subducting lithosphere.

3.1.2 South American Margin

19 seismic reflection profiles have been assembled from the Foz do Amazonas and Pará Maranhão Basins. This region extends from the northwestern edge of the Amazon Fan southeastwards onto the Demarara Abyssal Plain and is obliquely cross-cut by east-west trending fracture zones that developed during the opening of the Central Atlantic Ocean from ~ 120 Ma onwards (Figure 3.5a). The residual depth measurements calculated in this region show a northwest-southeast gradient in dynamic topography from lows of ~ -1.5 km in the northern Foz do Amazonas basin to highs approaching 500 m at the boundary between the Demerara and Pernambuco Abyssal Plains (Figure 3.5b).

A positive long wavelength gravity anomaly coincides with the elevated residual depths around the Eastern Cape of Brazil (Figure 3.5b). This bathymetric anomaly is fringed by emergent Miocene coastal deposits and marine terraces of Pleistocene and Holocene age (Barreto *et al.*, 2002; Rossetti *et al.*, 2013; Rodríguez Tribaldos *et al.*, 2017). The short wavelength of this topographic anomaly and its clear positive correlation with the long wavelength gravity point to an upper mantle origin for the thermal anomaly responsible.
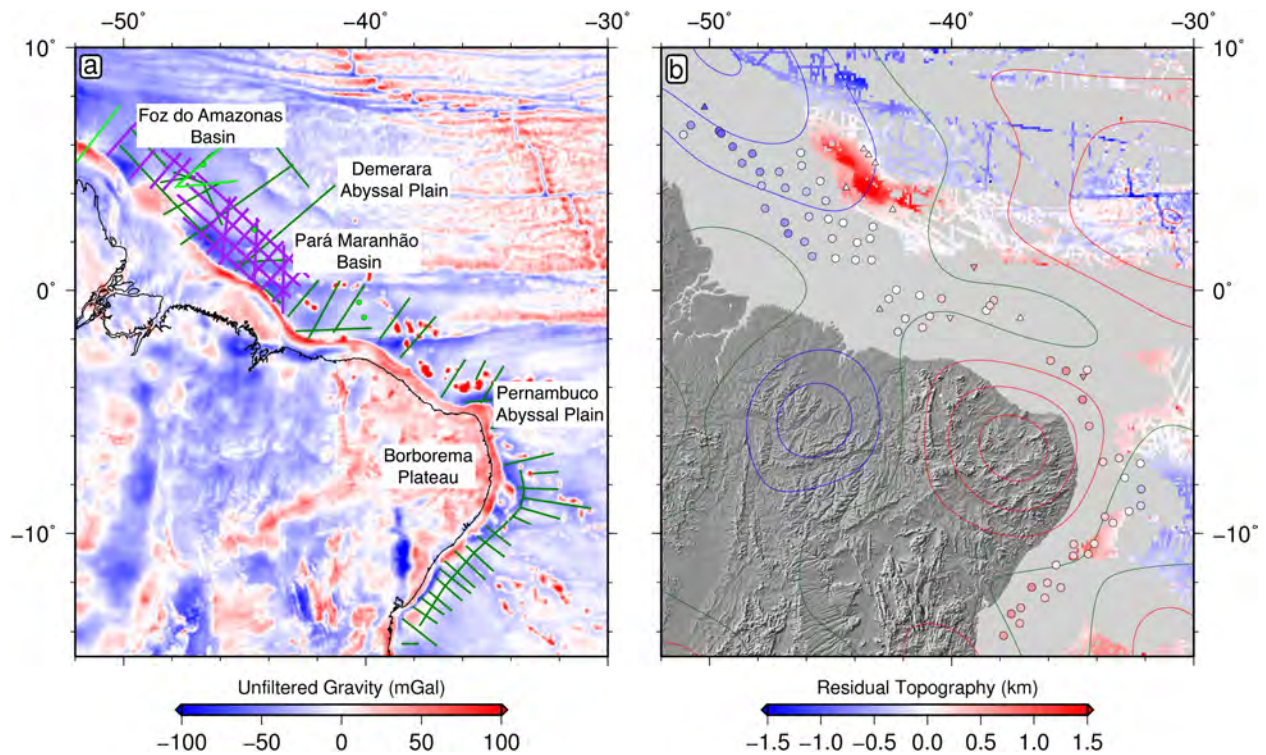
Figure 3.5: Seismic profile locations and residual depth measurements offshore north-eastern Brazil. (a) Location map. Dark green lines = pre-existing seismic reflection profiles; light green lines = pre-existing seismic wide-angle and refraction data; light green circles = vintage slope-intercept experiments; purple = new seismic reflection profiles. (b) Residual depth map. Circles = measurements with crustal and sedimentary correction; upward/downward pointing triangles = measurements with sedimentary correction, direction of arrow indicates whether estimate is an upper or lower bound; filigree = residual measurements from ship-track bathymetry where sedimentary correction is made using Whittaker *et al.* (2013) sediment thickness dataset and regions affected by plate flexure or anomalous crustal thickness are excluded using polygons of Hoggard *et al.* (2017). Long wavelength free-air gravity anomaly (1,000 km $\geqslant \lambda \geqslant$ 5,000 km) is contoured at 25 mGal intervals; red = positive; blue = negative; green = neutral.

Although residual depth anomalies had previously been calculated in the Rio Grande Rise area by Hoggard *et al.* (2016), available seismic profiles did not clearly image the base of the oceanic crust. The seismic reflection profiles analysed here clearly image the Moho, significantly improving constraint on the substantial crustal thickness variation in this area and yielding 9 residual depth measurements (Figure 3.1f & 3.6a).

Residual topography is elevated by ∼ 750 m across the Rio Grande Rise. However, the long wavelength gravity anomaly anti-correlates with residual depth (Figure 3.6b). This discrepancy could imply that oceanic lithosphere beneath the region is heavily depleted giving rise to a mass deficit that is expressed as a gravity low and topography high (O'Connor & Duncan, 1990). However, the lack of correlation may also reflect the differing depth sensitivities of gravity anomalies and

dynamic topography to density structure in the convecting mantle (Hager *et al.*, 1985).
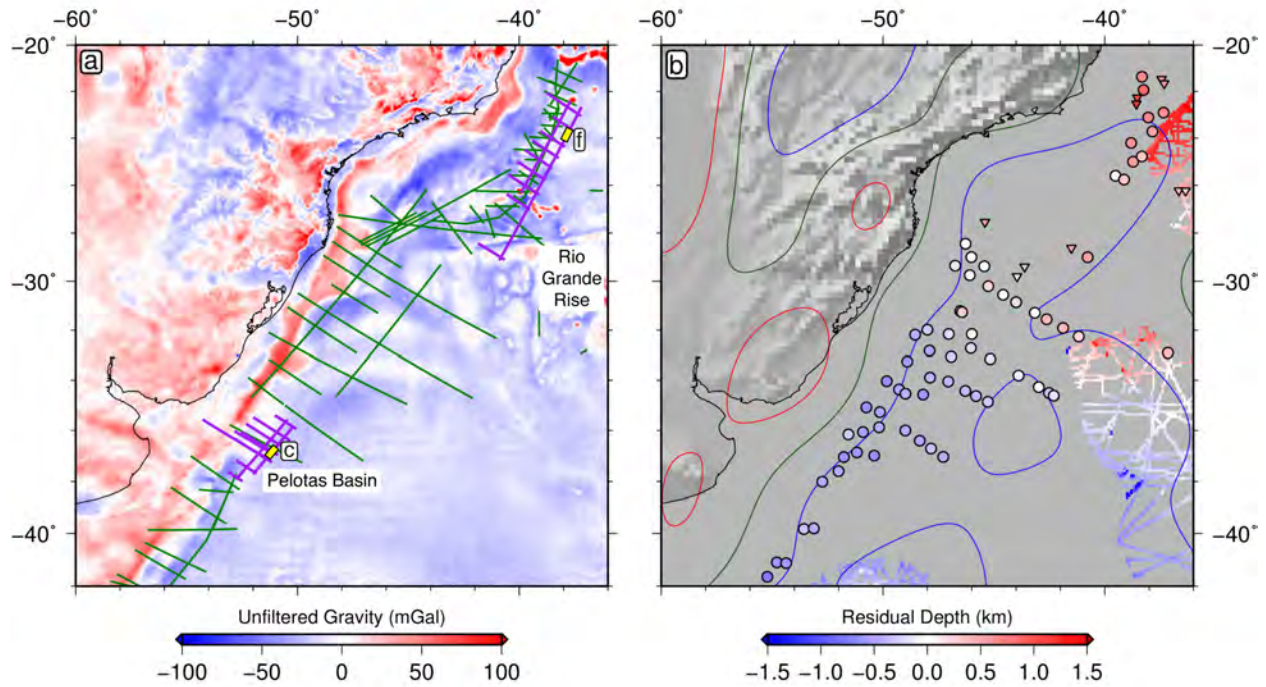
Figure 3.6: Seismic profile locations and residual depth measurements offshore south-eastern Brazil and Uruguay. (a) Location map. Dark green lines = pre-existing seismic reflection profiles; light green lines = pre-existing seismic wide-angle and refraction data; light green circles = vintage slope-intercept experiments; purple = new seismic reflection profiles; yellow bars = locations of seismic profiles in Figure 3.1c & f. (b) Residual depth map. Circles = measurements with crustal and sedimentary correction; upward/downward pointing triangles = measurements with sedimentary correction, direction of arrow indicates whether estimate is an upper or lower bound; filigree = residual measurements from ship-track bathymetry where sedimentary correction is made using Whittaker *et al.* (2013) sediment thickness dataset and regions affected by plate flexure or anomalous crustal thickness are excluded using polygons of Hoggard *et al.* (2017). Long wavelength free-air gravity anomaly ($1,000\text{ km} \geqslant \lambda \geqslant 5,000\text{ km}$) is contoured at 25 mGal intervals; red = positive; blue = negative; green = neutral.

Further south along the South American margin, in the Pelotas Basin, a suite of seismic reflection profiles have been processed to add 11 residual depth anomalies to the global database (Figure 3.1c & 3.6a). Average residual depth is ~ -500 m in this region, consistent with observations made previously on either side of the basin (Figure 3.6b). This portion of the South American margin represents the northern extreme of a long wavelength ($\sim 5,000$ km) residual depth anomaly that extends southwards along the margin towards the Argentine Abyssal Plain; an oceanic region that reaches residual depths of $\leqslant -2$ km.

3.1.3   West African Margin

Residual depth data coverage along the Central West African Coast was patchy before this study with most information derived from a single wide-angle study across the Cape Verde archipelago. However a $\sim$ 1,500 km-long seismic reflection profile, covering the West African margin between offshore Mauritania and Guinea, augments the existing database and is supplemented by smaller east-west trending profiles away from the main transect (Figure 3.7a). 12 residual depth points were added from the 10 profiles collected here, with all but one imaging a sufficiently clear Moho to accurately correct for crustal thickness variation as well as sedimentary thickness changes (Figure 3.1d). These spot measurements represent some of the largest positive anomalies on Earth, peaking at $\sim$ +1.5 km close to the Cape Verde Rise and decaying southwards, reaching $\sim$ +200 m offshore Guinea-Bissau, before rising again towards $\sim$ +600 m offshore Liberia (Figure 3.7b).

The $\sim$ 4 m km^{-1} decrease in residual topography away from the Cape Verde Rise suggests the presence of a relatively localised asthenospheric upwelling beneath the archipelago. Correlations between elevated topography, heat flow and long wavelength free-air gravity across the region confirm that the Cape Verde Rise is a dynamically supported feature (Courtney & White, 1986; Wilson *et al.*, 2013). These surface expressions show a clear link with slow shear wave speed anomalies in seismic tomography models and are consistent with an asthenospheric temperature anomaly of $\sim$ 100°C between 100 and 200 km depth (Lodhia *et al.*, 2018). Basaltic volcanism in the region from 15 Ma onwards provides further evidence for the existence of a significant thermal perturbation in the upper mantle beneath this region and places useful constraints on the timing of its arrival beneath the African plate (Gerlach *et al.*, 1988; Duprat *et al.*, 2007). A major Oligo-Miocene unconformity ($\sim$ 23 Ma) expressed in the margin stratigraphy of this region records a large-scale erosional event associated with regional uplift (Lodhia *et al.*, 2018). Upwelling may therefore have initiated $\sim$ 10 Ma prior to the production of the volcanic rocks.

Data coverage offshore Gabon is already excellent; however, 5 additional residual depth points have been added using new seismic reflection data. The negative residual topography retrieved ($\sim$ −300 m) is roughly consistent with previous estimates and helps to confirm the existence of high-amplitude, $\sim$ 1,500 km-wavelength variation of residual depth anomalies along the West African margin highlighted by Hoggard *et al.* (2016).

Although the database has some residual depth points from offshore Namibia and the Orange Basin, they are sparsely distributed. Here, 31 residual depth anomalies are added to the global
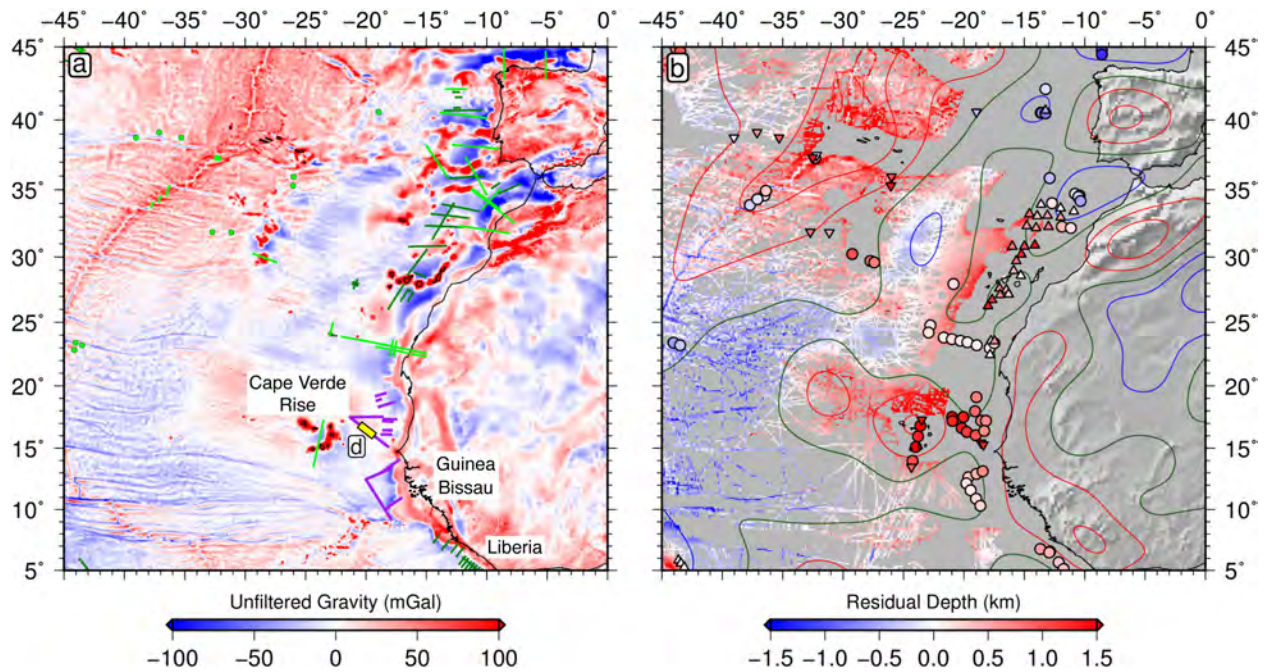
Figure 3.7: Seismic profile locations and residual depth measurements offshore Northwest Africa. (a) Location map. Dark green lines = pre-existing seismic reflection profiles; light green lines = pre-existing seismic wide-angle and refraction data; light green circles = vintage slope-intercept experiments; purple = new seismic reflection profiles; yellow bar = location of seismic profile in Figure 3.1d. (b) Residual depth map. Circles = measurements with crustal and sedimentary correction; upward/downward pointing triangles = measurements with sedimentary correction, direction of arrow indicates whether estimate is an upper or lower bound; filigree = residual measurements from ship-track bathymetry where sedimentary correction is made using Whittaker *et al.* (2013) sediment thickness dataset and regions affected by plate flexure or anomalous crustal thickness are excluded using polygons of Hoggard *et al.* (2017). Long wavelength free-air gravity anomaly (1,000 km $\geqslant$ λ $\geqslant$ 5,000 km) is contoured at 25 mGal intervals; red = positive; blue = negative; green = neutral.

database (Figure 3.1e & 3.8a). Only 5 of the new residual depth anomalies are corrected for both sedimentary and crustal thickness variation as many of the new seismic reflection profiles have a recording time that is too short to image the Moho. Nonetheless, spatial coverage adjacent to the Southwest African margin is improved by the addition of these measurements. The updated dataset reveals a broad, anomalously elevated region that climbs from +350 m in offshore Namibia to +1.05 km giving an average of $\sim$ +750 m (Figure 3.8b & 3.9b).

The average positive elevation is consistent with previous estimates of dynamic topography in southern Africa, with Nyblade & Robinson (1994) determining $\sim$ 500 m from residual topography analysis and Jones *et al.* (2017) retrieving an average of $\sim$ 670 m from probabilistic inversion of geoid anomalies, surface wave dispersion measurements, magnetotelluric data, and surface heat flow.
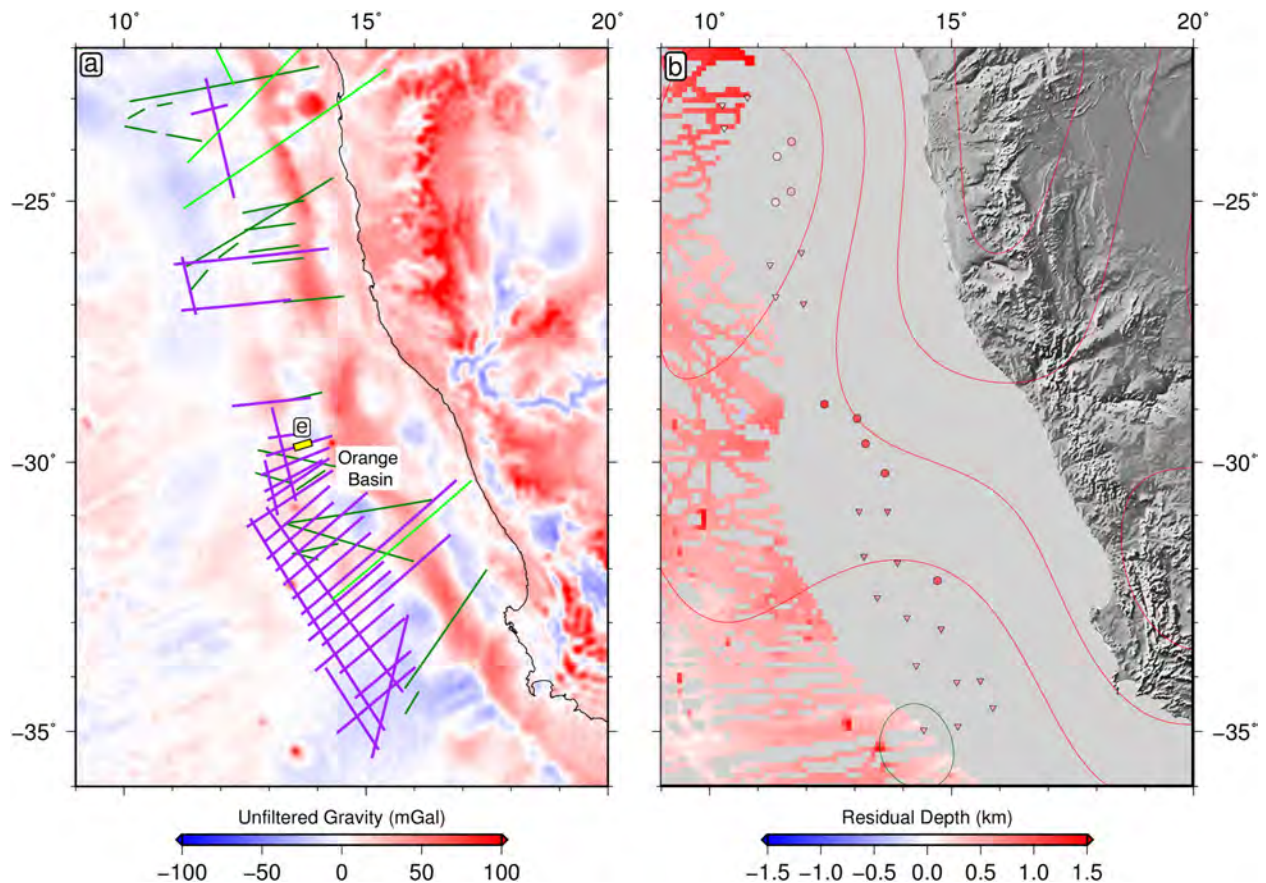
Figure 3.8: Southwest African seismic data locations and residual depth measurements. (a) Location map. Dark green lines = pre-existing seismic reflection profiles; light green lines = pre-existing seismic wide-angle and refraction data; light green circles = vintage slope-intercept experiments; purple = new seismic reflection profiles; yellow bar = location of seismic profile in Figure 3.1e. (b) Residual depth map. Circles = measurements with crustal and sedimentary correction; upward/downward pointing triangles = measurements with sedimentary correction, direction of arrow indicates whether estimate is an upper or lower bound; filigree = residual measurements from ship-track bathymetry where sedimentary correction is made using Whittaker *et al.* (2013) sediment thickness dataset and regions affected by plate flexure or anomalous crustal thickness are excluded using polygons of Hoggard *et al.* (2017). Long wavelength free-air gravity anomaly (1,000 km $\geqslant$ λ $\geqslant$ 5,000 km) is contoured at 25 mGal intervals; red = positive; blue = negative; green = neutral.

The age of the elevated long wavelength topography of southern Africa is poorly constrained. However, the shorter wavelength variation observed in the residual depths is consistent with the significant post-20 Ma differential uplift between southern Namibia and South Africa inferred from dated marine deposits and inverse modelling of drainage networks (Paul *et al.*, 2014). Further, it has been argued that km-thick, 100 km-long gravity-driven collapse structures observed in seismic reflection profiles along the Namibian-South African margin may indicate that slope instability is related to convective upwelling (Hodgson & Rodriguez, 2016). The collapsed margin deposits

are composed of Paleogene sediment and overlain by undisturbed Neogene sedimentary rocks, suggesting that slope instability occurred around 30 Ma, consistent with the onshore constraints on the age of the basin and swell topography of Africa (Burke, 1996).

The pattern of residual topography obtained with the augmented dataset along South Atlantic margins is consistent with the previous results of Hoggard *et al.* (2017) (Figure 3.9). In particular, several complete cycles of residual topography can be identified along the west coast of Africa with characteristic wavelengths and amplitudes of $\sim$ 1500 km and ± 1 km, respectively. Residual depth variations along the South American margin are generally smaller in amplitude and longer wavelength than those along the African margin. Long wavelength gravity anomalies generally correlate with the residual topography pattern along both margins, although there is ~ 1 km of discrepancy between the observed positive residual depth and gravity-derived estimates across the Rio Grande Rise. The good spatial correlation between residual depth anomalies and gravity-derived estimates, in conjunction with the short wavelengths of the signals, suggest that upper mantle density anomalies are responsible for the observed variation. The discrepancy in the Rio Grande Rise area may reflect local depletion of the lithosphere during melting, leading to reduced densities and gravity anomalies but high residual topography.

3.1.4   Offshore East Africa

Seismic reflection lines acquired across the Madagascar Plateau have been processed, adding two residual depth data points in a location with no other data in a $\sim$ 1,000 km radius (Figure 3.10a). Oceanic basement is anomalously elevated by $\sim$ +250 m in this region, considerably less than the $\sim$ 1.2 km observed closer to the East African margin (Figure 3.10b). This west-east residual topographic gradient suggests that the Madagascar Plateau lies close to the eastern edge of the South African 'superswell'. However, residual depths are also slightly elevated to the north and east near Réunion Island and the Gallieni Fracture Zone on the Southwest Indian Ridge. Réunion is the site of extensive recent intraplate volcanism and is thought to be the present-day locus of a deep-seated mantle plume (Montelli *et al.*, 2006). It has also been suggested that the section of the Southwest Indian Ridge between the Indomed and Gallieni fracture zones is underlain by hot upwelling material, in this case transported from the Crozet hotspot to the south (Breton *et al.*, 2013). Positive residual depth anomalies in these regions therefore appear to have a more localised origin compared with the broad region of elevated topography further west that extends from the eastern edge of the Madagascar Plateau to the Orange Basin.
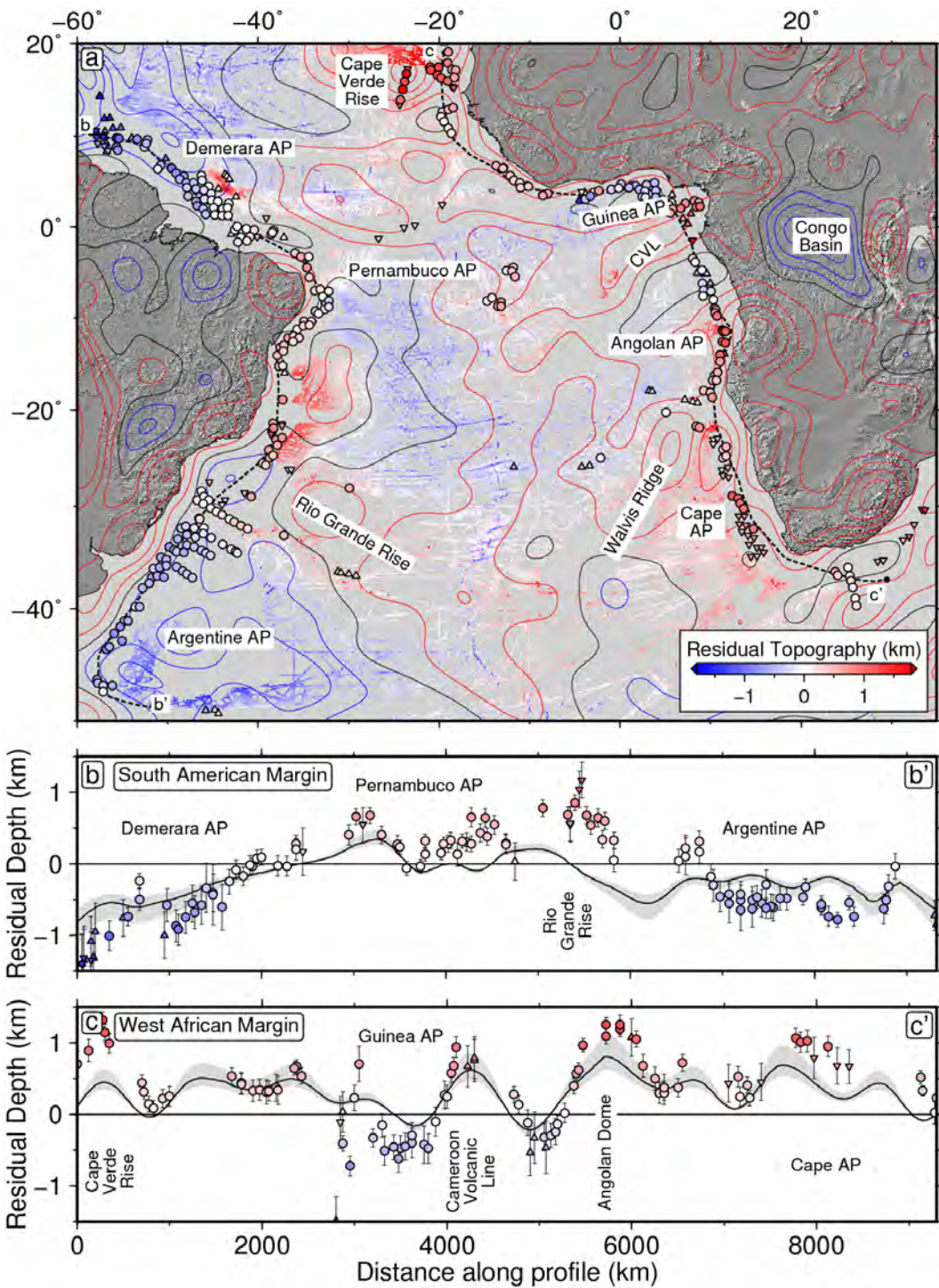
Figure 3.9: Residual depth anomalies along of South Atlantic margins. (a) Map of South Atlantic residual depth anomalies. Circles = measurements with crustal and sedimentary correction; upward/downward pointing triangles = measurements with sedimentary correction, direction of arrow indicates whether estimate is an upper or lower bound. Gravity contours = 10 mGal. AP = Abyssal Plain. Dashed black lines = transect locations. (b–b′) North-south transect along South American margin. Points within 80 km are plotted with uncertainties. Black line with grey bounds = predicted dynamic topography from long wavelength gravity anomaly from Chambat *et al.* (2010) bandpass-filtered (730 km $\leqslant \lambda \leqslant$ 9,000 km) and scaled using admittance (Z) of 35 mGal km^{-1}. Error envelopes represent equivalent values for $Z = 25\text{-}45$ mGal km^{-1}. (c–c′) Transect along the west African margin.

Two seismic lines extending westwards from West Madagascar into the Mozambique Channel have also added a point each to the residual depth database (Figure 3.10a). In both cases, the Moho is not clearly imaged and each point likely represents an upper bound on residual topography as oceanic crust is generally >7.1 km thick across this region. However, the +700m to +1 km anomalies are consistent with the regional picture and suggest the western edge of Madagascar is anomalously elevated (Figure 3.10b).
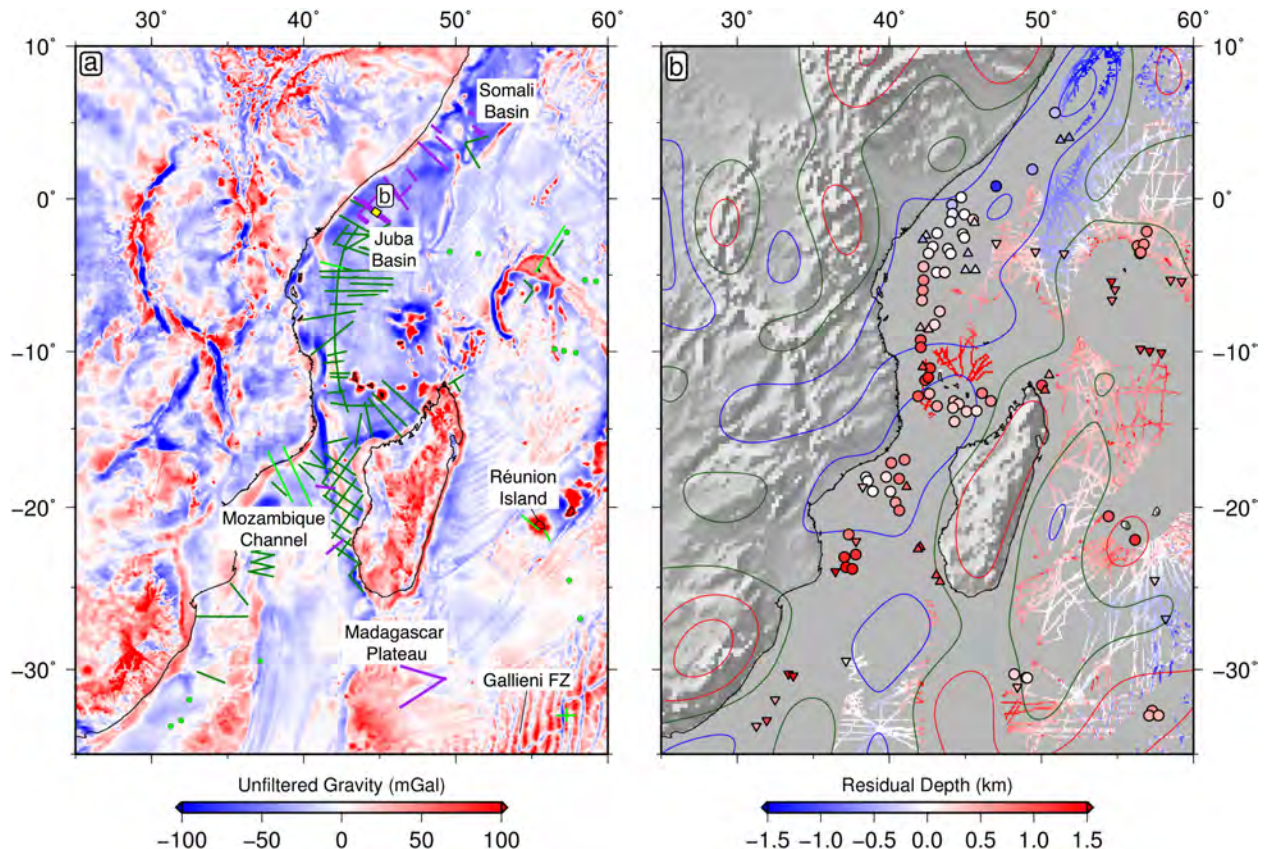
Figure 3.10: Seismic profile locations and residual depth measurements offshore East Africa. (a) Location map. Dark green lines = pre-existing seismic reflection profiles; light green lines = pre-existing seismic wide-angle and refraction data; light green circles = vintage slope-intercept experiments; purple = new seismic reflection profiles; yellow bar = location of seismic profile in Figure 3.1b. (b) Residual depth map. Circles = measurements with crustal and sedimentary correction; upward/downward pointing triangles = measurements with sedimentary correction, direction of arrow indicates whether estimate is an upper or lower bound; filigree = residual measurements from ship-track bathymetry where sedimentary correction is made using Whittaker *et al.* (2013) sediment thickness dataset and regions affected by plate flexure or anomalous crustal thickness are excluded using polygons of Hoggard *et al.* (2017). Long wavelength free-air gravity anomaly (1,000 km $\geqslant$ λ $\geqslant$ 5,000 km) is contoured at 25 mGal intervals; red = positive; blue = negative; green = neutral.

17 seismic reflection profiles collected in the Juba and Somali Basins between northern offshore

Kenya and central Somalia have been analysed to calculate 10 residual depth points, the majority of which can be corrected for both crustal and sedimentary thickness variations (Figure 3.1b & 3.10a). These residual depth points reveal a major northward decrease in dynamic support from ~ 500 m offshore southern Kenya to ~ -500 m offshore Somalia (Figure 3.10b). Uplifted marine terraces along the Kenyan coast suggest that the southern region is actively uplifting (Odada, 1996). However, constraints on uplift and subsidence in the Somalian sector are limited. Margin stratigraphy suggests a recent increase in accommodation space but placing tight constraints on this subsidence event is complicated by the lack of exploration well data in this region.

3.2   Spherical Harmonic Analysis

Although the updated residual depth database compiled here provides useful constraints on regional dynamic topography, when comparing these observations to predictive models it is desirable to make a globally continuous field. The intervening regions between the 2,030 spot measurements of residual depth must therefore be seeded with other observational constraints. Offshore, oceanic residual depth measurements are supplemented with residual topography computed from global ship-track bathymetry, the predicted subsidence of the complete plate model and corrected for sediment loading using the global NGDC sediment thickness grid (Smith & Sandwell, 1997; Whittaker *et al.*, 2013). Regions that are affected by plate flexure or have anomalous crustal thickness are excluded from this dataset using the polygons of Hoggard *et al.* (2017). Onshore, the approach of Hoggard *et al.* (2016) is adopted whereby a constant admittance value of 50 mGal km^{-1} is used to scale long wavelength free-air gravity anomalies ($\lambda > 730$ km) from the GGM03C gravity model into dynamic topography. Spherical harmonic functions are fitted sequentially to this augmented dataset, with higher degree functions only added if residual misfit between the model and observations is larger than data uncertainty. The revised spherical harmonic representation of dynamic topography is then compared to the model of Hoggard *et al.* (2016).

3.2.1   Damped Inverse Model

Spherical harmonic functions are fitted to the observations using the inverse method outlined in Hoggard *et al.* (2016). Observations are weighted by an uncertainty that reflects the weaker constraints offered by the continental admittance-derived dataset (± 250 m) and residual depth measurements that have not been corrected for crustal thickness variation (± 200 m). Uncertainties

in the crustal and sedimentary correction are used for residual depths where both corrections are applied.

Although the methodology employed here follows that of Hoggard *et al.* (2016), it is important to emphasise four differences. First, residual depth data in locations with previously sparse data coverage is included. Secondly, the updated magnetic age grid of Müller *et al.* (2016) is applied in the residual depth calculation, adapted to correct gridding errors north of Iceland and in the Gulf of California. Thirdly, following Hoggard *et al.* (2017), the reference level for residual depths is sea-level with the non-hydrostatic geoid subtracted to correct for the influence of convection. Finally, the reference model used to calculate residual values is the complete plate model described in Chapter 2 rather than the subsidence curve of Crosby & McKenzie (2009) applied by Hoggard *et al.* (2016).

Having compiled the full observational dataset, a least squares inversion is undertaken to find a smooth interpolating function that minimises misfit between the input data at each location, d_i, such that $f(\lambda'_i, \varphi_i) \approx d_i$. The interpolating function is expressed as the sum of a series of spherical harmonics using

$$f(\lambda', \varphi) = \sum_{l=1}^{l_{max}} \sum_{m=-l}^{l} f_{lm} \mathcal{Y}_{lm}(\lambda', \varphi). \tag{3.5}$$

In this expression, l and m represent spherical harmonic degree and order, $\mathcal{Y}_{lm}$ are fully normalised real spherical harmonic coefficients and f_{lm} are expansion coefficients. As the integral of dynamic topography over the surface of the Earth is equal to zero, degree zero components are not included in the expansion (Conrad & Husson, 2009).

To determine the best-fitting spherical harmonic representation of the observations, a cost function, J, is minimised that combines the least squares misfit between the interpolating function and the input data with two regularisation terms to prevent overfitting of the data. The cost function is written as

$$J = \frac{1}{2} \sum_{i=1}^{N} \frac{1}{\sigma_i^2} \left[f(\lambda'_i, \varphi_i) - d_i \right]^2 + \frac{1}{2} \int_{\mathbb{S}^2} \left[\lambda_1 \|\nabla_1 f\|^2 + \lambda_2 f^2 \right] \mathrm{d}S \tag{3.6}$$

where λ_1 and λ_2 are non-negative smoothing terms and $\mathbb{S}^2$ represents the unit two sphere. The first term on the right-hand side of Equation 3.6 represents the misfit between the data and the spherical harmonic expansion. This expression is proportional to

$$\chi^2 = \frac{1}{N} \sum_{i=1}^{N} \frac{1}{\sigma_i^2} \left[f(\lambda'_i, \varphi_i) - d_i \right]^2 \tag{3.7}$$

and measures how well the interpolating function is able to fit the data. When $\chi^2 \sim 1$, the misfit between the observations and interpolating function is approximately equal to the uncertainty, σ_i. Therefore, when $\chi^2 > 1$ the model is likely underparameterised and short wavelength signal in the data may be aliased; however, if $\chi^2 < 1$ the model is overparameterised and artefacts may be introduced into the final model.

The second expression on the right-hand side is a regularisation term that comprises a gradient damping function, $\lambda_1 \|\nabla_1 f\|^2$, that acts to favour smooth best-fitting interpolating functions, and a norm damping function $\lambda_2 f^2$ that prevents the recovery of excessively large coefficients. This combination of gradient regularisation and amplitude damping ensures that spurious short-wavelength features are removed and realistic values of dynamic topography are retrieved in unconstrained regions.

During the least squares inversion, spherical harmonic functions are sequentially fitted up to a maximum spherical harmonic degree of 40, i.e. $l_{max} = 40$ in Equation 3.5. As noted by Hoggard *et al.* (2016), χ^2 drops below unity at degree 30, suggesting that the data may be overfit if the expansion is extended to higher degrees. The final model therefore only includes coefficients up to degree and order 30. The smoothing parameters in the cost function, λ_1 and λ_2, are varied between 0.3–3 km^{-2} and from 100–1,000 km^{-2}, respectively to find values that produce an acceptably smooth model whilst minimising data misfit. The trade-off between misfit and roughness is optimised when λ_1 = 1 km^{-2} and λ_2 = 400 km^{-2}, identical to the optimal values retrieved by Hoggard *et al.* (2016). These values are applied to generate an optimal spherical harmonic representation.

3.2.2   Spherical Harmonic Representations

The final spherical harmonic function recovered here retains the characteristic wavelengths and amplitudes of the Hoggard *et al.* (2016) model (Figure 3.11a & b). However, certain differences are observable between the Hoggard *et al.* (2016) model and the updated representation (Figure 3.11c). First, the application of the revised age-depth subsidence relationship leads to more positive residual topography at ages between 70 and 150 Ma. Secondly, because the updated plate model leads to slower rates of subsidence, residual depths tend to be more negative between 0 and 70 Ma. Thirdly, changes in the lithospheric age grid between Müller *et al.* (2008) and Müller *et al.* (2016) have made substantial changes locally. For example, younger ages in the Scotia Sea lead to more negative residual topography values in this region. Fourthly, the addition of new residual depth points,
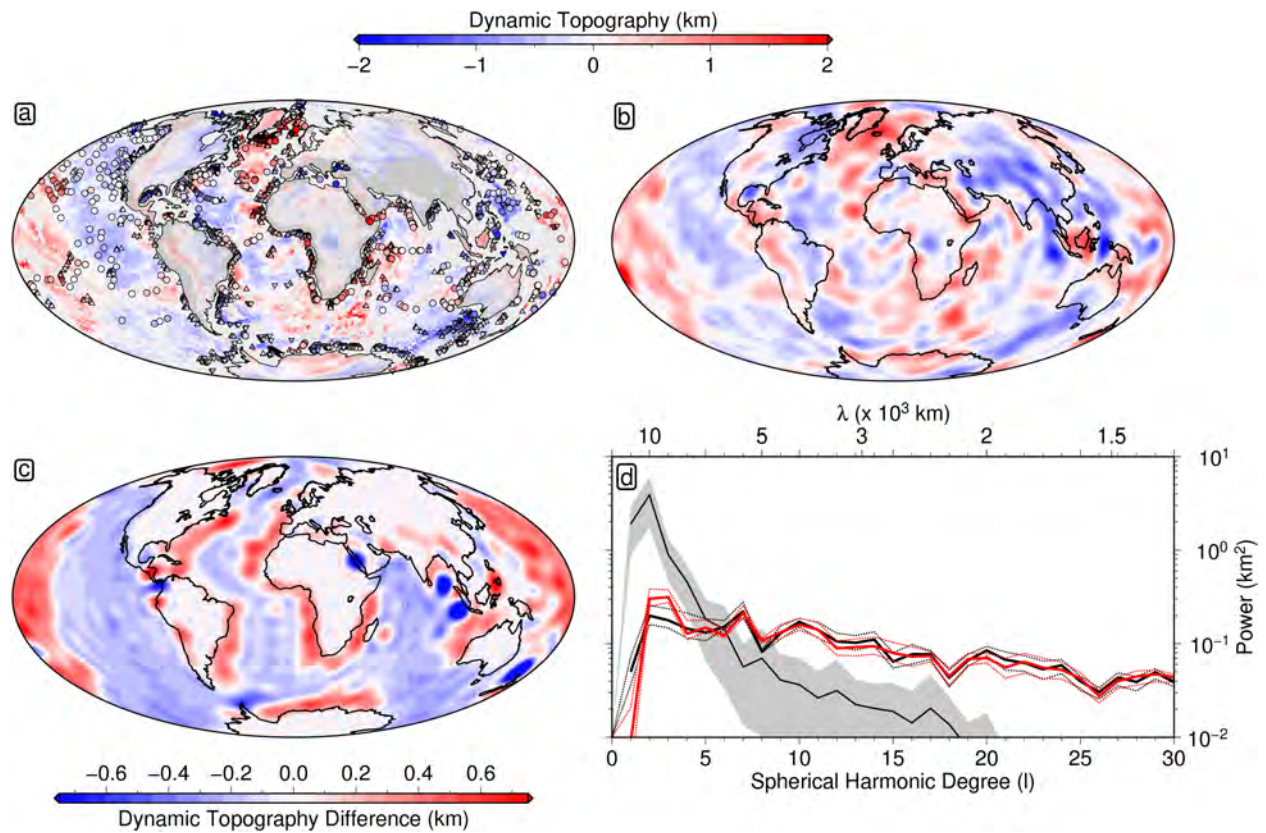
Figure 3.11: Difference between spherical harmonic representations. (a) Input data for spherical harmonic expansion. Circles = residual depth measurements with crustal and sedimentary correction; upward/downward pointing triangles = residual depth measurements with sedimentary correction, direction of arrow indicates whether estimate is an upper or lower bound. Offshore grid calculated from ship-track data, sampled every $1°$. Onshore nodes spaced every $1°$ calculated by scaling long-wavelength (> 730 km) free-air gravity anomalies by $Z = 50$ mGal km^{-1} and excising locations of orogens and flexure. (b) Spherical harmonic expansion to degree and order 30 of updated dataset, referenced to complete plate model and non-hydrostatic geoid. (c) Difference between updated spherical harmonic representation of dynamic topography observations and that of Hoggard *et al.* (2016). (d) Spectral comparison of observations and predictions of dynamic topography. Thick black line = mean power spectrum of predictive model ensemble (Ricard *et al.*, 1993; Steinberger, 2007; Conrad & Husson, 2009; Spasojevic & Gurnis, 2012; Flament *et al.*, 2013); grey envelope = $\pm 1\sigma$ standard deviation of predictive model ensemble power spectrum; thin black line = Hoggard *et al.* (2016) spherical harmonic fit to observations; thin red line = updated spherical harmonic fit to observations. Dashed lines represent maximum and minimum limits of the power recovered for all combinations of damping parameters within the ranges $\lambda_1 = 10^2$–10^4 km^{-2} and $\lambda_2 = 10^{-0.5}$–$10^{0.5}$ km^{-2}.

and removal of some unreliable data from the previous dataset, have clarified regional trends in a number of locations. A single elevated value of $\sim +2.5$ km in the Central Red Sea was removed due to poor original data quality, leading to $\sim +1$ km drop in dynamic topography. Regional residual topography now peaks adjacent to the locus of the Afar plume, where the highest mantle buoyancy flux would be expected. Finally, removal of the non-hydrostatic geoid signal reduces the amplitude

of long wavelength residual topography ($\lambda \sim 10{,}000$ km) by up to 150 m. Overall, however, the spatial pattern of residual highs and lows is very consistent between models, confirming the robustness of the anomalies to choice of reference model.

3.2.3 Power Spectral Representations

Having assessed the difference between the two spherical harmonic representations, spectral differences are investigated by calculating power spectra for each model as a function of spherical harmonic degree. Power at a given spherical harmonic degree, P_l is calculated from spherical harmonic coefficients using

$$P_l = \sum_{m=-l}^{l} f_{lm}^2 \qquad (3.8)$$

This calculation is performed for each observational dataset and an ensemble of five predictive geodynamic models of dynamic topography for comparison (Figure 3.11d). For $l \geqslant 4$, the observation-based power spectra match closely. However, within reasonable bounds of uncertainty, the updated spherical harmonic expansion has $\sim 50\%$ more power than that of Hoggard *et al.* (2016) at $l = 2$–3, principally reflecting different reference model choices and the correction of basement depths for the non-hydrostatic geoid. Nevertheless, despite these changes, the major discrepancy between observations and predictions of dynamic topography remains. At $l = 2$ predictions yield $\sim \pm 2$ km of dynamic topography, while the new observational dataset retrieves $\sim \pm 550$ m. At the opposite end of the power spectrum, $l = 30$ dynamic topography accounts for $\sim \pm 150$ m; the geodynamic models predict no dynamic topography at this spherical harmonic degree. This fundamental discrepancy, first highlighted by Hoggard *et al.* (2016), remains.

3.3 Summary

Best-fitting subsidence from the optimal plate model developed in Chapter 2 is used to determine 123 new residual depth anomalies and update the pre-existing database, adding important constraints on residual depth in regions with previously sparse or non-existent data coverage. Application of this reference model predicts oceanic residual depth anomalies that are evenly distributed about zero with minimal skewness, consistent with the expectation that dynamic topography should sum to zero when integrated over the surface of the Earth (Conrad & Husson, 2009). The pattern of

residual depth anomalies revealed by these measurements is consistent with previous observations suggesting that dynamic topography varies significantly at 1,000–5,000 km wavelengths.

The augmented residual depth anomaly database is then combined with onshore gravity data and offshore ship-track bathymetry grids to create a new global observation-based dynamic topography database. An inversion is performed to make a globally continuous spherical harmonic representation of the discrete data points for direct comparison with model predictions. The new dataset is subtly different from that of Hoggard *et al.* (2016), with residual depths deepening on young seafloor and shoaling on older seafloor as a result of the adapted reference model. Other local differences result from application of a non-hydrostatic geoid correction, implementation of a revised magnetic age grid and addition of new residual depth measurements.

Although amplitudes of long wavelength dynamic topography are marginally increased in the new dataset (550 m vs. 400 m), short-wavelength amplitudes are identical. Significantly, the gradient of the observational spectrum is demonstrated to be robust and a fundamental spectral discrepancy between predictions and observations of dynamic topography therefore remains. It can be concluded that previous predictions of dynamic topography significantly overestimate long wavelength dynamic topography and underestimate contributions at shorter wavelengths.

Chapter 4

Dynamic Topography of India

In the previous chapter, an augmented oceanic basement depth database was combined with an updated thermal model of the oceanic lithosphere to generate a revised spherical harmonic representation of present-day dynamic topography based on observations. Although this database provides useful bounds on the typical wavelengths and amplitudes of global dynamic topography, it does not constrain the temporal evolution of convectively maintained topography. However, transient vertical motions caused by mantle convection may be recorded in the stratigraphy and landscape evolution of the continents and their margins (Shaw Champion *et al.*, 2008; Roberts & White, 2010; Hartley *et al.*, 2011; Czarnota *et al.*, 2013; Paul *et al.*, 2014). In this chapter, the Cenozoic landscape evolution of India is investigated to place stronger constraints on the characteristic timescales over which dynamic topography evolves.

The physiography of Peninsular India is characterised by eastward tilting and predominantly eastward-flowing drainage (Powar, 1993; Collier *et al.*, 2008; Figure 4.1a). The age and origin of this asymmetric configuration is much debated. For example, it has been argued that the Western Ghats escarpment is a topographic relic of rifting and magmatism that developed at ∼ 65 Ma along the Western Indian continental margin (White & McKenzie, 1989; Cox, 1989; Pandey *et al.*, 1996; Figure 4.1a). Alternatively, it has been suggested that regional uplift is much younger with neotectonic activity playing an important role (Valdiya, 2001; Vita-Finzi, 2004). With regard to mechanism, a flexural response to combined onshore denudation and offshore sedimentary loading has been invoked to account for elevation of the western coastline (Watts & Cox, 1989; Whiting *et al.*, 1994; Gunnell & Fleitout, 1998; Campanile *et al.*, 2008). Regional epeirogenic uplift caused by thermal anomalies within the convecting mantle have also been proposed (Kailasam, 1975; Radakrishna, 1991). These different suggestions make testable predictions about the temporal and spatial pattern of uplift and tilting that is currently poorly known.

Active tectonic deformation is unlikely to account for the present-day topographic tilt of the Indian Peninsula. Background seismicity is modest in magnitude and frequency. Although, rare large
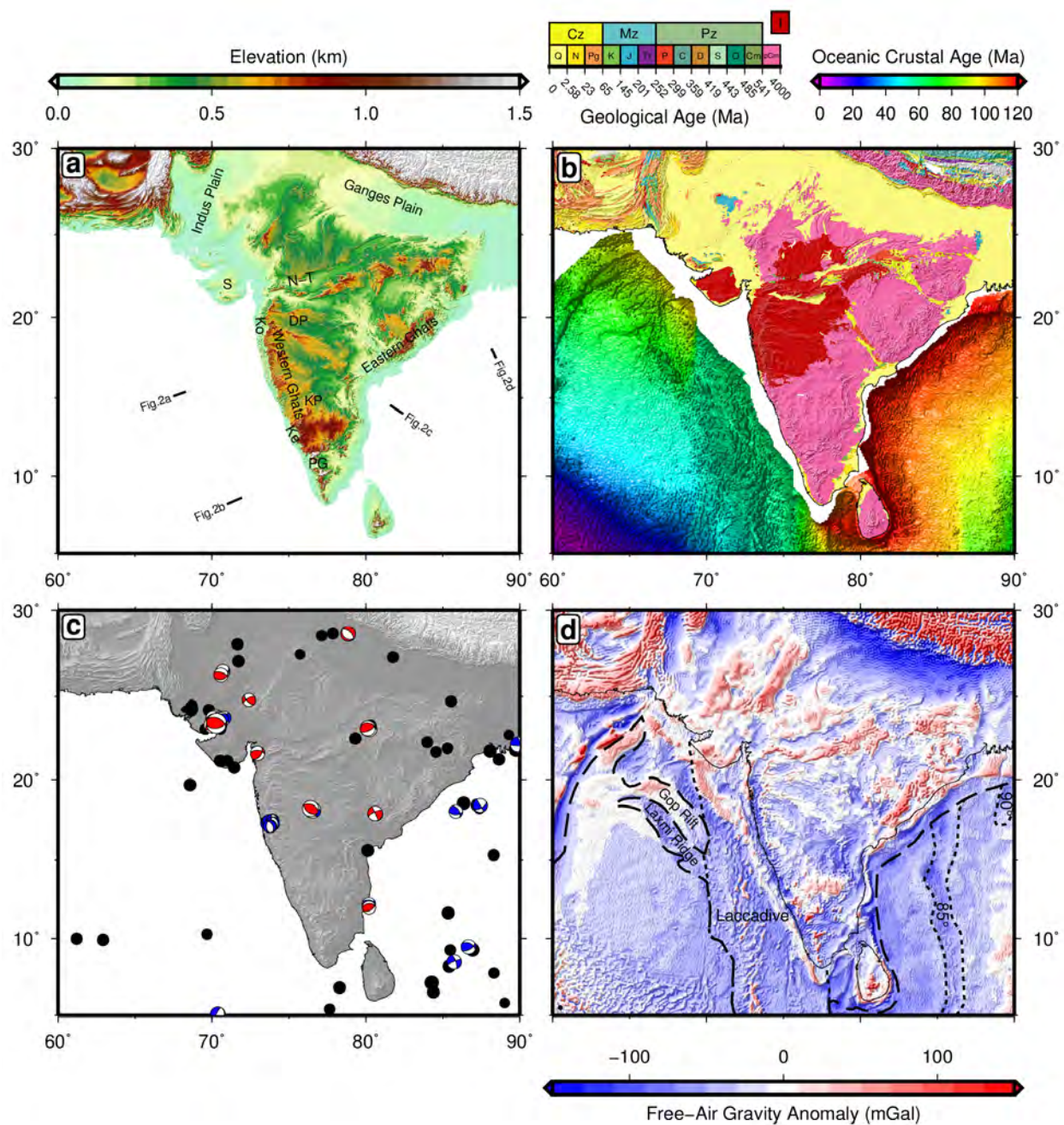
Figure 4.1: Indian topography, geology, active deformation and free-air gravity anomalies. (a) Topographic map based on SRTM30_PLUS model (Becker *et al.*, 2009). DP = Deccan Plateau; Ke = Kerala Coastal Plain; Ko = Konkan Coastal Plain; KP = Karnataka Plateau; N-T = Narmada-Tapti Valley; S = Saurashtra Peninsula. Black lines = seismic profiles shown in Figure 4.2. (b) Simplified geologic map with oceanic crustal ages (Wandrey & Law, 1997; Müller *et al.*, 2008). (c) Intraplate earthquake seismicity. Black circles = earthquakes with $M_b \geqslant 3$ for 1964–2015 taken from EHB catalogue (Engdahl *et al.*, 1998); blue beach balls = focal mechanisms from Centroid Moment Tensor catalogue (www.globalcmt.org); scaled red beach balls = focal mechanisms calculated by inverse modelling of body waveforms from Copley *et al.* (2014), size is proportional to magnitude. (d) Free-air gravity anomaly map (Sandwell *et al.*, 2014). Dashed lines = continent-ocean boundary; dotted lines = volcanic tracks including 85°E and 90°E ridges.

magnitude (i.e. $M_b \geqslant 6$) earthquakes do occur, most of these events are located within Proterozoic mobile belts that are oblique to the axis of regional tilting (Widdowson & Mitchell, 1999; Valdiya, 2001; Mishra *et al.*, 2004; Veeraswamy & Raval, 2005; Copley *et al.*, 2014; Figure 4.1c). Along the western coastline, focal mechanisms are mostly extensional. Within the continental interior and along the eastern seaboard strike-slip and shortening mechanisms predominate, consistent with north-south directed compressional stress (Yamato *et al.*, 2013; Müller *et al.*, 2015).

Here, Indian epeirogeny is investigated by analysing and combining three different datasets which bear upon this regional problem. First, residual depth anomalies are analysed across the Indian Peninsula. These anomalies typically have water-loaded amplitudes of $\pm 10^2$–10^3 m and wavelengths of 10^2–10^3 km. By measuring the distribution of these anomalies on either side of India, it is possible to frame the epeirogenic consequences for the peninsula itself. Of particular interest is the connection between offshore bathymetric anomalies and their expression within the adjacent continental topography. Secondly, a digital database of longitudinal river profiles that drain the sub-continent is generated. This drainage inventory is inverted using a stream-power formulation to determine the spatial and temporal pattern of regional rock uplift subject to independent geologic calibration and testing. Thirdly, the relationship between these observations and the distribution of seismic velocity anomalies from tomographic models is investigated. The principal goal is to show how disparate offshore, onshore and sub-plate observations can be combined to generate an improved quantitative understanding of the timing and causes of Indian epeirogeny.

4.1 Regional Framework

4.1.1 Residual Depth Measurements

The Indian sub-continent is bounded to the east and west by Cretaceous and Paleogene oceanic lithosphere, respectively (Figure 4.1b). It is well known that significant residual depth anomalies occur in the oceanic realm and that these anomalies are a useful guide for determining the spatial pattern of dynamic topography adjacent to continental margins (Czarnota *et al.*, 2013; Hoggard *et al.*, 2016). Residual depth analysis of a database of regional seismic reflection images, generously provided by ION Geophysical Corporation, has been conducted across the Indian Peninsula (Figures 4.1a & 4.2). On each of these images, the sedimentary pile overlying *bona fide* oceanic crust together with the base of the crust are clearly visible. These observations are used to accurately calculate the water-loaded depth to basement following the methodology of Hoggard *et al.* (2016).

During this analysis, considerable care was taken to avoid areas where crustal flexure was evident or where the presence of oceanic crust is ambiguous (Todal & Edholm, 1999; Chaubey *et al.*, 2002; Figures 4.1d & 4.2).
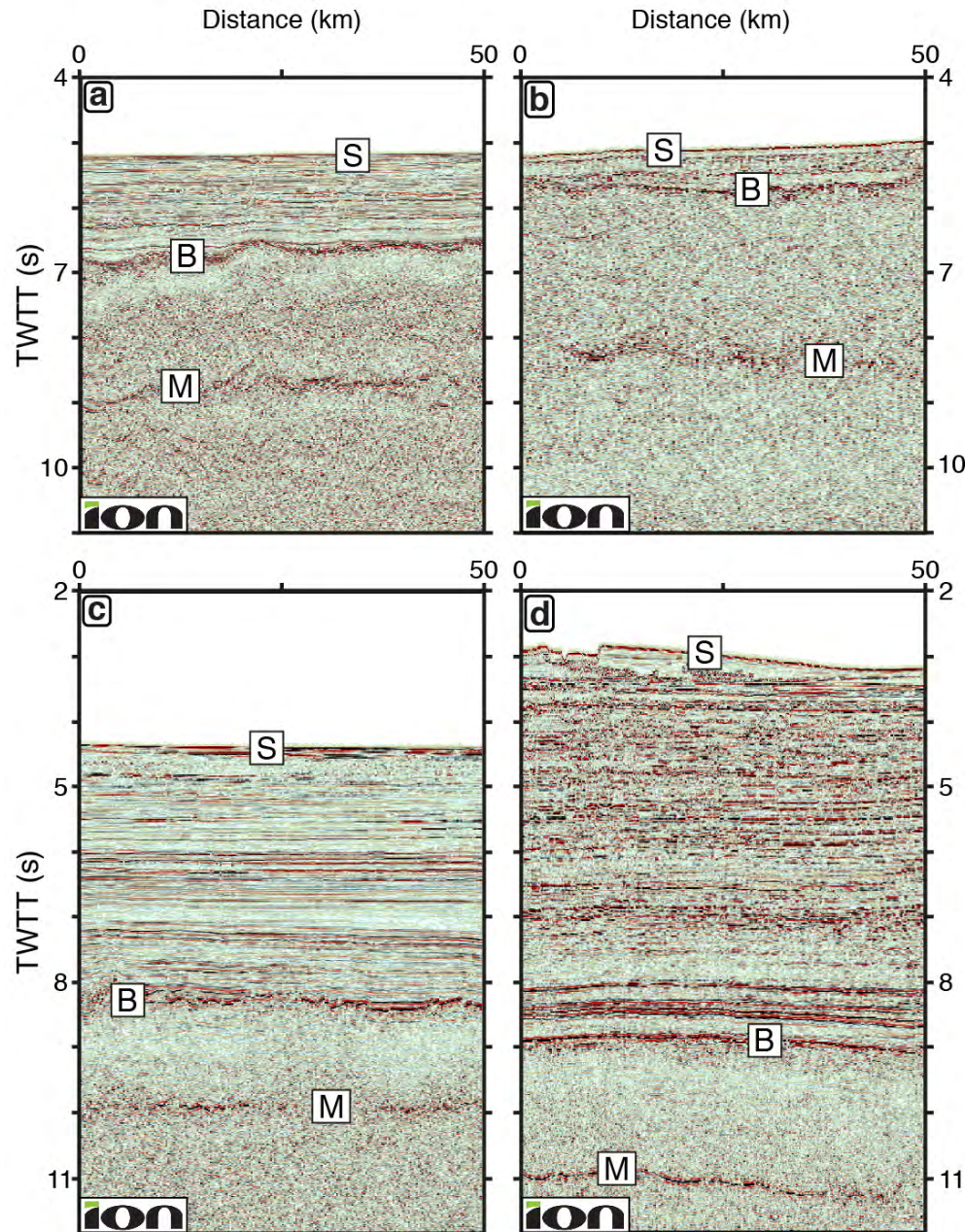
Figure 4.2: Portions of seismic reflection profiles used to calculate residual depth anomalies of oceanic lithosphere (Figure 4.1a). (a) 60 Ma oceanic crust located south-west of Mumbai. S = seabed; B = sediment-basement interface; M = Moho. Crustal age from magnetic anomalies (Müller *et al.*, 2008). (b) 54 Ma oceanic crust located west of Kerala. (c) 115 Ma oceanic crust located south of Krishna-Godavari delta. (d) 110 Ma oceanic crust beneath southern Bengal Fan. Images shown courtesy of ION Geophysical Corporation.

On each image, residual depth anomalies are calculated by measuring the difference between water-loaded subsidence of the top of oceanic basement and an assumed age-depth relationship. The age-depth compilation of Crosby & McKenzie (2009) is used in this instance. However, the size and polarity of these residual depth anomaly measurements is not significantly altered by using an alternative age-dependent plate subsidence model (e.g. Hoggard *et al.*, 2016; Figure 4.3a).
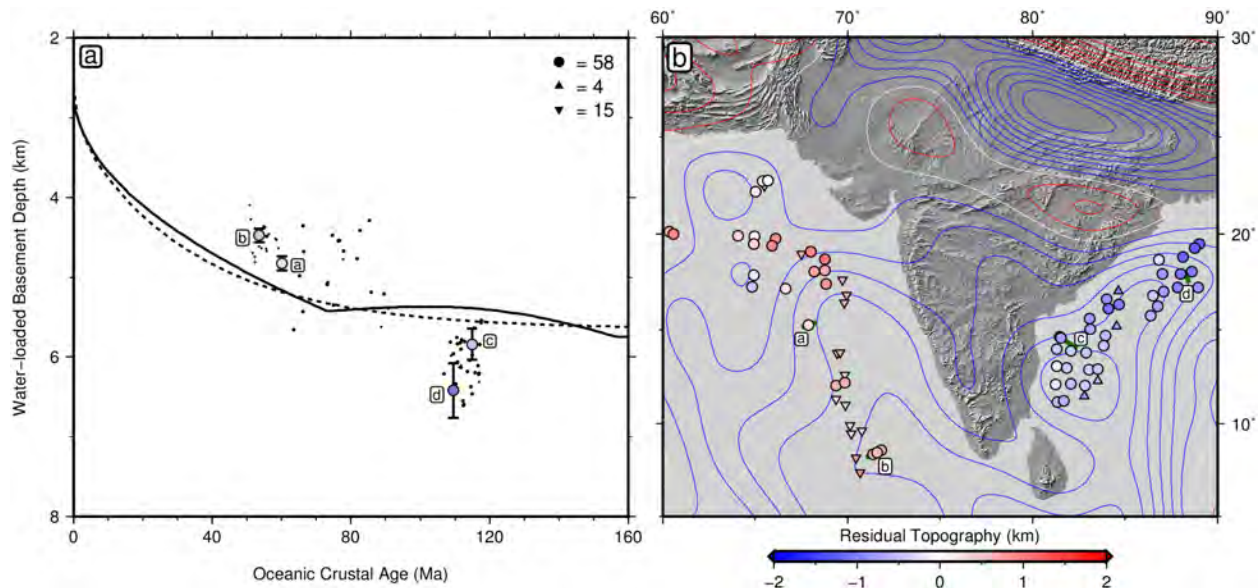
Figure 4.3: Residual depth anomalies of oceanic crust. (a) Water-loaded subsidence of oceanic lithosphere as function of age. Solid line = age-depth relationship of Crosby *et al.* (2006); dotted line = age-depth relationship of Stein & Stein (1992); solid circles/triangles = age-depth measurements averaged in 1 ° bins; red/blue circles with vertical bars = age-depth measurements and uncertainties calculated from seismic profiles shown in Figure 4.2. (b) Red/blue circles and upward/downward-pointing triangles = positive/negative residual depth anomaly measurements and upper/lower bounds; red/blue contours = positive/negative long-wavelength (> 730 km) free-air gravity anomalies at 10 mGal intervals calculated from GGMO3C dataset (Tapley *et al.*, 2007); labelled green lines = locations of seismic profiles shown in Figure 4.2.

These results show that there is a marked difference in residual depth anomalies on either side of India. To the west, Paleogene oceanic crust is up to 1 km shallower than expected. To the east, Cretaceous oceanic crust is up to 1.2 km deeper than expected. It is important to emphasise that these water-loaded anomalies are not caused by differences in the thickness of either sediment or crust, whose effects have been carefully removed. Instead, they reflect the presence of regional negative and positive density anomalies either within the lithospheric mantle, the sub-lithospheric mantle, or both. Figure 4.3b shows the spatial distribution of these residual depth anomalies. West of India, amplitudes of positive residual depth anomalies decrease slightly from east to west away from the coastline but there is little evidence for a north-south gradient. East of India, amplitudes
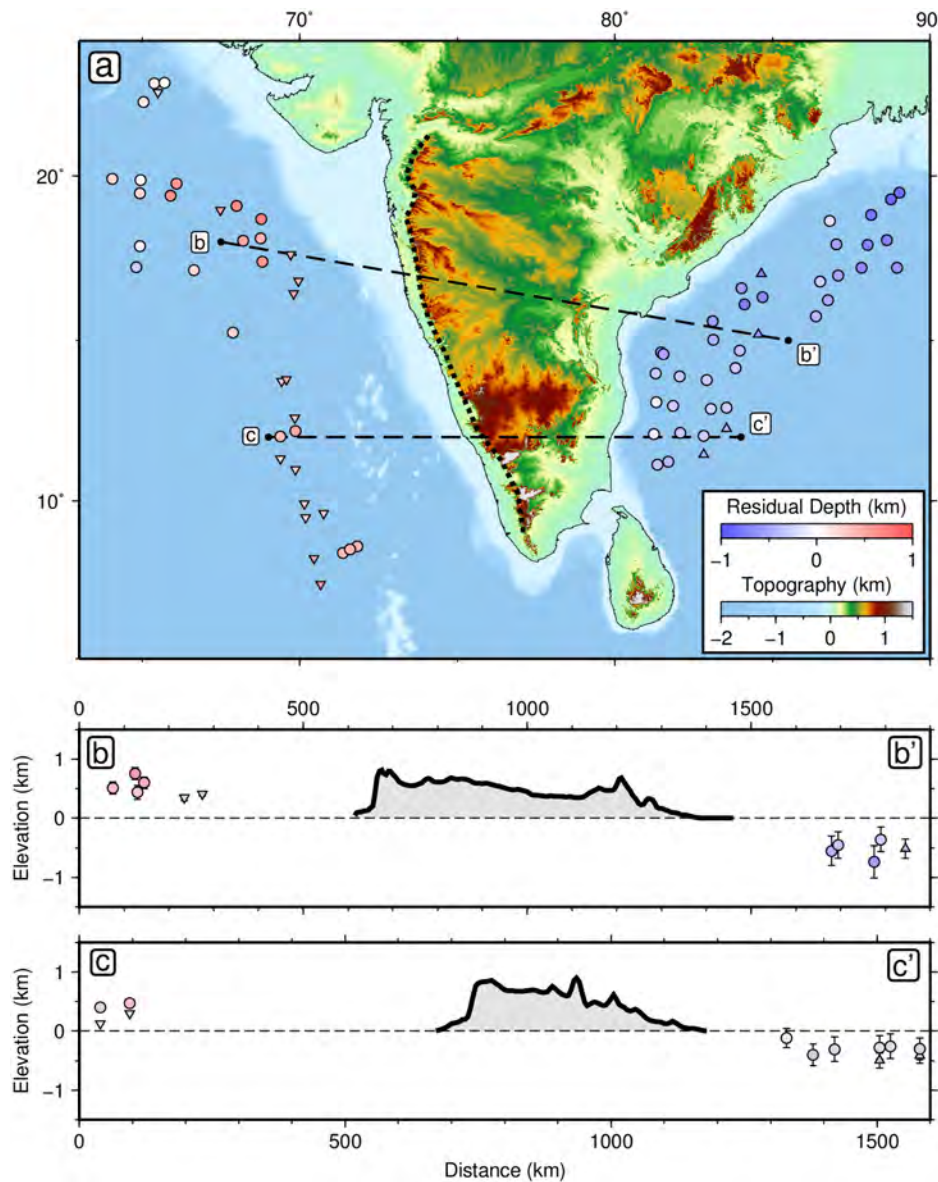
Figure 4.4: Air-loaded residual depths and onshore topography. (a) Topographic and bathymetric map from SRTM30_PLUS model (Becker *et al.*, 2009). Red/blue circles and upward/downward-pointing triangles = air-loaded residual depth anomaly measurements and upper/lower bounds; dotted line = Western Ghats drainage divide; dashed lines labelled b–b′ and c–c′ = location of transects shown in (b) and (c). (b) Northern transect showing offshore air-loaded residual depth anomalies and onshore topographic profile. Solid line = low-pass filtered topography (Gaussian function with 25 km moving window); horizontal dashed line = reference level. (c) Southern transect.

of negative anomalies increase steadily from south to north. These results build upon previously published estimates that only corrected for sedimentary loading (Ajay & Chaubey, 2008).

Given the assumed compositional homogeneity of oceanic lithosphere, these residual depth anomalies are probably maintained by density variations that occur within the sub-lithospheric mantle

since their size would require what are currently regarded as implausibly large variations in mantle composition (Dalton *et al.*, 2014). Elsewhere, a good correlation between long-wavelength (700–9,000 km) free-air gravity anomalies and residual depth measurements has been observed (Winterbourne *et al.*, 2014; Hoggard *et al.*, 2016). No such correlation is observed here where negative long-wavelength gravity anomalies predominate, consistent with the existence of a significant (~ 100 m) geoid low (Kaula, 1963; Bruinsma *et al.*, 2014). This lack of correlation between geoid and surface deflection implies that the positive mass anomaly that generates and maintains the geoid low is deep-seated (Hager *et al.*, 1985; Colli *et al.*, 2016; Nerlich *et al.*, 2016).

The offshore pattern of residual depth anomalies mirrors the onshore asymmetry of topographic relief (Figure 4.4). Peninsular India is dominated by a long-wavelength eastward tilt from the Western Ghats escarpment, where average elevation is ~ 1.5 km, down to the alluvial floodplains along the east coast. This pattern of relief is matched by a strongly asymmetric drainage configuration whereby rivers with headwaters positioned < 50 km from the Arabian Sea drain eastward into the Bay of Bengal. The close match between the polarity and gradient of regional tilting either side of, and across, India is striking (Figure 4.4). The wavelength of $\sim 2,000$ km and amplitude of ± 1 km, coupled with its continuity across both oceanic and continental lithosphere, is suggestive of an underlying, sub-plate mechanism (Panasyuk & Hager, 2000). Offshore, it is difficult to determine the temporal evolution of residual depth anomalies. In contrast, the growth of onshore regional topography can, in principle, be determined by combined studies of stratigraphic, geomorphic and thermochronologic observations. In order to place this approach in context, first the large-scale structure of the crust and lithosphere is examined.

4.1.2   Crustal and Lithospheric Isostasy

The continental realm contains indirect information about the temporal evolution of regional topography. However, determining continental residual topography is less straightforward since the density and thickness of heterogeneous crust and lithospheric mantle are relatively poorly known. An appropriate starting point is a database of crustal thickness measurements assembled from a combination of seismic refraction experiments and receiver function analyses (Kaila, 1979; Kaila *et al.*, 1981; Saul *et al.*, 2000; Ravi Kumar *et al.*, 2001; Sarkar *et al.*, 2003; Gupta *et al.*, 2003; Reddy, 2005; Tiwari *et al.*, 2006; Jagadeesh & Rai, 2008; Mitra *et al.*, 2008; Julià *et al.*, 2009; Acton *et al.*, 2011; Behera, 2011; Kayal *et al.*, 2011; Mandal, 2012; Borah *et al.*, 2014; Praveen Kumar & Mohan, 2014; Singh *et al.*, 2015; Figure 4.5). Bulk P wave velocities are 6.23–6.89 km s^{-1}

which yield average crustal densities of 2.76–2.9 Mg m^{-3}, according to empirical velocity-density relationships (Brocher, 2005; Maceira & Ammon, 2009).
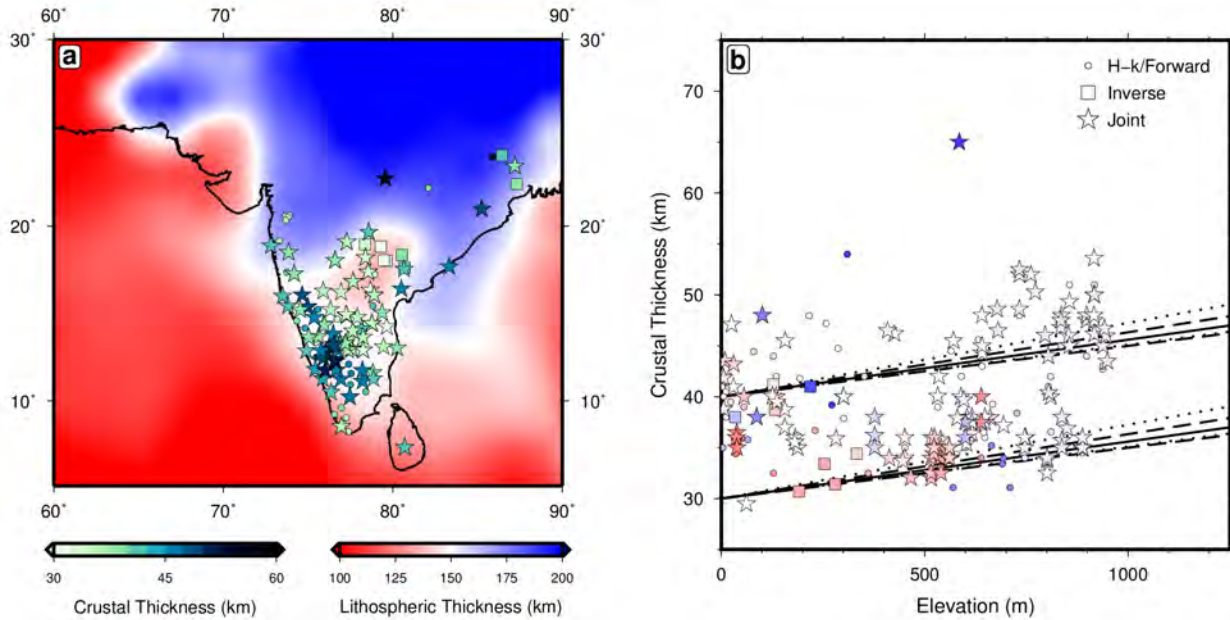
Figure 4.5: Crustal isostasy and lithospheric thickness. (a) Lithospheric thickness based upon surface wave tomographic model (Priestley & McKenzie, 2013). Symbols are published crustal thickness estimates. Stars = crustal thicknesses calculated by joint inversion of receiver functions and surface wave dispersion curves (e.g. Rai, 2003; Julià *et al.*, 2009; Rai *et al.*, 2009; Acton *et al.*, 2010, 2011; Vijay Kumar *et al.*, 2012; Mandal, 2012; Borah *et al.*, 2014); squares = crustal thicknesses from inverse modelling of receiver functions (e.g. Mitra *et al.*, 2008; Kayal *et al.*, 2011; Singh *et al.*, 2012; Praveen Kumar & Mohan, 2014); dots = crustal thicknesses calculated by either forward modelling or *H-k* stacks of receiver functions (e.g. Saul *et al.*, 2000; Ravi Kumar *et al.*, 2001; Gupta *et al.*, 2003; Rai *et al.*, 2005; Pathak *et al.*, 2006; Tiwari *et al.*, 2006; Jagadeesh & Rai, 2008; Rai *et al.*, 2013). (b) Crustal thickness plotted as function of elevation for different lithospheric thicknesses. Coloured stars/squares/dots = crustal thicknesses calculated as before where colour indicates lithospheric thickness at that location; solid lines = isostatic relationships determined by setting zero-elevation crustal thickness to 30 and 40 km using crustal density of 2.7 Mg m^{-3}; dashed lines = relationships calculated for crustal densities of 2.65 and 2.75 Mg m^{-3}; dotted lines = relationships calculated for crustal densities of 2.76 and 2.9 Mg m^{-3} (i.e. density range estimated from v_p/v_s ratios; Brocher, 2005).

An isostatic model can be used to predict elevation from these crustal thicknesses and densities. Observed elevations deviate substantially from this Airy isostatic relationship which implies that some fraction of elevation is maintained by other means (Rai *et al.*, 2013; Figure 4.5). The narrow range of crustal density variation combined with an absence of an east-west trend suggest that observed isostatic deviations are not easily accounted for by crustal heterogeneity. In particular, there is little evidence for magmatic underplating along the Western Ghats south of 20 °N where

the highest average elevation occurs (Tiwari *et al.*, 2006; Rao *et al.*, 2015). Instead, it is more likely that sub-crustal heterogeneity plays an important role in generating and maintaining some proportion of Indian topography.

Although much of northern India is dominated by thick ($>$ 150 km) lithosphere, there is evidence that continental lithosphere as thin as 100 km lies beneath the southwestern portion of the peninsula (Kumar *et al.*, 2013a,b; Priestley & McKenzie, 2013). This variation in lithospheric thickness could play a role in supporting the elevation of the Western Ghats. However, the relationship between crustal thickness, lithospheric thickness, and regional elevation is not consistent with a straightforward isostatic balance which implies that a component of sub-plate support may be required.

4.1.3 Flexural Analysis

The spectral relationship between free-air gravity anomalies and topography is analysed to determine the flexural rigidity of the Indian plate (Becker *et al.*, 2009; Förste *et al.*, 2011). First, the admittance, $Z(k)$, which is the ratio of free-air gravity and topographic anomalies as a function of wavenumber, k, is calculated within a 1550×1950 km^2 box that encompasses the bulk of Peninsular India (Figures 4.6a & b). Z is a measure of the degree of compensation and is often used to determine T_e, the elastic thickness. At short-wavelengths, Z approaches a constant value of ~ 120 mGal km^{-1}. Using the infinite slab approximation, $Z \sim 2\pi\rho_{cu}G$ where $G = 6.67 \times 10^{-11}$ m^3 kg^{-1} s^{-2} (Watts, 2001). This approximation yields an upper crustal density of $\rho_{cu} \sim 2.9$ Mg m^{-3}. It is consistent with estimates of crustal density obtained from receiver function studies and reflects the fact that basaltic rocks and Precambrian basement of amphibolite-granulite facies are the predominant lithologies (Newton & Hansen, 1986).

An inverse model is used to calculate T_e and to estimate the percentage of sub-surface loading (McKenzie & Fairhead, 1997; McKenzie, 2003). This model seeks a value of T_e that minimises the misfit between observed and calculated values of Z (Figures 4.6c & d). A T_e of $9.8^{+3.7}_{-2.0}$ km is obtained with a sub-surface loading percentage of 17^{+27}_{-13} %. This value agrees with that of McKenzie *et al.* (2015) who analysed a smaller box located in the northern half of the box used here. It is also consistent with the average regional value obtained by coherency analysis of Bouguer gravity anomalies by Mouthereau *et al.* (2013). This result supports the finding that admittance and Bouguer coherency studies yield similar values of T_e provided that large topographic signals exist, which are at least partially coherent with the free-air gravity field (McKenzie, 2016).
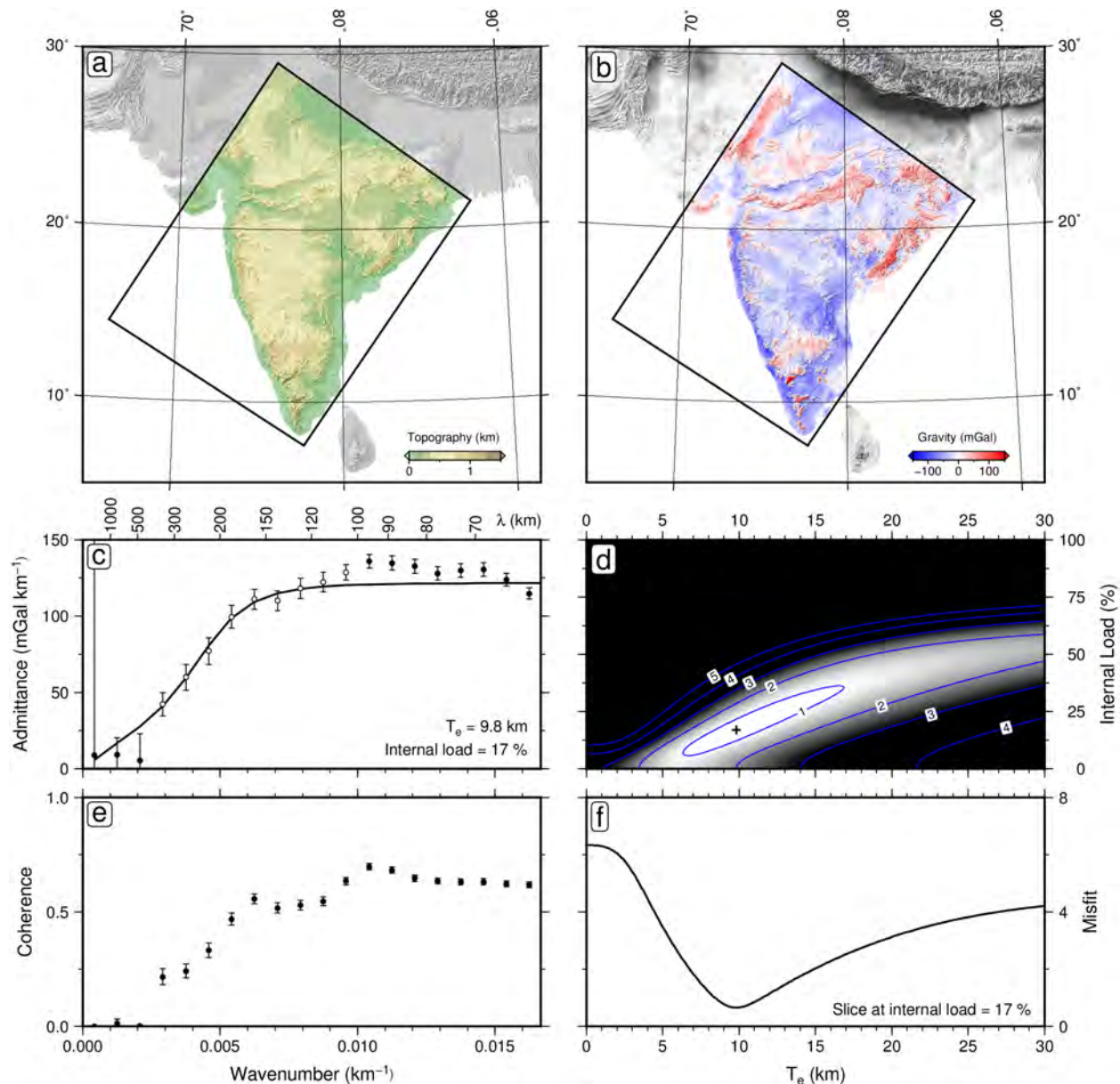
Figure 4.6: Admittance analysis of gravity and topography. (a) Map of topography based upon SRTM30_PLUS model (Becker *et al.*, 2009). Oblique box = region of analysis (1550 × 1950 km^2). (b) Map of free-air gravity anomalies calculated from EIGEN-6C3stat dataset at 6 minute resolution (Förste *et al.*, 2011). (c) Open/solid circles with vertical bars = observed admittance values with ± 1σ plotted as function of wavenumber; solid line = theoretical admittance function that best fits open circles (100 km ⩽ λ ⩽ 400 km) calculated for elastic plate model where T_e = 9.8 km, internal load = 17%, crustal thickness = 35 km, upper crustal thickness = 15 km, upper crustal density = 2.9 Mg m^{-3}, lower crustal density = 2.95 Mg m^{-3}. (d) RMS misfit between observed and calculated admittance plotted as function of T_e and internal load. Black cross = locus of global minimum. (e) Coherence between free-air gravity anomaly and topography plotted as function of wavenumber. (f) Slice through misfit function shown in (d) for internal load of 17%. Doubling of minimum misfit value yields T_e range of 7.8–12.5 km.

The value of T_e determines the wavelength over which flexural deformation can be supported (Watts, 2001). This wavelength is approximately $\pi\alpha_f$ where

$$\alpha_f = \left[\frac{(\rho_m - \rho_s)\, g}{4D} \right]^{-1/4}, \tag{4.1}$$

and

$$D = \frac{E_Y T_e^3}{12\left(1 - \nu^2\right)}, \tag{4.2}$$

$\rho_m = 3.3$ Mg m^{-3} is mantle density, $\rho_s = 2.0$ Mg m^{-3} is the density of infilling sedimentary rocks, $g = 9.81$ m s^{-2}, $E_Y = 10^{11}$ N m^{-2} is Young's modulus and $\nu = 0.25$ is Poisson's ratio. Substitution yields a $\pi\alpha_f$ of 126^{+28}_{-19} km. This value is significantly smaller than the $> 2,000$ km wavelength of regional tilting and suggests that regional epeirogeny is not exclusively generated and maintained by flexural processes.

At the very longest wavelengths, the coherence between the free-air gravity field and topography tends to zero. This lack of coherence directly arises from the lack of correlation between negative long-wavelength free-air gravity anomalies and positive topographic tilting (Figure 4.3b).

4.2   Drainage Analysis

Indian physiography is markedly asymmetric (Figure 4.1a). This asymmetry dominates many aspects of its geomorphology including the drainage network. In principle, ubiquitous drainage networks should preserve coherent signals of temporally and spatially varying rock uplift rates (Whipple, 2009). Pritchard *et al.* (2009) and Roberts & White (2010) have shown that longitudinal river profiles can be inverted as a function of regional uplift subject to independent geologic calibration.

Cox (1989) argued that the present-day topography and drainage of India was created during Paleogene times when the Seychelles rifted away from the western margin of the peninsula in the presence of a mantle plume. However, there is increasing evidence that any elevated topography generated during Deccan volcanism was rapidly eroded away and that relief was negligible by the beginning of Neogene times. During Eocene and Oligocene times, widespread lateritic deposits developed inboard of both margins (Bonnet *et al.*, 2014, 2016; Figure 4.7a). Combined with additional palaeoclimatic observations, this lateritisation suggests that a wet, tropical climate with low relief prevailed across most of Peninsular India at this time (Kent & Muttoni, 2008; Thorne

et al., 2012; Chatterjee *et al.*, 2013). Offshore, the Kerala-Konkan, Mahanadi, Krishna-Godavari and Cauvery deltas were dominated by fringing carbonate reef complexes, which suggests that the flux of clastic sediment was modest, despite humid climatic conditions. This observation provides further evidence for moderate topographic relief within drainage catchments during this period (Raju, 2008).
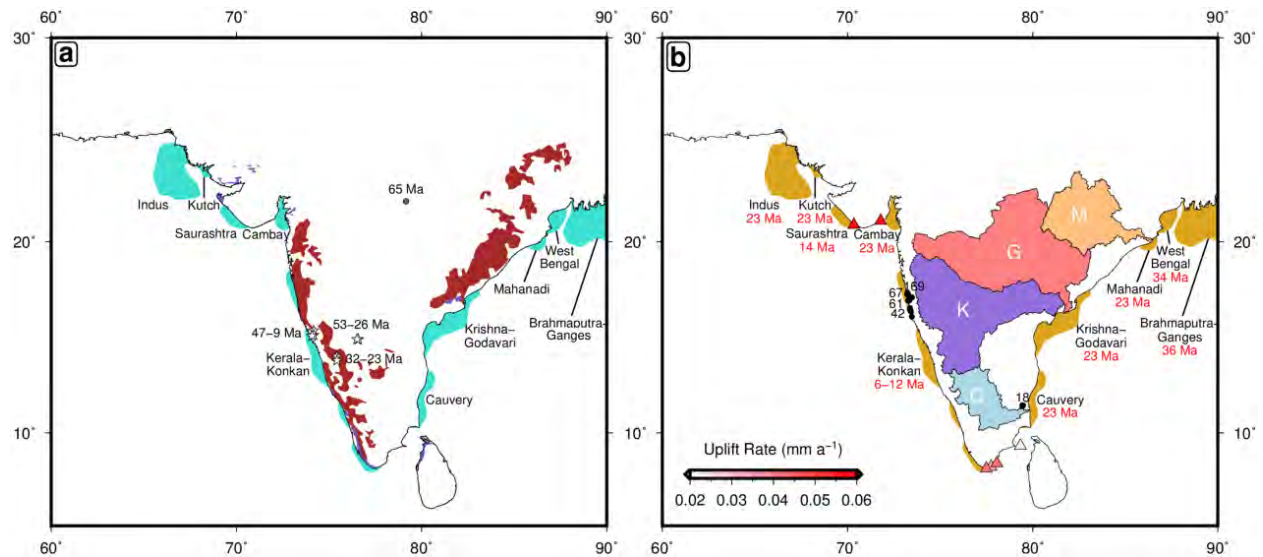
Figure 4.7: Cenozoic palaeogeography. (a) Summary of Eocene-Oligocene palaeogeography. Red polygons = lateritic deposits (FAO-UNESCO, 2007); labelled stars = locations and ages of laterites dated by $^{40}Ar/^{39}Ar$ analysis of cryptomelane (Bonnet *et al.*, 2016); blue circle = Early Paleocene (64.8 Ma) marine deposits (Keller *et al.*, 2009); blue polygons = Miocene marine deposits (Wandrey & Law, 1997); turquoise polygons = carbonate-dominated deltaic sedimentary deposits (Raju, 2008). (b) Miocene-Recent palaeogeography. Orange/red/purple/blue polygons = Mahanadi/Godavari/Krishna/Cauvery drainage catchments; labelled yellow polygons = clastic-dominated deltaic sedimentary deposits (number in red = age of transition from carbonate to clastic-dominated deposition; Raju, 2008); coloured triangles = elevated Pleistocene marine terraces with uplift rate given by colour scale bar (Pedoja *et al.*, 2011); solid labelled circles = Mio-Pliocene lignite deposits with elevations (Brückner, 1987; Singh *et al.*, 1992; Suryawanshi & Golekar, 2014).

Between Miocene times and the present day, these deltas have evidently experienced major influxes of clastic material that rapidly prograded over adjacent continental shelves (Figure 4.7b). The dramatic change in palaeogeography suggests that the present-day topography is relatively youthful. An important corollary is that the drainage network probably contains useful information about the spatial and temporal distribution of topographic growth. Circumstantial evidence for modest pre-Neogene topographic relief suggests that it is reasonable to prescribe a flat, zero elevation, starting condition for inverse modelling of drainage networks. However, although any starting condition could be used for inverse modelling, the inclusion of moderate topographic relief would be unlikely to

dramatically alter the principal conclusions. A combination of stratigraphic relationships, incision patterns, and the great distances over which Paleocene lavas flowed, imply that eastward-directed drainage patterns were established by this time (Cox, 1989; Knight *et al.*, 2003; Sheth, 2007). Deep incision of the Eastern Ghats region by eastward-flowing rivers provides corroborative evidence that these drainage patterns are probably antecedent and have therefore been relatively stable over a long period (Widdowson & Cox, 1996; Gunnell & Harbor, 2010).

4.2.1   Drainage Inventory

A digital elevation model was compiled using the Advanced Spaceborne Thermal Emission and Reflection Radiometer (ASTER) dataset, which was decimated to yield a pixel size of 60 m. Vertical resolution is 17 m at the 95% confidence level (Meyer *et al.*, 2011). First, anomalous spikes and sinks were removed using ArcGIS hydrologic tools. Drainage networks were then recreated using standard flow-routing algorithms. Overland flow is set to occur when upstream drainage area exceeds 15 km^2, which is reasonable for a valley slope of intermediate gradient (Montgomery & Dietrich, 1988).

1916 longitudinal river profiles were extracted, from which a smaller peninsular inventory of 530 rivers was selected. This smaller dataset specifically excludes the Narmada and Tapti basins where Cenozoic faulting may have modified or even reversed local drainage planforms (Tarboton, 1997; Copley *et al.*, 2014). In areas where there is negligible topography and/or internal drainage, the ability to adequately recover drainage networks can be compromised and the effective horizontal resolution decreases to hundreds of metres. In all regions, fidelity of the recovered drainage pattern was carefully checked using Landsat imagery (Figure 4.8). Extracted rivers that deviated significantly from their true courses were excised. In general, drainage recovery is excellent across Peninsular India.

A useful by-product of drainage extraction is the landscape response time, τ_G, which records the potential length of the 'tape recorder' that the drainage network represents (Roberts *et al.*, 2012; Figure 4.9). Note that strictly speaking, τ_G only applies within river channels. The maximum value of τ_G for India is 80 Ma which suggests that the peninsula-wide drainage pattern has the potential to record Cenozoic rock uplift history. τ_G was calculated by assuming that $v = 3.7$ and $m' = 0.37$. These values were chosen by an independent calibration procedure that is described in Section 4.3. Within the Western Ghats, there is a marked disparity in τ_G at the drainage divide that separates rivers draining into the Arabian Sea from those draining into the Bay of Bengal.
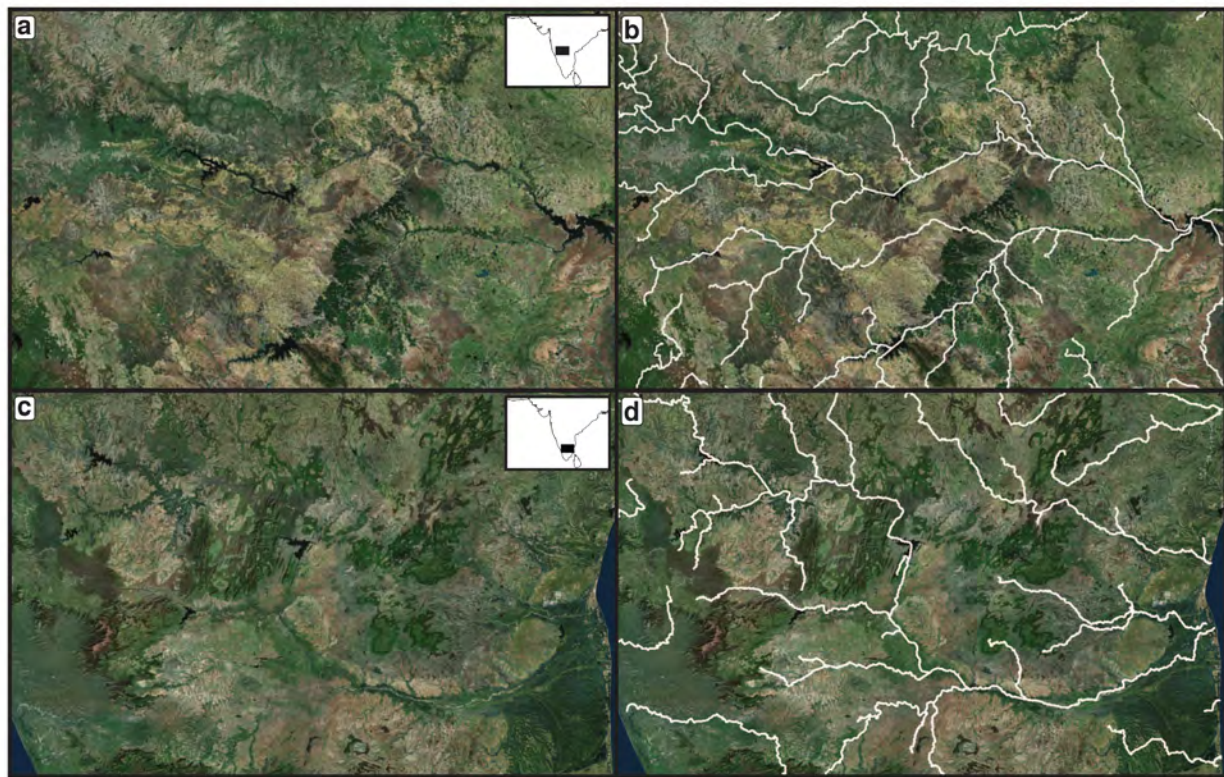
Figure 4.8: Landsat images of drainage patterns. (a) Map showing Landsat image of portion of southern Deccan Plateau (see inset map). (b) Landsat image overlain by drainage pattern recovered from flow-routing algorithms. (c) Map showing Landsat image of portion of southern Karnataka and Palghat Gap region (see inset map). (d) Landsat image overlain by recovered drainage pattern.

It has been proposed that disparities in τ_G (or its dimensionless equivalent χ) at drainage divides are indicative of migration of the divide toward the catchment with a longer response time (Willett *et al.*, 2014). Landscape response time assumes that rock uplift signals are inserted at river mouths and propagate upstream. In many regions such as India, Australia and North America, regional uplift has a spatially asymmetric distribution which means that rock uplift signals have been inserted at positions other than coastlines. Consequently, the juxtaposition of markedly different values of τ_G on either side of a drainage divide probably reflects the way in which the drainage networks are arranged with respect to the pattern of regional uplift. At the head of a given river, $A' \rightarrow 0$ and $\tau_G \rightarrow \infty$ which means that the magnitude of any actual disparity in τ_G is also dependent upon the chosen overland flow threshold (Willett *et al.*, 2014; Rudge *et al.*, 2015).

From a practical perspective, the Western Ghats escarpment— despite having an apparently pronounced cross-divide disparity in τ_G— can only have retreated by $\leqslant 100$ km since India-Seychelles rifting. This upper limit is the maximum distance between the continental shelf break and the
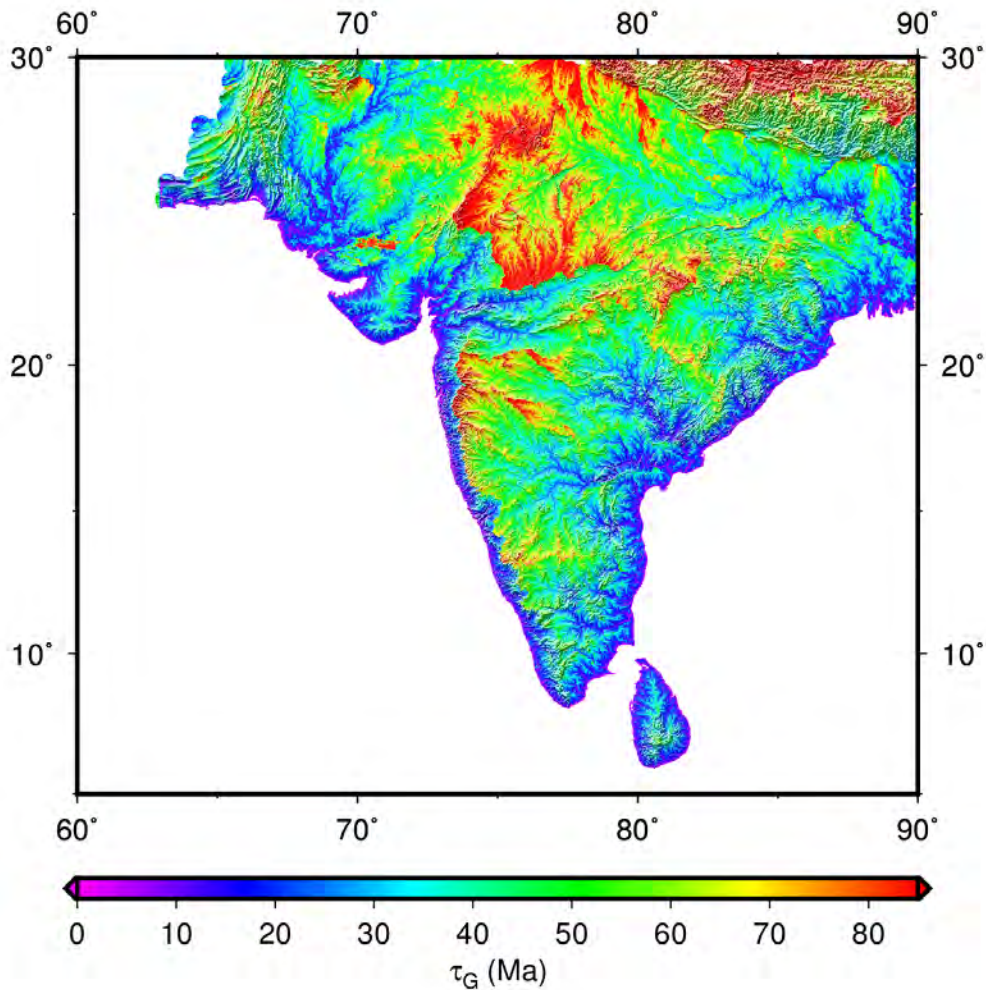
Figure 4.9: Landscape response time. Map of landscape response time, τ_G, calculated by solving Equation (4.11) for each drainage catchment where $v = 3.7$ m$^{0.26}$ Ma^{-1} and $m' = 0.37$. Note that, strictly speaking, τ_G only applies within river channels.

present-day escarpment (Gunnell, 1997; Widdowson & Mitchell, 1999; Kale & Subbarao, 2004; Figure 4.9). Lack of significant retreat implies that there has been a negligible change in upstream drainage area of the principal catchments. In the stream power formulation, upstream drainage area is taken to a fractional power which means that it can vary by $\pm 50\%$ without significantly changing regional uplift histories determined by inverse modelling (Paul *et al.*, 2014). This inference implies that changes in upstream drainage area triggered by drainage capture may not necessarily invalidate an inverse modelling strategy. Nevertheless, capture events could create knickzones that are not explicitly generated by regional uplift. Such knickzones probably occur close to watersheds and should be incoherent in space and time. If so, significant misfit excursions between observed and calculated rivers in affected catchments may be diagnostic of drainage capture. Thus, a range of geologic observations justify the simplifying assumptions used in inverse modelling of drainage
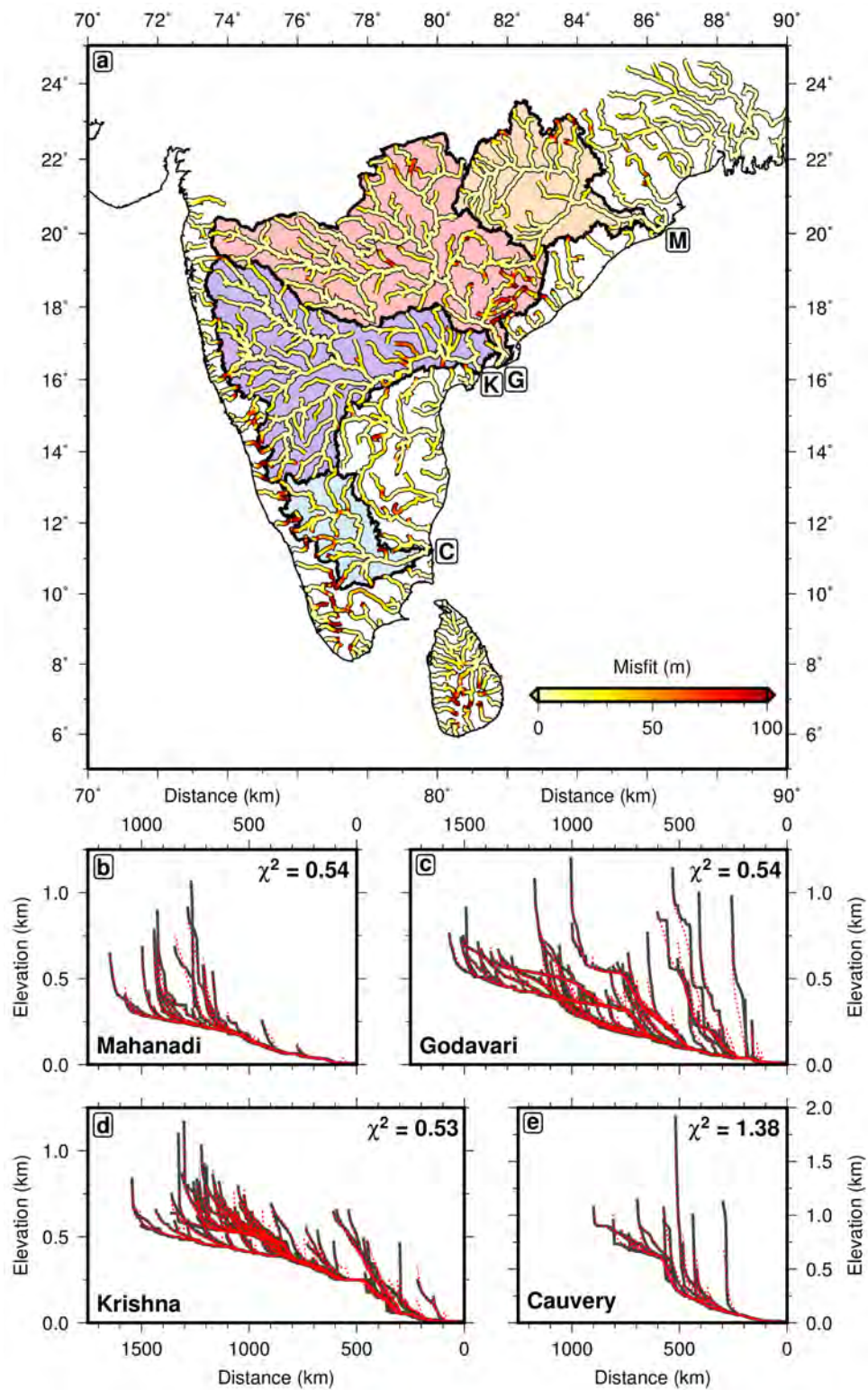
Figure 4.10: Observed and calculated river profiles (a) Map showing locations of four largest drainage catchments and residual misfit between observed and calculated river profiles ($v = 3.7$ m$^{0.26}$ Ma^{-1}, $m' = 0.37$, $\lambda_S = \lambda_T = 1$). Labels M/G/K/C = Mahanadi/Godavari/Krishna/Cauvery catchments; colour scale = size of residual misfit in meters. (b) Godavari catchment. Black lines = observed river profiles; red dotted lines = calculated river profiles obtained by inverse modelling. Residual misfit shown in top right-hand corner. (c) Mahanadi catchment. (d) Krishna catchment. (e) Cauvery catchment.

networks, particularly the significant assumptions that the initial topography at ~ 50 Ma had minimal relief and that the drainage planform has remained largely invariant.

In India, the recovered drainage network is dominated by four major river catchments: Mahanadi, Godavari, Krishna and Cauvery (Figure 4.10). Three of these rivers, together with their major tributaries, rise along the Western Ghats or Sahyadri escarpment and drain into the Bay of Bengal. The Mahanadi river originates in the foothills of the Eastern Ghats, also known as Mahendra Parvatam.

Longitudinal river profiles for each of these four catchments are shown in Figures 4.10b–e. Most of these river profiles have prominent long-wavelength knickzones that are indicative of disequilibrium. These knickzones have wavelengths of up to 300 km with amplitudes that consistently exceed 150 m. These wavelengths and amplitudes exceed changes in base level that are attributable to glacio-eustatic sea-level fluctuations (Siddall *et al.*, 2003; Miller *et al.*, 2005). There is poor correlation between major changes in geology and knickzone development, indeed the majority of knickzones occur within the relatively homogeneous Precambrian basement or Deccan basalt of the cratonic interior (Ambili & Narayana, 2014; Mandal *et al.*, 2016). Furthermore, major knickzones do not coincide with the location of Archaean and Proterozoic fault systems, pointing to limited Cenozoic tectonic reactivation of these ancient structures (Gunnell & Harbor, 2008; Kale *et al.*, 2014). The challenge is to exploit these sets of river profiles to constrain the spatial and temporal pattern of uplift rate for Cenozoic times.

4.2.2   Inverse Modelling

Change in elevation, z', as a function of time, t, along a longitudinal river profile depends upon the balance between the rate of regional rock uplift, $U(x,t)$, and the rate of erosion, $E(x,t)$, where x is distance along the profile. Thus

$$\frac{\partial z'}{\partial t} = E(x,t) - U(x,t). \tag{4.3}$$

The fluvial geomorphic community is primarily interested in developing a quantitative understanding of erosional processes. Here, the aim is to use river profiles to determine U, which means that $E(x,t)$ must be parameterised. It is usually assumed that E can be written in accordance with a

stream power formulation such that

$$E(x,t) = -vA(x)^m \left(\frac{\partial z'}{\partial x} \right)^n + \kappa_e \frac{\partial^2 z'}{\partial x^2}, \tag{4.4}$$

where v is a constant with dimensions of velocity if $m' = 0$, $A'(x)$ is the upstream drainage area along a river profile, m' and n' are the concavity indices, and κ_e represents erosional 'diffusivity'. The first term on the right-hand side of Equation (4.4) is advective and represents detachment-limited or 'backwearing' processes. In other words, it determines the velocity at which knickzones migrate toward the head of a river (Howard & Kerby, 1983; Whipple & Tucker, 1999). The second term is diffusive and represents transport-limited or 'downwearing' processes (Sklar & Dietrich, 1998; Sklar, 2001; Whipple, 2002; Tomkin, 2003).

Previous studies show that the non-linear inverse problem can be posed and solved (Roberts & White, 2010; Roberts *et al.*, 2012). Inverse modelling of large inventories of river profiles suggests that Equation (4.4) can be simplified in several important respects. First, river profiles are usually sampled every 5 km, yielding a minimum resolvable κ_e of $\sim 5 \times 10^6$ m^2 Ma^{-1}. This value is significantly greater than reported estimates which indicates that the diffusive term can be safely ignored (Rosenbloom & Anderson, 1994). Secondly, Paul *et al.* (2014) and Czarnota *et al.* (2014) showed that the residual misfit between observed and calculated river profiles has a global minimum at $n' = 1$, regardless of the degree of model regularisation and smoothing. This controversial result is not universally accepted but there is limited evidence from field studies that $n' \sim 1$ (Whittaker *et al.*, 2007; Whittaker & Boulton, 2012). Furthermore, at the length scales of 10^2–10^3 km considered here, there is no convincing evidence for shockwave behaviour (Pritchard *et al.*, 2009).

In the light of these earlier studies, the change in elevation along a river profile can be expressed as

$$-\frac{\partial z'}{\partial t} = -vA^m \frac{\partial z'}{\partial x} + U \tag{4.5}$$

This equation can be solved using the method of characteristic curves (Luke, 1972, 1974, 1976; Weissel & Seidl, 1998; Pritchard *et al.*, 2009; Goren *et al.*, 2014; Rudge *et al.*, 2015). The solution is written in the form $z'(x,t) = z'(x(t),t)$ since

$$\frac{\mathrm{d}z'}{\mathrm{d}t} = \frac{\partial z'}{\partial t} + \frac{\mathrm{d}x}{\mathrm{d}t} \frac{\partial z'}{\partial x} = \left(vA^{m'} + \frac{\mathrm{d}x}{\mathrm{d}t} \right) \frac{\partial z'}{\partial x} - U(x(t),t). \tag{4.6}$$

which is expressed as two ordinary differential equations

$$\frac{\mathrm{d}x}{\mathrm{d}t} = -vA^{m'},$$

(4.7)

$$\frac{\mathrm{d}z'}{\mathrm{d}t} = -U(x(t), t).$$

(4.8)

The boundary conditions are

$$x = x^*, z' = z^* \text{ at } t = 0,$$

(4.9)

and

$$x = 0, z' = 0 \text{ at } t = \tau_G.$$

(4.10)

The first boundary condition refers to the present-day landscape, where elevation is z^* at an upstream distance of x^* along a river profile. The landscape response time, τ_G, represents the time taken for a knickzone to propagate from the mouth of a river to any given point, x, upstream. The second boundary condition represents a time in the past, τ_G, where the characteristic curve intersects the river mouth (i.e. $x = 0$ and $z' = 0$). Equations (4.7), (4.8) and (4.10) must satisfy

$$\tau_G = \int_0^{x^*} \frac{\mathrm{d}x}{vA^m}.$$

(4.11)

Solutions to Equations (4.7)–(4.10) take the form

$$\tau_G - t = \int_0^{x(t)} \frac{\mathrm{d}x}{vA^m},$$

(4.12)

$$z^* = \int_0^{\tau_G} U(x(t), t)\mathrm{d}t.$$

(4.13)

These equations determine the evolution of a single river profile. The algorithm developed by Rudge *et al.* (2015) has been used to simultaneously invert hundreds of river profiles (i.e. multiple observations of x^* against z^*) in order to determine the spatial and temporal evolution of regional uplift. This linear problem can be spatially and temporally discretised by employing a triangular mesh and by specifying a finite number of timesteps, respectively. The resultant set of spatial and temporal nodes is represented by a vector, $\mathbf{U}$, where intermediate values are obtained by linear interpolation. Since A' and x^* are known, Equation (4.8) can be integrated using the trapezoidal rule to yield τ_G. Characteristic curves are calculated from Equation (4.12) and combined with

linear interpolation to discretise Equation (4.13) using the trapezoidal rule. In this way, a matrix equation is constructed

$$\mathbf{z'} = \mathrm{M}\mathbf{U} \tag{4.14}$$

that describes elevation, $\mathbf{z'}$, at different loci along observed river profiles. This equation can be inverted to determine $\mathbf{U}$. A non-negativity constraint is imposed to suppress positive and negative oscillations. Since M usually has fewer rows than columns, it is appropriate to employ a damped least-squares approach. The non-negative least squares (NNLS) inverse problem is solved by minimising

$$\left| \mathrm{M}\mathbf{U} - \mathbf{z'} \right|^2 + \lambda_S^2 \left| \mathrm{S}\mathbf{U} \right|^2 + \lambda_T^2 \left| \mathrm{T}\mathbf{U} \right|^2. \tag{4.15}$$

The essential regularisation is imposed using spatial and temporal smoothing parameters, λ_S and λ_T, and their corresponding matrices, S and T, such that

$$\left| \mathrm{S}\mathbf{U} \right|^2 = \int_S \int_{t=0}^{t_{max}} \left| \nabla U \right|^2 \, \mathrm{d}t \, \mathrm{d}S, \tag{4.16}$$

and

$$\left| \mathrm{T}\mathbf{U} \right|^2 = \int_S \int_{t=0}^{t_{max}} \left| \frac{\partial U}{\partial t} \right|^2 \, \mathrm{d}t \, \mathrm{d}S. \tag{4.17}$$

A limited-memory Broyden-Fletcher-Goldfarb-Shanno algorithm (L-BFGS-B) is employed to solve this NNLS inverse problem since it is computationally fast and well-suited to sparse matrix problems (Broyden *et al.*, 1973).

For significant reasons, the approaches described by Goren *et al.* (2014) and by Fox *et al.* (2014), who developed alternative linear least squares algorithms that use an empirical Bayesian scheme, are not exploited here. In their algorithms, an *a priori* model of uplift history is selected. This *a priori* model is based upon a guess of the average uplift rate that is calculated from channel elevation and upstream drainage area. By updating this *a priori* model with the observations, an *a posteriori* model is calculated. This *a posteriori* model is prevented from straying away from the *a priori* model and therefore inherits its attributes. In this sense, observational constraints are being exploited twice. Goren *et al.* (2014) do not incorporate spatial and temporal damping. Instead, they chose to damp departures from their *a priori* model. An important consequence of this approach is that oscillatory behavior can only be reduced by forcing the *a posteriori* model to stay close to the *a priori* model. Fox *et al.* (2014) damp spatial gradients of uplift rate by specifying an arbitrary correlation length scale parameter but chose not to damp temporal gradients of uplift

rate. Both algorithms achieve best-fit solutions with residual misfits of up to ±150 m and ±500 m, respectively.

4.2.3   Cumulative Uplift History

An inventory of 530 river profiles were simultaneously inverted to determine regional rock uplift rate as a function of space and time (Figures 4.10 & 4.11). Residual misfits between observed and calculated river profiles from the major catchments are $\chi^2 \sim 0.5$–1.5. Quality of fit suggests that knickzones are generated when spatially coherent signals propagate through drainage networks according to the stream power formulation. Calculated profiles match laterally continuous, but time-transgressive, palaeosurfaces that delineate upland plateaux. These palaeosurfaces age upward and tilt eastward with increasing dip (Gunnell, 1997; Bonnet *et al.*, 2016). They attest to a prolonged phase of regional rock uplift that is focused along the Western Ghats. Vertical separation between palaeosurfaces increases through time, which suggests that regional uplift has increased toward the present if these surfaces are equally separated in time.

Calculated cumulative rock uplift histories depend upon the degree of spatial and temporal smoothing and upon the chosen values of the erosional parameters (Figure 4.11). Here, $v = 3.7$ and $m' = 0.37$ are selected. These values are determined by independent calibration described below. The values of λ_S and λ_T are chosen to ensure that the smoothest model which yields the smallest misfit between observed and calculated river profiles is obtained for a given set of erosional parameters (i.e. v, m'). To choose the optimal values of λ_S and λ_T, a large suite of individual inverse models are computed in which λ_S and λ_T were simultaneously co-varied (Figure 4.12a). Residual misfit, χ^2, is plotted as a function of λ_S and λ_T so that the smoothest model that yields the best fit between observed and calculated river profiles can be identified (Parker, 1994).

Identification of the optimal model is neither a precise nor an objective art. Although some misfit reduction inevitably results from the choice of smoothing parameters, visual inspection suggests that NNLS linearised inversion yields small residual misfits along the majority of river profiles. Quality of fit may reflect the lower degree of numerical smearing that is achievable using the method of characteristic curves since it permits finer discretisation than non-linear finite difference or finite volume methods with equivalent computation times (Goren *et al.*, 2014; Campforts & Govers, 2015; Figure 4.10).
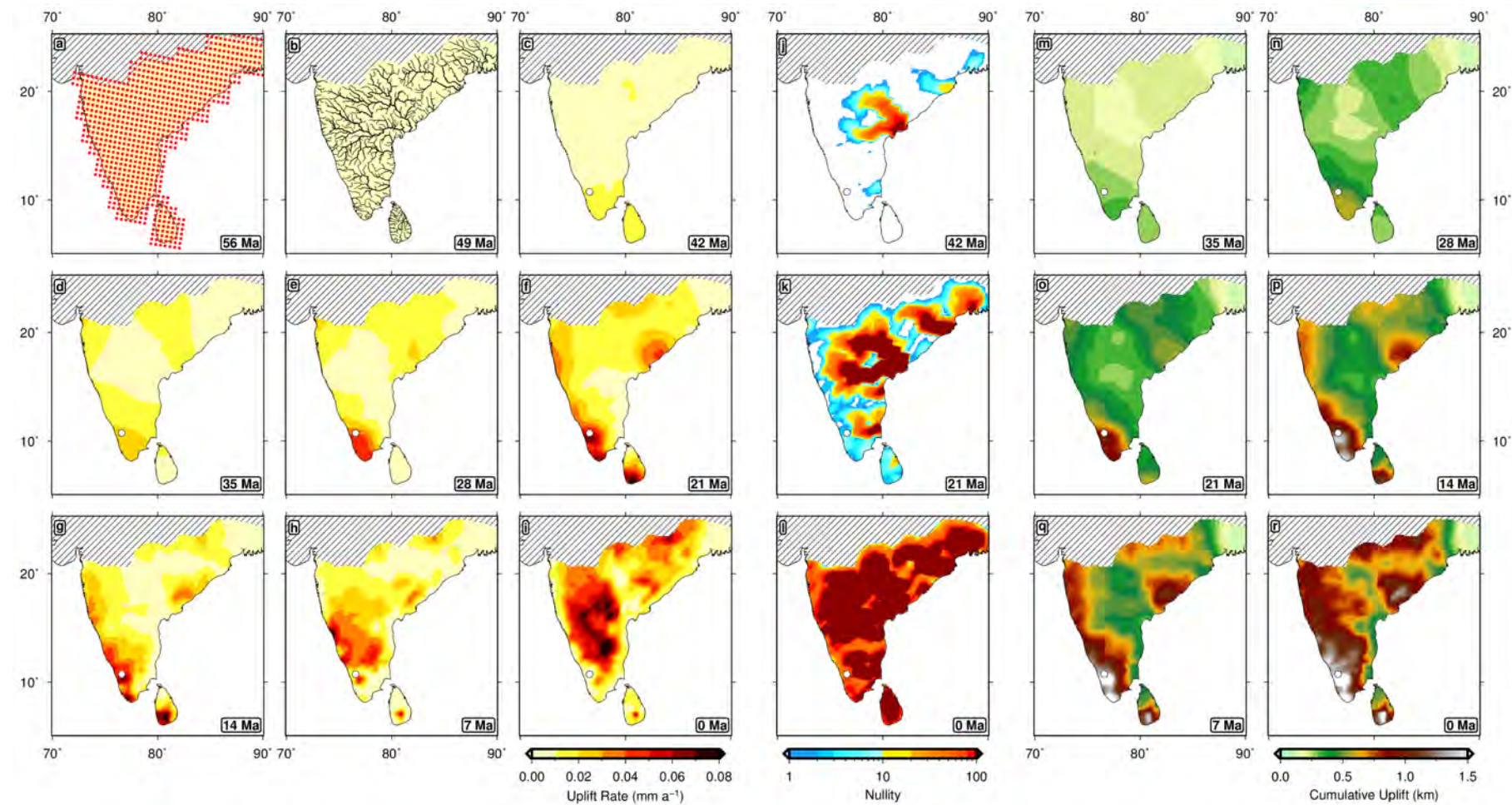
Figure 4.11: Uplift history of Peninsular India. (a) Map showing minimal uplift rate at 56 Ma. Red grid = spatial distribution of nodes at which rock uplift rate, U, is permitted to vary during inverse modelling where $v = 3.7 \text{ m}^{0.26} \text{ Ma}^{-1}$, $m' = 0.37$, $\lambda_S = \lambda_T = 1$. Hashed polygon = region excluded from inverse modelling. (b) Map showing distribution of drainage network overlain on uplift rate at 49 Ma. (c)–(i) Spatial uplift rate calculated as function of time between 42 and 0 Ma. White circle = locus of Palghat Gap (Figure 4.14). (j)–(l) Nullity plots at 42, 21 and 0 Ma showing number of non-zero entries in model matrix. (m)–(r) Cumulative uplift calculated as function of time between 35 and 0 Ma.

Observed and calculated river profiles from the Cauvery catchment have higher residual misfit compared with other major catchments (Figure 4.10e). It has been suggested that significant residual misfit may be a consequence of river capture events or drainage divide migration that could potentially generate knickzones which would be spatially and temporally inconsistent with respect to a stream-power formulation (Radakrishna, 1992; Fox *et al.*, 2014).

For the chosen values of v and m', negligible cumulative rock uplift occurred between 56 and 42 Ma (Figure 4.11). At 35 Ma, regional uplift commenced at the southern tip of India and propagated northward. By 21 Ma, most of the peninsula appears to have been uniformly uplifted by a total of 300–400 m. The calculated rate of uplift is $\leqslant 0.02$ mm a^{-1} with the exception of the Southern Granulite Terrain and the Deccan Plateau where calculated rates are 0.05–0.06 mm a^{-1} and 0.02–0.03 mm a^{-1}, respectively. The Eastern Ghats experienced an uplift rate of ~ 0.03 mm a^{-1} but, after 28 Ma, its rate lagged behind that of the Deccan Plateau. Rock uplift of the Southern Granulite Terrain then spread northwestward while uplift of the Deccan Plateau spread southeastward, forming a continuous corridor with a uniform uplift of ~ 500 m along the Western Ghats and Kerala-Konkan coastal plain. Between 21 and 14 Ma, eastward tilt of the Indian Peninsula rapidly developed at rates of 0.03–0.08 mm a^{-1} with regional rock uplift focused along the western margin. During the same period, uplift rates of 0.02–0.04 mm a^{-1} are predicted for the Eastern Ghats. Uplift rate decreased to $\leqslant 0.06$ mm a^{-1} between 14 and 7 Ma but remained focused on existing elevated areas, apart from a switch to comparatively modest rates at the northern extremity of the western margin. After 7 Ma, the spatial pattern changed again and rock uplift rates of up to 0.07 mm a^{-1} occurred within the central plateaux and along parts of the western margin.

How well resolved is this cumulative uplift history? The spatial distribution of τ_G suggests that Indian river profiles potentially record Cenozoic rock uplift signals (Figure 4.9). A more rigorous assessment of spatial and temporal resolution is obtained by calculating the number of non-zero values in the model matrix, M, as a function of time (Figures 4.11j–l). The spatial distribution of these values shows that uplift signals between ~ 20 Ma and the present day are well resolved. Prior to ~ 42 Ma, spatial resolution significantly deteriorates. This result suggest that the drainage network is primarily sensitive to Neogene rock uplift signals.

Significant Neogene uplift disagrees with the conclusions drawn by Mandal *et al.* (2015b). Based on the apparent consistency between millennial ^{10}Be erosion rates and Cenozoic AFTA rates, they suggested that the landscape of the southern Indian Peninsula is in steady state (i.e. slow isostatic rebound is balanced by landscape erosion). Available evidence suggests that their conclusions may

not be correct for two key reasons. First, their spatially averaged ^{10}Be erosion rate of 30.8 $\pm$ 8.5 m Ma^{-1} is, in fact, significantly greater than the AFTA-derived rates (15–20 m Ma^{-1}). This discrepancy is not consistent with a steady-state interpretation (Gunnell *et al.*, 2007). Secondly, if regional uplift mostly occurred between 35 and 7 Ma, as the inverse modelling suggests, slower millennial erosion rates may simply reflect a subsequent reduction in uplift rate (Figure 4.11).

4.2.4   Precipitation

The age of onset of the Indian monsoon is generally considered to be $\sim$ 8 Ma with two major intensifications after 3.6 Ma (An *et al.*, 2001; Cronin, 2010). A significantly earlier onset date of $\sim$ 15 Ma has also been proposed (Clift & Plumb, 2008; Iaffaldano *et al.*, 2011). Variable precipitation is not included in the stream power formulation for three reasons. First, cosmogenic nuclide ^{10}Be studies suggest that no clear link exists between precipitation and erosion rates (von Blanckenburg, 2004; Mandal *et al.*, 2015b). Secondly, it has been argued that no appreciable change in spatially averaged precipitation rates occurred over the Indian Peninsula since Eocene times (Reuter *et al.*, 2013; Shukla *et al.*, 2014). Finally, it has been shown that varying precipitation rate only affects calculated rock uplift histories if it has a periodicity of several million years or more (Paul *et al.*, 2014; Wilson *et al.*, 2014; Stephenson *et al.*, 2014).

Nevertheless, there is likely to be positive feedback between precipitation pattern and topographic relief (Gunnell, 1997). Modern precipitation patterns can be orographically controlled and the monsoon intensification observed between 15 and 8 Ma could be related to the Western Ghats having reached some threshold elevation (Nair, 2006). Faunal and floral shifts in Early to Mid-Miocene (23–14 Ma) times suggest that a topographic barrier did develop, implying that Neogene growth of the Western Ghats and modification of precipitation patterns are indeed coupled (Van Bocxlaer *et al.*, 2009; Kern *et al.*, 2013).

4.3   Calibration and Testing

4.3.1   Erosional Parameters

The calculated cumulative rock uplift history presented in Figure 4.11 is predicated upon having selected particular values of v and m'. v and m' are chosen using an objective strategy that exploits

the computational speed of the NNLS linear inverse algorithm. First, it is straightforward to carry out a parameter sweep where m' is varied at increments of 0.05 between 0 and 1 with minimal damping (i.e. $\lambda_S = \lambda_T = 10^{-3}$; Figure 4.12b). This systematic sweep reveals that there is a weak global minimum at $m' = 0.37^{+0.16}_{-0.11}$ where the quoted uncertainty reflects values of m' that yield misfit values < 125% of that at the global minimum. This range of values broadly agrees with published estimates (Stock & Montgomery, 1999; van der Beek & Bishop, 2003; Mandal *et al.*, 2016). The shape of the misfit function emphasises that m' is unlikely to have a fractional value significantly greater than 0.5.

λ_S and λ_T are then co-varied between 10^{-3} and 10^3 for $m' = 0.37$ to identify the smoothest model that yields the smallest residual misfit (Figure 4.12a). The chosen optimal model is at $\lambda_S = \lambda_T = 1$. If the parameter sweep for m' is repeated for these values of λ_S and λ_T, the global minimum shifts to $m' = 0.57^{+0.15}_{-0.21}$ (Figure 4.12b). A weak positive trade-off exists between m' and the values of λ_S and λ_T. This trade-off is expected: a highly damped inverse model can only find an appropriately small misfit between observed and calculated river profiles by increasing the rate of upstream incision which is achievable by increasing m'. To address this issue, it is noted that the suite of observed and calculated rock uplift rates should also agree, subject to the negative trade-off that exists between m' and v (Roberts & White, 2010). When $m' = 0.37$, there is an improved fit ($\sim$ 20%) between calculated and observed uplift rates than when $m' = 0.57$, irrespective of the value of v applied at either value of m' (Figure 4.12c). Further, $m' = 0.37$ falls within a statistically acceptable range of misfit tolerance for $\lambda_S = \lambda_T = 1$. A value of $m' = 0.37$ is therefore applied, as fits to uplift rate constraints are optimised whilst preserving acceptable fit between observed and modelled river profiles.

The value of v sets the pace for landscape erosion but it does not directly affect the residual misfit between observed and calculated rivers. Since published values of v have considerable variation, its value is determined here through calibration against independent rock uplift rate estimates (Figure 4.12c; Table 4.1). These estimates comprise U/Th dates from emergent marine terraces, heights and biostratigraphic ages of lignite deposits, together with elevations and magnetostratigraphic ages of shallow marine inter-trappean horizons. ^{40}Ar/^{39}Ar dates from lateritised palaeosurfaces are also considered, although their original elevation is uncertain.

Although measurements are sparse, U/Th dates exist from Marine Isotopic Stage (MIS) 5e coral terraces that are exposed at 3–15 m above sea level along the west coast. These dates imply a NW-SE gradient of rock uplift rate from 0.02 to 0.1 mm a^{-1} (this range is 0.0 to 0.09 mm a^{-1}
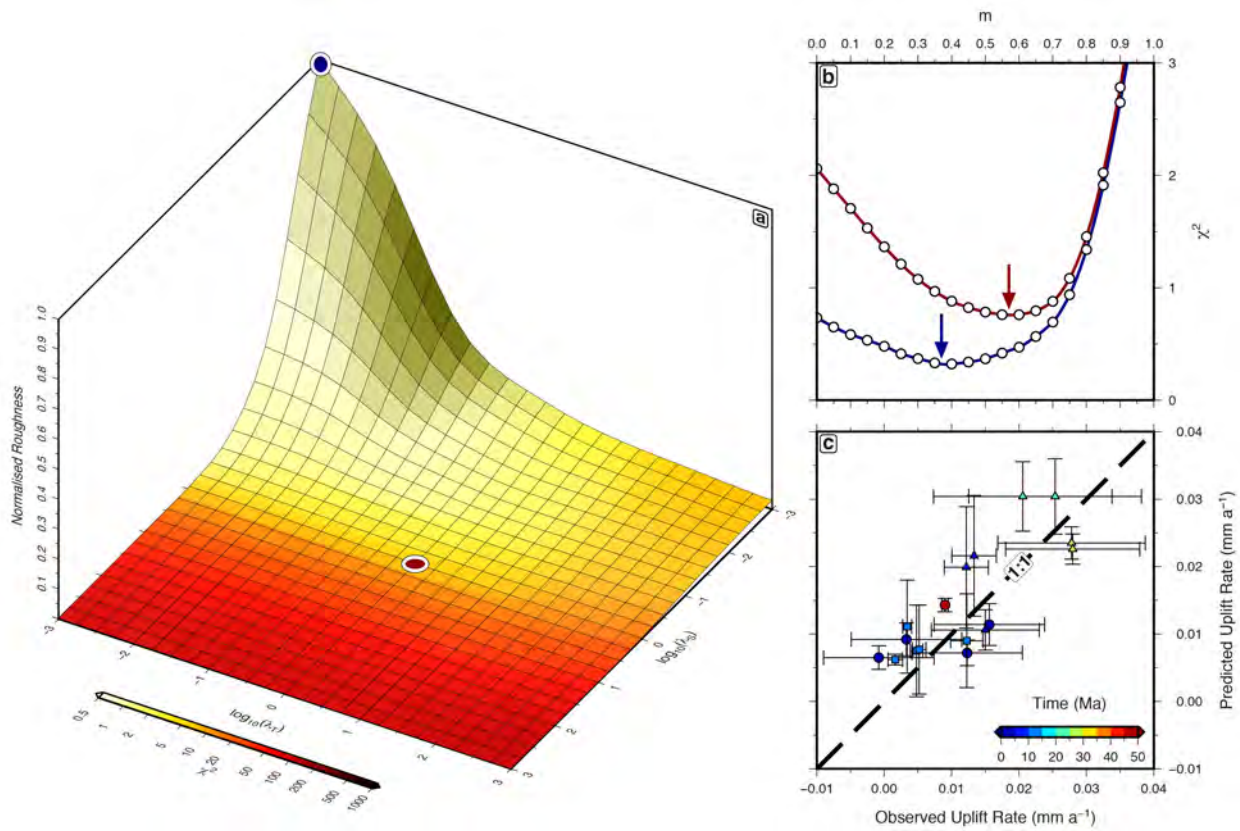
Figure 4.12: Calibration of model parameters. (a) Model misfit and roughness plotted as function of λ_T and λ_S. Blue/red circles = loci of inverse models where $\lambda_T = \lambda_S = 10^{-3}$ and $\lambda_T = \lambda_S = 1$, respectively. (b) Residual misfit, χ^2, plotted as function of m' for $\lambda_T = \lambda_S = 10^{-3}$ (blue curve) and $\lambda_T = \lambda_S = 1$ (red curve). Open circles = calculated values; arrows = loci of global minima at $m' = 0.37$ (blue) and at $m' = 0.57$ (red). (c) Observed uplift rates from emergent marine terraces (circles), lignite deposits (squares), and incised palaeosurfaces (triangles) plotted against calculated rock uplift rates. Optimal calculated rates determined by inverse modelling where $v = 3.7^{+0.8}_{-1.2}$ m$^{0.26}$ Ma^{-1}, $m' = 0.37$ and $\lambda_T = \lambda_S = 1$. Coloured circles/squares/triangles with vertical/horizontal bars = observed vs. calculated uplift rates and their uncertainties averaged over different timespans according to scale bar; dashed line = 1:1 relationship. Uncertainty on calculated rates corresponds to upper/lower bounds for values of v whose RMS uplift rate misfit is $< 125\%$ of global minimum (i.e. $v = 2.5$–4.5 m$^{0.26}$ Ma^{-1}); uncertainty on observed rates corresponds to errors in age and elevation of a given deposit.

when corrected for MIS 5e sea level of 3 m; Siddall *et al.*, 2006; Pedoja *et al.*, 2011). The highest terraces crop out along the Saurashtra coast where rift structures have been reactivated as reverse faults (Bodin & Horton, 2004). Elevated terraces also occur in tectonically inactive regions such as Kerala (Figure 4.1c). Holocene emergent marine terraces and raised beach deposits that were dated using ^{14}C and U/Th techniques are also exposed 2–3 m above sea level along the west coast. These features are typically ~ 1 m higher than equivalent features exposed along the east coast, suggesting that long-wavelength tilting is ongoing (Banerjee, 2000; Alappat *et al.*, 2015; Figure 4.7b). The

youthfulness of these terraces and deposits, combined with the possible existence of a mid-Holocene eustatic highstand, implies that reliable long-term uplift rates cannot be extrapolated (Woodroffe & Horton, 2005; Kench *et al.*, 2009).

Extensive lignite horizons, dominated by mangrove swamp flora, are found within the Mio-Pliocene Warkalli and Cuddalore Formations on both sides of the peninsula. Along the west coast at Malvan, lignites are exposed at elevations of 80–150 m. On the east coast at Neyveli, similar deposits occur at 10 m (Figure 4.7b). Additional evidence for Neogene uplift along the west coast comprises shallow marine deposits of the Late Burdigalian to Early Langhian ($\sim$ 15 Ma) Quilon Formation. These deposits are now exposed at elevations of $\leqslant$ 92 m in the hinterland of the Kerala coastal plain (Singh, 1998; Reuter *et al.*, 2013; Figure 4.7b).

The existence of $\sim$ 65 Ma old inter-trappean shallow marine deposits at elevations of $\sim$ 600 m near Jhimili indicates that regional topography was subdued following the main phase of Deccan volcanism. Present-day topography is inferred to have grown significantly in the intervening period (Keller *et al.*, 2009). This inference in conjunction with the subsequent onset of pervasive lateritisation suggest that regional relief was probably modest during Eocene and Oligocene times. Studies that combine digital elevation models with ^{40}Ar/^{39}Ar dating of cryptomelane suggest there are up to three topographically concordant lateritic palaeosurfaces in the western highlands (Gunnell, 1998; Bonnet *et al.*, 2014, 2016). These deposits crop out at elevations of 650–1200 m and have ages of 23–53 Ma. If these lateritic palaeosurfaces originally formed at elevations of 0–600 m, rock uplift rates of 0.02–0.03 mm a^{-1} since 23 Ma can be inferred (Widdowson, 1997; Sheth, 2007; Bonnet *et al.*, 2014). The inferred range of 0–600 m is conservative and the higher value is determined from the average elevation above sea level of incised valleys. Also included are uplift rates estimated from the separation of stacked palaeosurfaces and from the youngest ^{40}Ar/^{39}Ar ages obtained from underlying weathering profiles. These values assume that the youngest ages represent abandonment of the palaeosurface and onset of incision (Beauvais & Chardon, 2013).

A parameter sweep, where v was varied at increments of 0.1 between 2.2 and 5.2 m$^{0.26}$ Ma^{-1}, was used to identify the value of v which minimises the misfit between observed and calculated rock uplift rates. For $m' = 0.37$, the optimal value of v is $3.7^{+0.8}_{-1.2}$ m$^{0.26}$ Ma^{-1}. The upper and lower bounds correspond to values of v that yield root mean square (RMS) misfit values $< 125\%$ of its value at the global minimum.

Table 4.1: Observed and calculated uplift rates for Peninsular India. * = in decimal degrees; El. Range = Elevation Range; O.U.R. = Observed Uplift Rate; P.U.R. = Predicted Uplift Rate; [a]Keller *et al.* (2009): magnetostratigraphic dating of shallow marine intertrappean beds; [b]Bonnet *et al.* (2016): $^{40}Ar/^{39}Ar$ dating of cryptomelane from weathering profiles beneath lateritic palaeosurfaces; [c]Singh *et al.* (1992), [d]Brückner (1987), [e]Kumaran *et al.* (2004), [f]Suryawanshi & Golekar (2014): biostratigraphic dating of lignite deposits; [g]Banerjee (2000): U/Th dating of emergent marine terraces.

Locality	Lon.*	Lat.*	Age Range (Ma)	El. Range (m)	O.U.R. (mm a^{-1})	P.U.R. (mm a^{-1})	Constraints
Jhimili	79.16	22.05	$64.9\pm0.1 - 0$	$0^{+30}_{-25} - 591$	0.009 ± 0.001	0.014 ± 0.001	a
Kappataswamy	76.51	14.96	$27.5\pm0.8 - 0$	$250\pm250 - 1019$	0.028 ± 0.010	0.022 ± 0.002	b
Channanghi	76.58	14.95	$26.3\pm1.3 - 0$	$250\pm250 - 981$	0.028 ± 0.011	0.023 ± 0.002	b
Triveni	75.43	13.84	$23.9\pm0.2 - 0$	$300\pm300 - 906$	0.025 ± 0.013	0.030 ± 0.006	b
Kumsi	75.42	14.05	$23.2\pm0.3 - 0$	$300\pm300 - 777$	0.021 ± 0.013	0.030 ± 0.005	b
Naveli	74.18	15.17	$8.7\pm0.2 - 0$	$25\pm25 - 141$	0.013 ± 0.003	0.022 ± 0.009	b
Caurem	74.08	15.13	$8.7\pm0.2 - 0$	$25\pm25 - 131$	0.012 ± 0.003	0.020 ± 0.009	b
Cudnem	74.08	15.13	$2.5\pm0.2 - 0$	$12.5\pm12.5 - 50$	0.015 ± 0.008	0.011 ± 0.003	b
Neyveli	79.46	11.45	$11.2\pm5.6 - 0$	$0^{+15}_{-5} - 18$	0.002 ± 0.001	0.006 ± 0.001	c
Parchuri	73.48	17.14	$10.9\pm2.9 - 0$	$0^{+15}_{-5} - 169$	0.012 ± 0.002	0.009 ± 0.007	d
Malvan	73.49	16.10	$10.9\pm2.9 - 0$	$0^{+15}_{-5} - 42$	0.003 ± 0.001	0.001 ± 0.007	e
South Ratnagiri	73.32	16.93	$10.9\pm2.9 - 0$	$0^{+15}_{-5} - 61$	0.005 ± 0.001	0.008 ± 0.001	f
North Ratnagiri	73.30	17.02	$10.9\pm2.9 - 0$	$0^{+15}_{-5} - 67$	0.005 ± 0.001	0.008 ± 0.001	f
Rameswaram	79.33	9.31	$0.122\pm0.005 - 0$	$3.0 - 2.9\pm1$	-0.001 ± 0.008	0.006 ± 0.002	g
Idindakarai	77.75	8.18	$0.122\pm0.005 - 0$	$3.0 - 3.4\pm1$	0.003 ± 0.008	0.009 ± 0.002	g
Manappad	78.07	8.37	$0.122\pm0.005 - 0$	$3.0 - 4.5\pm1$	0.012 ± 0.008	0.007 ± 0.002	g
Cape Comorin	77.50	8.09	$0.122\pm0.005 - 0$	$3.0 - 4.9\pm1$	0.016 ± 0.008	0.011 ± 0.003	g

4.3.2 Independent Tests

Spot measurements of observed and calculated rock uplift rates are in reasonable agreement. Nevertheless, it is important to ensure that the cumulative rock uplift history presented in Figure 4.11 is tested against a geographically and temporally broader set of onshore and offshore observations. The growth and distribution of lateritised surfaces, low-temperature thermochronologic measurements, solid sedimentary flux measurements at major deltas and offshore sequence stratigraphic architecture are used here to test the reliability of inverted uplift histories (Halkett, 2002; Gunnell *et al.*, 2003; Sahu *et al.*, 2013; Mandal *et al.*, 2015a). It is important to emphasise that these tests are independent of the calibration of the erosional parameter v that was used to calculate the cumulative uplift history.

Lateritised Paleosurfaces

Extensive laterite deposits are consistent with a prolonged period during which relief was subdued and regional climate was sufficiently humid for thick ($\leqslant$ 200 m) chemical weathering deposits to develop (Figure 4.7a). These lateritised surfaces are often deeply incised, which suggests that their present-day elevation is disequilibrated with respect to the modern landscape. An important corollary is that they probably formed at lower elevations (Widdowson, 1997). Although these surfaces are heavily dissected, they exhibit low relief and are topographically continuous, suggesting that they represent former base levels that once graded toward sea level (Valeton, 1983; Chardon et al., 2006). Development of Western Ghat laterites that drape Deccan basalts demonstrates that they are post-Cretaceous in age (Widdowson & Cox, 1996). Studies that combine high-resolution digital elevation models with $^{40}\mathrm{Ar}/^{39}\mathrm{Ar}$ dating of cryptomelane suggest there are up to three topographically concordant lateritic palaeosurfaces in the western highlands whose ages range between 52 and 23 Ma (Gunnell, 1998; Bonnet et al., 2014, 2016). These time-transgressive surfaces, with the oldest, increasingly tilted ones cropping out at the greater elevation, point toward successive cycles of incision and valley widening in response to changes in base level followed by topographic quiescence (Green et al., 2013). If these stacked surfaces represent former base levels that developed at similar elevations, rock uplift rates of < 0.02 mm a^{-1} can be inferred. After 23 Ma, laterite formation within the uplands appears to have ceased. The current elevation of these surfaces (1200–650 m) together with their strongly incised appearance point toward a rapid increase in relief during Neogene times. Any such increase during this period would prevent the channel migration and extensive planation required to form these surfaces (Widdowson, 1997; Sheth, 2007; Bonnet et al., 2014).

The situation for lower-lying areas is less clear since there is considerable debate about the interpretation of $^{40}\mathrm{Ar}/^{39}\mathrm{Ar}$ weathering dates and their relationship to palaeosurface evolution. Paleomagnetic ages suggest that the lowland surface developed in Late Cenozoic times whereas those from elevated uplands yield Early Cenozoic ages (Schmidt et al., 1983). However, in the western lowlands near Goa, two ages of $\sim$ 46 Ma have been obtained for a weathered profile beneath a lateritised lowland plateau at $\sim$ 150 m elevation (Beauvais et al., 2016). This pediment is capped by ferricrete composed of reworked and cemented lateritic clasts (Bonnet et al., 2016). It has been suggested that some lowland laterites are allochthonous, having been generated by the dissection and gravitational collapse of upland surfaces (Fox, 1923; Ghosh & Guchhait, 2015). However, if the dated material did precipitate in situ, preservation of these ages on either side of the escarpment

suggests either that there was differential rock uplift between the uplands and lowlands between ~ 23 and 9 Ma or that the Western Ghats escarpment has been close to its present-day position with similar relief since ~ 60 Ma.

This possibility, invoked by Beauvais *et al.* (2016), necessitates escarpment formation by ~ 60 Ma with minimal subsequent denudation. It cannot easily be reconciled with 1–1.5 km of denudation following eruption of Deccan basalts that is required to form the Konkan coastal plain. It also disagrees with thermochronologic evidence for significant post-40 Ma denudation at rates of ~ 60 m Ma^{-1} across the Kerala-Konkan lowlands since Late Miocene times (Kalaswad *et al.*, 1993; Gunnell *et al.*, 2003; Campanile *et al.*, 2008; Mandal *et al.*, 2015b). These rates are consistent with cosmogenic nuclide studies and with evidence for ongoing escarpment retreat (Mandal *et al.*, 2015a, 2016). Differential uplift could have occurred as a result of a combination of offshore sedimentary loading and onshore denudational unloading that is manifest in seaward downwarping of the lowland pediment. Nevertheless, these surfaces are evidently not co-genetic since one forms on the original crest of the Deccan lava pile and the other is demonstrably located by as much as 1–1.5 km within the interior of the same lava pile (Widdowson & Cox, 1996; Campanile *et al.*, 2008). The most plausible explanation is that a progressive drop in regional base level triggered by Neogene uplift caused the development and preservation of lateritic palaeosurfaces with the lowland surface postdating its time-transgressive upland counterparts. However, it is acknowledged that it is difficult to reconcile the earliest Cenozoic ^{40}Ar/^{39}Ar dates from the lowland pediment with abundant and convincing evidence for post-Neogene uplift and denudation (e.g. emergent marine and lignite deposits, incision of palaeosurfaces, thermochronologic observations, sedimentary flux measurements).

Warm and humid climatic conditions are probably key prerequisites for the formation of laterites (Widdowson & Mitchell, 1999). Present-day rainfall patterns preclude laterite formation in parts of the high plateaux to the east of the Western Ghats escarpment. These patterns are primarily controlled by the orographic effect associated with the Western Ghats (Fawcett, 1994; Tawde & Singh, 2015). Palynologic evidence suggests that temperature and precipitation were both sufficiently high to permit laterites to form across lowland areas throughout Cenozoic times (Meher-Homji, 1989; Brückner, 1992). The existence of an orographic effect would suggest that time-transgressive lateritisation of southern Indian palaeosurfaces between 53 and 23 Ma could be accounted for by a steady increase in elevation. This interpretation could explain the abrupt cessation of upland laterite formation because uplift of the Western Ghats beyond a threshold elevation would trigger

an orographic climatic regime with precipitation increasingly concentrated along the coastline.

An alternative hypothesis is that these plateaux were already elevated and that dating of cryptomelane records a rapid post-23 Ma lowering of the elevation window within which humidity and temperature were appropriate for laterite formation (Beauvais *et al.*, 2016; Bonnet *et al.*, 2016). This hypothesis requires the existence of both significant relief and widespread high precipitation rates (e.g. > 1 m a^{-1}) between 52 and 23 Ma (Thorne *et al.*, 2012). Such conditions are at odds with the notable absence of clastic sedimentary flux into the principal deltas during this period (Figure 4.7a). The orographic interpretation of laterite ages is more consistent with these observations and permits the inclusion of palaeosurficial elevations for calibration purposes. Significantly, if these ^{40}Ar/^{39}Ar dates are omitted, the calibrated value of v is unchanged, although its uncertainty increases.

Thermochronology and Denudation

Apatite fission track ages are consistently older than 55 Ma with short track lengths. This distribution suggests a complex denudation history that cannot be attributed to a single cooling event (Gunnell *et al.*, 2003). Similar denudation histories are recovered across eastern India with a late Cenozoic peak observed in the T-t (temperature-time) relationships derived from many samples (Sahu *et al.*, 2013). The inferred low geothermal gradient for India (i.e. $15°$C km^{-1}) suggests that, for a stable geothermal profile, exhumation of 4.7–6.7 km is required to cool samples now found at the surface through their closure temperatures (i.e. $110 \pm 10°$C, depending on cooling rate; Dodson, 1973; Roy & Rao, 2000; Agrawal & Pandey, 2004; Lisker *et al.*, 2009). The paucity of Cenozoic ages suggests that no more than 4.7 km of exhumation has occurred since 65 Ma. However, this conclusion yields little insight into potentially significant Cenozoic denudation below this threshold. The apatite (U-Th-Sm)/He (AHe) system has a closure temperature of 45–70$°$C, depending upon cooling rate, and is therefore capable of resolving exhumation within the 1–3.3 km range (Zeitler *et al.*, 1987; Wolf *et al.*, 1996; Farley, 2000). Although only one AHe study has been published, it yields Mesozoic ages for samples from elevated sections of the Western Ghats Escarpment with ages ~ 40 Ma from the Palghat Gap (Mandal *et al.*, 2015a). This distribution suggests negligible erosion (< 1 km) throughout Cenozoic times on relict palaeosurfaces and inselbergs within the highlands, followed by rapid Neogene denudation (> 1 km) in the vicinity of major rivers that drain the Nilgiri and Kodakainal plateaux. The T-t relationships from these studies provide strong evidence for Cenozoic rock uplift and denudation with the greatest erosion confined to major rivers and minimal

erosion of low-relief palaeosurfaces stranded at high elevation along the principal watersheds.
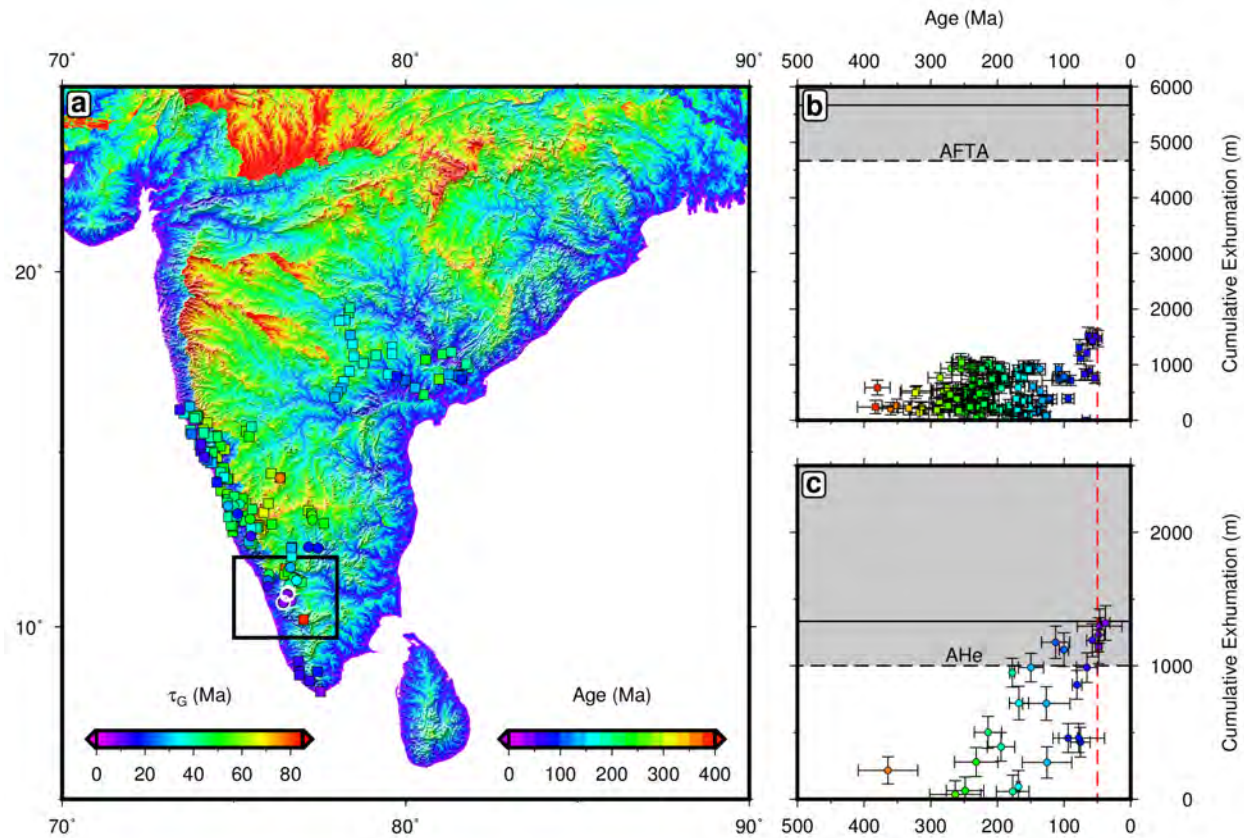
Figure 4.13: Comparison of thermochronologic measurements and calculated exhumation. (a) Map of landscape response time, τ_G, calculated from drainage catchments. Coloured squares/circles = AFTA/AHe ages (Gunnell *et al.*, 2003; Sahu *et al.*, 2013; Mandal *et al.*, 2015a); black box = locus of Palghat Gap (Figure 4.14a); white circles = locations of AHe samples whose cooling histories are shown in Figures 4.14c–e. (b) Calculated exhumation plotted as function of AFTA age. Solid line = mean exhumation since 50 Ma required to record $\leqslant$ 50 Ma AFTA age; grey band with dashed lines = envelope reflecting uncertainties in mean surface ($25 \pm 5°C$) and closure temperatures ($110 \pm 10°C$), assuming constant geothermal gradient of $15°C$ km^{-1} (Roy & Rao, 2000; Agrawal & Pandey, 2004). Exhumation since 50 Ma calculated using $v = 3.7^{+0.8}_{-1.2}$ m$^{0.26}$ Ma^{-1} and $m' = 0.37$ for $\lambda_S = \lambda_T = 1$. (c) Calculated exhumation plotted as function of AHe ages. Solid line = mean exhumation since 50 Ma required to record $\leqslant$ 50 Ma AHe age; grey band with dashed lines = envelope reflecting uncertainties in mean surface and closure temperatures ($57.5 \pm 12.5°C$), assuming constant geothermal gradient. Uncertainty on predicted cumulative exhumation corresponds to values for upper/lower bounds on v; uncertainty on sample ages corresponds to 1σ error.

Denudational histories recovered by inverse modelling of drainage networks can be compared with thermochronologic estimates (Figure 4.13). By assuming Cenozoic geothermal gradients and average surface temperatures equivalent to those of the present day ($\sim 15°C$ km^{-1} and $25 \pm 5°C$, respectively), observed T-t histories for different AFTA and AHe samples can be converted into time-exhumation (T-z) histories. These histories can then be compared with calculated denuda-

tional values obtained by inverse modelling. Predicted cumulative denudation is calculated by subtracting modern topography from the cumulative rock uplift predicted by the inversion between a given timestep and the present day. This approach is predicated on the existence of negligible topography at 50 Ma and so it represents an upper limit for cumulative denudation.
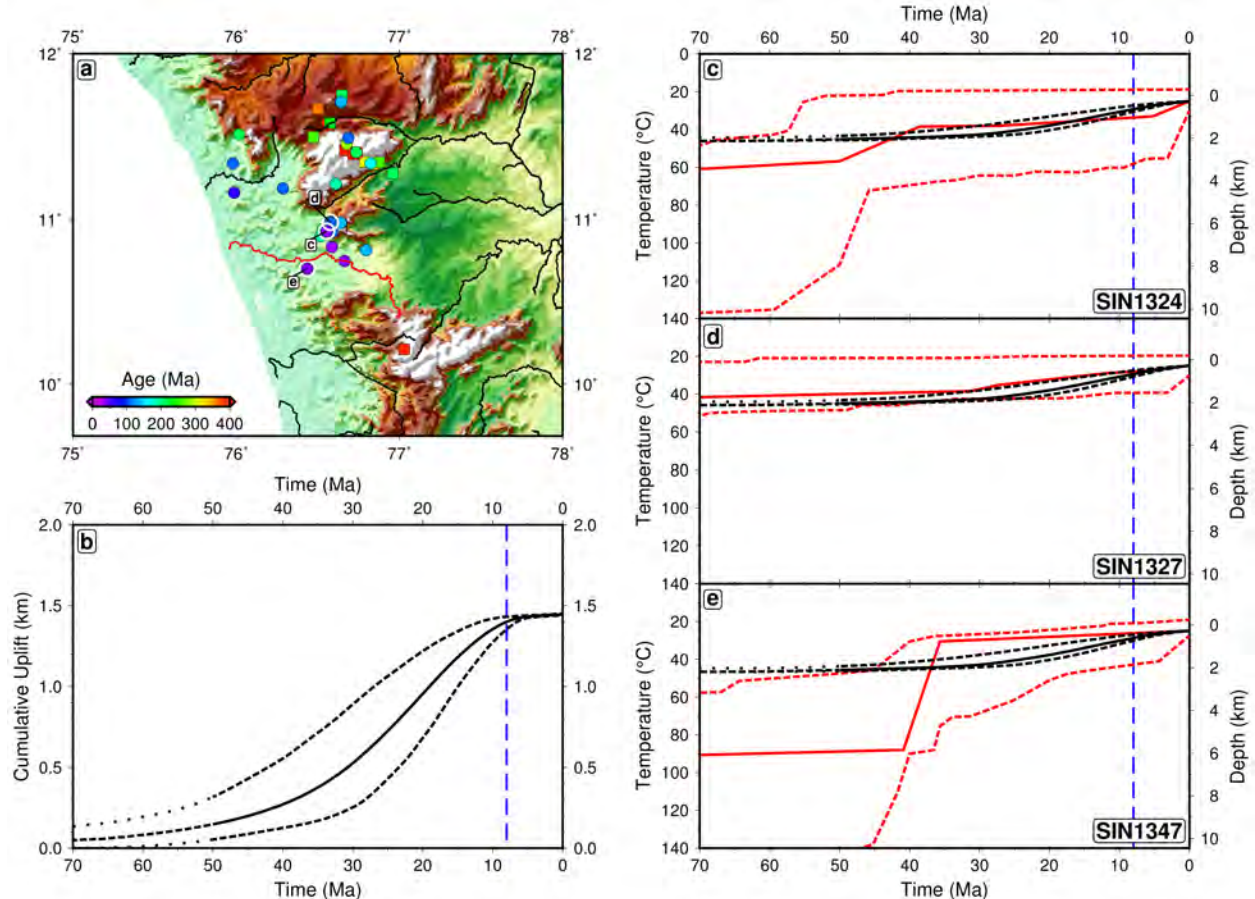
Figure 4.14: Thermochronologic measurements and denudation history at Palghat Gap. (a) Map of Palghat Gap region. Coloured circles/squares = AFTA/AHe dates (Gunnell *et al.*, 2003; Mandal *et al.*, 2015a). Black lines = drainage, red line = location of Bharathappuzha river whose incision history is shown in (c)–(e); white circles = locations of samples SIN1324, SIN1327 & SIN1347 from Mandal *et al.* (2015a) used to construct time-temperature relationships in (c)–(e). (b) Calculated cumulative uplift history of Palghat Gap region for $v = 3.7^{+0.8}_{-1.2}$ m$^{0.26}$ Ma^{-1} and $m' = 0.37$. Solid/dashed lines = mean cumulative uplift history with uncertainty corresponding to values for upper/lower bounds on v; dotted lines = poorly constrained history for period when $\geqslant 50\%$ of model nodes are null; dashed blue line = onset of monsoon intensification at 8 Ma. (c) Denudation history of Palghat Gap region for sample SIN1324. Solid/dashed lines = mean incision history at closest point along river to SIN1324 with uncertainty corresponding to values for upper/lower bounds on v; dotted lines = poorly constrained incision history as before; red solid/dashed lines = statistically favoured time-temperature (T-t) paths for SIN1324 with envelope of 'acceptable' T-t paths ($p > 0.05$) generated by HeFTY algorithm (Ketcham, 2005). Depth axis calculated by assuming geothermal gradient of 15°C km^{-1} (Roy & Rao, 2000; Agrawal & Pandey, 2004). (d) Denudational history for sample SIN1327. (e) Denudational history for sample SIN1347.

This calculation is performed from 50 Ma onward since this period is one for which inverse modelling yields adequate spatial coverage (Figure 4.13a). By comparing these predicted values with thermochronologic measurements for India, it is straightforward to demonstrate that Neogene epeirogeny has not generated sufficient exhumation to be recorded by apatite fission track analysis (i.e. 4.7–6.7 km or 100–120°C cooling; Figure 4.13b). However, where predicted denudation is large enough to cross the lower AHe closure temperature threshold of 45–70°C (i.e. 1–3.3 km), ages younger than 50 Ma are obtained (Figure 4.13c). This observation, combined with an obvious age-cumulative exhumation correlation for both AFTA and AHe samples, shows that Neogene denudation has left a clear and pervasive signal within basement rocks of the coastal plain. This result also agrees with 1–1.5 km Cenozoic denudation estimates for the Kerala-Konkan coastal plain calculated from basaltic stratigraphy by Widdowson & Cox (1996). These estimates suggest that the 3–4 km estimated by Gunnell *et al.* (2003) from thermochronologic modelling and the < 250 m value estimated by Beauvais *et al.* (2016) from lowland palaeosurfaces are upper and lower limits, respectively.

For a given rock uplift rate history, the shape of a river profile can be reconstructed through time. The integrated erosion between reconstructed river profiles at two different time steps constrains the volume of rock removed during that period. This calculation is carried out for the Bharathappuzha river that drains the Palghat Gap in order to determine an incision rate history which can be compared with the AHe *T-t* histories calculated by Mandal *et al.* (2015a) (Figures 4.14a & b). This comparison reveals clear evidence for post-50 Ma uplift and incision (Figures 4.14b–e). This incision history fits the mean *T-t* path for post-50 Ma AHe samples, falling within 95% probability bounds (Figures 4.14c–e). Crucially, onset of more rapid cooling after 40 Ma broadly coincides with increased incision. It also immediately post-dates the initiation of rapid uplift, although the exact timing of cooling varies between samples (Figures 4.14b–e). Sufficient incision is recorded (i.e. $\geqslant 1.33$ km for a 45°C closure temperature) to record an AHe age but not an AFTA age.

Solid Sedimentary Flux Estimates

Circumstantial evidence for Neogene uplift is provided by a post-23 Ma switch from carbonate- to clastic-dominated sedimentation within offshore deltas (Raju, 2008; Figures 4.7a & b). This switch to clastic deposition clearly pre-dates onset of monsoon intensification at 8 (or 15) Ma, although the exact timing of intensification is uncertain (Burckle, 1989; Kroon *et al.*, 1991; Wang *et al.*, 2005; Clift, 2010). Cosmogenic nuclide studies suggest that erosion rates are less sensitive to precipitation

but that they primarily scale with channel gradient and relief. This suggestion implies that rock uplift, and not climate *per se*, is primarily responsible for the switch (Mandal *et al.*, 2015b).
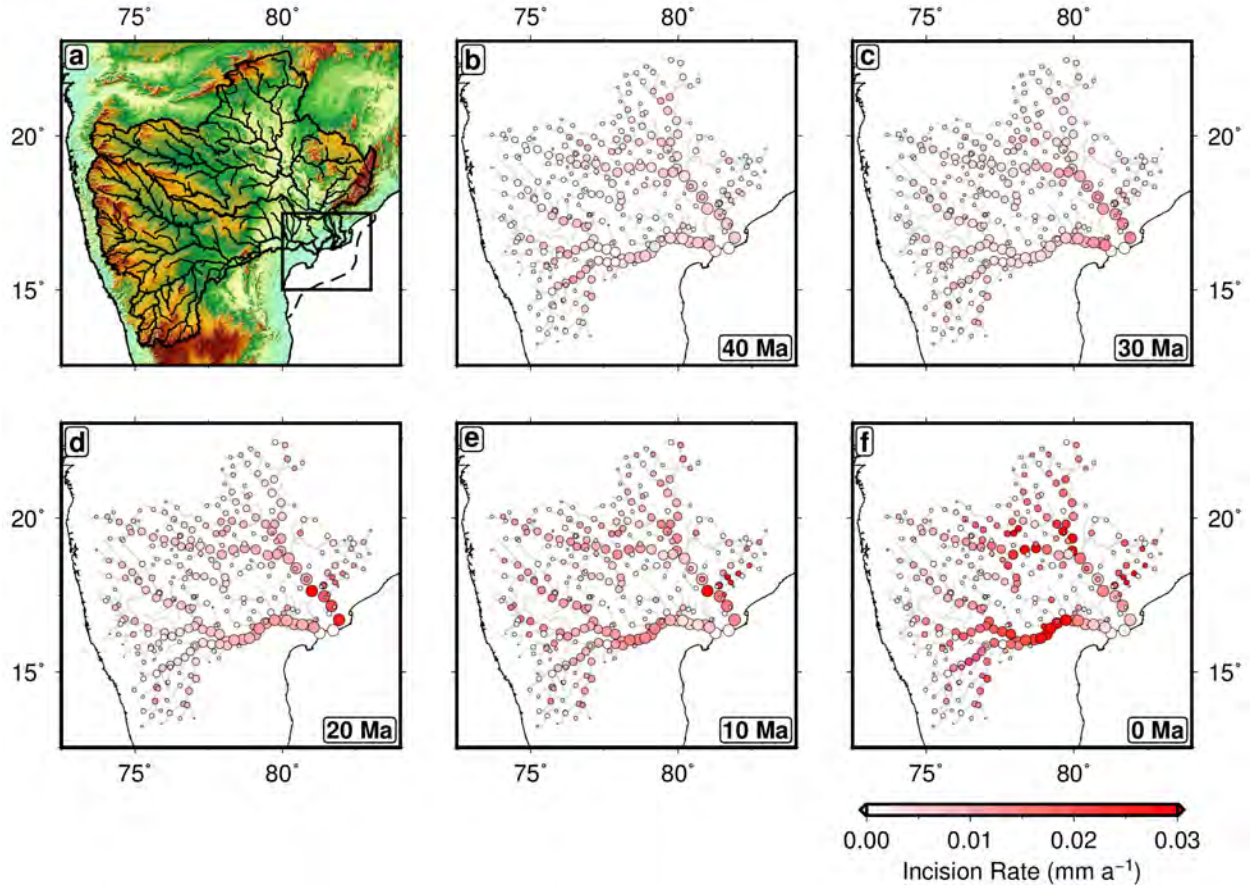
Figure 4.15: Predicted incision history of Krishna & Godavari catchments. (a) Topographic map of central India. Thick black line = outline of Krishna and Godavari catchments; thin black lines = principal rivers and their tributaries; black box = Krishna-Godavari delta region shown in Figure 4.16; dashed line = edge of offshore delta; (b) Predicted incision rates calculated at 40 Ma for $v = 3.7$ m$^{0.26}$ Ma^{-1}, $m' = 0.37$ and $\lambda_S = \lambda_T = 1$ (see scale bar). Grey lines = drainage within catchment. (c)–(f) Predicted incision rates at 30 Ma, 20 Ma, 10 Ma and 0 Ma.

Here, the relationship between cumulative rock uplift history and sedimentary efflux is investigated in more detail. Calculated uplift histories can be tested by attempting to match observed sedimentary deposition at major deltas. By carrying out incision calculations for all non-repeating sections of river profiles within the Krishna & Godavari catchments, incision rate history for the two largest catchments of the Indian Peninsula are determined (Figure 4.15). By integrating these incision rates over time, the total amount of rock eroded along a river profile as a function of time, $Q_s(t)$, can be reconstructed using

$$Q_s(t) = \int_0^{L_r} -vA(x)^{m'} \left(\frac{\partial z'}{\partial x} \right) \mathrm{d}x \tag{4.18}$$

where L_r is the length of a river profile. By integrating these values throughout the Krishna-Godavari drainage system, a sedimentary flux history is retrieved for both deltas. Sedimentary flux calculated in this way provides a minimum estimate since drainage recovery is incomplete and erosion of interfluves, hillslope processes or variable channel width are not taken into account. Although this calculation inevitably underestimates the true sedimentary flux, the relative changes are probably robust. Model coverage is well resolved between 50 Ma and the present day but earlier predictions are less certain.
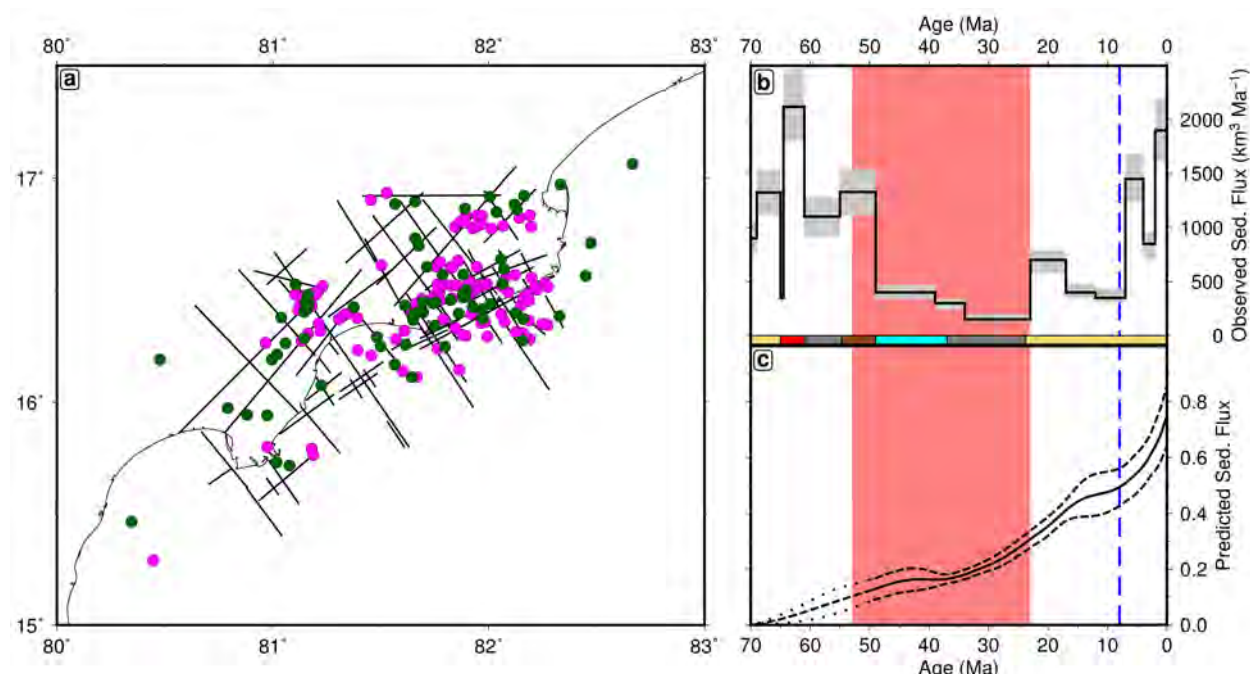
Figure 4.16: Testing uplift histories against sedimentary flux observations. (a) Map of seismic reflection survey and wells from Krishna-Godavari delta (see Figure 4.15 for location). Solid lines = seismic profiles; magenta circles = wells without sonic logs; green circles = well with sonic logs. (b) Sedimentary flux history of delta calculated using seismic survey calibrated by well data (Halkett, 2002). Solid line and grey band = mean sedimentary flux $\pm 1\sigma$; horizontal colour bar shows lithology (yellow = sandstone, blue = limestone, grey = mudstone, red = volcanic rocks, brown = siltstone); red vertical band = period of laterite formation for Western Ghats (Bonnet *et al.*, 2016); dashed blue line = onset of monsoon intensification at 8 Ma. (c) Predicted sedimentary flux for $v = 3.7^{+0.8}_{-1.2}$ m$^{0.26}$ Ma^{-1}, $m' = 0.37$ and $\lambda_S = \lambda_T = 1$. Solid/dashed lines = mean predicted sedimentary flux with uncertainty corresponding to values for upper/lower bounds on v; dotted lines = period when model resolution is less good.

Predicted sedimentary flux is compared with the observed record of Halkett (2002) who mapped a grid of regional seismic reflection profiles calibrated with well logs to estimate the volume of solid sediment within the proximal Krishna-Godavari delta as a function of time (Figures 4.16a & b). This record has two prominent peaks in sedimentation. The first one occurs at 70–48 Ma and is

associated with regional uplift of the Deccan traps following plume-related rifting between the Seychelles and India. The second one occurs at 23–0 Ma. Clastic deposition dominates during these two pulses of increased sedimentation. The pulses are separated by a 25 Ma period of lower sedimentation where carbonate and mud are the dominant lithologies. This quiescent period correlates with weathering ages of lateritised palaeosurfaces that crop out in upland areas. Topographic relief was probably modest since precipitation is inferred to have been significant enough to facilitate pervasive chemical weathering (Bonnet *et al.*, 2014, 2016; Figure 4.16c). The first peak cannot be matched since calculated cumulative rock uplift history is poorly resolved pre-50 Ma. However, slow sedimentation from 50–25 Ma followed by an increase in sedimentary flux toward the present day agrees with the observational record. Spatio-temporal smoothing imposed on the inverse model means that shorter period features observed in the sedimentary record are not accurately matched. Observed and predicted Neogene increases in sedimentation precede monsoon intensification by $\sim$ 15 Ma, suggesting that rock uplift, and not climate change, is the main driver for increased erosion over the peninsula during Cenozoic times (An *et al.*, 2001).

Offshore Sequence Stratigraphy

The large-scale stratigraphic architecture of surrounding rifted margins provides independent evidence for the existence of Neogene tilting. Along the northwest coast, a regional discontinuity truncates foresets of Lower Miocene to Lower Pliocene strata (Kumar *et al.*, 2009). The angle of truncation decreases toward the shelf edge, suggesting that this discontinuity records a regional regressive event that occurred after $\sim$ 16 Ma (Raju, 2008; Figures 4.17a & c). This discontinuity can be mapped onshore up to an elevation of $\sim$ 150 m. The depth of its offshore extent, corrected for sediment loading, is $\sim$ 150 m, indicating a relative sea-level fall of at least 300 m. Since there is no evidence for a glacio-eustatic drop of this magnitude during that period, it is more plausible that regional uplift of the margin occurred (e.g. Miller *et al.*, 2005).

Along the east coast, locations of the rollover crests of clinoformal surfaces within a Middle Miocene to Recent sedimentary sequence can be tracked. A switch from progradation to aggradation occurred during Middle Miocene times and is followed by Pleistocene to Holocene retrogradation. This sequence stratigraphic architecture is diagnostic of a rapid increase in accommodation space. By decompacting and unloading the sequence, it is estimated that $\sim$ 600 m of water-loaded subsidence occurred within $\sim$ 10 Ma (Figures 4.17b & d). Thus, multiple stratigraphic observations indicate that Neogene regional tilting of the Indian Peninsula is a significant phenomenon.
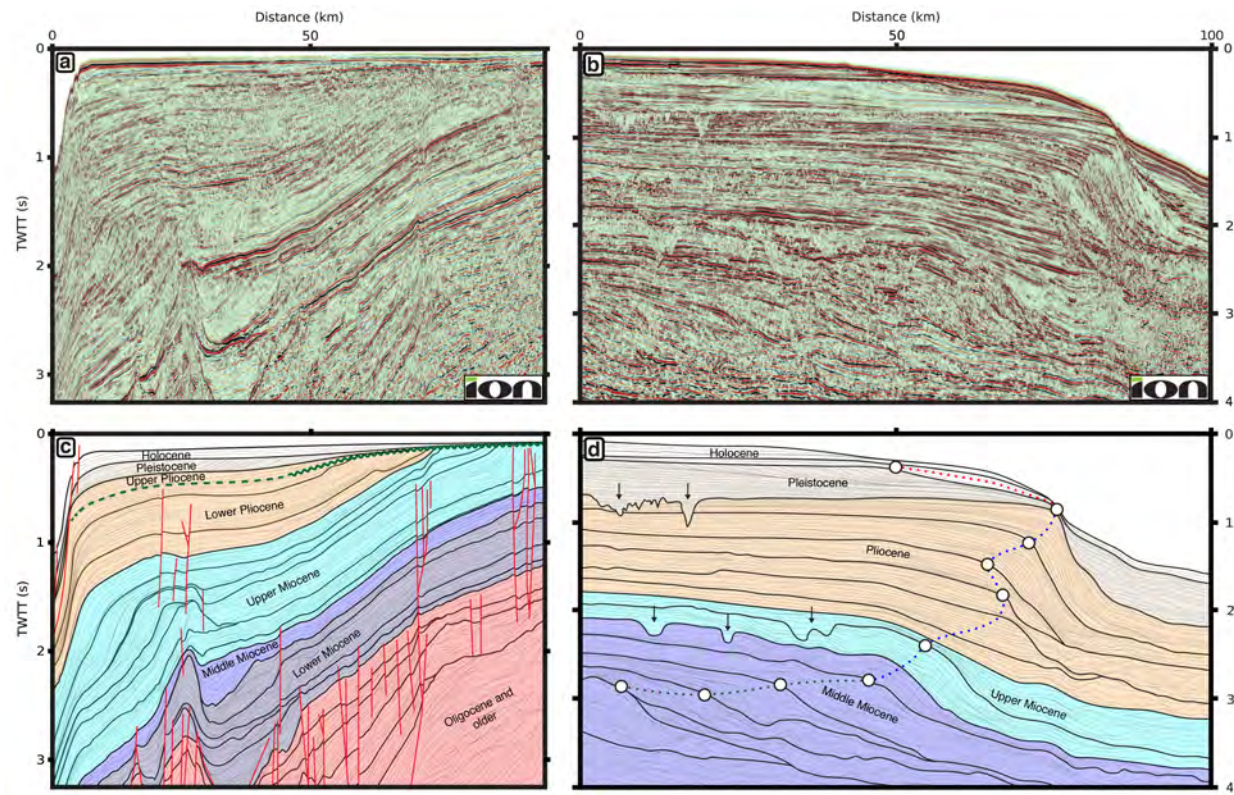
Figure 4.17: Seismic profiles from Indian margins. (a) Profile located offshore Saurashtra on western shelf. (b) Profile from edge of Mahanadi Delta on eastern shelf. (c) Interpretation of panel (a). Wiggly/dashed green line = angular unconformity with transition into sequence boundary; thin/grey lines = depositional/other boundaries; red lines = normal faults. Note topsets truncated by post-16 Ma angular unconformity. (d) Interpretation of panel (b). White circles = locations of clinoformal crests; green/blue/red circles = progradational/aggradational/retrogradational depositional sequences within Mio-Pliocene strata representing $\sim$ 600 m of water-loaded subsidence; black arrows = palaeochannels.

4.4 Origin of Indian Tilting

Offshore residual depth measurements, inverse modelling of drainage networks and supporting geologic constraints suggest that long-wavelength uplift of the western half of the Indian Peninsula has occurred during Neogene times. This inference does not preclude an earlier cycle of Paleocene rock uplift and denudation. It is unlikely that active tectonic deformation, crustal isostasy or plate flexure are responsible for regional eastward tilting. Nevertheless, although combined offshore and onshore tilting is very unlikely to be supported by lithospheric flexure, on shorter wavelengths, flexural rigidity can, and probably does, play a role in downwarping the lowland pediment and in maintaining high relief across the rim of the Western Ghats escarpment (Gilchrist & Summerfield, 1990; Whiting *et al.*, 1994; Gunnell & Fleitout, 1998; Campanile *et al.*, 2008).
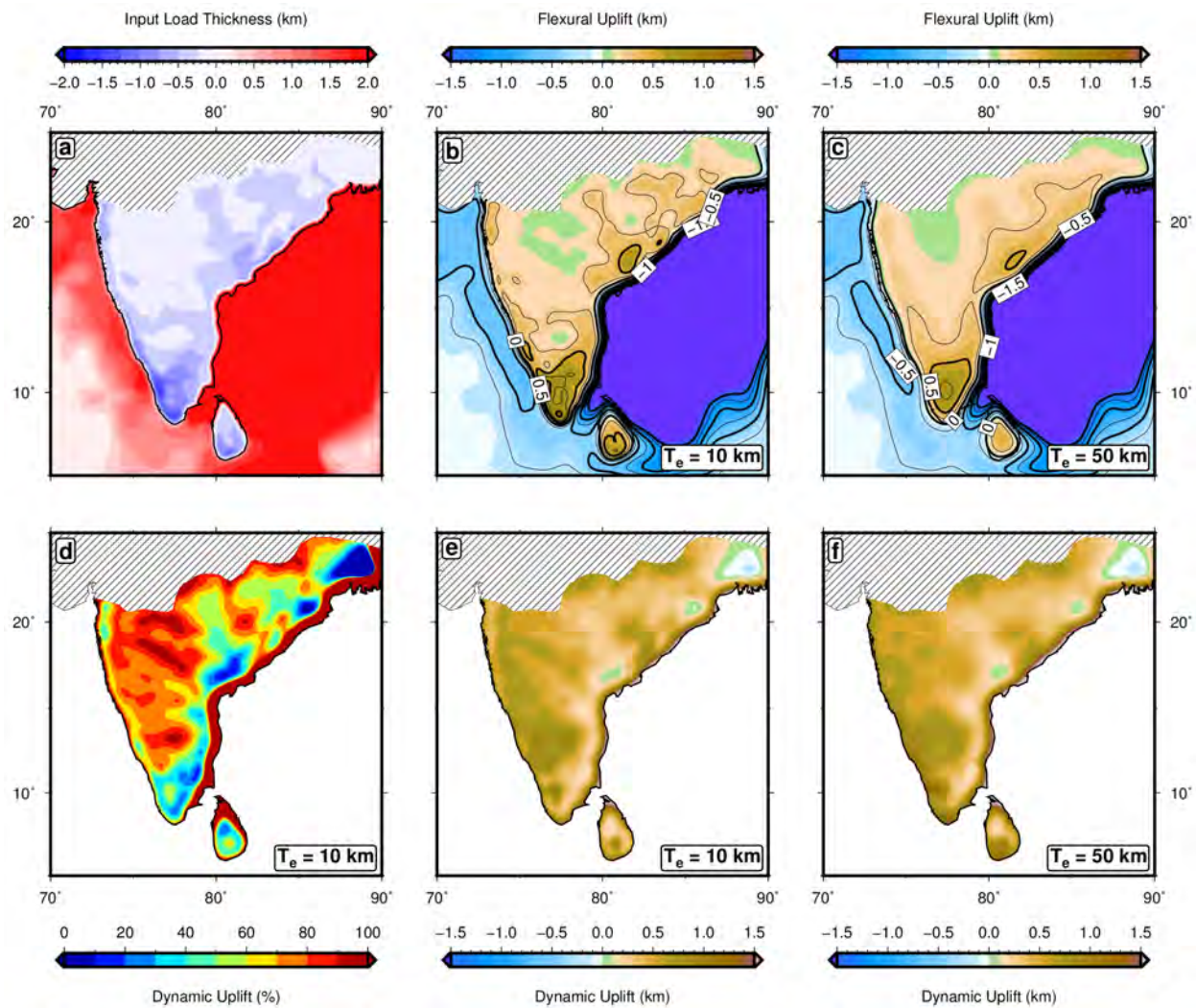
Figure 4.18: Flexural contributions to uplift over Peninsular India. (a) Onshore/offshore load configurations. Onshore load = maximum denudation between 50–0 Ma from inverse model (crustal density, $\rho_c = 2.7$ Mg m^{-3}); offshore load = total sedimentary thickness taken from National Geophysical Data Center (NGDC) grid (average sediment density, $\overline{\rho_s} = 2.0$ Mg m^{-3}); elastic thickness of oceanic lithosphere = 20 km (Whittaker *et al.*, 2013). (b) Flexural response to loads for onshore elastic thickness, $T_e = 10$ km. (c) Flexural response to loads for onshore elastic thickness, $T_e = 50$ km. (d) Percentage contribution of non-flexural topographic component. (e) Difference between observed topography and flexural contribution for $T_e = 10$ km. (f) Difference between observed topography and flexural contribution for $T_e = 50$ km.

The flexural effect of combined offshore sedimentary loading and onshore denudational unloading is calculated for different values of elastic thickness. Flexural modelling was carried out in the frequency domain using a spectral method with mirrored-edge symmetry (Watts, 2001). A heterogeneous load consisting of the offshore distribution of sedimentary deposits and the onshore, post-50 Ma, cumulative denudation determined by inverse modelling was constructed (Whittaker *et al.*, 2013; Figure 4.18a). The results suggest that no more than about 30% of post-50 Ma

epeirogenic uplift can be generated by lithospheric flexure, irrespective of the exact value of T_e (Figures 4.18b–f).

A more appealing mechanism is a change in the density structure of the lithospheric, or sub-lithospheric, mantle. The age and duration of regional uplift is incompatible with a progressive decrease in lithospheric density along the western margin since such a decrease would require significant and widespread melt extraction for which there is little evidence (Turcotte & Emerman, 1983; Hawkesworth *et al.*, 1990; Turner & Hawkesworth, 1995; Todal & Edholm, 1999). Thus, the observed spatio-temporal rock uplift pattern can be attributed to convective processes within the sub-lithospheric mantle.

This inference is supported by earthquake tomographic models (e.g. SMEAN, S40RTS, SL2013sv) and corroborated by receiver function studies. Both indicate the existence of predominantly slow upper mantle shear wave velocity anomalies beneath the western side of the peninsula and fast upper mantle shear wave velocity anomalies beneath the eastern side (Becker, 2002; Ritsema *et al.*, 2011; Mohan *et al.*, 2012; Schaeffer & Lebedev, 2013). The planform of this distribution shows good spatial correlation with oceanic residual depth measurements (Figure 4.19a). Significantly, a band of increased cumulative rock uplift visible in the last timestep of the inverse model coincides with the maximum gradient of the shear wave velocity anomaly. This correlation is consistent with expectations about the surficial expression of convective circulation (Braun *et al.*, 2013). The existence of a low density anomaly within the upper mantle immediately beneath the plate could maintain an west-east dynamic topographic gradient (Becker & Faccenna, 2011; Figures 4.19b & c). Residual depth measurements from the oceanic realm broadly agree with this premise.

It has also been suggested that a low viscosity asthenospheric channel beneath the lithosphere, within which pressure-driven Poiseuille flow occurs, can act to decouple the Earth's surface from convective circulation of the deeper mantle (Weismüller *et al.*, 2015). The best evidence for the existence of a low viscosity asthenosphere comes from ridge bathymetric, plate motion, glacial rebound, and seismic anisotropic studies (Buck *et al.*, 2009; Iaffaldano & Bunge, 2015; van der Wal *et al.*, 2015; Lin *et al.*, 2016). Low asthenospheric viscosity may be controlled by high temperatures, by partial melting, by the presence of water, or by some combination of all three (Anderson & Sammis, 1970; Karato & Jung, 1998; Stixrude & Lithgow-Bertelloni, 2005). Above such channels, surface deflections are probably dominated by the effects of thermal buoyancy and, to a lesser extent, by viscous tractions at the lithosphere-asthenosphere boundary (Robinson *et al.*, 1987). Surface wave dispersion studies of southern India are consistent with the presence of a 180 ± 40 km thick
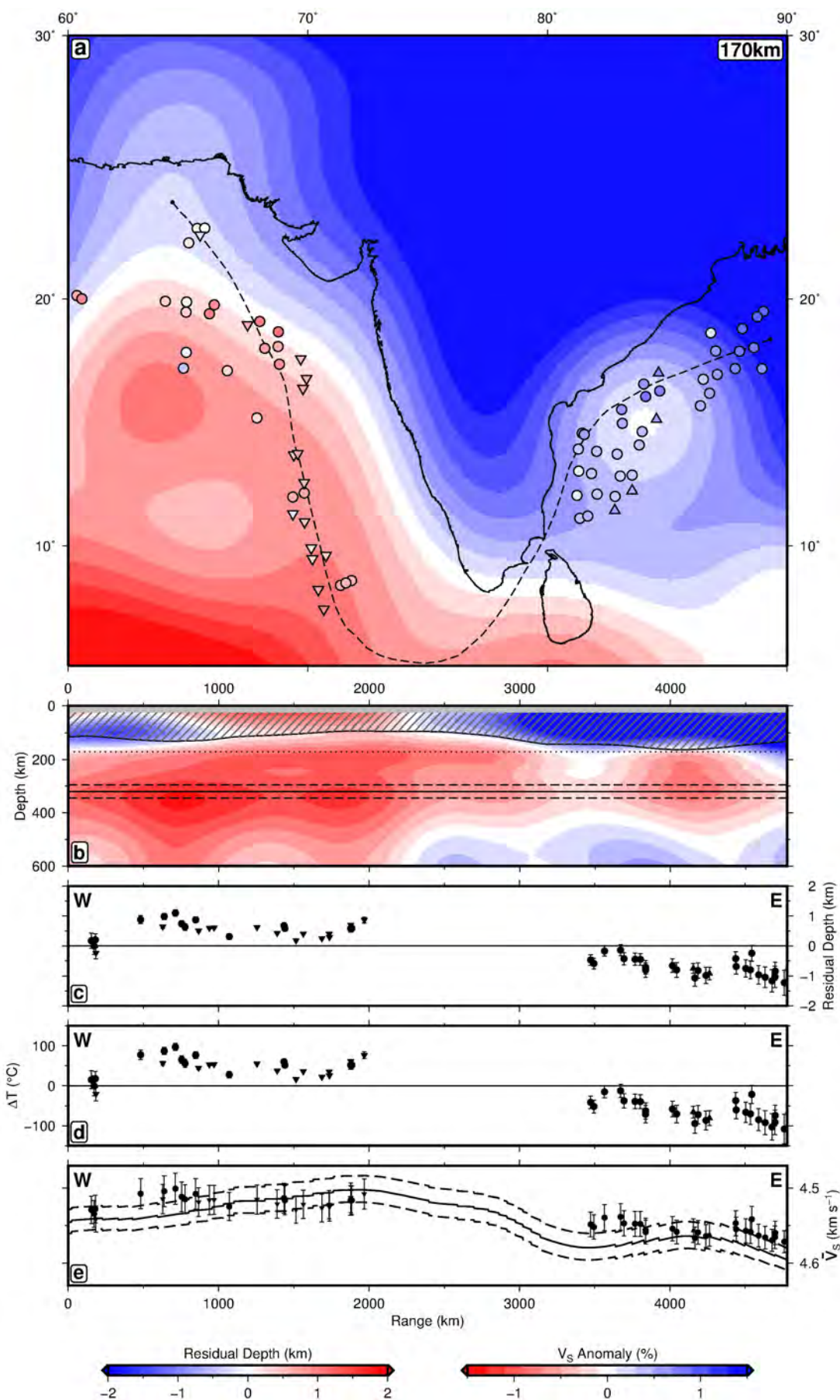
Figure 4.19 *(previous page)*: **Seismic tomographic model and residual depth anomalies.**
(a) Horizontal slice through S40RTS model at 170 km depth. Red/blue colours = slow/fast shear
wave, V_S, anomalies; coloured circles and upward/downward-pointing triangles = water-loaded
residual depth measurements; dashed line = locus of transect shown in panels (b)–(e). (b) Vertical
slice through S40RTS model along transect. Transparent grey box = oceanic lithosphere (Priestley
& McKenzie, 2013); dotted line = depth of horizontal slice shown in panel (a); solid/dashed lines
= putative base of proposed low viscosity channel at 320 ± 25 km. (c) Residual depth measure-
ments as function of distance along transect. (d) Asthenospheric temperature variation, ΔT, along
transect calculated using Equation 4.19 where $h = 200 \pm 25$ km. (e) Solid/dashed lines = shear
wave velocities determined from S40RTS by averaging over putative asthenospheric channel (i.e.
200 ± 25 km); solid circles, upward/downward-pointing triangles = shear wave velocity anoma-
lies calculated from empirical relationship between average ΔT and average V_S for asthenospheric
channel; vertical lines = errors estimated from uncertainties in h and T.

low-velocity layer beneath the lithosphere (Mitra *et al.*, 2008).

Residual depth, δz_w, as a function of channel thickness, h, and the average temperature deviation,
δT, is given by

$$\delta z_w = \frac{h\alpha\delta T}{(1 - \alpha T_\circ)} \tag{4.19}$$

where $\alpha = 3.3 \times 10^{-5}$ K^{-1} and $T_\circ$ is the background asthenospheric temperature (McKenzie &
Bickle, 1988; Hartley *et al.*, 2011). For a given channel thickness, the average temperature anomaly
for each residual depth measurement can be estimated (Figure 4.19d). The depth-averaged value
of V_S over the thickness of the channel is calculated from any given tomographic model. This value
is used to determine the best-fit linear relationship between V_S and T. The smallest misfit between
observed and calculated V_S is obtained for a channel thickness of 200 ± 25 km and a temperature
anomaly of $\pm 100°$C (Figure 4.19e). Note the absence of Neogene volcanism associated with this
temperature anomaly which could be cooler if a thicker channel is assumed.

The Yamauchi & Takei (2016) parameterisation is not used here, as in Chapter 5, due to difficulties
in converting S40RTS to accurate absolute velocities. These problems arise due to the use of PREM
as a reference model. As discontinuities in PREM are not solved for in the inversion, spurious
perturbations in absolute velocity occur either side of 220 km in the centre of the proposed channel.
Instead, the V_S-T relationship derived from the residual depth measurements is compared to that
predicted by matching surface wave dispersion measurements with a combination of the plate
model and continental thermobarometric constraints (Priestley & McKenzie, 2013). An optimal fit
is obtained for channel thicknesses of 200 ± 25 km using S40RTS (Ritsema *et al.*, 2011; Figure 4.20).
Similar results are obtained using S20RTS, albeit with a larger gradient misfit (Ritsema *et al.*, 1999).
An improved fit to the V_S-T gradient is obtained using the SL2013sv tomographic model, although
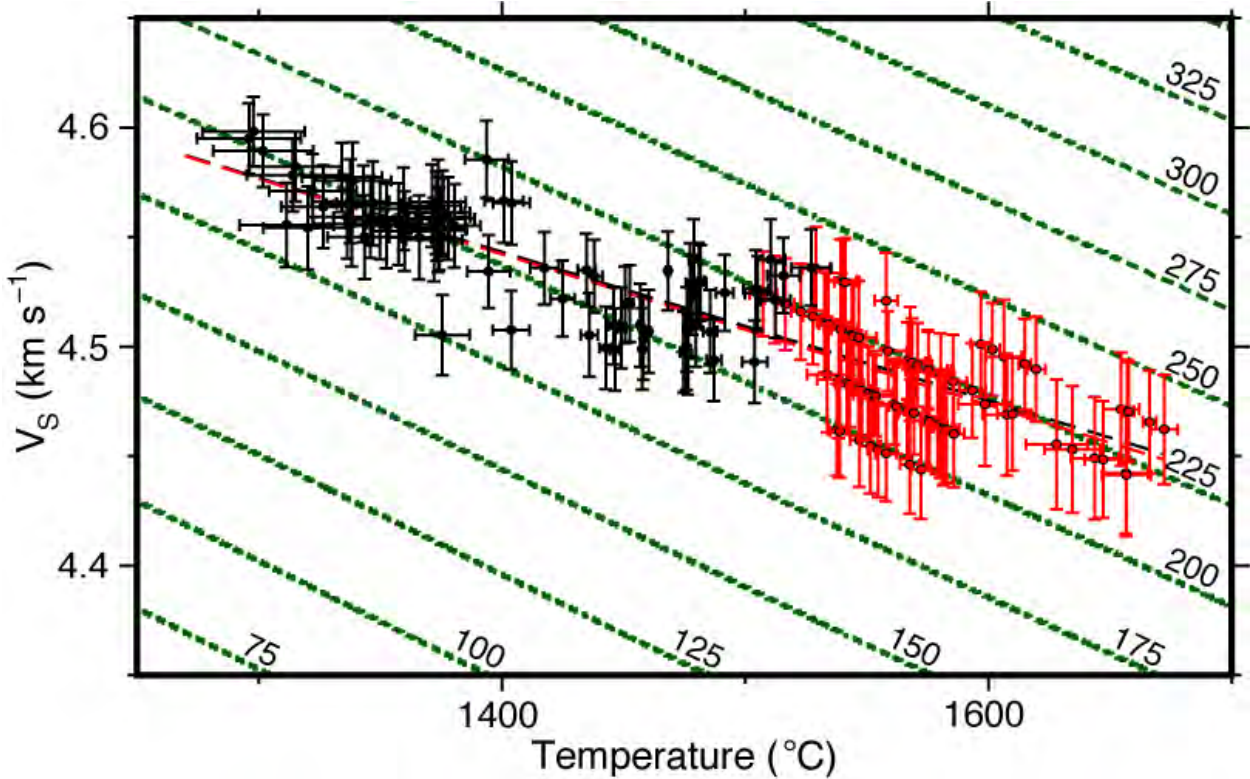
Figure 4.20: Relationship between shear wave velocity and temperature. Solid circles and crosses = relationship between average asthenospheric V_S from S40RTS and T inferred from residual depth anomalies with uncertainties that reflect $h = 200 \pm 25$ km; red circles and crosses = relationship between V_S and T predicted by parameterisation of Priestley & McKenzie (2013) for $h = 200 \pm 25$ km; dashed line = best-fitting line to solid circles; red dashed line = best-fitting line to red circles; green dashed lines = V_S-T relationships predicted by (Priestley & McKenzie, 2013) for individual depths (labelled in km).

there is a large negative offset in absolute V_S (Schaeffer & Lebedev, 2013). A similarly high offset was recovered for the 3D2015_07Sv model for which the fit to the gradient is less good (Debayle *et al.*, 2016). The larger V_S offset for the SL2013sv and 3D2015_07Sv models probably arises from the different reference velocities used, which are generally slower than for the PREM model at equivalent upper mantle depths. However, gradient misfits may have other possible causes. For example, the parameterisation of Priestley & McKenzie (2013) is less well resolved below a depth of ~ 200 km where there is insufficient mantle nodule data to calibrate the V_S-T relationship.

Furthermore, gradient misfits could be caused by the damping function used to stabilise tomographic models. In this instance, V_S variations are oversmoothed, which can give rise to excessively shallow V_S-T gradients. Takei *et al.* (2014) show that the Maxwell time-normalised frequency-attenuation (f'-Q^{-1}) relationship of McCarthy *et al.* (2011) does not apply to the seismic frequency range ($10^8 \leqslant f' \leqslant 10^{11}$). Their results show that at high temperatures, for a given f', Q^{-1} will

be higher and V_S will be lower than would be predicted by extrapolating the relationship. The anelastic part of the Priestley & McKenzie (2013) parameterisation will therefore underestimate attenuation at near-solidus temperatures, leading to overestimates of V_S at seismic frequencies and insufficiently steep decreases in V_S as temperatures approach the solidus temperature. Finally, viscous stresses are ignored here when relating residual depth anomalies to V_S anomalies. If these forces make a significant contribution, smaller temperature anomalies would be needed for a channel of equivalent thickness, resulting in higher gradient V_S-T relationships that would more closely match those predicted by Priestley & McKenzie (2013). Notwithstanding these complexities, the spatial correlation between residual depth observations and V_S anomaly gradients supports the inference that regional topographic asymmetry is linked to asthenospheric temperature anomalies (Ritsema *et al.*, 1999; Becker, 2002; Ritsema *et al.*, 2011; Schaeffer & Lebedev, 2013; Debayle *et al.*, 2016).

Many tomographic models show a substantial fast shear wave velocity anomaly within the lower mantle beneath the Indian plate. The lack of coherence observed between gravity and topography at wavelengths $>$ 400 km stems from the presence of a deeper-seated anomaly (Figures 4.3b & 4.6c). Topography is mainly sensitive to deflections induced by density variations immediately beneath the base of the plate. In contrast, the long-wavelength gravity field is also affected by density anomalies deeper within the mantle. The large, fast velocity anomaly beneath the Indian Ocean probably represents a positive density anomaly. According to Stokes' flow, this anomaly is expected to be actively sinking and should generate negative deflection of the core-mantle boundary (Hager & Richards, 1989a; Steinberger *et al.*, 2010). Although this interface is deep, the density contrast across it is large ($\geqslant$ 4.4 Mg m^{-3}) and deflection of this boundary will have an associated negative gravity anomaly (Dziewonski & Anderson, 1981; Colli *et al.*, 2016). This inference is consistent with a flow model suggesting that the presence of this anomaly is consistent with the accumulation of sinking Tethyan slab material (Nerlich *et al.*, 2016).

Inferred Neogene rock uplift rates of nearly 0.1 mm a^{-1} and the co-location of residual depth anomalies with shear wave anomalies immediately beneath the lithosphere together suggest that regional tilting of peninsular India and its surrounding oceanic lithosphere is principally maintained by shallow thermal isostasy. Onset of regional uplift at about 35 Ma across southern India broadly coincides with a major slowdown in plate velocity caused by collision with Eurasia (Molnar, 2009; Copley *et al.*, 2010; Cande & Patriat, 2015). Following this hard collision, the speed of northward flow of hot asthenospheric material may have surpassed that of the slowing plate above, resulting in

the observed northward propagation of regional uplift. This suggestion means that asthenospheric velocity must have exceeded that of the overriding plate throughout Neogene times ($\geqslant$ 40 mm a^{-1}). Asthenospheric velocities as fast as 400 mm a^{-1} have been documented beneath the North Atlantic Ocean (Vogt, 1971; Hartley *et al.*, 2011; Parnell-Turner *et al.*, 2014). It is therefore possible that thermal anomalies in an asthenospheric channel may have progressively impinged from the southwest, following continental collision.

4.5   Summary

To investigate the spatial and temporal pattern of vertical movements of the Indian Peninsula, a combination of offshore and onshore observations are presented and analysed. Oceanic lithosphere occurs on both sides of India and is characterised by significant residual age-depth anomalies. The asymmetry of these anomalies is consistent with Indian topography. Onshore, the drainage network contains coherent rock uplift signals that are non-linear in space and can be inverted to determine regional uplift histories. A stream power formulation is used to pose a damped linear inverse problem which has enabled 530 longitudinal river profiles to be fitted. The calculated regional rock uplift history suggests that the present-day topography primarily grew during Neogene times.

This history has been calibrated and tested using independent geologic constraints. Prior to $\sim$ 23 Ma, the development of the eastward tilt was slow, with rock uplift rates along the western margin $\leqslant$ 0.02 mm a^{-1}. After $\sim$ 23 Ma uplift rates along the Western Ghats increased rapidly to $\leqslant$ 0.1 mm a^{-1}. This Neogene increase in uplift rate is consistent with thermochronologic observations, sedimentary flux observations and sequence stratigraphic observations along the continental margins.

This rock uplift history, in conjunction with evidence for modest flexural rigidity and for crustal isostatic anomalies, suggests that the elevated topography of the Western Ghats escarpment is maintained by sub-lithospheric convective processes. The spatial pattern of regional uplift is consistent with the presence of a slow shear wave velocity anomaly directly beneath the plate. By converting residual depth measurements into depth-averaged temperature anomalies and by comparing these anomalies with the shear wave velocity structure beneath India, the size and variation of residual depth anomalies is shown to be consistent with a thermal isostatic response to $\pm$ 100°C temperature variations within a 200 $\pm$ 25 km thick asthenospheric channel.

The specific model proposed here to account for the generation and maintenance of elevated Indian

topography is likely applicable to other great escarpments on Earth (Hoggard *et al.*, 2016). From a broader perspective, the interconnectivity of dynamic topography, landscape development, and offshore stratigraphy described here testifies to the fundamental influence of mantle convection on evolution of the Earth's surface over a range of temporal and spatial scales. By applying integrated methodologies similar to those outlined here, it may be possible to reconstruct the Cenozoic spatio-temporal pattern of global dynamic topography.

Chapter 5

Asthenospheric Temperature Anomalies

Estimates of maximum dynamic topography based on observations show significant ± 1 km variation at wavelengths as short as 1,200 km (Figure 3.11). However, predictive models of dynamic topography consistently calculate amplitudes of ± 1 km at $\sim 10{,}000$ km wavelengths with relatively little power at wavelengths less than 5,000 km (Figure 5.1; Flament $et\ al.$, 2013). This discrepancy suggests that contributions from the uppermost mantle ($\leqslant 300$ km depth) are underestimated in predictive models as, in order for a radial viscosity profile to satisfy the Haskell constraint, its associated sensitivity kernels dictate that high-amplitude, short wavelength dynamic topography can only be generated by shallow structure (Richards & Hager, 1984). Many seismic tomographic models show a larger degree of short wavelength variation within the uppermost mantle than in deeper regions of the mantle, suggesting that the asthenosphere may host significant lateral variations in temperature and composition (Figures 4.19 & 4.20; Becker, 2002).

Mid-ocean ridge depth variations, plate motion changes, glacial isostatic adjustment studies and seismic anisotropy observations combine to provide strong evidence for the existence of a low-viscosity, thermally heterogeneous asthenospheric channel immediately beneath the lithospheric plates (Buck $et\ al.$, 2009; Iaffaldano & Bunge, 2015; van der Wal $et\ al.$, 2015; Lin $et\ al.$, 2016). The thickness, viscosity and ubiquity of this channel are debated. A trade-off exists between low-viscosity channel thickness, h, and the viscosity contrast between the channel and underlying mantle, η^*, such that equally good fits to glacial isostatic adjustment and geoid constraints can be obtained for any combination of parameters satisfying $h^3 \propto \eta^*$ (Paulson & Richards, 2009). However, recent studies of abrupt plate motion change and post-seismic relaxation recover the best fits between predictions and observations when asthenospheric channel thickness is 100–200 km and viscosity is 10^{19}–10^{20} Pa s (Iaffaldano & Lambeck, 2014; Hu $et\ al.$, 2016). Multiple independent observations of rapidly propagating (~ 40 cm a^{-1}) asthenospheric temperature anomalies in the North Atlantic also provide evidence for the existence low asthenospheric viscosities (Hartley $et\ al.$, 2011; Parnell-Turner $et\ al.$, 2014; Schoonman $et\ al.$, 2017).
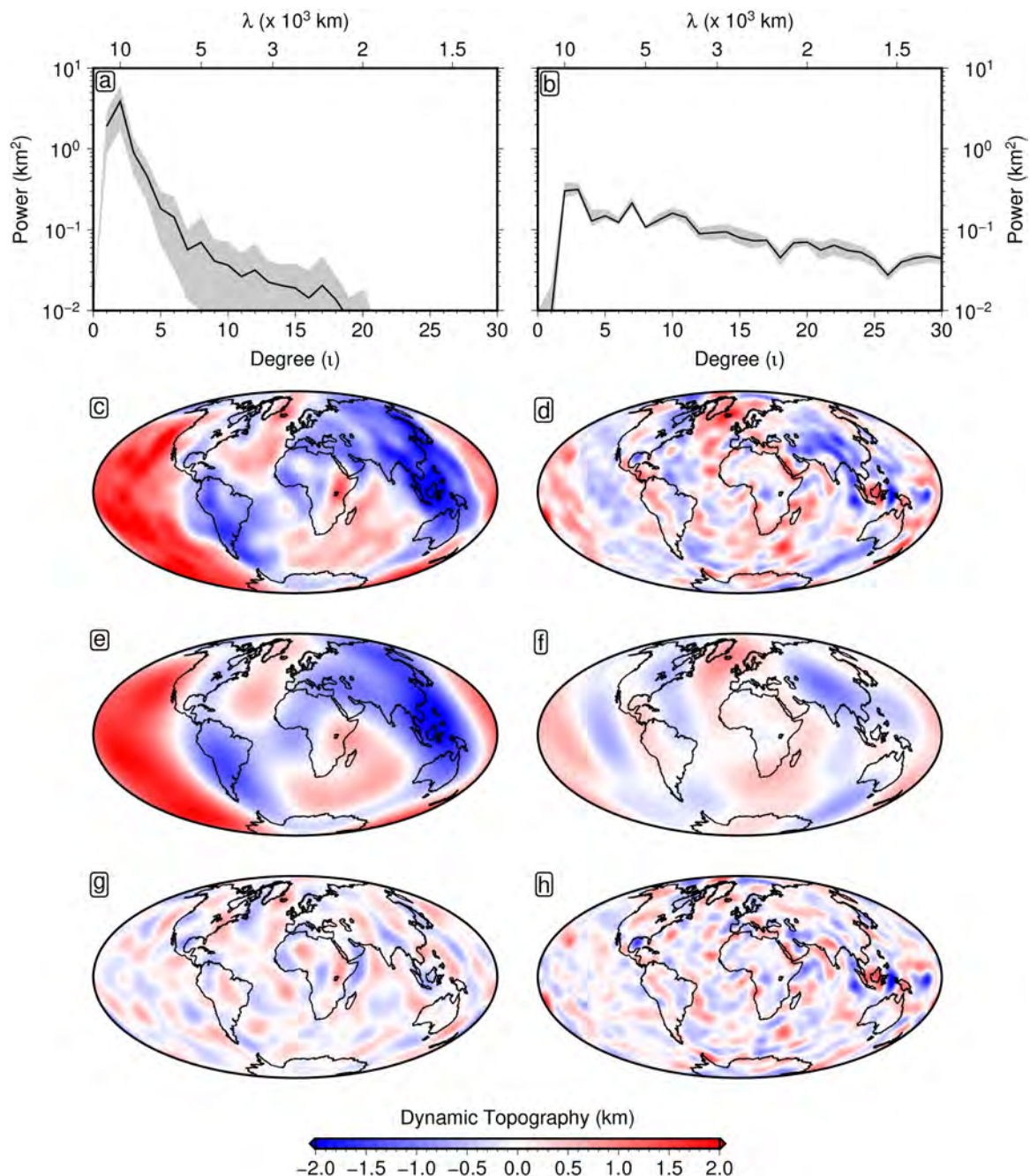
Figure 5.1: Spherical harmonic comparison of observations and predictions of dynamic topography. (a) Power spectrum of dynamic topography predictions. Thick black line = mean power spectrum of predictive model ensemble (Ricard *et al.*, 1993; Steinberger, 2007; Conrad & Husson, 2009; Spasojevic & Gurnis, 2012; Flament *et al.*, 2013); grey envelope = $\pm 1\sigma$ (standard deviation). (b) Power spectrum of observation-based water-loaded dynamic topography. Thick black line = power spectrum of spherical harmonic fit to dynamic topography observations; grey envelope = maximum and minimum limits of the power recovered for all combinations of damping parameters within the ranges $\lambda_1 = 10^2$–10^4 km^{-2} and $\lambda_2 = 10^{-0.5}$–$10^{0.5}$ km^{-2}. (c) Spherical harmonic fit to predicted dynamic topography of Steinberger (2007) for degree 1–30. (d) Spherical harmonic fit to dynamic topography observations from degree 1–30. (e) Degree 1–7 components of predicted dynamic topography field of Steinberger (2007). (f) Degree 1–7 components of dynamic topography observations. (g) Degree 8–30 components of predicted dynamic topography of Steinberger (2007). (h) Degree 8–30 components of dynamic topography observations.

In this chapter, I examine the extent to which short wavelength spectral discrepancy between observations and predictions of dynamic topography can be reconciled by constraining the amplitude and wavelength of thermal heterogeneity in the asthenosphere, building on initial results obtained across the Indian Peninsula in Chapter 4. First, the spatial correlation between asthenospheric shear wave velocities and residual depth anomalies is examined using seismic tomographic models. Next, the optimal thermal model developed in Chapter 2 is used, alongside a range of constraints on mantle temperature, viscosity and attenuation, to calibrate an experimentally-derived anelasticity parameterisation that converts shear wave velocity into temperature. The temperature predictions of the calibrated relationship are tested against independent geochemical observations to confirm the accuracy of the method. Finally, temperatures are converted to density anomalies and used to assess the extent to which residual depths can be reliably calculated from asthenospheric thermal anomalies alone.

5.1   Origin of Short Wavelength Spectral Discrepancy

Richards & Hager (1984) showed that, if the Earth's viscosity does not vary laterally, the spherical harmonic components of the geoid and dynamic topography can be calculated directly from the spherical harmonic components of mantle density structure using a set of sensitivity kernels that vary only as a function of radius and spherical harmonic degree, l (Figure 5.2a-b). Geoid sensitivity kernels, K_l^N, can be positive or negative depending on the details of the radial viscosity structure, whereas surface topography kernels, K_l^S, are positive throughout the mantle (Figure 5.2c-d).

Many predictive models of dynamic topography are calculated by inferring density structure from seismic tomography models and iteratively altering viscosity structure until the misfit between observed and calculated geoid undulations is minimised. However, most models do not calculate geoid and dynamic topography resulting from density anomalies in the uppermost ~ 300 km of the mantle for several reasons. First, simple velocity-density conversions in this layer are complicated by major compositional differences between thick cratonic roots and normal oceanic upper mantle. Secondly, lithospheric thickness differences cause significant lateral viscosity variation making the use of one-dimensional radial profiles less robust. Thirdly, values of K_l^S approach unity in this layer, resulting in implausibly large dynamic topography ($> \pm 5$ km). Finally, many global models generate input density structure by converting directly from seismic tomographic models constructed primarily from body-wave data, so have poor resolution in the uppermost mantle due
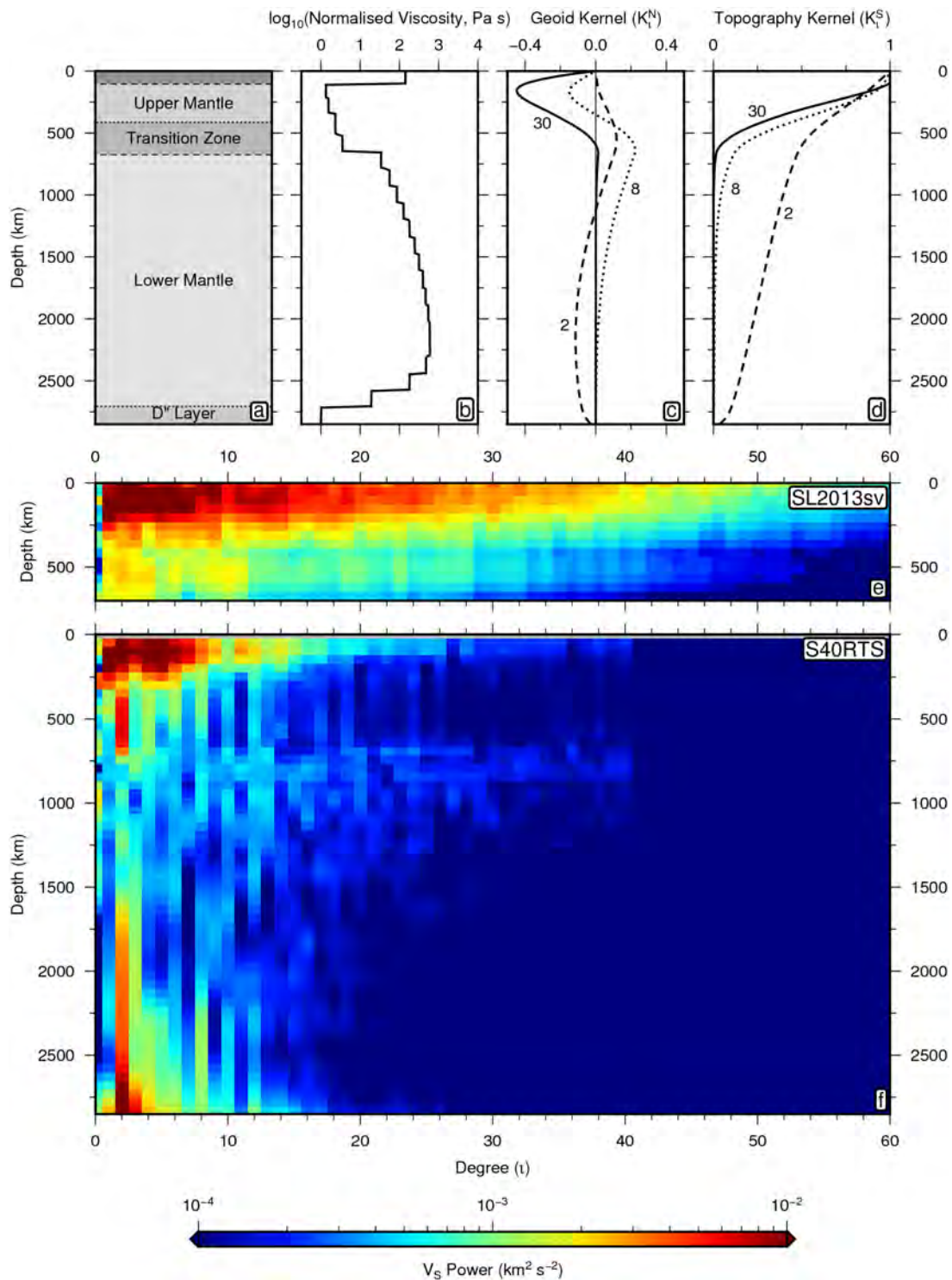
Figure 5.2: Instantaneous flow calculations and seismic tomographic inputs. (a) Generalised radial mantle structure. (b) Radial viscosity profile as a function of depth from Steinberger & Calderwood (2006). (c) Geoid sensitivity kernels as a function of depth calculated using methodology of Forte & Peltier (1991) and Steinberger & Calderwood (2006) viscosity profile. (d) Dynamic topography sensitivity kernels as a function of depth calculated using methodology of Forte & Peltier (1991) and Steinberger & Calderwood (2006) viscosity profile. (e) Power spectrum of shear wave velocity heterogeneity as a function of depth for SL2013sv (Schaeffer & Lebedev, 2013). (f) Power spectrum of shear wave velocity heterogeneity as a function of depth for S40RTS (Ritsema et al., 2011).

to the low density of crossing rays in this region (Steinberger, 2007; Spasojevic & Gurnis, 2012).

However, it is clear from kernel calculations that neglecting mantle density anomalies above 300 km depth will result in a small short wavelength ($l = 8$–30) contribution to predicted dynamic topography (Figure 5.2d). Previous seismic tomographic models constructed primarily from body wave data image relatively modest asthenospheric shear wave velocity anomaly signal at $l > 8$ (Figure 5.2f). In contrast, more recent surface wave models suggest significant shear wave velocity heterogeneities exist in the uppermost mantle, down to at least 400 km at $l \leqslant 50$ ($\lambda \geqslant 800$ km; Figure 5.2e). These two features imply that most previous models of global dynamic topography have underestimated the short wavelength component of the signal. Spectral discrepancy between the observations and predictions of dynamic topography at wavelengths shorter than 5,000 km may therefore result from model set-up.

5.2 Correlation between Residual Depth and Shear Wave Tomography

Seismic tomographic models can be constructed through inverse modelling of seismic waveform, travel time or phase velocity data. Starting from a given reference model, the gradient of the misfit between input data and predictions is used to iteratively update model parameters. Once the misfit has decreased below a prescribed threshold the inversion procedure is terminated to leave a final velocity model that provides acceptable fit to the input seismic data. A combination of theoretical advances, increased computing power and improved data coverage have led to the development of increasingly sophisticated and high-resolution seismic tomographic models. However, ray coverage remains sparse across much of the mantle meaning that inversions must be regularised, generally through amplitude damping or gradient damping, to prevent the introduction of artefacts (Rawlinson *et al.*, 2010). The adopted regularisation scheme must be sufficient to stabilise the inversion in parts of the model space that have minimal data constraint (Zaroli *et al.*, 2013). Often this condition leads to considerable damping and smoothing of velocity anomalies that are well constrained (Charléty *et al.*, 2013). As a result, the resolution of a particular tomography model can be highly variable and difficult to evaluate (Rawlinson *et al.*, 2014; Zaroli *et al.*, 2017). Furthermore, the selection of damping parameters and reference models is somewhat subjective and may lead to differences between tomographic models that are unrelated to the true velocity structure of the solid Earth (Kissling *et al.*, 2001).

Whole-mantle models are primarily constrained by body wave and normal mode data with some

surface wave data (Kustowski *et al.*, 2008; Ritsema *et al.*, 2011). As ray coverage is poor across much of the mid-mantle these models are often more strongly damped resulting in poorer vertical resolution (50–100 km) and typical horizontal resolution of ~ 1000 km in the upper mantle. By contrast, recent upper mantle models that are dominantly constructed from surface wave data have denser ray coverage and are generally less heavily regularised (Priestley *et al.*, 2012; French *et al.*, 2013; Schaeffer & Lebedev, 2013; Debayle *et al.*, 2016). These models tend to recover higher amplitude velocity anomalies and have vertical resolution of 25–50 km and typical horizontal resolutions of 300–600 km. While these characteristic resolution values help to constrain the average properties of each model, locally resolution may be significantly poorer. Model resolution tends to be particularly low across Africa, Antarctica and in the middle of ocean basins due to sparse ray coverage, so caution must be exercised when interpreting velocity structure in these regions. Moreover, in the shallow mantle, seismic tomographic models are dominated by signal from plate cooling in the oceans and cratonic roots in the continents (Figure 5.3a). Signal from the convecting mantle is therefore convolved with that of stable mantle lithosphere, making it difficult to disentangle dynamic and isostatic contributions to topography (Gvirtzman *et al.*, 2016).

Determining residual topography in the continents is problematic as their complex density structure is poorly constrained. However, the density structure of the oceanic lithosphere is significantly more homogeneous and the bathymetric signal of plate cooling places reasonable constraints on isostatic topography. Residual depth anomalies are defined relative to this background lithospheric isostasy. Thus, in order to assess the contribution of upper mantle density anomalies to dynamic topography, seismic velocity anomalies associated with plate cooling must be subtracted from observed velocity structure (Figure 5.3b). The resulting velocity structure is termed 'residual' tomography and reveals significant shear wave velocity anomaly structure in the uppermost mantle that is unrelated to plate cooling (Wen & Anderson, 1997). Furthermore, the pattern and characteristic wavelength of the anomalies mirrors that of the residual depth data with spatial anti-correlation observed between dynamic topography and shear wave velocities. This anti-correlation is expected if slow seismic velocity indicates hotter mantle and faster velocities are linked to cooler regions (Figure 5.3c & d).

For SL2013sv (Schaeffer & Lebedev, 2013), the optimal spatial correlation between shear wave speed and residual depth, both expanded up to spherical harmonic degree 30, occurs when residual tomography is stacked between 75 and 175 km ($r = -0.47$; Figure 5.3e & f). This depth range coincides with the thickness of the low-viscosity asthenosphere estimated from glacial isostatic adjustment, post-seismic rebound, seismic anisotropy and plate motion force balance studies
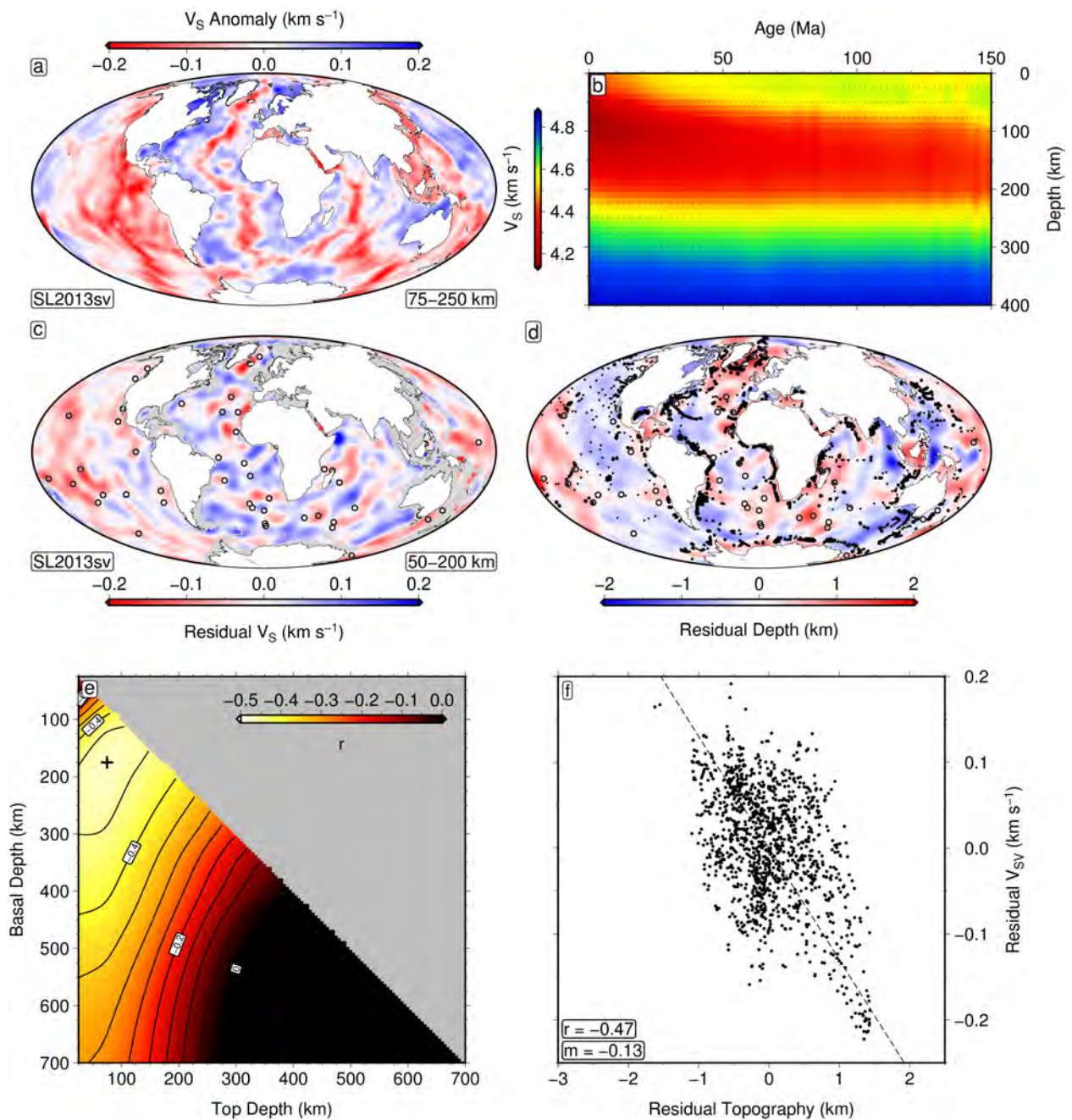
Figure 5.3: Comparison between residual topography and residual tomography. (a) Stacked shear wave velocity anomalies between 50 and 125 km depth from SL2013sv. (b) Oceanic V_S from SL2013sv stacked globally as a function of plate age, excluding regions with anomalous oceanic crust determined by Hoggard *et al.* (2017). (c) Stacked residual shear wave velocity anomalies between 75 and 175 km depth from SL2013sv (Schaeffer & Lebedev, 2013). Unfilled circles = oceanic intraplate hotspots. (d) Spherical harmonic fit to residual depth measurements. Unfilled circles = oceanic intraplate hotspots; filled circles = oceanic residual depth measurements isostatically corrected for both sediment and crustal thickness variations; filled up/down triangles = upper/lower bound oceanic residual depth measurements isostatically corrected for sedimentary thickness variations only. (e) Correlation between residual depth measurements and stacked residual shear wave velocity as a function of depth and layer thickness. r = Pearson's correlation coefficient. (f) Correlation between residual depth measurements and residual shear wave velocity stacked between 75 and 175 km. r = Pearson's correlation coefficient; m = gradient of best-fitting relationship.

(Iaffaldano & Lambeck, 2014; van der Wal *et al.*, 2015; Hu *et al.*, 2016; Lin *et al.*, 2016). 90% of oceanic hotspots occur within 200 km of anomalously low shear wave speed regions (Figure 5.3c; Courtillot *et al.*, 2003). Bouvet is the only putative hotspot outside such an area that is not deemed 'poor-reliability' in the catalogue of Courtillot *et al.* (2003). However, even this hotspot is less than 300 km from a low-velocity anomaly and is located in the South Atlantic where a low density of crossing rays make seismic tomographic models less well constrained. Overall, the reasonable correlation between slow upper mantle shear wave velocities, elevated residual depths and intraplate volcanism suggests that recent surface wave models generally have sufficient resolution to image small-scale asthenospheric temperature anomalies ($\lambda \sim 1{,}000$ km).

The gradient of the best-fitting linear relationship between residual depths and stacked residual shear wave velocity is -0.13 km s^{-1} per km . Application of this factor to the residual velocities yields a power spectrum that closely matches that of observation-based dynamic topography at wavelengths shorter than 5,000 km. The observed spatial correlation between these two independent datasets indicates that asthenospheric density structure may account for approximately 50% of the total variance in the residual depth database. The strong spectral correlation demonstrates that inclusion of these shallow contributions is important in reconciling short wavelength discrepancy between observations and models of dynamic topography.

Similar results are obtained for other tomographic models but correlations are generally weaker. The correlation between residual tomography and residual depth obtained for SEMUM2 is close to that of SL2013sv ($r = -0.44$) across a similar depth range (50–200 km; French *et al.*, 2013). However, correlations at asthenospheric depths are poorer for other surface wave models; $r = -0.35$ and $r = -0.32$ for 3D2015_07Sv and PM2012, respectively (Priestley *et al.*, 2012; Debayle *et al.*, 2016). The poorest correlation is obtained for the global, body-wave dominated model S362ANI (Kustowski *et al.*, 2008). Overall, the best correlations are obtained for seismic tomographic models that are constructed predominantly from surface wave data and use more higher mode data (e.g. SL2013sv and SEMUM2 fits waveforms up to the 9th overtone). This observation suggests that seismic tomographic inversion strategies that sacrifice larger numbers of seismograms in favour of fitting more of each waveform produce better models of asthenospheric velocity structure, provided the trade-off is not too heavily weighted towards the latter. For example, SL2013sv is unique in combining a large number of seismograms ($\sim$750,000) with more sophisticated waveform fitting (Schaeffer & Lebedev, 2013). This balanced trade-off between model complexity and data coverage, combined with an inversion strategy that inverts directly for crustal structure, is likely responsible

for the improved correlations obtained for this model. By contrast, the poor correlations obtained for S362ANI are to be expected given that this model is global, has the poorest horizontal resolution and uses only the fundamental mode of ∼250,000 surface waves.

A proportion of the scatter in the relationship between residual topography and residual tomography may reflect compositional effects or long wavelength residual depth deviations related to lower mantle density anomalies (Dalton *et al.*, 2014; Colli *et al.*, 2016). However, differences in residual depth anti-correlation between seismic tomographic models indicate that some discrepancy will reflect resolution limitations (Schoonman *et al.*, 2017). Nevertheless, the observation that better correlations can be directly tied to modelling strategy and input data suggests that these improvements are unlikely to be due to random variation between models; instead, they probably reflect increased resolution of upper mantle temperature perturbations. Thus, recent global surface wave models, such as SL2013sv, may be used to place useful constraints on upper mantle temperature and density anomalies in the absence of more direct observations.

5.3   Shear Wave Velocity Calibration

A reasonable spatial and spectral correlation exists between residual depth anomalies and residual shear wave tomography. However, it is not obvious that the amplitudes of imaged density anomalies are sufficient to generate the ±2 km dynamic surface perturbations identified in the observational database. To quantitatively assess the contribution of these asthenospheric buoyancy anomalies, shear wave speeds can be converted to temperature. The methodology adopted here is that described by Priestley & McKenzie (2006), where multiple constraints on the covariation of temperature and shear wave structure are used to calibrate optimal input parameters for an experimentally-constrained anelasticity model (Priestley & McKenzie, 2013; Yamauchi & Takei, 2016; Takei, 2017). This inverse, observation-driven approach is preferred over thermodynamic calculations as it allows separate parameter sets to be calculated for different seismic tomographic models (Connolly, 2009; Stixrude & Lithgow-Bertelloni, 2011; Cottaar *et al.*, 2014). This feature is desirable as shear wave velocity structure diverges significantly between models due to differences in damping and model parameterisation. As a result, if a single conversion were applied, variation in calculated temperatures would reflect model set-up rather than the thermal state of the upper mantle.

5.3.1 Parameterising Shear Wave Anelasticity

Over the past decade, many anelasticity models have been proposed for the upper mantle based on the results of forced oscillation experiments on either pure olivine or polycrystalline analogues (Faul & Jackson, 2005; Jackson *et al.*, 2010; McCarthy & Takei, 2011; Yamauchi & Takei, 2016). Olivine-based experiments have the advantage of being compositionally more similar to the upper mantle but are disadvantaged by the requirement for very fine-grained samples ($d < 50$ μm). Calculated relationships must therefore be extrapolated over 3 orders of magnitude to approximate upper mantle conditions ($d \sim$ 5–10 mm; Jackson *et al.*, 2014). By contrast, experiments on polycrystalline analogues can be carried out at representative grain sizes (Holtzman, 2016). Borneol, an organic compound, is commonly used in anelasticity studies as it forms a simple binary eutectic system with diphenylamine that behaves in an analogous way to the olivine-basalt system, producing very similar equilibrium microstructure (McCarthy *et al.*, 2011). However, the drawback of using borneol is that it is compositionally dissimilar to the upper mantle. Nevertheless, McCarthy *et al.* (2011) demonstrated that broad similarity exists between the anelastic responses of borneol and olivine when measurements are scaled by the relevant Maxwell frequency, $f_M = \mu_U/\eta$, where μ_U is the unrelaxed shear modulus and η is the diffusion creep viscosity of the material. Priestley & McKenzie (2013) exploited this scaling relationship to show that a representative range of independent shear wave velocity, attenuation and viscosity observations could be adequately fit with a single set of input parameters that are broadly consistent with independent experimental values. However, due to a lack of available measurements at the time, calibrating the anelasticity model necessarily involved extrapolation of the Maxwell frequency scaling relationship into the seismically relevant normalised frequency band ($10^8 \leqslant f/f_M \leqslant 10^{11}$). Subsequently, Yamauchi & Takei (2016) showed that, at these higher frequencies, the simple scaling relationship breaks down and an additional term must be added to the background trend to fully describe the experimental data. Importantly, their new anelasticity model more accurately fits the rapid decrease in V_S as oceanic lithospheric temperature nears the solidus, T_s. Moreover, the imposition of an unconstrained step change in viscosity at the melting point is no longer required (cf. Priestley & McKenzie, 2013). Calculated attenuation within this temperature and depth range is also more consistent with independent data. Due to these significant improvements, the parameterisation of Yamauchi & Takei (2016) is adopted here.

The parameterisation expresses V_S and shear wave attenuation, Q_S^{-1}, using

$$\begin{cases} V_S = \frac{1}{\sqrt{\rho J_1}} \left(\frac{1+\sqrt{1+(J_2/J_1)^2}}{2} \right)^{-\frac{1}{2}} \simeq \frac{1}{\sqrt{\rho J_1}} \\ Q_S^{-1} = \frac{J_2}{J_1} \left(\frac{1+\sqrt{1+(J_2/J_1)^2}}{2} \right)^{-1} \simeq \frac{J_2}{J_1}, \end{cases} \tag{5.1}$$

where J_1 and J_2 represent the real and imaginary components of the complex compliance J^*, a quantity that describes the sinusoidal strain resulting from the application of a unit of sinusoidal stress. J_1 represents the amplitude of the strain that is in phase with the stress; J_2 represents the component that is $\pi/2$ out of phase and results in dissipation. These complex compliance terms are expressed as

$$\begin{cases} J_1(\tau_S') = J_U \left[1 + \frac{A_B(\tau_S')^{\alpha_B}}{\alpha_B} + \frac{\sqrt{2\pi}}{2} A_P \, \sigma_P \left\{ 1 - \mathrm{erf} \left(\frac{\ln(\tau_P'/\tau_S')}{\sqrt{2}\sigma_P} \right) \right\} \right] \\ J_2(\tau_S') = J_U \frac{\pi}{2} \left[A_B(\tau_S')^{\alpha_B} + \frac{\sqrt{2\pi}}{2} A_P \exp\left(-\frac{(\ln(\tau_P'/\tau_S'^2))}{2\sigma_P^2} \right) \right] + J_U(\tau_S'). \end{cases} \tag{5.2}$$

$A_B = 0.664$ and $\alpha_B = 0.38$ represent the amplitude and slope of the background stress relaxation trend, respectively. $\tau_P' = 6 \times 10^{-5}$, σ_P and A_P represent the normalised timescale, amplitude and width of the relaxation peak that is superimposed on the background trend at high frequency. These last two terms are given as functions of homologous temperature ($T' = T/T_s$), where

$$\sigma_P(T') = \begin{cases} 4 & \text{for } T' < 0.91 \\ 4 + 37.5(T' - 0.92) & \text{for } 0.92 \leqslant T' < 1 \\ 7 & \text{for } T' \geqslant 1 \end{cases} \tag{5.3}$$

and

$$A_P(T') = \begin{cases} 0.01 & \text{for } T' < 0.91 \\ 0.01 + 0.4(T' - 0.91) & \text{for } 0.91 \leqslant T' < 0.96 \\ 0.03 & \text{for } 0.96 \leqslant T' < 1 \\ 0.03 + \beta(\phi_m) & \text{for } T' \geqslant 1. \end{cases} \tag{5.4}$$

ϕ_m is melt fraction and $\beta(\phi_m)$ describes the direct poroelastic effect of melt (~ 0 in the upper mantle). Assuming that the poroelastic effect is negligible under upper mantle conditions, the unrelaxed compliance (J_U in Equation 5.2) becomes $1/\mu_U(P, T)$ where

$$\mu_U(P, T) = \mu_U^0 + \frac{\partial \mu_U}{\partial T}(T - T_0) + \frac{\partial \mu_U}{\partial P}(P - P_0). \tag{5.5}$$

$\mu_U^0 = \mu_U(P_0, T_0)$ and the differential terms are assumed to be constant. The normalised shear wave period (τ_S' in Equation 5.2) is equal to $\tau_S/2\pi\tau_M$ where τ_S is shear wave period, τ_M ($= \eta/\mu_U$) is the normalised Maxwell relaxation time and η is described by

$$\eta = \eta_r \left(\frac{d}{d_r}\right)^{m_d} \exp\left[\frac{E_a}{R}\left(\frac{1}{T} - \frac{1}{T_r}\right)\right] \exp\left[\frac{V_a}{R}\left(\frac{P}{T} - \frac{P_r}{T_r}\right)\right] A_\eta. \tag{5.6}$$

In this expression, $\eta_r = \eta(T_r, P_r, d_r)$, m_d is a grain size exponent, E_a is activation energy and V_a is activation volume, while $d_r = 1$ mm, $P_r = 1.5$ GPa and $T_r = 1200°$C are reference grain size, reference pressure and reference temperature, respectively. A_η represents the extra reduction of viscosity due to an increase in E_a near the solidus and is expressed as

$$A_\eta(T') = \begin{cases} 1 & \text{for } T' < T_\eta' \\ \exp\left[-\frac{(T'-T_\eta')}{(T'-T'T_\eta')}\ln(\gamma)\right] & \text{for } T_\eta' \leqslant T' < 1 \\ \gamma^{-1}\exp(\lambda\phi) & \text{for } T' \geqslant 1. \end{cases} \tag{5.7}$$

T_η is the homologous temperature above which activation energy becomes $E_a + \Delta E_a$ and γ is the factor of extra reduction ($= 5$). The term $\lambda\phi$ describes the direct effect of melt on the viscosity and is assumed to be ~ 0 for the upper mantle (Takei, 2017).

5.3.2 Anelasticity Model Calibration

A_B, α_B, τ_P', $\beta(\phi_m)$, γ, T_η' and $\lambda\phi$, are directly constrained by the forced oscillation experiment data. However, μ_U^0, $\frac{\partial\mu_U}{\partial T}$, $\frac{\partial\mu_U}{\partial P}$, η_r, E_a and V_a must be independently determined by inverting available observational constraints on temperature, shear wave velocity, attenuation and viscosity. Inverse modelling is carried out separately for each shear wave velocity model since variations in damping parameters, reference V_S models, input seismograms and modelling strategies mean that no single set of parameters can provide a good fit to all seismic tomographic models (SL2013sv, SEMUM2, PM2012, 3D2015_07Sv and S362ANI). When calculating homologous temperatures, $T_s(z)$ can either be imposed *a priori* or left free to vary using the expression

$$T_s(z) = T_s(50 \text{ km}) + \frac{\partial T_s}{\partial z}(z - 50 \text{ km}), \tag{5.8}$$

where z is depth in km and the solidus gradient ($\frac{\partial T_s}{\partial z}$) is inverted for.

Observational Constraints

To determine best-fitting values for the unknown parameters in the anelasticity model, misfit between observational constraints and model calculations and on T, V_S, Q_S^{-1} and η is minimised using Powell's conjugate gradient algorithm (Press et $al.$, 1996). The datasets that underpin this inversion are similar to those used by Priestley & McKenzie (2013). There are, however, some important modifications. The best constraint on the relationship between temperature and shear wave velocity is the covariance of these quantities within the oceanic lithosphere as it cools and subsides. Previous studies derived both empirical and semi-empirical relationships between V_S and T using the McKenzie et $al.$ (2005) plate model (Priestley & McKenzie, 2006, 2013). In Chapter 2, by exploiting improved seafloor subsidence and heat flow databases, in conjunction with updated experimental data on the temperature and pressure dependence of key thermal properties, a revised plate model is developed. Unlike previous models, this parameterisation obtains an optimal fit to both heat flow and subsidence data for a mantle potential temperature that is consistent with geochemical constraints. Predicted evolution of lithospheric thickness is also in better agreement with constraints from global seismic tomographic models and seismic anisotropy constraints (Burgos et $al.$, 2014; Steinberger & Becker, 2017). This model may therefore constrain oceanic thermal structure more accurately at depth, potentially improving the calibration of shear wave velocity to temperature conversions (Figure 5.4a). The principal difference between this model and the model of McKenzie et $al.$ (2005), is the larger stable plate thickness and slower cooling of the plate, both of which better fit the seismological, subsidence and heat flow observations.

Beneath the thermal boundary layer, mean temperature variation as a function of depth is expected to be isentropic, allowing globally-averaged oceanic V_S to be tied to average temperature at a given depth (Figure 5.4b; Turcotte & Schubert, 2002). This observational constraint is restricted to a depth range of 225–400 km because non-isentropic temperature has been proposed as the cause of the low seismic velocity zone above 225 km and resolution of many surface wave tomographic models deteriorates significantly below 400 km (Figure 5.4b; Anderson, 2011; Morgan et $al.$, 2013). The exact isentropic gradient over this depth range is uncertain. A range of isentropic temperature profiles are therefore investigated, including $1333°C + 0.44°C$ km^{-1} (e.g. Katz et $al.$, 2003) and $1315°C + 0.6°C$ km^{-1} (e.g. Priestley & McKenzie, 2006). An additional pressure-, temperature- and composition-dependent isentrope is determined for a potential temperature of $1333°C$ using the Perple_X Gibbs free-energy minimisation routine and the mineral database of Stixrude & Lithgow-Bertelloni (2011) to investigate the potential impact of depth-dependent isen-

tropic gradients (Connolly, 2009). A pyrolitic mantle composition is assumed when calculating this isentrope (Workman & Hart, 2005).

As in Priestley & McKenzie (2006, 2013), P-T conditions calculated from thermobarometry of mantle xenoliths are used as a constraint on deep temperature structure (50–200 km). First, a profile of V_S as a function of depth is determined from a given seismic tomographic model at each xenolith sample location. Secondly, profiles are interpolated at 5 km intervals and sampled at depths corresponding to the inferred origin of the mantle xenolith. Finally, by repeating this sampling process, depth of origin, present-day shear wave velocity and equilibration temperature is determined for each xenolith in the database (Figure 5.4c; Mather *et al.*, 2011). This constraint depends on the assumption that the thermal structure of the host lithosphere has changed little since the time the xenolith was transported to the surface. The long thermal time constant of thick cratonic lithosphere ($\geqslant$ 100 Ma) precludes geologically rapid alterations of the geotherm, suggesting this assumption holds for the relatively young mantle xenoliths used here. This approach also presupposes that any systematic compositional differences between oceanic and continental lithosphere have a relatively minor effect on V_S structure. Priestley & McKenzie (2006) validated this simplification by showing that, for reasonable amounts of sub-continental melt extraction (20–25%), V_S of residual harzburgite is $\sim$ 0.03 km s^{-1} greater than undepleted peridotite, suggesting that lithospheric V_S structure is relatively insensitive to compositional heterogeneity.

As well as providing a relationship between V_S and temperature, the anelasticity model of Yamauchi & Takei (2016) can be used to estimate Q_S^{-1} and η. Beneath plates older than 100 Ma, both V_S and Q_S^{-1} do not vary significantly with age at depths of 150 to 400 km (Figure 5.4d). Therefore, to constrain attenuation estimated by the anelasticity model, the QRFSI12 attenuation model of Dalton *et al.* (2009) is stacked according to age in the same manner as the V_S tomographic models to determine an average Q_S^{-1} profile that is tied to average V_S over the same depth and age range (Figure 5.3b; Priestley & McKenzie, 2013). Temperatures are inverted from V_S to allow for the possibility that temperature structure in the shallow asthenosphere may be non-isentropic. Finally, viscosity is constrained by penalising solutions that give average upper mantle viscosities between 225 and 400 km that differ from the value of 3×10^{20} Pa s estimated by Lau *et al.* (2016) for a depth range of 100–670 km depth (Figure 5.4e).

To determine best-fitting parameters for the anelasticity model, a cost function is minimised in two stages. First a parameter sweep is carried out to find the approximate global minimum of the function. Secondly, Powell's conjugate direction algorithm is used to further minimise the

cost function using the parameters corresponding to the approximate global minimum as starting values (Press *et al.*, 1996). This two-step optimisation procedure is adopted to ensure that the final parameter values represent global minima as initial tests using Powell's algorithm with randomised starting models revealed that the cost function contains multiple local minima. The cost function implemented here is almost identical to that presented in Priestley & McKenzie (2013) and is composed of five separate misfit functions. Misfits to stacked oceanic seismic velocities, to isentropic seismic velocity,constraints, to xenolith velocity data, to attenuation observations and to average viscosity are denoted as H_1, H_2, H_3, H_4 and H_5, respectively.

H_1 is determined using

$$H_1 = \left[\frac{1}{N} \sum_{i=1}^{N} \left(\frac{V_i^o - V_i^c}{\sigma_i} \right)^2 \right]^{\frac{1}{2}} . \tag{5.9}$$

where V_i^o are observed stacked velocities, σ_i are the standard deviations of V_i^o and V_i^c are calculated velocities. H_2, is expressed in an identical manner. H_3 and H_4 are given by

$$H_3 = \left[\frac{1}{N} \sum_{i=1}^{N} (V_i^o - V_i^c)^2 \right]^{\frac{1}{2}} \text{ and } H_4 = \left[\frac{1}{N} \sum_{i=1}^{N} \left(\frac{Q^{-1}{}_i{}^o - Q^{-1}{}_i{}^c}{\sigma_i^*} \right)^2 \right]^{\frac{1}{2}}, \tag{5.10}$$

where $Q^{-1}{}_i{}^o$ are observed stacked attenuation measurements at a given depth, $Q^{-1}{}_i{}^c$ are calculated attenuation values and σ_i^* are the standard deviations of $Q^{-1}{}_i{}^o$. Note that this expression differs from that used by Priestley & McKenzie (2013), where misfit is normalised by average attenuation within a given depth range. Finally, H_5 is given by

$$H_5 = \left[\frac{1}{N} \sum_{i=1}^{N} (\log_{10}(\eta_{ref}) - \log_{10}(\eta_i^c))^2 \right]^{\frac{1}{2}}, \tag{5.11}$$

where η_{ref} is and η_i^c are observed average viscosity and computed viscosity, respectively. Individual misfit functions are then combined into a final cost function, H_w, using the expression

$$H_w = \sum_{i=1}^{N} w_i H_i, \tag{5.12}$$

where w_i represents the weights assigned to individual misfit functions. After setting w_1 to a given value, w_2, w_3, w_4 and w_5 are determined using the approximate ratios of H_1 relative to H_2, H_3, H_4 and H_5, respectively, as calculated using the parameters calibrated by Yamauchi & Takei (2016).

The inversion is carried out for several different combinations of misfit weights, solidus param-

eterisations, isentrope parameterisations and five different shear wave velocity models (S362ANI, PM2012, SEMUM2, SL2013sv & 3D2015_07Sv) to investigate the effect of different model assumptions and inputs on recovered parameter values (Kustowski *et al.*, 2008; Priestley *et al.*, 2012; French *et al.*, 2013; Schaeffer & Lebedev, 2013; Debayle *et al.*, 2016). In all cases the initial parameter sweep to constrain the global minimum and determine a starting model is carried out for value ranges and increments listed in Table 5.1. Extrema are chosen that lie outside the range of values proposed by mineral physics experiments on olivine and previous anelasticity calibrations to ensure that the minimisation procedure is not preconditioned to obtain results that match previous studies (Isaak, 1992; Kohlstedt *et al.*, 1995; Hirth & Kohlstedt, 2013; Cammarano *et al.*, 2003; Karato, 2010; Priestley & McKenzie, 2013; Mao *et al.*, 2015; Thomson *et al.*, 2016; Yamauchi & Takei, 2016; Takei, 2017).

Table 5.1: Parameter sweep values. Value ranges and increments for initial parameter sweep.

Value	μ_0 (GPa)	$\frac{\partial\mu}{\partial T}$ (GPa$^\circ$C^{-1})	$\frac{\partial\mu}{\partial P}$	η_0 (Pa s)	E_a (kJ mol^{-1})	V_a (cm^{-3} mol^{-1})	$\frac{\partial T_s}{\partial z}$ ($^\circ$C km^{-1})
Minimum	72	-0.020	1.7	10^{19}	300	4	0.6
Maximum	80	-0.008	2.4	10^{23}	600	11	d1.4
Increment	0.5	0.001	0.1	$10^{0.5}$	50	0.5	0.1

5.3.3 Results

As found by Priestley & McKenzie (2013) and Yamauchi & Takei (2016), parameter sets are broadly in agreement with independent mineral physics data (Table 5.2). Indeed, inverted values of μ_0 and $\frac{\partial\mu}{\partial T}$ generally agree better with experimental data than previous studies (Isaak, 1992; Cammarano *et al.*, 2003). However, as recognised in earlier work, inverted $\frac{\partial\mu}{\partial P}$ values are generally higher than the experimentally constrained value of ~ 1.8 (Mao *et al.*, 2015). For the most part, activation energies and volumes are consistent with previous experimental results but vary considerably between models (cf. Kohlstedt *et al.*, 1995; Hirth & Kohlstedt, 2013; Fei *et al.*, 2012).

When the solidus is free to vary, as in Yamauchi & Takei (2016), the inverted solidus gradient, $\sim 1^\circ$C km^{-1}, is significantly lower than the $\sim 4^\circ$C km^{-1} expected for dry peridotite (Katz *et al.*, 2003). When a dry peridotite solidus is imposed, fits to attenuation, viscosity and the isentrope become poorer. Depressing the solidus by increasing the water content of the mantle to 112 ppm

Table 5.2: Summary of anelastic parameter inversion results. H_w = weighted misfit ($w_1 = 0.5$, $w_2 = 0.05$, $w3 = 0.5$, $w_4 = 0.1$, $w_5 = 0.1$). KSL03 = ~ 0.44°C km^{-1} isentrope of Katz *et al.* (2003); PM06 = ~ 0.6°C km^{-1} isentrope of Priestley & McKenzie (2006); $d(z)$ = depth-dependent grain size-dependence (Dannberg *et al.*, 2017); YT16 = same input as Yamauchi & Takei (2016) with SL2013sv velocity model. Unless otherwise specified, H_w is minimised and the 1333°C pyrolitic isentrope of Stixrude & Lithgow-Bertelloni (2011) is used.

Model Run	μ_0 (GPa)	$\frac{\partial \mu}{\partial T}$ (GPa°C^{-1})	$\frac{\partial \mu}{\partial P}$	η_0 (Pa s)	E_a (kJ mol^{-1})	V_a (cm^{-3} mol^{-1})	$\frac{\partial T_s}{\partial z}$ (°C km^{-1})	H_w	Misfit Function
SL2013sv (YT16)	72.8	-0.0125	2.15	1.38×10^{21}	461	9.44	1.108	0.748	H_w
SL2013sv (V_S no nod.)	76.87	-0.0181	2.59	2.24×10^{22}	599	6.42	1.059	0.699	H_1 & H_2
SL2013sv (V_S)	77.2	-0.0184	2.60	1.39×10^{22}	531	7.013	1.014	0.729	H_1-H_3
SL2013sv (no nod.)	74.7	-0.0161	2.56	2.50×10^{21}	304	3.04	0.946	0.638	H_1, H_2, H_4 & H_5
SL2013sv (no plate)	72.4	-0.0146	2.58	3.27×10^{22}	496	3.00	0.969	0.792	H_2-H_5
SL2013sv (dry solidus)	75.5	-0.0167	2.56	3.23×10^{18}	300	9.24	—	0.914	H_w
SL2013sv (wet solidus)	76.2	-0.0175	2.60	3.37×10^{21}	576	4.01	—	0.938	H_w
SL2013sv (KSL03)	73.5	-0.0151	2.56	2.32×10^{21}	384	5.11	0.962	0.691	H_w
SL2013sv (PM06)	73.5	-0.0151	2.60	9.79×10^{20}	301	5.28	1.195	0.773	H_w
SL2013sv ($d(z)$)	72.0	-0.0135	2.47	4.38×10^{21}	561	3.01	0.919	0.778	H_w
SL2013sv	72.0	-0.0130	2.40	3.02×10^{20}	309	5.74	1.098	0.623	H_w
SEMUM2	73.8	-0.0140	2.22	2.10×10^{21}	328	4.00	0.869	0.789	H_w
PM2012	75.5	-0.0161	2.41	4.02×10^{21}	343	3.03	0.997	1.099	H_w
S362ANI	79.2	-0.0181	2.27	6.46×10^{22}	551	3.05	0.922	0.533	H_w
3D2015_07Sv	75.7	-0.0170	2.36	1.53×10^{22}	448	3.01	0.957	0.881	H_w

improves the fit to attenuation data. However, misfit below 200 km depth remains high as homologous temperatures become too low to produce the observed high attenuation and lower viscosity. It therefore appears that low $\frac{\partial T_s}{\partial z}$ is required by the data. The presence of small quantities of CO_2 in the upper mantle could create the necessary gradient and has been invoked to explain high attenuation values in the asthenosphere (Thomson *et al.*, 2016; Eilon & Abers, 2017).

Choice of isentropic gradient has a relatively small effect on the recovered parameters but misfits are ∼ 15% smaller when isentropic gradients are reduced. Best fits are obtained using the isentrope predicted for pyrolite using thermodynamically self-consistent calculations. This result suggests that inclusion of a depth-dependent isentropic gradient can better account for the changes in average V_S, Q_S^{-1} and η with depth.

V_S, and in particular Q_S^{-1} and η, are expected to vary significantly with changing grain size (Faul & Jackson, 2005; Jain *et al.*, 2018). It is possible that significant depth-dependent grain size variations occur within the oceanic upper mantle due to systematic changes in the balance between dynamic recrystallisation and grain growth (Hall & Parmentier, 2003; Ricard & Bercovici, 2009; Turner *et al.*, 2015). At present, grain size profiles cannot be measured directly so numerical simulations performed at geological strain rates provide the only available estimates (e.g. Behn *et al.*, 2009). Dannberg *et al.* (2017) carried out global convection simulations incorporating feedbacks between strain rate, dynamic recrystallisation and viscosity. Their predicted grain-size distributions are broadly similar to previous predictions but better satisfy a number of independent seismological and rheological constraints. Here, the ensemble mean and standard deviation of their variable grain size models are used as input parameters for the anelasticity model to assess the effect of non-constant grain size distribution on inversion results. Inverted activation volume (3.01 cm^{-3}) is reduced compared to values obtained for constant grain size ($5.74 \text{ cm}^{-3} \text{ mol}^{-1}$). The smaller activation volume may indicate that modulation of viscosity through grain size variation accounts for some proportion of the observed anelasticity, relaxing the requirement for elevated temperatures to explain low asthenospheric shear wave velocities (cf. Morgan *et al.*, 2013). However, this inference is necessarily tentative as recovered activation volume varies substantially between models suggesting that this parameter may not be very well constrained by the data.
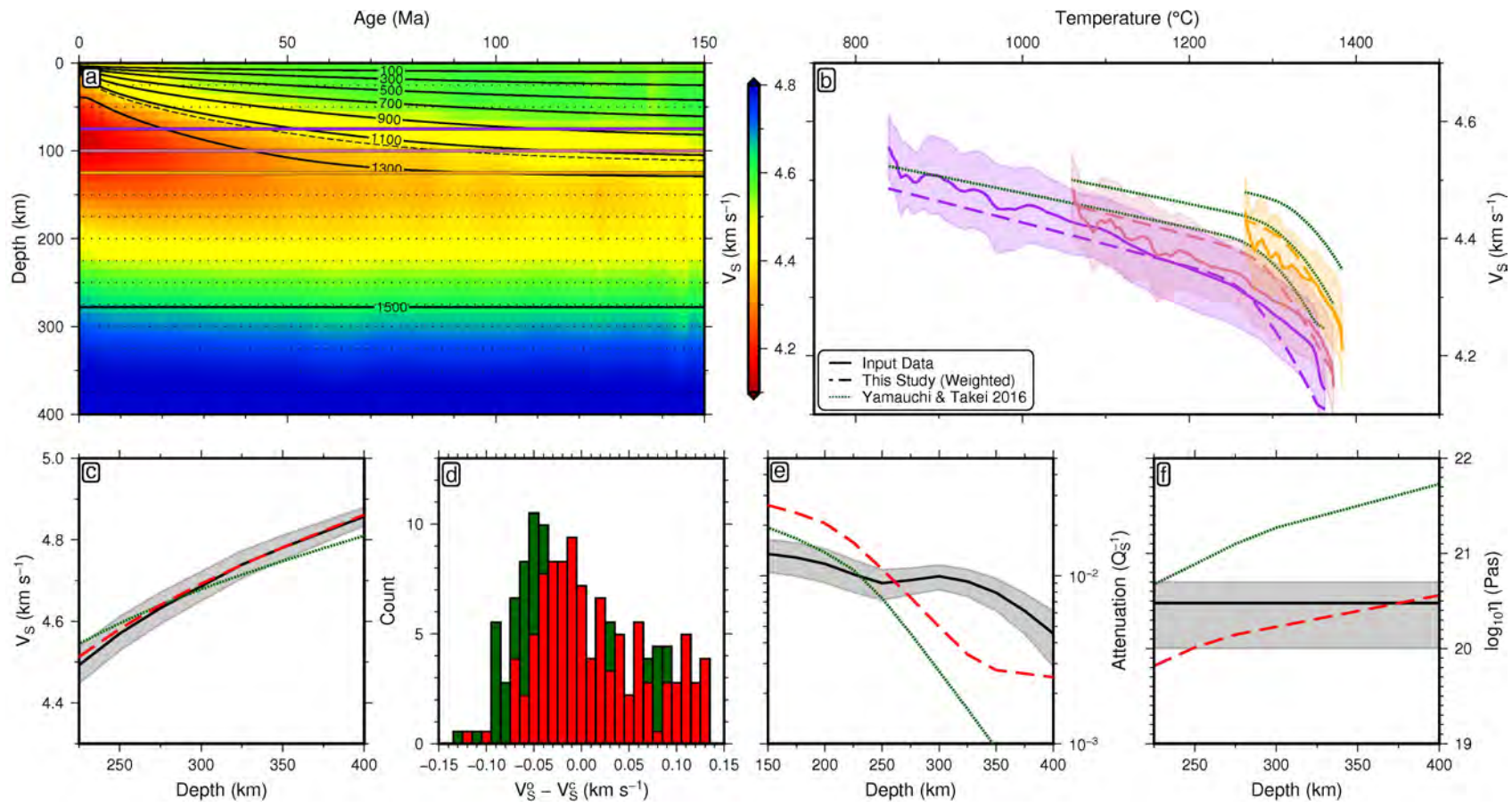
Figure 5.4: Anelasticity model calibration. (a) Oceanic V_S (SL2013sv). Solid black lines = isotherms from optimal plate model (Chapter 2). Purple line = 75 km; red line = 100 km; yellow line = 125 km. (b) V_S and plate temperature. Solid lines = V_S from SL2013sv vs. T from optimal plate model; coloured dashed lines = relationships calculated from best-fitting parameters; green dotted lines = Yamauchi & Takei (2016) relationships (YT16). Purple = 75 km; red = 100 km; yellow = 125 km; error envelopes = $\pm 1\sigma$. (c) V_S and isentropic temperature. Solid line = average oceanic V_S (SL2013sv) and T from 1333°C depth-dependent pyrolitic isentrope; grey envelopes = $\pm 1\sigma$; red dashed line = best-fit relationship; green dotted line = YT16. (d) V_S of xenoliths. Red bars = difference between observed V_S at xenolith origin and best-fit parameter calculations; green bars = YT16. (e) Q_S^{-1} beneath > 100 Ma plate. Solid line = average Q_S^{-1} from QRFS12; red dashed line = best-fit relationship; green dotted line = YT16. (f) Upper mantle viscosity. Solid line = upper mantle average (Lau *et al.*, 2016); upper/lower bounds = Zhao *et al.* (2012)/Lambeck *et al.* (2014); red dashed line = best-fit relationship; green dotted line = YT16.

Overall, there is some agreement between results obtained using different seismic tomographic models. However, the pressure- and temperature-dependence of the shear modulus varies significantly (Table 5.2). Inspection of the V_S-T relationships for these models suggests that choice of reference model, regularisation and constituent datasets in each tomographic inversion causes this variation. The substantially different absolute V_S structure obtained for each model underlines the need for independent calibration of anelasticity model parameters in order to develop conversions between shear wave velocity, temperature and density that are consistent with observational constraints.

5.3.4   Testing Temperature Predictions

After calibration of individual parameter sets, V_S estimated from tomographic models can be converted to temperature perturbations (Figure 5.5a). Predicted asthenospheric temperatures averaged between 75 and 250 km have a global range of $\sim 250^{\circ}$C, in agreement with the estimate of Dalton $et\ al.$ (2014). In Iceland, recent crystallisation temperature estimates from olivine-spinel aluminium exchange thermometry have been combined with melt chemistry and crustal thickness data to suggest that the plume is 162^{+41}_{-31} $^{\circ}$C hotter than the isentropic background temperature (Matthews $et\ al.$, 2016). V_S-derived temperatures show good agreement with these figures, predicting an average thermal anomaly of $156 \pm 19^{\circ}$C between depths of 100 and 200 km. The maximum depth-averaged value of 181°C is centred below Akureyri (Figure 5.5b).

Crustal thicknesses at mid-ocean ridges can be compared with melt production predicted by the parameterisation of Shorttle $et\ al.$ (2014) to estimate mantle potential temperatures at the time of crystallisation (Figure 5.5a). Reasonable correlation ($r = 0.53$) exists between inverted and V_S-derived potential temperatures, with the latter tending to slightly exceed the former (Figure 5.5c). The reduced correlation between these values may partly reflect temperature changes beneath the ridge since the crust was formed. Small-scale variation in the efficiency of melt extraction may also lead to local differences in crustal thickness. Nevertheless, broad agreement between these two independent measures of sub-ridge temperature state lend confidence to the V_S-T conversion.

Another means of testing the accuracy of temperatures predicted from V_S is to compare them directly to geochemical proxies. Sodium is incompatible during melting, occurring in high concentrations in low melt fraction igneous rocks and much lower concentrations as melt fraction rises. Na_8, is defined as the concentration of Na_2O per 8 wt.% MgO and acts as a proxy for melt fraction. Gale $et\ al.$ (2014) found strong positive correlations ($r = 0.77$) between axial ridge depth
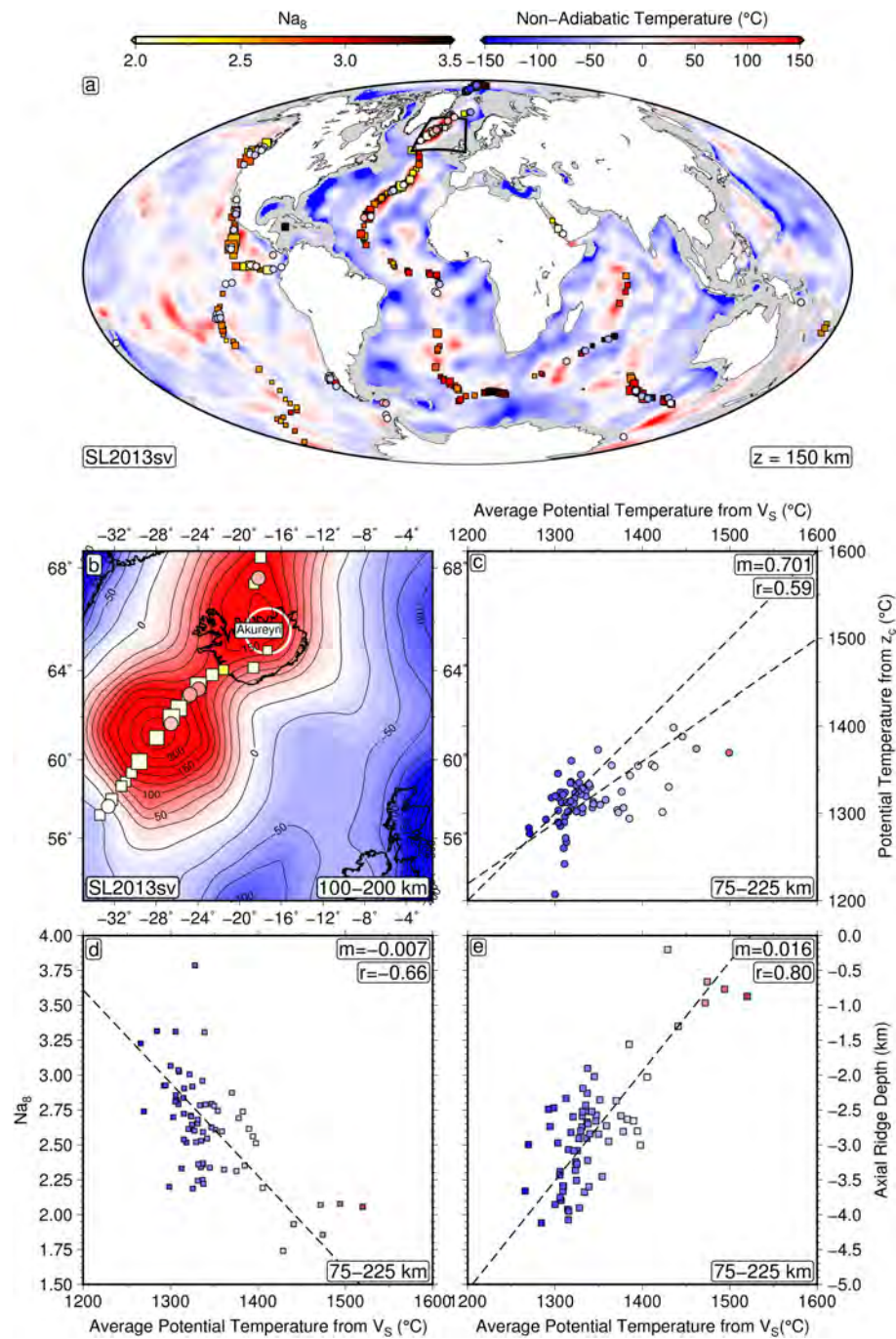
Figure 5.5: Testing V_S-T conversions. (a) Predicted temperature vs. geochemical constraints (150 km). Filled circles = z_c-derived potential temperature deviations (Hoggard *et al.*, 2017); filled squares = mean Na_8 values per ridge segment (Gale *et al.*, 2014). Size of square scales with number of samples (n). Black square = boundary of Figure 5.5b. (b) Predicted temperature deviations around Iceland (100–200 km). White circle = area within 100 km radius of sample locations of Matthews *et al.* (2016). (c) Predicted potential temperature (75–225 km average) vs. potential temperature from crustal thicknesses (z_c). Circles = z_c-derived potential temperature (Hoggard *et al.*, 2017); black dotted line = 1:1 relationship; black dashed line = best-fitting linear relationship; m = gradient; r = correlation coefficient. (d) Predicted potential temperature (75–225 km average) vs. Na_8. Squares = Average Na_8 per ridge segment where $n > 30$ (Gale *et al.*, 2014). (e) Predicted potential temperature (75–225 km average) vs. axial ridge depth. Squares = Axial ridge depth per ridge segment where $n > 30$ (Gale *et al.*, 2014).

and Na_8, suggesting that elevated temperatures, melt fractions and bathymetry are correlated, and that asthenospheric temperature is a major control on residual depth along the global ridge system. Along mid-ocean ridge axes, a strong negative correlation ($r \sim 0.7$) exists between predicted asthenospheric temperature and basalt Na_8 (Figure 5.5d). Moreover, correlation between V_S-derived potential temperature and axial ridge depth is remarkably strong ($r = 0.8$), further supporting a direct link between asthenospheric temperature and dynamic topography at the ridge axis (Figure 5.5e). The close agreement between these independent observations strongly suggests that temperature, not composition, is the major control on sub-plate density anomalies and the associated topographic response.

The correlation between V_S and geochemically-derived temperature estimates, melting conditions and anomalous ridge elevations suggest that it may be possible to estimate palaeo-dynamic topography using temperatures determined from basaltic petrology (Shorttle & Maclennan, 2011; Van Avendonk *et al.*, 2017). However, output temperature distributions are negatively skewed, with mean values 5–10% lower than the median throughout the upper mantle. This result contrasts with the roughly symmetrical distribution of temperature anomalies that would be expected in a vigorously convecting mantle (Jarvis & Peltier, 1986). This negative skew appears to be spurious and results from the approximately normal distribution of V_S anomalies at each depth, a feature that is an inevitable result of the damping that must be applied to stabilise seismic tomographic inversions (Schuberth & Bunge, 2009). The non-linear mapping of V_S into temperature therefore creates a long negative anomaly tail on the temperature distribution at each depth. Moreover, the non-linear mapping means that small errors in V_S translate into disproportionately large errors in temperature when $T < 900°C$, further skewing the temperature distribution (see Priestley & McKenzie, 2013).

5.4   The Relationship Between Asthenospheric Temperature and Residual Depth

Here, the extent to which improved constraints on shallow mantle density structure can reconcile predictions and observations of short wavelength dynamic topography is investigated. The normal stress applied to the base of the lithosphere by convective processes is a combination of both buoyancy forces resulting from density anomalies and dynamic stresses resulting directly from mantle flow (Molnar *et al.*, 2015). Since flow in the Earth's mantle is buoyancy-driven, disentangling these static and dynamic contributions is not straightforward (Richter, 1978).

There is evidence from post-seismic rebound, glacial isostatic adjustment, seismic anisotropy, rapid changes in plate motion and convection simulations that the asthenosphere is characterised by low viscosities ($\sim 10^{19}$–10^{20} Pa s) and, away from sinking slabs and upwelling plumes, predominantly tangential flow (Phipps Morgan *et al.*, 1995; Iaffaldano & Lambeck, 2014; van der Wal *et al.*, 2015; Lin *et al.*, 2016; Dannberg *et al.*, 2017). Under these conditions the direction of maximum dynamic pressure is approximately parallel to the base of the lithosphere. Buoyancy forces thus form the dominant contribution to the radial component of normal stress. In addition, the dynamic topography kernel (K_l^S) approaches unity in the upper 250 km of the mantle. For simplicity, it is therefore reasonable to assume that shallow density anomalies are compensated at the base of the asthenosphere (i.e. that $K_l^S = 1$ in this layer). Residual depth (δz_w) can therefore be estimated using

$$\delta z_w = \frac{-\rho_r \alpha}{\rho_b - \rho_w} \int_0^{z_l + h} \Delta T(t, z)\, \mathrm{d}z, \qquad (5.13)$$

where z_l is lithospheric thickness, h is asthenospheric layer thickness, ρ_b is mantle density at the base of the asthenospheric layer, ρ_w is water density, ρ_r is a reference density and α is thermal expansivity. $\Delta T(t, z)$ is the difference between the V_S-derived temperature, calculated at a given location and depth, relative to the average geotherm calculated for oceanic lithosphere of the same age. These average age-dependent geotherms are calculated individually for each seismic tomographic model using globally-averaged $V_S(t, z)$ profiles (Figure 5.4a). Note that although the assumption that $K_l^S = 1$ is reasonable in the upper $\sim$ 250 km of the mantle, K_l^S decreases with depth and does so most sharply for high spherical harmonic degrees ($l \geqslant 8$). The isostatic approximation may therefore overestimate the influence of short wavelength density anomalies in the deep upper mantle (250–400 km). However, these contributions are likely to be small given the minor V_S variation for $l \geqslant 8$ at depths greater than 250 km. Furthermore, the strong correlation between average asthenospheric temperature and axial ridge depth suggests that assuming $K_l^S = 1$ in the upper mantle is a reasonable first order approximation (Figure 5.5e). A further simplification is that compositional density heterogeneity in the oceanic lithosphere and asthenosphere is assumed to be negligible. Given its inferred low viscosity, the oceanic asthenosphere is likely well mixed, while recent studies suggest that temperature is the dominant control on geophysical and geochemical observables in this layer. Both observations justify the assumption of negligible compositional heterogeneity (Dalton *et al.*, 2014).
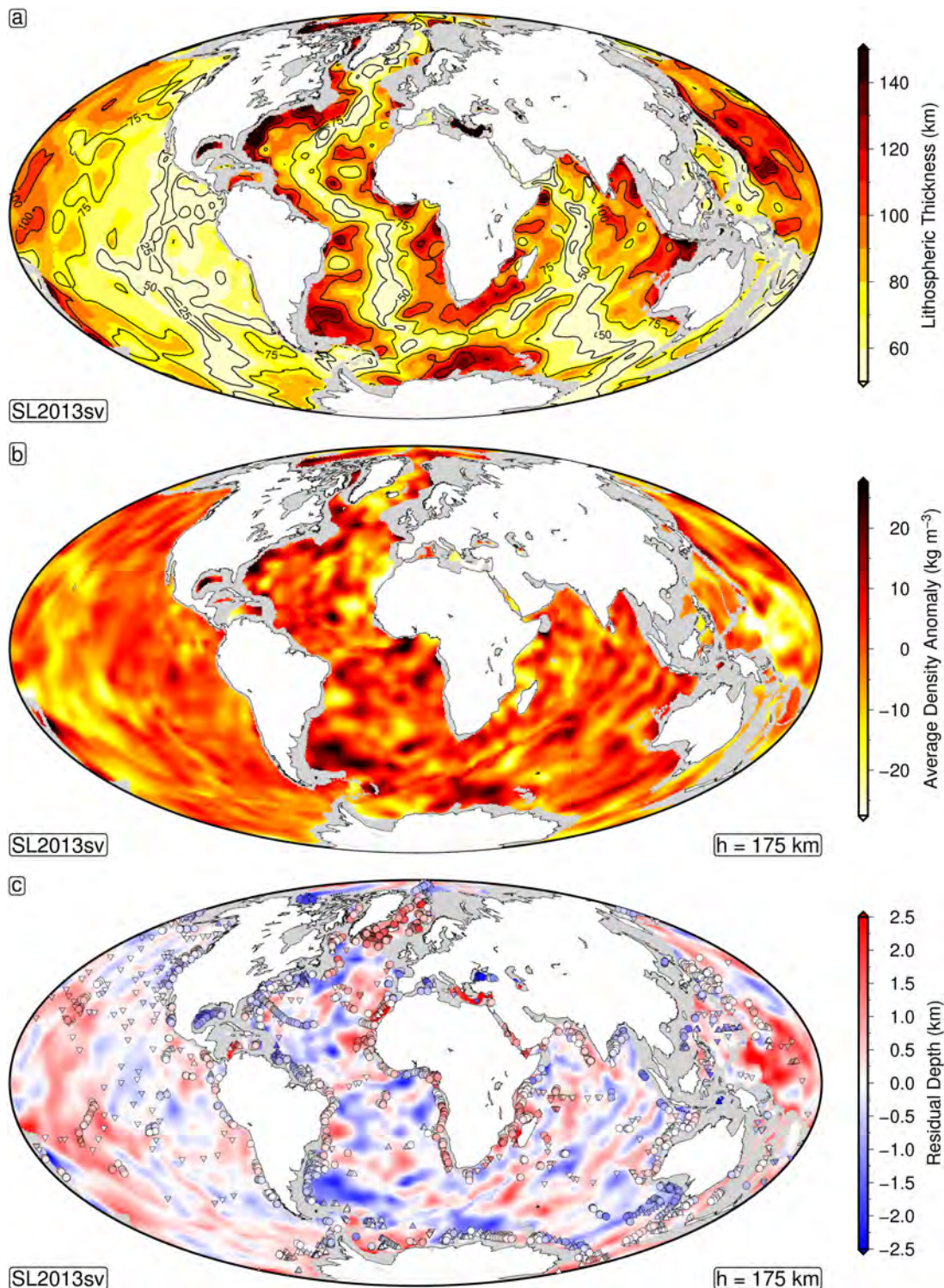
Figure 5.6: Lithospheric thickness and residual depth predictions from temperature and density inverted from SL2013sv. (a) Predicted lithospheric thickness based on depth to $1150°C$ isotherm. (b) Predicted density anomaly, relative to oceanic background, stacked between 50 and 250 km depth ($h = 175$ km). (c) Predicted vs. observed residual depths for stacked density anomalies compensated at 250 km depth ($h = 175$ km). Filled circles = oceanic residual depth measurements isostatically corrected for both sedimentary and crustal thickness variations; filled up/down triangles = upper/lower bound oceanic residual depth measurements isostatically corrected for sedimentary thickness variations only.

5.4.1   Global Correlations

Sub-oceanic density anomalies, when stacked over the depth of the lithosphere and asthenosphere (75–225 km) have peak-to-peak variation of ~ 60 kg m^{-3} (Figure 5.6b). These density anomalies, assuming isostatic compensation at the base of the asthenosphere, lead to residual depth variations of ± 2.5 km, which are consistent with the amplitudes measured in the observational database (Figure 5.6c). Predicted values are in reasonable agreement with observations, yielding a median root mean square (RMS) misfit of < 200 m and correlation of ~ 0.45 (Figure 5.7). Note that this value is equivalent to the best correlations obtained by Steinberger (2007) and Guerri *et al.* (2016) using full mantle simulations and density models that try to account for phase transitions.
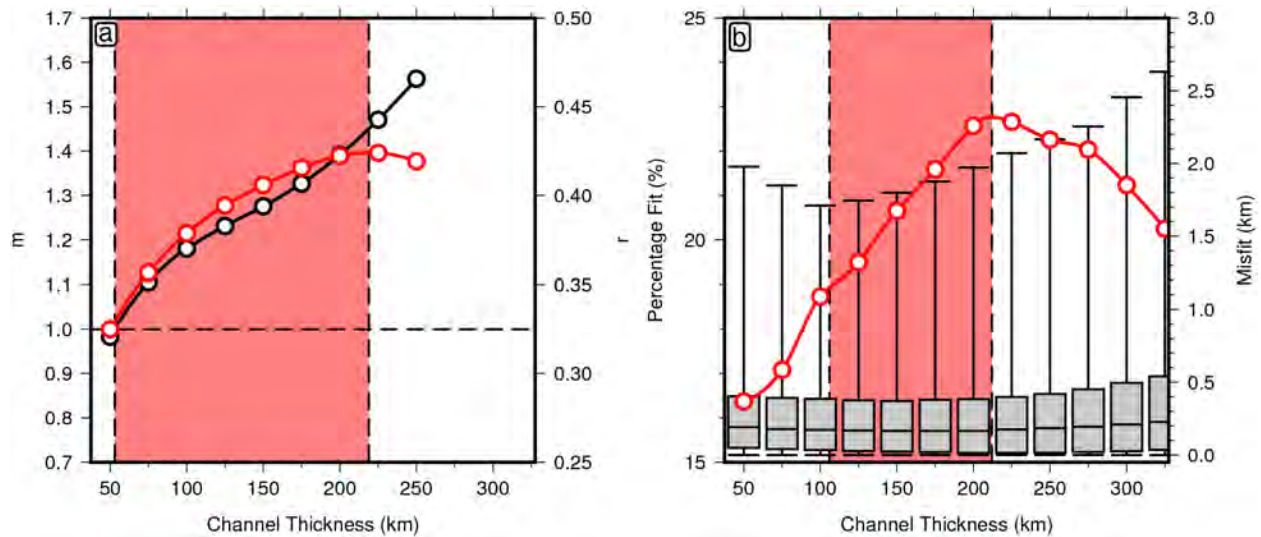
Figure 5.7: Correlation and misfit between predicted and observed residual depth anomalies as a function of channel thickness. (a) Correlation coefficient, r, and gradient, m, of best-fitting linear relationship between predicted and observed residual depth as function of channel thickness. Solid black line = gradient of best-fitting relationship between predicted and observed residual depths; solid red line = Pearson's product moment correlation coefficient of relationship between predicted and observed residual depths; horizontal black dashed line = 1:1 relationship, i.e. $m = 1$; vertical black line at ~ 50 km = value of h for which $m = 1$; vertical black line at ~ 225 km = value of h at which r is at global maximum; red box = envelope enclosing values of h for which $m = 1$ and r is at global maximum. (b) Misfit between predicted and observed residual depths as a function of channel thickness. Grey boxes and bars = median, interquartile range and full range of misfit between predicted and observed residual depths; solid red line = percentage of residual depth points for which observations and predictions fit within error; vertical black line at ~ 100 km = value of h for which variance reduction is maximised; vertical black line at ~ 200 km = value of h at which percentage of residual depth fits is at global maximum; red box = envelope enclosing values of h for which variance reduction and percentage of residual depth fits are at global maxima.

Best-fitting values for the thickness of the asthenospheric layer vary according to the measure of fit

used (Figure 5.7). If the maximum variance reduction is chosen as the measure of fit, an average global channel thickness of ~ 100 km is obtained. When the percentage of predictions that fit within error is selected as the measure of fit, a ~ 200 km channel thicknesses is preferred. Meanwhile, if maximum correlation is the best-fit measure a ~ 225 km channel thickness gives the best results. Finally, $h \sim 50$ km is the optimal result if the value giving a best-fit relationship closest to 1:1 is used. The range of best-fit h obtained using different measures ($h \sim 150 \pm 50$ km) may reflect the fact that the viscosity jump defining the base of the asthenosphere is likely to be variable in both depth and magnitude. p, the probability that observations and predictions of residual topography are not correlated, is $< 10^{-5}$, indicating that the global correlation is statistically significant. However, there are certain regions that correlate poorly. For example, although the predictions fit the residual depths in the vicinity of Iceland well, observations suggest that anomalously high residual depths extend to the Northeast Canadian margin and Norway, whereas cold temperatures and high densities are predicted from seismic tomography. This discrepancy highlights two aspects of global seismic tomographic models that complicate interpretations. First, due to computational expense, the amount of higher mode information that can be included in seismic waveform fitting is necessarily limited. The ability of models to clearly resolve anomalies such as the thin, low-velocity channel extending far from the Iceland plume conduit in full-waveform studies is thus reduced (cf. Rickers *et al.*, 2013). Secondly, in areas of the model with poorer resolution, imaged anomalies may be smeared along the ray path (Ekström *et al.*, 1997). This feature of models is particularly problematic in regions close to the ocean-continent boundary, where fast shear wave velocities from cold continental roots can bleed out into oceanic regions and result in predictions of implausibly cold mantle temperature and depressed residual depth. Predicted and observed residual depths may therefore diverge significantly in regions such as the Norwegian Sea, not because of inconsistency between measured residual depths and the true thermal state of the underlying mantle, but because of uneven tomographic model resolution. In spite of these difficulties, the correlation between predicted and observed residual depths suggests that temperature anomalies in the upper 250 km of the mantle play a significant role in maintaining observed residual topography.

5.4.2   Regional Correlations

The spatial coverage of the residual depth dataset of Hoggard *et al.* (2017) is uneven. However, relatively continuous measurements exist along certain passive margins such as Australia, West Africa and South America (Figure 5.8a & b). Comparison of observations and predictions of residual depth

in these regions is therefore a useful assessment of the ability of the thermal isostatic method to accurately determine shorter wavelength trends in the measurements. Lithosphere and asthenosphere are deconvolved in this analysis to investigate whether lithospheric isostasy plays a significant role in generating residual depth anomalies. Lithosphere-asthenosphere boundary depth is defined using the $1150°C$ isotherm as this surface coincides with the base of the lithosphere inferred from seismic anisotropy observations (Figures 2.11b & 5.6a; Burgos et $al.$, 2014). Overall, correlation between residual depths and topography predicted from lithospheric contributions are $\sim 50\%$ poorer than for asthenospheric equivalents. Interpreting the significance of this result is complicated both by the limited vertical resolution (~ 25 km) of tomographic models and uncertainty on the temperature conditions that define the lithosphere-asthenosphere boundary. Nevertheless, the large difference in correlation does suggest that residual depth variations are controlled more strongly by upper mantle convection than by deviations in lithospheric thickness from expected plate cooling trends. This may not be the case in continental regions where greater compositional heterogeneity and lithospheric thickness may allow a larger proportion of topography to be supported by lithospheric isostasy.

Australian Passive Margin

Good spatial correlation between residual depth observations and residual V_S anomalies is observed along the Australian margin (Figure 5.8a). Further, cold temperatures and negative dynamic topography predicted west of the Australian-Antarctic discordance are corroborated by anomalously depressed axial ridge depths (~ 4 km) and elevated Na_8 values (Figure 5.8a; Gale et $al.$, 2014). Decomposition of the transect into lithospheric and asthenospheric contributions reveals a particularly strong correlation between asthenospheric density anomalies and observed residual depths. 90% of residual depth measurements, corrected for both crustal and sediment thickness variations, fit within error (Figure 5.8c & e). Large misfit between observations and predictions occurs around the central west coast where fast shear wave velocities in the upper 100 km extend out from the cratonic interior into the oceanic realm. These anomalously fast wave speeds may be an artefact of model regularisation or higher error in the V_S-T conversion at the lower end of the temperature range (Section 5.3). Importantly, this method of predicting residual depths produces much better results than using a single value of admittance to scale long wavelength gravity anomalies (Figure 5.8e).
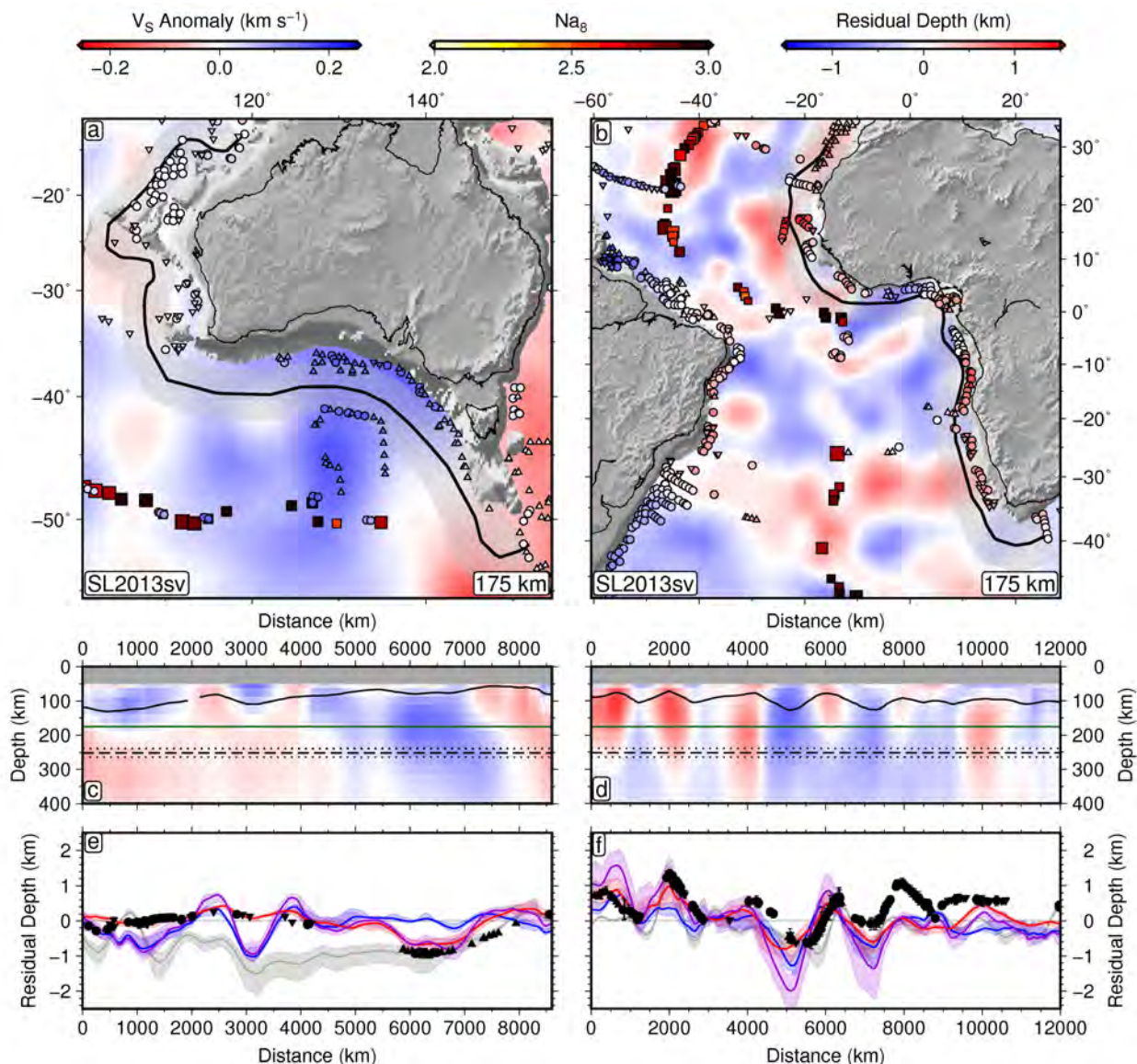
Figure 5.8: Transects of predicted and observed residual depths. (a) Residual depth and 'residual' V_S around Australia. Background = 'residual' V_S anomaly at 175 km (SL2013sv); black line = transect; translucent grey envelope = region within which mean and 1σ for predicted residual depth is calculated perpendicular to transect; filled circles = residual depths isostatically corrected for both sediment and crustal thickness variations; filled up/down triangles = upper/lower bounds on oceanic residual depth measurements isostatically corrected for sediment thickness variations only. (b) Residual depth and 'residual' V_S around West Africa. (c) Cross-section through SL2013sv 'residual' V_S model along Australian transect. Solid black line = lithosphere-asthenosphere boundary (1150°C isotherm); dashed black line = inferred base of asthenosphere ($h = 175$ km); dotted black lines = uncertainty on base of asthenosphere (reflects maximum vertical resolution of 25 km). (d) Cross-section through SL2013sv 'residual' V_S model along West African transect. (e) Predicted and observed residual depths along Australian transect. Blue line = predicted lithospheric contribution; red line = predicted asthenospheric contribution; purple line = predicted combined (lithospheric and asthenospheric) contribution; error envelopes = 1σ along 500 km cross-lines perpendicular to transect (grey region in panel a); grey line = long wavelength gravity anomaly (730 km $\leqslant \lambda \leqslant 9{,}000$ km) scaled using admittance of 35 mGal km^{-1}; error envelopes = 25–45 mGal km^{-1}. (f) Predicted and observed residual depths along West African transect.

West African Passive Margin

Spatial correlation between observations and predictions of residual depth is excellent along the northern West African margin but progressively worsens towards the southern tip of the continent (Figure 5.8b). Asthenospheric contributions account for most of the observed variation along the West African margin, fitting 95% of residual depth measurements within error. Although fits deteriorate significantly between North Angola and South Africa, the short wavelength pattern of highs and lows are fairly coherent across datasets despite some amplitude mismatch (Figure 5.8d & f). The ~ 500 km long wavelength offset between the two datasets might be explained by the presence of a large positive buoyancy anomaly in the deep mantle (Colli *et al.*, 2016). While there is still debate over the sign of the density contrast between large low shear wave velocity provinces (LLSVPs) and ambient lower mantle material, the prevailing view is that the African LLSVP constitutes a net low-density anomaly of approximate wavelength 10,000 km and may be able to account for this discrepancy (Schuberth *et al.*, 2012; Davies *et al.*, 2012; Garnero *et al.*, 2016; Koelemeijer *et al.*, 2017). Onshore, recent joint inversions of geochemical and geophysical datasets suggest that the whole southern African region is elevated by ~ 650 m (air-loaded) due to dynamic support, in accordance with the offset observed here (Jones *et al.*, 2017).

Some of the increased misfit along the central section of the profile seems to result from small phase shifts in the sinusoidal variations of each dataset. These horizontal offsets are likely to result from inaccuracies in the location of shear wave speed anomalies. Such inaccuracies are common in parts of tomographic models with low crossing ray densities, as is the case for the central section of the West African margin (Schaeffer & Lebedev, 2013; Rawlinson *et al.*, 2014). Much of the residual depth anomaly variation along the West African coast occurs at ~ 1150 km wavelengths, meaning that small phase shifts (< 400 km) can create ~ 1 km of RMS misfit between predictions and observations. In any case, phase offsets are generally smaller than the minimum half-wavelength of shear wave velocity variation resolved by the seismic inversions (300–600 km; Priestley & McKenzie, 2013).

5.5   Asthenospheric Viscosity

Calibrated anelasticity parameterisations obtained for each seismic tomographic model can also be used to make predictions of viscosity structure beneath the plate. Although no direct constraints exist to test the viscosity predictions, olivine *c*-axes preferentially align with the prevailing
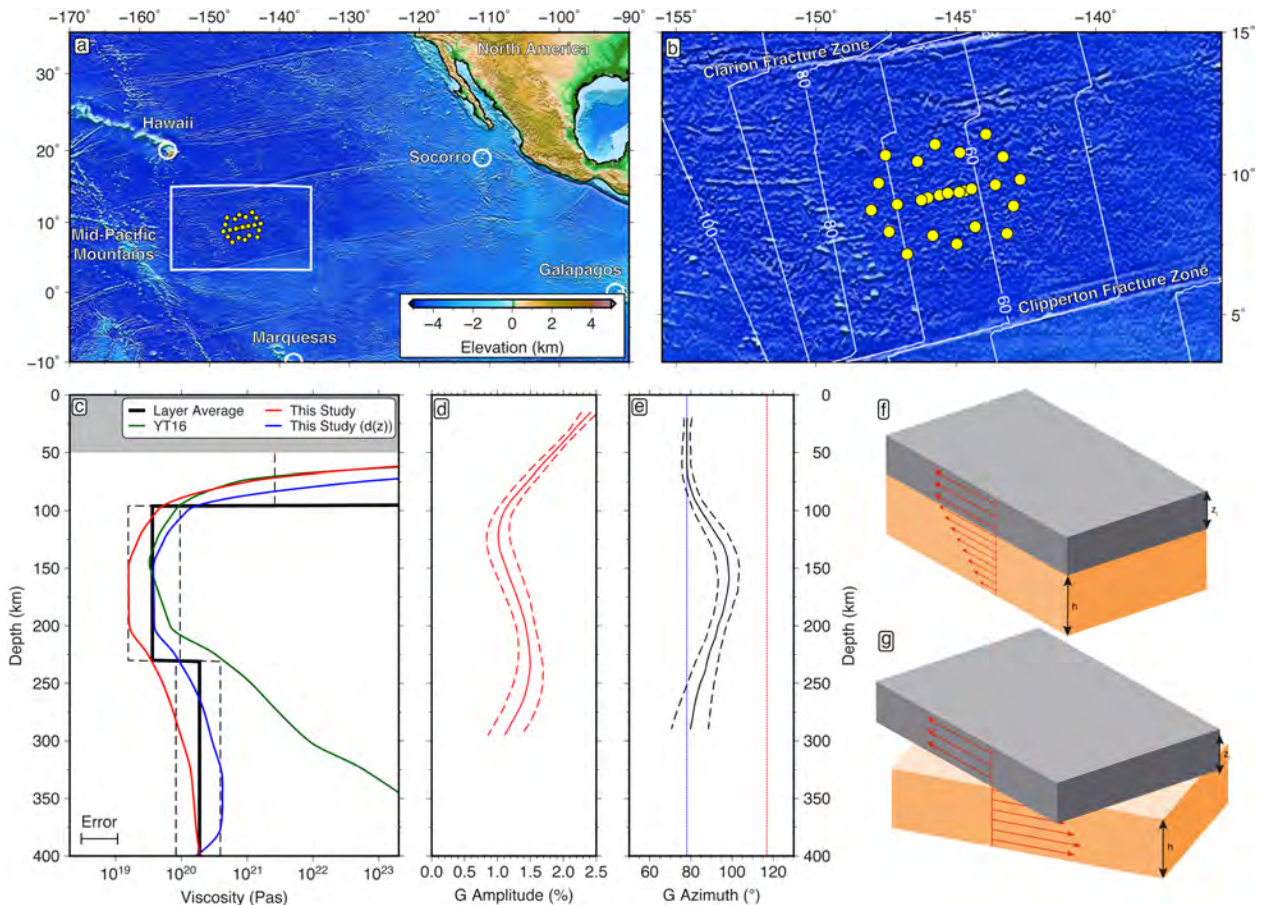
Figure 5.9: Viscosity vs. depth compared with seismic anisotropy. (a) Location map of NoMelt region. White circles = oceanic hotspots (Courtillot *et al.*, 2003); yellow circles = broadband ocean-bottom seismometer deployment sites; white box = region covered by panel (b) (b) Inset map of NoMelt region. White contours = age of oceanic lithosphere from revised age grid (see Section 2.1.1); yellow circles = broadband ocean-bottom seismometer deployment site. (c) Mean viscosity vs. depth within 500 km radius of NoMelt region ($\sim 9.5°$N/$\sim 145.5°$W). Red solid line = predicted viscosity using parameters inverted for SL2013sv using weighted misfit (H_w); blue line = predicted viscosity using parameters inverted for SL2013sv using weighted misfit (H_w) and depth-dependent grain size variation; green line = predicted viscosity using parameters of Yamauchi & Takei (2016); black solid/dashed lines = layer average and range of SL2013sv predictions from inverted parameters. Error bar refers to range of viscosity values within 500 km radius of NoMelt region. (d) Seismic anisotropy amplitude vs. depth from Lin *et al.* (2016). Red solid/dashed lines = mean/$\pm 1\sigma$ of average seismic anisotropic strength (G amplitude) profile within NoMelt region. (e) Azimuth of seismic anisotropy vs. depth from Lin *et al.* (2016). Black solid/dashed lines = mean/$\pm 1\sigma$ of average seismic anisotropic azimuth (G azimuth) profile within NoMelt region. (f) Expected velocity profile for Couette flow in asthenosphere. z_l = lithospheric thickness; h = asthenospheric channel thickness; arrows show velocities of plate and mantle material. (g) Expected velocity profile for Poiseuille flow in asthenosphere.

direction of flow in the asthenosphere (Zhang & Karato, 1995). This lattice-preferred orientation (LPO) causes horizontally-polarised shear waves to travel faster through the asthenosphere than vertically-polarised shear waves ($V_{SH} > V_{SV}$) (Dziewonski & Anderson, 1981). Thus, the locations

of significant viscosity gradients can be inferred from the magnitude and orientation of seismic anisotropy.

The NoMelt seismic experiment was conducted in a Mid-Pacific location remote from hotspot volcanism, in order to investigate the seismic character and fabric of 'normal' oceanic upper mantle (Figure 5.9a & b; Lin *et al.*, 2016). The characteristic pattern of flow beneath oceanic lithosphere determined from NoMelt seismic anisotropy data can therefore be used to test viscosity predictions in the same region. Viscosity profiles predicted using SL2013sv identify high-viscosity lithosphere down to ~ 75 km overlying an 150 km thick low-viscosity ($\sim 10^{19}$) asthenospheric channel. Viscosity increases by almost an order of magnitude between 225 and 275 km, indicating that the low-viscosity channel has a relatively sharp base (Figure 5.9c). This result holds whether or not grain size variation with depth is taken into account (Table 5.2; Dannberg *et al.*, 2017). Viscosity predictions using the parameters calibrated by Yamauchi & Takei (2016) give comparable asthenospheric viscosities but predict implausibly large viscosities beneath 250 km depth (cf. Lau *et al.*, 2016). Other V_S models give similar results but yield slightly different viscosity gradients below 225 km. The inferred base of the asthenosphere coincides with a sub-lithospheric peak in seismic anisotropy (Figure 5.9d; Lin *et al.*, 2016). Significantly, the fast direction within this layer is oblique to both fossil spreading direction and present-day plate motion (Figure 5.9e). The rotational alignment of olivine *c*-axes required to form these anisotropic fabrics is maximised where shear strain gradients are highest (Hansen *et al.*, 2016). Taken together, these observations indicate that the deep peak in anisotropy represents the boundary between fast-flowing, low-viscosity asthenospheric material and more sluggish, higher viscosity underlying mantle.

Traditionally the flow regime in the upper mantle has been assumed to be Couette-type, i.e. driven predominantly by plate motion-induced shear with the more viscous lower mantle acting as a stationary bottom boundary (Turcotte & Schubert, 2002). In this regime, flow velocity and shear strain gradients decrease linearly from the lithosphere-asthenosphere boundary down to the base of the asthenosphere (Figure 5.9f). Azimuthal anisotropy would therefore be expected to align with plate motion and decrease in amplitude with depth (Becker, 2008). By contrast, in a Poiseuille-type flow regime, horizontal pressure gradients in the asthenosphere lead to a parabolic velocity profile with peak velocities at mid-asthenospheric depths and slow velocities near the base of the lithosphere and asthenosphere (Figure 5.9g; Morgan & Smith, 1992). In this case, flow is in the direction of maximum horizontal pressure gradient and the highest shear strain gradients occur at the upper and lower boundaries of the asthenosphere. Thus, the dominance of Poiseuille flow

over Couette flow in the asthenosphere could explain both the obliquity of the fast direction and the presence of the deep anisotropy peak in the NoMelt region (Figure 5.9d & e; e.g. Natarov & Conrad, 2012).

Evidence for a low viscosity asthenosphere helps explain the success of the isostatic approximation employed here, as this region becomes effectively decoupled from underlying flow, with the result that the dynamic topography kernel approaches unity for $l \geqslant 8$. However, while a relatively low-viscosity asthenosphere is required by attenuation and shear wave velocity profiles, the calibrated anelasticity relationships employed here implicitly assume that high temperatures and/or grain size variations are responsible. Water content and strain rate variation may further reduce asthenospheric viscosities, and these estimates may therefore constitute a lower bound (Karato & Jung, 1998; Behn *et al.*, 2009; Dannberg *et al.*, 2017).

5.6   Correlation as a Function of Spherical Harmonic Degree

Although the isostatic approximation used to determine upper mantle contributions to dynamic topography is valid for $l \geqslant 8$, correlation and misfit between predicted and observed dynamic topography are expected to deteriorate for longer wavelength signals. To assess correlation as a function of wavelength, spherical harmonic functions up to degree 30 are fit to both the best-fitting predictive geodynamic model (Steinberger, 2007) and the calculated dynamic topography of the five seismic tomography models investigated here. The geodynamic predictions perform more poorly than all other models at short wavelengths ($l \geqslant 8$; Figure 5.10a). Although the predictive model is better correlated with observations at long wavelengths $l < 8$ ($r = 0.29$ vs. $r = 0.0$), peak-to-peak predicted dynamic topography is $> 200\%$ that of observed values. By contrast, isostatic predictions yield good correlations for $l = 8\text{--}30$ (Figure 5.10b-f). However, as expected, correlations approach zero at longer wavelengths. All isostatic models moderately overpredict short wavelength dynamic topography. This overprediction occurs because the isostatic approach implicitly assumes that the normalised dynamic topography kernel, K_l^S, is unity within the asthenospheric channel and zero below for all spherical harmonic degrees. In reality, sensitivity will decrease with depth for density anomalies of any wavelength, reducing most sharply for higher spherical harmonic degrees. An important corollary is that, although the isostatic approximation is valid for short wavelength density anomalies, long wavelength dynamic topography may be underestimated if large-scale ($\lambda \geqslant 5,000$ km) deep mantle buoyancy anomalies exist. Nevertheless,

the isostatic models consistently outperform the geodynamic predictions at short wavelengths. Moreover, isostatic predictions using SL2013sv match residual depth observations better than the best-fitting predictive model at all wavelengths ($1 \leqslant l \leqslant 30$) in terms of both maximum predicted amplitude and correlation ($r = 0.45$ vs. 0.36). These results suggest that better constraint on asthenospheric density anomalies is essential to improve predictive models of dynamic topography.
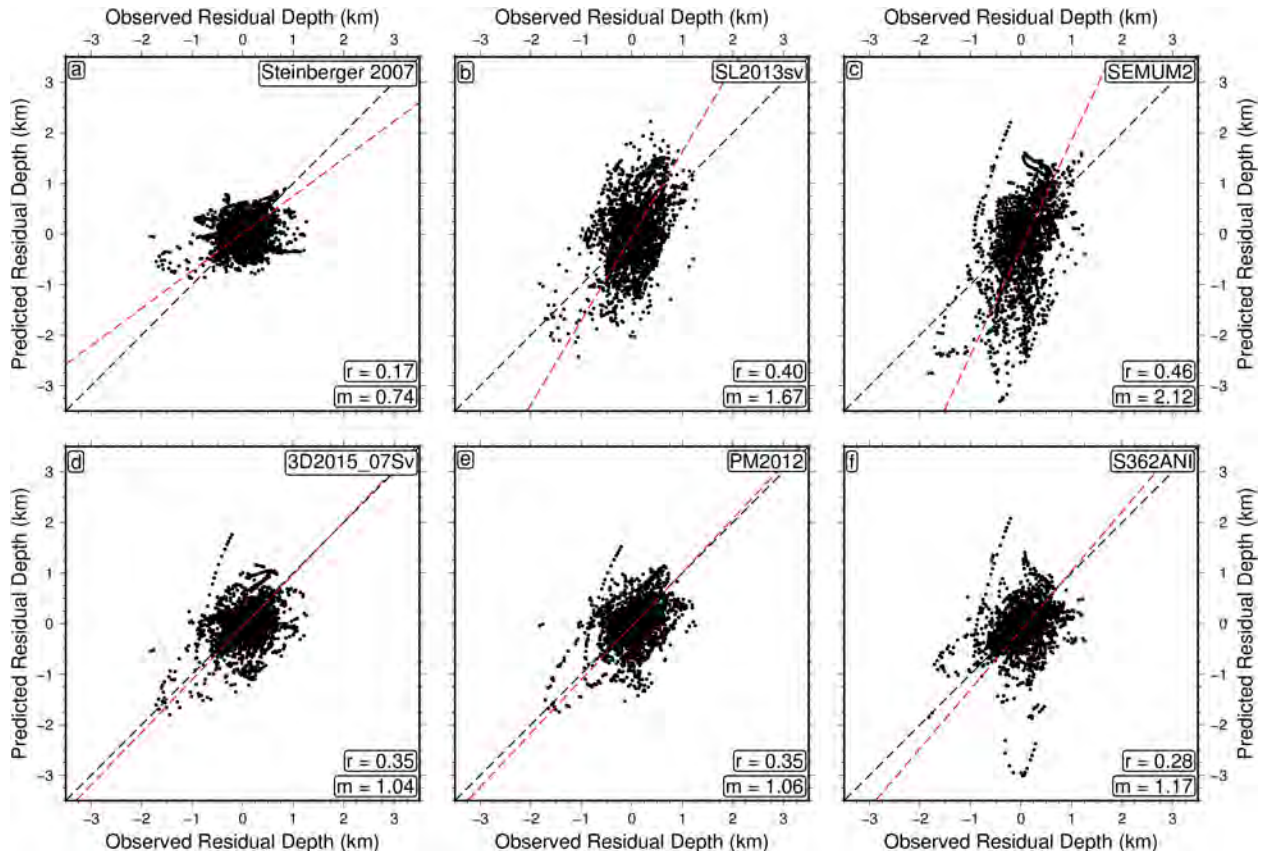
Figure 5.10: Correlation between predicted and observed residual depth as a function of spherical harmonic degree. (a) Observed residual depths vs . whole-mantle predictive model of Steinberger (2007) for $8 \leqslant l \leqslant 30$. Black line = 1:1 linear relationship; red line = best-fitting linear relationship; r = Pearson's correlation coefficient; m = gradient. (b) Observed residual depths vs. isostatic predictions from SL2013sv for $8 \leqslant l \leqslant 30$ (Schaeffer & Lebedev, 2013). (c) Observed residual depths vs. isostatic predictions from SEMUM2 for $8 \leqslant l \leqslant 30$ (French *et al.*, 2013). (d) Observed residual depths vs. isostatic predictions from 3D2015_07Sv for $8 \leqslant l \leqslant 30$ (Debayle *et al.*, 2016). (e) Observed residual depths vs. isostatic predictions from PM2012 for $8 \leqslant l \leqslant 30$ (Priestley *et al.*, 2012). (f) Observed residual depths vs. isostatic predictions from S362ANI for $8 \leqslant l \leqslant 30$ (Kustowski *et al.*, 2008).

For each seismic tomographic model, correlations between observations and predictions of residual depth are similar to those obtained between residual depth and residual V_S. This result suggests

that, irrespective of the accuracy of the V_S-T conversion, the predictive power of the methodology developed in this chapter will depend on the spatial distribution, wavelength and amplitude of V_S anomalies in a given tomographic model. SL2013sv gives the best results of the models tested here for $l = 1$–30, likely as a result of its combination of a large dataset ($\sim 750,000$ seismograms) with waveform fits up to the 9th overtone and direct inversion for crustal structure. However, comparison of SL2013sv with a regional full-waveform model in the North Atlantic suggests that the resolution of the best global models remains too low to consistently image thin ($\leqslant 50$ km) asthenospheric structures that may nevertheless have a large impact on residual depth predictions (Schoonman *et al.*, 2017). As computing power increases and further theoretical advances are made, full-waveform inversion of increasingly large seismic datasets will become possible, potentially leading to the development of global full-waveform models (Bozdağ *et al.*, 2016; Fichtner *et al.*, 2018). The better correlations achieved with models that fit larger proportions of the seismic waveform whilst maintaining high data coverage suggest that results obtained here will improve further as the resolution of seismic tomographic inversions increases.

5.7 Summary

Comparisons between observations and predictions of dynamic topography show that short wavelength contributions are consistently underestimated in predictive geodynamic models. This underestimation is a direct result of model set-up, wherein density anomaly contributions above ~ 300 km are removed and body wave-dominated models with poor upper mantle ray coverage provide input density structure. Removing the plate cooling signal from recent surface wave-based upper mantle tomographic models reveals an anti-correlation between oceanic residual depth anomalies and so-called 'residual' V_S anomalies. Correlation between the two datasets is maximum between 50 and 250 km depth, suggesting asthenospheric temperature anomalies are an important control on dynamic topography.

Temperature structure from the optimal plate model presented in Chapter 2 is exploited alongside constraints on the geotherm based on mantle xenoliths, isentropic temperature, attenuation and viscosity to derive a best-fit anelasticity model for converting upper mantle V_S to temperature, viscosity and attenuation. The resulting V_S-derived temperature estimates are used to assess the extent to which the oceanic dynamic topography signal can be explained by asthenospheric thermal anomalies alone, assuming that the associated buoyancy variations are compensated at the base

of the asthenosphere. These temperature estimates are corroborated by strong correlations with a number of independent constraints including Na_8, axial ridge depth and oceanic crustal thickness.

Resulting oceanic residual depth predictions, which assume isostatic compensation at the base of the asthenosphere, yield an average misfit of <200 m and correlations of $r \sim 0.45$ for asthenospheric channel thicknesses of $\sim 150 \pm 50$ km. This channel thickness is consistent with predicted viscosity profiles and independent seismic anisotropy observations, supporting the validity of the isostatic approximation. All isostatic models outperform previous geodynamic models for $l \geqslant 8$. This finding suggests that asthenospheric temperature anomalies play a significant role in maintaining convective surface deflections. Geochemically-derived basaltic melting temperatures may therefore provide a useful proxy for approximating past dynamic topography.

Chapter 6

Observed & Predicted Dynamic Topography

The observation that long wavelength geoid anomalies spatially anti-correlate with large low shear velocity provinces (LLSVPs) in the lower mantle forms the basis of our understanding of Earth's internal viscosity structure (Pekeris, 1935; Richards & Hager, 1984). By converting shear wave velocity anomalies into density anomalies and modelling the instantaneous flow that results from the inferred buoyancy variations, Hager *et al.* (1985) were able to make a prediction of the long wavelength geoid that closely matched satellite observations. In making this prediction, the deflection of the Earth's surface in response to normal stresses arising from viscous flow was calculated, providing the first estimate of global dynamic topography. Since this pioneering work, many studies have made predictions of dynamic topography using increasingly complex modelling approaches, updated density models and different assumptions about Earth's viscosity structure (Ricard *et al.*, 1993; Steinberger, 2007; Conrad & Husson, 2009; Spasojevic & Gurnis, 2012; Flament *et al.*, 2013). These models are constrained to fit the long wavelength geoid and, despite differences in their construction, recover dynamic topography predictions that are broadly consistent and are dominated by degree two structure (i.e., wavelengths of $\sim$ 20,000 km, Figure 6.1). However, as demonstrated in Chapter 3, spherical harmonic fits to observations consistently recover $\sim$ 75% less dynamic topography at these wavelengths.

This discrepancy between observations and predictions of dynamic topography has led to considerable debate within the geodynamic community (Yang & Gurnis, 2016; Coltice *et al.*, 2017). Yang *et al.* (2017) have contended that the disagreement is not as large in practice if the spherical harmonic inversion used to fit the observations applies damping parameters that scale with the maximum spherical harmonic degree used in the fitting process. Nevertheless, Yang *et al.* (2017) recover a peak-to-peak long wavelength ($1 \leqslant l \leqslant 3$) dynamic topographic amplitude of ± 900 m, double that of the observations. Moreover, the results of the spherical harmonic inversions presented in Chapter 3 and in Hoggard *et al.* (2016) are corroborated by independent studies. Lecroart *et al.* (1997) found similarly modest values of long wavelength dynamic topography (± 426 m) by
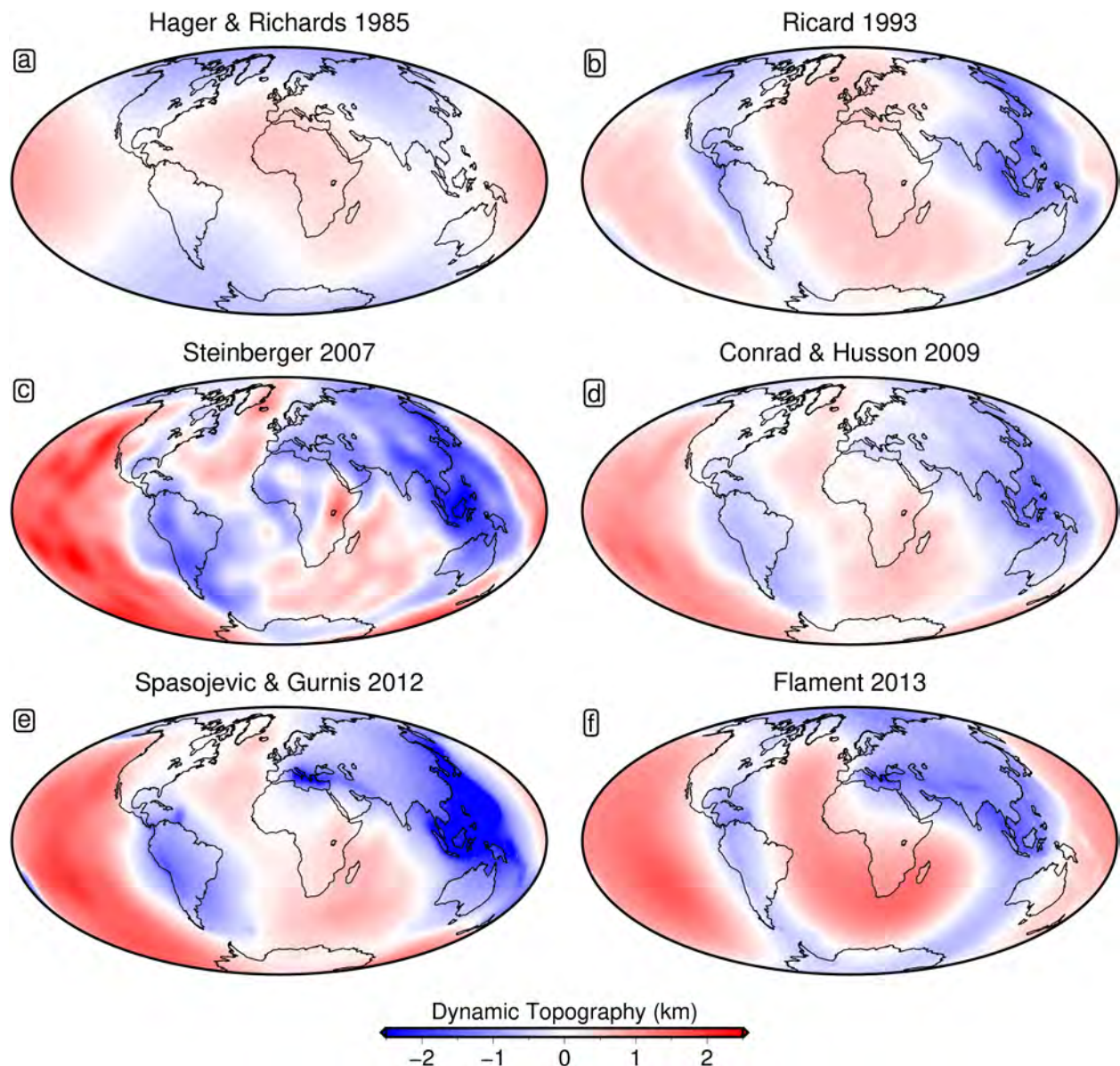
Figure 6.1: Predictive models of dynamic topography. (a) Hager *et al.* (1985) prediction ($l = 2$–3; density derived from seismic tomography). (b) Ricard *et al.* (1993) prediction (density derived from slab subduction histories). (c) Steinberger (2007) prediction (density derived from seismic tomography). (d) Conrad & Husson (2009) prediction (density from seismic tomography). (e) Spasojevic & Gurnis (2012) prediction (density from seismic tomography in the lower mantle, slab subduction histories in the upper mantle). (f) Flament *et al.* (2013) prediction (density from slab subduction histories).

analysing variations in crustal thickness and density along the global ridge system. More recently, Watkins & Conrad (2018) found no more than ± 500 m of long wavelength dynamic topography by investigating the asymmetry of seafloor subsidence across both the East Pacific Rise and the Mid Atlantic Ridge. The agreement of these different studies suggests that the $\sim 500 \pm 100$ m estimate of long wavelength dynamic topography is reasonable.

The cause of the discrepancy between observations and predictions of dynamic topography is unclear. Seismic tomographic models indicate that lower mantle density structure is dominantly degree two and will therefore account for most dynamic topographic signal at these longest wavelengths ($\sim 10,000$ km), despite reduced sensitivity below the 660 km discontinuity (Figure 6.2). Thus, the mismatch between observed and predicted long wavelength dynamic topography implies that our current understanding of deep Earth density and viscosity structure is incomplete (Steinberger *et al.*, 2017).

In this chapter, constraints on upper mantle temperature variation obtained in Chapter 5 are combined with deep mantle density structure with the aim of developing a geodynamic model that is consistent with observations of dynamic topography, whilst honouring constraints on the non-hydrostatic geoid and core-mantle boundary (CMB) topography. First, it is demonstrated that incorporation of significant anelastic behaviour throughout the mantle reduces amplitude misfit between predicted and observed dynamic topography and geoid anomalies. Secondly, inclusion of a dense basal layer within Earth's large low shear velocity provinces (LLSVPs) is shown to greatly reduce discrepancy between observed and predicted geoid and dynamic topography amplitudes at degree two. Finally, by inverting geoid, dynamic topography, free-air gravity anomaly and CMB excess ellipticity data, improved constraints are placed on the Earth's radial viscosity structure. The revised viscosity and density structure are consistent with previous estimates and predict dynamic topography, geoid and CMB topography fields that improve fit to available data. These results suggest that it is possible to reconcile observations and models of dynamic topography and the geoid with plausible input parameters.

6.1   Instantaneous Flow Kernels

To predict instantaneous mantle flow in response to internal buoyancy variations, I use the kernel formalism originally developed by Parsons & Daly (1983) but since updated to include spherical geometry, radially varying viscosity, self-gravitation and the effect of compressibility (Hager & O'Connell, 1979, 1981; Richards & Hager, 1984; Forte & Peltier, 1991; Corrieu *et al.*, 1995). The advantage of using this analytical method is that computation times are minimal compared to numerical mantle convection codes such as Citcom-S, StagYY, Terra or ASPECT, making the method more amenable to use in inversion schemes (Bunge *et al.*, 1996; Zhong *et al.*, 2000; Tackley, 2008; Heister *et al.*, 2017). Applying this method comes at the cost of being unable to include laterally

varying viscosity structure or to impose plate velocity-derived boundary conditions. However, the focus here is on the longest wavelength features of the Earth's geoid and dynamic topography, suggesting that these limitations are unlikely to affect the main conclusions (cf. Richards & Hager, 1989).

Using the kernel-based approach, given a particular radial viscosity structure, predicted geophysical fields can be calculated for a specified radial and lateral distribution of internal density anomalies expressed in spherical harmonics. The internal density anomalies are expressed as equivalent surface mass anomalies for mathematical simplicity. Provided that layer spacing is appropriately fine ($\leqslant 100$ km) this approximation is valid (cf. Hager & Richards, 1989b). The kernels are calculated using the propagator matrix technique to solve the system of ordinary differential equations governing compressible mantle flow in a self-gravitating Earth (Gantmacher, 1959; Gilbert & Backus, 1966; Hager & Clayton, 1989; Corrieu *et al.*, 1995). Free-slip boundary conditions are applied at both the surface and the CMB, such that the vertical velocity and the shear stresses are assumed to be equal to zero. The propagator matrix method assumes spherical boundaries between internal layers. The boundary conditions are therefore imposed by analytical continuation from the physically deformed exterior boundaries to the mathematically imposed spherical interfaces using a first-order Taylor expansion (e.g. Forte & Peltier, 1991). As a result, the boundary conditions on the mathematical interfaces are expressed as continuity of velocity and shear traction with a jump condition in radial normal stress, $\tau_{r'r'}$,

$$\tau_{r'r'}(b)]_{-}^{+} = \Delta\rho g(b)\delta b. \tag{6.1}$$

Here, b is the radius of a given internal boundary, e.g., the surface or CMB, $g(b)$ is the value of gravity at that radius, $\Delta\rho$ is the density contrast across the boundary and δb is the dynamic topography on the boundary. δb is equivalent to the difference between the physically deformed boundary and the mathematically imposed spherical surface. The spherical boundary approximation assumed by the propagator matrix technique is robust provided that δb is small compared to the depth of the convecting mantle, a condition that is satisfied at the Earth's surface and CMB.

Since viscosity is assumed to vary only with radius, kernels depend on spherical harmonic degree but not order (Richards & Hager, 1984). As a result, the spherical harmonic components of geophysical fields (F_{lm}), including non-hydrostatic geoid (N_{lm}), dynamic surface topography (S_{lm}), CMB topography (C_{lm}) and dynamic admittance (Z_{lm}), can be computed from the kernels in the
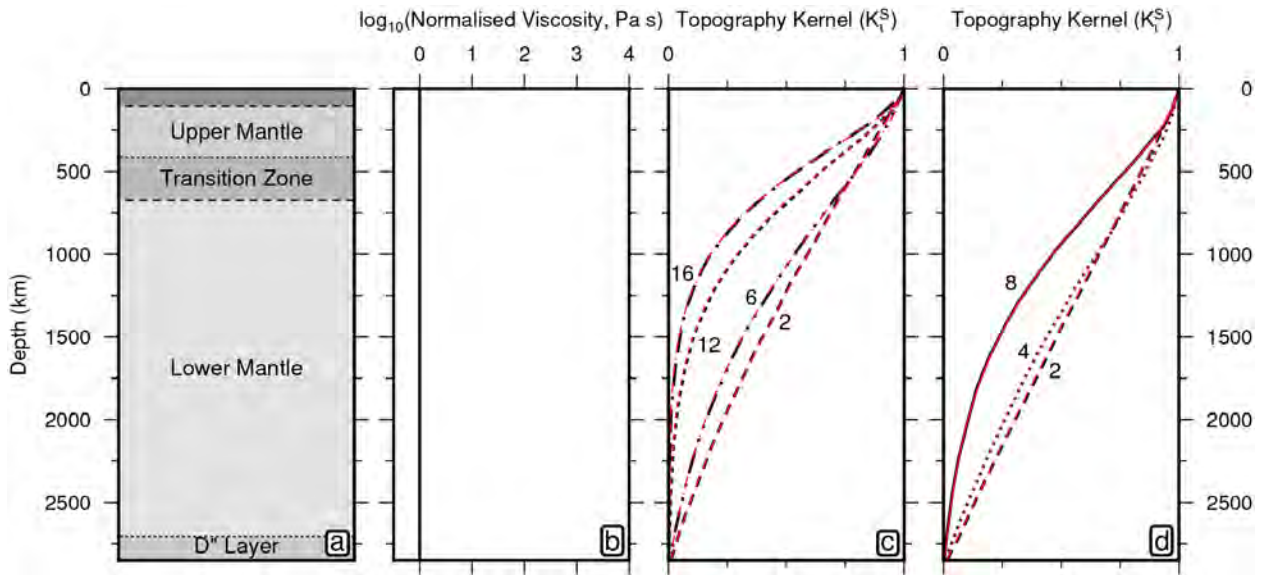
Figure 6.2: Benchmark of instantaneous flow kernel code. (a) Schematic mantle structure as a function of depth. (b) Viscosity structure as a function of depth (isoviscous). (c) Dynamic topography kernel predicted if self-gravitation is neglected, i.e. $g = 10 \text{ m s}^{-2}$ throughout the mantle. Black lines = degree 2, 6, 12 and 16 kernels obtained by Hüttig *et al.* (2013); red lines = calculated degree 2, 6, 12 and 16 kernels. (d) Dynamic topography kernel predicted if self-gravitation is included using a constant radial density profile throughout the mantle. Black lines = degree 2, 4 and 8 kernels obtained by Hager & Clayton (1989); red lines = calculated degree 2, 4 and 8 kernels.

spectral domain using the general formula

$$F_{lm} = \int_{R_C}^{R_\oplus} K_l^F(r')\delta\rho_{lm}(r')dr', \tag{6.2}$$

where $\delta\rho_{lm}(r')$ is the relevant spherical harmonic component of the density anomaly field as function of radius, r', $R_\oplus = 6371$ km, $R_C = 3486$ km and $K_l^F(r')$ is the relevant kernel function. The free-air gravity anomaly field, Δg_{lm}, is computed from geoid undulations, N_{lm}, using

$$\delta g_{lm} = \frac{\gamma_r}{R_\oplus}(l-1)N_{lm}, \tag{6.3}$$

where γ_r is the reference gravitational acceleration at the surface of the Earth. The dynamic topography kernel is expressed as K_l^S and CMB topography as K_l^C, while the dynamic admittance kernel, K_l^Z, is expressed as the ratio of the free-air gravity anomaly and dynamic topography, using

$$K_l^Z = \frac{K_l^{\Delta g}}{K_l^S}. \tag{6.4}$$
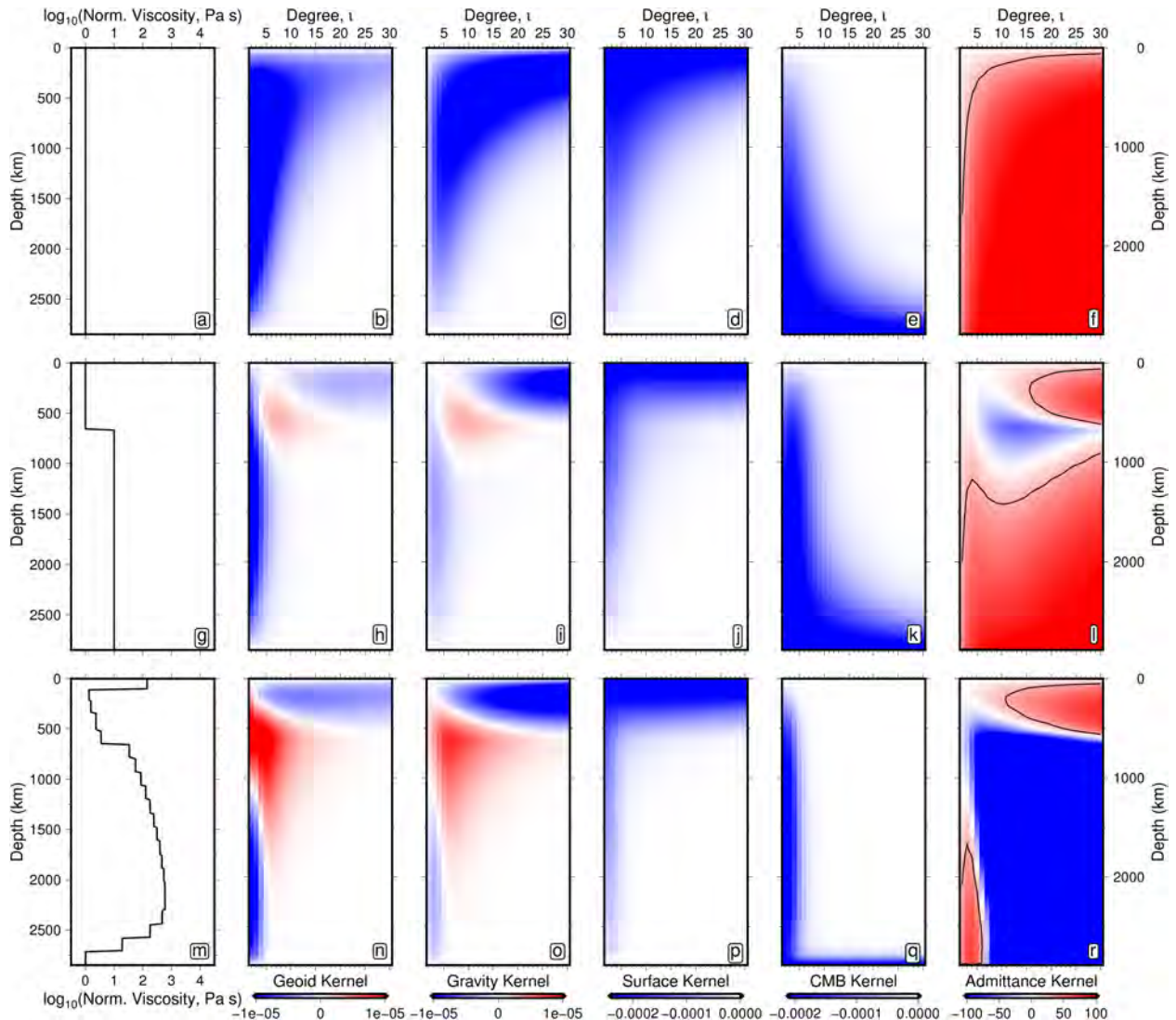
Figure 6.3: Instantaneous flow kernels as a function of viscosity, depth and spherical harmonic degree. (a) Isoviscous profile. (b) Geoid undulation kernel (m^3 kg^{-1}). (c) Free-air gravity anomaly kernel (mGal m^2 kg^{-1}). (d) Dynamic topography kernel (m^3 kg^{-1}). (e) CMB topography kernel (m^3 kg^{-1}). (f) Dynamic admittance kernel (mGal km^{-1}). Black contour = 30 mGal km^{-1}, the average value in the oceanic realm (Anderson *et al.*, 1973; Crosby *et al.*, 2006; Crosby & McKenzie, 2009). (g–l) Same as above for viscosity profile of (Hager *et al.*, 1985). (m–r) Same as above for viscosity profile of (Steinberger & Calderwood, 2006).

The code used here to calculate the instantaneous flow kernels has been benchmarked against previous studies to ensure that results are robust. These tests show that the code correctly accounts for self-gravitation and can accurately recreate previous results at all spherical harmonic degrees, providing important validation of the results obtained with this methodology (Figure 6.2). Although the exact form of the kernel will vary as a function of radial viscosity structure, there are

important commonalities that exist, provided that lower mantle viscosity is greater than or equal to upper mantle viscosity (Figure 6.3; Haskell, 1935; Mitrovica, 1996). First, as postulated by Pekeris (1935), long wavelength geoid and free-air gravity anomalies anti-correlate with density structure in the deep mantle. Second, both CMB and surface topography are insensitive to shorter wavelength density structure ($l \geqslant 8$) that is distant from the interface in question. As a result, short wavelength dynamic topography on these boundaries must originate in the two boundary layers of the terrestrial mantle.

6.2   Density Structure of Mantle

Two key unknowns are involved in making predictions of geophysical fields from instantaneous flow calculations: internal density structure and average radial viscosity structure of the Earth. Recent advances in theoretical seismology combined with increased computing power have improved resolution of Earth's internal velocity structure, particularly in the upper mantle (Kustowski *et al.*, 2008; Ritsema *et al.*, 2011; Priestley & McKenzie, 2013; Schaeffer & Lebedev, 2013; French & Romanowicz, 2015; Bozdağ *et al.*, 2016). Moreover, mineral physics databases have been expanded and computational thermodynamics packages have been developed that allow for elastic wave speeds to be related to changes in composition, temperature and density in a self-consistent manner (Powell *et al.*, 1998; Stixrude & Lithgow-Bertelloni, 2005, 2011; Connolly, 2009; de Capitani & Petrakakis, 2010; Cottaar *et al.*, 2014; Jennings & Holland, 2015; Chust *et al.*, 2017). Although, these computational packages are likely to be more accurate than applying single conversion values between V_S and ρ, caution is warranted as the mineral physics databases that underpin the technique remain incomplete, leading to density uncertainties of $\sim 3\%$ throughout the mantle (Steinberger & Calderwood, 2006; Connolly & Khan, 2016). Despite these caveats, taken together, recent seismological and mineral physics advances suggest that the density structure of the Earth may be constrained more accurately than was previously possible.

In the past, a number of different approaches have been taken to convert seismic velocity anomalies into density anomalies. The simplest involves multiplying the V_S anomaly by an empirically determined factor, R_ρ (~ 0.2), whereas more complicated approaches use a radially varying conversion factor that is based on mineral physics experiments (e.g. Becker & O'Connell, 2001; Steinberger, 2007). Conrad & Husson (2009) used a scaling of 0.15 Mg m^{-3} per km s^{-1} to convert velocity anomalies from S20RTS into density anomalies below 300 km, before running three-dimensional

convection simulations with the finite element code CitcomS using a viscosity structure that varied radially but not laterally (Zhong *et al.*, 2000; Karato & Karki, 2001; Ritsema *et al.*, 2004). By applying the same scaling, radial viscosity profile and removing density anomalies in the upper 300 km of the mantle, reasonably good fits to the Earth's geoid can be achieved using the kernel methodology (RMS misfit = 30 m and $r = 0.8$; Figure 6.4a & b). Moreover, the analytical approach faithfully recreates the spatial pattern and power spectrum of the dynamic topography obtained by Conrad & Husson (2009) using the more complex numerical model, providing an additional benchmark of the code implemented here (Figure 6.4c–f). These calculations demonstrate that imposing a 300 km cutoff depth can provide a good fit to the Earth's geoid and reasonable maximum amplitudes of dynamic topography ($\sim \pm 1.5$ km). However, the spectral discrepancy between observations and these predictions is significant (Figure 6.4f). Predicted long wavelength ($l = 1$–3) dynamic topography is three times larger than observations, while predicted short wavelength ($l > 3$) contributions are approximately six times smaller, on average.

A key aim of this study is to find a density and viscosity structure that allows observations of dynamic topography to be fitted at all wavelengths above 1,000 km ($l \leqslant 30$). The short wavelength discrepancy obtained previously results both from exclusion of uppermost mantle (< 300 km) density anomalies and the use of input seismic tomographic models with low resolution in the upper mantle (e.g. S20RTS; Figure 6.5a). As demonstrated in Chapter 5, better accounting for upper mantle density anomalies using surface wave tomographic models can significantly improve agreement between observed and predicted dynamic topography at wavelengths $< 5,000$ km. It is therefore desirable to include asthenospheric density structure from surface wave tomographic models in convection simulations. However, the velocity anomalies that are imaged by surface wave-dominated models are generally confined to the upper ~ 400 km of the mantle and additional inputs are required to model whole mantle convection. To address this issue, a hybrid shear wave velocity model of the mantle is developed, using the SL2013sv model of Schaeffer & Lebedev (2013) between 50 and 400 km in the upper mantle and the SEMUCB-WM1 model of French & Romanowicz (2015) beneath 400 km. This combination of models is chosen to maximise resolution of shorter wavelength velocity structure in the upper and mid-mantle. In the hybrid model, layer spacing is 25 km between 50 and 400 km and 50 km below 400 km, reflecting the different vertical resolutions of the constituent models. Although input models are normalised to different reference velocity profiles, potential discontinuities in output density structure between 400 and 450 km are avoided by defining anomalies relative to mean density in each layer. Further, the resultant model is linearly interpolated between input layers to smooth the transition between the two tomographic models
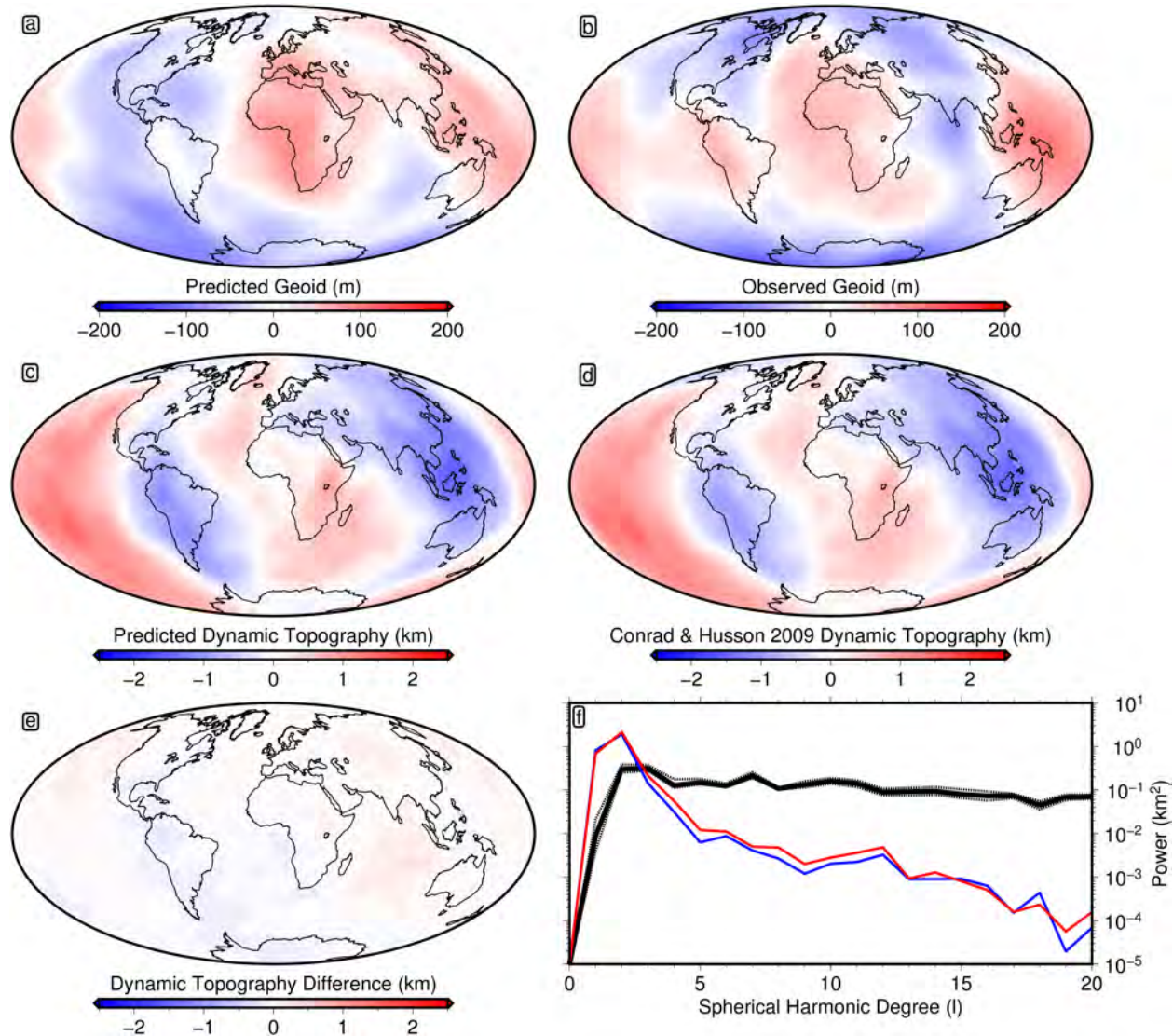
Figure 6.4: Geophysical fields predicted from constant scaling model with 300 km cutoff depth. (a) Predicted geoid. (b) Observed geoid (Chambat *et al.*, 2010). (c) Predicted dynamic topography using instantaneous flow kernels. (d) Predicted dynamic topography calculated by Conrad & Husson (2009) using three-dimensional finite element code CitcomS. (e) Difference between dynamic topography predicted using analytical and numerical approaches. RMS misfit $= \sim 75$m. (f) Power spectrum of dynamic topography. Solid black line = power spectrum of observational model; dashed black line = maximum and minimum limits of power recovered for damping parameters within the ranges $\lambda_1 = 10^2$–10^4 km^{-2} and $\lambda_2 = 10^{-0.5}$–$10^{0.5}$ km^{-2}; red line = power spectrum of dynamic topography calculated using instantaneous flow kernels; blue line = power spectrum of dynamic topography calculated by Conrad & Husson (2009).

(Figure 6.5b).

The definition of dynamic topography used here excludes topography generated by the background cooling and subsidence of oceanic lithosphere. As a result it is necessary to remove the plate cooling signal from density models when including upper mantle layers in convection simulations.
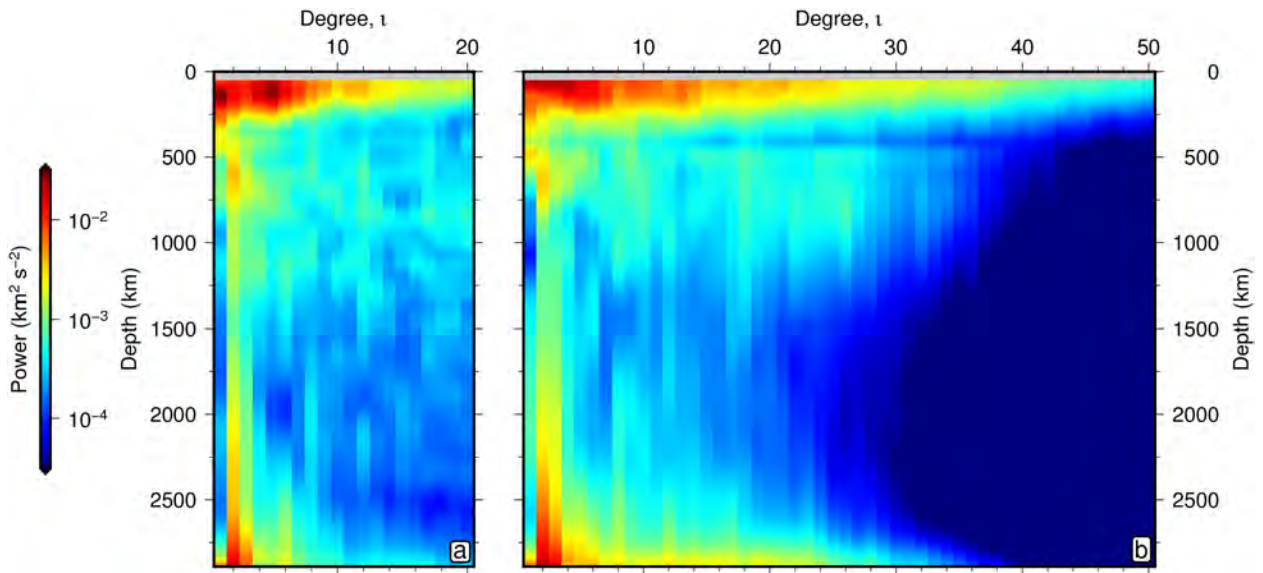
Figure 6.5: Shear wave velocity model power spectra. (a) V_S power spectrum of S20RTS as a function of depth. (b) V_S power spectrum of hybrid model as a function of depth. Above 400 km V_S is taken from SL2013sv and corrected for the effects of plate cooling (Schaeffer & Lebedev, 2013). Below 400 km V_S is taken from SEMUCB-WM1 (French & Romanowicz, 2015).

In addition, lithospheric and asthenospheric density anomalies must be distinguished and the former removed before calculating the instantaneous flow field. To remove the plate cooling signal in the oceans, the average age-dependent residual V_S anomaly structure of the upper mantle observed in SL2013sv, determined in Chapter 5, is subtracted from observed absolute shear wave velocities at a given location, depending on lithospheric age and the depth of the tomography slice in question (Müller *et al.*, 2016). To correct the velocity structure in continental areas, the reference residual V_S profile of the continents is set to the average for the oldest oceanic lithosphere ($\sim$ 170 Ma), following the approach of Steinberger (2016).

Lithospheric thickness is defined using the 1150°C isotherm for two reasons (Figure 5.6a). First, rock physics experiments suggest that, at geologically observed strain rates, the creep strength of dry, olivine-rich materials tends to zero at approximately this temperature (Ranalli & Murphy, 1987; Kohlstedt *et al.*, 1995). Secondly, the age-dependent deepening of the Pacific lithosphere-asthenosphere boundary closely follows this interface in the calibrated plate model developed in Chapter 2. However, in continental areas with thick crust, low shear wave velocities are observed down to $\sim$ 75 km depth (Schaeffer & Lebedev, 2013). In this case, the low shear wave velocity anomalies are caused by the smaller shear moduli of the minerals comprising continental crust and not by high temperatures in rocks with mantle compositions. Assuming pyrolitic composition when converting these shear wave velocities will therefore assign erroneously high temperatures to

these regions, resulting in spuriously thin lithosphere. To circumvent this problem, a minimum lithospheric thickness of 75 km is assigned to continental regions, consistent with the maximum observed thickness of continental crust (Laske *et al.*, 2013).

6.2.1 Simple Models

Having delineated and removed lithospheric contributions to shear wave velocity structure, the hybrid V_S model must be converted to a density model to calculate instantaneous mantle flow. In the first instance, a simple scaling value (0.15 Mg m^{-3} per km s^{-1}) is applied to convert V_S into temperature following Conrad & Husson (2009). This value is towards the lower end of conversion factors suggested by mineral physics experiments (Karato & Karki, 2001). At shallow depths, lithospheric regions are assigned the mean density of the surrounding mantle layers so that they do not contribute density anomalies or skew the average of the convecting regions in each depth slice. The final density model is then produced by interpolating density values to create 256 equally spaced layers from 0 to 2980 km depth before subtracting the average density from each layer to determine relative density anomalies. Each layer is then expanded into spherical harmonics up to degree and order 50. Predicted dynamic topography, geoid, free-air gravity anomaly and CMB topography fields are calculated using the viscosity profile of Steinberger & Calderwood (2006) (SC06) without imposing a cutoff depth (Figure 6.3m–r). SC06 is selected here as it is calibrated against a wide range of independent constraints including heat flow, glacial isostatic adjustment and geoid undulations. This viscosity profile is adopted in all subsequent calculations in this section to ensure that results are comparable.

Results

Simple models yield good fit to the geoid (RMS misfit = 26 m and r= 0.88); however, dynamic topography amplitudes are $\sim$ 50% higher than observed (Figure 6.6). Comparison of this result with those of previous predictions (Figures 6.1& 6.4) suggests that inclusion of asthenospheric anomalies constrained by surface wave tomographic models, significantly increases correlation with observed dynamic topography (+ $\sim$15%) and yields a power spectrum that is in better agreement with observations (Figure 6.6g). Nevertheless, overprediction of the long wavelength component of dynamic topography remains, suggesting that the lower mantle dynamic topography signal is overestimated using this scaling value. Further reduction of the scaling value uniformly decrease
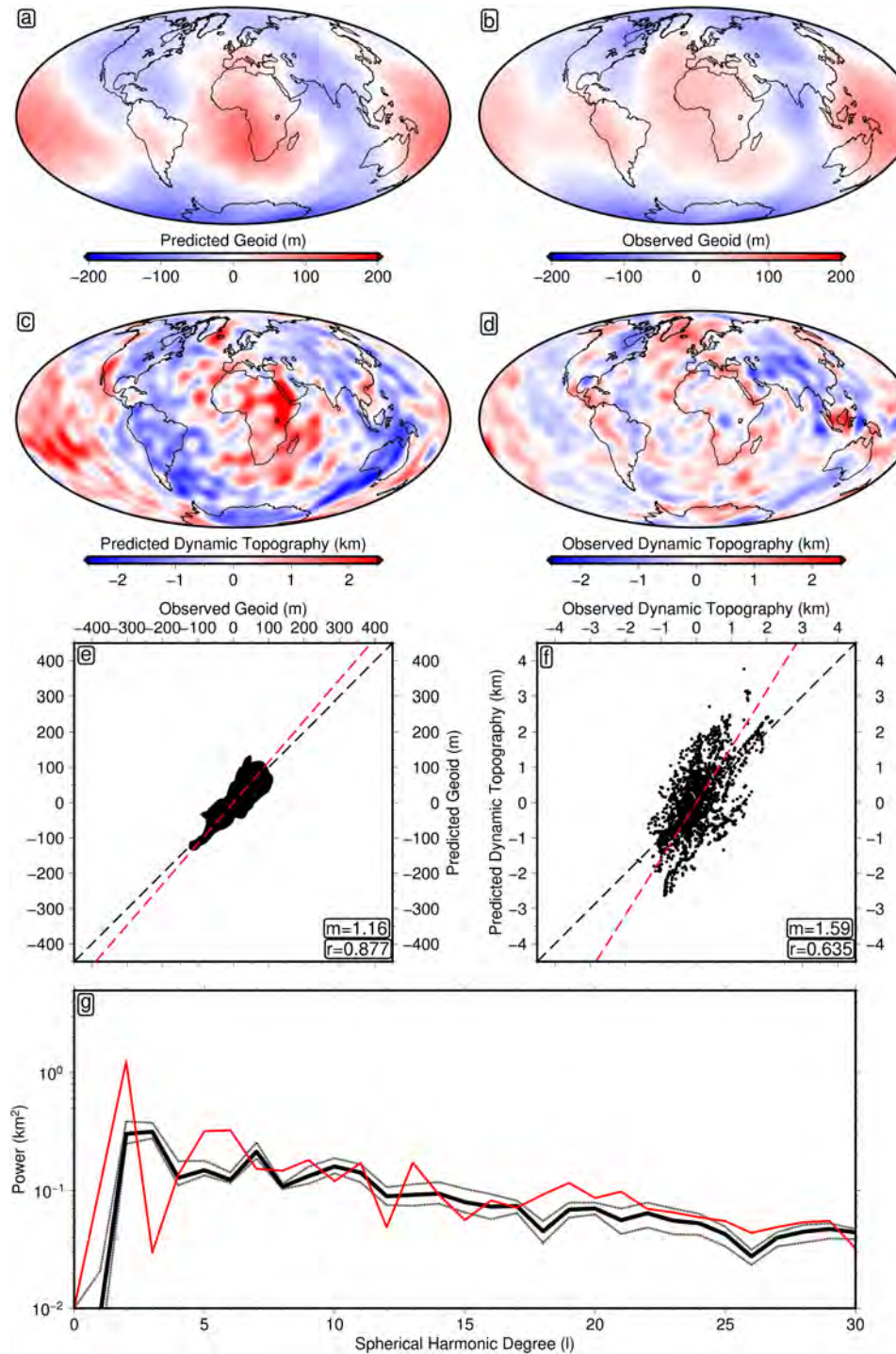
Figure 6.6: Geophysical fields predicted from density model generated using constant scaling factor. (a) Predicted geoid. (b) Observed geoid (Chambat *et al.*, 2010). (c) Predicted dynamic topography. (d) Observed dynamic topography. (e) Correlation between observed and predicted dynamic topography. (f) Correlation between observed and predicted geoid. (g) Power spectrum of dynamic topography. Solid black line = power spectrum of observational model; dashed black line = maximum and minimum limits of power recovered for damping parameters within the ranges $\lambda_1 = 10^2$–10^4 km^{-2} and $\lambda_2 = 10^{-0.5}$–$10^{0.5}$ km^{-2}; red line = power spectrum of predicted dynamic topography. Fields are calculated using the viscosity profile of Steinberger & Calderwood (2006). Densities are derived from hybrid V_S model (Figure 6.5b) using a scaling factor of 0.15 Mg m^{-3} per km s^{-1}.

amplitudes at all wavelengths and is therefore unable to resolve the relative overestimation of the degree two component of dynamic topography. Moreover, such a reduction comes at the expense of poorer fit to the geoid and is inconsistent with mineral physics constraints on the covariance of shear wave velocity and density in the mantle (cf. Karato & Karki, 2001). In summary, although the hybrid V_S model improves correlation with observed dynamic topography, especially at shorter wavelengths ($l < 8$), predicted geoid and long wavelength dynamic topography cannot be reconciled when a single conversion factor is used to estimate density.

6.2.2   Elastic Density Models

Although discrepancy between predicted and observed dynamic topography can be reduced using the simple scaling applied above, the inability of these models to reconcile long wavelength dynamic topography and the geoid suggests that a more complex density scaling may be required. Mineral physics experiments and seismological studies suggest that the relationship between V_S and density as a function of temperature is likely to be highly non-linear as large changes in the temperature and pressure dependence of physical properties occur across major phase transitions (Shearer & Flanagan, 1999; Stixrude & Lithgow-Bertelloni, 2012). With the development of software that can calculate stable phase assemblages throughout the whole mantle as a function of temperature, pressure and major oxide composition, it is now possible to directly convert V_S into temperature and density using experimentally calibrated elastic moduli and thermodynamic parameters (Connolly, 2005; Stixrude & Lithgow-Bertelloni, 2005, 2011; Chust *et al.*, 2017). This more comprehensive approach is tested to investigate the effect of exploiting a more thermodynamically self-consistent conversion between V_S and density.

First, stable phase assemblages are calculated using the software package MMA-EoS for a range of pressures (0–140 GPa) and temperatures (300–4500 K) to create a look-up table of density and V_S for a pyrolitic composition (Workman & Hart, 2005; Chust *et al.*, 2017). Post-perovskite is included as a possible stable phase in these calculations. Next, V_S derived from the hybrid tomographic model is converted to temperature and then density via the look-up file with linear interpolation used to estimate values that fall between temperature and pressure nodes. As physical properties can vary significantly across phase transitions, at a given depth in the mantle, more than one value of temperature may correspond to a single value of V_S or density. In these cases, for each depth slice, temperature and density at the longitude and latitude in question are estimated by taking the average values of the nearest geographical neighbours weighted by the spatial distance

between the points.

The shear wave velocities calculated by MMA-EoS are anharmonic V_S ($V_{S\ anh}$) and calculated directly from the pressure and temperature dependence of shear moduli. In this approach, V_S, is calculated as a function of phase composition (X), temperature (T) and pressure (P), using

$$V_S(X) = \sqrt{\frac{\mu_0(X) + \frac{\partial \mu(X)}{\partial T}T + \frac{\partial \mu(X)}{\partial P}P}{\rho_0(X) + \frac{\partial \rho(X)}{\partial T}T + \frac{\partial \rho(X)}{\partial P}P}}.$$ (6.5)

This equation holds under the assumption that anelastic effects are negligible at seismic frequencies, so that $V_S = V_{S\ anh}$. This assumption is likely to be a fair approximation across most of the mantle; however, significant seismic wave attenuation observed in the asthenosphere and the base of LLSVP regions suggests that it may break down in these regions (Karato & Karki, 2001; Romanowicz & Durek, 2013; Liu & Grand, 2018). By applying anharmonic V_S to density conversions in convection simulations, Nakagawa *et al.* (2009) suggested that seismological observations of the mantle could be better recreated if significant geochemical heterogeneity was present in the deep mantle. The effect of using anharmonic conversions to convert V_S to density is explored here using the methodology outlined above and assuming that the mantle is pyrolitic.

Results

Model predictions yield good spatial correlations with observed geoid ($r = 0.87$) and oceanic dynamic topography ($r = 0.65$) but predicted amplitudes are overestimated by up to 350% (Figure 6.7). As with previous predictions of dynamic topography, these models significantly overestimate degree two dynamic topography. Similarly, although inclusion of density anomalies in the uppermost mantle gives predictions that match the gradient of the observed power spectrum at shorter wavelengths, amplitude is overestimated by 150–175% (Figure 6.7g).

The strong spatial correlations between observations and predictions suggest that the distribution of density anomalies prescribed by the input density structure is relatively accurate. However, the amplitude offset suggests that density anomaly magnitudes are overpredicted. The greatest magnitude of V_S variation occurs in the asthenosphere, a region where the assumption of negligible anelasticity is weakest as temperatures are expected to be close to the solidus. Overestimation of short wavelength dynamic topography would therefore be expected to originate in this depth range. Indeed, the assumption of pure elasticity leads to the prediction of asthenospheric temperature
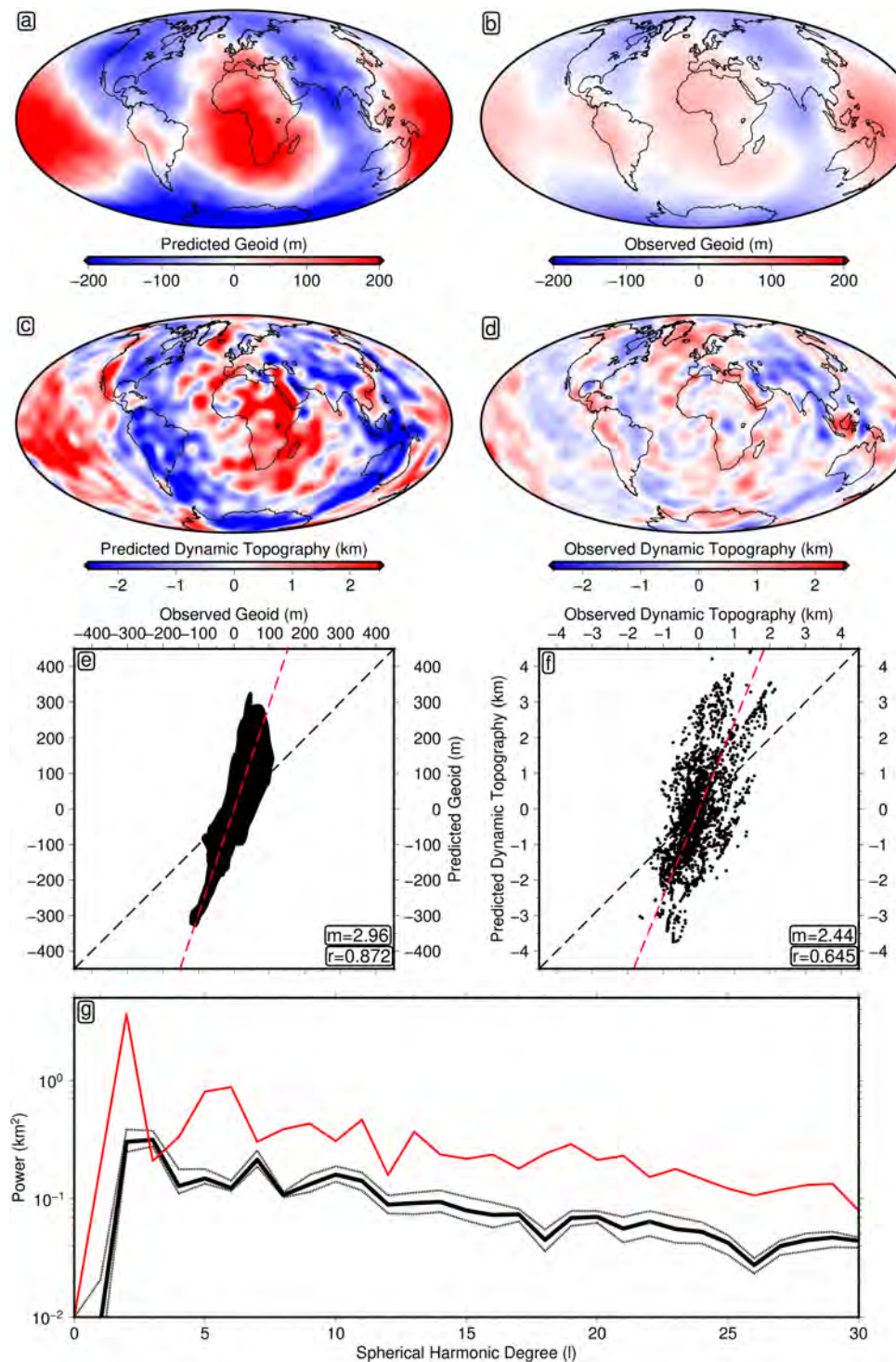
Figure 6.7: Geophysical fields predicted from elastic density model. (a) Predicted geoid. (b) Observed geoid (Chambat *et al.*, 2010). (c) Predicted dynamic topography. (d) Observed dynamic topography. (e) Correlation between observed and predicted dynamic topography. (f) Correlation between observed and predicted geoid. (g) Power spectrum of dynamic topography. Solid black line = power spectrum of observational model; dashed black line = maximum and minimum limits of power recovered for damping parameters within the ranges $\lambda_1 = 10^2$–10^4 km^{-2} and $\lambda_2 = 10^{-0.5}$–$10^{0.5}$ km^{-2}; red line = power spectrum of predicted dynamic topography. Fields are calculated using the viscosity profile of Steinberger & Calderwood (2006). Densities are derived from hybrid V_S model (Figure 6.5b) using anharmonic V_S calculated for pyrolite.

anomalies $\sim \pm 500^\circ$C, far outside the $\sim \pm 150^\circ$C range suggested by geochemical constraints (Dalton *et al.*, 2014).

Overestimation of upper mantle temperature anomalies occurs because the significant decrease in V_S at high temperatures caused by anelasticity, as shown in Chapter 5 and previous studies, is ignored in constructing the density model (Priestley & McKenzie, 2006, 2013; Yamauchi & Takei, 2016). As a result, the lowest V_S values in the seismic tomography models correspond to unreasonably high temperatures ($T_p \sim 1800^\circ$C). As anelastic effects, if present, only become important at high temperatures, density models that erroneously ignore them will be skewed towards lower densities and result in overestimation of positive dynamic topography.

Some overestimation of degree two dynamic topography may also result from anelastic effects but, given the generally lower attenuation measured seismologically in these regions, a more modest impact is to be expected (Liu & Grand, 2018). Further, lack of positive skew in the geoid anomaly, which is more sensitive to deep mantle structure, suggests that anelasticity is a less important consideration in the deep mantle.

Inclusion of a thermodynamically self-consistent V_S to density conversion slightly increases spatial correlation (+ $\sim$2%) between observed and predicted dynamic topography and the predicted power spectral gradient is nearly identical to observations (Figure 6.7). However, significant overestimation of upper mantle temperature anomalies, and therefore short wavelength dynamic topography, indicate that more accurate parameterisation of upper mantle anelasticity may improve results.

6.2.3   Anelastic Density Models

As shown in the previous chapter, there is strong evidence that significant portions of the Earth's mantle deform anelastically and that accounting for this anelasticity is required to accurately convert upper mantle V_S velocity variation to temperature and density anomalies.

To investigate the effect of including anelastic density models in instantaneous flow predictions the model construction process is adapted in two important ways. In the upper mantle, the calibrated anelasticity models developed in Chapter 5 are used to convert directly from V_S into density using predicted temperatures and the expression

$$\rho = \rho_0 \left[1 - \alpha(T - T_r) + \frac{P}{K} \right], \tag{6.6}$$
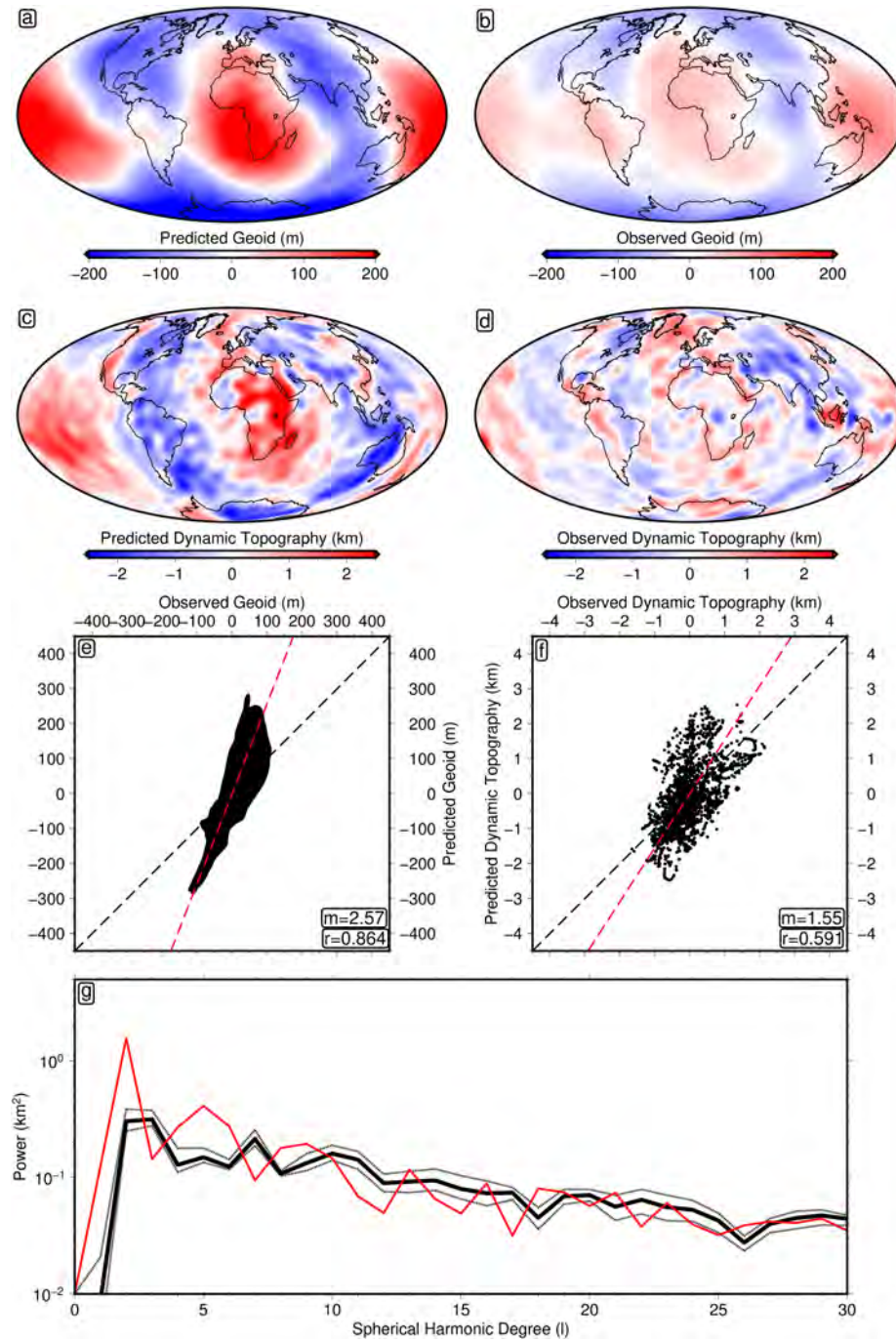
Figure 6.8: Geophysical fields predicted from density model incorporating anelastic-ity. (a) Predicted geoid. (b) Observed geoid (Chambat *et al.*, 2010). (c) Predicted dynamic topography. (d) Observed dynamic topography. (e) Correlation between observed and predicted dynamic topography. (f) Correlation between observed and predicted geoid. (g) Power spectrum of dynamic topography. Solid black line = power spectrum of observational model; dashed black line = maximum and minimum limits of power recovered for damping parameters within the ranges $\lambda_1 = 10^2$–10^4 km^{-2} and $\lambda_2 = 10^{-0.5}$–$10^{0.5}$ km^{-2}; red line = power spectrum of predicted dynamic topography. Fields are calculated using the viscosity profile of Steinberger & Calderwood (2006). Between 50 and 400 km, densities are determined using anelastic V_S-T conversion calibrated for SL2013sv (Chapter 5). Between 450 and 2890 km, V_S from SEMUCB-WM1 is converted to density after applying Q4 anelasticity correction to anharmonic V_S calculated for pyrolite (Cammarano *et al.*, 2003).

where T is temperature, T_r is reference temperature (600°C), ρ_0 is reference density (3921 kg m^{-3}), α is thermal expansivity (3.59 × 10^{-5} K^{-1}), P is pressure and K is the bulk modulus (115.2 GPa; Isaak, 1992). Below 400 km V_S is converted into density using a pyrolitic look-up table as before but with V_S corrected for anelasticity *a priori* using the Q4 attenuation profile of Cammarano *et al.* (2003).

Results

Instantaneous flow calculations performed using these anelastic density models and the calibrated radial viscosity structure of Steinberger & Calderwood (2006) yield correlations with geoid and dynamic topography that are very similar to elastic counterparts (< 10% difference) but fits to observed amplitudes are improved (Figure 6.8). Further, the observational power spectrum is fit well at spherical harmonic degrees greater than two (Figure 6.8g). However, the predicted peak-to-peak geoid amplitude is three times higher than observations and peak-to-peak dynamic topography is ∼ 1.5 times larger than observed. The dynamic topography power spectrum demonstrates that most of the remaining discrepancy results from overestimation of the degree two contribution (Figure 6.8g).

As in the elastic calculations, amplitude discrepancy is greater for the geoid than dynamic topography. The geoid is more sensitive to degree two density structure than dynamic topography, suggesting that this discrepancy is related to incorrect density structure at these longest wavelengths. Although tomographic models image some degree two structure in the upper mantle, instantaneous flow calculations considering only the upper 400 km of the mantle reveal that these contributions are negligible above the transition zone (Figure 6.9). Degree two discrepancy between observations and predictions must therefore originate deeper than 400 km. Moreover, in contrast to predictions that assume the Earth behaves elastically at seismic frequencies, the more symmetrical distribution of dynamic topography predicted by the anelastic density model indicates that upper mantle temperatures are normally distributed, consistent with theoretical expectations for a vigorously convecting planet like the Earth (Jarvis & Peltier, 1986).

The LLSVPs are the largest contiguous structures in the Earth's deep mantle and are consistently imaged by a range of seismic tomographic models (Garnero & McNamara, 2008; Lekic *et al.*, 2012; Cottaar & Lekic, 2016). Having excluded the upper mantle as the origin of degree two discrepancy, reduced buoyancy may be required in these regions to explain available data. Two
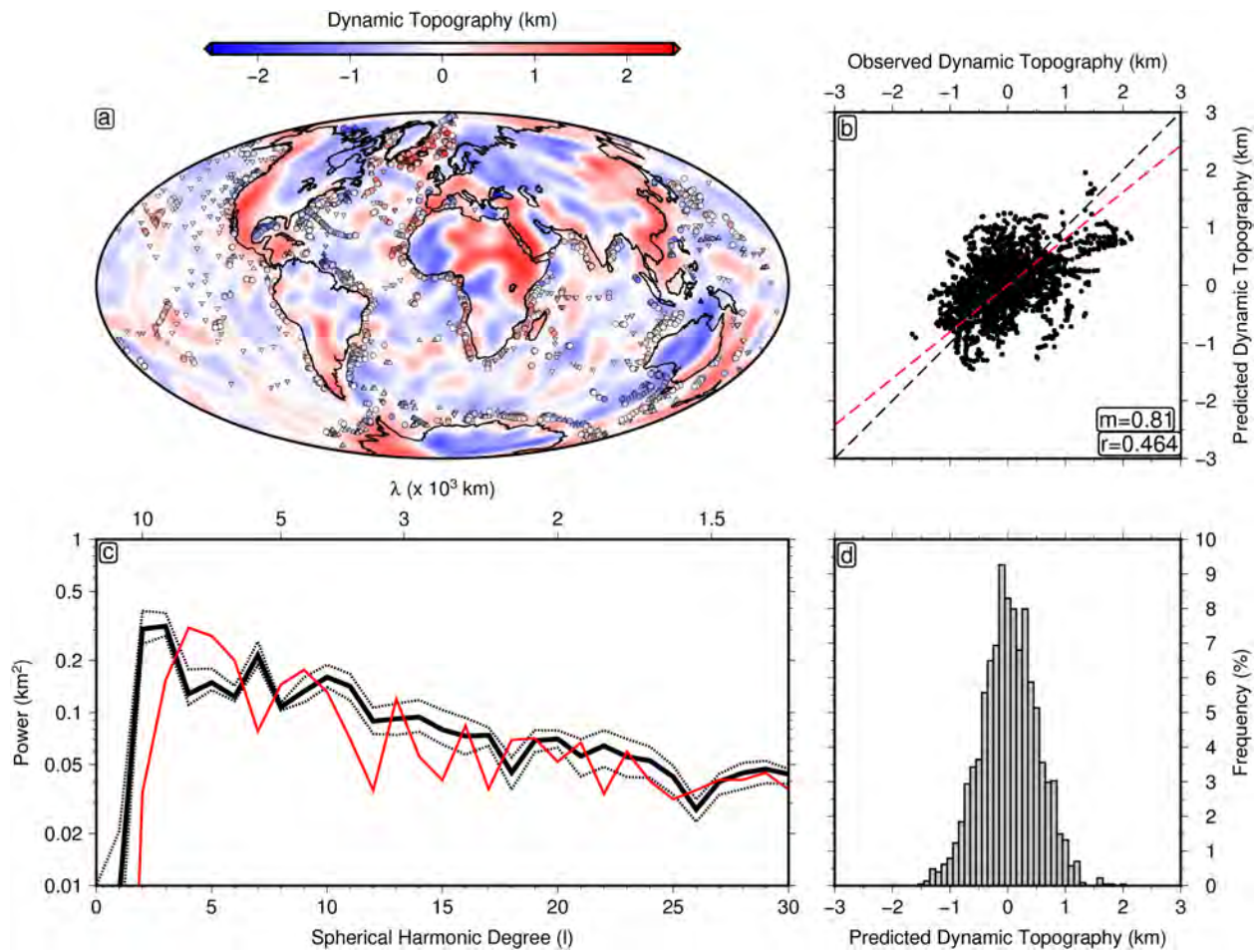
Figure 6.9: Upper mantle instantaneous flow calculations. (a) Upper mantle (50–400 km) dynamic topography predicted using density structure from calibrated anelasticity models and SC06 viscosity profile. Contributions beneath 400 km are ignored in these calculations. Filled circles = oceanic residual depth measurements isostatically corrected for both sediment and crustal thickness variations; filled up/down triangles = upper/lower bound oceanic residual depth measurements isostatically corrected for sediment thickness variations only. (b) Correlation between observed and predicted dynamic topography. (c) Power spectrum of dynamic topography. Solid black line = power spectrum of observational model; dashed black line = maximum and minimum limits of power recovered for damping parameters within the ranges $\lambda_1 = 10^2$–10^4 km^{-2} and $\lambda_2 = 10^{-0.5}$–$10^{0.5}$ km^{-2}; red line = power spectrum of predicted dynamic topography. (d) Frequency distribution of predicted upper mantle dynamic topography.

possible candidates for achieving this reduction are stronger anelastic effects in the LLSVP regions and compositionally dense LLSVPs. The amplitude of attenuation in the lowermost mantle is highly uncertain but recent results suggest that the Q4 attenuation profile used here may underestimate the true magnitude of anelasticity within the LLSVPs (Liu & Grand, 2018). However, given the magnitude of the degree two discrepancy, anelasticity alone is unlikely to be the cause of the remaining disagreement. Further, anelastic effects will reduce geoid and dynamic topography amplitudes by similar proportions and will therefore be unable to resolve the proportionally higher

mismatch observed for the geoid. Instead, chemical heterogeneity in the deepest mantle is likely to account for the residual mismatch for two reasons. First, it can produce the right magnitude of change (Figure 6.10). Secondly, it can reduce the degree two geoid to a greater extent than degree two dynamic topography, provided the viscosity of the upper mantle is lower, on average, than the lower mantle. In such a configuration, geoid sensitivity to degree two density structure peaks in the mid-lower mantle, while dynamic topography sensitivity tends to zero with depth (Figure 6.3). As a result, if the deepest sections of the LLSVP are denser than their surroundings, dynamic topography will be reduced but to a lesser extent than the geoid. Furthermore, several studies have suggested that a range of independent geophysical observations can be better explained if LLSVPs are compositionally distinct from their surroundings over a particular depth range (Garnero *et al.*, 2016).

6.2.4   Compositionally Distinct LLSVPs

Over the past decades there has been much debate over the chemical composition of the Pacific and African LLSVPs (Garnero *et al.*, 2016). Seismological studies find that the LLSVPs, at least locally, have sharp sides with decreases in V_S and V_P of up to 5% and 3%, respectively, over a distance of 50-100 km (He & Wen, 2012; Frost & Rost, 2014). These strong seismic velocity gradients have led many to infer that these regions are chemically distinct from ambient lower mantle. Further evidence for geochemical heterogeneity in the deep mantle comes from normal mode studies that find the deepest sections of LLSVP regions to be $\sim$ 1% denser than their surroundings (Ishii & Tromp, 1999; Trampert *et al.*, 2004; Moulik & Ekström, 2016). Some geodynamic studies also favour a thermochemical origin for the LLSVPs, arguing that the long-term stability of these features requires positive density anomalies to anchor the structures (Tackley, 2002; McNamara & Zhong, 2005; Simmons *et al.*, 2007; Steinberger & Torsvik, 2008; Deschamps *et al.*, 2018). However, many studies have suggested that the present-day resolution of seismological methods is insufficient to accurately determine whether LLSVPs are purely thermal or thermochemical anomalies (Schuberth *et al.*, 2009; Schuberth & Bunge, 2009; Davies *et al.*, 2012). Indeed some seismological studies explicitly favour chemically light LLSVPs (Koelemeijer *et al.*, 2017). Further, the anti-correlation of geoid anomalies with LLSVPs suggests that a dominant portion of these low shear velocity regions are buoyant and upwelling (Hager *et al.*, 1985).

The origin and intrinsic density of the LLSVPs remain controversial due to the ambiguity of previous seismological results. However, the recent development of body tide tomography to investigate deep
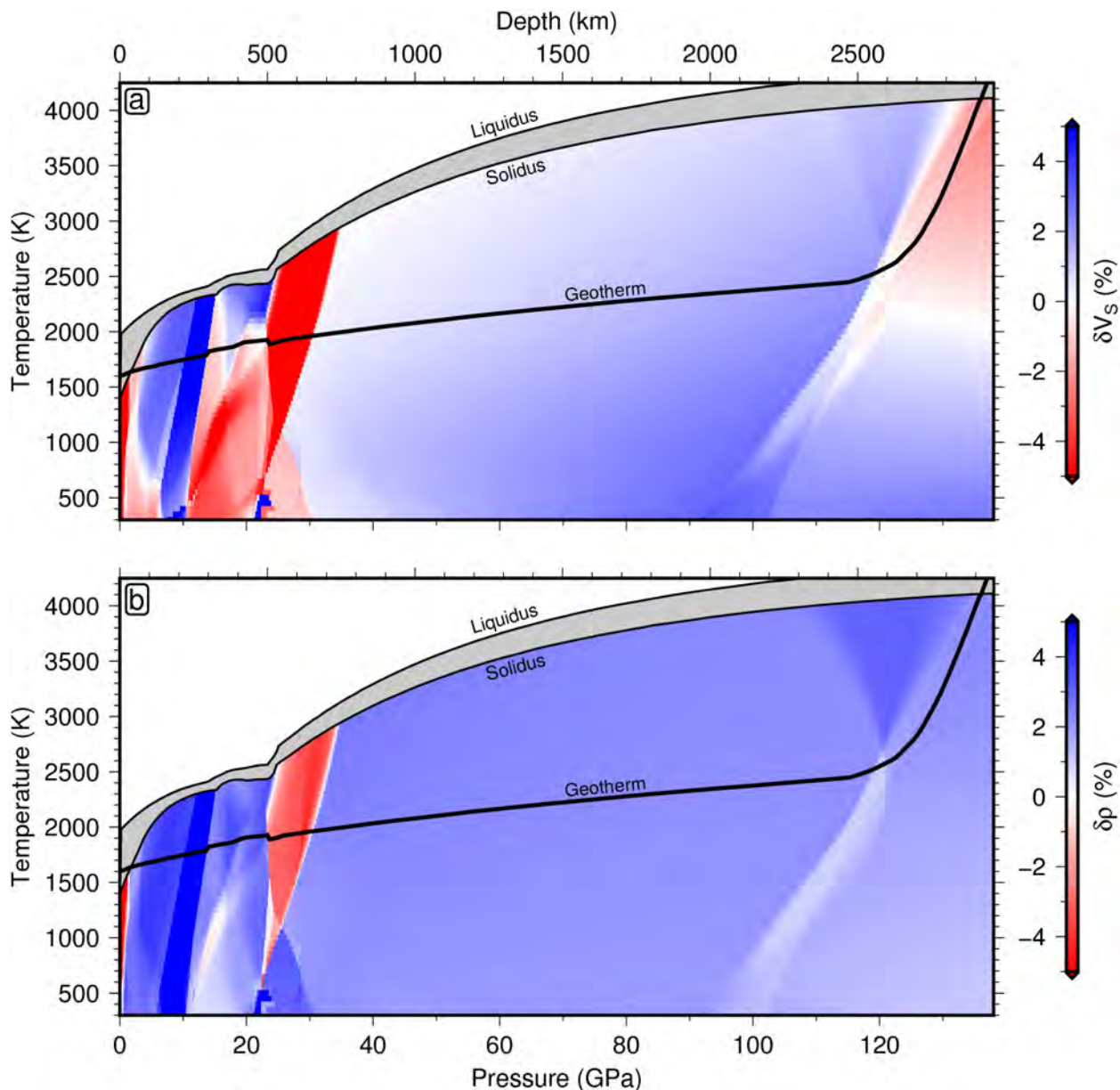
Figure 6.10: Variation in physical properties as a function of composition. (a) Difference in V_S between basaltic and pyrolitic mantle. (b) Difference in density between basaltic and pyrolitic mantle. Solidus, liquidus and 1600 K geotherm from Stixrude *et al.* (2009).

mantle density structure has provided independent evidence that the lowest 300 km of the LLSVPs are on average 1% more dense than ambient mantle (Lau *et al.*, 2017). Dense basal portions of LLSVPs can potentially explain modest long wavelength dynamic topography as negative buoyancy near the CMB will partially cancel out the positive buoyancy of the upper reaches of these provinces.

To investigate this possibility, below a prescribed depth, regions with shear wave velocity anomalies $\leqslant 0.65\%$ are assumed to contain basaltic material, such that their excess density approximately matches the average value obtained by Lau *et al.* (2017). The mantle outside the LLSVPs is
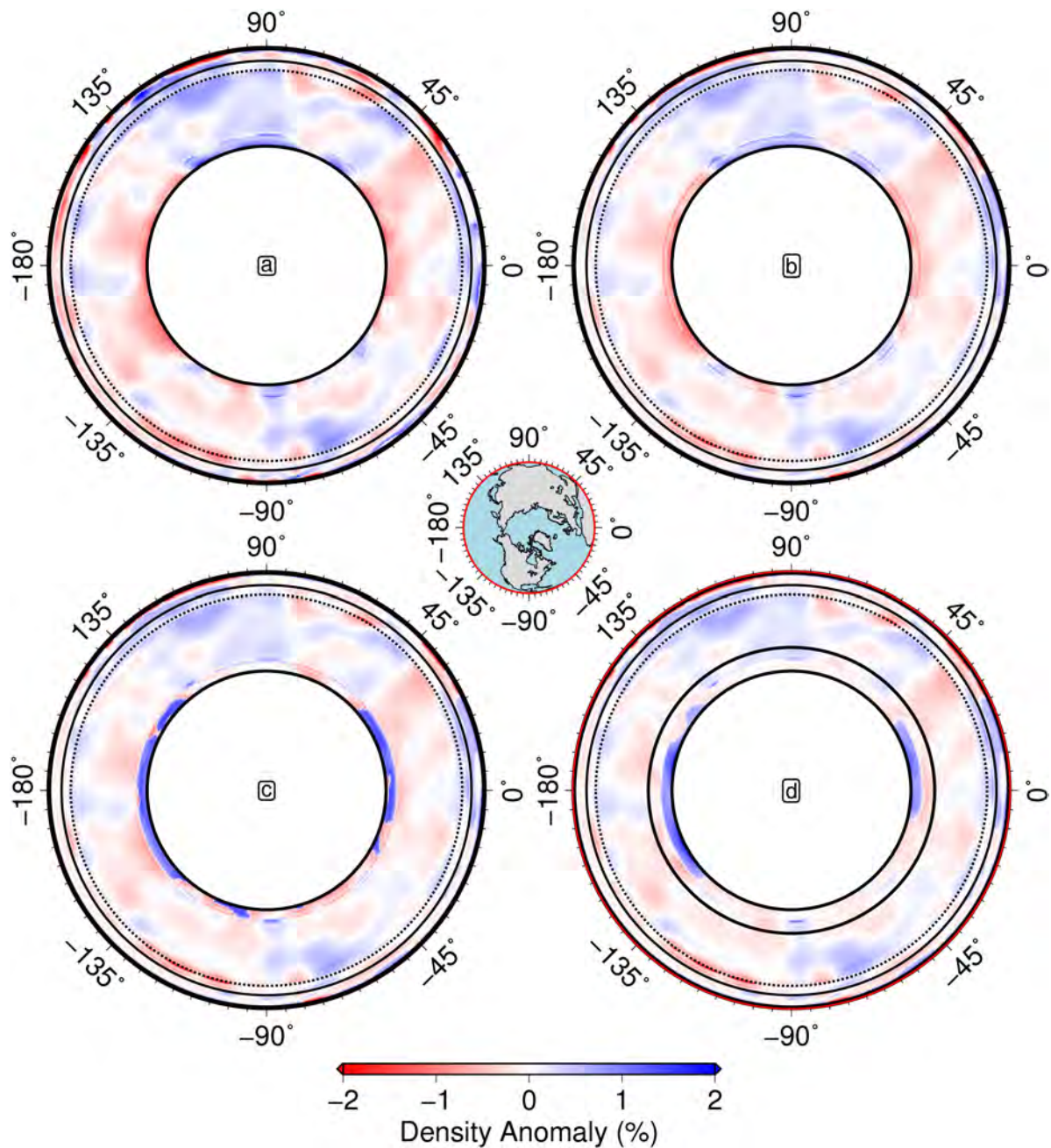
Figure 6.11: Variation in density structure as a function of composition and anelasticity. (a) Density model constructed assuming no anelastic effects. Solid line at 400 km = boundary separating density structure derived from SL2013sv ($z \leqslant 400$ km) and SEMUCB-WM1 ($z > 400$ km); dotted line = 660 km discontinuity. (b) Density model including anelastic effects based on calibrated model in upper mantle and Q4 profile of Cammarano *et al.* (2003) below 400 km. (c) Density model including anelastic effects based on calibrated anelasticity model in upper mantle and Q4 profile of Cammarano *et al.* (2003) below 400 km. LLSVP regions ($\delta V_S < -0.65\%$) are assumed to be basaltic below 2600 km. (d) Density model including anelastic effects based on calibrated model in upper mantle and Q4 profile of Cammarano *et al.* (2003) below 400 km. Below 2200 km, density anomalies are taken directly from Lau2. Solid line at 2200 km = boundary separating density structure derived from SEMUCB-WM1 (400 km $> z \leqslant 2200$ km) and Lau2 ($z > 2200$ km). All models assume pyrolitic mantle composition unless stated otherwise. Inset map gives location of equatorial transect along which cross-sections are assembled.

assumed to be pyrolitic in composition (Green & Ringwood, 1970; Workman & Hart, 2005). In the lower mantle, key thermoelastic parameters pertaining to both basaltic and pyrolitic compositions are calculated using the MMA-EoS software and the Stixrude & Lithgow-Bertelloni (2011) mineral physics database (Figure 6.10). Shear wave velocities have been corrected for anelasticity using the Q4 profile of Cammarano *et al.* (2003). In the upper mantle, density structure is taken directly from the anelasticity model calibrated for SL2013sv in Chapter 5. The depth below which LLSVPs are assumed to be dense is varied between 1900 km and 2850 km to determine the effect of different density structures on the fit between observed and predicted geophysical fields, particularly the geoid and dynamic topography. Instantaneous flow arising from the adapted density models are calculated using the viscosity profile of Steinberger & Calderwood (2006) for comparison with previous results.

Another suite of models, that directly incorporate the tidal tomography-derived density models of Lau *et al.* (2017) below 1900 km, are also tested. This depth threshold is chosen as the sensitivity of the body tide models to density structure above 1900 km is effectively zero. Between 400 km and 1900 km the mantle is assumed to be pyrolitic and the density is determined using the thermoelastic parameters predicted by MMA-EoS with V_S corrected using the Q4 anelasticity profile (Cammarano *et al.*, 2003). Above 400 km, the density is derived from the calibrated anelasticity model. The three density models implemented here cover the range of possible solutions to the tidal tomography inversions in the Lau *et al.* (2017) study. These models differ in how they partition the anomalous density of the LLSVP regions between the lowermost mantle (2550–2890 km) and the middle lower mantle (2200–2550 km): Lau1 has a relatively equal distribution, Lau2 has anomalous density concentrated in the lowermost mantle, whereas, Lau3 places the majority of the anomalous density in the middle lower mantle (Table 6.1).

Results

Modelling the basal sections of LLSVPs as positive density anomalies improves fit to geophysical observables in four important respects: first, it reduces the misfit between peak amplitudes of observed and predicted geoid and dynamic topography; secondly, it improves the correlation between observed and predicted geoid and dynamic topography; thirdly, it reduces the long wavelength spectral discrepancy between predictions and observations; finally, misfit between observed and predicted excess CMB ellipticity is reduced (Figures 6.12 & 6.13). However, optimal dense LLSVP depth values, i.e. the depth below which the mantle is assumed to be basaltic in regions where
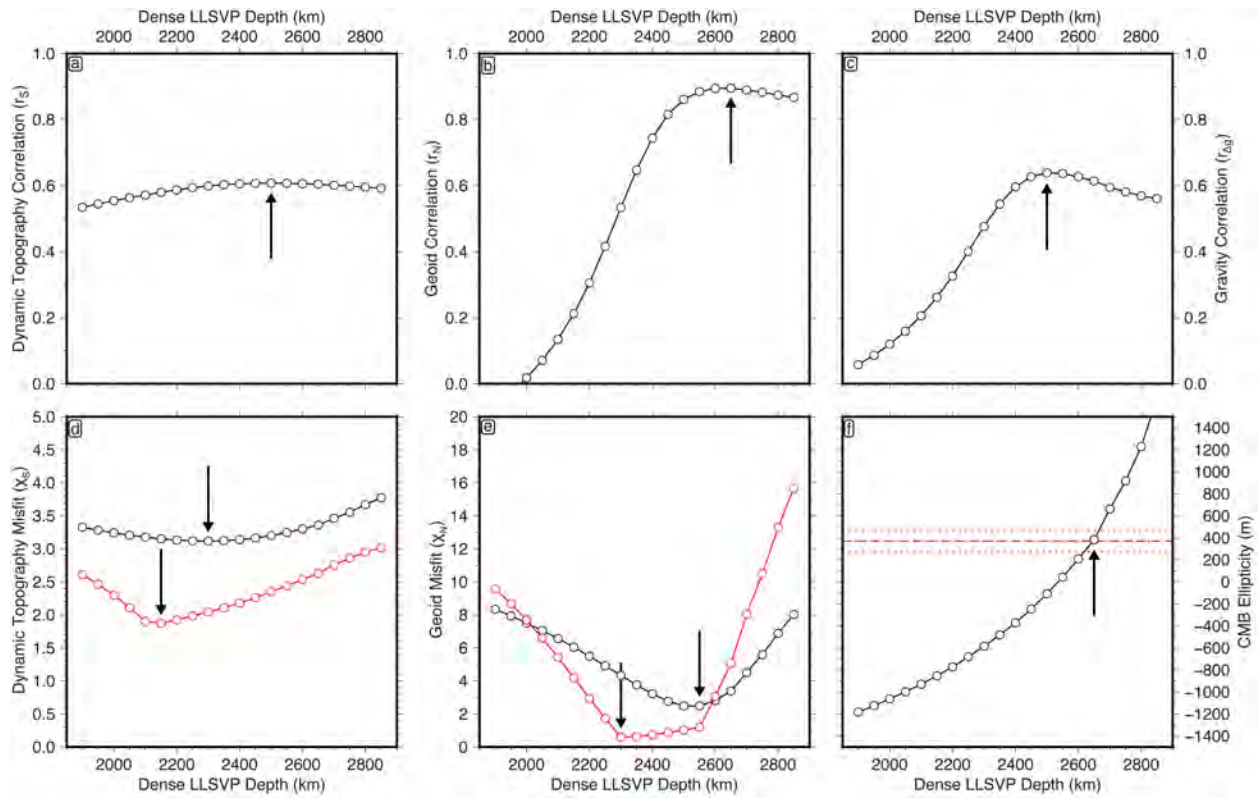
Figure 6.12: Dense LLSVP tests. (a) Correlation between observed and predicted dynamic topography as a function of dense LLSVP depth (i.e. depth below which mantle is assumed to be basaltic in regions where $\delta V_S \leqslant 0.65\%$). Black line = correlation vs. dense LLSVP depth; circles = tested dense LLSVP depths; black arrow = dense LLSVP depth giving optimal correlation. (b) Geoid correlation. (c) Free-air gravity anomaly correlation. (d) Root mean square (RMS) misfit between observed and predicted dynamic topography as a function of dense LLSVP depth. Black line = global RMS misfit assuming $1\sigma = \pm 200$ m; red line = RMS misfit between peak amplitudes. (e) Geoid RMS misfit. Black line = global RMS misfit assuming $1\sigma = \pm 10$ m; red line = RMS misfit between peak amplitudes. (f) Predicted CMB excess ellipticity ($C_{2,0}$) as a function of dense LLSVP depth. Dashed/dotted red line = observed $C_{2,0}$ (370 ± 100 m; Dehant *et al.*, 2017).

$\delta V_S \leqslant 0.65\%$, differ according to the measures of fit used. A trade-off therefore arises between improving fit to one set of parameters whilst minimising the increased misfit to others. The optimum trade-off is achieved when the deepest ~ 300 km of the LLSVP are assumed to be basaltic. This result is corroborated by the outputs of models that directly incorporate the density structure obtained by Lau *et al.* (2017) through inverse modelling of body tide data (Table 6.1; Figure 6.14).

The key outcome of these calculations is that the long wavelength discrepancy between predicted and observed dynamic topography can be resolved while improving fit to the geoid. This result is significant because it has been suggested that the $\sim \pm 500$ m long wavelength dynamic topography observed by Hoggard *et al.* (2016) cannot be reconciled with the strong long wavelength signal observed in geoid undulations (Coltice *et al.*, 2017). This work demonstrates that the power
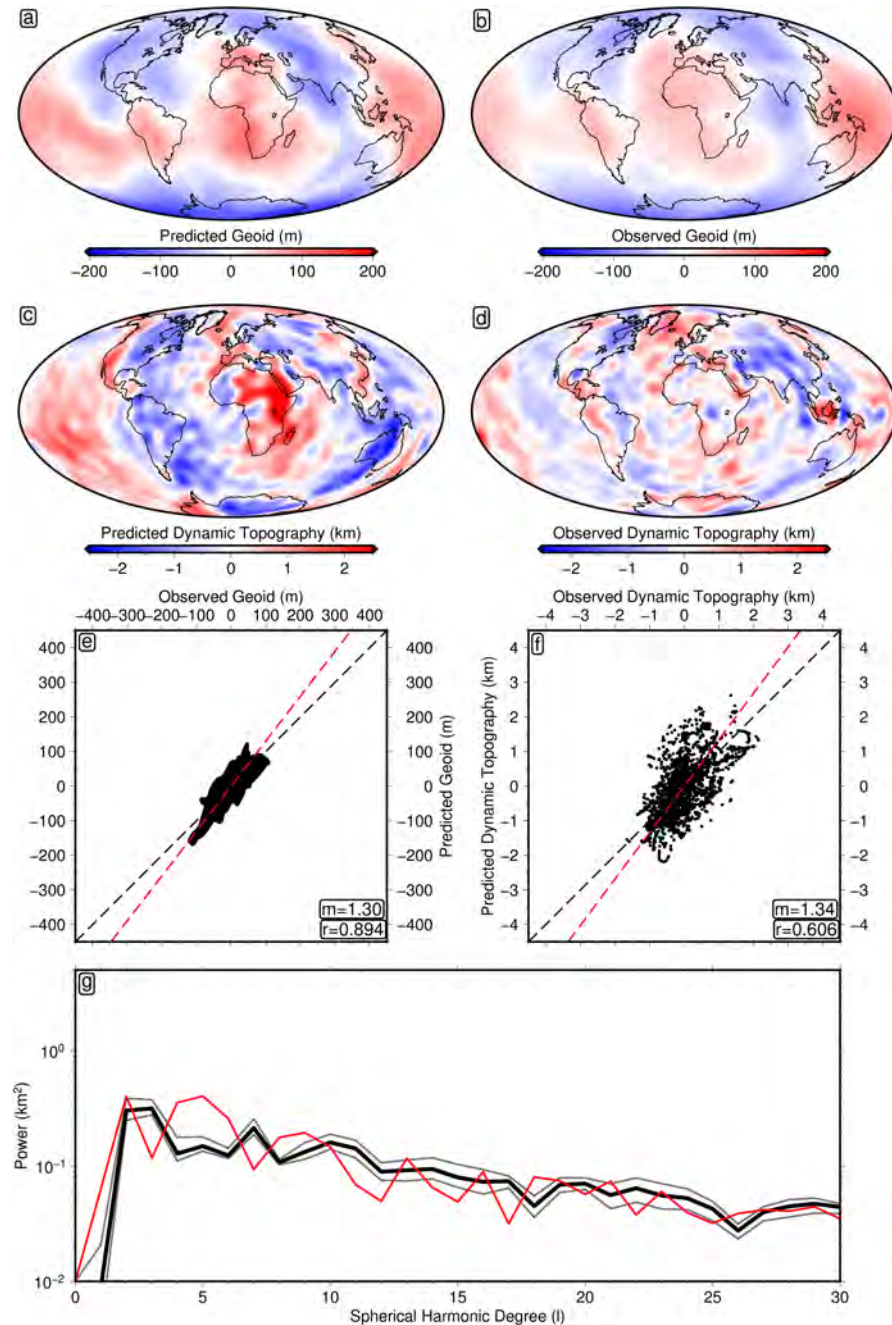
Figure 6.13: Geophysical fields predicted from density model incorporating anelasticity and dense basal LLSVP. (a) Predicted geoid. (b) Observed geoid (Chambat *et al.*, 2010). (c) Predicted dynamic topography. (d) Observed dynamic topography. (e) Correlation between observed and predicted dynamic topography. (f) Correlation between observed and predicted geoid. (g) Power spectrum of dynamic topography. Solid black line = power spectrum of observational model; dashed black line = maximum and minimum limits of power recovered for damping parameters within the ranges $\lambda_1 = 10^2$–10^4 km^{-2} and $\lambda_2 = 10^{-0.5}$–$10^{0.5}$ km^{-2}; red line = power spectrum of predicted dynamic topography. Fields are calculated using the viscosity profile of Steinberger & Calderwood (2006). Between 50 and 400 km, densities are determined using anelastic V_S-T conversion calibrated for SL2013sv (Chapter 5). Between 450 and 2890 km, V_S from SEMUCB-WM1 is converted to density after applying Q4 anelasticity correction to anharmonic V_S calculated for pyrolite and basalt (Cammarano *et al.*, 2003). Below 2600 km, the mantle is assumed to be basaltic where $\delta V_S \leqslant 0.65\%$ and pyrolitic elsewhere, above 2600 km the mantle is assumed to be pyrolitic.
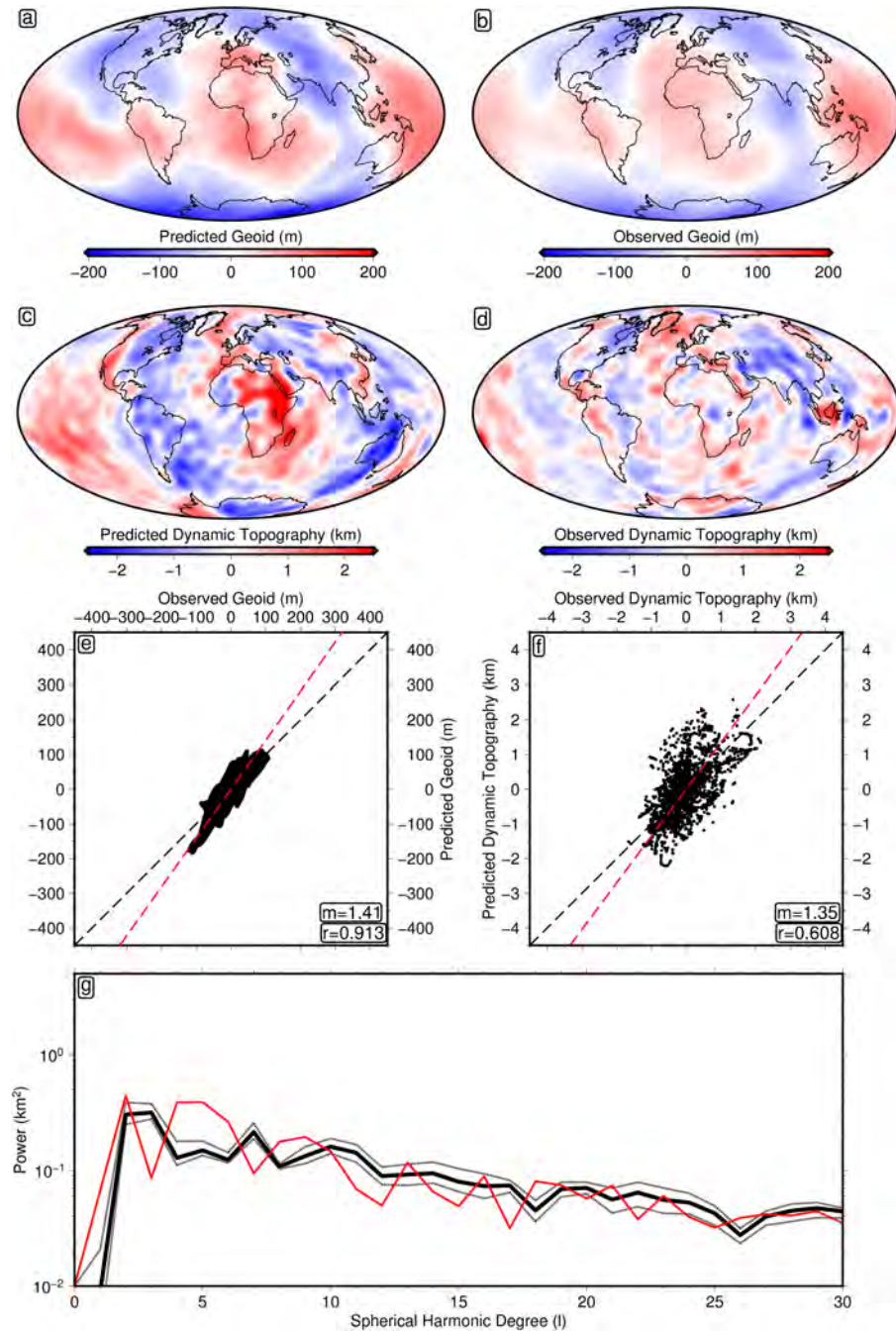
Figure 6.14: Geophysical fields predicted from density model incorporating anelasticity and tidal tomographic inversions. (a) Predicted geoid. (b) Observed geoid (Chambat *et al.*, 2010). (c) Predicted dynamic topography. (d) Observed dynamic topography. (e) Correlation between observed and predicted dynamic topography. (f) Correlation between observed and predicted geoid. (g) Power spectrum of dynamic topography. Solid black line = power spectrum of observational model; dashed black line = maximum and minimum limits of power recovered for damping parameters within the ranges $\lambda_1 = 10^2$–10^4 km^{-2} and $\lambda_2 = 10^{-0.5}$–$10^{0.5}$ km^{-2}; red line = power spectrum of predicted dynamic topography. Fields are calculated using the viscosity profile of Steinberger & Calderwood (2006) and a hybrid density model. Between 50 and 400 km, densities are determined using anelastic V_S-T conversion calibrated for SL2013sv (Chapter 5). Between 450 and 2200 km, V_S from SEMUCB-WM1 is converted to density after applying Q4 anelasticity correction to anharmonic V_S calculated for pyrolite (Cammarano *et al.*, 2003). Below 2200 km, mantle density structure derived from Lau2.

Table 6.1: Summary of tidal tomography-derived model outputs. $R_\rho = \delta \ln \rho / \delta \ln V_S$; D = deep lower mantle (2,551 km – 2,891 km); M = mid-lower mantle (2,211 km – 2,551 km); L = inside LLSVP; O = outside LLSVP. LLSVP boundary taken as 0.65% V_S anomaly contour. r_S = dynamic topography correlation; r_N = geoid correlation; $r_{\Delta g}$ = free-air gravity anomaly correlation; $C_{2,0}$ = predicted excess CMB ellipticity; χ_S = root mean square (RMS) misfit between observed and predicted dynamic topography; χ_N = RMS misfit between observed and predicted geoid. Bracketed values represent RMS misfit between peak amplitudes.

Model	R_ρ(ML)	R_ρ(DL)	R_ρ(DO)	r_S	r_N	$r_{\Delta g}$	$C_{2,0}$	χ_S	χ_N
Lau1	-0.6	-0.85	0.2	0.609	0.914	0.529	448	3.286 (2.488)	2.913 (2.359)
Lau2	-0.35	-1.0	0.2	0.608	0.913	0.529	434	3.305 (2.450)	3.016 (2.407)
Lau3	-0.9	-0.7	0.2	0.610	0.912	0.528	444	3.264 (2.468)	2.782 (2.283)

spectra of predicted and observed dynamic topography agree when input density models include a compositionally dense basal layer in LLSVP regions, higher-resolution seismic tomography models in the upper mantle and more accurate conversion of V_S into temperature and density.

6.3   Viscosity Structure

The preceding instantaneous flow calculations have involved modifying Earth's density structure whilst keeping the radial viscosity profile fixed. However, although the profile of Steinberger & Calderwood (2006), SC06, is calibrated against heat flow, glacial isostatic adjustment and geoid constraints, considerable uncertainties remain. Other attempts to constrain Earth's internal viscosity structure using glacial isostatic adjustment, precession and geoid data have retrieved viscosity profiles that diverge markedly despite similar inversion methods and inputs (Mitrovica & Forte, 1997; Rudolph *et al.*, 2015; Lau *et al.*, 2017; Figure 6.15).

The updated observed dynamic topography database obtained in Chapter 3 can be incorporated as an additional constraint in these inversions. Inclusion of this dataset, combined with the more accurate density models developed in this study, should significantly reduce the non-uniqueness of the solution. In the following section, inverse modelling is undertaken to assess whether Earth's radial viscosity profile can be better constrained through optimisation of the fit between observed and predicted dynamic topography, geoid undulations, free-air gravity anomalies and CMB excess ellipticity.
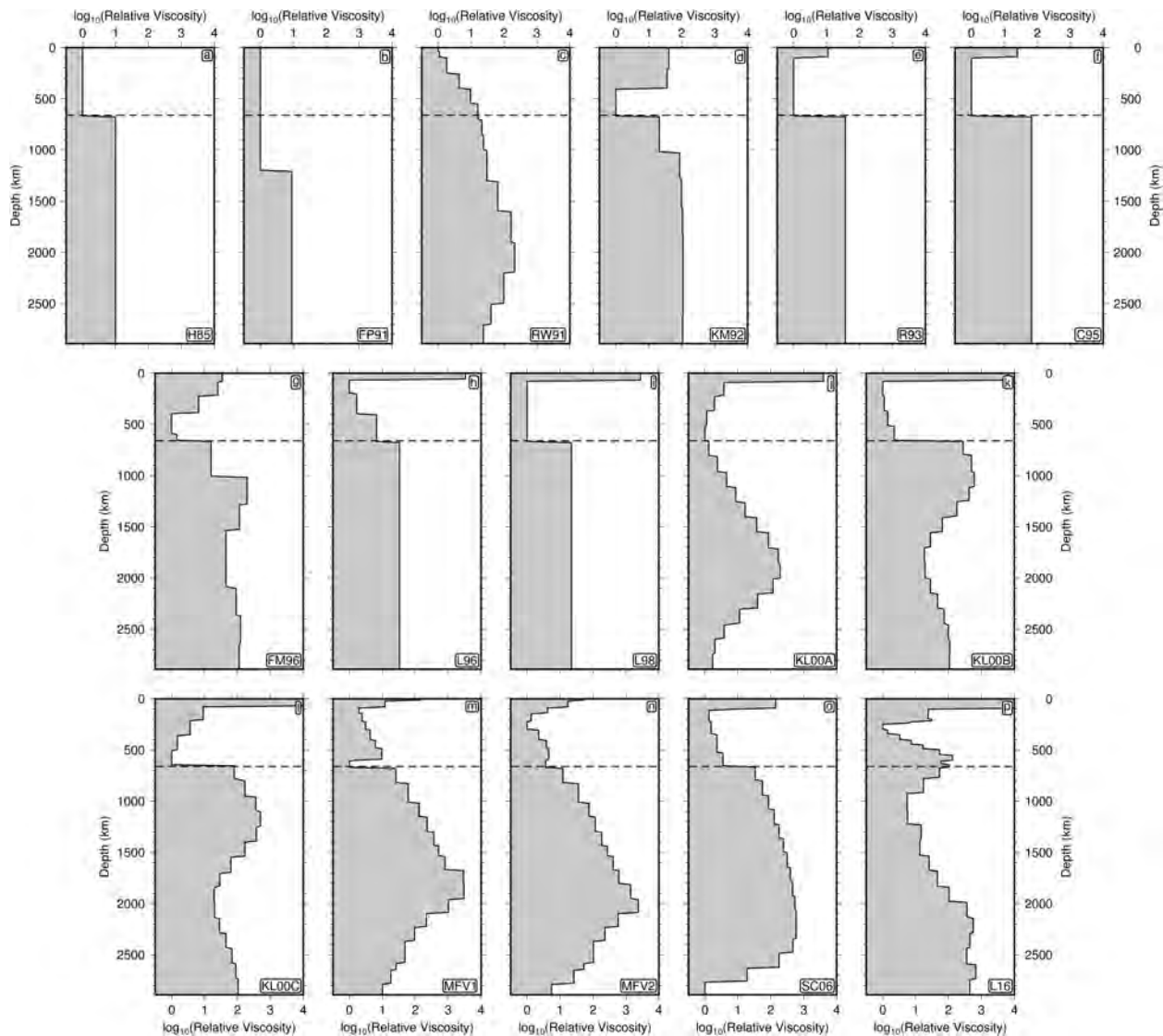
Figure 6.15: Proposed radial viscosity profiles of the Earth. (a) Hager *et al.* (1985). (b) Forte & Peltier (1991). (c) Ricard & Wuming (1991). (d) King & Masters (1992). (e) Ricard *et al.* (1993). (f) Corrieu *et al.* (1995). (g) Forte & Mitrovica (1996). (h) Lambeck *et al.* (1996). (i) Lambeck *et al.* (1998). (j) Kaufmann & Lambeck (2000), profile A. (k) Kaufmann & Lambeck (2000), profile B. (l) Kaufmann & Lambeck (2000), profile C. (m) Mitrovica & Forte (2004), profile V1. (n) Mitrovica & Forte (2004), profile V2. (o) Steinberger & Calderwood (2006). (p) Lau *et al.* (2016).

6.3.1   Methodology

To improve constraint on Earth's radial viscosity structure it is desirable to maximise the number of independent datasets used in the inversion. Of the fields that are explicitly predicted by instantaneous flow calculations, the non-hydrostatic geoid is the best constrained, both in terms of measurement error and spatial coverage (Chambat *et al.*, 2010). The gravity field is similarly well constrained but is likely to be more contaminated by lithospheric signals than the geoid, which is

dominated by the very longest wavelength components that likely originate deep within the convecting mantle (Förste *et al.*, 2011). Thanks to the development of more accurate residual depth anomaly datasets, combined with the refinements made in this study, dynamic topography is now relatively well constrained across much of the global ocean (Winterbourne *et al.*, 2014; Hoggard *et al.*, 2016, 2017). Constraint on dynamic topography is poorer in regions with fewer residual depth measurements. However, dynamic topography highs in the globally continuous dataset remain in good agreement with independent observations including the locations of hotspots, amagmatic swells and elevated passive margins (Hoggard *et al.*, 2016). An additional dataset that can be used to invert for viscosity is CMB topography. Despite numerous attempts to constrain this field, considerable divergence in peak-to-peak amplitude and spatial pattern is observed between proposed models, suggesting that the whole field may be too uncertain to incorporate in an inversion scheme (Morelli & Dziewonski, 1987; Ishii & Tromp, 1999; Koelemeijer *et al.*, 2017). However, the excess ellipticity of the CMB (i.e., $C_{2,0}$) is a parameter for which there is excellent constraint, with recent Very Long Baseline Interferometry (VLBI) studies retrieving a value of 370 ± 100 m (Gwinn *et al.*, 1982; Dehant *et al.*, 2017). By defining and iteratively minimising a joint misfit function based on these independent observations it should be possible to converge on a more accurate radial viscosity structure. In the joint inversion, a misfit function is calculated for each field in the spatial domain in the form

$$M_x = \sqrt{\frac{1}{N} \sum_{i=1}^{N} \left(\frac{F_x(\lambda_i', \phi_i)^o - F_x(\lambda_i', \phi_i, \eta, \rho)^c}{\sigma(\lambda_i', \phi_i)} \right)^2}, \qquad (6.7)$$

where F_x^o is the observed field of interest, F_x^c is calculated field, λ_i' and ϕ_i are the latitude and longitude, respectively, σ_i is the error and N is the total number of measurements. In the calculated field term, η represents the viscosity profile and ρ represents the specified input density structure. The sum of the individual misfit functions is then minimised using Powell's algorithm to iteratively adapt the radial viscosity structure within a specified stratification and value range (Press *et al.*, 1996). The viscosity profile is parameterised as a series of constant viscosity layers to simplify the application of the propagator matrix approach and accurately capture the substantial viscosity jumps that are likely to occur at major phase transitions and internal boundaries. The logarithm of the viscosity is used in this optimisation scheme to ensure non-negativity and render the inverse problem quasi-linear, thus ensuring relatively rapid convergence to a solution. As the instantaneous flow calculations are sensitive to only relative viscosity changes, the depth profile is normalised such that the minimum value is unity.

Powell's algorithm is preferred because it does not require the Frèchet derivatives of the function

$F_x(\lambda_i', \phi_i, \eta, \rho)^c$ to be calculated. This feature is desirable as accurately calculating the gradient of the misfit function would require solution of the Stokes equations and impose excessively large computational costs on the inversion. For similar reasons, Bayesian inversion techniques are not considered as they typically require $\sim 100{,}000$ forward calculations to fully sample a given parameter space (Sambridge, 1999). Bounds are placed on individual parameters so that normalised viscosity may not exceed 10^4, the maxima retrieved by previous studies (Figure 6.15). These bounds are implemented following the methodology of Newville *et al.* (2014), whereby the parameters at a given iteration are transformed from bounded values, $P_{bounded}$, to internally varied parameters, $P_{internal}$, using

$$P_{internal} = \arcsin\left(\frac{2(P_{bounded} - P_{min})}{P_{max} - P_{min}} - 1\right), \tag{6.8}$$

where P_{min} and P_{max} are 10^0 and 10^4, respectively. This implementation ensures that bounded parameter values cannot exceed specified limits whilst allowing the internal parameter to vary freely during optimisation. The bounds placed on the viscosity of each layer are intentionally wide and uniform to ensure that they do not bias the inversion towards any particular solution.

6.3.2   Synthetic Tests

Although Powell's algorithm is one of the more effective minimisation schemes for this type of inverse problem, data errors and the nonlinearity of the forward problem may result in solutions that represent local rather than global minima. It is therefore important to test the degree to which the inversion is sensitive to different parameterisations and starting assumptions. Choice of starting model, random noise in the data, relative weighting of different constraints, the number of layers and the prescribed locations of layer boundaries all have the potential to affect the final model. In the following section, numerous tests are carried out using synthetic data to assess the impact of these different features and inform the interpretation of inversions carried out using real data. In all cases, the input density model includes a basaltic LLSVP below 2600 km and a calibrated anelasticity model in the upper mantle, as this configuration produces an improved fit to geoid and dynamic topography observations (see Section 6.2.4).

Oceanic vs. Global Dynamic Topography Constraints

The observational dynamic topography dataset developed in this dissertation is well constrained at locations in the global ocean by accurate oceanic residual depth measurements. In oceanic locations

away from these points, observed dynamic topography is estimated using shiptrack bathymetry with a less accurate correction made for variable sedimentary thickness and no correction applied for variation in crustal thickness. Potential errors are reduced by applying this approach only in locations that have modest sediment thicknesses and are distant from regions of anomalously thick or thin crust such as oceanic plateaux or fracture zones. In continental regions, a constant admittance value, $Z = 50$ mGal km^{-1}, is applied to scale long wavelength free-air gravity anomalies following McKenzie (2010). Uncertainty is thus significantly higher in continental regions and oceanic locations distant from residual depth measurements. Subsequently, it may be preferable to use only oceanic residual depth measurements in the inversions, provided the advantages of reduced uncertainty outweigh any loss of resolving power due to reduced spatial coverage. To test whether using only oceanic data provides acceptable results, dynamic topography and geoid fields are forward modelled using a given viscosity profile. The dynamic topography field is then sampled either globally ($1°$ bins) or locally, at the latitude and longitude of the residual depth measurements. Inversions are then carried out using both the global and local dynamic topography datasets combined with the global geoid.

The target viscosity profile is retrieved with similar accuracy whether or not the input dynamic topography is globally or locally sampled (RMS misfit is $10^{0.4}$ in both cases). Fits to the target geophysical fields are also good irrespective of spatial coverage of dynamic topography data: respective geoid and dynamic topography misfits are 1.2 m and 8 m for the global dataset and 1.3 m and 9 m for the ocean-only dataset. These minimal differences validate the use of ocean-only dynamic topography constraints in future inversions.

Discretisation

The different mantle viscosity profiles that have been proposed over the past decades use different numbers and thicknesses of constituent layers (Figure 6.15). In all inverse problems, a fundamental trade-off exists between model variance (i.e. the error in an unknown parameter at any point in the model) and model resolution (i.e. the degree to which model parameters are spatially averaged; Backus & Gilbert, 1970). As the number of free parameters in an inversion increases, both resolution and variance increase. It is therefore desirable to find a parameterisation that is sufficiently finely discretised to maintain an acceptable fit to the data but also coarse enough to prevent high values of model variance or 'roughness' (Parker, 1994). To determine the optimal radial discretisation of the viscosity profile, a suite of inverse models are constructed in which the number of layers
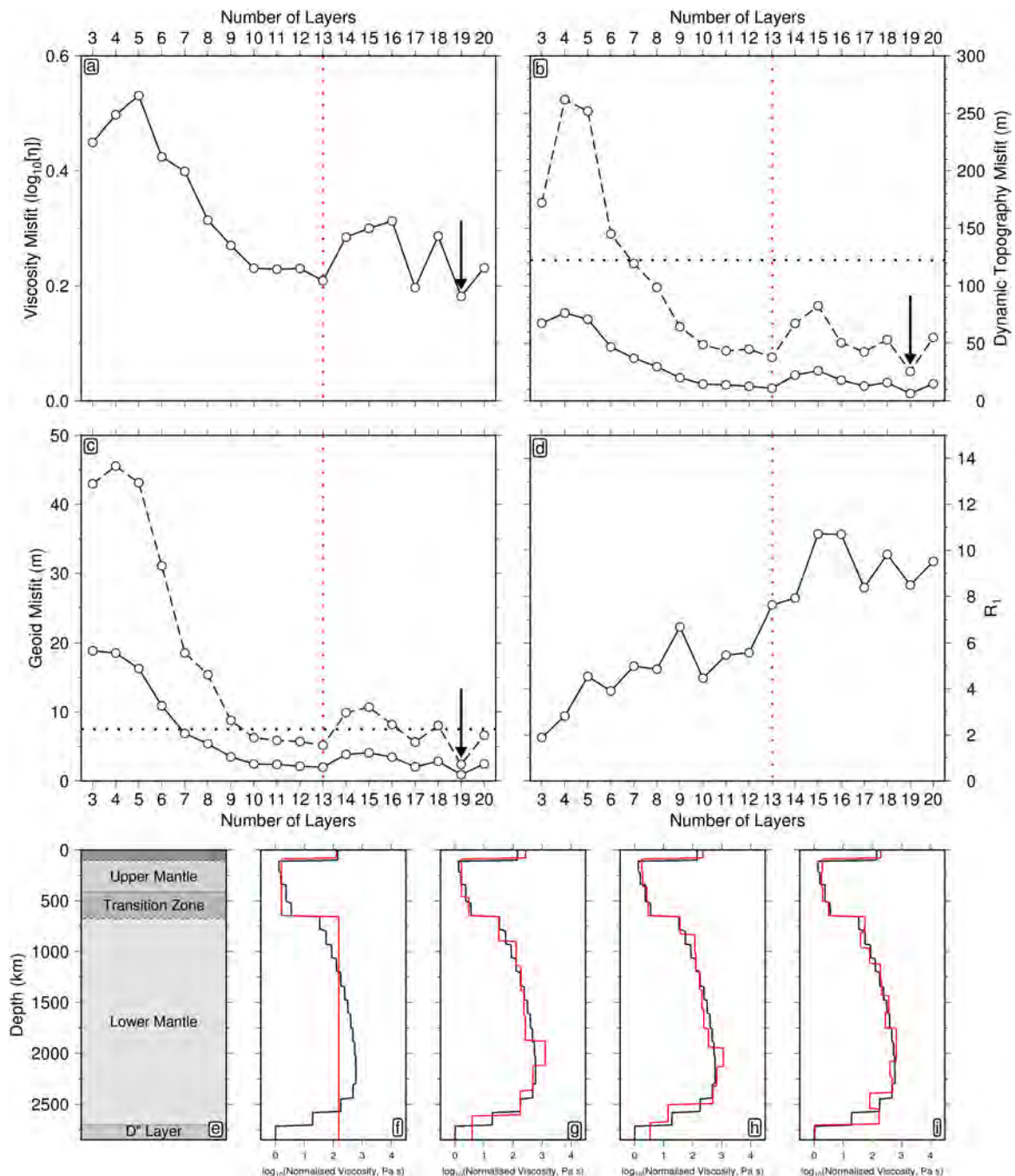
Figure 6.16: Fit to synthetic data as function of discretisation. (a) Misfit between inverted and target viscosity profile as a function of discretisation. Black solid line = RMS misfit; black arrow = global RMS misfit minimum; red dotted line = preferred discretisation. (b) Misfit between inverted and target dynamic topography as a function of discretisation. Black dashed line = maximum misfit; black dotted line = average data error. (c) Misfit between inverted and target geoid as a function of discretisation. (d) Roughness, R_1, of model as a function of discretisation. Data errors from residual depth observations in case of dynamic topography and hydrostatic correction uncertainty in case of geoid (Nakiboglu, 1982; Chambat *et al.*, 2010). R_1 defined as in Equation 1 of Constable *et al.* (1987). (e) Schematic mantle structure as a function of depth. (f) Fit of 3-layer model to target viscosity profile. Black = Steinberger & Calderwood (2006) viscosity structure; red = inverted viscosity structure. (g) Fit of 13-layer model to target viscosity profile. (h) Fit of 17-layer model to target viscosity profile. (i) Fit of 20-layer model to target viscosity profile.

is systematically varied from 3 to 20. Synthetic geoid and dynamic topography fields generated using the viscosity profile of Steinberger & Calderwood (2006) are used as input data in these inversions. This target profile was chosen to evaluate the extent to which available geoid and dynamic topography data can constrain more complex end members of previously proposed viscosity profiles. All model parameterisations include a boundary at the base of the lithosphere ($\sim$ 100 km) and at the 660 km discontinuity with equally spaced layers between these fixed boundaries.

Misfit to the target viscosity profile, geoid and dynamic topography reduces significantly as discretisation increases from 3 to 10 layers, eventually reaching a minimum for 13 layer inversions (Figure 6.16a-c). Misfit values recovered by models with more than 13 layers are highly variable, suggesting that beyond this level of discretisation the optimisation procedure begins to converge on local rather than global minima. Maximum misfit between inverted and target fields falls below characteristic data errors at 7 layers for dynamic topography and 10 layers for the geoid, indicating that inverted fields for models with more than 10 layers can fit the target data within the bounds of uncertainty (Figure 6.16b-c). As expected, model roughness (R_1), defined as the integral of first derivatives using Equation 1 in Constable *et al.* (1987), progressively increases as more layers are added to the inversion (Figure 6.16d). These results suggest that 13 layers represents the optimal level of discretisation as these models yield the best trade-off between misfit and roughness (Figure 6.16g). Although 17- and 19-layer models yield similar results, they come at the cost of introducing additional roughness and extra free parameters that increase computation times by a factor of $\sim$ 2–3 (Figure 6.16h-i). Moreover, these models yield spurious high-amplitude, high-frequency viscosity variations, indicating that the optimisation procedure is converging on local minima and cannot uniquely constrain viscosity at this level of discretisation without the inclusion of regularisation terms in the misfit function (Figure 6.16i).

Complexity of Input Viscosity Structure

Proposed models for Earth's internal viscosity structure vary from simple isoviscous profiles, through two-layer models with a low-viscosity upper mantle and high-viscosity lower mantle, to more elaborate models with numerous layers (Hager *et al.*, 1985; Corrieu *et al.*, 1995; Kaufmann & Lambeck, 2000; Mitrovica & Forte, 2004; Steinberger & Calderwood, 2006; Lau *et al.*, 2016; Figure 6.15). To test the degree to which different levels of complexity can be constrained by the data, geoid and dynamic topography are calculated using a given viscosity profile then inverted to test whether the optimisation scheme can recover the original fields. Initial profiles are isoviscous except when in-

verting for the constant viscosity profile. In this case, a three layer profile including a more viscous

lithosphere and lower mantle is used.
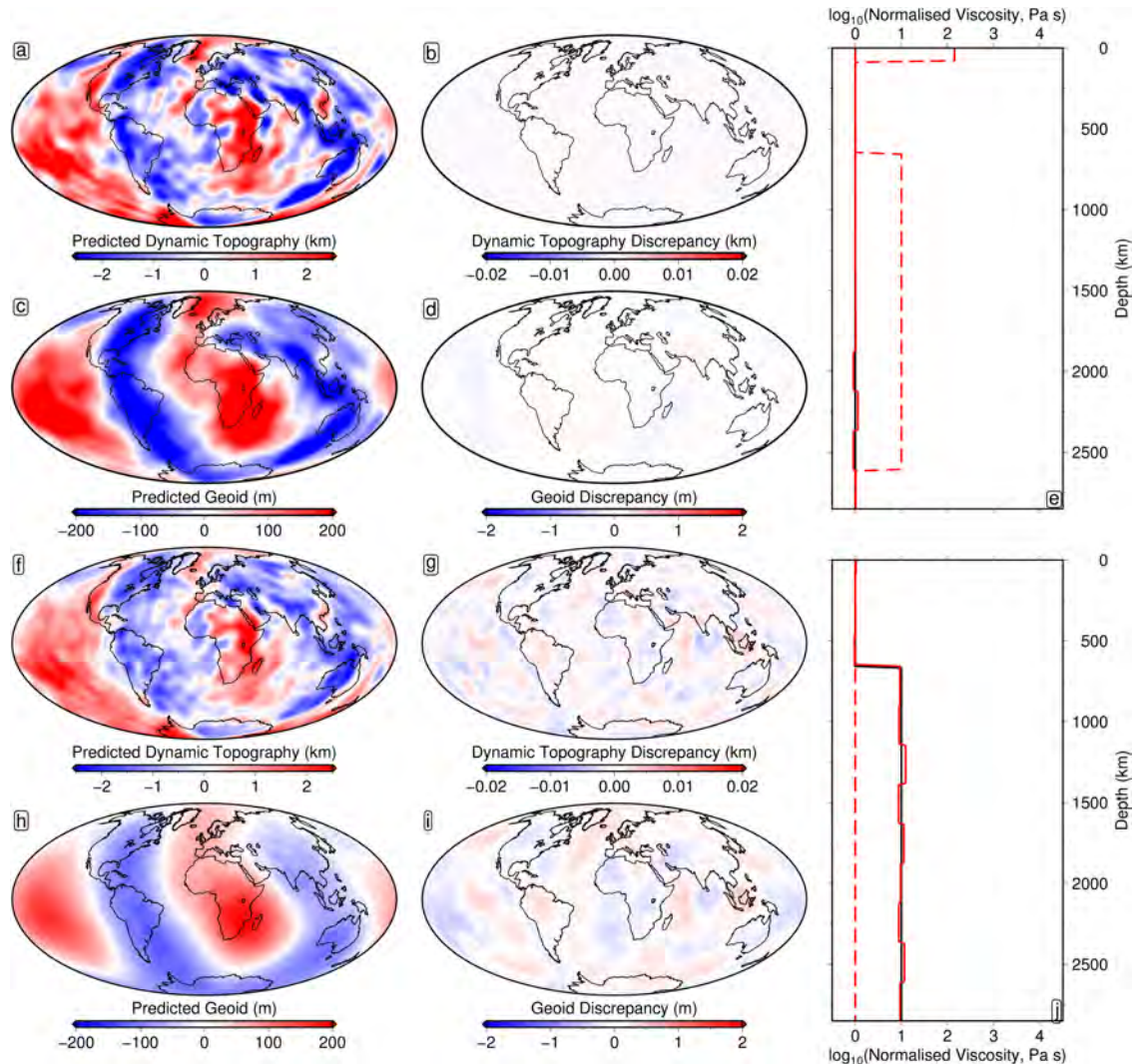
Figure 6.17: Fit to synthetic data for simple viscosity models. (a) Inverted dynamic topography field for isoviscous profile. (b) Difference between inverted and target dynamic topography fields. (c) Inverted geoid field for isoviscous profile. (d) Difference between inverted and target geoid fields. (e) Viscosity profiles. Black solid line = target profile (isoviscous); red dashed line = starting profile; red solid line = inverted profile. (f)–(j) As above for two-layer viscosity profile.

The constant viscosity profile is recovered accurately but deviates increasingly below 1500 km depth, with the largest discrepancy, $\pm 10^{-0.3}$, occurring between 1800 and 2600 km depth (Figure 6.17e). Nevertheless, the inverted viscosity profile produces fields that are essentially identical to those produced by the isoviscous profile with model misfits to dynamic topography and the geoid of ± 7 m and ± 0.4 m, respectively. These misfit values are far smaller than the data errors (Figure 6.17a–

d). The inability of the data to constrain viscosity in the deepest mantle must therefore reflect the relative insensitivity of dynamic topography and geoid kernels to viscosity variation in this region. Two-layer viscosity models are well recovered by the inversion. However, as with the isoviscous profile, fit deteriorates in the lower mantle despite predicted dynamic topography and geoid differing from the target fields by $< 0.5\%$ (Figure 6.17f–j). However, CMB topography associated with the inverted viscosity profile differs by up to 220 m from the original prediction, confirming that this field is most sensitive to deep mantle structure. Inclusion of CMB constraints may therefore improve the accuracy of the inversion, especially in the D'' region. The first of the more elaborate models
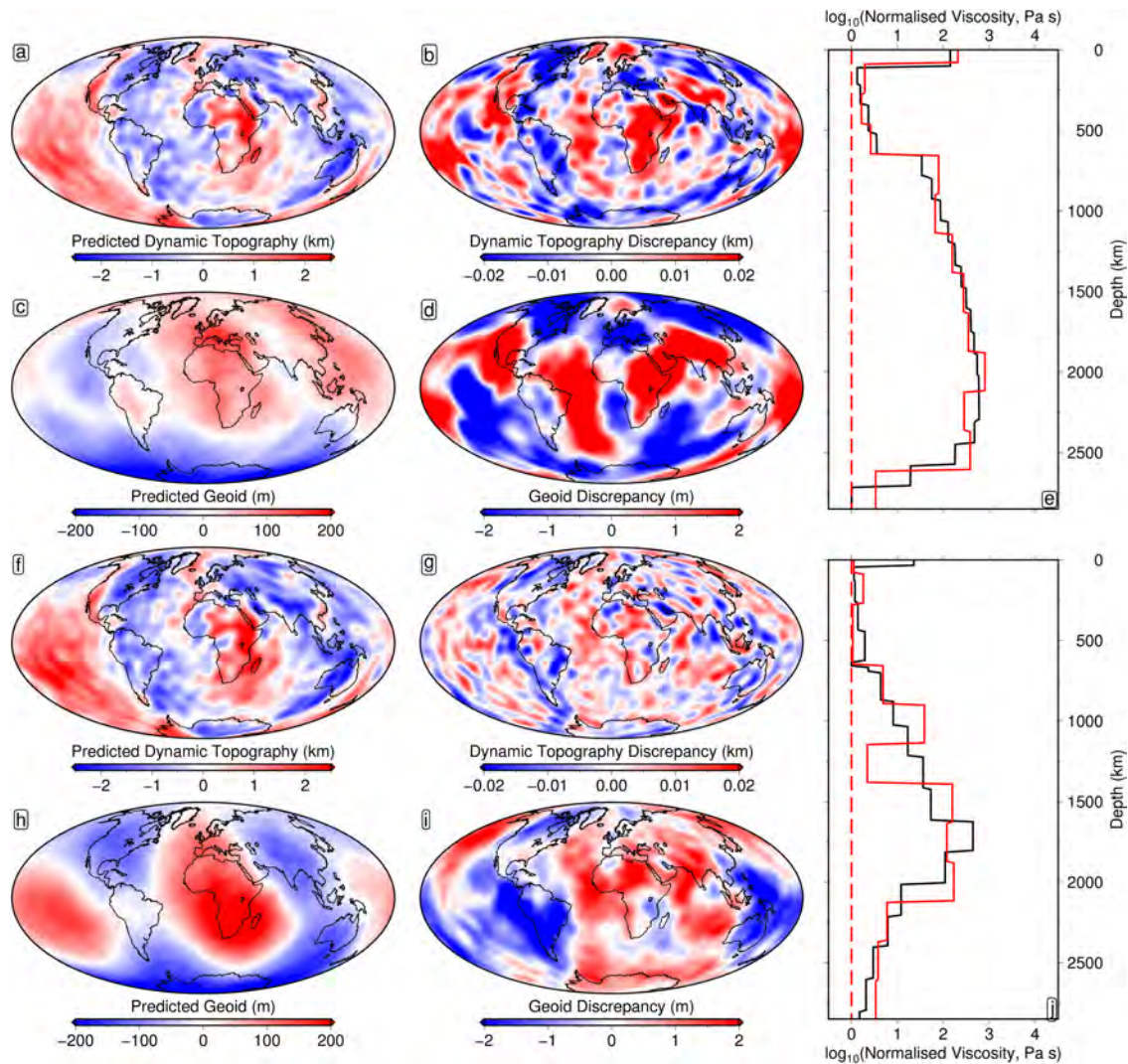
Figure 6.18: Fit to synthetic data for complex viscosity models (a) Inverted dynamic topography field for SC06. (b) Difference between inverted and target dynamic topography fields. (c) Inverted geoid field for SC06. (d) Difference between inverted and target geoid fields. (e) Viscosity profiles. Black solid line = target profile (SC06); red dashed line = starting profile; red solid line = inverted profile. (f)–(j) As above for MFV1 viscosity profile.

tested here, SC06, consists of 22 layers and has been determined using fits to the geoid, radial heat flux and the Haskell constraint (Steinberger & Calderwood, 2006). The 13-layer inversion is thus unable to recover the exact shape of the original profile but does accurately retrieve the predicted fields and the key features of the viscosity profile (Figure 6.18a-e). Fit to the original viscosity profile deteriorates less clearly in the deep mantle than for the simple models. This result possibly reflects the larger variations in viscosity at these depths (Figure 6.18e). Overall, RMS misfit between original and inverted fields is below the error threshold of relevant observational datasets: 9 m for dynamic topography, 1 m for the geoid, 90 m for CMB topography and 1 mGal for the free-air gravity anomaly (Figure 6.18b).
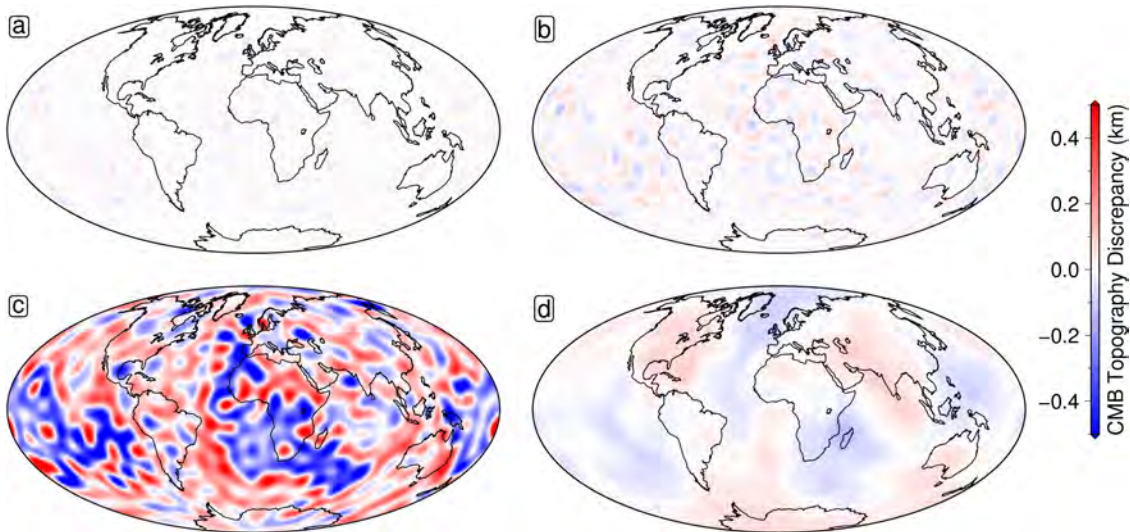
Figure 6.19: Fit to synthetic CMB topography for different viscosity models. (a) Difference between inverted and target CMB topography fields for isoviscous model. (b) For two-layer viscosity model. (c) For SC06 viscosity model (Steinberger & Calderwood, 2006). (d) For MFV1 viscosity model (Mitrovica & Forte, 2004).

The second and third of the more complex viscosity profiles tested here, MFV1 and MFV2, are 25-layer profiles determined by Mitrovica & Forte (1997) and Mitrovica & Forte (2004) from joint inversion of glacial isostatic adjustment constraints, free-air gravity anomalies, plate motion histories and CMB excess ellipticity using Occam's algorithm. Inversions recover the geoid and dynamic topography fields well within the error bounds on those datasets (RMS misfit is 32 m and 3 m for MFV1; 12 m and 0.9 m or MFV2; Figure 6.18f–i). However, RMS misfit to CMB topography is ~ 125 m for both profiles, suggesting again that including some constraint on this field in the inversion scheme may reduce the non-uniqueness of the solution. The higher misfits for MFV1 seem to reflect poorer recovery of the true profile in the uppermost mantle, suggesting that the datasets are sensitive to viscosity changes at these shallower depths but that local minima exist in the misfit

function (Figure 6.18j). This result suggests that some form of regularisation may be required to stabilise 13-layer inversions when applied to real data (Parker, 1994).

Overall, these synthetic tests show that, given the data errors on geoid and dynamic topography observations, 13-layer inversions are sufficiently finely discretised to constrain viscosity variation in the Earth's mantle. Viscosity variation is more poorly constrained in the deep mantle (below 1500 km). However, the poorer fits obtained between synthetic and inverted CMB topography implies that the inclusion of constraints on the deflection of this boundary may improve the recovery of viscosity at these depths (Figure 6.19). Finally, these inversions suggest that geophysical fields do contain sufficient information to differentiate between relatively simple and complex internal viscosity profiles.

Influence of Data Error

Measurements of the geoid have small errors ($\leqslant$ 0.03 m). However, residual depth observations have greater errors ($\sim$ 100 m on average) due to uncertainty in sedimentary and crustal corrections. To test the sensitivity of inversion results to these uncertainties, at each location an error value is drawn from a Gaussian distribution with standard deviation equivalent to the mean uncertainty in the residual depth dataset. These values are added to the predicted dynamic topography field for a particular viscosity profile to generate a synthetic dataset that is then inverted alongside the geoid data. This process is repeated 50 times to fully investigate the effect of randomly distributed data error on the recovered viscosity profile.

In all 100 cases, inverted viscosity profiles closely match the target viscosity profiles. Average standard deviation between inverted and original profiles is $10^{0.6}$ (Figure 6.20b). Errors in the viscosity profile are larger towards the surface, reflecting the greater sensitivity of dynamic topography observations to shallow mantle variation. This effect at least partially counteracts poor sensitivity in the lower mantle which leads to uncertainty in the deep viscosity profile. This result suggests that while overall shapes of inverted viscosity profiles are robust to data errors, absolute magnitudes of individual viscosity jumps are less well constrained.

Impact of Chosen Starting Profiles

Deterministic inversion algorithms require the specification of starting parameters to initialise the optimisation procedure. In most previous tests, the initial profiles are isoviscous to prevent a
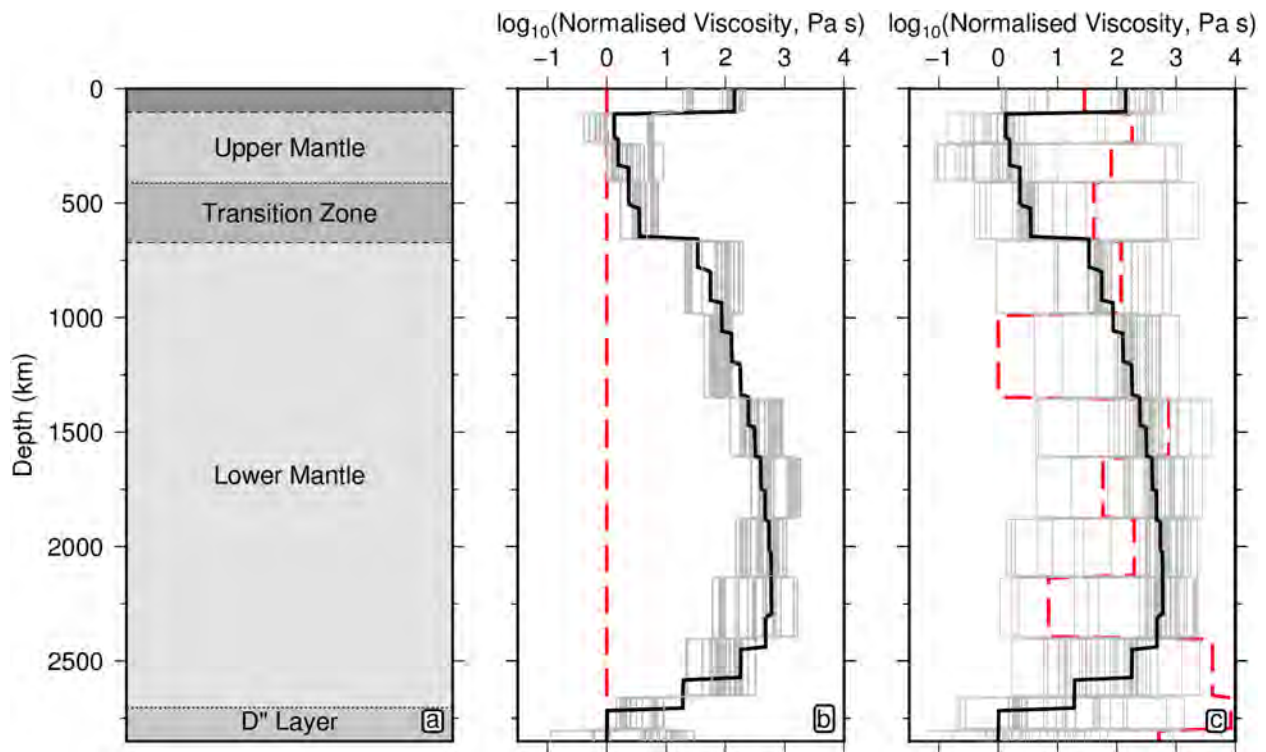
Figure 6.20: Effect of data error and starting profile on inversion. (a) Schematic mantle structure as a function of depth. (b) Data error sensitivity tests. Grey line = inverted viscosity profiles for synthetic dataset with random noise added ($1\sigma = 100$ m); red dashed line = starting profile; black line = target profile (SC06). (c) Starting profile sensitivity tests. Grey line = inverted viscosity profiles for different random starting profiles; red dashed line = example random starting profile; black line = target profile (SC06).

priori introduction of artefacts. The target profile could be accurately retrieved in these tests if the inverse problem was well-posed and possessed a unique solution. Observed discrepancies between final models and target profiles demonstrate that this inverse problem is non-unique and underdetermined. When an inverse problem has these characteristics, it is common for the starting model to influence the final solution. Consequently, it is essential to test the robustness of the inversion scheme to different initial viscosity profiles.

To test sensitivity to choice of initial model, 50 13-layer inversions are carried out using Steinberger & Calderwood (2006) as the target profile. In each inversion the starting value for each layer in the initial profile is drawn at random from a normal distribution with the same mean and standard deviation as the target profile ($\mu = 10^2$; $1\sigma = 10^1$). In all cases, inverted geoid and dynamic topography fields closely match the synthetic data (RMS misfit values are $\leqslant 1\%$ of maximum amplitudes). However, in many cases, high-frequency, high-amplitude variation is inherited from the initial viscosity profile. This result indicates that geoid and dynamic topography fields are not

sufficient to uniquely constrain the true viscosity profile at all depths. It is therefore important not to include large, unconstrained viscosity jumps in the initial profile as some may create only modest misfit increases and will not be removed during the optimisation process.

The mean of the 50 inverted viscosity profiles closely resembles the target profile (RMS misfit $\sim 10^{0.3}$). This fit suggests that, despite the existence of local minima, it is possible to converge on the global minimum provided a sufficient number of inversions are carried out from different starting points (Figure 6.20c).

6.3.3   Inverse Modelling of Observational Datasets

Coltice *et al.* (2017) suggest that the ± 500 m of long wavelength ($0 < l < 3$) dynamic topography recovered by Hoggard *et al.* (2016) is "too small for mantle convection models to fit the geoid". However, as demonstrated earlier in this chapter, discrepancies between predictions and observations of long wavelength dynamic topography and the geoid originate in the lower mantle and can be reduced by including a dense basal LLSVP. This is a feature of mantle density structure for which there is growing independent evidence from a wide range of studies (Ishii & Tromp, 1999; Trampert *et al.*, 2004; Moulik & Ekström, 2016; Lau *et al.*, 2017). However, predicted geoid amplitudes remain $\sim 30\%$ higher than observed. The aim of the inversions performed here is to determine whether, by varying radial viscosity structure within acceptable limits, the fit between predictions and observations of Earth's geophysical fields can be significantly improved.

Based on the results of synthetic tests, observational datasets are inverted using a 13-layer parameterisation with dynamic topography sampled only at locations with oceanic residual depth measurements. As in the synthetic tests, input densities include a basaltic LLSVP below 2600 km and a calibrated anelasticity model in the upper mantle. CMB excess ellipticity and free-air gravity anomaly constraints are included in the misfit functions as synthetic tests indicate that deep viscosity structure may be better constrained by these datasets (Figure 6.19). As implied by the results of the synthetic tests, initial testing of the optimisation procedure on real data indicated that inverted results are unstable without the introduction of regularisation. In the first instance, regularisation was imposed by rewriting the misfit function to give

$$M = M_S + M_N + M_{\Delta g} + M_C + \lambda_\eta \int \left(\frac{d\eta(z)}{dz} \right)^2 dz, \tag{6.9}$$

where M_S, M_N, $M_{\Delta g}$ and M_C are the misfit functions for dynamic topography, the geoid, the free-

air gravity anomaly and CMB excess ellipticity, respectively (Equation 6.7). The sum of these four values is hereafter referred to as the joint misfit. The last term in Equation 6.9 is a regularisation function (R_1) that penalises the cumulative gradient of the viscosity profile in order to reduce model roughness (Constable et $al.$, 1987). λ_η controls the trade-off between reducing joint misfit and increasing smoothness. $\log_{10}(\lambda_\eta)$ is varied between -6 and 3 in 0.25 increments to find the smoothest model that yields the smallest residual misfit (Figure 6.21).
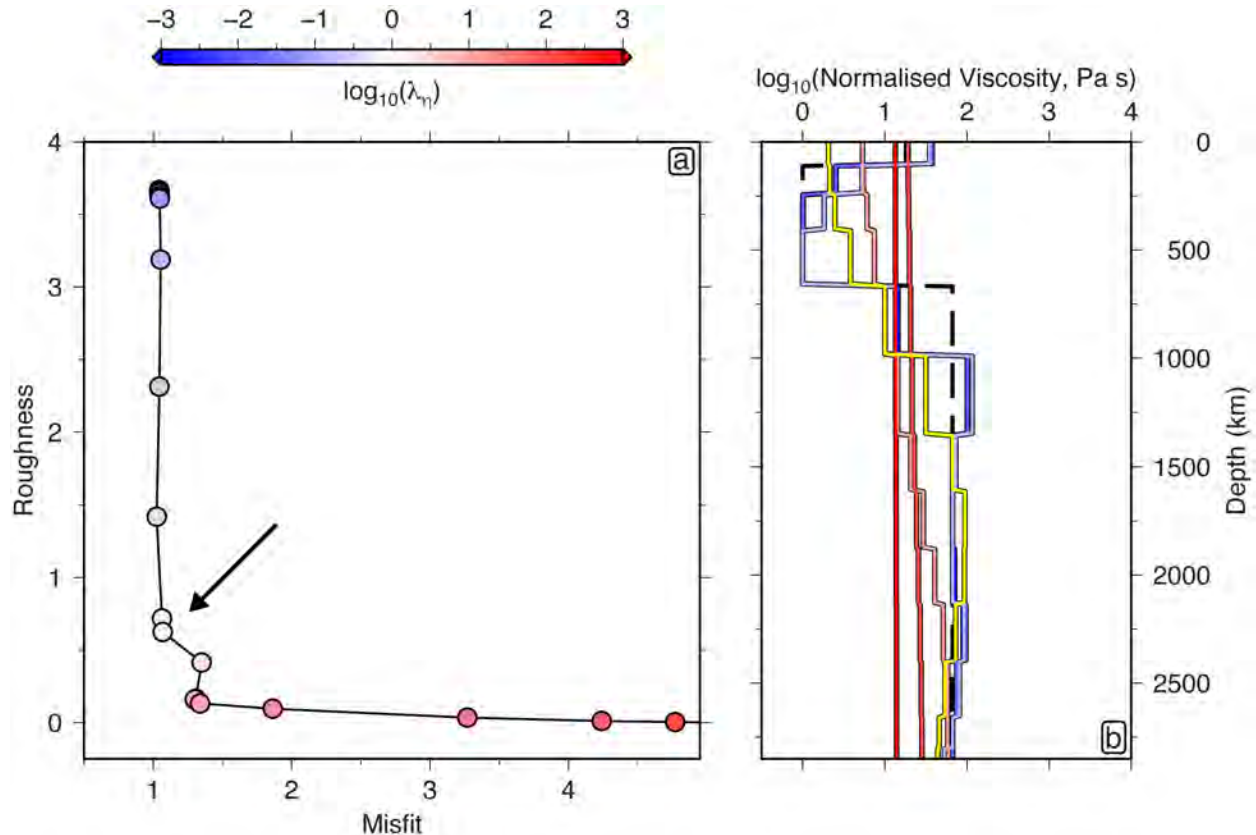
Figure 6.21: Effect of model regularisation. (a) Trade-off between model roughness (R_1) and misfit as a function of λ_η. Black arrow = optimal model. (b) Change in inverted viscosity profile as a function of λ_η. Yellow line = optimal model; black dashed line = starting model (Corrieu et $al.$, 1995); coloured lines = models with $\log_{10}(\lambda_\eta) = -3$–3 in increments of 1.

The optimal trade-off between model roughness and misfit is obtained for $\lambda_\eta \sim 1$. Although the inverted profile is smooth ($R_1 \sim 0.5$), viscosity increases by a factor of ~ 400 between 400 and 1300 km, reaching a peak at 1700 km before decreasing by a factor of ~ 3 towards the CMB. This viscosity structure closely resembles the result obtained by Ricard & Wuming (1991) through regularised inverse modelling of plate velocity, geoid and dynamic topography data. The tomographic models used by these authors to constrain density structure had lower horizontal and vertical resolution than those exploited here. Thus, the good agreement between these results

implies that radial viscosity structure is largely constrained by the longest wavelength features of the Earth's geoid and dynamic topography.

Although the smooth model provides acceptable misfit to the data constraints, geoid and dynamic topography correlations (0.86 and 0.60, respectively) are poorer than those obtained using the SC06 profile. Moreover, the relationship between misfit and model roughness is non-linear as a function of λ_η suggesting that the location and magnitude of viscosity discontinuities are important controls on the misfit. Given the nonlinearity of the problem and the expectation that large jumps in viscosity may occur across phase boundaries, it is not necessarily clear that a smooth model of viscosity is desirable (Sammis & Dein, 1974; Sammis *et al.*, 1977). Subsequently, an alternative method of stabilising the inversion is tested that allows for large viscosity discontinuities and is based on the approach of Steinberger (2016). In this scheme, model solutions that deviate from glacial isostatic adjustment constraints on Earth's viscosity structure are penalised by introducing two additional terms to the misfit function. The first of these penalty functions, $P_{um-tz} = (\eta_{um} - \eta_{tz})^2$, is applied if upper mantle viscosity, η_{um}, in a particular iteration exceeds that of the transition zone, η_{tz}. P_{um-tz} is otherwise set to zero. The second penalty function, $P_{tz-lm} = (\eta_{tz} - \eta_{lm})^2$, penalises models that yield η_{tz} in excess of the lower mantle average, η_{lm}, and is otherwise set to zero. The misfit function to be minimised by Powell's algorithm then becomes

$$M = M_S + M_N + M_{\Delta g} + M_C + P_{um-tz} + P_{tz-lm}. \tag{6.10}$$

To explore the stability of the inverse model, 50 separate optimisations are performed with initial viscosity values in the lithosphere, asthenosphere, transition zone, lower mantle and D'' region that are selected at random subject to the constraint that $\eta_{um} \leqslant \eta_{tz} \leqslant \eta_{lm}$. This mix of Monte Carlo-style sampling and deterministic inversion is applied in an attempt to incorporate the advantages of Powell's algorithm, which can find local minima rapidly, and a probabilistic method that attempts to find the global minimum. This approach avoids assigning too much significance to a single computation and allows a range of acceptable models to be identified.

For the best-fitting model, viscosity increases by a factor of ~ 50 across the 410 km discontinuity (Figure 6.22). Viscosity generally increases further with depth until an additional jump by a factor of 10 at ~ 1000 km. From ~ 1000 km to ~ 2800 km viscosity is constant and approximately two orders of magnitude larger than the upper mantle average. Below ~ 2800 km, viscosity decreases abruptly by $\sim 80\%$. Although the inverted profile predicts less variability in lower mantle viscosity, the main features closely resemble the MFV2 profile obtained by Mitrovica & Forte (2004) through
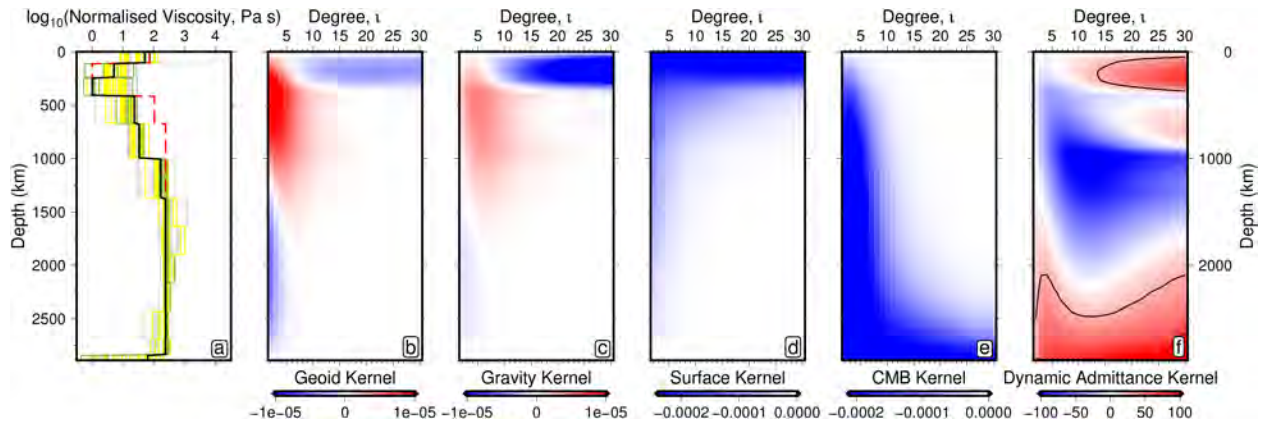
Figure 6.22: Inverted viscosity profile and sensitivity kernels. (a) Inverted viscosity profiles. Black line = best-fitting inverted profile; red dashed line = starting profile for best-fitting inversion; green lines = inverted profiles within 2.5% of the global minimum; yellow lines =inverted profiles within 10% of global minimum. (b) Geoid undulation kernel (m^3 kg^{-1}). (c) Free-air gravity anomaly kernel (mGal m^2 kg^{-1}). (d) Dynamic topography kernel (m^3 kg^{-1}). (e) CMB topography kernel (m^3 kg^{-1}). (f) Dynamic admittance kernel (mGal km^{-1}). Black contour = 30 mGal km^{-1}, the average value in the oceanic realm (Anderson *et al.*, 1973; Crosby *et al.*, 2006; Crosby & McKenzie, 2009).

inverse modelling of both glacial isostatic adjustment and convection-related observables. The range of models that fit within 10% of the global minimum show good agreement in the lower mantle, with an average lower mantle viscosity around 100–300 times higher than that of the asthenosphere. Interestingly, a viscosity jump at 1,000 km is consistently retrieved by the best-fitting models, corroborating the result of Rudolph *et al.* (2015). Recovered upper mantle viscosities are more variable but give the same mean value when averaged between 100 and 400 km. Significantly, the solutions obtained using Equation 6.10 are relatively stable and insensitive to the starting model. This stability suggests that the first order features of the acceptable models (i.e. those that give misfit values within 10% of the global minimum) are robust. Encouragingly, the main features of the viscosity profile are very similar to those obtained in the regularised inversion. However, larger jumps in viscosity are invoked at 660 km and 1000 km.

Joint misfit to the geoid, dynamic topography, free-air gravity anomalies and CMB excess ellipticity data is $\sim$ 40% lower for the best-fitting model than that obtained using the SC06 profile (Figures 6.23). Compared with purely pyrolitic anelastic density models, dynamic topography correlation rises from $r = 0.59$ to $r = 0.62$, geoid correlation increases from $r = 0.86$ to $r = 0.91$ and RMS misfit between geoid predictions and observations decreases by $\sim$ 70%. Furthermore, this inverted viscosity profile improves fit to excess CMB ellipticity (280 m vs. 1960 m) and free-air gravity anomaly constraints, with misfit reductions of $\sim$ 85% and $\sim$ 40%, respectively. Finally,
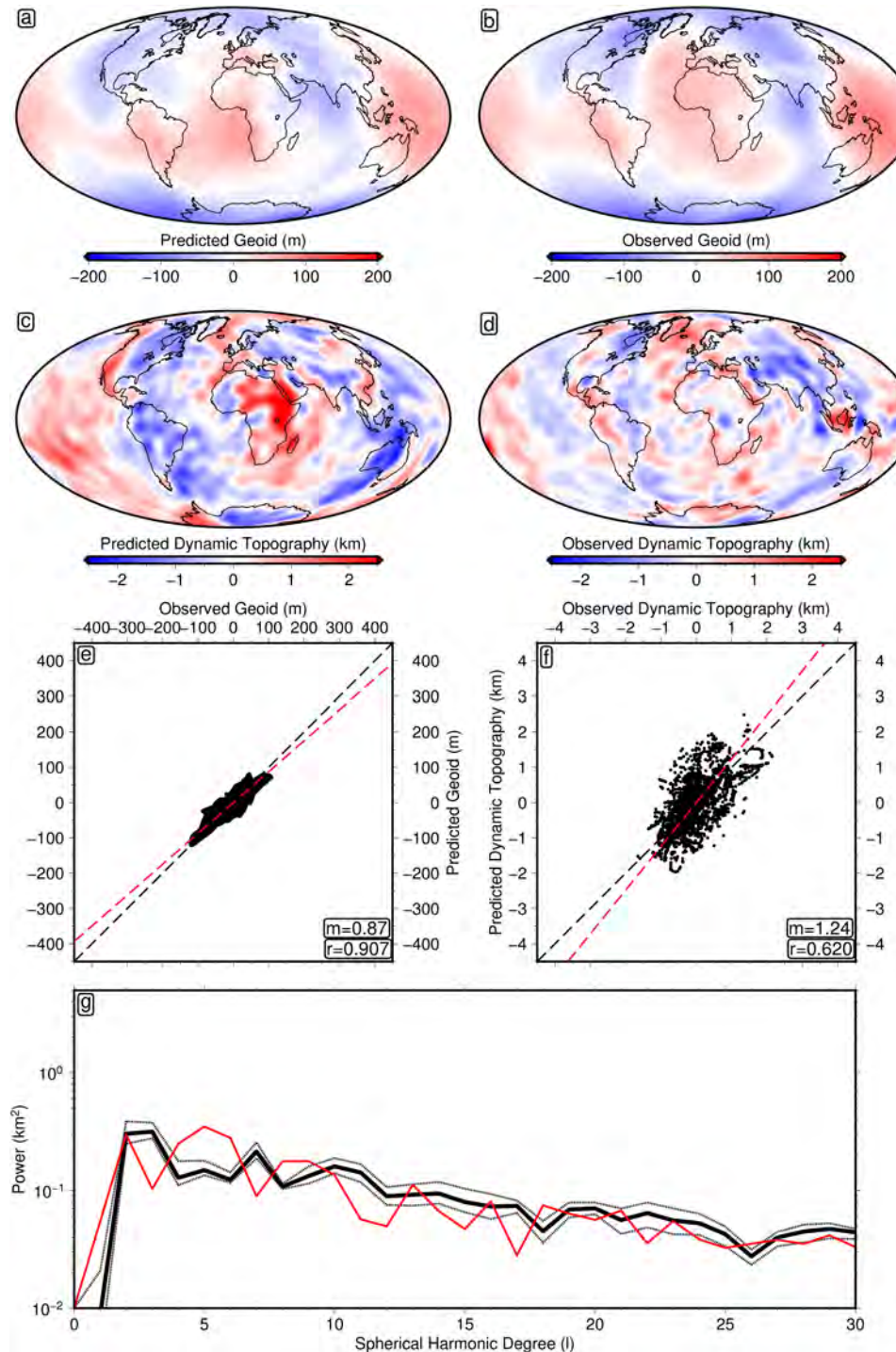
Figure 6.23: Geophysical fields predicted from inverted viscosity profile and density model incorporating anelasticity and dense basal LLSVP. (a) Predicted geoid. (b) Observed geoid (Chambat *et al.*, 2010). (c) Predicted dynamic topography. (d) Observed dynamic topography. (e) Correlation between observed and predicted dynamic topography. (f) Correlation between observed and predicted geoid. (g) Power spectrum of dynamic topography. Solid black line = power spectrum of observational model; dashed black line = maximum and minimum limits of power recovered for damping parameters within the ranges $\lambda_1 = 10^2$–10^4 km^{-2} and $\lambda_2 = 10^{-0.5}$–$10^{0.5}$ km^{-2}; red line = power spectrum of predicted dynamic topography. Fields are calculated using the best-fitting inverted viscosity profile (Figure 6.22) and a hybrid density model including a basaltic layer in the LLSVPs below 2600 km (Figure 6.11c).

these inverted models yield dynamic topography predictions that fit the power spectrum of dynamic topography observations from $l = 2$–30. Significantly, the results demonstrate that, given a reasonable viscosity profile and more accurate input density structure, observations of modest long wavelength dynamic topography can be reconciled with the geoid (*contra* Coltice *et al.*, 2017).

Joint misfit is >10% lower and geoid and dynamic topography correlations are improved by $\sim 5\%$ compared to the regularised model, suggesting that larger jumps in viscosity at 660 km and 1000 km depth are favoured by the available data. Moreover, the agreement between results initialised with different starting profiles suggests that the penalty function approach yields robust results despite the lack of explicit regularisation. The best-fitting model obtained with this method may therefore provide a more accurate representation of Earth's viscosity structure than the model determined by the regularised inversion scheme.

Inversions calculated using the Lau2 density model produce intermediate fits to the dynamic topography and geoid but better fits to free-air gravity anomalies and CMB constraints than other models. A notable feature of these models is that the magnitude of density anomalies inferred in the LLSVP regions are smaller than for models derived from conversion of seismic velocity into density. Improved fit to observed CMB excess ellipticity and free-air gravity anomalies may therefore indicate that density models assuming purely basaltic compositions in the basal layer of LLSVPs overestimate the magnitude of density heterogeneity in the lowermost 300 km of the mantle. If so, anelastic effects in the deep mantle may be underestimated by the Q4 attenuation profile. Alternatively, the composition of the basal layer may be only partly basaltic.

Significantly, if the inversion is repeated using a density structure that does not include a dense basal layer in LLSVP regions, fit to both the geoid and dynamic topography deteriorate, with misfit increasing by $\sim 25\%$. It can therefore be concluded that available data require the presence of significant chemical heterogeneity in the lower portion of these low seismic velocity provinces.

6.4   Testing Model Performance: India

In Chapter 4, a strong correlation between inferred asthenospheric temperature anomalies and observed residual depth anomalies was identified (Figure 4.19). However, unlike other locations, such as the West African Margin, the long wavelength ($\lambda > 730$ km) free-air gravity anomaly over India is uniformly negative; whereas, dynamic topography shows a clear west-east tilt from the
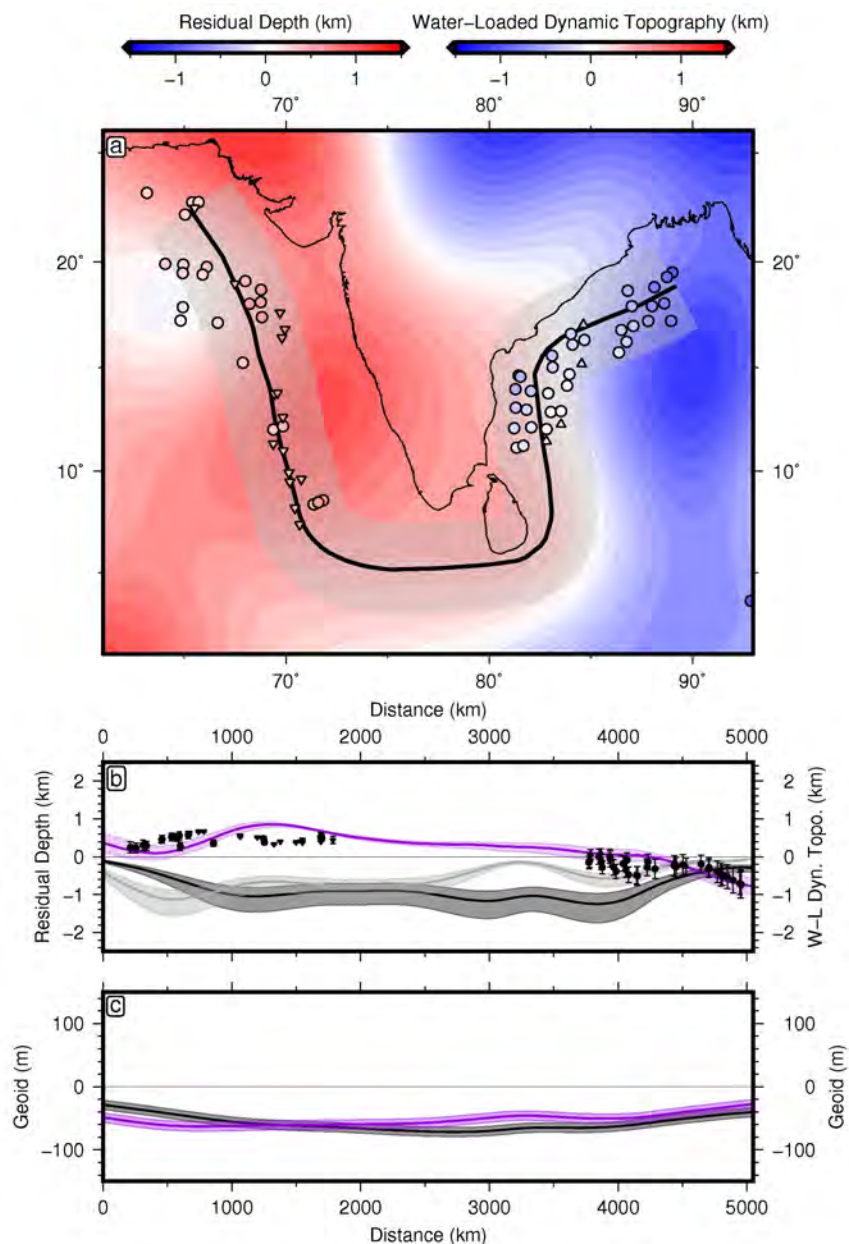
Figure 6.24: Predicted vs. observed dynamic topography and geoid (a) Instantaneous flow prediction using inverted viscosity profile and hybrid density model including a basaltic layer in the LLSVPs below 2600 km. Red/blue colours = high/low predicted dynamic topography (water-loaded); coloured circles and upward/downward-pointing triangles = observed dynamic topography from spherical harmonic representation (l_{max}=30); solid line = transect shown in panels (b) & (c); grey band = coverage of 500 km cross-lines perpendicular to transect. (b) Predicted vs. observed dynamic topography along transect. Solid circles, upward/downward-pointing triangles = observed dynamic topography from spherical harmonic representation (l_{max}=30); purple line = instantaneous flow prediction; error envelopes = 1σ along 500 km cross-lines perpendicular to transect; black line = observed long-wavelength ($\lambda \geqslant 730$ km) gravity anomaly of Förste *et al.* (2011) scaled using admittance (Z) of 35 mGal km^{-1}; grey line = instantaneous flow prediction of long wavelength gravity anomaly ($\lambda \geqslant 730$ km) scaled using $Z = 35$ mGal km^{-1}; error envelopes = $25 \leqslant Z \leqslant 45$ mGal km^{-1}. (c) Predicted vs. observed geoid along transect. Black line = long-wavelength geoid ($\lambda \geqslant 730$ km; Förste *et al.*, 2011); purple line = instantaneous flow prediction; error envelopes = 1σ error in hydrostatic correction (Nakiboglu, 1982; Chambat *et al.*, 2010).

Arabian Sea across Peninsular India to the Bay of Bengal. Here, predictions of the instantaneous flow model developed in Section 6.3.3 are tested locally by revisiting the previously identified lack of correlation between residual depth anomalies and long wavelength gravity across the Indian Peninsula (Figure 4.3b).

Predicted dynamic topography accurately recreates the strong west-east gradient in observed dynamic topography across the peninsula (Figure 6.24a). Although the transition from positive to negative dynamic topography occurs further east in the predictions, $\sim 70\%$ of the residual depth points fit within error (Figure 6.24b). By contrast dynamic topography estimates obtained by applying constant values of admittance to observed and predicted gravity anomalies agree relatively well with each other but fit $< 20\%$ of dynamic topography observations within error (Figure 6.24b). The observed geoid low over the Indian Ocean is well recovered by the predicted geoid undulations, with both fields retrieving values $\leqslant -40$ m over the whole region.

Dynamic topography and gravity have differing sensitivity to density anomalies as a function of depth and spherical harmonic degree, potentially resulting in very different integrated admittance values (Figure 6.3; Colli *et al.*, 2016). The breakdown of a simple relationship between free-air gravity anomalies and dynamic topography over India may therefore relate to the anti-correlation between negative density anomalies in the asthenosphere and positive density anomalies in the deep mantle (Figure 6.11). By contrast, negative density anomalies in the asthenosphere beneath the West African Margin are underlain by deep mantle density anomalies of the same sign.

These calculations suggest that it is indeed possible to reconcile observations and predictions of dynamic topography with the large gravity and geoid low observed across the Indian Peninsula. Moreover, these results emphasise the importance of shallow density anomalies for maintaining dynamic topography and demonstrate that substantial long wavelength free-air gravity anomaly and geoid lows can coincide with substantial positive dynamic topography at shorter wavelengths (cf. Molnar *et al.*, 2015). Finally, this analysis implies that application of a single value of admittance to scale long wavelength free-air gravity anomalies into dynamic topography, while valid in some cases, cannot be implemented globally.

6.5   Discussion

The modelling undertaken here suggests that the discrepancy between observations and previous predictions of dynamic topography can be resolved by including asthenospheric density anomalies,

accurately accounting for anelasticity and assuming the basal sections of LLSVPs are $\sim 1\%$ denser than their surroundings. Significantly, models that fit dynamic topography observations also generate geoid undulations and CMB excess ellipticities that are consistent with observations. However, given the large uncertainties in the density and viscosity structure of the Earth, it may be possible to reconcile predictions and observations of dynamic topography without appealing to geochemical heterogeneity in the deep mantle.

First, the magnitude of lower mantle density anomalies predicted from seismic tomographic models is dependent on V_S anomaly amplitudes. These amplitudes are sensitive to the regularisation applied in the tomographic inversion procedure and will therefore reflect modelling choices, as well as shear wave velocity heterogeneity in the Earth's mantle. The distribution of spectral power as a function of spherical harmonic degree will also be affected by amplitude damping which will, in turn, lead to dynamic topography predictions with different spectral properties. Although, the combination of seismic tomographic models used here is likely to be amongst the more accurate representations of mantle V_S structure, it would be useful to test the degree to which the results presented here depend on V_S model choices. Secondly, considerable uncertainty remains regarding the strength of anelastic effects in the lower mantle. The Q4 profile of Cammarano *et al.* (2003) predicts relatively strong attenuation in the deep mantle, with $Q_S^{-1} \sim 5 \times 10^{-2}$ beneath 2500 km compared to $\sim 2 \times 10^{-2}$ predicted by other profiles. However, a recent study suggests that Q_S^{-1} may be as high as 9×10^{-2} within the African LLSVP (Liu & Grand, 2018). If lower mantle anelastic effects are indeed stronger than predicted here, less strong chemically derived density heterogeneity is required within LLSVPs to explain dynamic topography observations. Finally, it is possible that consideration of the deflections of the 410 km and 660 km phase boundaries may help reconcile predictions and observations of dynamic topography. If strong viscosity contrasts exist across these boundaries, convection models predict significant perturbation of these interfaces (Thoraval *et al.*, 1995). Accommodation of convectively induced deflections at these boundaries would reduce deformation at the Earth's surface, leading to more modest lower mantle-derived, long wavelength contributions. Nevertheless, although these alternative hypotheses are plausible, it is unclear that they are sufficient to explain the magnitude of the observed discrepancy.

Instead, the hypothesis that the deepest sections of the LLSVP are negatively buoyant is more appealing for several reasons. First, it is consistent with the findings of tidal tomographic inversions that require an average density anomaly of $\sim 1\%$ in the lower sections of the LLSVPs to explain body tide data (Lau *et al.*, 2017). Secondly, it provides a mechanism for stabilising these structures

over long periods of time, as inferred from palaeomagnetic observations (Torsvik *et al.*, 2008; Conrad *et al.*, 2013). Finally, the presence of a dense basaltic layer would provide a mechanism for preserving the considerable geochemical heterogeneity inferred from ocean island basalts since this material would be less easily entrained by convective upwellings (Hofmann & White, 1982; Sobolev *et al.*, 2007; Mulyukova *et al.*, 2015).

6.6   Summary

Observations of Earth's present-day dynamic topography consistently retrieve lower long wavelength amplitudes than predicted by geodynamic models. This major discrepancy has provoked much debate within the geodynamic community, with some studies suggesting that the ± 500 m of long wavelength dynamic topography determined through spherical harmonic expansion of observations cannot be reconciled with the spectral characteristics of the geoid.

Previous geodynamic predictions of dynamic topography, in addition to excluding the upper 220–350 km of the Earth's mantle, generally use simple conversions between seismic wave velocities and density to determine internal buoyancy structure. While this approach yields good fit to the geoid, long wavelength dynamic topography is overpredicted and short wavelength dynamic topography is underpredicted.

Inclusion of the uppermost mantle in instantaneous flow predictions yields improved correlation with observed geoid and dynamic topography; however, predicted amplitudes are two to three times larger than observed. However, when the calibrated anelasticity model derived in Chapter 5 is substituted in the upper mantle and an attenuation model applied beneath it, the excessive amplitudes of the geophysical fields are reduced while correlations remain essentially unchanged. The improvement in amplitude misfit suggests that it is important to accurately account for the non-linear reduction of V_S at high temperature due to anelasticity. However, geoid and dynamic topography amplitudes remain $\sim 150\%$ larger than the observed values at degree two.

It has been proposed that at least the basal portions of the LLSVP regions are chemically dense. Geodynamic models that include compositional density heterogeneity in the lower 300 km of the LLSVP regions yield peak-to-peak amplitudes of dynamic topography and geoid that match observations at all wavelengths. Furthermore, geoid correlation is improved compared to models that do not include chemical heterogeneity. This result demonstrates that the observed long wavelength

geoid is compatible with modest degree two dynamic topography provided the basal sections of LLSVPs are $\sim 1\%$ denser than their surroundings.

The details of Earth's radial viscosity structure are not well constrained, with numerous studies deriving significantly different profiles (Figure 6.15). Inverse models are therefore carried out to determine whether the revised dynamic topography database, combined with existing geoid, gravity and CMB topography measurements, can be used to improve constraint on viscosity variation with depth. Synthetic tests demonstrate that the inverted viscosity profiles are not significantly affected by data errors and that acceptable fit to complex viscosity structures can be obtained with 8– 13 equal thickness layers. Randomisation of initial starting profiles suggests that although the inversion may converge on local minima, the global minimum can be reached by running a suite of inversions with different starting profiles. Applying the inversion to real data demonstrates that it is possible to simultaneously fit the geoid and dynamic topography at all wavelengths with a plausible viscosity profile, whilst satisfying CMB topography and free-air gravity anomaly constraints. This result further corroborates the finding that modest long wavelength dynamic topography and geoid observations can be reconciled.

Finally, the relationship between dynamic topography, free-air gravity anomalies and geoid undulations across the Indian Peninsula are reassessed to test the predictions of updated instantaneous flow calculations. The calculations accurately predict the west-east gradient in dynamic topography across the peninsula that is observed in both offshore and onshore topography. Significantly, the lack of coherence observed between gravity and topography at long wavelengths is accurately recreated, demonstrating that high-amplitude positive dynamic topography can coincide with substantial negative long wavelength free-air gravity anomalies. This result reaffirms the importance of asthenospheric density anomalies in generating observed dynamic topography.

Chapter 7

Conclusions

7.1 Summary

Although it is well established that viscous stresses imposed by mantle convection modulate Earth's surface topography, there remains debate about the magnitude and wavelength of this deformation. Over the past 30 years, theoretical advances, increased computing power and ever-improving seismological constraint on Earth's density structure, have spurred the development of complex, three-dimensional simulations of mantle convection. Although the geoid predicted by these models is broadly consistent with satellite data, until recently, dynamic topography predictions remained largely unconstrained due to a lack of robust observations (Flament *et al.*, 2013).

The last 30 years has also seen a rapid proliferation of oceanic seismic reflection datasets, driven largely by petroleum exploration. The high quality of these data has allowed sedimentary and oceanic crustal thickness variations to be carefully mapped throughout the global ocean, permitting accurate measurement of residual depth anomalies (Winterbourne *et al.*, 2014; Hoggard *et al.*, 2016, 2017). These anomalies provide the strongest constraint on the spatial pattern of present-day dynamic topography.

The existing water-loaded basement depth dataset is supplemented with a further 123 measurements in Chapter 2. This new data, combined with an updated heat flow database, is used to determine the average thermal structure of oceanic lithosphere by minimising the misfit between these observations and the predictions of a series of increasingly complex models. The optimal model predicts a mantle potential temperature of $1304 \pm 60°C$ and a plate thickness of 135 ± 30 km, consistent with geochemical and seismological constraints. The base of the seismogenic zone is predicted to coincide with the $700°C$ isotherm, towards the upper end of experimental constraints, while integrated oceanic heat flow is ~ 28 TW.

In Chapter 3, subsidence predicted by the optimal model is subtracted from water-loaded basement

depths to yield a revised residual depth database. The additional measurements fill significant gaps in the existing data coverage and are generally consistent with previously inferred regional anomalies. Finally, this dataset is combined with updated ship-track bathymetric constraints and onshore long wavelength gravity anomalies to create a spherical harmonic representation of observed dynamic topography. Spectral analysis of the revised dataset demonstrates that the fundamental disagreement between observations and model predictions of dynamic topography initially identified by Hoggard *et al.* (2016) remains. Predicted degree two dynamic topography is $\sim 250\%$ larger than observations whilst observed short wavelength dynamic topography is not recreated by the models.

Having augmented and improved constraints on observed dynamic topography, in Chapter 4, the Cenozoic landscape evolution of Peninsular India is investigated to place constraints on the spatio-temporal pattern of convectively maintained vertical motions. Through analysis of residual depths offshore and long wavelength topography onshore, an eastward tilt can be identified across the Indian Peninsula, extending over 2,000 km from the Arabian Sea to the Bay of Bengal. Admittance between free-air gravity and topography yields an elastic thickness of ~ 10 km for the peninsular region, suggesting that the asymmetry cannot be flexurally maintained. To further investigate the timing and mechanism of tilting, inverse modelling of a database of 530 rivers profiles is undertaken, with erosional parameters calibrated against independent geological uplift rate constraints. These drainage inversions suggest that regional tilting was initiated by uplift in the south of the peninsula at *ca.* 30 Ma, before uplift propagated north and eastwards, continuing up to the present day at rates of up to 0.1 mm a^{-1}. This uplift history is corroborated by low-temperature thermochronological measurements, the sedimentary flux history of the Krishna-Godavari delta and sequence stratigraphic constraints along fringing margins. Flexural modelling suggests $\leqslant 30\%$ of the inverted rock uplift could be explained through onshore denudation and sediment loading offshore. However, strong anti-correlation exists between residual depth measurements and shear wave speeds observed beneath the Indian Plate in a number of seismic tomographic models. Isostatic calculations suggest that the observed shear wave anomalies are consistent with temperature perturbations of $\pm 100^{\circ}$C within a 200 ± 25 km-thick asthenospheric channel. It is speculated that late Cenozoic dynamic uplift may be linked to the rapid post-35 Ma slowdown in Indian plate velocities. Initiation of western margin uplift may reflect progressive impingement of anomalously hot mantle beneath the Indian Peninsula once northeastward asthenospheric flow began to outpace plate motion following hard collision between India and Eurasia.

Chapter 5 demonstrates that short wavelength discrepancy between predictions and observations of

dynamic topography can be attributed to the excision of density anomalies in the upper ~ 300 km of the mantle in most geodynamic models. Removal of the globally averaged plate cooling signal from seismic tomographic models reveals that the strongest anti-correlation between residual depth anomalies and shear wave velocities occurs when anomalies are stacked between ~ 50 and 250 km. Inclusion of the asthenosphere is therefore necessary to accurately match observed dynamic topography. By calibrating an experimentally determined anelasticity model against a range of constraints, including the thermal structure of the optimal plate model recovered in Chapter 2, a V_S-temperature conversion method is developed that accurately constrains the thermal state of the upper mantle for multiple seismic tomography models. Residual depths are then predicted by assuming that density anomalies are compensated at the base of a low-viscosity asthenospheric channel. For the model of Schaeffer & Lebedev (2013), residual depth anomaly predictions fit $> 25\%$ of residual anomaly observations and yield good spatial correlations ($r \sim 0.45$) when the channel is 150 ± 50 km thick. Although results are poorer for other tomographic models, all asthenosphere-only isostatic calculations provide significantly better fit to short wavelength residual depths than the best-fitting predictive model. These results indicate that the asthenosphere plays a dominant role in the generation of oceanic dynamic topography and that constraints on palaeo-mantle temperature from basalt geochemistry may be used to reconstruct past dynamic topography.

The overall discrepancy between predictions and observations of dynamic topography is investigated in Chapter 6. This chapter shows that using linear conversion factors to scale shear wave velocity anomalies into density anomalies is flawed due to significant anelasticity in the mantle, especially in the asthenosphere. Although correlations between predicted and observed geoid and dynamic topography are strong when anharmonic conversions are used, predicted amplitudes are 2–3 times larger than observed. Inclusion of anelastic effects in input density models leads to significant improvements in the amplitude fit between predicted and observed geophysical fields; however, degree two dynamic topography remains $\sim 100\%$ higher than observed. By contrast, models that include geochemically induced negative buoyancy anomalies in the lower 300 km of the large low shear wave velocity provinces (LLSVPs), as constrained by tidal tomography models, largely resolve the remaining long wavelength discrepancy. Moreover, these models improve geoid correlation relative to models that assume an isochemical pyrolitic mantle; however, predicted geoid amplitudes remain $\sim 40\%$ higher than observations. Viscosity inversions are carried out that are constrained by dynamic topography, geoid, core-mantle boundary (CMB) topography and gravity observations, revealing that all geophysical fields can be reconciled with a plausible radial profile. Lower misfits are recovered in inversions using density models with dense LLSVPs, suggesting that

geochemical heterogeneity in the lowermost mantle is required by the data. The ability to fit the entire observation-based dynamic topography spectrum and maintain fit to the geoid challenges assertions to the contrary made in previous studies. Finally, inverted density and viscosity models are tested regionally by revisiting relationships between dynamic topography, free-air gravity anomalies and geoid undulations across the Indian Peninsula. Both the observed long wavelength negative free-air gravity anomaly and west-east gradient in dynamic topography are accurately recovered by the revised instantaneous flow model. This result underlines the dominant role of asthenospheric temperature in maintaining dynamic topography and demonstrates that high amplitude dynamic topography can coincide with free-air gravity anomalies of opposite sign.

7.2   Further Work

The research presented here refines existing constraints on dynamic topography in the oceanic realm. Additional seismic reflection and refraction surveys, outwith continental margins, would further improve this dataset but oceanic dynamic topography is now relatively well constrained. By contrast, dynamic topography in continental regions remains poorly known owing to a lack of constraints on the complex density structure of the continental lithosphere. Uncertainties in crustal thickness, lithospheric thickness and chemical composition typically propagate into km-scale errors in isostatic calculations, preventing determination of accurate residual topography. Joint inversion of receiver function and surface wave dispersion measurements yield useful constraints on the relative thicknesses and seismic velocity structure of continental crust and lithosphere, but wave speeds rarely provide unequivocal evidence for compositional versus thermal heterogeneity (e.g. Julià *et al.*, 2009). A promising approach is the use of multi-dimensional thermochemical inversions that reduce the non-uniqueness inherent in seismic velocity structure interpretation by integrating other geochemical and geophysical data constraints, such as xenolith compositions and gravity gradients, alongside more traditional seismic velocity information (e.g. Afonso *et al.*, 2013a,b; Jones *et al.*, 2017). These inversions solve directly for the density structure and layer thicknesses of the continental crust and lithosphere, thereby obviating the use of uncertain, empirical conversions from seismic velocity to temperature and density. The disadvantage of these complex inversions is that they are computationally expensive, limiting their application to regional studies. Further, their reliability is dependent on availability of high-quality geochemical and geophysical data throughout the study region, a condition that is rarely met outside of Western Europe, Australia and North America. Nevertheless, integration of results from these inversions with more traditional multi-

observable studies in areas with poorer data coverage should significantly improve estimates of present-day continental dynamic topography.

Although consideration has been given here to the spatio-temporal evolution of dynamic topography across Peninsular India, a more global assessment of the time-dependence of dynamic topography is desirable. Essential to this endeavour will be the development of a comprehensive database of observations that constrain convective vertical motions back through geological time. The stratigraphy of passive continental margins constitutes a relatively complete archive of changing sea-level through at least Late Cenozoic times. Provided sufficiently narrow age bounds can be placed on different sedimentary packages, analysis of a global database should allow variations in accommodation space due to eustasy to be separated from those caused by vertical motion of the Earth's surface. Global analysis of seaward-dipping reflectors may add further constraints on palaeo-dynamic topography, as these lava flows often record palaeo-sea level via a transition from sub-aerial to submarine eruption style that is observable in seismic reflection profiles (Buck, 2017). Further, the relative success of simple isostatic scaling between dynamic topography and asthenospheric temperature anomalies demonstrated here, suggests that palaeo-mantle temperature derived from oceanic crustal thickness and rare earth element inversion may provide a useful proxy for palaeo-dynamic topography (McKenzie & O'Nions, 1991; Van Avendonk *et al.*, 2017). Construction of this multi-observable palaeo-dynamic topography database will allow much stronger constraints to be placed on the lateral and radial variation of Earth's viscosity structure, secular variation in the cooling and convection of the mantle, and the relationship between plate motion and dynamic topography.

Finally, the geodynamic modelling undertaken in this work was necessarily simplified to carry out multi-observable inversions. Although, to first order, dynamic topography is controlled by radial viscosity variation, lateral viscosity variations (LVVs) may modify the signal, particularly at shorter wavelengths (Yang & Gurnis, 2016). A detailed assessment of the effect of LLVs on recovered dynamic topography could be made by feeding the adapted density model and inverted radial viscosity profile developed here into a three-dimensional mantle convection code that can effectively handle large lateral variations in viscosity (e.g. ASPECT). This modelling would also provide an independent test of the extent to which the input model is consistent with other observables like surface heat flux, plate motions and rates of vertical motion. Further work should also be undertaken to refine the inversion scheme presented here and to test the robustness of results to different density inputs based on other tomographic models and compositional components. Optimisation of the

instantaneous flow calculations may also allow for the application of Bayesian inversion techniques, such as transdimensional reversible jump Markov chain Monte Carlo algorithms. Recent adaptation of these algorithms allows polynomial functions within individual layers in addition to jumps across partitions. Given that viscosity is likely to vary smoothly with temperature and pressure between mantle phase transitions but could potentially change dramatically across these boundaries, inverting the relevant geophysical data with these algorithms may allow for recovery of a more accurate viscosity profile and better constraint on uncertainties.

References

Acton, C. E., Priestley, K., Gaur, V. K., & Rai, S. S., 2010. Group velocity tomography of the Indo-Eurasian collision zone, *J. Geophys. Res. Solid Earth*, **115**(B12), B12335.

Acton, C. E., Priestley, K., Mitra, S., & Gaur, V. K., 2011. Crustal structure of the Darjeeling-Sikkim Himalaya and southern Tibet, *Geophys. J. Int.*, **184**(2), 829–852.

Afonso, J., Fullea, J., Yang, Y., Connolly, J., & Jones, A., 2013. 3-D multi-observable probabilistic inversion for the compositional and thermal structure of the lithosphere and upper mantle. II: General methodology and resolution analysis, *J. Geophys. Res. Solid Earth*, **118**(4), 1650–1676.

Afonso, J. C., Ranalli, G., & Fernàndez, M., 2007. Density structure and buoyancy of the oceanic lithosphere revisited, *Geophys. Res. Lett.*, **34**(10), 2–6.

Afonso, J. C., Fullea, J., Griffin, W. L., Yang, Y., Jones, A. G., Connolly, J. A. D., & O'Reilly, S. Y., 2013. 3-D multiobservable probabilistic inversion for the compositional and thermal structure of the lithosphere and upper mantle. I: a priori petrological information and geophysical observables, *J. Geophys. Res. Solid Earth*, **118**(5), 2586–2617.

Agrawal, P. K. & Pandey, O. P., 2004. Unusual lithospheric structure and evolutionary pattern of the cratonic segments of the South Indian shield, *Earth Planets Space*, **56**(2), 139–150.

Airy, G. B., 1855. On the Computation of the Effect of the Attraction of Mountain-Masses, as Distributing the Apparent Astronomical Latitude of Stations in Geodetic Surveys, *Phil. Trans. R. Soc.*, **145**, 101–104.

Ajay, K. K. & Chaubey, A. K., 2008. Depth anomalies in the Arabian Basin, NW Indian Ocean, *Geo-Mar. Lett.*, **28**, 15–22.

Alappat, L., Frechen, M., Sree Kumar, S., Suresh Babu, D., Ravur, R., & Tsukamoto, S., 2015. Evidence of Late Holocene shoreline progradation in the coast of Kerala, South India obtained from OSL dating of palaeo-beach ridges, *Geomorphology*, **245**, 73–86.

Ambili, V. & Narayana, A., 2014. Tectonic effects on the longitudinal profiles of the Chaliyar River and its tributaries, southwest India, *Geomorphology*, **217**, 37–47.

An, Z., Kutzbach, J. E., Prell, W. L., & Porter, S. C., 2001. Evolution of Asian monsoons and phased uplift of the Himalaya-Tibetan plateau since Late Miocene times, *Nature*, **411**(6833), 62–66.

Anderson, D. L., 2011. Hawaii, boundary layers and ambient mantlegeophysical constraints, *J. Pet.*, **52**(7-8), 1547–1577.

Anderson, D. L. & Sammis, C., 1970. Partial melting in the upper mantle, *Phys. Earth Planet. In.*, **3**, 41–50.

Anderson, R. N., McKenzie, D., & Sclater, J. G., 1973. Gravity, bathymetry and convection in the earth, *Earth Plan. Sci. Lett.*, **18**(3), 391–407.

Athy, L. F., 1930. Density, Porosity, and Compaction of Sedimentary Rocks, *Nat. Geosci.*, **14**(1), 1–24.

Auer, L., Becker, T. W., Boschi, L., & Schmerr, N., 2015. Thermal structure, radial anisotropy, and dynamics of oceanic boundary layers, *Geophys. Res. Lett.*, **42**(22), 9740–9749.

Backus, G. & Gilbert, F., 1970. Uniqueness in the inversion of inaccurate gross earth data, *Phil. Trans. R. Soc. A*, **266**(1173), 123–192.

Bagley, B. & Revenaugh, J., 2008. Upper mantle seismic shear discontinuities of the Pacific, *J. Geophys. Res. Solid Earth*, **113**(B12), B12301.

Banerjee, P., 2000. Holocene and Late Pleistocene relative sea level fluctuations along the east coast of India, *Mar. Geol.*, **167**, 243–260.

Barreto, A. M. F., Bezerra, F. H. R., Suguio, K., Tatumi, S. H., Yee, M., Paiva, R. P., & Munita, C. S., 2002. Late Pleistocene marine terrace deposits in northeastern Brazil: sea-level change and tectonic implications, *Palaeogeog. Palaeoclim., Palaeoecol.*, **179**, 57–69.

Beauvais, A. & Chardon, D., 2013. Modes, tempo, and spatial variability of Cenozoic cratonic denudation: The West African example, *Geochem. Geophys. Geosyst.*, **14**(5), 1590–1608.

Beauvais, A., Bonnet, N. J., Chardon, D., Arnaud, N., & Jayananda, M., 2016. Very long-term stability of passive margin escarpment constrained by $^{40}Ar/^{39}Ar$ dating of K-Mn oxides, *Geology*, **44**(4), 299–302.

Becker, J. J., Sandwell, D. T., Smith, W. H. F., Braud, J., Binder, B., Depner, J., Fabre, D., Factor, J., Ingalls, S., Kim, S.-H., Ladner, R., Marks, K., Nelson, S., Pharaoh, A., Trimmer, R., Von Rosenberg, J., Wallace, G., & Weatherall, P., 2009. Global Bathymetry and Elevation Data at 30 Arc Seconds Resolution: SRTM30_PLUS, *Mar. Geod.*, **32**(4), 355–371.

Becker, T., 2002. A comparison of tomographic and geodynamic mantle models, *Geochem. Geophys. Geosyst.*, **3**(1), 1003.

Becker, T. W., 2008. Azimuthal seismic anisotropy constrains net rotation of the lithosphere, *Geophys. Res. Lett.*, **35**(5), L05303.

Becker, T. W. & Faccenna, C., 2011. Mantle conveyor beneath the Tethyan collisional belt, *Earth Plan. Sci. Lett.*, **310**(3-4), 453–461.

Becker, T. W. & O'Connell, R. J., 2001. Predicting plate velocities with mantle circulation models, *Geochem. Geophys. Geosyst.*, **2**(12), 1060.

Beghein, C., Yuan, K., Schmerr, N., & Xing, Z., 2014. Changes in Seismic Anisotropy Shed Light on the Nature of the Gutenberg Discontinuity, *Science*, **343**(6176), 1237–1240.

Behera, L., 2011. Crustal tomographic imaging and geodynamic implications toward south of Southern Granulite Terrain (SGT), India, *Earth Plan. Sci. Lett.*, **309**(1-2), 166–178.

Behn, M. D., Hirth, G., & Ii, J. R. E., 2009. Implications of grain size evolution on the seismic structure of the oceanic upper mantle, *Earth Plan. Sci. Lett.*, **282**(1-4), 178–189.

Benisek, A., Kroll, H., Dachs, & Edgar, 2012. The heat capacity of fayalite at high, *Am. Mineral.*, **97**, 657–660.

Berman, R. G., 1988. Internally-consistent thermodynamic data for minerals in the system $Na_2O-K_2O-CaO-MgO-FeO-Fe_2O_3-Al_2O_3-SiO_2-TiO_2-H_2O-CO_2$, *J. Pet.*, **29**(2), 445–522.

Berman, R. G. & Aranovich, L. Y., 1996. Optimized standard state and solution properties of minerals .1. Model calibration for olivine, orthpyroxene, cordierite, garnet, ilmenite in the system $FeO-MgO-CaO-Al_2O_3-TiO_2-SiO_2$, *Contrib. Min. Pet.*, **126**(1-2), 1–24.

Bodin, P. & Horton, S., 2004. Source parameters and tectonic implications of aftershocks of the Mw 7.6 Bhuj earthquake of 26 January 2001, *Bull. Seismol. Soc. Am.*, **94**(3), 818–827.

Boettcher, M. S., Hirth, G., & Evans, B., 2007. Olivine friction at the base of oceanic seismogenic zones, *J. Geophys. Res. Solid Earth*, **112**(1), 1–13.

Bonnet, N. J., Beauvais, A., Arnaud, N., Chardon, D., & Jayananda, M., 2014. First $^{40}Ar/^{39}Ar$ dating of intense Late Palaeogene lateritic weathering in Peninsular India, *Earth Plan. Sci. Lett.*, **386**, 126–137.

Bonnet, N. J., Beauvais, A., Arnaud, N., Chardon, D., & Jayananda, M., 2016. Cenozoic lateritic weathering and erosion history of peninsular India from $^{40}Ar/^{39}Ar$ dating of supergene K-Mn oxides, *Chem. Geol.*, **446**, 33–53.

Borah, K., Rai, S. S., Priestley, K., & Gaur, V. K., 2014. Complex shallow mantle beneath the Dharwar Craton inferred from Rayleigh wave inversion, *Geophys. J. Int.*, **198**(2), 1055–1070.

Bouhifd, M. A., Andrault, D., Fiquet, G., & Richet, P., 1996. Thermal expansion of forsterite up to the melting point, *Geophys. Res. Lett.*, **23**(10), 1143–1146.

Bozdağ, E., Peter, D., Lefebvre, M., Komatitsch, D., Tromp, J., Hill, J., Podhorszki, N., & Pugmire, D., 2016. Global adjoint tomography: first-generation model, *Geophys. J. Int.*, **207**(3), 1739–1766.

Braun, J., Robert, X., & Simon-Labric, T., 2013. Eroding dynamic topography, *Geophys. Res. Lett.*, **40**(8), 1494–1499.

Breton, T., Nauret, F., Pichat, S., Moine, B., Moreira, M., Rose-Koga, E. F., Auclair, D., Bosq, C., & Wavrant, L.-M., 2013. Geochemical heterogeneities within the Crozet hotspot, *Earth Plan. Sci. Lett.*, **376**, 126–136.

Brocher, T. M., 2005. Empirical relations between elastic wavespeeds and density in the Earth's crust, *Bull. Seism. Soc. Am.*, **95**(6), 2081–2092.

Brown, E. & Lesher, C., 2016. REEBOX PRO: A forward model simulating melting of thermally and lithologically variable upwelling mantle, *Geochem. Geophys. Geosyst.*, **17**, 3929–3968.

Broyden, C. G., Dennis, J. E., & Moré, J. J., 1973. On the Local and Superlinear Convergence of Quasi-Newton Methods, *IMA J. Appl. Math.*, **12**(3), 223–245.

Brückner, H., 1987. New Data on the Evolution of Konkan (Western Ghats), in *Exploration in the Tropics*, edited by V. S. Datye, pp. 173–184, Prof. K. R. Dikshit Felicitation Volume Committee, 1987, Pune.

Brückner, H., 1992. Aspects of weathering and peneplanation in Southern India, *Z. Geomorph.*, **91**(1), 43–66.

Bruinsma, S. L., Förste, C., Abrikosov, O., Lemoine, J.-M., Marty, J.-C., Mulet, S., Rio, M.-H., & Bonvalot, S., 2014. ESA's satellite-only gravity field model via the direct approach based on all GOCE data, *Geophys. Res. Lett.*, **41**(21), 7508–7514.

Bry, M. & White, N., 2007. Reappraising elastic thickness variation at oceanic trenches, *J. Geophys. Res. Solid Earth*, **112**(B8), B08414.

Buck, W. R., 2017. The role of magmatic loads and rift jumps in generating seaward dipping reflectors on volcanic rifted margins, *Earth Plan. Sci. Lett.*, **466**, 62–69.

Buck, W. R., Small, C., & Ryan, W. B. F., 2009. Constraints on asthenospheric flow from the depths of oceanic spreading centers: The East Pacific Rise and the Australian-Antarctic discordance, *Geochem. Geophys. Geosyst.*, **10**(9), 1–23.

Buffler, R. T. & Sawyer, D. S., 1985. Distribution of Crust and Early History, Gulf of Mexico Basin, *Gulf Coast Ass. Geol. Soc. Trans.*, **35**, 333–344.

Bunge, H.-P., Richards, M. A., & Baumgardner, J. R., 1996. Effect of depth-dependent viscosity on the planform of mantle convection, *Nature*, **379**(6564), 436–438.

Bunge, H.-P., Hagelberg, C. R., & Travis, B. J., 2003. Mantle circulation models with variational data assimilation: inferring past mantle flow and structure from plate motion histories and seismic tomography, *Geophys. J. Int.*, **152**(2), 280–301.

Burckle, L. H., 1989. Distribution of diatoms in sediments of the northern Indian Ocean: Relationship to physical oceanography, *Mar. Micropal.*, **15**(1-2), 53–65.

Burgos, G., Montagner, J. P., Beucler, E., Capdeville, Y., Mocquet, A., & Drilleau, M., 2014. Oceanic lithosphere-asthenosphere boundary from surface wave dispersion data, *J. Geophys. Res. Solid Earth*, **119**(2), 1079–1093.

Burke, K., 1996. The African Plate, *S. Afr. J. Geol.*, **99**(4), 341–409.

Cammarano, F., Goes, S., Vacher, P., & Giardini, D., 2003. Inferring upper-mantle temperatures from seismic velocities, *Phys. Earth Planet. In.*, **138**(3-4), 197–222.

Campanile, D., Nambiar, C. G., Bishop, P., Widdowson, M., & Brown, R., 2008. Sedimentation record in the Konkan-Kerala Basin: implications for the evolution of the Western Ghats and the Western Indian passive margin, *Basin Res.*, **20**, 3–22.

Campforts, B. & Govers, G., 2015. Keeping the edge: A numerical method that avoids knickpoint smearing when solving the stream power law, *J. Geophys. Res. Earth Surf.*, **120**(7), 1189–1205.

Cande, S. C. & Patriat, P., 2015. The anticorrelated velocities of Africa and India in the Late Cretaceous and early Cenozoic, *Geophys. J. Int.*, **200**(1), 227–243.

Carlson, R. L. & Herrick, C. N., 1990. Densities and porosities in the oceanic crust and their variations with depth and age, *J. Geophys. Res. Solid Earth*, **95**(B6), 9153–9170.

Cazenave, A. & Lago, B., 1991. Long wavelength topography, seafloor subsidence and flattening, *Geophys. Res. Lett.*, **18**(7), 1257–1260.

Cazenave, A., Dominh, K., Rabinowicz, M., & Ceuleneer, G., 1988. Geoid and depth anomalies over ocean swells and troughs: Evidence of an increasing trend of the geoid to depth ratio with age of plate, *J. Geophys. Res. Solid Earth*, **93**(B7), 8064–8077.

Chambat, F., Ricard, Y., & Valette, B., 2010. Flattening of the Earth: further from hydrostaticity than previously estimated, *Geophys. J. Int.*, **183**(2), 727–732.

Chang, Y.-Y., Hsieh, W.-P., Tan, E., & Chen, J., 2017. Hydration-reduced lattice thermal conductivity of olivine in Earth's upper mantle, *Proc. Natl. Acad. Sci.*, **114**(16), 4078–4081.

Chardon, D., Chevillotte, V., Beauvais, A., Grandin, G., & Boulangé, B., 2006. Planation, bauxites and epeirogeny: One or two paleosurfaces on the West African margin?, *Geomorphology*, **82**(3-4), 273–282.

Charléty, J., Voronin, S., Nolet, G., Loris, I., Simons, F. J., Sigloch, K., & Daubechies, I. C., 2013. Global seismic tomography with sparsity constraints: Comparison with smoothing and damping regularization, *J. Geophys. Res. Solid Earth*, **118**(9), 4887–4899.

Chatterjee, S., Goswami, A., & Scotese, C. R., 2013. The longest voyage: Tectonic, magmatic, and paleoclimatic evolution of the Indian plate during its northward flight from Gondwana to Asia, *Gondwana Res.*, **23**(1), 238–267.

Chaubey, A. K., Gopala Rao, D., Srinivas, K., Ramprasad, T., Ramana, M. V., & Subrahmanyam, V., 2002. Analyses of multichannel seismic reflection, gravity and magnetic data along a regional profile across the central-western continental margin of India, *Mar. Geol.*, **182**(3-4), 303–323.

Christensen, N. I., 1982. Seismic Velocities, in *Handbook of Physical Properties of Rocks, Vol. II*, edited by R. S. Carmichael, pp. 57–74, CRC Press, Boca Raton, Florida.

Chust, T. C., Steinle-Neumann, G., Dolejš, D., Schuberth, B. S., & Bunge, H. P., 2017. MMA-EoS: A Computational Framework for Mineralogical Thermodynamics, *J. Geophys. Res. Solid Earth*, **122**(12), 9881–9920.

Clift, P. D., 2010. Enhanced global continental erosion and exhumation driven by Oligo-Miocene climate change, *Geophys. Res. Lett.*, **37**(9), 1–6.

Clift, P. D. & Plumb, R. A., 2008. *The Asian Monsoon: Causes, History and Effects*, Cambridge University Press, Cambridge.

Cochran, J. R. & Talwani, M., 1977. Free-air gravity anomalies in the worlds oceans and their relationship to residual elevation, *Geophys. J. Roy. Astr. Soc.*, **50**, 495–552.

Coffin, M. F. & Eldholm, O., 1994. Large igneous provinces: Crustal structure, dimensions, and external consequences, *Rev. Geophys.*, **32**(1), 1–36.

Colli, L., Ghelichkhan, S., & Bunge, H.-P., 2016. On the ratio of dynamic topography and gravity anomalies in a dynamic Earth, *Geophys. Res. Lett.*, **43**(6), 2510–2516.

Collier, J. S., Sansom, V., Ishizuka, O., Taylor, R. N., Minshull, T. A., & Whitmarsh, R. B., 2008. Age of Seychelles-India break-up, *Earth Plan. Sci. Lett.*, **272**(1-2), 264–277.

Coltice, N., Gérault, M., & Ulvrová, M., 2017. A mantle convection perspective on global tectonics, *Earth-Sci. Rev.*, **165**, 120–150.

Connolly, J. A., 2009. The geodynamic equation of state: What and how, *Geochem. Geophys. Geosyst.*, **10**(10), Q10014.

Connolly, J. A. D., 2005. Computation of phase equilibria by linear programming: A tool for geodynamic modeling and its application to subduction zone decarbonation, *Earth Plan. Sci. Lett.*, **236**(1-2), 524–541.

Connolly, J. A. D. & Khan, A., 2016. Uncertainty of mantle geophysical properties computed from phase equilibrium models, *Geophys. Res. Lett.*, **43**(10), 5026–5034.

Conrad, C. P. & Husson, L., 2009. Influence of dynamic topography on sea level and its rate of change, *Lithosphere*, **1**, 110–120.

Conrad, C. P., Steinberger, B., & Torsvik, T. H., 2013. Stability of active mantle upwelling revealed by net characteristics of plate tectonics, *Nature*, **498**(7455), 479.

Constable, S. C., Parker, R. L., & Constable, C. G., 1987. Occam's inversion: A practical algorithm for generating smooth models from electromagnetic sounding data, *Geophysics*, **52**(3), 289–300.

Copley, A., Avouac, J. P., & Royer, J. Y., 2010. India-Asia collision and the Cenozoic slowdown of the Indian plate: Implications for the forces driving plate motions, *J. Geophys. Res. Solid Earth*, **115**(3), 1–14.

Copley, A., Mitra, S., Sloan, R. A., Gaonkar, S., & Reynolds, K., 2014. Active faulting in apparently stable peninsular India : Rift inversion and a Holocene-age great earthquake on the Tapti Fault, *J. Geophys. Res. Solid Earth*, **119**(8), 6650–6666.

Corrieu, V., Thoraval, C., & Ricard, Y., 1995. Mantle dynamics and geoid Green functions, *Geophys. J. Int.*, **120**(2), 516–523.

Cossey, S. P. J., Van Nieuwenhuise, D., Davis, J., Rosenfeld, J. H., & Pindell, J., 2016. Compelling evidence from eastern Mexico for a Late Paleocene/Early Eocene isolation, drawdown, and refill of the Gulf of Mexico, *Interpretation*, **4**(1), SC63–SC80.

Cottaar, S. & Lekic, V., 2016. Morphology of seismically slow lower-mantle structures, *Geophys. J. Int.*, **207**(2), 1122–1136.

Cottaar, S., Heister, T., Rose, I., & Unterborn, C., 2014. BurnMan: A lower mantle mineral physics toolkit, *Geochem. Geophys. Geosyst.*, **15**(4), 1164–1179.

Courtillot, V., Davaille, A., Besse, J., & Stock, J., 2003. Three distinct types of hotspots in the Earth's mantle, *Earth Plan. Sci. Lett.*, **205**(3-4), 295–308.

Courtney, R. C. & White, R. S., 1986. Anomalous heat flow and geoid across the Cape Verde Rise: evidence for dynamic support from a thermal plume in the mantle, *Geophys. J. Int.*, **87**, 815–867.

Cox, K. G., 1989. The role of mantle plumes in the development of continental drainage patterns, *Nature*, **342**(6252), 873–877.

Craig, T. J., Copley, A., & Jackson, J., 2014. A reassessment of outer-rise seismicity and its implications for the mechanics of oceanic lithosphere, *Geophys. J. Int.*, **197**(1), 63–89.

Cronin, T., 2010. *Paleoclimates: Understanding climate change past and present*, Columbia University Press, New York.

Crosby, A. G. & McKenzie, D. P., 2009. An analysis of young ocean depth, gravity and global residual topography, *Geophys. J. Int.*, **178**, 1198–1219.

Crosby, A. G., McKenzie, D., & Sclater, J. G., 2006. The relationship between depth, age and gravity in the oceans, *Geophys. J. Int.*, **166**(2), 553–573.

Crough, S. T., 1983. The Correction for Sediment Loading on the Seafloor, *J. Geophys. Res. Solid Earth*, **88**(B8), 6449–6454.

Crough, S. T. & Jarrard, R. D., 1981. The Marquesas-Line Swell, *J. Geophys. Res. Solid Earth*, **86**(B12), 11763–11771.

Czarnota, K., Hoggard, M. J., White, N., & Winterbourne, J., 2013. Spatial and temporal patterns of Cenozoic dynamic topography around Australia, *Geochem. Geophys. Geosyst.*, **14**(3), 634–658.

Czarnota, K., Roberts, G. G., White, N. J., & Fishwick, S., 2014. Spatial and temporal patterns of Australian dynamic topography from River Profile Modeling, *J. Geophys. Res. Solid Earth*, **119**(2), 1384–1424.

Dalton, C. A., Ekström, G., & Dziewonski, A. M., 2009. Global seismological shear velocity and attenuation: A comparison with experimental observations, *Earth Plan. Sci. Lett.*, **284**(1-2), 65–75.

Dalton, C. A., Langmuir, C. H., & Gale, A., 2014. Geophysical and Geochemical Evidence for Deep Temperature Variations Beneath Mid-Ocean Ridges, *Science*, **344**(6179), 80–83.

Dannberg, J., Eilon, Z., Faul, U., Gassmöller, R., Moulik, P., & Myhill, R., 2017. The importance of grain size to mantle dynamics and seismological observations, *Geochem. Geophys. Geosyst.*, **18**, 1–28.

Davaille, A. & Jaupart, C., 1994. Onset of thermal convection in fluids with temperature-dependent viscosity: Application to the oceanic mantle, *J. Geophys. Res. Solid Earth*, **99**(B10), 19853–19866.

Davies, D. & Davies, J., 2009. Thermally-driven mantle plumes reconcile multiple hot-spot observations, *Earth Plan. Sci. Lett.*, **278**(1-2), 50–54.

Davies, D. R., Goes, S., Davies, J. H., Schuberth, B. S. A., Bunge, H. P., & Ritsema, J., 2012. Reconciling dynamic and seismic models of Earth's lower mantle: The dominant role of thermal heterogeneity, *Earth Plan. Sci. Lett.*, **353–354**, 253–269.

Davies, G. F., 1992. Whole-mantle convection and plate tectonics, *Geophys. J. R. Astr. Soc.*, **49**(2), 459–486.

Davies, J. H. & Davies, D. R., 2010. Earth's surface heat flux, *Solid Earth*, **1**(1), 5–24.

de Capitani, C. & Petrakakis, K., 2010. The computation of equilibrium assemblage diagrams with Theriak/Domino software, *American Mineralogist*, **95**(7), 1006.

Debayle, E., Dubuffet, F., & Durand, S., 2016. An automatically updated S-wave model of the upper mantle and the depth extent of azimuthal anisotropy, *Geophys. Res. Lett.*, **43**(2), 674–682.

Dehant, V., Laguerre, R., Rekier, J., Rivoldini, A., Triana, S. A., Trinh, A., Hoolst, T. V., & Zhu, P., 2017. Understanding the effects of the core on the nutation of the earth, *Geod. Geodyn.*, **8**(6), 389–395.

Deschamps, F., Rogister, Y., & Tackley, P. J., 2018. Constraints on core-mantle boundary topography from models of thermal and thermochemical convection, *Geophys. J. Int.*, **212**(1), 164–188.

Dodson, M. H., 1973. Closure temperature in cooling geochronological and petrological systems, *Contrib. Min. Pet.*, **40**(3), 259–274.

Doin, M. P. & Fleitout, L., 1996. Thermal evolution of the oceanic lithosphere: An alternative view, *Earth Plan. Sci. Lett.*, **142**, 121–136.

Duprat, H. I., Friis, J., Holm, P. M., Grandvuinet, T., & Sø rensen, R. V., 2007. The volcanic and geochemical development of São Nicolau, Cape Verde Islands: Constraints from field and $^{40}Ar/^{39}Ar$ evidence, *J. Volcanol. Geoth. Res.*, **162**, 1–19.

Dziewonski, A. M. & Anderson, D. L., 1981. Preliminary reference Earth model, *Phys. Earth Planet. In.*, **25**(4), 297–356.

Dziewonski, A. M. & Anderson, D. L., 1984. Seismic tomography of the earth's interior: The first three-dimenstional models of the earth's structure promise to answer some basic questions of geodynamics and signify a revolution in earth science, *American Scientist*, **72**(5), 483–494.

Eaton, D. W., Darbyshire, F., Evans, R. L., Grütter, H., Jones, A. G., & Yuan, X., 2009. The elusive lithosphere-asthenosphere boundary (LAB) beneath cratons, *Lithos*, **109**(1-2), 1–22.

Eilon, Z. C. & Abers, G. A., 2017. High seismic attenuation at a mid-ocean ridge reveals the distribution of deep melt, *Sci. Adv.*, **3**(5), E1602829.

Ekström, G., Tromp, J., & Larson, E. W., 1997. Measurements and global models of surface wave propagation, *J. Geophys. Res. Solid Earth*, **102**(B4), 8137–8157.

Engdahl, E. R., Van der Hilst, R., & Buland, R., 1998. Global teleseismic earthquake relocation with improved travel times and procedures for depth determination, *Bull. Seism. Soc. Am.*, **88**(3), 722–743.

FAO-UNESCO, 2007. Digital Soil Map of the World (v3.6).

Farley, K. A., 2000. Helium diffusion from apatite: General behavior as illustrated by Durango fluorapatite, *J. Geophys. Res. Solid Earth*, **105**(B2), 2903–2914.

Faul, U. H. & Jackson, I., 2005. The seismological signature of temperature and grain size variations in the upper mantle, *Earth Plan. Sci. Lett.*, **234**(1), 119–134.

Fawcett, P., 1994. The climatic evolution of India and Australia from the Late Permian to mid-Jurassic: A comparison of climate model results with the geologic record, *Geol. Soc. Am. Sp. Pap.*, **288**(1), 139–157.

Fei, H., Hegoda, C., Yamazaki, D., Wiedenbeck, M., Yurimoto, H., Shcheka, S., & Katsura, T., 2012. High silicon self-diffusion coefficient in dry forsterite, *Earth Plan. Sci. Lett.*, **345**, 95–103.

Fei, Y. & Saxena, S., 1987. An equation for the heat capacity of solids, *Geochim. Cosmochim. Acta*, **51**, 251–254.

Fichtner, A., van Herwaarden, D.-P., Afanasiev, M., Simutè, S., Krischer, L., Çubuk Sabuncu, Y., Taymaz, T., Colli, L., Saygin, E., Villaseñor, A., Trampert, J., Cupillard, P., Bunge, H.-P., & Igel, H., 2018. The Collaborative Seismic Earth Model: Generation 1, *Geophys. Res. Lett.*, **45**.

Flament, N., Gurnis, M., & Müller, R. D., 2013. A review of observations and models of dynamic topography, *Lithosphere*, **5**(2), 189–210.

Förste, C., Bruinsma, S. L., Shako, R., Flechtner, F., Dahle, C., Abrikosov, O., Marty, J., Lemoine, J., Neumayer, H., Biancale, R., Barthelmes, F., Koenig, R., Balmino, G., & Eigen-Team, 2011. EIGEN-6– The new Combined Global Gravity Field Model including GOCE data from the collaboration of GFZ Potsdam and GRGS Toulouse, *AGU Fall Meeting Abstracts*, pp. G43A–0747.

Forte, A. M. & Mitrovica, J. X., 1996. New inferences of mantle viscosity from joint inversion of long-wavelength mantle convection and post-glacial rebound data, *Geophys. Res. Lett.*, **23**(10), 1147–1150.

Forte, A. M. & Peltier, R., 1991. Viscous flow models of global geophysical observables: 1. Forward problems, *J. Geophys. Res. Solid Earth*, **96**(B12), 20131–20159.

Fox, C. S., 1923. *The bauxite and aluminous laterite occurrences of India*, Office of the Geological Survey of India, Calcutta.

Fox, M., Goren, L., May, D. A., & Willett, S. D., 2014. Inversion of fluvial channels for paleorock uplift rates in Taiwan, *J. Geophys. Res. Earth Surf.*, **119**(9), 1853–1875.

French, S., Lekic, V., & Romanowicz, B., 2013. Waveform Tomography Reveals Channeled Flow at the Base of the Oceanic Asthenosphere, *Science*, **342**(6155), 227–230.

French, S. W. & Romanowicz, B., 2015. Broad plumes rooted at the base of the Earth's mantle beneath major hotspots, *Nature*, **525**(7567), 95–99.

Frost, D. A. & Rost, S., 2014. The P-wave boundary of the Large-Low Shear Velocity Province beneath the Pacific, *Earth Plan. Sci. Lett.*, **403**, 380–392.

Gale, A., Langmuir, C. H., & Dalton, C. A., 2014. The global systematics of ocean ridge basalts and their origin, *J. Pet.*, **55**(6), 1051–1082.

Gantmacher, F. R., 1959. *The Theory of Matrices*, vol. 1, Chelsea Publishing Company.

Garnero, E. J. & McNamara, A. K., 2008. Structure and dynamics of Earth's lower mantle, *Science*, **320**(5876), 626–628.

Garnero, E. J., McNamara, A. K., & Shim, S.-H., 2016. Continent-sized anomalous zones with low seismic velocity at the base of Earth's mantle, *Nat. Geosci.*, **9**(7), 481.

Gerlach, D. C., Cliff, R. A., Davies, G. R., Norry, M., & Hodgson, N., 1988. Magma sources of the Cape Verdes archipelago: Isotopic and trace element constraints, *Geochim. Cosmochim. Acta*, **52**, 2979–2992.

Ghiorso, M. S., Hirschmann, M. M., Reiners, P. W., & Kress, V. C., 2002. The pMELTS: A revision of MELTS for improved calculation of phase relations and major element partitioning related to partial melting of the mantle to 3 GPa, *Geochem. Geophys. Geosyst.*, **3**(5), 1–35.

Ghosh, S. & Guchhait, S. K., 2015. Characterization and evolution of primary and secondary laterites in northwestern Bengal Basin , West Bengal, *J. Palaeogeog.*, **4**(2), 203–230.

Gilbert, F. & Backus, G. E., 1966. Propagator Matrices in Elastic Wave and Vibration Problems, *Geophysics*, **31**(2), 326–332.

Gilchrist, A. R. & Summerfield, M. A., 1990. Differential denudation and flexural isostasy in formation of rifted-margin upwarps, *Nature*, **346**(6286), 739–742.

Gillet, P., Richet, P., Guyot, F., & Fiquet, G., 1991. High-Temperature Thermodynamic Properties of Forsterite, *J. Geophys. Res. Solid Earth*, **96**(B7), 11805–11816.

Goetze, C., 1978. The mechanisms of creep in olivine, *Philos. Trans. R. Soc. Lond. A*, **288**(1350), 99–119.

Goren, L., Willett, S. D., Herman, F., & Braun, J., 2014. Coupled numerical-analytical approach to landscape evolution modeling, *Earth Surf. Process. Landforms*, **39**(4), 522–545.

Goutorbe, B., 2010. Combining seismically derived temperature with heat flow and bathymetry to constrain the thermal structure of oceanic lithosphere, *Earth Plan. Sci. Lett.*, **295**(3-4), 390–400.

Green, D. H. & Ringwood, A. E., 1970. Mineralogy of peridotitic compositions under upper mantle conditions, *Phys. Earth Planet. In.*, **3**(C), 359–371.

Green, P. F., Lidmar-Bergström, K., Japsen, P., Bonow, J. M., & Chalmers, J. A., 2013. Stratigraphic landscape analysis, thermochronology and the episodic development of elevated, passive continental margins, *Geol. Surv. Denmark Greenl. Bull.*, **30**.

Griggs, D. T., 1939. A theory of mountain-building, *Am. J. Sci.*, **237**(9), 611–650.

Grose, C. J., 2012. Properties of oceanic lithosphere: Revised plate cooling model predictions, *Earth Plan. Sci. Lett.*, **333-334**, 250–264.

Grose, C. J. & Afonso, J. C., 2013. Comprehensive plate models for the thermal evolution of oceanic lithosphere, *Geochem. Geophys. Geosyst.*, **14**(9), 3751–3778.

Guerri, M., Cammarano, F., & Tackley, P. J., 2016. Modelling Earth's surface topography: Decomposition of the static and dynamic components, *Phys. Earth Planet. In.*, **261**, 172–186.

Guliyev, I. S., Mamedov, P. Z., Feyzullayev, A. A., Huseynov, D. A., Kadirov, F. A., Aliyeva, E. H.-M., & Tagiyev, M. F., 2003. *Hydrocarbon Systems of the South Caspian Basin*, Nafta-Press, Baku.

Gunnell, Y., 1997. Relief and climate in south Asia: The influence of the western ghats on the current climate pattern of peninsular India, *Int. J. Climatol.*, **17**(11), 1169–1182.

Gunnell, Y., 1998. The interaction between geological structure and global tectonics in multistoreyed landscape development: a denudation chronology of the South Indian Shield, *Basin Res.*, **10**(3), 281–310.

Gunnell, Y. & Fleitout, L., 1998. Shoulder uplift of the Western Ghats passive margin, India: A denudational model, *Earth Surf. Process. Landforms*, **23**(5), 391–404.

Gunnell, Y. & Harbor, D., 2008. Structural Underprint and Tectonic Overprint in the Angavo (Madagascar) and Western Ghats (India) Implications for Understanding Scarp Evolution at Passive Margins, *J. Geol. Soc. India*, **71**, 763–779.

Gunnell, Y. & Harbor, D. J., 2010. Butte detachment: How pre-rift geological structure and drainage integration drive escarpment evolution at rifted continental margins, *Earth Surf. Proc. Land.*, **35**(12), 1373–1385.

Gunnell, Y., Gallagher, K., Carter, A., Widdowson, M., & Hurford, A. J., 2003. Denudation history of the continental margin of western peninsular India since the early Mesozoic–reconciling apatite fission-track data with geomorphology, *Earth Plan. Sci. Lett.*, **215**, 187–201.

Gunnell, Y., Braucher, R., Bourlès, D., & André, G., 2007. Quantitative and qualitative insights into bedrock landform erosion on the South Indian craton using cosmogenic nuclides and apatite fission tracks, *Bull. Geol. Soc. Am.*, **119**(5-6), 576–585.

Gupta, S., Rai, S. S., Prakasam, K. S., Srinagesh, D., Chadha, R. K., Priestley, K., & Gaur, V. K., 2003. First evidence for anomalous thick crust beneath mid-Archean western Dharwar craton, *Curr. Sci.*, **84**(9), 1219–1226.

Gvirtzman, Z., Faccenna, C., & Becker, T. W., 2016. Isostasy, flexure, and dynamic topography, *Tectonophysics*, **683**, 255–271.

Gwinn, C. R., Herring, T. A., & Shapiro, I. I., 1982. Geodesy by radio interferometry: Studies of the forced nutations of the Earth: 2. Interpretation, *J. Geophys. Res. Solid Earth*, **91**(B5), 4755–4765.

Hager, B. H. & Clayton, R. W., 1989. Constraints on the structure of mantle convection using seismic observations, flow models, and the geoid, pp. 657–763.

Hager, B. H. & O'Connell, R. J., 1979. Kinematic models of large-scale flow in the Earth's mantle, *J. Geophys. Res.*, **84**(B3), 1031–1048.

Hager, B. H. & O'Connell, R. J., 1981. A simple global model of plate dynamics and mantle convection, *J. Geophys. Res. Solid Earth*, **86**(B6), 4843–4867.

Hager, B. H. & Richards, M. A., 1989. Long-Wavelength Variations in Earth's Geoid: Physical Models and Dynamical Implications, *Philos. Trans. R. Soc. Lond. A*, **328**(1599), 309–327.

Hager, B. H. & Richards, M. A., 1989. Long-wavelength variations in earth's geoid: physical models and dynamical implications, *Phil. Trans. R. Soc. A*, **328**(1599), 309–327.

Hager, B. H., Clayton, R. W., Richards, M. A., Comer, R. P., & Dziewonski, A. M., 1985. Lower mantle heterogeneity, dynamic topography and the geoid, *Nature*, **313**(6003), 541–545.

Halkett, A., 2002. Mantle Plumes and the Sedimentary Record: Onshore-Offshore India, Ph.D. Thesis, University of Cambridge.

Hall, C. E. & Parmentier, E. M., 2003. Influence of grain size evolution on convective instability, *Geochem. Geophys. Geosyst.*, **4**(3), 1029.

Hansen, L. N., Qi, C., & Warren, J. M., 2016. Olivine anisotropy suggests Gutenberg discontinuity is not the base of the lithosphere, *Proc. Natl. Acad. Sci.*, **113**(38), 10503–10506.

Hartley, R. A., Roberts, G. G., White, N., & Richardson, C., 2011. Transient convective uplift of an ancient buried landscape, *Nat. Geosci.*, **4**(8), 562–565.

Haskell, N. A., 1935. The Motion of a Viscous Fluid Under a Surface Load, *Physics*, **6**(8), 265–269.

Hasterok, D., 2013. A heat flow based cooling model for tectonic plates, *Earth Plan. Sci. Lett.*, **361**, 34–43.

Hasterok, D., Chapman, D., & Davis, E., 2011. Oceanic heat flow: Implications for global heat loss, *Earth Plan. Sci. Lett.*, **311**(3), 386–395.

Hawkesworth, C., Kempton, P., Rogers, N., Ellam, R., & van Calsteren, P., 1990. Continental mantle lithosphere, and shallow level enrichment processes in the Earth's mantle, *Earth Plan. Sci. Lett.*, **96**(3-4), 256–268.

He, Y. & Wen, L., 2012. Geographic boundary of the "Pacific Anomaly" and its geometry and transitional structure in the north, *J. Geophys. Res. Solid Earth*, **117**(B9), 1–16, B09308.

Heister, T., Dannberg, J., Gassmöller, R., & Bangerth, W., 2017. High Accuracy Mantle Convection Simulation through Modern Numerical Methods. II: Realistic Models and Problems, *Geophys. J. Int.*, **210**(2), 833–851.

Herzberg, C., Asimow, P. D., Arndt, N., Niu, Y., Lesher, C. M., Fitton, J. G., Cheadle, M. J., & Saunders, A. D., 2007. Temperatures in ambient mantle and plumes: Constraints from basalts, picrites, and komatiites, *Geochem. Geophys. Geosyst.*, **8**(2).

Hillier, J. K., 2010. Subsidence of "normal" seafloor: Observations do indicate "flattening", *J. Geophys. Res. Solid Earth*, **115**(3), 1–6.

Hillier, J. K. & Watts, A. B., 2005. Relationship between depth and age in the North Pacific Ocean, *J. Geophys. Res. Solid Earth*, **110**(2), 1–22.

Hirth, G. & Kohlstedt, D., 2013. Rheology of the Upper Mantle and the Mantle Wedge: A View from the Experimentalists, in *Inside the Subduction Factory*, edited by J. Eiler, pp. 83–105, American Geophysical Union (AGU), Washington, D.C.

Hodgson, N. & Rodriguez, K., 2016. Shelf stability and mantle convection on Africa's passive margins (Part 1), *First Break*, **35**, 93–97.

Hofmann, A. W. & White, W. M., 1982. Mantle plumes from ancient oceanic crust, *Earth Plan. Sci. Lett.*, **57**(2), 421–436.

Hofmeister, A. M., 1999. Mantle Values of Thermal Conductivity and the Geotherm from Phonon Lifetimes, *Science*, **283**, 1699–1706.

Hofmeister, A. M., 2005. Dependence of diffusive radiative transfer on grain-size, temperature , and Fe-content: Implications for mantle processes, *J. Geodyn.*, **40**, 51–72.

Hofmeister, A. M., 2007. Pressure dependence of thermal transport properties, *Proc. Natl. Acad. Sci.*, **104**(22), 9192–9197.

Hofmeister, A. M. & Pertermann, M., 2008. Thermal diffusivity of clinopyroxenes at elevated temperature, *Eur. J. Mineral.*, **20**, 537–549.

Hoggard, M. J., White, N., & Al-Attar, D., 2016. Global dynamic topography observations reveal limited influence of large-scale mantle flow, *Nat. Geosci.*, **9**, 456–463.

Hoggard, M. J., Winterbourne, J., Czarnota, K., & White, N., 2017. Oceanic residual depth measurements, the plate cooling model, and global dynamic topography, *J. Geophys. Res. Solid Earth*, **122**(3), 2328–2372.

Holtzman, B. K., 2016. Questions on the existence, persistence, and mechanical effects of a very small melt fraction in the asthenosphere, *Geochem. Geophys. Geosyst.*, **17**(2), 470–484.

Howard, A. D. & Kerby, G., 1983. Channel changes in badlands, *Geol. Soc. Am. Bull.*, **94**(6), 739–752.

Hu, Y., Bürgmann, R., Banerjee, P., Feng, L., Hill, E. M., Ito, T., Tabei, T., & Wang, K., 2016. Asthenosphere rheology inferred from observations of the 2012 Indian Ocean earthquake, *Nature*, **538**(7625), 368–372.

Huang, J. & Zhong, S., 2005. Sublithospheric small-scale convection and its implications for the residual topography at old ocean basins and the plate model, *J. Geophys. Res. Solid Earth*, **110**(5), 1–17.

Hüttig, C., Tosi, N., & Moore, W. B., 2013. An improved formulation of the incompressible NavierStokes equations with variable viscosity, *Phys. Earth Planet. In.*, **220**, 11–18.

Iaffaldano, G. & Bunge, H.-P., 2015. Rapid Plate Motion Variations Through Geological Time: Observations Serving Geodynamic Interpretation, *Annu. Rev. Earth Plan. Sci.*, **43**(1), 571–592.

Iaffaldano, G. & Lambeck, K., 2014. Pacific plate-motion change at the time of the Hawaiian-Emperor bend constrains the viscosity of Earth's asthenosphere, *Geophys. Res. Lett.*, **41**(10), 3398–3406.

Iaffaldano, G., Husson, L., & Bunge, H. P., 2011. Monsoon speeds up Indian plate motion, *Earth Plan. Sci. Lett.*, **304**(3-4), 503–510.

Isaak, D. G., 1992. High-temperature elasticity of iron-bearing olivines, *J. Geophys. Res. Solid Earth*, **97**(B2), 1871–1885.

Ishii, M. & Tromp, J., 1999. Normal-Mode and Free-Air Gravity Constraints on Lateral Variations in Velocity and Density of Earth's Mantle, *Science*, **285**(5431), 1231–1236.

Jackson, I., Faul, U. H., Suetsugu, D., Bina, C., Inoue, T., & Jellinek, M., 2010. Grainsize-sensitive viscoelastic relaxation in olivine: Towards a robust laboratory-based model for seismological application, *Phys. Earth Planet. In.*, **183**(1-2), 151–163.

Jackson, I., Faul, U. H., & Skelton, R., 2014. Elastically accommodated grain-boundary sliding: New insights from experiment and modeling, *Phys. Earth Planet. In.*, **228**, 203–210.

Jagadeesh, S. & Rai, S. S., 2008. Thickness, composition, and evolution of the Indian Precambrian crust inferred from broadband seismological measurements, *Precambrian Res.*, **162**, 4–15.

Jain, C., Korenaga, J., & Karato, S.-i., 2018. On the grain size sensitivity of olivine rheology, *J. Geophys. Res. Solid Earth*, **123**(1), 674–688.

Jarvis, G. & Peltier, W., 1986. Lateral heterogeneity in the convecting mantle, *J. Geophys. Res. Solid Earth*, **91**(B1), 435–451.

Jaupart, C. & Mareschal, J.-C., 2007. Heat Flow and Thermal Structure of the Lithosphere, in *Treatise on Geophysics*, pp. 217–252.

Jennings, E. S. & Holland, T. J. B., 2015. A simple thermodynamic model for melting of peridotite in the system NCFMASOCr, *J. Pet.*, **56**(5), 869–892.

Jones, A. G., Afonso, J. C., & Fullea, J., 2017. Geochemical and geophysical constrains on the dynamic topography of the Southern African Plateau, *Geochem. Geophys. Geosyst.*.

Julià, J., Jagadeesh, S., Rai, S. S., & Owens, T. J., 2009. Deep crustal structure of the Indian shield from joint inversion of P wave receiver functions and Rayleigh wave group velocities: Implications for Precambrian crustal evolution, *J. Geophys. Res. Solid Earth*, **114**, 1–25.

Kaila, K., 1979. Crustal structure alonf Kavali-Udipi profile in the Indian Peninsular Shield from deep seismic sounding, *J. Geol. Soc. India*, **20**(7), 307–333.

Kaila, K., Murty, P., Rao, V., & Kharetchko, G., 1981. Crustal structure from deep seismic soundings along the Koyna II (Kelsi-Loni) profile in the Deccan Trap area, India, *Tectonophysics*, **73**(4), 365–384.

Kailasam, L. N., 1975. Epeirogenic studies in India with reference to recent vertical movements, *Tectonophysics*, **29**, 505–521.

Kalaswad, S., Roden, M. K., Miller, D. S., & Morisawa, M., 1993. Evolution of the Continental Margin of Western India: New Evidence from Apatite Fission-Track Dating, *J. Geol.*, **101**(5), 667–673.

Kale, V. S. & Subbarao, K. V., 2004. Some observations on the recession of the Western Ghat escarpment in the Deccan Trap Region, India: Based on geomorphological evidence, *Trans. Japanese Geomorphol. Union*, **25**(3), 231–245.

Kale, V. S., Sengupta, S., Achyuthan, H., & Jaiswal, M. K., 2014. Tectonic controls upon Kaveri River drainage, cratonic Peninsular India: Inferences from longitudinal profiles, morphotectonic indices, hanging valleys and fluvial records, *Geomorphology*, **227**, 153–165.

Karato, S.-i., 2010. Rheology of the deep upper mantle and its implications for the preservation of the continental roots: A review, *Tectonophysics*, **481**(1), 82–98.

Karato, S.-i. & Jung, H., 1998. Water, partial melting and the origin of the seismic low velocity and high attenuation zone in the upper mantle, *Earth Plan. Sci. Lett.*, **157**(3-4), 193–207.

Karato, S.-i. & Karki, B. B., 2001. Origin of lateral variation of seismic wave velocities and density in the deep mantle, *J. Geophys. Res. Solid Earth*, **106**(B10), 21771–21783.

Katsura, T., Yamada, H., Nishikawa, O., Song, M., Kubo, A., Shinmei, T., Yokoshi, S., Aizawa, Y., Yoshino, T., Walter, M. J., Ito, E., & Funakoshi, K.-i., 2004. Olivine-wadsleyite transition in the system $(Mg,Fe)_2SiO_4$, *J. Geophys. Res. Solid Earth*, **109**(B2), 1–12.

Katz, R. F., Spiegelman, M., & Langmuir, C. H., 2003. A new parameterization of hydrous mantle melting, *Geochem. Geophys. Geosyst.*, **4**(9), 1–19.

Kaufmann, G. & Lambeck, K., 2000. Mantle dynamics, postglacial rebound and the radial viscosity profile, *Phys. Earth Planet. In.*, **121**(3), 301–324.

Kaula, W. M., 1963. Tesseral Harmonics of the Gravitational Field and Geodetic Datum Shifts Derived from Camera Observations of Satellites, *J. Geophys. Res.*, **68**(2), 473–494.

Kawakatsu, H., Kumar, P., Takei, Y., Shinohara, M., Kanazawa, T., Araki, E., & Suyehiro, K., 2009. Seismic Evidence for Sharp Lithosphere-Asthenosphere Boundaries of Oceanic Plates, *Science*, **324**(5926), 499–502.

Kayal, J. R., Srivastava, V. K., Kumar, P., Chatterjee, R., & Khan, P. K., 2011. Evaluation of crustal and upper mantle structures using receiver function analysis: ISM broadband observatory data, *J. Geol. Soc. India*, **78**(1), 76–80.

Kelemen, P., Kikawa, E., & Miller, D., 2004. Shipboard Scientific Party, 2004. Leg 209 Summary, in *Proc. ODP, Init. Repts., 209*, pp. 1–139, Ocean Drilling Program, College Station TX.

Keller, G., Khosla, S. C., Sharma, R., Khosla, A., Bajpai, S., & Adatte, T., 2009. Early Danian Planktic Foraminifera From Cretaceous-Tertiary Intertrappean Beds At Jhilmili, Chhindwara District, Madhya Pradesh, India, *J. Foram. Res.*, **39**(1), 40–55.

Kench, P. S., Smithers, S. G., McLean, R. F., & Nichol, S. L., 2009. Holocene reef growth in the Maldives: Evidence of a mid-Holocene sea-level highstand in the central Indian Ocean, *Geology*, **37**(5), 455–458.

Kent, D. V. & Muttoni, G., 2008. Equatorial convergence of India and early Cenozoic climate trends., *Proc. Natl. Acad. Sci. U. S. A.*, **105**(42), 16065–16070.

Kern, A. K., Harzhauser, M., Reuter, M., Kroh, A., & Piller, W. E., 2013. The Miocene coastal vegetation of southwestern India and its climatic significance, *Palaeoworld*, **22**(3-4), 119–132.

Ketcham, R. A., 2005. Forward and Inverse Modeling of Low-Temperature Thermochronometry Data, *Rev. Min. Geochem.*, **58**(1), 275–314.

King, D. S. H. & Marone, C., 2012. Frictional properties of olivine at high temperature with applications to the strength and dynamics of the oceanic lithosphere, *J. Geophys. Res. Solid Earth*, **117**(12), 1–16.

King, S. D. & Masters, G., 1992. An inversion for radial viscosity structure using seismic tomography, *Geophys. Res. Lett.*, **19**(15), 1551–1554.

Kirby, S. H. & Kronenberg, A. K., 1987. Rheology of the lithosphere: Selected topics, *Rev. Geophys.*, **25**(6), 1219–1244.

Kissling, E., Husen, S., & Haslinger, F., 2001. Model parametrization in seismic tomography: a choice of consequence for the solution quality, *Physics of the Earth and Planetary Interiors*, **123**(2-4), 89–101.

Knight, K. B., Renne, P. R., Halkett, A., & White, N., 2003. ^{40}Ar/^{39}Ar dating of the Rajahmundry Traps, Eastern India and their relationship to the Deccan Traps, *Earth Plan. Sci. Lett.*, **208**(1-2), 85–99.

Koelemeijer, P., Deuss, A., & Ritsema, J., 2017. Density structure of Earth's lowermost mantle from Stoneley mode splitting observations, *Nat. Commun.*, **8**, 15241.

Kohlstedt, D. L. & Goetze, C., 1974. Low-stress high-temperature creep in olivine single crystals, *J. Geophys. Res.*, **79**(14), 2045–2051.

Kohlstedt, D. L., Evans, B., & Mackwell, S. J., 1995. Strength of the lithosphere: Constraints imposed by laboratory experiments, *J. Geophys. Res. Solid Earth*, **100**(B9), 17587–17602.

Korenaga, J., 2007. Effective thermal expansivity of Maxwellian oceanic lithosphere, *Earth Plan. Sci. Lett.*, **257**(1-2), 343–349.

Korenaga, J., 2007. Thermal cracking and the deep hydration of oceanic lithosphere: A key to the generation of plate tectonics?, *J. Geophys. Res. Solid Earth*, **112**(B5), B05408.

Korenaga, J., 2015. Seafloor topography and the thermal budget of Earth, *Geol. Soc. Am. Sp. Pap.*, **514**(SPE514-11), 167–185.

Korenaga, T. & Korenaga, J., 2008. Subsidence of normal oceanic lithosphere, apparent thermal expansivity, and seafloor flattening, *Earth Plan. Sci. Lett.*, **268**(1), 41–51.

Korenaga, T. & Korenaga, J., 2016. Evolution of young oceanic lithosphere and the meaning of seafloor subsidence rate, *J. Geophys. Res. Solid Earth*, **121**, 6315–6332.

Kroon, D., Steens, T., Troelstra, S. R., & Kingdom, U., 1991. Onset of Monsoonal Related Upwelling in the Western Arabian Sea As Revealed by Planktonic Foraminifers, *Proc. Ocean Drill. Program, Sci. Results*, **117**(13), 257–263.

Kumar, N., Zeyen, H., Singh, A. P., & Singh, B., 2013. Lithospheric structure of southern indian shield and adjoining oceans: Integrated modelling of topography, gravity, geoid and heat flow data, *Geophys. J. Int.*, **194**(1), 30–44.

Kumar, P., Saraswati, P. K., & Banerjee, S., 2009. Early Miocene shell concentration in the mixed carbonate-siliciclastic system of Kutch and their distribution in sequence stratigraphic framework, *J. Geol. Soc. India*, **74**(4), 432–444.

Kumar, P., Ravi Kumar, M., Srijayanthi, G., Arora, K., Srinagesh, D., Chadha, R. K., & Sen, M. K., 2013. Imaging the lithosphere-asthenosphere boundary of the Indian plate using converted wave techniques, *J. Geophys. Res. Solid Earth*, **118**, 5307–5319.

Kumaran, K. P. N., Shindikar, M., & Limaye, R. B., 2004. Mangrove associated lignite beds of Malvan, Konkan: Evidence for higher sea-level during the Late Tertiary (Neogene) along the west coast of India, *Curr. Sci.*, **86**(2), 335–340.

Kustowski, B., Ekström, G., & Dziewoński, A. M., 2008. Anisotropic shear-wave velocity structure of the Earth's mantle: A global model, *J. Geophys. Res. Solid Earth*, **113**(B6), B06306.

Lambeck, K., Johnston, P., Smither, C., & Nakada, M., 1996. Glacial rebound of the british islesiii. constraints on mantle viscosity, *Geophys. J. Int.*, **125**(2), 340–354.

Lambeck, K., Smither, C., & Johnston, P., 1998. Sea-level change, glacial rebound and mantle viscosity fornorthern europe, *Geophys. J. Int.*, **134**(1), 102–144.

Lambeck, K., Rouby, H., Purcell, A., Sun, Y., & Sambridge, M., 2014. Sea level and global ice volumes from the Last Glacial Maximum to the Holocene, *Proc. Natl. Acad. Sci.*, **111**(43), 15296–15303.

Laske, G., Masters, G., Ma, Z., & Pasyanos, M., 2013. Update on CRUST1.0 — A 1° Global Model of Earth's Crust, **15**, EGU2013–2658.

Lau, H. C., Mitrovica, J. X., Davis, J. L., Tromp, J., Yang, H. Y., & Al-Attar, D., 2017. Tidal tomography constrains Earth's deep-mantle buoyancy, *Nature*, **551**(7680), 321–326.

Lau, H. C. P., Mitrovica, J. X., Austermann, J., Crawford, O., Al-Attar, D., & Latychev, K., 2016. Inferences of mantle viscosity based on ice age data sets : Radial structure, *J. Geophys. Res. Solid Earth*, **121**, 6991–7012.

Lay, T. & Buffett, B., 2008. Core–mantle boundary heat flow, *Nat. Geosci.*, **1**, 13–15.

Le Douaran, S. & Parsons, B. E., 1982. A Note on the Correction of Ocean Floor Depths for Sediment Loading, *J. Geophys. Res. Solid Earth*, **87**(B6), 4715–4722.

Le Roy, C., Rangin, C., Le Pichon, X., Thi Ngoc, H. N., Andreani, L., & Aranda-Garcia, M., 2008. Neogene crustal shear zone along the western Gulf of Mexico margin and its implications for gravity sliding processes. Evidences from 2D and 3D multichannel seismic data, *Bull. Soc. Geol. Fr.*, **179**(2), 175–193.

Lecroart, P., Cazenave, A., Ricard, Y., Thoraval, C., & Pyle, D. G., 1997. Along-axis dynamic topography constrained by major-element chemistry, *Earth Plan. Sci. Lett.*, **149**(1), 49–56.

Lekic, V., Cottaar, S., Dziewonski, A., & Romanowicz, B., 2012. Cluster analysis of global lower mantle tomography: A new class of structure and implications for chemical heterogeneity, *Earth Plan. Sci. Lett.*, **357**, 68–77.

Lin, P.-Y. P., Gaherty, J. B., Jin, G., Collins, J. A., Lizarralde, D., Evans, R. L., & Hirth, G., 2016. High-resolution seismic constraints on flow dynamics in the oceanic asthenosphere, *Nature*, **535**(7613), 538.

Lisker, F., Ventura, B., & Glasmacher, U. A., 2009. Apatite thermochronology in modern geology, *Geol. Soc. Lond. Sp. Pub.*, **324**(1), 1–23.

Lister, C. R. B., 1972. On the Thermal Balance of a Mid-Ocean Ridge, *Geophys. J. Int.*, **26**(5), 515–535.

Lithgow-Bertelloni, C. & Silver, P. G., 1998. Dynamic topography, plate driving forces and the african superswell, *Nature*, **395**(6699), 269.

Liu, C. & Grand, S. P., 2018. Seismic attenuation in the African LLSVP estimated from PcS phases, *Earth Plan. Sci. Lett.*, **489**, 8–16.

Lodhia, B. H., Roberts, G. G., Fraser, A. J., Fishwick, S., Goes, S., & Jarvis, J., 2018. Continental margin subsidence from shallow mantle convection: Example from west africa, *Earth Plan. Sci. Lett.*, **481**, 350–361.

Luke, J., 1972. Mathematical models for landform evolution, *J. Geophys. Res.*, **77**(14), 2460–2464.

Luke, J. C., 1974. Special solutions for nonlinear erosion problems, *J. Geophys. Res.*, **79**(26), 4035–4040.

Luke, J. C., 1976. A note on the use of characteristics in slope evolution models, *Z. Geomorph. Supp.*, **25**, 114–119.

Maceira, M. & Ammon, C. J., 2009. Joint inversion of surface wave velocity and gravity observations and its application to central Asian basins shear velocity structure, *J. Geophys. Res. Solid Earth*, **114**(2), 1–18.

Mandal, P., 2012. Passive-source seismic imaging of the crust and upper mantle beneath the 2001 Mw 7.7 Bhuj earthquake region, Gujarat, India, *Bull. Seism. Soc. Am.*, **102**(1), 252–266.

Mandal, S. K., Fellin, M. G., Burg, J.-P., & Maden, C., 2015. Phanerozoic surface history of southern Peninsular India from apatite (U-Th-Sm)/He data, *Geochem. Geophys. Geosyst.*, **16**, 1–23.

Mandal, S. K., Lupker, M., Burg, J.-P., Valla, P. G., Haghipour, N., & Christl, M., 2015. Spatial variability of [10]Be-derived erosion rates across the southern Peninsular Indian escarpment: A key to landscape evolution across passive margins, *Earth Plan. Sci. Lett.*, **425**, 154–167.

Mandal, S. K., Burg, J.-P., & Haghipour, N., 2016. Geomorphic fluvial markers reveal transient landscape evolution in tectonically quiescent southern Peninsular India, *Geological Journal*, **52**(4), 681–702.

Mao, Z., Fan, D., Lin, J.-F., Yang, J., Tkachev, S. N., Zhuravlev, K., & Prakapenka, V. B., 2015. Elasticity of single-crystal olivine at high pressures and temperatures, *Earth Plan. Sci. Lett.*, **426**, 204–215.

Marty, J. C. & Cazenave, A., 1989. Regional variations in subsidence rate of oceanic plates: a global analysis, *Earth Plan. Sci. Lett.*, **94**(3-4), 301–315.

Mather, K. A., Pearson, D. G., McKenzie, D., Kjarsgaard, B. A., & Priestley, K., 2011. Constraints on the depth and thermal history of cratonic lithosphere from peridotite xenoliths, xenocrysts and seismology, *Lithos*, **125**(1-2), 729–742.

Matthews, S., Shorttle, O., & Maclennan, J., 2016. The temperature of the Icelandic mantle from olivine-spinel aluminum exchange thermometry, *Geochem. Geophys. Geosyst.*, **17**, 4725–4752.

McCarthy, C. & Takei, Y., 2011. Anelasticity and viscosity of partially molten rock analogue: Toward seismic detection of small quantities of melt, *Geophys. Res. Lett.*, **38**(18), 3–7.

McCarthy, C., Takei, Y., & Hiraga, T., 2011. Experimental study of attenuation and dispersion over a broad frequency range: 2. The universal scaling of polycrystalline materials, *J. Geophys. Res. Solid Earth*, **116**(9), 1–18.

McKenzie, D., 1977. Surface deformation, gravity anomalies and convection, *Geophys. J. R. Astr. Soc.*, **48**(2), 211–238.

McKenzie, D., 2003. Estimating T_e in the presence of internal loads, *J. Geophys. Res. Solid Earth*, **108**(B9), 1–21.

McKenzie, D., 2010. The influence of dynamically supported topography on estimates of te, *Earth Plan. Sci. Lett.*, **295**(1), 127–138.

McKenzie, D., 2016. A note on estimating Te from Bouguer coherence, *Int. J. Geomath.*, **7**(1), 103–116.

McKenzie, D. & Bickle, M. J., 1988. The volume and composition of melt generated by extension of the lithosphere, *J. Pet.*, **29**(3), 625–679.

McKenzie, D. & Fairhead, D., 1997. Estimates of the effective elastic thickness of the continental lithosphere from Bouguer and free air gravity anomalies, *J. Geophys. Res. Solid Earth*, **102**(B12), 27523–27552.

McKenzie, D. & O'Nions, R. K., 1991. Partial Melt Distributions from Inversion of Rare Earth Element Concentrations, *J. of Petrology*, **32**(5), 1021–1091.

McKenzie, D., Jackson, J., & Priestley, K., 2005. Thermal structure of oceanic and continental lithosphere, *Earth Plan. Sci. Lett.*, **233**(3-4), 337–349.

McKenzie, D., Daly, M. C., & Priestley, K., 2015. The lithospheric structure of Pangea, *Geology*, **43**(9), 783–786.

McKenzie, D. P., 1967. Some remarks on heat flow and gravity anomalies, *J. Geophys. Res.*, **72**(24), 6261.

McKenzie, D. P., Roberts, J., & Weiss, N., 1973. Numerical models of convection in the Earth's mantle, *Tectonophysics*, **19**, 89–103.

McNamara, A. K. & Zhong, S., 2005. Thermochemical structures beneath Africa and the Pacific Ocean, *Nature*, **437**(7062), 1136–1139.

Meher-Homji, V. M., 1989. History of vegetation of peninsular India, *Man Environ.*, **13**(1), 1–10.

Menard, H. W., 1973. Depth Anomalies and the Bobbing Motion of Drifting Islands, *J. Geophys. Res.*, **78**(23), 5128–5137.

Meyer, D., Tachikawa, T., Kaku, M., Iwasaki, A., Gesch, D., Oimoen, M., Zheng, Z., Danielson, J., Krieger, T., Curtis, W., Haase, J., Abrams, M., Crippen, R., & Carabajal, C., 2011. ASTER Global Digital Elevation Model Version 2 - Summary of Validation Results, Tech. rep.

Miller, K. G., Kominz, M. A., Browning, J. V., Wright, J. D., Mountain, G. S., Katz, M. E., Sugarman, P. J., Cramer, B. S., Christie-Blick, N., & Pekar, S. F., 2005. The Phanerozoic record of global sea-level change., *Science*, **310**, 1293–1298.

Mishra, D. C., Laxman, G., & Arora, K., 2004. Large-wavelength gravity anomalies over the Indian continent: Indicators of lithospheric flexure and uplift and subsidence of Indian Peninsular Shield related to isostasy, *Curr. Sci.*, **86**, 861–867.

Mitra, S., Bhattacharya, S. N., & Nath, S. K., 2008. Crustal structure of the Western Bengal basin from joint analysis of teleseismic receiver functions and Rayleigh-wave dispersion, *Bull. Seismol. Soc. Am.*, **98**(6), 2715–2723.

Mitrovica, J. X., 1996. Haskell [1935] revisited, *J. Geophys. Res. Solid Earth*, **101**(B1), 555–569.

Mitrovica, J. X. & Forte, A. M., 1997. Radial profile of mantle viscosity: Results from the joint inversion of convection and postglacial rebound observables, *J. Geophys. Res. Solid Earth*, **102**(B2), 2751–2769.

Mitrovica, J. X. & Forte, A. M., 2004. A new inference of mantle viscosity based upon joint inversion of convection and glacial isostatic adjustment data, *Earth Plan. Sci. Lett.*, **225**(1-2), 177–189.

Mohan, G., Kumar, M. R., Saikia, D., Kumar, K. A. P., Tiwari, P. K., & Surve, G., 2012. Imprints of volcanism in the upper mantle beneath the NW Deccan volcanic province, *Lithosphere*, **4**, 150–159.

Molnar, P., 2009. The state of interactions among tectonics, erosion, and climate: A polemic, *GSA Today*, **19**(7), 44–45.

Molnar, P., England, P. C., & Jones, C. H., 2015. Mantle dynamics, isostasy, and the support of high terrain, *J. Geophys. Res. Solid Earth*, **120**(3), 1932–1957.

Montelli, R., Nolet, G., Dahlen, F. A., & Masters, G., 2006. A catalogue of deep mantle plumes: New results from finite-frequency tomography, *Geochem. Geophys. Geosyst.*, **7**(11), Q11007.

Montgomery, D. R. & Dietrich, W. E., 1988. Where do channels begin?, *Nature*, **336**(6196), 232–234.

Morelli, A. & Dziewonski, A. M., 1987. Topography of the core–mantle boundary and lateral homogeneity of the liquid core, *Nature*, **325**(6106), 678.

Morgan, J., Hasenclever, J., & Shi, C., 2013. New observational and experimental evidence for a plume-fed asthenosphere boundary layer in mantle convection, *Earth Plan. Sci. Lett.*, **366**, 99–111.

Morgan, J. P. & Smith, W. H., 1992. Flattening of the sea-floor depth-age curve as a response to asthenospheric flow, *Nature*, **359**(6395), 524.

Moulik, P. & Ekström, G., 2016. The relationships between large-scale variations in shear velocity, density, and compressional velocity in the Earth's mantle, *J. Geophys. Res. Solid Earth*, **121**(4), 2737–2771.

Mouthereau, F., Watts, A. B., & Burov, E., 2013. Structure of orogenic belts controlled by lithosphere age, *Nat. Geosci.*, **6**(8), 1–5.

Müller, R. D., Sdrolias, M., Gaina, C., & Roest, W. R., 2008. Age, spreading rates, and spreading asymmetry of the world's ocean crust, *Geochem. Geophys. Geosyst.*, **9**(4), Q04006.

Müller, R. D., Seton, M., Zahirovic, S., Williams, S. E., Matthews, K. J., Wright, N. M., Shephard, G. E., Maloney, K. T., Barnett-Moore, N., Bower, D. J., & Cannon, J., 2016. Ocean basin evolution and global-scale reorganization events since Pangea breakup, *Annu. Rev. Earth Plan. Sci. Lett.*, **44**(1), 107–138.

Müller, R. D. D., Yatheesh, V., & Shuhail, M., 2015. The tectonic stress field evolution of India since the Oligocene, *Gondwana Res.*, **28**(2), 612–624.

Mulyukova, E., Steinberger, B., Dabrowski, M., & Sobolev, S. V., 2015. Survival of LLSVPs for billions of years in a vigorously convecting mantle: Replenishment and destruction of chemical anomaly, *J. Geophys. Res. Solid Earth*, **120**(5), 3824–3847.

Nair, V. G., 2006. *Impact of Western Ghats Orography on the Weather and Climate Over Southern Peninsular India–A Mesoscale Modelling Study*, Ph.D. thesis, Cochin University of Science and Technology.

Nakagawa, T., Tackley, P. J., Deschamps, F., & Connolly, J. A. D., 2009. Incorporating self-consistently calculated mineral physics into thermochemical mantle convection simulations in a 3-D spherical shell and its influence on seismic anomalies in Earth's mantle, *Geochem. Geophys. Geosyst.*, **10**(3), Q03004.

Nakiboglu, S. M., 1982. Hydrostatic theory of the Earth and its mechanical implications, *Phys. Earth Planet. In.*, **28**(4), 302–311.

Natarov, S. I. & Conrad, C. P., 2012. The role of Poiseuille flow in creating depth-variation of asthenospheric shear, *Geophys. J. Int.*, **190**(3), 1297–1310.

Nerlich, R., Colli, L., Ghelichkhan, S., Schuberth, B., & Bunge, H.-P., 2016. Constraining central Neo-Tethys Ocean reconstructions with mantle convection models, *Geophys. Res. Lett.*, **43**(18), 9595–9603.

Newton, R. C. & Hansen, E. C., 1986. The South India-Sri Lanka high-grade terrain as a possible deep-crust section, *Geol. Soc. Lond. Sp. Pub.*, **24**(1), 297–307.

Newville, M., Stensitzki, T., Allen, D. B., & Ingargiola, A., 2014. LMFIT: Non-Linear Least-Square Minimization and Curve-Fitting for Python.

Nyblade, A. A. & Robinson, S. W., 1994. The African Superswell, *Geophys. Res. Lett.*, **21**(9), 765–768.

O'Connor, J. M. & Duncan, R. A., 1990. Evolution of the Walvis Ridge-Rio Grande Rise Hot Spot System: Implications for African and South American Plate motions over plumes, *J. Geophys. Res. Solid Earth*, **95**(B11), 17475–17502.

Odada, E. O., 1996. Geological evolution of coastal Kenya as inferred from sedimentary sequences and marines terraces, *Afr. Geosci. Rev.*, **3**(3), 1–18.

Oxburgh, E. R. & Parmentier, E. M., 1977. Compositional and density stratification in oceanic lithosphere-causes and consequences, *J. Geol. Soc.*, **133**(4), 343.

Panasyuk, S. V. & Hager, B. H., 2000. Models of isostatic and dynamic topography, geoid anomalies, and their uncertainties, *J. Geophys. Res. Solid Earth*, **105**(B12), 28199–28209.

Pandey, O. P., Agrawal, P. K., & Negi, J. G., 1996. Evidence of low density sub-crustal underplating beneath western continental region of India and adjacent Arabian Sea: Geodynamical considerations, *J. Geodyn.*, **21**(4), 365–377.

Parker, R. L., 1994. *Geophysical Inverse Theory*, Princeton University Press, Princeton, N.J.

Parnell-Turner, R., White, N., Henstock, T., Murton, B., Maclennan, J., & Jones, S. M., 2014. A continuous 55-million-year record of transient mantle plume activity beneath Iceland, *Nat. Geosci.*, **7**(12), 914–919.

Parsons, B. & Daly, S., 1983. The relationship between surface topography, gravity anomalies, and temperature structure of convection, *J. Geophys. Res. Solid Earth*, **88**(B2), 1129.

Parsons, B. & McKenzie, D., 1978. Mantle convection and the thermal structure of the plates, *J. Geophys. Res.*, **83**(B9), 4485–4496.

Parsons, B. & Sclater, J. G., 1977. An analysis of the variation of ocean floor bathymetry and heat flow with age, *J. Geophys. Res.*, **82**(5), 803–827.

Pathak, A., Ravi Kumar, M., & Sarkar, D., 2006. Seismic structure of Sri Lanka using receiver function analysis: A comparison with other high-grade Gondwana terrains, *Gondwana Res.*, **10**(1-2), 198–202.

Paul, J. D., Roberts, G. G., & White, N., 2014. The African landscape through space and time, *Tectonics*, **33**(6), 898–935.

Paulson, A. & Richards, M. A., 2009. On the resolution of radial viscosity structure in modelling long-wavelength postglacial rebound data, *Geophys. J. Int.*, **179**(3), 1516–1526.

Pedoja, K., Husson, L., Regard, V., Cobbold, P. R., Ostanciaux, E., Johnson, M. E., Kershaw, S., Saillard, M., Martinod, J., Furgerot, L., Weill, P., & Delcaillau, B., 2011. Relative sea-level fall since the last interglacial stage: Are coasts uplifting worldwide?, *Earth-Sci. Rev.*, **108**(1-2), 1–15.

Peel, F. J., Travis, C. J., & Hossack, J. R., 1995. Genetic Structural Provinces and Salt Tectonics of the Cenozoic Offshore US Gulf of Mexico: A Preliminary Analysis, in *Salt Tectonics: A Global Perspective*, edited by M. P. A. Jackson, D. G. Roberts, & S. Snelson, chap. 7, pp. 153–175.

Pekeris, C. L., 1935. Thermal convection in the interior of the Earth, *Geophys. J. Int.*, **3**, 343–367.

Pertermann, M. & Hofmeister, A. M., 2006. Thermal diffusivity of olivine-group minerals at high temperature, *Am. Mineral.*, **91**(2005), 1747–1760.

Phipps Morgan, J., Morgan, W. J., Zhang, Y.-S., & Smith, W. H. F., 1995. Observational hints for a plume-fed, suboceanic asthenosphere and its role in mantle convection, *J. Geophys. Res. Solid Earth*, **100**(B7), 12753–12767.

Pollack, H. N., 1980. On the use of the volumetric thermal expansion coefficient in models of ocean floor topography, *Tectonophysics*, **64**(3-4), T45–T47.

Pollack, H. N. & Chapman, D. S., 1977. On the regional variation of heat flow, geotherms, and lithospheric thickness, *Tectonophysics*, **38**(3-4), 279–296.

Pollack, H. N., Hurter, S. J., & Johnson, J. R., 1993. Heat flow from the Earth's interior: Analysis of the global data set, *Rev. Geophys.*, **31**(3), 267–280.

Powar, K. B., 1993. Geomorphological evolution of Konkan Coastal Belt and adjoining Sahyadri Uplands with reference to Quaternary uplift, *Curr. Sci.*, **64**(11-12), 793–796.

Powell, R., Holland, T., & Worley, B., 1998. Calculating phase diagrams involving solid solutions via non-linear equations, with examples using THERMOCALC, *J. Metamorph. Geol.*, **16**(4), 577–588.

Pratt, J. H., 1855. On the attraction of the Himalaya Mountains, and of the elevated regions beyond them, upon the plumb-line in India, *Phil. Trans. R. Soc.*, **145**, 53–100.

Praveen Kumar, K. & Mohan, G., 2014. Crustal velocity structure beneath Saurashtra, NW India, through waveform modeling: Implications for magmatic underplating, *J. Asian Earth Sci.*, **79**, 173–181.

Press, W. H., Teukolsky, S. A., Vetterling, W. T., & Flannery, B. P., 1996. *Numerical Recipes in Fortran 90 (2nd Ed.): The Art of Parallel Scientific Computing*, Cambridge University Press, New York, NY, USA.

Priestley, K. & McKenzie, D., 2006. The thermal structure of the lithosphere from shear wave velocities, *Earth Plan. Sci. Lett.*, **244**(1-2), 285–301.

Priestley, K. & McKenzie, D., 2013. The relationship between shear wave velocity, temperature, attenuation and viscosity in the shallow part of the mantle, *Earth Plan. Sci. Lett.*, **381**, 78–91.

Priestley, K., McKenzie, D., Barron, J., Tatar, M., & Debayle, E., 2012. The Zagros core: Deformation of the continental lithospheric mantle, *Geochem. Geophys. Geosyst.*, **13**(11), Q11014.

Pritchard, D., Roberts, G. G., White, N. J., & Richardson, C. N., 2009. Uplift histories from river profiles, *Geophys. Res. Lett.*, **36**(24), 1–5.

Radakrishna, B. P., 1991. Neogene uplift and geomorphic rejuvenation of the Indian Peninsula, *Curr. Sci.*, **64**(11-12), 787–793.

Radakrishna, B. P., 1992. Evolution of river Cauvery: A point of view, *Curr. Sci.*, **63**(7), 348–353.

Rai, A., Gaur, V. K., Rai, S. S., & Priestley, K., 2009. Seismic signatures of the Pan-African orogeny: Implications for southern Indian high-grade terranes, *Geophys. J. Int.*, **176**(2), 518–528.

Rai, S. S., 2003. Crustal shear velocity structure of the south Indian shield, *J. Geophys. Res. Solid Earth*, **108**(B2), 2088.

Rai, S. S., Kumar, T. V., & Jagadeesh, S., 2005. Seismic evidence for significant crustal thickening beneath Jabalpur earthquake, 21 May 1997, source region in Narmada-Son lineament, central India, *Geophys. Res. Lett.*, **32**(May 1997), 1–5.

Rai, S. S., Borah, K., Das, R., Gupta, S., Srivastava, S., Prakasam, K. S., Sivaram, K., Kumar, S., & Meena, R., 2013. The South India Precambrian crust and shallow lithospheric mantle: Initial results from the India Deep Earth Imaging Experiment (INDEX), *J. Earth Syst. Sci.*, **122**(6), 1435–1453.

Raju, D., 2008. MEGA CHART-I: Major Hiatuses, Stratigraphic Sequences, Lithology, Thickness and Rates of Sedimentation of Lithounits of the Proterozoic and Phanerozoic of India, *ONGC Bull.*, **43**(1).

Ranalli, G. & Murphy, D. C., 1987. Rheological stratification of the lithosphere, *Tectonophysics*, **132**, 281–295.

Rao, K. M., Kumar, M. R., & Rastogi, B. K., 2015. Crust beneath the Northwestern Deccan Volcanic Province, India : Evidence for uplift and magmatic underplating, *J. Geophys. Res. Solid Earth*, **120**, 3385–3405.

Ravi Kumar, M., Saul, J., Sarkar, D., Kind, R., & Shukla, A. K., 2001. Crustal structure of the Indian Shield: New constraints from teleseismic receiver functions, *Geophys. Res. Lett.*, **28**(7), 1339–1342.

Rawlinson, N., Pozgay, S., & Fishwick, S., 2010. Seismic tomography: A window into deep Earth, *Phys. Earth Planet. Int.*, **178**(3), 101–135.

Rawlinson, N., Fichtner, A., Sambridge, M., & Young, M. K., 2014. Seismic tomography and the assessment of uncertainty, *Adv. Geophys.*, **55**, 1–76.

Reddy, P. R., 2005. Crustal velocity structure of western India and its use in understanding intraplate seismicity, *Curr. Sci.*, **88**(10), 1652–1657.

Reuter, M., Piller, W. E., Harzhauser, M., & Kroh, A., 2013. Cyclone trends constrain monsoon variability during late Oligocene sea level highstands (Kachchh Basin, NW India), *Clim. Past*, **9**, 2101–2115.

Ricard, Y. & Bercovici, D., 2009. A continuum theory of grain size evolution and damage, *J. Geophys. Res. Solid Earth*, **114**(B1).

Ricard, Y. & Wuming, B., 1991. Inferring the viscosity and the 3-D density structure of the mantle from geoid, topography and plate velocities, *Geophys. J. Int.*, **105**(3), 561–571.

Ricard, Y., Richards, M., Lithgow-Bertelloni, C., & Lestunff, Y., 1993. A Geodynamic Model of Mantle Density Heterogeneity, *J. Geophys. Res. Solid Earth*, **98**(B12), 21895–21909.

Richards, M. A. & Hager, B. H., 1984. Geoid anomalies in a dynamic Earth, *J. Geophys. Res. Solid Earth*, **89**(B7), 5987–6002.

Richards, M. A. & Hager, B. H., 1989. Effects of lateral viscosity variations on long-wavelength geoid anomalies and topography, *J. Geophys. Res. Solid Earth*, **94**(B8), 10299–10313.

Richter, F. M., 1978. Mantle Convection Models, *Ann. Rev. Earth Plan. Sci.*, **6**(1), 9–19.

Rickers, F., Fichtner, A., & Trampert, J., 2013. The Iceland-Jan Mayen plume system and its impact on mantle dynamics in the North Atlantic region: Evidence from full-waveform inversion, *Earth Plan. Sci. Lett.*, **367**, 39–51.

Ritsema, J., van Heijst, H. J., & Woodhouse, J. H., 1999. Complex Shear Wave Velocity Structure Imaged Beneath Africa and Iceland, *Science*, **286**(5446), 1925–1928.

Ritsema, J., van Heijst, H. J., & Woodhouse, J. H., 2004. Global transition zone tomography, *J. Geophys. Res. Solid Earth*, **109**(B2).

Ritsema, J., Deuss, A., Van Heijst, H. J., & Woodhouse, J. H., 2011. S40RTS: A degree-40 shear-velocity model for the mantle from new Rayleigh wave dispersion, teleseismic traveltime and normal-mode splitting function measurements, *Geophys. J. Int.*, **184**, 1223–1236.

Roberts, G. G. & White, N., 2010. Estimating uplift rate histories from river profiles using African examples, *J. Geophys. Res. Solid Earth*, **115**(2), 1–24.

Roberts, G. G., White, N. J., Martin-Brandis, G. L., & Crosby, A. G., 2012. An uplift history of the Colorado Plateau and its surroundings from inverse modeling of longitudinal river profiles, *Tectonics*, **31**(4), 1–25.

Robinson, E. M., Parsons, B., & Daly, S. F., 1987. The effect of a shallow low viscosity zone on the apparent compensation of mid-plate swells, *Earth Plan. Sci. Lett.*, **82**(3), 335–348.

Rodríguez Tribaldos, V., White, N. J., Roberts, G. G., & Hoggard, M. J., 2017. Spatial and temporal uplift history of South America from calibrated drainage analysis, *Geochem. Geophys. Geosyst.*, **18**(6), 2321–2353.

Romanowicz, B. & Durek, J. J., 2013. Seismological Constraints on Attenuation in the Earth: a Review, in *Earth's Deep Interior: Mineral Physics and Tomography From the Atomic to the Global Scale*, edited by S. Karato, A. Forte, R. Liebermann, G. Masters, & L. Stixrude, pp. 161–179, American Geophysical Union (AGU), Washington, D.C.

Rosenbloom, N. A. & Anderson, R. S., 1994. Hillslope and channel evolution in a marine terraced landscape, Santa Cruz, California, *J. Geophys. Res. Solid Earth*, **99**(B7), 14013.

Ross, M. I. & Scotese, C. R., 1988. A hierarchical tectonic model of the gulf of mexico and caribbean region, *Tectonophysics*, **155**(1-4), 139–168.

Rossetti, D. F., Bezerra, F. H. R., & Dominguez, J. M. L., 2013. Late Oligocene-Miocene transgressions along the equatorial and eastern margins of Brazil, *Earth-Science Reviews*, **123**, 87–112.

Rowan, M. G., Peel, F. J., & Vendeville, B. C., 2004. Gravity-driven Fold Belts on Passive Margins, in *Thrust Tectonics and Hydrocarbon Systems*, edited by K. R. McClay, pp. 157–182, Tulsa, Oklahoma.

Roy, S. & Rao, R. U. M., 2000. Heat flow in the Indian Shield, *J. Geophys. Res. Solid Earth*, **105**(B11), 587–625.

Rudge, J. F., Roberts, G. G., White, N. J., & Richardson, C. N., 2015. Uplift histories of Africa and Australia from linear inverse modeling of drainage inventories, *J. Geophys. Res. Earth Surf.*, **120**(5), 894–914.

Rudolph, M. L., Lekić, V., & Lithgow-Bertelloni, C., 2015. Viscosity jump in Earth's mid-mantle., *Science*, **350**(6266), 1349–52.

Runcorn, S. K., 1965. Changes in the convection pattern in the Earth's mantle and continental drift: evidence for a cold origin of the Earth, *Phil. Trans. R. Soc. A*, **258**, 228–251.

Rychert, C. A., Schmerr, N., & Harmon, N., 2012. The Pacific lithosphere-asthenosphere boundary: Seismic imaging and anisotropic constraints from SS waveforms, *Geochem. Geophys. Geosyst.*, **13**(1), Q0AK10.

Sahu, H. S., Raab, M. J., Kohn, B. P., Gleadow, A. J. W., & Kumar, D., 2013. Denudation history of Eastern Indian peninsula from apatite fission track analysis: Linking possible plume-related uplift and the sedimentary record, *Tectonophysics*, **608**, 1413–1428.

Sambridge, M., 1999. Geophysical inversion with a neighbourhood algorithmI.Searching a parameter space, *Geophys. J. Int.*, **138**, 479–494.

Sammis, C. G. & Dein, J. L., 1974. On the possibility of transformational superplasticity in the Earth's mantle, *J. Geophys. Res.*, **79**(20), 2961–2965.

Sammis, C. G., Smith, J. C., Schubert, G., & Yuen, D. A., 1977. Viscositydepth profile of the Earth's mantle: Effects of polymorphic phase transitions, *J. Geophys. Res.*, **82**(26), 3747–3761.

Sandwell, D. T., Müller, R. D., Smith, W. H. F., Garcia, E., & Francis, R., 2014. New global marine gravity model from CryoSat-2 and Jason-1 reveals buried tectonic structure, *Science*, **346**(6205), 65–67.

Sarkar, D., Kumar, M. R., Saul, J., Kind, R., Raju, P. S., Chadha, R. K., & Shukla, A. K., 2003. A receiver function perspective of the Dharwar craton (India) crustal structure, *Geophys. J. Int.*, **154**(1), 205–211.

Saul, J., Kumar, M. R., & Sarkar, D., 2000. Lithospheric and upper mantle structure of the Indian Shield, from teleseismic receiver functions, *Geophys. Res. Lett.*, **27**(16), 2357–2360.

Schaeffer, A. J. & Lebedev, S., 2013. Global shear speed structure of the upper mantle and transition zone, *Geophys. J. Int.*, **194**(1), 417–449.

Schatz, J. F. & Simmons, G., 1972. Thermal conductivity of Earth Materials at High Temperatures, *J. Geophys. Res.*, **77**(35), 6966–6983.

Schmeling, H., Marquart, G., & Nawa, V., 2017. The role of hydrothermal cooling of the oceanic lithosphere for ocean floor bathymetry and heat flow, *J. Geophys. Res. Solid Earth*, **122**, 3934–3952.

Schmerr, N., 2012. The Gutenberg Discontinuity: Melt at the Lithosphere-Asthenosphere Boundary, *Science*, **335**(6075), 1480–1483.

Schmidt, P., Prasad, V., & Ramam, P., 1983. Magnetic ages of some Indian laterites, *Palaeogeog. Palaeoclimatol. Palaeoecol.*, **44**(3-4), 185–202.

Schoonman, C., White, N., & Pritchard, D., 2017. Radial viscous fingering of hot asthenosphere within the icelandic plume beneath the north atlantic ocean, *Earth Plan. Sci. Lett.*, **468**, 51–61.

Schouten, H. & Klitgord, K. D., 1994. Mechanistic solutions to the opening of the gulf of mexico, *Geology*, **22**(6), 507–510.

Schuberth, B. S. A. & Bunge, H. P., 2009. Tomographic filtering of high-resolution mantle circulation models: Can seismic heterogeneity be explained by temperature alone?, *Geochem. Geophys. Geosyst.*, **10**(5), Q05W03.

Schuberth, B. S. A., Bunge, H. P., Steinle-Neumann, G., Moder, C., & Oeser, J., 2009. Thermal versus elastic heterogeneity in high-resolution mantle circulation models with pyrolite composition: High plume excess temperatures in the lowermost mantle, *Geochem. Geophys. Geosyst.*, **10**(1), Q01W01.

Schuberth, B. S. A., Zaroli, C., & Nolet, G., 2012. Synthetic seismograms for a synthetic Earth: Long-period P- and S-wave traveltime variations can be explained by temperature alone, *Geophys. J. Int.*, **188**(3), 1393–1412.

Schutt, D. L. & Lesher, C. E., 2006. Effects of melt depletion on the density and seismic velocity of garnet and spinel lherzolite, *J. Geophys. Res. Solid Earth*, **111**(5), 1–24.

Sclater, J. G., Jaupart, C., & Galson, D., 1980. The heat flow through oceanic and continental crust and the heat loss of the Earth, *Rev. Geophys.*, **18**(1), 269–311.

Shaw Champion, M. E., White, N. J., Jones, S. M., & Lovell, J. P. B., 2008. Quantifying transient mantle convective uplift: An example from the Faroe-Shetland basin, *Tectonics*, **27**(1), TC1002.

Shearer, P. M. & Flanagan, M. P., 1999. Seismic velocity and density jumps across the 410-and 660-kilometer discontinuities, *Science*, **285**(5433), 1545–1548.

Sheth, H., 2007. Plume-related regional pre-volcanic uplift in the Deccan Traps: Absence of evidence, evidence of absence, *Geol. Soc. Am. Sp. Pap.*, **430**(1), 785–813.

Shorttle, O. & Maclennan, J., 2011. Compositional trends of icelandic basalts: Implications for short-length scale lithological heterogeneity in mantle plumes, *Geochem. Geophys. Geosyst.*, **12**(11), Q11008.

Shorttle, O., Maclennan, J., & Lambart, S., 2014. Quantifying lithological variability in the mantle, *Earth Plan. Sci. Lett.*, **395**, 24–40.

Shukla, A., Mehrotra, R. C., Spicer, R. A., Spicer, T. E., & Kumar, M., 2014. Cool equatorial terrestrial temperatures and the South Asian monsoon in the Early Eocene: Evidence from the Gurha Mine, Rajasthan, India, *Palaeogeog. Palaeoclimatol. Palaeoecol.*, **412**, 187–198.

Siddall, M., Rohling, E. J., Almogi-Labin, A., Hemleben, C., Meischner, D., Schmelzer, I., & Smeed, D. A., 2003. Sea-level fluctuations during the last glacial cycle., *Nature*, **423**(6942), 853–858.

Siddall, M., Bard, E., Rohling, E. J., & Hemleben, C., 2006. Sea-level reversal during termination II, *Geology*, **34**(10), 817–820.

Simmons, N. A., Forte, A. M., & Grand, S. P., 2007. Thermochemical structure and dynamics of the African superplume, *Geophys. Res. Lett.*, **34**(2), 1–5.

Singh, A., Misra, B. K., Singh, B. D., & Navale, G. K. B., 1992. The Neyveli lignite deposits (Cauvery basin), India: organic composition, age and depositional pattern, *Int. J. Coal Geol.*, **21**(1-2), 45–97.

Singh, A., Kumar, M. R., Kumar, N., Saikia, D., Solomon Raju, P., Srinagesh, D., Rao, N. P., & Sarkar, D., 2012. Seismic signatures of an altered crust and a normal transition zone structure beneath the Godavari rift, *Precambrian Res.*, **220-221**, 1–8.

Singh, A., Singh, C., & Kennett, B. L. N., 2015. A review of crust and upper mantle structure beneath the Indian subcontinent, *Tectonophysics*, **644-645**, 1–21.

Singh, A. D., 1998. Early-Middle Miocene Planktic Foraminifera from the Quilon Formation, Kerala, *Geol. Soc. India*, **52**(3), 313–316.

Sklar, D. W. E., 2001. Sediment and rock strength controls on river incision into bedrock, *Geology*, **29**(12), 1087–1090.

Sklar, L. & Dietrich, W. E., 1998. River Longitudinal Profiles and Bedrock Incision Models: Stream Power and the Influence of Sediment Supply, in *Rivers Over Rock: Fluvial Processes in Bedrock Channels*, edited by J. Tinkler & E. Wohl, vol. 107, pp. 237–260, American Geophysical Union, Washington, D.C.

Smith, W. H. & Sandwell, D. T., 1997. Global Sea Floor Topography from Satellite Altimetry and Ship Depth Soundings, *Science*, **277**(September), 1956–1962.

Sobolev, A. V., Hofmann, A. W., Kuzmin, D. V., Yaxley, G. M., Arndt, N. T., Chung, S.-L., Danyushevsky, L. V., Elliott, T., Frey, F. A., Garcia, M. O.,*et al.*, 2007. The amount of recycled crust in sources of mantle-derived melts, *Science*, **316**(5823), 412–417.

Spasojevic, S. & Gurnis, M., 2012. Sea level and vertical motion of continents from dynamic earth models since the late Cretaceous, *AAPG Bull.*, **96**(11), 2037–2064.

Stein, C. A. & Stein, S., 1992. A model for the global variation in oceanic depth and heat flow with lithospheric age, *Nature*, **356**, 133–135.

Steinberger, B., 2007. Effects of latent heat release at phase boundaries on flow in the Earth's mantle, phase boundary topography and dynamic topography at the Earth's surface, *Phys. Earth Planet. In.*, **164**(1-2), 2–20.

Steinberger, B., 2016. Topography caused by mantle density variations: Observation-based estimates and models derived from tomography and lithosphere thickness, *Geophys. J. Int.*, **205**(1), 604–621.

Steinberger, B. & Becker, T. W., 2017. A comparison of lithospheric thickness models, *Tectonophysics*, pp. 1–14.

Steinberger, B. & Calderwood, A. R., 2006. Models of large-scale viscous flow in the Earth's mantle with constraints from mineral physics and surface observations, *Geophys. J. Int.*, **167**(3), 1461–1481.

Steinberger, B. & Torsvik, T. H., 2008. Absolute plate motions and true polar wander in the absence of hotspot tracks., *Nature*, **452**(7187), 620–623.

Steinberger, B., Werner, S. C., & Torsvik, T. H., 2010. Deep versus shallow origin of gravity anomalies, topography and volcanism on Earth, Venus and Mars, *Icarus*, **207**(2), 564–577.

Steinberger, B., Conrad, C. P., Tutu, A. O., & Hoggard, M. J., 2017. On the amplitude of dynamic topography at spherical harmonic degree two, *Tectonophysics*.

Stephenson, S. N., Roberts, G. G., Hoggard, M. J., & Whittaker, A. C., 2014. A Cenozoic uplift history of Mexico and its surroundings fromlongitudinal river profiles, *Geochem. Geophys. Geosyst.*, pp. 4734–4758.

Stern, T. A., Henrys, S. A., Okaya, D., Louie, J. N., Savage, M. K., Lamb, S., Sato, H., Sutherland, R., & Iwasaki, T., 2015. A seismic reflection image for the base of a tectonic plate, *Nature*, **518**(7537), 85–88.

Stixrude, L. & Lithgow-Bertelloni, C., 2005. Mineralogy and elasticity of the oceanic upper mantle: Origin of the low-velocity zone, *J. Geophys. Res. Solid Earth*, **110**(3), 1–16.

Stixrude, L. & Lithgow-Bertelloni, C., 2011. Thermodynamics of mantle minerals–II. Phase equilibria, *Geophys. J. Int.*, **184**(3), 1180–1213.

Stixrude, L. & Lithgow-Bertelloni, C., 2012. Geophysics of Chemical Heterogeneity in the Mantle, *Ann. Rev. Earth Plan. Sci.*, **40**(1), 569–595.

Stixrude, L., de Koker, N., Sun, N., Mookherjee, M., & Karki, B. B., 2009. Thermodynamics of silicate liquids in the deep earth, *Earth Plan. Sci. Lett.*, **278**(3), 226–232.

Stock, J. D. & Montgomery, D. R., 1999. Geologic constraints on bedrock river incision using the stream power law, *J. Geophys. Res. Solid Earth*, **104**(B3), 4983–4993.

Stocker, R. L. & Ashby, M. F., 1973. On the rheology of the upper mantle, *Rev. Geophys.*, **11**(2), 391–426.

Suryawanshi, R. A. & Golekar, R. B., 2014. Geochemistry of sub-surface Tertiary–Sediments of Ratnagiri District, Maharashtra, India, *Int. J. Adv. Earth Sci.*, **3**(1), 1–12.

Tackley, P. J., 2002. Strong heterogeneity caused by deep mantle layering, *Geochem. Geophys. Geosyst.*, **3**(4), 1–22.

Tackley, P. J., 2008. Modelling compressible mantle convection with large viscosity contrasts in a three-dimensional spherical shell using the yin-yang grid, *Phys. Earth Planet. In.*, **171**(1-4), 7–18.

Takei, Y., 2017. Effects of Partial Melting on Seismic Velocity and Attenuation: A New Insight From Experiments, *Annu. Rev. Earth Plan. Sci.*, **45**, 1–25.

Takei, Y., Karasawa, F., & Yamauchi, H., 2014. Temperature, grain size, and chemical controls on polycrystal anelasticity over a broad frequency range extending into the seismic range, *J. Geophys. Res. Solid Earth*, **119**(7), 5414–5443.

Tapley, B., Ries, J., Bettadpur, S., Chambers, D., Cheng, M., Condi, F., & Poole, S., 2007. The GGM03 Mean Earth Gravity Model from GRACE, *AGU Fall Meeting Abstracts*, pp. G42A–03.

Tarboton, D. G., 1997. A new method for the determination of flow directions and upslope areas in grid digital elevation models, *Water Resour. Res.*, **33**(2), 309–319.

Tawde, S. A. & Singh, C., 2015. Investigation of orographic features influencing spatial distribution of rainfall over the Western Ghats of India using satellite data, *Int. J. Climatol.*, **35**(9), 2280–2293.

Thomson, A. R., Walter, M. J., Kohn, S. C., & Brooker, R. A., 2016. Slab melting as a barrier to deep carbon subduction, *Nature*, **529**(7584), 76–79.

Thoraval, C., Machetel, P., & Cazenave, A., 1995. Locally layered convection inferred from dynamic models of the Earth's mantle, *Nature*, **375**(6534), 777–780.

Thorne, R. L., Roberts, S., & Herrington, R., 2012. Climate change and the formation of nickel laterite deposits, *Geology*, **40**(4), 331–334.

Thybo, H., 2006. The heterogeneous upper mantle low velocity zone, *Tectonophysics*, **416**(1), 53–79.

Tiwari, P. K., Surve, G., & Mohan, G., 2006. Crustal constraints on the uplift mechanism of the Western Ghats of India, *Geophys. J. Int.*, **167**(3), 1309–1316.

Todal, A. & Edholm, O., 1999. Continental margin off Western India and Deccan Large Igneous Province, *Mar. Geophys. Res.*, (1995), 273–291.

Tomkin, J. H., 2003. Quantitative testing of bedrock incision models for the Clearwater River, NW Washington State, *J. Geophys. Res. Solid Earth*, **108**(B6), 2308.

Torsvik, T. H., Smethurst, M. A., Burke, K., & Steinberger, B., 2008. Long term stability in deep mantle structure: Evidence from the~ 300 Ma Skagerrak-Centered Large Igneous Province (the SCLIP), *Earth Plan. Sci. Lett.*, **267**(3-4), 444–452.

Trampert, J., Deschamps, F., Resovsky, J., & Yuen, D., 2004. Probabilistic Tomography Maps Chemical Heterogeneities Throughout the Lower Mantle, *Science*, **306**(5697), 853–856.

Turcotte, D. L. & Emerman, S. H., 1983. Mechanisms of active and passive rifting, *Tectonophysics*, **94**(1-4), 39–50.

Turcotte, D. L. & Oxburgh, E. R., 1967. Finite amplitude convective cells and continental drift, *J. Fluid Mech.*, **28**, 29–42.

Turcotte, D. L. & Oxburgh, E. R., 1969. Convection in a mantle with variable physical properties, *J. Geophys. Res.*, **74**(6), 1458–1474.

Turcotte, D. L. & Schubert, G., 2002. *Geodynamics (2nd Ed.)*, Cambridge University Press, Cambridge.

Turner, A. J., Katz, R. F., & Behn, M. D., 2015. Grain-size dynamics beneath mid-ocean ridges: Implications for permeability and melt extraction, *Geochem. Geophys. Geosyst.*, **16**(3), 925–946.

Turner, S. & Hawkesworth, C., 1995. The nature of the sub-continental mantle: constraints from the major-element composition of continental flood basalts, *Chem. Geol.*, **120**(3-4), 295–314.

Ueki, K. & Iwamori, H., 2013. Thermodynamic model for partial melting of peridotite by system energy minimization, *Geochem. Geophys. Geosyst.*, **14**(2), 342–366.

Valdiya, K. S., 2001. Tectonic resurgence of the Mysore plateau and surrounding regions in cratonic Southern India, *Curr. Sci.*, **81**(8), 1068–1089.

Valeton, I., 1983. Palaeoenvironment of lateritic bauxites with vertical and lateral differentiation, *Geol. Soc. Lond. Sp. Pub.*, **11**(1), 77–90.

Van Avendonk, H. J., Davis, J. K., Harding, J. L., & Lawver, L. A., 2017. Decrease in oceanic crustal thickness since the breakup of pangaea, *Nat. Geosci.*, **10**(1), 58–61.

Van Bocxlaer, I., Biju, S., Loader, S. P., & Bossuyt, F., 2009. Toad radiation reveals into-India dispersal as a source of endemism in the Western Ghats-Sri Lanka biodiversity hotspot, *BMC Evol. Biol.*, **9**(1), 131.

van der Beek, P. & Bishop, P., 2003. Cenozoic river profile development in the Upper Lachlan catchment (SE Australia) as a test of quantitative fluvial incision models, *J. Geophys. Res. Solid Earth*, **108**(B6), 2309.

van der Wal, W., Whitehouse, P. L., & Schrama, E. J. O., 2015. Effect of GIA models with 3D composite mantle viscosity on GRACE mass balance estimates for Antarctica, *Earth Plan. Sci. Lett.*, **414**, 134–143.

van Hunen, J., Huang, J., & Zhong, S., 2003. The effect of shearing on the onset and vigor of small-scale convection in a Newtonian rheology, *Geophys. Res. Lett.*, **30**(19), 1991.

Veeraswamy, K. & Raval, U., 2005. Remobilization of the palaeoconvergent corridors hidden under the Deccan trap cover and some major stable continental region earthquakes, *Curr. Sci.*, **89**(3), 522–530.

Vijay Kumar, T., Jagadeesh, S., & Rai, S., 2012. Crustal structure beneath the Archean-Proterozoic terrain of north India from receiver function modeling, *J. Asian Earth Sci.*, **58**, 108–118.

Vita-Finzi, C., 2004. Buckle-controlled seismogenic faulting in peninsular India, *Quat. Sci. Rev.*, **23**(23-24), 2405–2412.

Vogt, P. R., 1971. Asthenosphere motion recorded by the ocean floor south of Iceland, *Earth Plan. Sci. Lett.*, **13**(1), 153–160.

von Blanckenburg, F., 2004. Cosmogenic nuclide evidence for low weathering and denudation in the wet, tropical highlands of Sri Lanka, *J. Geophys. Res. Earth Surf.*, **109**(F3), F03008.

Von Herzen, R. P. & Uyeda, S., 1963. Heat flow through the eastern Pacific ocean floor, *J. Geophys. Res.*, **68**(14), 4219–4250.

Wandrey, C. J. & Law, B. E., 1997. Maps showing geology, oil and gas fields and geologic provinces of South Asia, *USGS Open File Rep.*, **470**(C).

Wang, H., Gurnis, M., & Skogseid, J., 2017. Rapid Cenozoic Subsidence in the Gulf of Mexico Resulting From Hess Rise Conjugate Subduction, *Geophys. Res. Lett.*, **44**(21), 10930–10938.

Wang, P., Clemens, S., Beaufort, L., Braconnot, P., Ganssen, G., Jian, Z., Kershaw, P., & Sarnthein, M., 2005. Evolution and variability of the Asian monsoon system: state of the art and outstanding issues, *Quat. Sci. Rev.*, **24**(5-6), 595–629.

Waples, D. W. & Waples, J. S., 2004. A Review and Evaluation of Specific Heat Capacities of Rocks, Minerals, and Subsurface Fluids. Part 2: Fluids and Porous Rocks, *Nat. Resources Res.*, **13**(2), 123–130.

Watkins, C. E. & Conrad, C. P., 2018. Constraints on dynamic topography from asymmetric subsidence of the mid-ocean ridges, *Earth Plan. Sci. Lett.*, **484**, 264–275.

Watts, A., 2001. *Isostasy and Flexure of the Lithosphere*, Cambridge University Press, Cambridge.

Watts, A., Zhong, S., & Hunter, J., 2013. The Behavior of the Lithosphere on Seismic to Geologic Timescales, *Ann. Rev. Earth Plan. Sci.*, **41**(1), 443–468.

Watts, A. B. & Cox, K., 1989. The Deccan Traps: an interpretation in terms of progressive lithospheric flexure in response to a migrating load, *Earth Plan. Sci. Lett.*, **93**(1), 85–97.

Watts, A. B. & Zhong, S., 2000. Observations of flexure and the rheology of oceanic lithosphere, *Geophys. J. Int.*, **142**(3), 855–875.

Weismüller, J., Gmeiner, B., Ghelichkhan, S., Huber, M., John, L., Wohlmuth, B., Rüde, U., & Bunge, H. P., 2015. Fast asthenosphere motion in high-resolution global mantle flow models, *Geophys. Res. Lett.*, **42**(18), 7429–7435.

Weissel, J. K. & Seidl, M. A., 1998. Inland Propagation of Erosional Escarpments and River Profile Evolution Across the Southeast Australian Passive Continental Margin, in *Rivers Over Rock: Fluvial Processes in Bedrock Channels*, edited by K. J. Tinkler & E. E. Wohl, pp. 189–206, American Geophysical Union, Washington, D.C.

Wen, L. & Anderson, D. L., 1997. Slabs, hotspots, cratons and mantle convection revealed from residual seismic tomography in the upper mantle, *Phys. Earth Planet. In.*, **99**(96), 131–143.

Wessel, P., Sandwell, D., & Kim, S.-S., 2010. The Global Seamount Census, *Oceanography*, **23**(1), 24–33.

Whipple, K. X., 2002. Implications of sediment-flux-dependent river incision models for landscape evolution, *J. Geophys. Res. Solid Earth*, **107**(B2), 2039.

Whipple, K. X., 2009. The influence of climate on the tectonic evolution of mountain belts, *Nat. Geosci.*, **2**(2), 97–104.

Whipple, K. X. & Tucker, G. E., 1999. Dynamics of the stream-power river incision model: Implications for height limits of mountain ranges, landscape response timescales, and research needs, *J. Geophys. Res. Solid Earth*, **104**(B8), 17661–17674.

White, R. & McKenzie, D., 1989. Magmatism at rift zones: The generation of volcanic continental margins and flood basalts, **94**, 7685–7729.

White, R. S., McKenzie, D., & O'Nions, R. K., 1992. Oceanic crustal thickness from seismic measurements and rare earth element inversions, *J. Geophys. Res. Solid Earth*, **97**(B13), 19683–19715.

White, W. M. & Klein, E. M., 2013. *Composition of the Oceanic Crust*, vol. 4, Elsevier, 2nd edn.

Whiting, B. M., Karner, G. D., & Driscoll, N. W., 1994. Flexural and stratigraphic development of the west Indian continental margin, *J. Geophys. Res. Solid Earth*, **99**(94), 13791–13811.

Whittaker, A. C. & Boulton, S. J., 2012. Tectonic and climatic controls on knickpoint retreat rates and landscape response times, *J. Geophys. Res. Earth Surf.*, **117**(F2), 2156–2202.

Whittaker, A. C., Cowie, P. A., Attal, M., Tucker, G. E., & Roberts, G. P., 2007. Contrasting transient and steady-state rivers crossing active normal faults: new field observations from the Central Apennines, Italy, *Basin Res.*, **19**(4), 529–556.

Whittaker, J. M., Goncharov, A., Williams, S. E., Müller, R. D., & Leitchenkov, G., 2013. Global sediment thickness data set updated for the Australian-Antarctic Southern Ocean, *Geochem. Geophys. Geosyst.*, **14**(8), 3297–3305.

Widdowson, M., 1997. Tertiary palaeosurfaces of the SW Deccan, Western India: implications for passive margin uplift, *Geol. Soc. Lond. Sp. Pub.*, **120**(1), 221–248.

Widdowson, M. & Cox, K., 1996. Uplift and erosional history of the Deccan Traps, India: Evidence from laterites and drainage patterns of the Western Ghats and Konkan Coast, *Earth Plan. Sci. Lett.*, **137**(1-4), 57–69.

Widdowson, M. & Mitchell, C., 1999. Large-scale Stratigraphical, Structural and Geomorphological Constraints for Earthquakes in the Southern Deccan Traps, India: The Case for Denudationally-driven Seismicity, *Mem. Geol. Soc. India*, **43**(1), 425–452.

Wiens, D. A. & Stein, S., 1983. Age dependence of oceanic intraplate seismicity and implications for lithospheric evolution, *J. Geophys. Res. Solid Earth*, **88**(B8), 6455–6468.

Willett, S. D., McCoy, S. W., Perron, J. T., Goren, L., & Chen, C.-Y., 2014. Dynamic reorganization of river basins., *Science*, **343**(6175), 1248765.

Wilson, D. J., Peirce, C., Watts, A. B., & Grevemeyer, I., 2013. Uplift at lithospheric swellsII: is the Cape Verde mid-plate swell supported by a lithosphere of varying mechanical strength?, *Geophys. J. Int.*, **193**(2), 798–819.

Wilson, J. W. P., Roberts, G. G., Hoggard, M. J., & White, N. J., 2014. Cenozoic epeirogeny of the Arabian Peninsula from drainage modeling, *Geochem. Geophys. Geosyst.*, **15**(10), 3723–3761.

Winterbourne, J., White, N., & Crosby, A., 2014. Accurate measurements of residual topography from the oceanic realm, *Tectonics*, **33**(6), 982–1015.

Winterbourne, J. R., Crosby, A. G., & White, N. J., 2009. Depth, age and dynamic topography of oceanic lithosphere beneath heavily sedimented Atlantic margins, *Earth Plan. Sci. Lett.*, **287**, 137–151.

Wolf, R. A., Farley, K. A., & Silver, L. T., 1996. Helium diffusion and low temperature thermochronometry of apatite, *Geochim. Cosmochim. Acta*, **60**(21), 4231–4240.

Woodroffe, S. A. & Horton, B. P., 2005. Holocene sea-level changes in the Indo-Pacific, *J. Asian Earth Sci.*, **25**(1), 29–43.

Workman, R. K. & Hart, S. R., 2005. Major and trace element composition of the depleted MORB mantle (DMM), *Earth Plan. Sci. Lett.*, **231**(1-2), 53–72.

Xu, Y., Shankland, T. J., Linhardt, S., Rubie, D. C., Langenhorst, F., & Klasinski, K., 2004. Thermal diffusivity and conductivity of olivine, wadsleyite and ringwoodite to 20 GPa and 1373 K, *Phys. Earth Planet. In.*, **143**(1-2), 321–336.

Yamato, P., Husson, L., Becker, T. W., & Pedoja, K., 2013. Passive margins getting squeezed in the mantle convection vice, *Tectonics*, **32**(6), 1559–1570.

Yamauchi, H. & Takei, Y., 2016. Polycrystal anelasticity at near-solidus temperatures, *J. Geophys. Res. Solid Earth*, **121**(11), 7790–7820.

Yang, T. & Gurnis, M., 2016. Dynamic topography, gravity and the role of lateral viscosity variations from inversion of global mantle flow, *Geophys. J. Int.*, **207**(2), 1186–1202.

Yang, T., Moresi, L., Müller, R. D., & Gurnis, M., 2017. Oceanic residual topography agrees with mantle flow predictions at long wavelengths, *Geophysical Research Letters*, **44**(21), 10896–10906.

Yuan, H. & Romanowicz, B., 2010. Lithospheric layering in the north american craton, *Nature*, **466**(7310), 1063.

Yuen, D. A. & Fleitout, L., 1985. Thinning of the lithosphere by small-scale convective destabilization, *Nature*, **313**(5998), 125–128.

Yuen, D. A., Reuteler, D. M., Balachandar, S., Steinbach, V., Malevsky, A. V., & Smedsmo, J. J., 1994. Various influences on three-dimensional mantle convection with phase transitions, *Phys. Earth Planet. In.*, **86**, 185–203.

Zaroli, C., Sambridge, M., Lévêque, J.-J., Debayle, E., & Nolet, G., 2013. An objective rationale for the choice of regularisation parameter with application to global multiple-frequency S-wave tomography, *Solid Earth*, **4**(2), 357–371.

Zaroli, C., Koelemeijer, P., & Lambotte, S., 2017. Toward Seeing the Earth's Interior Through Unbiased Tomographic Lenses, *Geophys. Res. Lett.*, **44**(22), 11,399–11,408.

Zeitler, P. K., Herczeg, A. L., McDougall, I., & Honda, M., 1987. U-Th-He dating of apatite: A potential thermochronometer, *Geochim. Cosmochim. Acta*, **51**(10), 2865–2868.

Zhang, S. & Karato, S.-i., 1995. Lattice preferred orientation of olivine aggregates deformed in simple shear, *Nature*, **375**(6534), 774–777.

Zhao, S., Lambeck, K., & Lidberg, M., 2012. Lithosphere thickness and mantle viscosity inverted from GPS-derived deformation rates in Fennoscandia, *Geophys. J. Int.*, **190**(1), 278–292.

Zhong, S., Zuber, M. T., Moresi, L., & Gurnis, M., 2000. Role of temperature-dependent viscosity and surface plates in spherical shell models of mantle convection, *J. Geophys. Res. Solid Earth*, **105**(B5), 11063–11082.

Appendix A

New Reflection Seismic Profiles Included in Oceanic Residual Depth Database

Over 200 new seismic reflection profiles, generously provided by **Spectrum Geo Ltd.**, were analysed, with 123 sections interpreted and added to the oceanic residual depth database of Hoggard *et al.* (2017). Seabed and sediment-basement interfaces are picked on all profiles. The Moho is also interpreted where imaging quality permits unambiguous identification of this interface. Locations and interpretations of these profiles are given in Table A.1 and Figure A.1, respectively.

Table A.1: Multichannel reflection seismic profiles on ocean floor picked in two-way travel time. Regional estimates of whether the crustal thickness (z_c) is larger or smaller than the global average of 7.1 km are included (White *et al.*, 1992).

Profile No.	Source	Left Lon.[a]	Left Lat.[a]	Right Lon.[a]	Right Lat.[a]	z_c^b
1	Proprietary data	-57.86	11.84	-56.29	12.04	S
2	Proprietary data	-50.70	5.56	-49.49	6.90	S
3	Proprietary data	-49.72	4.65	-48.71	5.81	S
4	Proprietary data	-48.91	4.21	-47.61	5.69	S
5	Proprietary data	-48.37	4.14	-47.21	5.46	S
6	Proprietary data	-48.45	5.83	-47.03	4.57	S
7	Proprietary data	-40.89	-29.14	-40.08	-27.79	L
8	Proprietary data	-39.34	-26.53	-38.57	-25.17	L
9	Proprietary data	-38.60	-25.22	-37.85	-23.87	L
10	Proprietary data	-37.92	-24.01	-37.19	-22.67	L
11	Proprietary data	-41.85	-28.43	-40.65	-29.11	L
12	Proprietary data	-40.08	-24.99	-38.80	-25.78	L
13	Proprietary data	-39.74	-24.50	-38.51	-25.27	L
14	Proprietary data	-38.49	-23.09	-37.59	-23.66	L
15	Proprietary data	-38.76	-22.07	-37.20	-23.06	L
16	Proprietary data	-52.77	-37.91	-50.46	-35.57	L

Continued overleaf...

Table A.1 – continued

Profile No.	Source	Left Lon.[a]	Left Lat.[a]	Right Lon.[a]	Right Lat.[a]	z_c^b
17	Proprietary data	-52.00	-37.70	-50.17	-35.82	L
18	Proprietary data	-51.02	-35.40	-50.05	-35.93	L
19	Proprietary data	-52.00	-35.48	-50.33	-36.40	L
20	Proprietary data	-52.32	-35.73	-50.60	-36.68	L
21	Proprietary data	-52.53	-36.05	-50.88	-36.96	L
22	Proprietary data	-52.83	-36.32	-51.15	-37.25	L
23	Proprietary data	-52.76	-37.18	-51.84	-37.69	L
24	Proprietary data	-53.14	-37.62	-52.48	-37.98	L
25	Proprietary data	-52.85	-36.02	-51.11	-36.91	L
26	Proprietary data	-54.28	-35.56	-51.36	-37.10	L
27	Proprietary data	8.51	-4.17	8.77	-3.99	S
28	Proprietary data	8.32	-4.03	8.59	-3.84	S
29	Proprietary data	8.22	-3.82	8.64	-3.53	S
30	Proprietary data	8.11	-3.60	8.72	-3.21	S
31	Proprietary data	8.07	-3.54	8.47	-3.29	S
32	Proprietary data	46.34	-29.79	49.40	-30.60	L
33	Proprietary data	46.31	-32.29	49.37	-30.49	L
34	Proprietary data	41.48	-22.94	42.66	-21.99	S
35	Proprietary data	40.77	-18.66	42.09	-18.81	S
36	Proprietary data	12.22	-28.94	13.86	-28.78	L
37	Proprietary data	13.55	-30.73	13.05	-28.96	L
38	Proprietary data	12.98	-29.54	13.58	-29.47	L
39	Proprietary data	12.94	-29.88	14.30	-29.50	L
40	Proprietary data	12.95	-31.82	14.33	-30.76	L
41	Proprietary data	13.29	-32.30	14.95	-31.02	L
42	Proprietary data	14.16	-33.83	15.26	-35.34	L
43	Proprietary data	12.61	-31.06	15.38	-34.98	L
44	Proprietary data	12.61	-31.06	15.38	-34.98	L
45	Proprietary data	-95.33	18.88	-92.00	25.13	S
46	Proprietary data	-95.33	18.88	-92.00	25.13	S
47	Proprietary data	-95.62	20.04	-92.69	24.90	S
48	Proprietary data	-96.04	20.88	-94.10	23.66	S
49	Proprietary data	-96.43	21.37	-93.45	25.85	S
50	Proprietary data	-97.13	21.63	-94.41	26.00	S
51	Proprietary data	-96.93	21.61	-92.19	22.12	S
52	Proprietary data	-97.03	21.75	-93.87	20.05	S
53	Proprietary data	-97.31	22.55	-93.74	20.75	S
54	Proprietary data	-95.87	22.61	-92.47	20.81	S

Continued overleaf...

Table A.1 – **continued**

Profile No.	Source	Left Lon.[a]	Left Lat.[a]	Right Lon.[a]	Right Lat.[a]	z_c^b
55	Proprietary data	-96.59	22.92	-91.05	23.06	S
56	Proprietary data	-96.42	23.81	-92.60	21.85	S
57	Proprietary data	-96.24	24.58	-92.02	22.35	S
58	Proprietary data	-95.58	25.35	-91.44	22.59	S
59	Proprietary data	-95.38	25.74	-91.00	22.90	S
60	Proprietary data	-94.58	25.95	-90.13	23.08	S
61	Proprietary data	-93.28	23.45	-91.12	24.63	S
62	Proprietary data	-90.62	23.76	-91.19	24.65	S
63	Proprietary data	-88.84	23.80	-90.05	25.75	S
64	Proprietary data	-90.34	25.46	-89.79	25.75	S
65	Proprietary data	50.83	5.55	50.99	5.82	S
66	Proprietary data	48.52	2.79	49.49	1.85	S
67	Proprietary data	46.78	2.02	47.45	1.15	S
68	Proprietary data	46.41	0.19	47.07	0.89	S
69	Proprietary data	43.72	-0.90	45.02	0.40	S
70	Proprietary data	43.75	0.01	45.72	-1.53	S
71	Proprietary data	43.28	0.14	44.74	-1.00	S
72	Proprietary data	44.12	-0.51	45.54	-1.64	S
73	Proprietary data	43.52	-0.94	44.29	-1.52	S
74	Proprietary data	43.52	-1.13	44.20	-1.64	S
75	Proprietary data	-21.41	17.50	-18.53	17.53	L
76	Proprietary data	-21.39	17.54	-18.09	15.06	L
77	Proprietary data	-17.84	13.39	-20.06	12.45	L
78	Proprietary data	-20.04	12.53	-17.86	9.10	L
79	Proprietary data	-17.18	14.10	-18.78	12.99	L
80	Proprietary data	-18.79	16.11	-17.84	16.10	L
81	Proprietary data	-18.66	16.45	-17.79	16.44	L
82	Proprietary data	-18.67	17.17	-17.70	17.15	L
83	Proprietary data	-18.64	17.34	-17.41	17.32	L
84	Proprietary data	-19.04	18.30	-17.61	18.73	L
85	Proprietary data	-19.18	18.79	-18.68	18.95	L
86	Proprietary data	-19.26	19.16	-18.28	19.46	L
87	Proprietary data	11.18	-27.11	13.45	-26.91	L
88	Proprietary data	11.03	-26.22	14.22	-25.92	L
89	Proprietary data	11.20	-26.07	11.48	-27.19	L
90	Proprietary data	13.18	-31.00	12.91	-29.96	L
91	Proprietary data	12.83	-30.24	14.25	-29.72	L
92	Proprietary data	12.90	-30.55	14.11	-29.96	L

Table A.1 – continued

Profile No.	Source	Left Lon.[a]	Left Lat.[a]	Right Lon.[a]	Right Lat.[a]	z_c^b
93	Proprietary data	12.96	-30.73	14.24	-29.93	L
94	Proprietary data	12.54	-31.22	14.32	-30.15	L
95	Proprietary data	12.91	-31.50	14.25	-30.45	L
96	Proprietary data	13.13	-32.04	15.03	-30.57	L
97	Proprietary data	13.48	-32.56	15.10	-31.32	L
98	Proprietary data	13.66	-32.85	16.87	-30.34	L
99	Proprietary data	13.80	-33.06	15.37	-31.86	L
100	Proprietary data	13.81	-33.34	15.51	-32.04	L
101	Proprietary data	14.09	-33.42	16.74	-31.36	L
102	Proprietary data	13.95	-33.89	15.58	-32.66	L
103	Proprietary data	15.04	-33.50	15.80	-32.92	L
104	Proprietary data	14.46	-33.94	15.10	-33.45	L
105	Proprietary data	12.94	-30.85	15.77	-34.28	L
106	Proprietary data	14.77	-34.40	15.93	-33.52	L
107	Proprietary data	15.12	-35.49	15.87	-32.85	L
108	Proprietary data	14.40	-35.03	16.02	-33.82	L
109	Proprietary data	-46.09	1.08	-44.40	2.92	S
110	Proprietary data	-45.38	0.88	-43.90	2.49	S
111	Proprietary data	-45.38	0.88	-43.90	2.49	S
112	Proprietary data	-47.02	4.87	-42.34	0.54	S
113	Proprietary data	-47.41	4.42	-42.70	0.17	S
114	Proprietary data	-47.78	3.95	-43.10	-0.29	S
115	Proprietary data	-47.78	3.95	-43.10	-0.29	S
116	Proprietary data	-47.54	3.01	-44.38	0.15	S
117	Proprietary data	-46.91	2.14	-45.34	3.86	S
118	Proprietary data	-44.33	0.01	-42.91	1.57	S
119	Proprietary data	-44.83	0.45	-43.40	2.03	S
120	Proprietary data	-46.56	1.51	-44.85	3.38	S
121	Proprietary data	-43.43	-0.96	-43.38	1.90	S
122	Proprietary data	-44.61	0.34	-44.49	3.00	S
123	Proprietary data	-45.97	1.08	-45.62	3.84	S

[a] In decimal degrees

[b] L/S = larger/smaller than 7.1 km
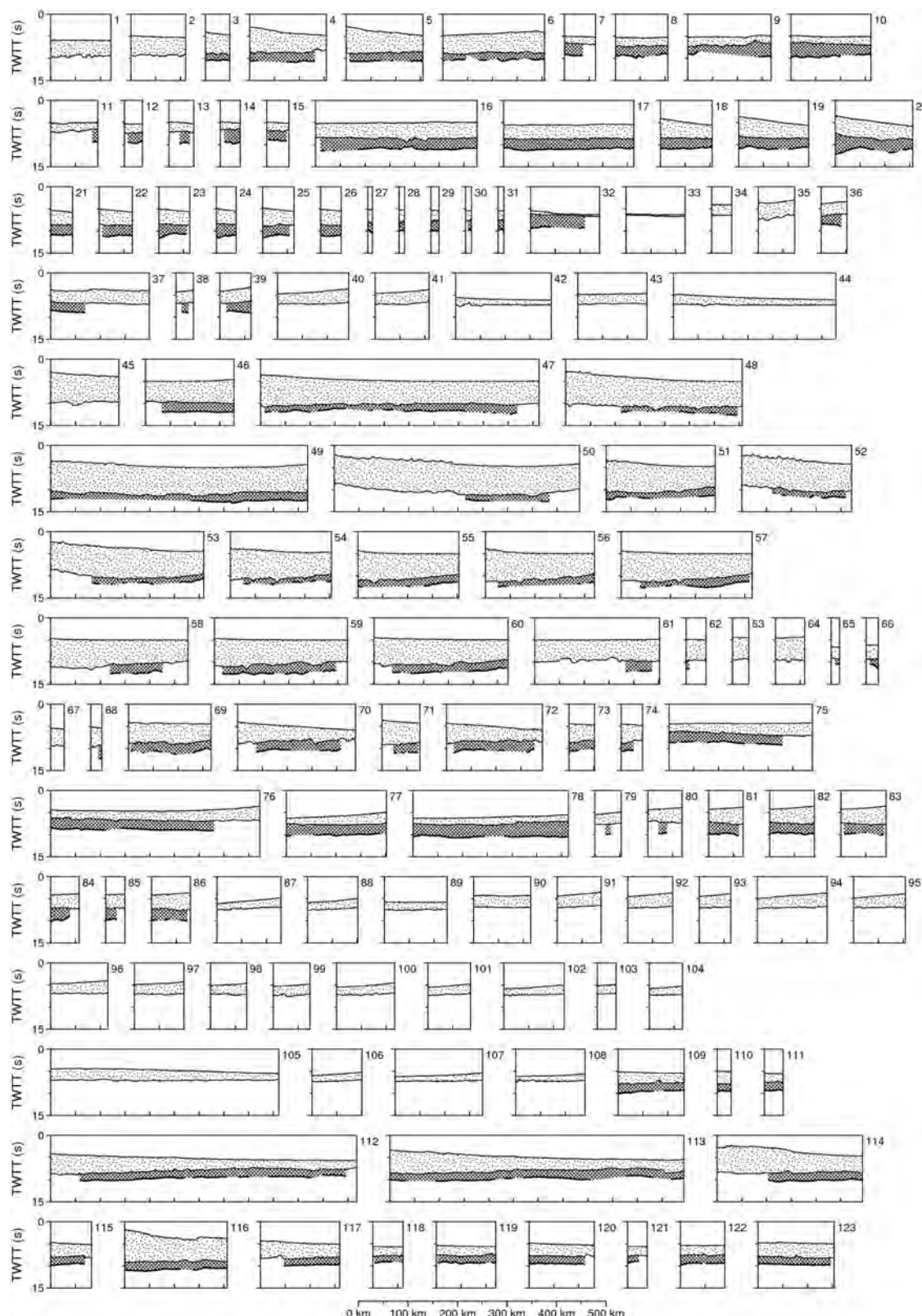
Figure A.1: 123 Interpreted oceanic seismic reflection profiles recorded in two-way travel time. Picked in two-way travel time (TWTT) and used to calculate residual topography. Stippled layer = sediments. Cross hatching = crustal layer. Thick black line = Moho, which is patchy and incomplete due to variable geology and data quality. Profile numbers listed in Table A.1.

Appendix B

Global Inventory of Water-Loaded Basement Depths

This compilation of water-loaded basement depth is derived from more than 1,440 seismic reflection profiles, 302 wide-angle seismic experiments and 395 legacy slope-intercept refraction studies. Sedimentary and crustal corrections have been applied to 1,160 spot measurements, each of which has a typical uncertainty of ±120 m. An additional 870 spot measurements have been included that have only been corrected for sedimentary loading, of which 471 are lower bounds on basement depth and 399 are maxima. The combined inventory of age-depth measurements has been averaged within 1° bins to yield 2,030 individual values.

Table B.1: 1,160 water-loaded basement depths measurements including a crustal correction and averaged over 1° bins (circles in Figure 2.2).

Age (Ma)	w (m)	Error (m)	Lon.[a]	Lat.[a]	Age (Ma)	w (m)	Error (m)	Lon.[a]	Lat.[a]
0.003	3956	43	114.445	-49.845	101.77	5708	102	-42.979	-34.272
0.023	2878	19	-112.974	-15.801	102.014	6199	189	2.132	4.127
0.089	3078	31	109.865	-49.645	102.036	4275	92	-44.48	50.375
0.098	3128	21	109.445	-49.515	102.103	5080	100	-8.517	3.562
0.112	3014	26	109.225	-49.448	102.172	6078	241	-46.078	2.006
0.131	3896	41	114.975	-49.96	102.212	5503	125	-34.4	-3.282
0.152	3916	38	126.955	-48.763	102.292	5598	62	-174.43	-28.3
0.187	1086	78	-24.64	63.04	102.334	5857	234	25.707	-38
0.193	2768	27	-103.988	8.467	102.43	6172	194	-57.711	-46.767
0.197	2815	11	101.846	-47.863	102.456	5438	105	-41.175	-32.258
0.223	2692	55	-105.26	16.109	102.807	6169	261	3.951	4.028
0.237	2938	12	-104.156	9.028	102.88	5625	60	-174.495	-28.521
0.242	2581	64	-129	47.979	103.028	6005	173	2.732	3.91
0.243	1233	47	-26.75	61.737	103.238	5168	137	5.797	2.029
0.253	2720	16	100.39	-47.409	103.258	5498	212	25.537	-37.357
0.266	3107	90	9.17	84.98	103.285	5592	58	-174.54	-28.674

Continued overleaf...

Table B.1 – continued

Age (Ma)	w (m)	Error (m)	Lon.	Lat.	Age (Ma)	w (m)	Error (m)	Lon.	Lat.
0.273	1715	7	-32.737	57.753	103.433	6257	203	0.1	4.719
0.298	2666	15	100.54	-47.483	103.433	6257	203	0.1	4.719
0.315	1283	106	-23.605	63.548	103.447	6118	423	-47.705	3.386
0.322	3717	79	23.33	85.93	103.799	5711	154	25.405	-36.858
0.352	2840	16	-104.12	10.003	103.83	6211	174	1.014	4.375
0.353	2461	4	-129.984	44.449	103.987	6022	342	-47.846	4.325
0.394	1939	11	-32.302	37.298	103.987	5673	115	25.19	-36.044
0.401	2807	17	101.072	-47.682	104.048	5332	60	-63.185	28.613
0.464	3885	83	20	85.79	104.159	5063	246	-2.38	4.001
0.475	2423	30	-11.955	-4.934	104.284	6401	303	-46.757	2.356
0.483	2865	25	-37.095	34.31	104.651	5849	213	-41.92	-1.166
0.501	2839	26	-112.775	-17.231	105.06	5142	114	-40.771	-29.006
0.513	2466	25	-130.051	44.651	105.145	5790	113	-43.885	-33.813
0.574	2451	24	-176.78	-22.255	105.196	5299	112	-41.88	-31.914
0.604	1172	78	-18.525	66.813	105.295	5108	73	8.405	-21.712
0.608	2536	50	-77.795	-44.894	105.325	6412	258	-55.535	8.494
0.618	3125	9	-106	-4.829	105.33	5061	85	-14.181	48.752
0.676	3358	96	-108.588	22.455	105.763	6577	254	-55.648	8.821
0.677	2578	28	-36.4	34.925	105.804	6213	295	88.949	17.225
0.741	1008	61	-18.375	67.183	105.837	5581	95	-34.115	-10.421
0.773	3267	4	133.17	-50.045	105.856	6398	192	1.36	4.524
0.79	3241	4	133.65	-50.077	105.857	4837	142	6.703	2.093
0.895	3204	56	153.853	-10.126	105.941	6251	178	1.71	4.529
0.932	2448	22	-176.51	-22.503	105.969	5451	93	-34.359	-10.844
0.933	2324	33	-176.452	-22.138	106.006	5913	42	106.03	-9.753
0.941	2604	55	-105.655	16.074	106.043	5555	178	-2.874	3.778
0.956	1229	21	-15.833	69.871	106.343	5746	92	-32.204	-7.133
0.97	1160	84	-23.998	63.219	106.431	5320	65	-63.635	28.875
0.994	3006	35	65.465	-27.593	106.543	5089	111	-35.272	-3.32
0.999	2941	28	-104.806	9.086	106.585	5600	161	-42.6	-0.346
1.057	2450	67	-91.655	2.291	106.662	6340	311	87.83	17.228
1.084	2887	27	-112.325	-17.175	107.006	6716	105	-8.583	44.757
1.095	2387	26	50.575	-37.664	107.011	6133	285	87.088	16.991
1.14	2215	12	-13.137	-8.746	107.023	6195	210	2.94	4.646
1.172	3040	19	-112	-15.661	107.028	6018	101	-45.275	-34.863
1.176	3322	48	1.37	84.26	107.079	6409	352	88.615	18.063
1.176	3322	48	1.37	84.26	107.263	5053	62	8.755	-21.866
1.187	3220	12	-105.882	-4.28	107.333	6451	135	-56.805	-43.744
1.236	2809	61	-128.821	46.701	107.4	6423	341	88.014	17.923
1.25	2758	30	-114.065	-17.391	107.426	5979	93	-32.19	-8.864
1.336	1192	35	-18.116	67.82	107.585	6383	115	-7.865	45.99
1.384	2475	69	-91.445	2.254	107.631	5958	231	86.381	15.729

Continued overleaf...

Table B.1 – continued

Age (Ma)	w (m)	Error (m)	Lon.	Lat.	Age (Ma)	w (m)	Error (m)	Lon.	Lat.
1.388	1716	67	38.69	19.585	107.781	5352	119	-42.62	-31.554
1.407	1305	31	-15.665	69.462	108.024	6590	437	89.015	19.505
1.424	2513	57	-94.345	2.689	108.085	6609	418	88.75	19.29
1.472	2546	63	-94.535	2.709	108.269	6062	251	86.761	16.237
1.514	2908	23	-114	-15.947	108.29	6550	372	88.129	18.82
1.521	2567	31	-11.821	-4.493	108.363	5355	145	-35.915	-2.897
1.573	2570	47	50.32	-37.693	108.435	5805	233	86.5	16.797
1.586	3371	52	127	-48.236	108.644	5790	75	40.022	-61.466
1.671	3040	34	-37.715	33.875	108.902	5029	178	7.215	2.618
1.687	2626	59	-129.911	47.06	108.961	6183	296	87.019	17.928
1.78	4179	73	15.29	85.5	109.053	6125	108	-45.805	-34.635
1.795	3133	21	-111.485	-15.588	109.129	5791	92	-32.676	-9.094
1.799	2985	63	-129.155	44.713	109.183	5442	116	-34.977	-10.914
1.806	3509	46	65.995	-27.654	109.366	5692	153	-43.156	-31.292
1.869	2462	108	41.675	15.981	109.434	5632	89	-33.335	-9.564
1.889	3181	12	-102.962	-4.136	109.477	6126	97	-32.165	-8.189
1.919	3364	63	153.005	-10.101	109.531	5967	287	-42.215	-1.705
1.974	3570	111	-108.085	22.179	109.602	6292	138	92.715	-60.46
1.982	1970	35	3.488	72.529	109.98	5455	99	-35.49	-12.212
1.998	2855	63	-129.855	48.166	110.201	6164	97	-47.286	-37.04
2.031	3677	87	-108.854	22.615	110.245	5353	132	9.21	-17.949
2.05	2309	30	-11.626	-5.526	110.325	5877	65	-66.49	22.137
2.115	1125	92	38.285	20.062	110.482	5932	134	-45.162	-33.16
2.175	678	45	-25.844	62.064	110.54	5635	261	86.815	18.654
2.202	2896	30	-114.725	-17.473	111.181	6137	119	-46.287	-34.428
2.25	3279	73	-3.41	83.57	111.223	5502	118	-34.955	-10.444
2.309	2692	32	-36.51	34.591	111.5	6319	320	3.816	4.865
2.323	2978	24	-114.535	-16.024	111.647	5506	108	-36.151	-12.63
2.362	2884	64	-128.115	47.785	112.055	6308	100	-56.445	-43.5
2.408	3055	67	-128.286	46.593	112.118	5536	172	-44	-30.86
2.527	2881	44	-77	-44.733	112.126	4912	222	8.415	2.23
2.773	1422	27	-15.043	69.81	112.173	5521	143	-10.972	4.316
2.886	2878	28	-115.22	-17.534	112.205	5858	98	-32.853	-7.721
3.002	2142	78	2.297	72.27	112.222	5564	95	-33.089	-6.915
3.002	2142	78	2.297	72.27	112.419	6107	99	-47.835	-36.708
3.114	3109	67	-127.955	46.394	112.423	5012	117	-37.31	-18.885
3.204	2721	16	-12.55	-4.852	112.646	5127	108	-34.595	-4.507
3.216	1979	60	-16.245	70.085	112.788	5118	259	8.258	2.881
3.281	2984	54	66.575	-27.541	112.987	5665	166	-35.69	-11.286
3.283	2127	23	-13.163	-8.287	113.05	6039	78	-67.255	22.248
3.303	3016	30	-115.505	-17.569	113.276	6080	160	-57.105	-46.971
3.304	2464	8	-13.515	-8.758	113.573	5736	187	-44.58	-30.554

Table B.1 – continued

Age (Ma)	w (m)	Error (m)	Lon.	Lat.	Age (Ma)	w (m)	Error (m)	Lon.	Lat.
3.542	1606	14	-32.23	57.607	113.606	5231	268	8.677	2.654
3.542	2911	47	65.949	-27.332	113.623	5493	127	-36.052	-12.013
3.748	3703	71	37.86	86.325	113.803	5472	127	9.954	-18.121
3.804	3401	105	-108.04	23.23	113.867	5454	123	-38.329	-24.779
3.842	2875	6	-14.175	-7.814	113.906	5485	93	-33.673	-9.315
3.955	1545	127	38.56	19.435	113.993	5977	120	9.2	-7.646
3.989	2977	47	57.076	-32.744	114.101	6162	191	9.134	-6.27
4.009	3199	74	-127.415	47.632	114.147	5530	130	-37.255	-15.249
4.016	3148	53	-76.39	-44.61	114.199	5130	119	10.21	-18.615
4.225	4011	37	127.585	-48.309	114.312	5996	149	-46.034	-32.72
4.376	2951	62	-130.735	48.359	114.385	4795	111	11.078	-14.041
4.378	3233	69	-125.517	40.711	114.4	5428	120	-37.185	-13.664
4.387	2783	60	-130.855	47.312	114.429	5380	130	-37.145	-13.033
4.94	1553	23	-26.233	61.451	114.469	6290	113	-48.34	-36.402
5.445	2805	47	-131.08	45.073	114.478	6216	141	-47.058	-34.051
5.445	3075	69	-126.59	44.64	114.482	5551	148	10.44	-16.266
5.501	3685	97	-125.499	40.505	114.489	5122	105	-37.35	-22.913
5.549	3267	76	-126.704	47.074	114.704	5737	230	-46.28	-28.447
5.754	1150	57	-25.067	62.09	114.708	4837	217	8.816	2.25
6.078	1666	153	38.455	19.314	114.815	6146	171	9.257	-6.969
6.192	3429	81	-126.16	44.643	114.863	6569	105	-55.915	-42.284
6.351	3592	123	-107.37	21.761	114.979	5476	116	-39.133	-25.756
6.44	3330	82	-126.375	46.681	114.989	5783	196	82.82	12.038
6.591	3514	113	-108.465	23.526	115.079	5589	111	89.4	-61.257
7.128	3429	60	-83.708	1.114	115.119	5862	147	-45.994	-32.154
7.406	3307	18	-14.685	-8.151	115.163	5452	143	-12.94	6.48
7.518	3478	124	-108.62	23.634	115.175	5206	119	-38.727	-25.005
7.817	2637	46	57.278	-32.461	115.182	4868	99	-43.485	44.728
8.199	1684	21	-14.03	69.701	115.26	5555	114	89.78	-61.32
8.899	3235	60	-131.545	45.294	115.285	5533	148	-11.751	5.118
9.119	3659	92	-125.495	40.46	115.46	5265	128	-37.849	-23.716
9.656	4235	92	-46.47	22.779	115.513	5579	174	-45.251	-30.201
9.756	3361	33	-77.96	-43.115	115.514	5326	73	-65.405	29.826
10.04	2597	91	-17.31	71	115.514	5726	111	91.166	-60.819
10.24	2808	96	-17.645	70.686	115.645	5885	79	-67.838	22.266
10.281	3842	67	48.75	86.73	115.65	5181	129	-37.541	-13.274
10.558	2414	75	3.572	72.007	115.668	5556	161	10.216	-16.844
10.576	3436	51	-80.12	2.025	115.808	6060	170	-46.925	-33.065
10.619	3311	70	35	86.13	115.918	5569	170	-11.079	4.846
11.035	4003	127	-56.005	-56.631	115.955	5767	165	-45.43	-29.382
11.045	3825	65	-77.19	-47.564	116	5445	151	-12.875	6.561
11.118	3726	98	-57.28	-56.354	116.057	5812	185	83.535	12.909

Continued overleaf...

Table B.1 – continued

Age (Ma)	w (m)	Error (m)	Lon.	Lat.	Age (Ma)	w (m)	Error (m)	Lon.	Lat.
11.511	3743	68	-77.52	-47.598	116.059	5369	162	10.758	-15.961
11.642	3469	38	-77	-43.005	116.12	5753	234	-46.017	-29.001
11.661	4015	3	-44.047	23.403	116.132	4594	89	11.369	-11.523
12.023	4227	102	-46.85	22.783	116.191	5190	158	11.03	-14.804
12.098	3777	59	-64.068	-61.883	116.258	5907	125	92.732	-61.033
12.683	3636	56	-76.37	-42.933	116.487	5353	117	-13.67	6.766
12.757	1801	46	-24.27	61.613	116.51	4674	115	11.336	-12.616
13.059	4211	92	-57.845	-56.232	116.526	5533	136	-37.686	-15.306
13.264	1987	32	-13	69.564	116.556	5176	137	-36.694	-12.193
13.32	3840	79	-66.385	-63.489	116.56	4576	91	11.343	-11.334
13.638	3109	24	-84.375	6.77	116.575	5565	123	-33.75	-7.066
13.675	3867	1	-43.499	23.205	116.741	5880	124	92.23	-61.299
13.738	3149	49	57.7	-32.736	116.804	6329	63	-13.63	40.504
14.099	3048	10	-84.535	6.931	116.819	5520	188	-10.251	4.559
14.689	2823	167	-19.37	70.08	116.827	6388	145	-48.19	-34.571
14.757	3405	60	42.08	86.55	116.923	5559	154	-12.155	5.666
15.28	2143	52	-23.965	61.466	116.977	4619	100	11.6	-11.483
15.62	2035	21	-12.48	69.503	117.08	5143	122	-38.039	-23.117
15.777	4591	39	137	29.836	117.086	5768	161	-39.515	-25.598
16.192	4808	75	-46.418	-63.92	117.086	6288	126	-48.992	-36
16.562	4236	57	63.64	86.93	117.092	4973	111	-38.253	-21.941
17.169	4742	92	138.205	42.614	117.154	5753	207	83.035	12.869
17.248	4835	90	137.715	42.403	117.173	5851	139	10.289	-8.055
17.968	2250	43	-11.975	69.443	117.184	6238	174	-47.88	-33.892
18.096	4910	88	137	42.096	117.209	4784	111	11.675	-11.514
18.169	4314	85	153.87	-64.33	117.296	5557	200	-10.115	4.481
18.321	4889	230	6.345	39.86	117.299	5710	120	91.03	-61.707
18.731	5573	237	5.92	40.941	117.304	5715	257	-46.084	-29.749
18.751	4509	145	2.494	37.474	117.422	5253	96	10.5	-9.5
18.779	3796	63	151.09	-62.269	117.471	4908	93	10.686	-9.865
18.862	4494	48	136.17	29.658	117.499	5508	143	-46.435	-31.266
18.954	4297	94	-70.815	-65.515	117.614	5555	118	90.44	-61.917
19.102	4856	81	136.38	41.829	117.637	5288	134	-37.859	-14.161
19.301	3113	151	-81.88	-1.394	117.683	6458	111	28.464	-62.934
19.88	3440	39	-86.185	9.265	117.711	4629	135	11.635	-12.77
19.933	4142	86	-70.09	-64.415	117.723	6537	67	-13.545	40.495
19.978	4306	89	-71.18	-65.408	117.759	6112	185	10.031	-7.103
19.985	4823	216	6.55	39.842	117.76	5655	158	-46.52	-31.218
20.033	4139	93	-72.099	-65.947	117.772	5304	96	10.555	-9.196
20.092	4327	61	137.695	29.985	117.785	5998	177	-47.035	-32.157
20.452	4122	120	-123.395	37.271	117.843	5845	124	92	-61.687
20.469	4483	53	-121.98	34.83	118.023	5144	108	-38.326	-21.372

Continued overleaf...

Table B.1 – continued

Age (Ma)	w (m)	Error (m)	Lon.	Lat.	Age (Ma)	w (m)	Error (m)	Lon.	Lat.
20.932	4177	89	-123.505	37.217	118.129	5507	184	10.629	-16.824
20.95	4531	147	2.517	37.387	118.134	5658	310	-46.745	-29.357
21.023	4531	95	-72.825	-66.281	118.167	5450	120	-34.323	-5.598
21.065	4441	144	2.446	37.649	118.24	5186	125	-38.811	-24.204
21.068	4501	171	5.675	37.418	118.466	5804	89	54.84	-62.331
21.168	3456	45	-86.5	9.502	118.635	5823	124	92.88	-61.755
21.185	4542	75	169.174	-31.847	118.716	5602	114	8.02	-3.489
21.434	3259	94	4.33	71.363	119.097	6294	210	-47.901	-32.825
21.901	4282	79	-72	-65.166	119.108	7090	146	-8.579	44.493
22.032	3409	105	-111.437	27.302	119.412	6263	178	-48.985	-34.54
22.086	3483	112	-111.6	27.407	119.497	5256	107	-45.349	43.867
22.137	3827	142	-111.793	27.532	119.58	5838	194	83.83	14.138
22.184	2467	61	-10.995	69.28	119.606	6371	270	84.685	16.327
22.633	3370	67	-87.54	9.604	119.648	5109	129	-43.85	44.911
22.751	3249	58	-87.089	9.817	119.705	5971	42	-68.07	24.95
22.981	4308	155	5.609	37.999	119.729	6456	143	-50.395	-36.986
23.065	5342	217	5.37	41.399	119.992	5456	77	-66.293	30.299
23.621	2432	61	-10.425	69.377	120.139	5669	105	11.385	-25.039
23.714	2346	53	-10.33	69.516	120.171	5902	207	83.95	14.683
23.882	5250	226	5.185	41.553	120.269	5816	202	81.837	12.973
23.925	3059	102	-87.96	10.773	120.334	5976	181	81.681	11.228
24.178	4082	75	153.59	-64.546	120.434	4699	137	12.395	-28.92
24.219	4285	73	-73.193	-64.985	120.439	6150	223	-47.997	-31.981
24.25	4890	106	115.705	16.3	120.53	5824	199	82.906	13.766
24.263	4331	153	5.548	38.527	120.599	5941	98	53.919	-62.778
24.745	3776	60	153.98	-55.725	120.65	6356	215	-49.275	-34.368
25.094	4242	70	-73.985	-65.1	120.667	5868	175	-57.1	-47.523
25.805	3788	249	14.515	75.405	120.734	5861	174	81.351	11.136
25.837	2031	83	6.355	76.658	120.749	5747	133	97.338	-62.398
25.95	2015	96	8.66	76.915	120.925	6576	141	-55.215	-41.65
26.665	4221	81	-54.74	-59.902	120.934	5839	208	82.07	12.127
26.841	3825	57	153.918	-55.012	120.937	5833	145	93.835	-62.297
27.184	3398	119	3.893	78.86	120.994	6316	161	-50.174	-35.875
27.355	3178	82	2.194	78.694	121.019	6626	94	-13.244	40.463
27.355	3178	82	2.194	78.694	121.062	5897	112	52.44	-63.42
27.48	4827	55	132.964	-41.698	121.106	5674	131	91.23	-62.861
27.504	4833	54	128.339	-41.077	121.254	5660	133	11.415	-24.148
27.672	4860	54	132.175	-41.592	121.307	5545	117	43.31	-7.382
27.885	5074	57	131.068	-41.443	121.347	5925	119	52.345	-63.536
27.99	4979	61	129.982	-41.297	121.425	5895	109	53.028	-63.207
28.317	4946	112	116.304	17.971	121.563	6410	271	-48.905	-33.254
29.063	4322	75	-81.635	-8.688	121.649	5553	61	106.685	-24.7

Continued overleaf...

Table B.1 – continued

Age (Ma)	w (m)	Error (m)	Lon.	Lat.	Age (Ma)	w (m)	Error (m)	Lon.	Lat.
29.38	4788	55	-81.435	-8.607	121.649	5710	105	65.585	-62.31
29.659	4310	23	-76.92	-37.467	121.745	5544	116	70.505	-62.06
29.894	4380	31	-76.635	-37.528	121.843	5507	97	63.709	-62.33
29.952	4621	120	115.542	16.637	122.056	5501	115	11.705	-24.832
29.981	4267	63	153.826	-53.957	122.065	5570	167	81.229	12.078
30.15	3839	100	-3.7	66.206	122.19	6368	188	-50.14	-35.271
30.421	4371	29	-76	-37.664	122.251	5640	139	91.53	-63.22
30.786	5769	146	119.224	18.991	122.26	5622	79	-66.53	30.425
30.96	4536	38	-75.345	-37.805	122.346	5638	103	67.215	-62.26
31.221	4756	85	138.092	32.25	122.379	5124	101	-45.641	44.026
31.691	3500	100	-3	65.971	122.38	5518	104	68.709	-62.279
33.714	3544	198	-60	68.309	122.389	5602	96	61.66	-62.418
33.819	4636	177	-62.115	69.613	122.48	5623	66	106.485	-20.987
35.334	3925	43	-74.255	-34.181	122.5	5288	72	-4.955	-67.07
35.344	4413	136	-53.185	58.175	122.505	5837	194	82.051	13.879
36.057	3986	61	151.84	-52.752	122.583	6315	256	-48.55	-32.185
36.708	4092	38	-74.014	-32.882	122.638	5539	187	81.305	13.074
36.868	4325	30	-74.221	-32.344	122.702	5620	74	106.725	-21.244
37.561	4198	33	-73.323	-32.903	122.753	6455	166	-51.177	-36.861
38.26	4140	19	-73.255	-32.085	122.985	6325	108	-53.123	-39.806
38.423	5234	66	-50.84	23.348	123.102	5842	141	72.111	-62.483
38.876	4278	59	-139.985	-27.113	123.389	5401	145	11.715	-23.858
39.011	3567	66	-31.01	64.431	123.462	6417	195	-50.903	-36.062
39.096	4314	4	-73.19	-31	123.497	6466	115	-54.784	-41.103
39.672	4077	97	-57.215	60.794	123.567	6045	224	83.123	15.019
39.773	3216	189	-59.39	68.154	123.635	4855	136	13.068	-29.193
39.799	4891	23	-79.715	-11.911	123.688	6523	284	-49.83	-34.039
39.906	2908	100	-14.955	72.223	123.748	5819	74	108.47	-18.972
41.354	3385	64	-31.335	64.566	123.82	6607	138	-55.035	-42.956
41.518	3674	104	-2.05	65.652	123.896	6460	273	84.1	16.101
41.804	4841	32	-78.17	-13.836	123.921	4916	145	13.242	-29.668
41.947	5712	78	141.04	-40.894	124.108	5883	77	109.215	-17.424
41.949	5557	71	139.275	-39.616	124.137	5774	90	108.375	-19.622
41.958	4183	74	-140.4	-29.154	124.137	5594	107	63.741	-63.007
42.206	4030	98	7.046	70.241	124.172	6355	161	-52.002	-37.596
42.613	5090	16	89.485	-17.025	124.173	4976	145	14.73	-32.239
42.676	3623	101	-1.545	65.482	124.181	5625	100	62.055	-63.001
43.239	4235	150	-61.715	70.342	124.193	5700	110	65.536	-63
43.446	4260	68	151.216	-51.786	124.216	5842	204	81.29	13.97
43.679	4309	67	-140.575	-29.457	124.328	5622	123	70.534	-62.992
43.683	5812	102	132.537	-61.094	124.347	6437	121	-54.368	-41.135
43.824	5502	99	117.47	-61.276	124.378	5658	120	68.725	-63.003

Table B.1 – continued

Age (Ma)	w (m)	Error (m)	Lon.	Lat.	Age (Ma)	w (m)	Error (m)	Lon.	Lat.
43.911	4306	98	-40.27	58.472	124.4	5763	134	72.139	-63.017
44.385	5577	71	139.29	-39.31	124.434	5682	111	67.26	-63.004
44.405	4610	143	-77.072	-15.379	124.473	5676	140	42.97	-8.249
44.507	4569	165	-76.794	-15.714	124.58	6194	108	-53.57	-39.835
44.782	4484	118	-76.355	-16.047	124.586	6491	185	-51.767	-37.042
44.809	3655	87	-20.905	59.785	124.718	5818	73	109.344	-17.806
44.868	4878	15	90	-17.025	124.727	5799	88	108.973	-18.893
45.011	4194	97	-40.44	58.516	124.783	5545	131	75.768	-63.108
45.184	4216	104	7.485	69.997	124.806	6382	119	-56.085	-46.996
45.388	4013	108	8.025	70.059	124.869	4901	70	-24.242	13.976
46.523	4131	175	-60.625	68.469	124.977	6193	251	83.093	15.578
46.54	4379	130	-57.87	60.227	124.981	5393	91	111.332	-32.759
46.563	4395	66	-140.845	-29.923	124.993	6216	257	84.018	16.606
46.673	5424	75	-52.257	23.714	125.151	4910	155	13.644	-30.228
46.743	4167	56	-137.12	-7.826	125.256	6110	229	81.535	14.566
46.772	5710	80	137.15	-37.818	125.373	5750	136	73.942	-63.434
46.87	3565	64	-24.823	57.229	125.38	5528	88	60.375	-63.486
46.94	4180	56	-137.45	-7.365	125.401	5590	92	60.425	-63.53
47.005	4150	56	-137.56	-7.211	125.496	5778	121	63.769	-63.589
47.025	3844	110	-1	65.299	125.518	5765	121	62.45	-63.584
47.345	4185	55	-138.14	-6.402	125.553	6204	245	81.45	14.621
47.394	5230	359	-74.535	74.306	125.632	5767	130	65.486	-63.676
47.718	4157	101	8.007	69.799	125.644	6146	71	-13.245	42.14
47.856	3905	118	-20.41	59.547	125.722	5966	84	109.887	-17.333
47.907	3966	11	-138.25	-8.341	125.809	5556	135	70.553	-63.613
47.968	3937	137	-32	64.844	125.881	6162	136	-40.475	-68.785
48.335	4143	137	-20.205	59.448	125.949	5424	68	112.435	-29.292
48.405	3552	81	1.075	65.91	125.956	5471	78	113.43	-30.382
48.479	4432	102	10.315	69.929	125.974	6179	208	-51.555	-36.153
48.517	4086	3	-138.47	-8.528	126.193	6041	76	110.37	-16.192
48.55	3546	98	-14.404	73.201	126.202	5536	129	75.735	-63.58
48.647	3626	91	0.98	67.714	126.433	5763	120	109.605	-18.784
48.687	4313	170	-61.12	68.595	126.515	5913	119	25.5	-64.91
48.782	4970	59	-2.14	-25.01	126.857	5747	94	109.978	-17.955
48.835	4282	106	-41	58.664	126.903	5503	138	68.741	-63.703
48.982	4422	62	-141.218	-30.568	126.955	5620	67	150.816	40.047
49.074	3936	114	-36.157	62.22	127.051	5949	69	110.565	-16.317
49.115	4213	21	-138.67	-8.698	127.275	5786	130	62.515	-63.68
49.126	3794	81	-24.07	56.944	127.284	5877	87	110.989	-21.993
49.372	4394	215	-68.71	74.227	127.497	5938	92	110.932	-22.777
49.445	3948	72	7.09	69.311	127.562	5685	130	67.303	-63.738
49.5	3810	104	-12.67	73.922	127.676	5659	76	-67.031	30.692

Continued overleaf...

Table B.1 – continued

Age (Ma)	w (m)	Error (m)	Lon.	Lat.	Age (Ma)	w (m)	Error (m)	Lon.	Lat.
49.708	4251	80	8.52	69.506	127.7	5953	87	110.295	-22.704
49.956	4637	130	-56.875	59.524	127.761	5679	140	72.174	-63.706
50.129	3834	89	-11.725	74.303	127.804	5995	89	110.411	-22.459
50.238	4261	136	-4.936	63.749	127.907	5671	94	60.565	-63.654
50.29	3745	59	-23.305	56.918	127.957	5684	85	109.775	-20.168
50.314	4116	168	-65.034	73.304	127.989	5851	37	159.95	41.1
50.337	4451	103	10.975	69.677	127.996	5266	73	113.735	-31.039
50.419	4702	317	-75.752	74.649	127.999	5810	93	111.026	-21.341
50.451	4483	174	-62.084	68.914	128.046	6028	151	-40.965	-69.084
50.803	3962	117	-23.845	56.491	128.081	5730	55	146.703	41.156
50.833	4035	143	-36.782	62.408	128.121	5862	89	111.7	-21.941
50.92	4663	24	-71.58	-23.419	128.322	5606	50	146.132	40.816
50.925	5773	103	100.751	-61.073	128.335	4156	80	-23.988	15.105
50.927	4013	111	-53.965	57.754	128.834	5815	55	145.39	40.238
51.226	4061	90	-8.691	75.158	129.305	5486	170	42.149	-6.657
51.312	3738	90	0	64.963	129.31	5664	41	146.83	40.339
51.312	3738	90	0	64.963	129.364	5822	77	147.575	40.525
51.346	4126	86	-7.21	75.447	129.443	5581	37	145.607	39.893
51.448	4118	86	-6.815	75.521	129.449	5740	69	143.35	33.255
51.532	4442	290	-33	65.261	129.769	5263	141	42.198	-6
51.707	3657	91	1.61	65.57	130.031	6002	95	111.984	-13.906
51.707	4524	141	-42	58.927	130.053	4810	147	42.068	-9.726
51.732	5159	59	-155.725	53.91	130.086	7131	369	-95.06	21.848
51.777	4518	104	9.015	69.271	130.193	5577	32	145.526	39.354
51.83	3948	160	-37.261	62.578	130.209	6027	95	111.365	-15.361
51.983	4440	102	11.47	69.489	130.263	6728	291	-87.968	26.127
51.998	5737	67	125.345	22.425	130.292	5790	72	147.945	40
52.085	4734	8	86.19	-17.025	130.433	5680	126	110.93	-17.822
52.144	4465	126	-57.221	59.343	130.76	6911	310	-88.928	26.13
52.308	5620	79	-53.352	24	130.773	6022	30	142.985	32.246
52.369	4126	157	-61.38	70.953	130.786	5919	103	111.071	-17
52.473	5893	88	125.255	22.65	130.937	5507	19	145.433	38.855
52.588	4252	175	-4.934	63.275	131.051	4914	143	42.058	-9.247
52.874	4495	363	-33.535	65.484	131.095	5630	68	147.095	39.238
52.895	5210	62	-159.745	53.066	131.289	6241	218	-86.227	25.45
52.912	4443	104	11.82	69.355	131.665	5470	28	145.335	38.331
52.99	4478	364	-33.595	65.509	131.68	4701	82	-23.795	15.962
53.081	4224	192	-37.933	62.78	131.76	7304	281	-93.171	24.148
53.088	4022	104	0.815	64.689	131.914	5831	64	148.128	39.086
53.111	4605	111	9.595	68.996	132.113	5878	62	143.74	31.864
53.183	4841	24	90.795	-17.025	132.305	5872	63	148.635	39.022
53.381	3579	75	2.115	65.25	132.751	4321	77	-23.606	16.804

Continued overleaf...

Table B.1 – continued

Age (Ma)	w (m)	Error (m)	Lon.	Lat.	Age (Ma)	w (m)	Error (m)	Lon.	Lat.
53.454	5127	85	140.06	-61.675	132.753	5818	65	147.69	38.469
53.804	4389	26	-140.245	-10.034	132.764	7155	391	-95.57	22.453
53.893	2941	50	2.634	64.919	132.811	7135	312	-89.95	25.985
54.085	4268	222	-38.665	63.019	132.913	6126	167	25.58	-66.35
54.555	5502	28	-163.585	52.542	133.248	6133	73	153.906	36.741
54.721	4431	66	69.375	12.014	133.365	7586	316	-94.048	23.976
54.727	5296	32	-163.525	52.452	133.699	6485	248	-86.964	26.033
54.859	5177	27	-163.475	52.377	133.833	5805	91	-20.868	27.951
55.004	4125	10	-140.65	-10.378	133.845	5915	61	143.982	31.069
55.025	4385	109	-57.595	59.147	133.888	7618	327	-93.983	24.989
55.113	4645	156	-59.082	59.604	134.025	7406	311	-93.09	24.95
55.233	4370	62	69.85	12.177	134.07	7427	374	-92.005	25.763
55.505	4013	24	-140.82	-10.522	134.104	7431	332	-90.884	25.922
55.591	4426	82	71.365	8.36	134.132	6063	71	154.963	36.816
55.927	6334	157	94.209	2.151	134.206	5825	78	-22.779	24.765
55.959	4469	99	71.59	8.459	134.221	6061	68	153.25	36.694
56.423	4795	182	-59.72	59.903	134.409	5215	136	42.248	-5.339
56.617	5415	86	154.879	-29.666	134.43	6058	67	152.64	36.4
56.892	6151	137	93.705	2.722	134.446	7534	383	-95.06	22.989
57.236	4664	76	151.243	-50.123	134.471	6120	69	155.575	36.86
57.319	4622	62	-145.42	-13.774	134.65	5985	60	144.772	31.005
57.556	4486	119	71.82	8.559	134.72	4762	136	42.673	-11.082
57.841	4375	56	-145.22	-28.256	134.853	5858	63	145.155	36.266
58.299	4321	113	-51.72	58.968	134.973	6381	227	-86.734	25.452
58.322	4716	63	-145.805	-13.958	134.976	6033	98	111.771	-15.35
58.52	4817	185	-59.079	59.395	135.102	5711	34	115.975	-11.788
58.639	4843	89	67.875	15.238	135.688	5869	122	111.98	-17.626
58.729	5660	143	64.812	17.243	135.778	5888	65	146.014	36.097
58.785	4547	170	-62.821	69.01	135.905	5782	123	111.818	-16.933
58.825	4984	110	66.64	17.143	136.218	5843	72	-22.93	24.203
58.983	5746	66	-54.425	24.283	136.44	7756	532	-134.336	71.892
59	5046	113	165.345	-24.979	136.735	5997	64	146.611	35.775
59	5099	117	165.78	-24.7	137.136	4672	149	42.555	-11.677
59	4912	114	166.13	-26.425	137.339	6049	64	146.55	35.386
59	4885	116	166.535	-26.379	137.344	6213	221	-86.254	25.913
59.314	4665	202	-42.655	59.099	137.54	7712	387	-94.879	24.057
59.678	4093	55	-145.475	-28.779	137.606	4853	153	42.356	-11.856
59.822	5430	142	64.924	17.876	138.474	7167	275	-92.25	24.731
60.411	4818	63	-129.375	-66.399	138.494	5931	80	-69.275	27.701
61	4341	63	56.925	-2.141	138.655	6045	64	146.477	34.531
61.148	4126	116	-54.213	57.021	138.678	5794	131	43.643	-4.831
61.278	4608	62	-142.123	-11.609	139.118	5416	106	6.015	-67.011

Continued overleaf...

Table B.1 – continued

Age (Ma)	w (m)	Error (m)	Lon.	Lat.	Age (Ma)	w (m)	Error (m)	Lon.	Lat.
61.283	4677	131	60.365	20.133	139.142	5903	134	112.076	-16.063
61.525	4357	90	60.57	20.004	139.311	5933	151	43.119	-4.828
61.847	4337	82	56.52	-3.517	139.39	6036	64	146.489	34.327
62.017	4295	83	56.48	-3.58	139.456	5743	77	-68	31.184
62.049	4712	72	151.745	-49.57	139.862	7530	423	-95.56	24.152
62.242	4378	76	56.73	-2.984	140.133	6003	63	147.07	34.059
62.443	5090	127	64.919	19.479	140.235	7534	381	-93.16	25.914
62.454	6074	74	129.618	-36.923	140.281	6004	58	147.665	34.035
62.584	5497	86	154.421	-29.666	140.478	6080	79	-69.679	27.814
62.681	5065	133	64.055	19.905	140.656	5897	65	154.56	34.021
62.802	4471	121	65.895	19.411	140.777	5944	62	153.915	33.997
62.859	4661	72	151.965	-49.328	141.041	7253	290	-93.892	23.123
62.904	4382	75	56.325	-3.093	141.195	7488	381	-143.235	71.719
63.094	5351	148	64.938	19.878	141.217	6433	262	-87.072	26.785
63.295	5257	16	-171.835	50.526	141.342	6946	393	-89.826	26.985
63.568	4538	132	66.095	19.766	141.364	5877	61	149.355	33.922
64.008	5715	112	92.875	3.598	141.387	7684	436	-132.6	73.078
64.562	5010	14	-171.66	50.251	141.64	5558	156	42.635	-12.739
64.567	4777	124	-55.41	57.629	141.849	5996	66	150.12	33.859
64.886	5390	111	156.763	-29.167	142.057	7477	376	-93.874	25.928
64.965	5657	116	156.46	-29.29	142.185	5149	78	6.036	-67.638
64.99	4211	12	54.41	-20.573	142.298	6171	64	152.845	33.876
65.144	4795	56	-142.955	-12.299	142.371	7730	463	-131.763	73.04
65.299	3955	50	56.15	-22.052	142.491	6652	230	-86.42	26.626
66.636	5681	42	133.87	21.41	142.523	6637	310	-88.008	26.945
66.885	4877	143	-55.971	57.773	142.527	6062	63	152.019	33.962
67.351	4548	96	68.815	17.406	143.162	6810	366	-88.944	27.054
67.354	4340	59	-149.25	-15.452	143.223	7737	365	-94.725	25.225
67.444	5837	79	79.91	-5.5	143.69	5738	77	-68.59	31.469
68.019	4786	115	-53.745	56.299	143.767	7061	257	-92.356	24.407
68.191	4134	89	50.033	-12.189	143.792	5010	161	41.892	-12.898
68.361	4348	116	-54.967	57.09	143.89	5597	157	42.25	-4.449
68.62	5928	120	93.23	3.223	144.141	7011	340	-94.857	21.219
69.256	5134	77	49.06	-30.51	144.334	6178	62	146.136	30.829
69.269	4332	59	-149.55	-16.073	144.42	5930	135	44.925	-2.541
69.345	5203	87	48.99	-30.492	144.54	5611	152	44.252	-13.218
69.61	4816	121	-53.255	55.867	144.647	4682	131	37.575	-23.866
70.09	5541	41	134.185	21.97	144.992	5944	146	44.035	-3.601
70.141	4672	103	68.202	18.038	145.608	4625	138	37.147	-23.754
70.486	6220	90	135.56	-37.201	145.636	5968	73	146.335	27.186
70.571	5351	83	158.125	-35.571	145.937	5711	156	44.565	-13.386
70.973	4399	81	-51.79	59.883	146.192	5896	65	147.115	27.588

<div align="right">Continued overleaf...</div>

Table B.1 – continued

Age (Ma)	w (m)	Error (m)	Lon.	Lat.	Age (Ma)	w (m)	Error (m)	Lon.	Lat.
71.664	6312	123	101.691	-7.132	146.225	6207	75	146.14	25.181
71.711	4769	114	68.758	18.112	146.349	5491	147	43.136	-13.538
71.958	5286	73	160.84	-38.505	146.414	5918	138	44.831	-2.325
71.985	5029	97	48.21	-30.285	146.702	5890	81	-69.01	31.671
72.244	4728	62	-29.937	-28.12	146.886	6273	63	147.199	30.69
72.262	5610	80	158.45	-35.366	146.899	5892	71	147.004	27.136
72.483	6248	95	101.405	-7.404	147.099	6341	139	50.895	5.661
72.652	5748	67	123.723	-36.937	147.491	5528	60	118.89	-11.423
72.702	6020	73	129.405	-36.609	147.544	5722	156	44.177	-13.646
72.829	6002	86	79.82	-3.51	147.639	6274	63	148.032	30.707
73.446	5380	78	161.17	-38.338	147.644	6915	286	-94.234	22.065
73.458	5918	167	-177.015	57.628	147.819	5956	100	-21.66	23.815
74.003	5340	72	160.29	-37.6	147.993	6855	250	-93.436	23.032
74.023	6034	124	177.207	57.42	148.34	6310	64	148.755	30.725
74.235	4778	135	-55.793	57.298	148.604	4854	121	37.796	-22.967
74.336	5926	161	-178.252	57.923	148.657	5540	64	118.873	-11.686
74.779	5359	101	-43.255	2.631	148.706	4810	146	37.048	-23.126
75.205	6027	132	177.201	57.998	148.794	6217	89	-71.071	28.166
75.333	5516	78	159.295	-36.704	149.55	5945	63	147.85	27.069
75.812	5781	100	150.874	-39.225	149.708	5229	205	40.655	-20.198
75.847	5325	99	-43.365	2.145	149.749	7248	235	47.02	0.833
75.942	5813	61	-56.96	24.944	149.915	6497	112	-12.9	35.847
76.014	5272	68	-97.987	-64.092	150.431	6016	115	-19.44	11.581
76.354	5352	74	160.49	-37.494	151.252	4685	108	-20.992	17.51
76.41	6035	58	-58.128	25.576	151.332	5892	101	-21	23.69
76.896	5414	86	150.77	-41.506	151.333	6332	99	-71.5	28.497
77.256	5537	93	150.63	-41.434	151.352	6101	83	-69.807	32.056
77.399	5777	156	177.19	58.999	151.632	5880	190	42.58	-3.581
77.536	5633	82	159.115	-34.947	151.67	4834	110	-20.95	17.203
77.611	5370	67	-97.982	-64.857	152.012	6204	77	114.819	-15.457
77.639	5040	82	-38.26	-0.411	152.207	5484	217	40.41	-19.698
77.921	5419	80	161.795	-38.021	152.373	6214	98	-71.629	28.543
77.935	5188	205	65.032	22.193	152.711	5889	125	-19	10.888
78.276	5431	101	150.024	-40.158	152.896	6113	73	114.892	-15.631
78.362	4292	102	68.77	18.695	153.389	5861	142	-18.635	10.313
78.425	5161	88	-38.415	-0.624	153.702	6469	98	118.485	-14.751
78.591	5749	107	150.213	-39.215	153.838	5767	164	44.285	-14.529
78.591	5533	103	150.125	-41.173	153.932	5772	116	45.5	-1.356
79.181	5390	99	-38.565	-0.83	154.309	6079	181	44.02	-1.506
79.316	5918	145	177.181	59.864	154.311	5313	133	46.093	-12.699
79.416	5581	80	159.728	-35.912	154.399	5900	158	43.856	-3.28
79.67	4454	43	-29.25	30.233	154.41	6104	23	149.324	27.167

Continued overleaf...

Table B.1 – continued

Age (Ma)	w (m)	Error (m)	Lon.	Lat.	Age (Ma)	w (m)	Error (m)	Lon.	Lat.
79.849	4369	83	-51.245	60.035	154.518	5930	188	42.851	-3.146
79.911	5613	130	-46.197	5.148	154.523	5283	155	37.328	-21.712
80	6268	320	37.866	42.846	154.548	6151	14	150.05	27.729
80	5572	240	38.026	42.333	154.708	6006	83	113.08	-15.345
80	6604	368	39.179	42.42	154.818	6004	18	149.802	26.972
80.087	4415	100	67.993	19.106	154.852	5746	160	45.074	-13.883
80.228	5503	105	-46.235	5.681	154.88	5919	247	40.07	-19.004
80.287	5407	109	-44.478	2.791	154.935	6548	157	49.405	1.934
80.369	5416	107	-43.903	1.98	155.058	6072	160	44.939	-1.018
80.397	5488	87	159.48	-35.538	155.075	5964	109	-19.797	12.147
80.706	5328	111	-43.306	1.259	155.418	6365	99	118.555	-14.791
80.912	5939	160	-52.2	9.626	155.465	5892	18	150.335	26.416
81.652	5528	102	150.025	-41.688	155.657	6277	75	117.467	-15.926
81.659	4913	95	-41.375	48.539	155.774	6150	206	44.15	-0.974
81.924	6006	79	129.183	-36.281	155.972	5460	148	46.67	-13.204
82.118	6106	68	-59.068	26.164	155.979	5730	85	119.096	-13.209
82.178	5482	76	160.898	-37.278	156.246	5227	215	40.645	-18.187
82.374	5510	83	159.635	-35.484	156.263	6273	75	117.641	-15.994
83.148	5522	131	-45.092	2.947	156.449	5985	63	150.02	14.832
84.124	5344	16	-158.756	27.519	156.521	6122	206	43.146	-2.256
84.155	5645	142	-45.201	3.702	156.542	5881	176	45.733	-13.841
84.236	4724	13	-158.754	26.992	156.611	6018	261	38.915	-18.99
84.289	5628	130	-44.937	2.142	156.974	6015	122	-20.295	23.557
84.324	4308	56	-157.551	23.395	157.117	4848	120	-20.042	17.518
84.41	4873	8	-158.751	26.192	157.215	5916	259	39.791	-18.077
84.593	5314	153	-45.425	4.509	157.323	6030	60	150.955	15.128
84.664	5212	255	65.384	22.752	157.324	6406	245	44.12	-0.388
85.204	6179	124	-53.38	9.651	157.528	4816	105	-20.185	16.63
85.573	5402	112	-43.974	1.256	157.676	6089	203	44.72	0.099
85.867	5947	157	-52.38	9.231	157.873	5362	214	41.003	-16.98
85.981	5935	115	100.698	-61.871	158.122	6056	288	38.59	-18.336
86.624	6097	60	-59.896	26.681	158.68	5962	288	38.47	-18.095
86.669	4684	18	-160.283	26.95	158.682	5395	251	40.125	-17.18
86.879	4818	13	-160.281	26.192	158.766	6219	92	-69.845	34.537
87.146	6155	229	-48.234	5.644	158.788	5825	105	-19.635	12.639
87.328	5947	228	-47.125	4.899	159.583	6056	48	157.704	25.528
87.644	5972	109	-3.8	3.088	160.801	5948	43	157.611	25.118
87.936	5383	283	65.697	22.763	160.808	6557	166	-57.385	41.378
88.362	5023	56	-14.719	48.599	161.185	5010	113	-19.755	16.308
88.786	5571	134	-44.801	1.321	161.863	6292	96	-70.54	34.141
89.135	5502	32	5.115	-20.265	163.602	6520	160	-57.47	41.562
89.219	4735	51	-27.74	29.709	163.667	5983	116	-12.715	34.01

Continued overleaf...

Table B.1 – continued

Age (Ma)	w (m)	Error (m)	Lon.	Lat.	Age (Ma)	w (m)	Error (m)	Lon.	Lat.
89.339	6255	222	-49.045	5.931	165.361	6036	139	-19.715	23.447
89.405	5769	173	-45.897	3.046	165.404	5596	38	157.105	22.885
89.711	5167	55	-173.87	-26.399	165.597	6650	106	-71.325	32.957
89.787	6426	217	-49.52	6.472	166.059	5358	30	156.98	22.335
90	7838	535	32.228	43.782	166.444	5987	69	155.235	19.997
90	8321	561	32.68	43.592	168.069	6562	101	-71.775	32.618
90	7506	493	32.156	43.064	168.277	6281	232	-53.37	43.452
90	8256	551	33.029	43.294	169.03	6688	108	-72.74	30.83
90.024	5262	113	-40.42	-0.335	169.067	5196	136	-19.023	16.038
90.05	6380	223	-49.611	6.569	169.233	6089	237	-53.28	43.535
90.129	5132	78	-37.15	-32.91	170.172	6077	45	156.216	18.961
90.185	5820	185	-45.997	4.071	170.646	6601	188	-57.67	41.993
90.918	5878	127	2.472	3.308	170.701	5299	155	-19.078	17.977
91.1	4855	50	-27.415	29.596	171.333	5947	36	156.004	18.025
91.133	6027	59	-60.745	27.191	173.58	5477	163	-18.571	17.22
91.424	5765	108	-52.58	8.792	174.393	6194	129	-71.927	34.633
92.613	5847	127	2.802	3.268	174.493	6972	145	-59.905	41.116
92.978	6124	229	-50.775	6.814	174.566	6102	131	-70.26	37.117
93.175	5375	58	-173.975	-26.755	175.66	6541	113	-72.185	33.737
93.227	5597	17	-160.231	32.636	176.564	5506	179	-18.972	19.099
93.301	5969	129	-0.932	4.16	176.654	6103	177	-18.936	23.21
93.385	5330	16	-160.224	31.999	176.877	5561	179	-18.318	16.395
93.516	5585	16	-160.219	31.483	177.946	5540	186	-18.177	17.212
94.317	6378	68	103.56	-8.583	178.649	5767	117	-18.964	12.915
94.344	6431	63	103.755	-8.316	179.146	6230	156	-68.88	38.065
94.796	5744	224	-51.08	6.42	181.129	6540	153	-72.692	34.752
94.889	5942	57	-61.455	27.605	183.879	5806	128	-11.89	32.282
95.649	5412	153	-40.9	-1.067	184.951	7105	190	-60.338	41.853
96.349	5649	138	-41.318	-0.201	185.363	6713	157	-73.15	33.998
96.731	6014	264	-46.875	4.229	185.61	6841	153	-73.45	33.419
96.898	4463	59	-159.31	19.58	185.784	6831	147	-73.6	33.129
97.556	5751	71	110.037	-35.727	185.958	7167	172	-60.54	41.794
97.568	5790	97	-42.3	-34.617	187.104	5583	130	-18.44	13.132
98.028	6161	208	3.952	3.286	187.478	5932	96	-67.692	14.015
98.185	5599	59	-62.077	27.967	187.996	6181	139	-10.794	34.709
98.237	6246	318	-46.895	2.802	189.461	7269	274	-58.199	43.035
98.418	5855	162	-0.133	4.277	190.503	7295	276	-58.535	42.983
98.418	5855	162	-0.133	4.277	191.375	6416	218	-64.25	41.449
98.422	5086	120	-42.025	48.392	191.9	6112	292	-17.862	22.988
98.777	5800	203	4.762	3.024	192.582	5928	121	-66.665	14.015
99.058	5068	96	-8.538	3.482	192.921	6209	223	-64.033	41.638
99.083	5951	103	-42.515	-34.508	193.375	5758	109	-66.345	14.415

Continued overleaf...

Table B.1 – continued

Age (Ma)	w (m)	Error (m)	Lon.	Lat.	Age (Ma)	w (m)	Error (m)	Lon.	Lat.
99.214	6620	209	-55.365	9.718	193.925	6548	144	-10.53	34.484
99.275	6194	266	-47.922	4.889	193.929	5708	104	-66.46	14.66
99.53	5353	68	24.03	-36.812	194.059	6323	208	-73.415	36.386
99.643	5452	185	-41.205	-1.533	194.242	6085	146	-11.145	32.182
99.643	5172	92	23.815	-36.441	194.404	5630	97	-66.56	14.872
99.766	6267	210	-57.785	-46.438	194.599	5909	335	-17.495	23.374
100.12	7244	274	-55.645	9.806	195.305	5684	100	-75.07	25.365
100.232	6150	258	-48.66	5.251	195.629	5614	92	-75.26	25.709
100.587	6450	141	-3.27	3.429	196.509	6273	218	-73.707	36.443
100.906	5042	119	5.55	1.497	196.728	6057	146	-10.422	34.573
101.029	6075	249	-45.765	1.411	196.833	7063	294	-72.27	38.598
101.099	5691	254	25.972	-39.001	197.016	6790	161	-10.347	34.171
101.178	5477	260	26.158	-39.708	199.251	6324	257	-74.04	36.507
101.196	5483	159	5.42	2.409	199.482	6613	295	-76.51	31.773
101.505	5345	61	-62.705	28.334	199.602	6547	230	-76.202	32.037
101.515	5701	141	-42.285	0.026	238.841	5846	362	34.61	32.398
101.553	5209	116	-7.964	3.649	240.676	5549	336	33.859	32.108
101.697	5468	194	5.655	2.687	245.792	6016	333	34.161	32.838

[a] In decimal degrees

Table B.2: 471 minimum water-loaded basement depth measurements averaged over $1°$ bins (upwards pointing triangles in Figure 2.2). Crustal corrections have not been applied, but crust is deemed to be thinner than average, based upon constraints from nearby lines, absence of seamounts, presence of fracture zones and regional tectonic setting.

Age (Ma)	w (m)	Error (m)	Lon.	Lat.	Age (Ma)	w (m)	Error (m)	Lon.[a]	Lat.[a]
0.117	2016	20	38.673	19.77	70.018	6130	36	-27.195	-65.355
0.126	3042	1	-103.865	12.04	70.549	6329	22	131.984	-36.889
0.167	2351	1	158.825	-62.274	70.551	5239	12	-119.98	-66.512
0.168	5487	15	128.13	-6.196	71.028	4560	10	-125.914	-67.936
0.231	2780	1	-127	42.604	71.118	4458	7	-125.079	-67.801
0.355	2159	4	-92.665	2.205	71.139	5229	25	-42.435	3.335
0.412	3163	1	-29.895	-57.483	71.623	4451	8	-124.06	-67.731
0.553	3098	1	-83.772	2.997	71.755	5612	36	150.265	-46.433
0.58	3621	2	144.79	18.152	72.593	5510	23	153	-43.91
0.743	3208	1	-30.4	-57.505	72.798	5071	50	-89	-69.313
0.777	2922	1	-30	-59.303	72.874	5322	12	163.025	-44.007
0.98	1710	21	38.287	20.204	73.334	5250	23	-37.165	-1.143
1.425	2895	2	-126.31	42.523	74.125	5389	16	163.39	-44.521
1.455	2551	1	-83.79	3.535	74.219	6043	33	-26.7	-65.598

Table B.2 – continued

Age (Ma)	w (m)	Error (m)	Lon.[a]	Lat.[a]	Age (Ma)	w (m)	Error (m)	Lon.	Lat.
1.49	2554	1	-29.275	-59.38	74.879	5620	50	-104.532	-66.244
1.624	3120	1	-103	12.155	74.888	5812	8	3.21	-17.904
1.676	2550	1	159.32	-62.622	75.174	3913	7	-150.39	-17.795
2.161	2562	1	158.115	-61.776	75.375	4568	13	-124.87	-68.659
2.186	3572	2	-31	-57.531	75.826	5761	55	-104.538	-67.002
2.452	3735	9	-29	-57.444	75.855	5216	12	150.645	-46.371
2.473	2023	1	37.745	22.435	76.11	5741	6	3.55	-17.988
2.594	3208	1	-31	-59.197	76.282	5326	29	-109.925	-67.023
2.632	2970	4	-125.805	42.463	76.355	5997	66	126.115	-62.549
2.73	3082	2	-128	42.722	76.939	5357	20	151.89	-47.823
2.827	3205	1	-102.4	12.235	77.14	4298	3	-150.69	-18.39
3.334	5555	15	128.21	-6.549	77.677	5570	32	151.83	-44.761
3.449	3504	10	-125.48	42.425	77.719	4341	3	-150.78	-18.57
3.555	1742	30	38.59	20.523	77.998	5122	31	-109.975	-67.713
3.743	2682	1	159.995	-63.095	78.154	5712	56	-104.545	-68.003
3.76	2783	1	157.61	-61.421	79.627	4446	1	-150.955	-19.72
3.955	2078	73	38.56	19.435	79.938	5520	46	-44.35	4.237
4.341	3817	11	-28.155	-57.407	79.956	5580	17	-26	-65.942
4.439	3111	1	-31.975	-59.093	80.104	5538	90	-50.255	53.34
4.503	3874	4	-32	-57.574	80.409	6074	66	131.505	-62.72
4.941	2786	1	157.255	-61.172	80.965	5675	68	-104.552	-69.005
5.204	3567	6	-129	42.839	80.979	5471	91	-50.485	53.514
5.964	3605	8	-32.59	-57.6	81.219	5054	41	-89.655	-69.39
6.078	2189	100	38.455	19.314	81.683	5373	27	152.015	-43.91
6.266	4197	2	144.045	18.003	81.757	5627	43	151.485	-44.608
6.953	2958	1	162.005	-63.574	81.79	5464	104	-51	53.905
7.375	3125	1	162.65	-63.513	83.2	6223	21	132.294	-36.377
7.652	3000	1	163.145	-63.467	83.429	5636	53	-102.995	-69.609
7.728	3557	5	-130	42.951	83.527	5527	51	-102	-69.5
7.736	4102	1	130.235	-47.95	83.797	5675	81	-104.558	-69.722
8.137	2919	1	164	-63.387	83.91	5800	44	-98.85	-69.065
9.806	2925	1	164.54	-63.336	83.945	5580	51	-101	-69.5
10.286	3791	5	-131	43.063	84.185	5796	40	-98.07	-68.921
10.688	4293	1	130.126	-46.999	84.294	5478	43	-100	-69.5
12.057	4005	2	-11.745	-25.965	84.651	5723	51	-99	-69.5
12.581	3830	4	-132.005	43.159	84.701	5658	59	-103.51	-69.986
12.585	4231	1	135.304	-46.514	84.755	5724	64	-103.535	-70.013
13.669	3805	1	-22.305	-60.114	84.879	7188	73	-57.48	14.365
13.701	4497	1	129.918	-46.036	85.081	5647	43	-98	-69.5
13.737	3676	66	-0.4	79.705	85.176	6941	61	-57.525	14.332
14.039	4577	1	128.972	-45.84	85.523	5544	36	-97	-69.5
14.353	4348	1	135.268	-46	85.555	5518	16	-25.18	-66.345

Table B.2 – continued

Age (Ma)	w (m)	Error (m)	Lon.[a]	Lat.[a]	Age (Ma)	w (m)	Error (m)	Lon.	Lat.
14.537	4452	1	128.483	-45.644	85.697	5573	36	-96.485	-69.5
14.753	3833	2	-133	43.089	87	5973	13	127.367	-36.013
15.544	4716	11	113.35	12.299	88.589	5487	127	-51.635	54.387
15.641	4600	7	114.24	12.999	88.642	5599	19	-24.685	-66.588
15.665	3955	4	-61.395	-60.466	90	7046	357	30.445	42.277
15.849	4584	1	128.43	-45.201	90	7185	370	30.72	42.402
16.578	3911	5	-91.34	7.21	90.333	7000	119	-56.4	12.025
16.98	4035	2	-134	42.978	90.692	6458	82	-55.195	10.95
17.617	3948	5	-61.115	-60.692	92.844	5886	29	-24	-66.925
17.664	3290	1	167.71	-64.096	93.941	7051	127	-56.96	11.955
17.784	4517	1	135.196	-45	95.675	6708	120	-56.028	10.844
17.924	4558	5	114.755	13.734	98.043	5843	27	-23.16	-67.337
18.061	3938	2	-22.92	-60.049	98.076	6160	6	-61.65	26.459
18.162	4749	11	113.63	11.918	99.252	5946	19	7.165	-18.904
18.33	4077	1	-134.61	42.911	101.81	6040	34	-22.665	-67.581
18.807	4920	1	138.77	17.991	102	6729	145	-56.92	10.554
19.326	4912	16	113.085	12.66	103.456	5841	20	8.001	-19.083
19.369	4844	12	115.14	12.784	104.236	5953	41	-28.935	-68.129
19.512	2986	1	167.245	-63.708	104.975	5103	89	6.93	0.942
20.967	4625	8	113.795	13.826	104.994	5906	37	-28	-68.126
21.03	4653	1	135.124	-44	105.466	5956	15	-65.508	21.39
21.268	3963	5	156.845	-56.5	105.643	5793	22	8.55	-19.19
21.505	3902	84	-3.15	79.962	105.77	6987	198	-57	9.955
21.702	4917	1	138	17.994	105.932	5835	33	-27	-68.123
21.911	2528	1	166.75	-63.295	106.687	6128	45	-26.315	-68.121
22.693	4806	11	114.929	12.275	107.334	7100	217	-57.925	10.516
22.931	4814	2	140.075	17.982	107.806	5947	21	46.87	-61.225
23.038	4943	1	127.35	-42.499	108.012	5039	94	7.425	0.421
23.053	4953	1	127.19	-42.501	108.257	6019	34	-22	-67.907
23.576	2768	1	166.435	-63.033	108.65	7063	233	-57.809	10.108
23.912	5054	1	127.806	-42.06	108.688	6666	200	-56.797	9.227
23.948	4872	1	135.052	-43	108.716	5010	92	7.515	0.327
24.125	3781	17	171.455	-65.523	109.406	5865	41	46.833	-62.007
24.235	3740	9	171.55	-65.509	109.705	6032	223	-56.73	8.287
24.439	4840	1	137	17.998	114.648	5982	5	-44.775	-49.071
24.628	3693	2	85	86.877	115.956	5858	67	46.788	-62.935
24.738	3812	10	172.055	-65.433	115.994	6120	39	-21.145	-68.327
25.172	3990	12	172.555	-65.358	117.255	6153	28	25.12	-62.463
25.721	5113	10	141	17.985	117.712	6199	33	53.629	-62.106
25.814	4744	8	157.885	-54.485	118.165	5987	29	55	-62.253
25.996	4694	1	136.445	18	118.553	6198	34	53.345	-62.32
26.257	4957	1	134.819	-42.193	118.557	6111	27	24.795	-62.812

Continued overleaf...

Table B.2 – continued

Age (Ma)	w (m)	Error (m)	Lon.[a]	Lat.[a]	Age (Ma)	w (m)	Error (m)	Lon.	Lat.
26.712	5314	18	141.695	17.987	118.673	6195	9	-45.815	-49.107
26.899	4372	5	158.17	-54.61	119.806	5934	33	-20.65	-68.571
27.232	5321	5	159.26	-55.075	119.879	6329	40	34.212	-63.108
27.373	3997	63	0.65	77.154	119.966	6389	36	51.825	4.018
28.17	4611	5	144.791	-46.786	120.073	5975	46	-46.285	41.857
28.88	4465	4	159.8	-55.31	120.083	6571	61	38.61	-64.51
29.273	5034	36	117.765	18.43	120.121	6693	56	28.416	-64.008
29.358	4159	2	162.28	-49.425	120.121	6223	45	39.105	-64.464
29.634	5117	41	118.11	18.534	120.138	6302	46	38	-64.567
29.779	4245	2	161.825	-49.687	120.237	5883	16	-53.45	38.986
29.9	4486	9	159.355	-56.5	120.262	6256	40	53.995	-62.742
30.021	4865	47	-140.583	58.059	120.338	6317	47	37.265	-64.635
30.389	4100	1	160.46	-50.473	120.374	6285	35	24.33	-63.313
30.485	4319	4	161	-50.162	120.389	6111	44	40.081	-64.382
30.527	4127	1	160.015	-50.73	120.436	5855	38	40.2	-64.503
30.764	4776	3	144.586	-45.955	120.525	6305	43	34.306	-63.84
31.435	4436	15	159.79	-56.5	120.57	5992	29	41.775	-63.337
31.49	4718	33	90	87.108	120.785	5545	52	-39.325	-51.089
31.789	4536	93	-2.7	77.759	120.951	6313	50	52.96	-63.081
32.299	4695	50	20.85	84.01	121.062	6291	56	52.44	-63.42
32.369	4541	91	-1.9	77.614	121.285	6688	59	27.259	-64.133
32.516	4677	24	-75.76	-66.628	121.984	6326	63	52.28	-63.615
32.643	4027	2	158.88	-50.858	122.679	5995	41	41	-64.099
32.893	4529	21	-75.545	-66.465	122.888	5871	41	-28.35	-69.013
33.122	4332	6	158.55	-50.449	123.221	5918	35	57.045	-63.075
33.511	5065	7	143.351	-44.046	123.342	6175	33	23.825	-63.856
34.42	4661	9	157.93	-51.01	123.565	6569	13	-51.605	-48.716
35.047	5916	19	123.61	18.792	123.586	5832	39	41.973	-64.156
35.568	4485	5	158.325	-50.17	123.701	5989	4	-44.41	-49.365
35.947	4977	5	144.151	-45.171	124.027	5672	36	-46.725	42.04
35.952	4804	4	144.353	-45.945	124.296	5685	73	-39.69	-51.358
35.963	4961	5	141.43	-42.654	124.54	6267	31	-53.997	39.028
36.256	4796	6	141.585	-42.555	124.979	5767	32	42.86	-64.114
36.465	4502	14	147.332	-63.092	125.068	6202	55	-29	-69.11
36.572	5257	22	123.19	18.622	125.351	5858	86	-40.195	-51.731
37.189	5030	19	157.465	-50.536	125.913	6038	39	-20	-68.89
37.447	5033	11	143.585	-43.386	126.02	6047	30	23.36	-64.356
37.919	5019	7	143.682	-44.059	126.325	6315	64	-30	-69.26
37.927	5077	8	143.175	-42.886	126.364	6029	95	-40.82	-52.191
38.602	4584	7	147.295	-49.224	126.977	6325	66	-31	-69.41
38.662	4805	3	-4.2	-25.97	127.004	6713	20	-51.318	-48.914
39.054	4985	47	95	87.338	127.394	6312	66	-31.545	-69.492

Continued overleaf...

Table B.2 – continued

Age (Ma)	w (m)	Error (m)	Lon.[a]	Lat.[a]	Age (Ma)	w (m)	Error (m)	Lon.	Lat.
39.431	4283	17	176.04	-69.28	127.792	6292	69	-32.05	-69.568
40.227	4951	13	156.97	-50.031	127.996	6223	42	22.865	-64.888
40.341	5083	19	107.335	-61.282	128.532	5983	42	56.65	-63.733
40.399	5689	23	-147.69	57.283	128.624	6301	71	-33	-69.71
40.405	5077	74	25.767	83.653	128.955	6062	44	-19.089	-69.332
40.513	5256	9	142.185	-42.017	129.422	5921	44	45.665	-4.67
40.726	4896	51	129.2	88.917	129.503	6273	73	-33.905	-69.846
40.906	5395	15	142.668	-42.061	129.856	6327	51	22.4	-65.388
41.685	5329	73	125	88.723	130.233	6902	72	28.383	-64.777
42.084	5386	35	112.231	-61.208	130.365	6154	48	-18.58	-69.518
42.195	3931	18	3.815	69.683	131.15	6167	60	45	-4.684
42.409	5234	81	27.65	83.584	131.284	5945	47	56.48	-64.017
42.45	4879	2	-3.345	-25.845	131.3	6650	47	-54.918	39.187
43.073	5383	37	122.845	18.483	131.387	5983	41	-18	-69.646
43.45	5398	73	97.95	87.475	132.498	6735	54	-54.23	39.761
43.461	5085	35	-80.455	-66.636	132.732	4805	65	41.88	-22.618
43.546	5613	2	127.054	-37.749	132.932	5827	35	-17	-69.867
43.614	5148	37	-80.515	-66.621	133.213	4797	65	42.035	-22.494
44.188	5449	76	118.8	88.437	133.568	6318	59	21.895	-65.931
44.194	4354	1	172.565	-62.304	134.169	6037	43	-16.45	-69.989
44.276	5221	65	121.35	88.555	134.408	6091	46	-16.36	-70.009
44.438	6236	18	131.481	-37.923	135.975	6440	37	51.245	3.858
44.943	5680	37	97.236	-60.404	136.38	6279	64	45.175	-3.584
45.132	5832	45	126.017	-61.278	138.384	6270	64	21.43	-66.431
45.434	5883	1	133.075	17.802	138.478	4977	51	43.088	-24.254
45.722	4693	7	-29.14	-36.858	139.297	6202	61	21.345	-66.522
45.874	5181	18	156.475	-49.527	139.332	6793	86	23.095	-66.767
46.054	3989	19	3.62	69.198	139.758	5017	42	43.335	-24.649
46.145	5784	2	133.775	17.822	142.031	6754	57	-54.839	40.169
46.159	5702	48	112.264	-61.515	142.316	6396	86	29	-66.591
46.432	5216	27	107.19	-61.799	142.684	7759	274	-147.545	72.169
46.48	5216	64	100.5	87.592	142.915	5462	26	-1.445	-67.662
46.786	5252	81	24.35	82.999	143.001	6545	84	28	-66.61
47.09	5076	10	154.641	-49.806	144.221	5466	28	-1.635	-67.774
47.319	5210	9	-22.945	-57.173	145.384	6942	65	-56	39.879
47.666	4845	9	154.029	-49.939	147.788	7026	77	-55.245	40.736
47.724	4662	3	172	-62.151	148.664	5411	43	-15.995	30.791
47.767	5893	9	133.015	-37.758	149.321	5288	30	-14.575	33.223
47.932	6260	19	131.541	-37.673	149.567	6702	117	25.465	-67.508
48.723	4723	49	-87.43	-69.13	150.04	6684	119	25.555	-67.537
48.788	3675	10	3.46	68.8	150.138	7190	82	-56.725	40.356
48.801	5489	77	105	87.8	150.573	5524	35	-14.8	32.339

Continued overleaf...

Table B.2 – continued

Age (Ma)	w (m)	Error (m)	Lon.[a]	Lat.[a]	Age (Ma)	w (m)	Error (m)	Lon.	Lat.
49.261	4646	10	-30	-36.694	151.137	7164	94	-55.765	41.236
49.699	5626	83	115	88.262	152.413	5276	7	167	6.399
49.837	5271	12	156.195	-49.241	152.414	6811	61	-58.605	39.695
49.892	4074	3	170.973	-61.873	152.437	5225	7	167.5	6.445
49.968	5622	100	28.9	82.984	153.159	7216	86	-58.1	40.14
50.515	5002	8	-22	-57.13	153.173	5253	5	166	6.309
51.227	4450	3	169.58	-61.473	153.684	5151	51	-14.993	30.8
51.262	4212	2	170.144	-61.643	153.901	5340	8	165	6.218
51.304	5284	46	-84.486	-66.72	153.918	5797	49	-13.926	33.074
51.715	5216	16	153.31	-49.838	154.109	7286	97	-57.122	40.968
51.822	5337	70	110	88.031	154.385	7348	112	-56.327	41.593
51.992	5327	47	-84.517	-66.576	154.385	5170	6	164.32	6.156
51.996	4280	1	169	-61.299	156.163	6443	87	29.63	-66.579
52.746	4886	54	-88	-69.196	156.434	5573	42	-14.029	32.189
52.984	5768	46	97.266	-61	158.31	4917	59	-15.245	30.206
53.232	5647	105	26.75	82.306	159.284	7249	119	-56.96	41.54
53.281	4702	6	168.235	-61.069	160.492	5363	74	-15.665	29.704
53.584	4722	8	-30.815	-36.553	161.773	7217	95	-57.914	41.08
53.724	4596	1	-144.093	-13.132	162.882	4808	63	-14.132	30.901
54.01	5234	38	-84.612	-66.147	164.242	5497	75	-17.06	27.624
55.96	5378	106	29.404	82.067	166.632	4912	46	-18	26.251
56.228	5968	53	131.48	-62.02	166.683	5088	50	-17.66	26.747
57.236	4746	9	-31.21	-36.485	167.195	5781	94	-15.883	28.969
57.413	5072	13	-132.515	-67.339	168.126	5555	78	-16.992	27.123
57.933	4963	11	-132.375	-67.424	170.568	7113	134	-57.754	41.943
58.391	5859	9	127.215	-37	171.274	5736	95	-16.48	27.506
58.514	6037	62	126.073	-62.001	174.834	5906	4	157.11	17.298
59.761	4853	10	-131.87	-67.73	175.34	5963	113	-16.303	27.17
60.1	5769	11	-2.055	-60.026	176.723	5925	5	158.425	17.729
60.361	4802	4	154.744	-48.708	176.964	6125	4	155.17	12.923
61.24	5947	11	128.056	-36.931	177.371	5888	4	158.625	17.585
62.224	4651	8	-131.045	-68.23	178.268	6154	122	-15.29	28.589
63.742	4924	9	154.105	-48.735	178.636	7355	119	-59	41.853
64.077	4685	11	-130.55	-68.529	178.978	5867	5	159.12	17.229
64.087	4499	6	-130.08	-67.999	179.687	6249	6	156	13.163
64.298	5025	21	-43.155	5.257	180.586	5909	5	159.56	16.913
65.367	5085	21	-158.745	-72.388	180.817	6327	7	156.53	13.317
65.635	5076	15	154.535	-48.486	181.801	5948	4	155.165	11.253
65.792	4526	10	-129.785	-68.599	182.48	5860	3	155.53	11.158
66.117	5431	36	-155.445	-72.408	185.074	6277	75	-11.305	33.533
66.254	4515	12	-129.415	-68.807	185.646	5610	55	-73.015	13.806
66.415	6360	23	132.729	-37.111	186.062	5624	63	-77.03	13.02

Continued overleaf...

Table B.2 – continued

Age (Ma)	w (m)	Error (m)	Lon.[a]	Lat.[a]	Age (Ma)	w (m)	Error (m)	Lon.	Lat.
66.682	5037	21	-43.425	5.588	186.805	4843	26	-74	14.205
66.748	4721	8	-126.992	-67.25	187.231	5099	34	-76.65	13.784
67.26	4621	5	-126.246	-67.131	187.524	4653	15	-74.615	14.454
67.367	6292	43	-27.51	-65.2	187.811	7167	189	-57.02	43.325
68.029	5295	29	149.47	-45.328	187.843	4348	13	-76.46	14.166
68.118	5067	20	-43.63	5.839	188.014	5099	26	-74.5	14.754
68.147	5128	17	154.149	-48.495	188.061	4822	19	-74.991	14.662
68.282	5373	17	153.995	-43.91	188.529	7381	201	-58.223	42.971
68.519	6266	19	130.903	-36.877	191.015	7404	222	-58.555	43.008
68.773	5217	27	149.54	-45.261	193.722	7327	219	-57.165	43.595
69.225	4554	7	-126.797	-67.743	196.033	5489	36	-65.62	15.65
69.567	5315	14	-119.99	-66.149					

[a] In decimal degrees

Table B.3: 399 maximum water-loaded basement depth measurements averaged over $1°$ bins (downwards pointing triangles in Figure 2.2). Crustal corrections have not been applied, but crust is deemed to be thicker than average, based upon constraints from nearby lines, presence of seamounts and regional tectonic setting.

Age (Ma)	w (m)	Error (m)	Lon.[a]	Lat.[a]	Age (Ma)	w (m)	Error (m)	Lon.[a]	Lat.[a]
0.048	3061	71	-113.75	-20.3	59.622	4810	56	75.083	-5.35
0.051	2710	46	-103.8	11.633	59.759	4255	42	58.483	-5.333
0.19	1180	1	-29.002	60.252	60.041	5258	28	-142.517	35.083
0.429	2272	1	-176.35	-18.317	60.563	5383	32	-143.117	37.25
0.629	2249	1	-176.44	-18.573	60.664	5888	44	128.117	23.858
0.812	2611	65	-110.633	-9.667	60.877	4933	66	-19.658	2.45
0.867	2641	1	-175.94	-19.515	60.938	5323	12	93.217	-13.15
1.268	2311	43	78.517	-37.25	61.072	5511	176	150.622	-14.804
2.241	2930	41	-104.767	10.883	61.24	3793	38	-26.042	35.292
2.321	2928	111	-128.409	40.9	62.303	5143	64	-148.05	22.967
2.519	3314	26	-110.617	-44.583	62.459	3929	39	57.883	-10.083
3.336	3385	53	-108.5	-13.467	62.846	5424	111	177.442	53.392
3.361	996	35	44.308	11.767	63.725	4519	25	69.8	16.426
4.849	3024	66	-117.833	-23.267	64.281	4941	101	-175.95	52.642
5.058	1639	2	-30	60.315	64.387	5082	46	-145.883	10.717
5.285	1671	3	-28	60.2	64.54	5162	47	135.725	23.708
5.769	1201	73	-28.792	61.275	64.74	4640	86	51.483	-3.6
6.534	3119	58	-106.933	-27.933	65.168	5019	58	-160.65	40.983
6.667	3297	67	-23.858	-0.075	65.433	5485	22	130.967	23.383
7.872	4675	58	-128.183	40.067	65.78	4640	56	49.6	-3.467

Table B.3 – continued

Age (Ma)	w (m)	Error (m)	Lon.[a]	Lat.[a]	Age (Ma)	w (m)	Error (m)	Lon.[a]	Lat.[a]
8.175	2536	34	53.067	13.692	65.877	5484	114	-176.067	53.9
8.295	2404	66	52.017	14.017	67.03	5677	126	-176.5	54.667
8.84	2880	78	76.383	-36.85	67.363	4534	30	69.945	16.826
8.842	2484	146	9.858	73.175	67.766	5961	120	-172.29	55.647
8.943	3961	67	-114.217	-3.617	67.853	6154	139	-177.955	54.962
9.138	3838	67	-98.783	12.183	68.461	6032	130	-177.212	55.352
9.589	3428	54	-119.167	-14.267	68.516	5641	117	-178.692	55.175
10.427	2139	7	-26.999	60.14	68.535	4995	19	-147.633	-21.7
10.492	1957	2	-31	60.371	68.755	5711	22	-152.467	29.333
10.817	2285	75	46.3	12.908	68.914	5955	126	-176.715	55.622
10.956	1866	3	-29	61.874	68.965	5595	54	-151	23
11.533	3611	59	-104.433	-43.767	69.385	5620	95	-18.958	40.558
12.04	3527	90	-111.05	12.217	69.449	6082	134	-173.865	56.177
12.442	3641	25	-22.683	0.175	69.485	5923	53	-57.375	17.942
12.45	2721	89	51.542	14.583	69.551	5930	123	-176	55.987
14.294	4547	16	-45.135	-55.365	69.672	5716	22	-174.817	46.883
14.419	4158	66	-118.667	-7.333	70.239	5977	127	-175.26	56.375
15.033	3687	74	73.667	-35.767	70.492	6036	131	-175.005	56.509
15.201	2528	3	-32.001	60.42	71.567	5206	77	-153.517	28.75
15.52	3433	68	-117.583	29.133	72.634	4173	39	56.5	-9.833
15.527	2251	5	-30	61.938	73.089	5480	41	-169.8	47.933
15.692	3550	50	-117.408	28.775	73.766	6351	132	133.98	-36.894
15.737	2526	8	-26	60.045	73.814	4430	107	-15.35	46.142
15.832	3767	125	-135.633	54.533	74.874	5607	20	-163.783	44.3
16.018	3717	81	-135.1	54.642	75.446	4827	82	-39.083	0.983
16.243	4038	63	-115.683	4.067	77.842	3996	94	57.117	-9.967
16.752	3358	104	-135.992	54.2	79.025	4563	22	54.64	-6.647
16.87	2132	9	-23.597	61.491	79.751	4222	30	-155.217	22.217
17.265	3923	36	-116.05	21.967	79.781	5752	73	-58.25	23.492
17.311	4486	32	138.775	23.442	80.163	5681	27	97.2	-20.717
17.33	3747	31	-116.633	24.5	80.224	4034	17	54.595	-5.429
17.422	3788	78	-116.083	1.45	81.094	4490	27	54.836	-5.958
17.887	4349	54	-96.083	-42.733	81.194	4202	12	-155.9	22.8
17.918	3394	20	-96.317	-28.017	81.416	4025	24	-156.133	23.617
17.945	3980	46	-134.45	43	83.378	5457	26	-152.675	30.45
18.195	3873	34	-120.125	30.925	83.569	5444	107	-53.433	32.867
18.378	3579	33	-93.483	9.8	84.502	5084	25	102.75	-32.75
18.643	4173	11	-44.825	-56.006	86.12	5665	30	-154.65	32.3
18.698	4096	36	87.65	-37.933	86.34	5634	38	-157.033	37.15
19.7	3900	1	-48	22.795	87.383	4488	22	-160.317	24.667
19.805	2692	4	-32.969	60.474	87.878	4700	1	-160.483	23.958
19.895	2431	15	-23	61.432	89.218	5092	77	103.5	-33.017

Continued overleaf...

Table B.3 – continued

Age (Ma)	w (m)	Error (m)	Lon.[a]	Lat.[a]	Age (Ma)	w (m)	Error (m)	Lon.[a]	Lat.[a]
20.018	4050	31	-120.9	31.3	90.098	5681	57	-151.9	14.683
20.089	2476	5	-31	62.005	92.565	4872	8	-163.7	25.5
20.83	4367	21	-121.583	27.4	93.419	5264	36	174.933	-9.017
21.129	4382	81	168.39	56.393	94.745	4685	71	-157.7	18.867
21.142	2643	8	-25	59.954	94.915	5608	37	-172.983	39.7
21.181	4881	12	138.35	19.05	97.279	5174	2	111.49	-35.84
21.3	3733	24	-121.733	29.867	97.926	4775	51	-166.117	22.5
21.313	4393	67	-123.267	35.15	98.36	5251	99	-57.5	32.858
21.465	4090	96	-124.917	39.15	99.205	4547	5	-161.417	20.3
21.478	4191	17	-44.565	-56.544	100.288	5219	51	-173.05	34.333
21.54	2153	63	45.008	10.883	100.315	5780	43	105.917	-34.183
21.738	4143	80	-138.75	53.133	100.356	5343	6	111.59	-35.663
21.85	4645	25	-136.267	40.3	102.157	4899	4	11.855	-61.991
22.243	3787	93	69.975	-5.659	103.781	5410	36	-36.36	-26.228
22.621	2980	4	-33.47	60.502	104.084	5054	27	-158.667	-17.533
22.773	4103	47	-137.1	43.75	105.12	5350	32	-36.66	-26.223
22.86	4270	72	-123.983	5.783	106.115	5379	10	112.037	-35.372
23.654	4648	71	-125.019	38.144	106.206	7041	204	-57.087	9.948
23.96	4664	34	136.783	15.625	106.915	7094	207	-57.905	10.581
24.752	3961	44	-128.95	-11.767	107.463	4576	27	-169.083	26.7
25.005	4009	53	-141.167	52.6	108.721	5611	42	-172.067	32.133
25.101	3918	124	177.567	-18.983	109.126	6380	203	-57.022	8.914
25.39	4942	59	176.767	-29.917	110.087	7004	242	-57.917	9.899
25.613	3820	19	-88.817	-27.067	110.173	4959	4	11.485	-62.489
25.739	2953	5	-33.999	60.52	110.237	5874	76	-168.517	-16.267
25.749	4929	51	140.992	18.092	111.123	6345	210	-57.772	9.237
25.797	2595	21	-22.001	61.339	112.433	6062	90	-43.615	-29.4
25.894	4428	57	-123.433	0.183	112.733	4881	46	-160.983	-17.467
26.168	5274	79	171.8	-23.533	113.232	5282	131	-45.366	-27.478
26.344	2782	6	-31.998	62.058	113.279	5293	131	-45.405	-27.542
26.364	4247	1	-48.997	22.878	114.089	5476	74	-174.175	28.337
26.476	4634	100	176	-29.5	114.97	5263	108	28.482	-35.487
26.725	5233	98	178.55	-21.917	116.25	5612	54	10.282	-23.146
26.818	4542	49	-125.1	34.978	116.337	5708	57	10.325	-23.597
27.074	4521	12	-125.033	35.517	116.903	5417	92	29.089	-35.369
27.14	4274	53	-125.933	32.983	117.149	4276	97	8.045	-1.468
27.393	4301	15	-124.2	14.967	117.548	5225	3	11.105	-63.001
27.553	4699	64	-125.867	37.467	118.27	5662	45	171.992	37.7
28.031	2750	12	-24	59.889	118.75	5577	39	11.39	-26.869
28.564	4580	20	-140.633	43.967	118.842	5604	42	11.273	-26.255
29.107	4324	42	-127.067	32.833	119.032	5573	41	108.15	-14.95
29.178	4491	42	143.267	1.858	119.093	5436	85	-9.85	46.892

Continued overleaf...

Table B.3 – continued

Age (Ma)	w (m)	Error (m)	Lon.[a]	Lat.[a]	Age (Ma)	w (m)	Error (m)	Lon.[a]	Lat.[a]
29.211	4633	128	-139.967	57.316	119.313	5457	62	10.802	-22.999
29.229	4639	25	-127.417	28.083	119.342	4804	41	104.2	-25.05
29.237	4797	60	170.833	-23.9	120.089	5446	101	109.617	-11.667
29.271	4678	131	-140.05	58.333	120.388	6026	10	110.115	-27.083
29.313	4468	42	138.167	2.908	120.577	5306	43	11.961	-27.001
29.759	4576	39	-125.889	35.622	120.719	5188	37	-177.317	19.033
29.759	4762	43	-126.033	34.483	121.089	6107	12	107.72	-25.395
30.365	4300	38	140.333	2.408	121.104	5277	109	-63.033	34.467
31.487	3152	7	-35	60.534	121.237	5161	60	13.21	-31.788
31.788	2828	19	-20.999	61.258	121.679	5311	58	13.49	-32.556
32.073	3543	188	13.46	72.09	121.728	5352	19	14.45	-34.992
32.331	4613	30	-143.117	43.817	121.773	5453	56	11.931	-26.004
32.406	3483	93	-35.292	38.75	121.852	5400	6	10.62	-63.654
32.456	3049	7	-33	62.078	122.329	5358	105	31.263	-33.367
32.96	4071	70	-81.55	-18.983	122.528	4865	104	31.943	-33.027
33.282	4281	32	-145.183	51.383	122.642	5505	7	10.455	-63.876
33.283	3661	45	61.5	-31.54	122.711	5558	13	109.319	-32.758
33.457	4748	47	-128	38.583	123.123	4567	59	33.68	-30.383
33.76	4262	52	61.867	-31.483	123.274	5416	35	14.293	-33.811
34.126	4624	45	96.017	-33.8	123.342	5262	40	-178.017	25.442
34.392	3124	21	-23	59.829	123.554	5241	35	15.618	-34.089
34.44	4578	47	-143.183	45.567	123.64	4531	61	33.375	-30.271
35.352	4306	37	63.733	-5.55	123.689	5283	29	15.875	-34.585
35.458	3894	27	62.6	-31.35	124.002	5412	24	15.152	-34.925
35.665	4116	184	15.41	74.31	125.254	5377	34	15.128	-34.118
36.27	4596	53	-144.466	45.025	126.425	5669	63	37.146	-29.492
36.472	3306	27	-19.967	61.13	126.773	6027	82	-69.258	24.658
36.54	4706	45	-127.004	21.271	128.511	5083	7	113.158	-32.097
36.669	4788	41	-131.517	-1.383	133.527	5467	114	32.49	-31.808
36.868	4619	42	-136.1	-15.033	133.927	5637	81	47.033	-2.917
36.941	4087	67	-26.667	-1.267	134.55	5439	69	115.35	-12.85
37.425	6230	100	123.625	2.925	134.839	5928	72	148.855	37.614
37.72	3471	12	-36.016	60.576	136.428	6122	77	147.758	36.343
38.322	4563	27	-148.367	50.733	136.857	5886	49	150.457	36.767
38.669	3630	70	63.067	-5.517	137.469	5449	105	169.183	0.783
38.891	3531	16	-34.014	62.117	137.679	5982	31	151.405	36.627
39.329	4723	36	62.075	-33.092	137.885	6084	59	150.845	36.17
40.35	4181	30	-133.583	-10.75	138.298	6254	46	145.042	34.302
40.672	4316	72	-135.4	31.083	138.866	5751	17	-60	37.9
40.885	4733	35	-128.5	19.367	139.174	6209	35	-60.82	37.612
41.29	4770	16	-136.167	38.9	139.225	6202	40	146.083	23.575
41.498	5777	22	130.525	14.158	139.24	6258	54	144.603	33.095

Continued overleaf...

Table B.3 – continued

Age (Ma)	w (m)	Error (m)	Lon.[a]	Lat.[a]	Age (Ma)	w (m)	Error (m)	Lon.[a]	Lat.[a]
41.693	5998	101	122.833	4.083	139.966	6262	82	-70.15	26.133
42.061	3834	83	-42.908	54.775	140.81	5944	25	-61.31	37.44
42.078	4400	29	-79.067	-21.55	141.768	6077	29	-59.349	38.229
42.528	3726	21	-37.01	60.786	143.707	6354	43	-61.85	37.443
42.951	4891	15	-132.883	-40.6	145.352	6082	33	151.758	32.488
44.066	5188	37	-134.25	34.45	145.563	6034	43	152.508	32.521
44.396	3320	23	-19.018	60.749	146.632	6350	42	-62.29	37.554
46.043	5676	89	122.142	5.558	147.099	6232	57	115.55	-13.783
46.302	4669	61	-141.433	-18.467	148.811	6443	43	-58.98	38.999
46.542	4487	59	-134.567	24.767	149.591	5918	25	-63	37.733
46.638	4238	122	-37.125	39.125	149.971	6165	83	-72.45	25.733
47.036	4466	65	120.283	7.575	151.868	5811	23	-64.555	37.516
47.642	5130	18	90.8	-13.833	152.181	6638	52	-58.725	39.562
47.741	3228	18	-18.539	60.47	152.527	5822	25	-65.05	37.348
47.748	4635	55	63.967	-39.75	152.63	5774	21	-64	37.704
47.953	4096	95	70.667	7.367	153.549	5976	31	-66	37.025
48.642	3185	15	-18.215	60.22	155.635	6017	31	-67	36.685
49.156	4057	47	-32.708	31.883	156.778	5713	28	-68.025	36.337
49.302	3814	31	-38	61.125	157.23	5540	18	-67.52	36.508
49.818	3458	48	2.99	68.564	159.915	5857	40	-68.898	36.216
49.994	4580	50	57.45	-24.567	166.655	6053	70	-73.34	29.331
50.275	4737	66	-154.467	51.5	166.808	5898	48	-69.945	36.064
50.407	3975	145	15.91	70.38	166.911	5737	42	-74.148	26.79
51.143	2957	58	3.3	68.394	167.677	5777	23	-74.115	26.342
51.283	3570	31	-38.705	61.41	168.785	5448	124	-66.175	38.233
51.96	7322	43	-161.683	53.367	171.241	6105	53	-74	29.01
52.131	2531	60	3.515	68.276	171.481	5228	67	165.167	11.2
52.262	5354	45	58.167	-26.933	174.215	5099	60	168.367	12.45
52.538	3361	34	-39.205	61.629	174.229	5889	39	-74.721	27.013
52.54	5353	21	153.808	-14.861	175.198	6112	65	-74	30.132
53.124	5013	57	-157.1	53.233	177.474	4731	80	161.583	11.333
53.154	4695	6	70.19	9.46	180.148	6052	41	-74.775	28.633
53.266	5129	35	-137.5	23.067	181.257	6551	52	-73.955	31.602
53.562	3151	37	-39.5	61.757	182.896	5942	32	-75.254	28.026
53.863	5197	16	153.44	-15.046	183.185	6402	62	-74.33	31.41
53.879	4579	41	74.3	-5.367	184.419	5898	58	-75.233	30.238
53.924	4637	9	70.755	9.596	185.767	5961	52	-75.585	30.143
54.283	4752	7	70.142	9.907	186.298	5818	94	-75.012	30.994
54.872	4612	6	69.865	10.985	189.11	5924	106	-75.566	30.932
55.161	4497	39	60.033	-5.45	189.667	6095	37	-75.798	28.087
55.443	5442	114	155.867	-27.1	190.06	6224	173	-70.72	38.569
55.57	5844	104	149.917	-12.583	191.484	6069	170	-70.004	38.828

Table B.3 – continued

Age (Ma)	w (m)	Error (m)	Lon.[a]	Lat.[a]	Age (Ma)	w (m)	Error (m)	Lon.[a]	Lat.[a]
55.599	5727	41	131.883	20.1	191.958	6120	74	-65.27	40.238
55.696	3995	69	-26	35.95	193.569	6028	156	-68.945	39.158
56.135	5193	134	156.1	-27.783	193.639	6111	35	-76.013	29.058
56.208	5450	37	154.109	-14.351	193.94	6791	130	-74.968	32.885
56.727	5068	74	-39.042	38.75	194.874	6115	43	-75.995	27.344
58.005	4675	14	69.415	13.73	195.892	6047	154	-68.21	39.402
58.651	4461	8	69.58	13.786	196.152	6390	155	-73.995	35.01
58.692	4104	74	59.217	-5.417	197.638	6724	154	-74.778	33.69
59	5096	50	162.32	-20.01	197.891	6806	222	-67.14	39.811
59	5012	47	162.744	-19.897	240.425	7032	229	17.859	36.004
59	4723	98	164.95	-23	266.264	7954	393	28.103	33.138
59.423	4620	60	-31.142	31.85					

[a] In decimal degrees

Appendix C

Updated Heat Flow Database

23,428 global oceanic heat flow data points are filtered and spatially binned over $0.1°$ regions following the methodology detailed in Section 2.1.2. Heat flow values are corrected for sedimentation using Equation 2.1 and a thermal diffusivity of 2.5 mm a^{-1}. At ages > 65 Ma data are not filtered as hydrothermal circulation is negligible. At ages < 25 Ma, site-specific values are taken from Hasterok (2013), as it is suggested the corrected database may systematically underpredict heatflow at these young ages, where hydrothermal circulation is at its most vigorous. All data are binned into 2.5 Ma age increments.

Table C.1: Updated heat flow database, filtered to remove effects of hydrothermal circulation, spatially binned over $0.1°$ regions, corrected for sedimentation and temporally binned into 2.5 Ma age increments. Ages are derived from updated version of Müller *et al.* (2016)

Age (Ma)	Number	Mean (W m^{-2})	Median (W m^{-2})	Q1 (W m^{-2})	Q3 (W m^{-2})
1.25	60	0.22750	0.20207	0.14208	0.26129
3.75	47	0.17126	0.15176	0.09852	0.21121
6.25	41	0.13902	0.13697	0.11094	0.16002
8.75	35	0.16051	0.15099	0.13176	0.18296
11.25	33	0.12612	0.13224	0.10852	0.15496
13.75	29	0.10740	0.11087	0.08234	0.11996
16.25	52	0.11535	0.10959	0.09027	0.13213
18.75	69	0.09667	0.10270	0.07557	0.11931
21.25	84	0.08774	0.09047	0.06698	0.11508
23.75	62	0.09922	0.10364	0.08490	0.11860
26.25	59	0.09979	0.09531	0.07780	0.12121
28.75	45	0.08573	0.08574	0.07163	0.10444
31.25	26	0.09585	0.09642	0.06797	0.10579

Continued overleaf...

Table C.1 – continued

Age (Ma)	Number	Mean (W m^{-2})	Median (W m^{-2})	Q1 (W m^{-2})	Q3 (W m^{-2})
33.75	51	0.09329	0.08633	0.06567	0.11393
36.25	33	0.07769	0.06997	0.03515	0.09805
38.75	26	0.07111	0.07428	0.06338	0.08450
41.25	27	0.07272	0.06929	0.06321	0.08676
43.75	25	0.08475	0.06936	0.06284	0.08341
46.25	30	0.06743	0.06897	0.05515	0.07840
48.75	33	0.07137	0.07028	0.05263	0.08513
51.25	28	0.06992	0.06770	0.04409	0.07622
53.75	31	0.06374	0.06633	0.05122	0.07364
56.25	18	0.06999	0.06614	0.05861	0.07845
58.75	21	0.06411	0.05940	0.04927	0.07240
61.25	17	0.05805	0.06493	0.04121	0.07288
63.75	23	0.09801	0.06461	0.05041	0.08736
66.25	62	0.06140	0.05950	0.04237	0.06902
68.75	70	0.06593	0.06443	0.05267	0.07526
71.25	68	0.06547	0.06544	0.04820	0.07399
73.75	66	0.06325	0.06004	0.04751	0.07628
76.25	63	0.08294	0.06248	0.05247	0.07520
78.75	54	0.06710	0.06446	0.05373	0.08021
81.25	71	0.06371	0.05896	0.04904	0.06888
83.75	68	0.06419	0.05923	0.05102	0.06841
86.25	64	0.06012	0.05783	0.04733	0.06903
88.75	76	0.06448	0.05484	0.04736	0.06781
91.25	104	0.05556	0.05547	0.04264	0.06727
93.75	47	0.05553	0.05771	0.05013	0.06371
96.25	61	0.06275	0.05739	0.04873	0.06654
98.75	54	0.06011	0.05684	0.04919	0.06431
101.25	53	0.06045	0.05494	0.04598	0.06749
103.75	54	0.06093	0.05671	0.04895	0.06600
106.25	66	0.05523	0.05420	0.04689	0.05994

Table C.1 – continued

Age (Ma)	Number	Mean (W m^{-2})	Median (W m^{-2})	Q1 (W m^{-2})	Q3 (W m^{-2})
108.75	56	0.06156	0.05621	0.04859	0.06362
111.25	40	0.05945	0.05641	0.04883	0.06755
113.75	43	0.06005	0.05933	0.04473	0.06786
116.25	46	0.05301	0.05203	0.04093	0.06467
118.75	59	0.05522	0.05307	0.04608	0.06348
121.25	52	0.06034	0.05449	0.04718	0.06336
123.75	57	0.05632	0.05460	0.04853	0.06033
126.25	46	0.05476	0.05210	0.04633	0.05812
128.75	56	0.05208	0.04806	0.03683	0.05889
131.25	37	0.05361	0.05325	0.04224	0.06395
133.75	47	0.05662	0.05127	0.04486	0.05733
136.25	31	0.05873	0.05408	0.04450	0.05827
138.75	36	0.05599	0.05486	0.04642	0.06672
141.25	37	0.04911	0.04931	0.04212	0.05251
143.75	30	0.06044	0.05405	0.04268	0.06257
146.25	38	0.05451	0.05279	0.04747	0.06009
148.75	33	0.05480	0.05030	0.04363	0.05241
151.25	52	0.06613	0.05830	0.04827	0.07780
153.75	18	0.05773	0.05233	0.04529	0.05900
156.25	22	0.06070	0.05837	0.04718	0.08042
158.75	20	0.05898	0.05442	0.04604	0.06496
161.25	10	0.05041	0.04986	0.04098	0.05881
163.75	19	0.05557	0.05026	0.04508	0.06508
166.25	10	0.05125	0.04916	0.03973	0.05398
168.75	7	0.04947	0.05436	0.04484	0.05520
171.25	11	0.05238	0.05187	0.04336	0.05732
173.75	13	0.06112	0.05941	0.04964	0.06740
176.25	6	0.05007	0.05073	0.04400	0.05454
178.75	6	0.04757	0.04770	0.04501	0.05076
181.25	11	0.05621	0.05048	0.04894	0.06672

Table C.1 – continued

Age (Ma)	Number	Mean (W m^{-2})	Median (W m^{-2})	Q1 (W m^{-2})	Q3 (W m^{-2})
183.75	23	0.05828	0.05436	0.04676	0.05993
186.25	23	0.05599	0.05494	0.04660	0.06028
188.75	15	0.05169	0.05134	0.04738	0.05492
191.25	13	0.07730	0.06453	0.04942	0.08392
193.75	11	0.05538	0.05264	0.04966	0.06101
196.25	13	0.07406	0.06255	0.05671	0.09502
198.75	9	0.05836	0.05626	0.05321	0.06270
243.75	8	0.06814	0.03551	0.01748	0.05264